



HAL
open science

Metal oxide heterostructures for efficient photocatalysts

Md. Tamez Uddin

► **To cite this version:**

Md. Tamez Uddin. Metal oxide heterostructures for efficient photocatalysts. Other. Université Sciences et Technologies - Bordeaux I; Technische Universität (Darmstadt, Allemagne), 2013. English. NNT : 2013BOR14859 . tel-00879226

HAL Id: tel-00879226

<https://theses.hal.science/tel-00879226>

Submitted on 2 Nov 2013

HAL is a multi-disciplinary open access archive for the deposit and dissemination of scientific research documents, whether they are published or not. The documents may come from teaching and research institutions in France or abroad, or from public or private research centers.

L'archive ouverte pluridisciplinaire **HAL**, est destinée au dépôt et à la diffusion de documents scientifiques de niveau recherche, publiés ou non, émanant des établissements d'enseignement et de recherche français ou étrangers, des laboratoires publics ou privés.

Order N°: 4859

THESIS

Presented at

UNIVERSITY OF BORDEAUX I AND TECHNICAL UNIVERSITY OF DARMSTADT

DOCTORAL SCHOOL OF CHEMICAL SCIENCES

By

Md. Tamez UDDIN

TO OBTAIN THE DEGREE OF

DOCTOR

SPECIALITY: PHYSICAL CHEMISTRY OF CONDENSED MATTER

METAL OXIDE HETEROSTRUCTURES FOR EFFICIENT PHOTOCATALYSTS

Defended on: **16th September 2013**

After approval of:

Mme C. LOUIS , Director of research CNRS, LRS, University Paris VI	Reviewer
Mme S. CASSAIGNON , Assistant Professor, LCMCP, University Paris VI	Reviewer

In front of a jury composed of:

Mme C. LOUIS , Director of research CNRS, LRS, University Paris VI	Reviewer
Mme S. CASSAIGNON , Assistant Professor, LCMCP, University Paris VI	Reviewer
M. R. RIEDEL , Professor, Technical University of Darmstadt	Examiner
M. H.-J. KLEEBE , Professor, Technical University of Darmstadt	Examiner
M. L. SERVANT , Professor, University Bordeaux 1	Examiner
M. J. ETOURNEAU , Professor, University Bordeaux 1	Examiner
M. T. TOUPANCE , Professor, University Bordeaux 1	Supervisor
M. W. JAEGERMANN , Professor, Technical University of Darmstadt	Supervisor

Acknowledgements

This work has been performed in the Material group, Institute of Molecular Sciences, University of Bordeaux I and in the Surface Science group, Technical University of Darmstadt. I express my deepest gratitude to a number of people, without whom it would have not been possible for me to undertake this rigorous academic programme during my 3 years at Bordeaux and Darmstadt.

First of all I would like to thank “International Doctoral School in Functional Materials (IDS FunMat)” under the umbrella of Erasmus Mundus PhD Programme of European Union for providing me financial support. This work was made in cooperation with Merck KGaA, Darmstadt (Germany). I would like to thank Dr. Bernd Oster for giving me an opportunity to do internship in Merck for one month.

I sincerely thank my thesis supervisors Prof. Dr. Thierry Toupance and Prof. Dr. Wolfram Jaegermann for their continuous support, encouragement, and insightful guidance during the course of my doctoral studies. I consider myself immensely fortunate and privileged to be able to work with them. I thank Dr. Toupance and Dr. Jaegermann for their reasoning and constructive criticisms that motivated me to delve deeper into my research. Their contribution has made me an independent thinker and researcher. I cannot forget their unconditional support in and out of the lab to facilitate my stay in Bordeaux and Darmstadt.

I would like to thank Prof. Jean Etourneau, EMMI Executive Director, University of Bordeaux I for presiding over my thesis jury. I am also grateful to Prof. Laurent Servant, Coordinator of IDS-FunMat for his help in the course of my work. I wish to express my gratitude and my appreciation to Dr. Catherine Louis (Director of research CNRS, LRS, University Paris VI) and Dr. Sophie Cassaignon, (Assistant Professor, LCMCP, University Paris IV) who generously provided time, energy and valuable suggestions in evaluating my thesis as reviewers. Special thanks to Prof. Ralf Riedel, Technical University of Darmstadt and Prof. Hans-Joachim Kleebe, Technical University of Darmstadt for their time, encouraging remarks about my work.

This work is the result of a teamwork and collaboration of many people without whom this work could not be completed. I would like to thank those who helped me to characterize my samples: Madam Odile Babot (ISM) for doing nitrogen adsorption-desorption measurement and thermogravimetric analysis; Dr. Jörg Zimmermann (TUD) for the UV-Vis diffuse reflectance spectrometry measurement; Jürgen Ziegler for interface

analysis by XPS and UPS. I also give my appreciation to Dr. Henrik Junge, LIKAT, Rostock for letting me use his lab for the photocatalytic hydrogen production experiment. I am also grateful to Dr. Céline Olivier and Dr. Yohann Nicolas for their continuous support in many ways in the laboratory.

Although I had many acquaintances during my PhD, I formed some true friendships with Svitlana Poix Shinkaruk, Christophe Pejoux, Samuel de Sousa, Anaëlle Girard, Guillaume Gruntz, Mathieu Meillan, Amandine Foulet, Liubovi Mitcova and Ludmila Cojocar. I would specially like to thank Svitlana for her help throughout my stay in Bordeaux in many ways, specially when I faced problem with accomodation.

In a general manner I would like to thank all members of the Material group for their generosity and cooperation and for maintaining a very competitive yet friendly environment in the group.

I consider myself fortunate to have M. A. Hannan Khan and Abdus Sobhan as my best friends forever. I thank you for being beside me in every critical phase of my personal life.

I deeply thank my parents for their unconditional love and support, without which I would not have been able to succeed in this endeavor. Last but not least I thank my wife Nadira Aktary and my daughter Tahira Tasnim Shaila for their incredible understanding, support and patient during the most difficult phase of my PhD.

SYNTHÈSE EN FRANÇAIS

Il est désormais bien établi que les sources d'énergie propres et les questions environnementales constituent des enjeux majeurs pour le 21^{ème} siècle. Ainsi, les ressources limitées en énergies fossiles et les règles environnementales de plus en plus strictes suscitent un effort de recherche considérable pour découvrir des sources d'énergie durables, efficaces et respectueuses de l'environnement. Tout d'abord, l'hydrogène (H₂) produit à partir de ressources renouvelables possède un très grand potentiel comme source d'énergie du futur. D'autre part, les problèmes environnementaux aigus liés à l'utilisation industrielle de composés organiques toxiques nécessitent des solutions urgentes. Dans ce contexte, les processus photocatalytiques à la surface d'oxydes métalliques semi-conducteurs ont fait l'objet ces deux dernières décennies d'intenses recherches au niveau mondial car ils constituent des alternatives efficaces, respectueuses de l'environnement et peu coûteuses aux méthodes conventionnelles dans les domaines de la purification de l'eau et de l'air, et de la production « verte » d'hydrogène. Cependant, les recombinaisons rapides des paires électron-trou générées par illumination conduisent à une diminution drastique des performances photocatalytiques ce qui a empêché l'industrialisation de cette technologie. Pour tracer de nouvelles perspectives dans ce domaine, ce travail a pour but d'améliorer les processus photocatalytiques en diminuant les phénomènes de recombinaison via un transfert de charge vectoriel. Dans ce but, de nouveaux photocatalyseurs à base d'hétérostructures ont été développés en déposant des oxydes aux propriétés conductrices métalliques sur des matériaux semiconducteurs ou en associant deux semiconducteurs dont les niveaux des bandes sont correctement positionnés.

Dans ce contexte, trois types d'hétérostructures telles que des nanomatériaux à base d'hétérojonction semiconducteur n/semiconducteur n (SnO₂/ZnO), metal/semiconducteur n (RuO₂/TiO₂ and RuO₂/ZnO) et semiconducteur p/semiconducteur n (NiO/TiO₂) ont été synthétisées, caractérisées et leurs propriétés photocatalytiques étudiées lors de la dégradation de colorants organiques et la production d'hydrogène (H₂). Dans ce qui suit, chaque type de catalyseur est décrit et discuté, une attention particulière étant portée sur les mécanismes de séparation des charges à l'interface des hétérostructures conduisant à des performances photocatalytiques améliorées dans la décomposition du bleu de méthylène (MB) et de l'orangé de méthyle (MO), d'une part, et, de la production de H₂, d'autre part. Pour chaque système, nous décrivons un nouvel outil efficace, mettant en jeu une combinaison des données de spectroscopie de photoélectron X (XPS) et UV (UPS) et de spectroscopie UV-

visible en réflexion diffuse, pour déterminer précisément l'alignement des bandes ce qui a ensuite permis de comprendre les propriétés photocatalytiques des matériaux synthétisés..

Dans un premier temps, le système SnO₂/ZnO a été étudié comme un modèle de photocatalyseur constitué d'une hétérojonction semiconducteur n/semiconducteur n de manière à établir la méthodologie scientifique générale développée dans ce travail. Des nanomatériaux mésoporeux SnO₂/ZnO (rapport molaire 1:1) ont tout d'abord été préparés avec succès via une procédure par voie liquide en deux étapes mettant en jeu la synthèse de nanoparticules de SnO₂ par précipitation en milieu homogène associée à un traitement hydrothermal, puis la réaction de ces particules avec de l'acétate de zinc suivie d'une calcination. Les études réalisées par spectroscopie UV-visible en réflexion diffuse ont montré que l'énergie de la bande interdite des hétérostructures SnO₂/ZnO était déplacée dans le rouge par rapport au SnO₂ pur. Une attention particulière a été apportée à la détermination de l'alignement des bandes à l'interface de l'hétérojonction SnO₂/ZnO. La spectroscopie XPS été utilisée comme une méthode de détermination directe du décalage des bandes de valence (VBO) dans les hétérostructures SnO₂/ZnO. Le décalage des bandes de valence (VBO) ΔE_V dans l'hétérostructure SnO₂/ZnO a été calculé à partir de l'équation (1)

$$\Delta E_V = (E_{Zn\ 2p} - E_{V.ZnO})_{bulk}^{ZnO} - (E_{Sn\ 3d} - E_{V.SnO_2})_{bulk}^{SnO_2} - \Delta E_{CL} \quad (1)$$

où $\Delta E_{CL} = (E_{Zn\ 2p} - E_{Sn\ 3d})_{heterostructure}$ est la différence d'énergie entre les niveaux de coeur (CLs) Zn 2p et Sn 3d, qui ont été mesurés dans l'échantillon SnO₂/ZnO. $E_{Zn\ 2p}$ et $E_{Sn\ 3d}$ sont les énergies de liaison dans les nanomatériaux purs ZnO et SnO₂, respectivement; $E_{V.ZnO}$ et $E_{V.SnO_2}$ sont les énergies du haut de la bande de valence des matériaux massiques ZnO et SnO₂, respectivement. Enfin, le décalage de la bande de conduction (CBO) a été estimée à partir de la formule $\Delta E_C = \Delta E_V + E_g^{ZnO} - E_g^{SnO_2}$, où E_g^{ZnO} et $E_g^{SnO_2}$ sont les « gap » optiques des nanomatériaux ZnO et SnO₂ purs, respectivement. Les valeurs correspondantes sont indiquées dans la **Figure 1**.

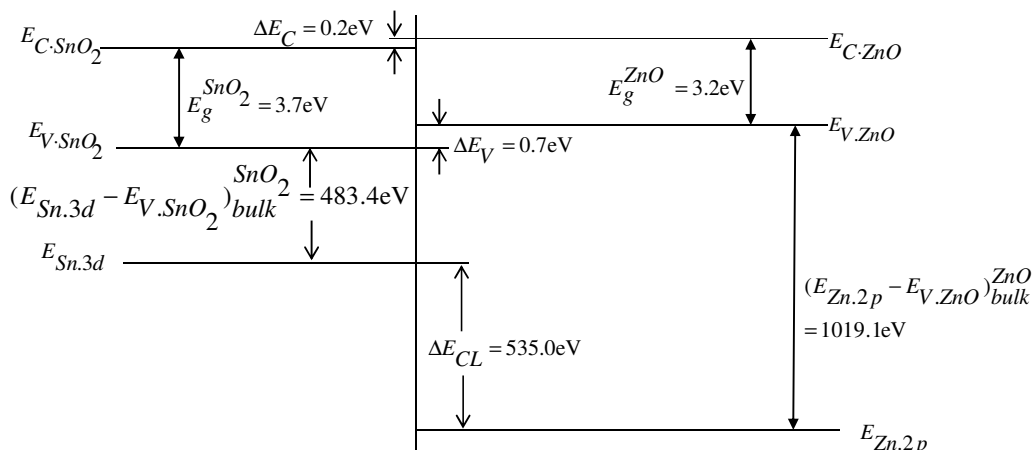


Figure 1: Diagramme d'alignement des bandes dans le nanocomposite SnO₂-ZnO.

Un alignement des bandes de type II (**Figure 1**) avec un décalage des bandes de valence (VBO) de $\Delta E_V = 0.7 \pm 0.05$ eV et des bandes de conduction (CBO) de $\Delta E_C = 0.2 \pm 0.05$ eV a aussi été déterminé. Les photocatalyseurs SnO₂/ZnO présentent une activité plus élevée pour la dégradation du MB sous irradiation UV que les nanomatériaux purs SnO₂ et ZnO (**Figure 2A**). La constante de vitesse de dégradation normalisée par l'aire spécifique BET du nanocomposite SnO₂/ZnO a été estimée à 12.1×10^{-4} g m⁻² min⁻¹ ce qui est 1,7 fois supérieur à celle de SnO₂ pur ($7,1 \times 10^{-4}$ g m⁻² min⁻¹) et environ 1,4 fois supérieur à celle de ZnO pur ($8,9 \times 10^{-4}$ g m⁻² min⁻¹). Cette vitesse de dégradation supérieure observée dans le cas de SnO₂/ZnO a été attribuée à un transfert vectoriel des électrons et des trous photogénérés provenant de la discontinuité des bandes de conduction et de valence à l'interface SnO₂/ZnO ce qui a été confirmé par l'alignement des bandes déduit des mesures XPS. Le transfert vectoriel des électrons et des trous photogénérés est expliqué dans la **Figure 2B**.

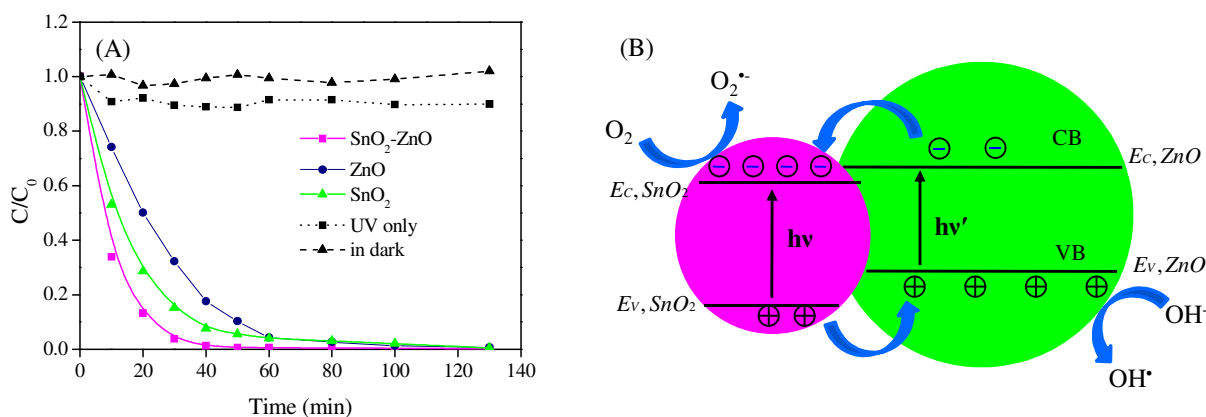


Figure 2: (A) Cinétique de dégradation du MB sur les différents photocatalyseurs (B) Représentation des phénomènes de transfert de charge dans l'hétérostructure SnO₂-ZnO.

Par ailleurs, ces photocatalyseurs à base d'hétérojonctions ont pu être recyclés plusieurs fois sans perte notable d'activité catalytique ce qui prouve leur stabilité et leur reproductibilité. En outre, les valeurs de pH élevées favorisant l'adsorption du colorant cationique MB à la surface de ces catalyseurs, une augmentation significative de l'efficacité de dégradation de ce colorant a été observée en milieu basique.

Dans une seconde étape, nous nous sommes intéressés au développement d'hétérostructures metal/semiconducteur n de type $\text{RuO}_2/\text{TiO}_2$ et RuO_2/ZnO , l'oxyde de ruthénium étant attendu présenter une conductivité de type métallique. L'hétérostructure cible $\text{RuO}_2/\text{TiO}_2$ a été préparée par imprégnation de nanoparticules de TiO_2 , synthétisées par voie sol-gel, avec une solution de pentan-2,4-dionate ruthenium (III) suivi d'un recuit sous air à $400\text{ }^\circ\text{C}$. Quelle que soit la teneur en RuO_2 , les nanocatalyseurs obtenus sont constitués d'un réseau mésoporeux de nanoparticules de TiO_2 anatase agrégées modifiées par RuO_2 d'après les études réalisées par porosimétrie de sorption d'azote et microscopie électronique en transmission (MET). La spectroscopie UV-visible en réflexion diffuse a montré que les nanocomposites $\text{RuO}_2/\text{TiO}_2$ absorbaient la lumière sur toute la gamme du visible ce qui a été attribué à des effets de résonance plasmonique de surface suggérant que ces matériaux pouvaient être actifs sous illumination solaire. De manière à clarifier les processus de séparation de charge à l'interface de l'hétérojonction $\text{RuO}_2/\text{TiO}_2$, le diagramme d'énergie d'alignement des bandes a été déterminé par XPS et UPS. Tout d'abord, une expérience aux interfaces a été réalisée par un dépôt progressif de RuO_2 sur un film de TiO_2 et des mesures XPS *in-situ* révélèrent un déplacement du niveau de coeur Ti $2p_{3/2}$ vers les basses énergies de 1.22 eV ce qui a été attribué à une courbure de bande à l'interface de l'hétérojonction $\text{RuO}_2/\text{TiO}_2$. Les travaux de sortie de TiO_2 (Φ_{TiO_2}) et de RuO_2 (Φ_{RuO_2}), mesurés par UPS, ont été estimés à $3,8$ and $6,2\text{ eV}$, respectivement. L'alignement des bandes d'énergie à l'interface entre RuO_2 et TiO_2 est représenté schématiquement **Figure 3**. La courbure de bande pour le nanocomposite $\text{RuO}_2/\text{TiO}_2$ a été évaluée à $0.2 \pm 0.05\text{ eV}$.

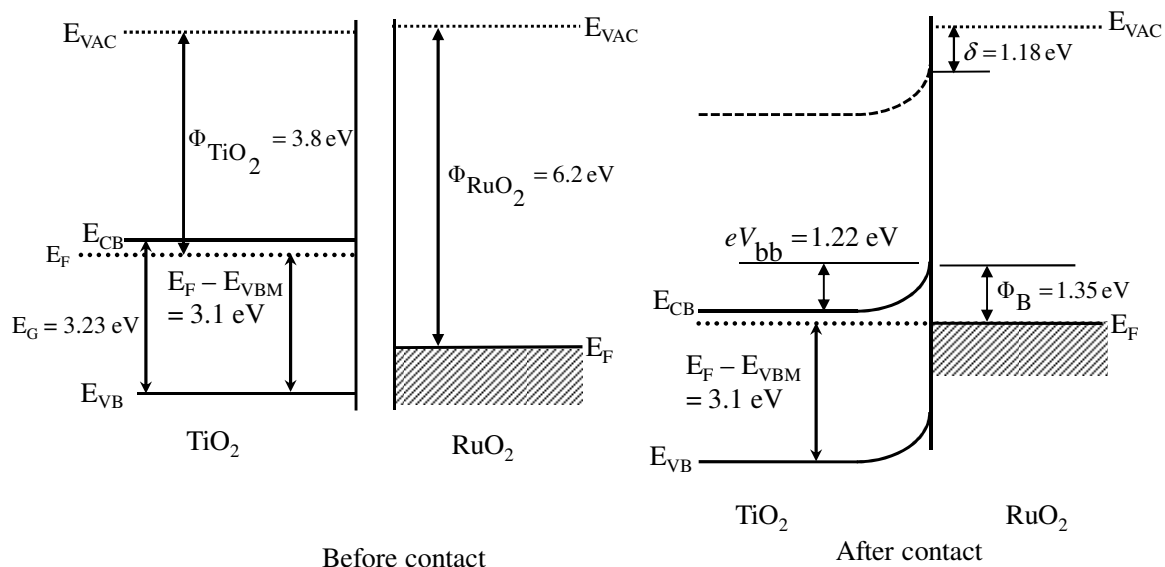


Figure 3: Représentation schématique de l'alignement des bandes d'énergie à l'interface entre RuO_2 et TiO_2 . E_{CB} , E_{VB} , E_F , E_g sont les énergies du bas de la bande de conduction, du haut de la bande de valence, du niveau de Fermi et de la bande interdite, respectivement. eV_{bb} correspond à la courbure de bande à l'interface entre RuO_2 et TiO_2 .

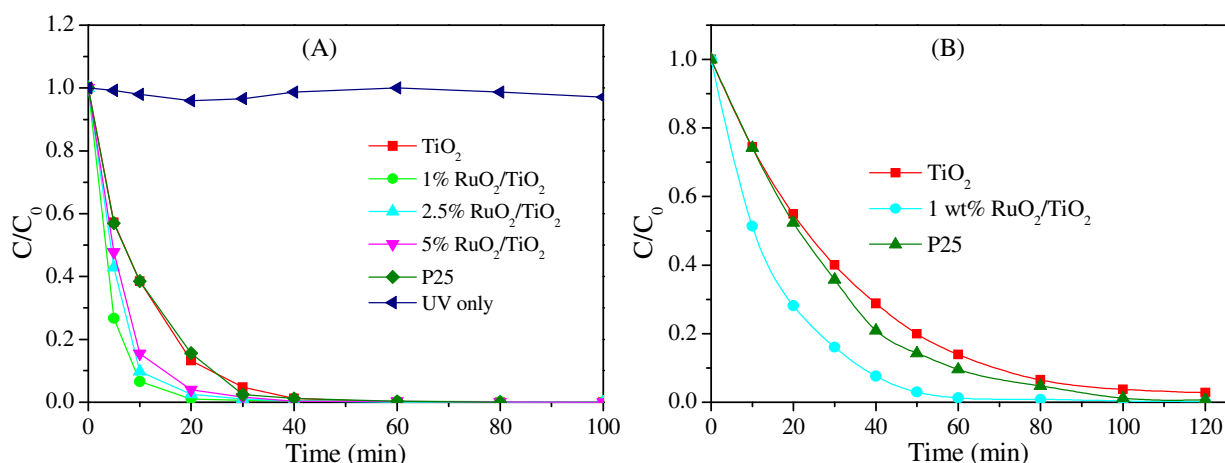


Figure 4: Cinétique de dégradation du MB (A) and du MO (B) en présence des différentes nanoparticules $\text{RuO}_2/\text{TiO}_2$ préparées.

La Figure 4 présente la décomposition photocatalytique du MB et du MO en solution sous irradiation UV en présence des photocatalyseurs $\text{RuO}_2/\text{TiO}_2$. L'hétérostructure 1 wt% $\text{RuO}_2/\text{TiO}_2$ a conduit aux meilleures performances photocatalytiques pour la dégradation du MB et du MO comparé au TiO_2 hydrothermal pur et au TiO_2 commercial (Degussa P25). Les constantes de vitesse de dégradation normalisées par l'aire spécifique BET des nanocomposites ont été estimées à $3.56 \times 10^{-3} \text{ g min}^{-2} \text{ min}^{-1}$ et $0.92 \times 10^{-3} \text{ g min}^{-2} \text{ min}^{-1}$ pour la dégradation du MB et du MO, respectivement, ce qui est 1,7 et 1,3 fois plus rapide que ce qui a été mesuré dans les mêmes conditions avec TiO_2 hydrothermal pur et TiO_2 P25,

respectivement. En outre, le recyclage des nanocomposites a été réalisé avec succès, aucune diminution de l'activité photocatalytique n'ayant été détectée après recyclage, ce qui confirme la stabilité des photocatalyseurs. D'autre part, la production de H_2 sous irradiation UV en présence de méthanol comme piège à trous a également été réalisée avec ce système. Quelle que soit la teneur en RuO_2 , la vitesse de production de H_2 sur les photocatalyseurs RuO_2/TiO_2 est plus élevée que celle observée dans les mêmes conditions sur TiO_2 hydrothermal pur et TiO_2 P25 (**Figure 5A**). Par ailleurs, le photocatalyseur 5 wt% RuO_2/TiO_2 a conduit à l'activité photocatalytique la plus élevée avec une vitesse moyenne de production de H_2 de $618 \mu\text{mol h}^{-1}$ (**Figure 5B**)

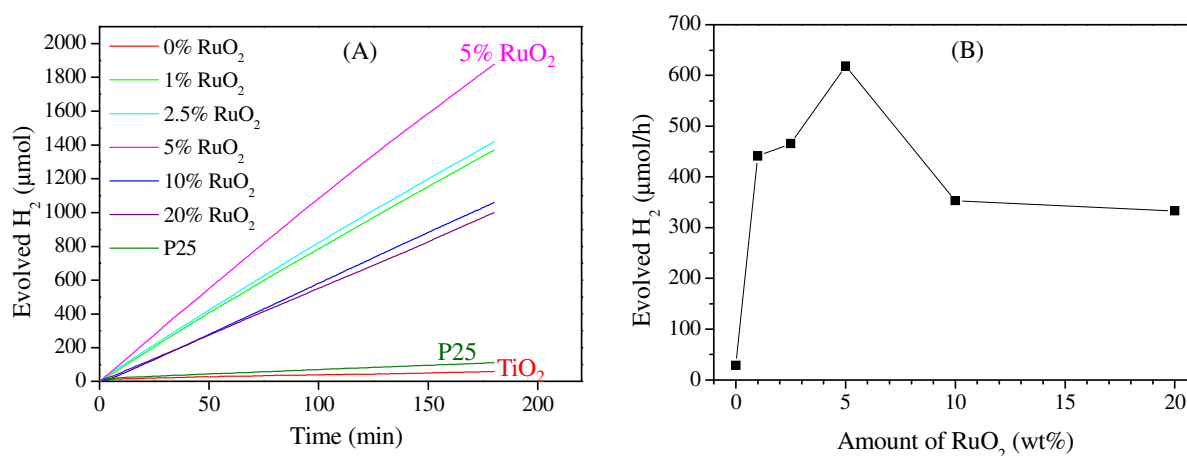


Figure 5: (A) Production photocatalytique de H_2 sur les photocatalyseurs TiO_2 et RuO_2/TiO_2 contenant différentes teneurs massiques de RuO_2 et (B) effet du taux de RuO_2 sur la production de H_2 . Toutes les expériences ont été effectuées pendant 3 h dans des conditions identiques. Volume de solvant 10 mL (H_2O : méthanol = 1:1), quantité en photocatalyseur : 0.05 g.

Comme l'énergie de la bande interdite de ZnO et les processus photocatalytiques à la surface de ZnO sont similaires à ceux de TiO_2 , nous avons également développé une hétérostructure originale contenant à la fois ZnO et RuO_2 en utilisant une méthode de préparation en deux étapes similaire à celle employée pour synthétiser les hétérostructures RuO_2/TiO_2 : préparation de nanoparticules de ZnO par précipitation en milieu homogène, puis imprégnation ultérieure avec le trichlorure de ruthénium (III) en solution, les matériaux résultants étant calcinés à $350 \text{ }^\circ\text{C}$ pendant 2 h. Comme les systèmes RuO_2/TiO_2 , les nanocomposites RuO_2/ZnO absorbent également dans le visible. De même, un diagramme d'énergie des bandes dans les nanocomposites RuO_2/ZnO a été déterminé par XPS et UPS à partir des déplacements des niveaux de coeur. Le déplacement des niveaux de coeur $Zn 2p_{3/2}$ ont été estimés à $0,42 \pm 0,05 \text{ eV}$ ce qui a été attribué à la courbure de bande à l'interface de

l'hétérojonction RuO_2/ZnO . Par ailleurs, le travail de sortie de ZnO dans ces systèmes a été évalué à 4.2 eV par UPS.

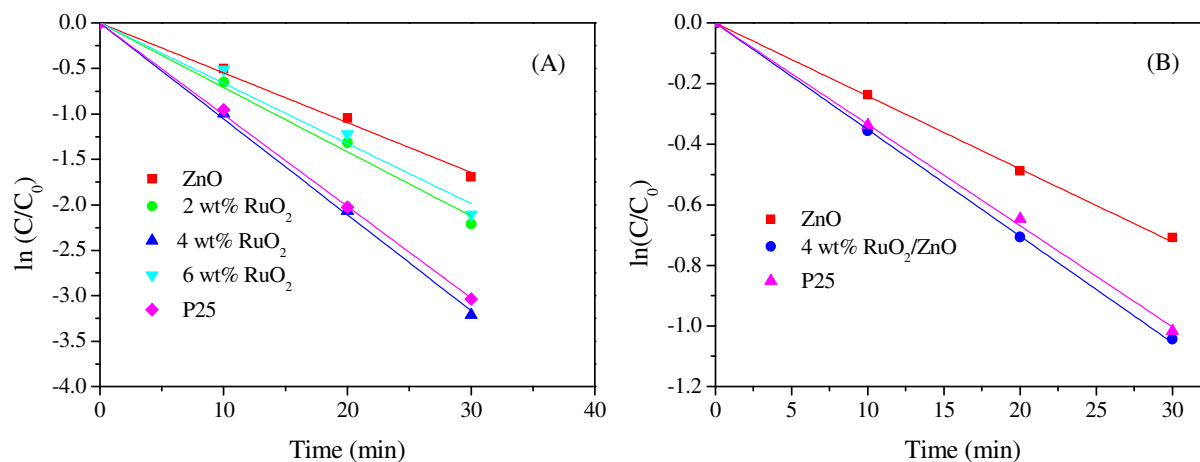


Figure 6: Loi cinétique du premier ordre $\ln C/C_0$ en fonction de t pour la dégradation photocatalytique de (A) MB et MO (B) en présence des systèmes RuO_2/ZnO étudiés.

Comme précédemment, les performances photocatalytiques des systèmes RuO_2/ZnO étudiés ont été étudiées via la dégradation de colorants organiques tels que le MB et le MO. D'après la **Figure 6**, le processus de dégradation suit une loi cinétique du 1^{er} ordre, le nanomatériau 4 wt% RuO_2/ZnO présentant une activité photocatalytique supérieure sous illumination UV pour la décomposition du MB (**Figure 6A**) et du MO (**Figure 6B**) comparé à celles du ZnO pur et du TiO_2 P25. Les constantes de vitesse de dégradation normalisées par l'aire spécifique BET des nanomatériaux ZnO , 2 wt% RuO_2/ZnO , 4 wt% RuO_2/ZnO , 6 wt% RuO_2/ZnO et P25 pour la dégradation de MB ont été estimées à $1,74 \times 10^{-3}$, $2,44 \times 10^{-3}$, $4,24 \times 10^{-3}$, $3,03 \times 10^{-3}$, $2,14 \times 10^{-3} \text{ g min}^{-2} \text{ min}^{-1}$, respectivement, suggérant que les meilleures performances photocatalytiques des nanocomposites RuO_2/ZnO n'étaient pas dues à des variations de surface spécifique, mais à la synergie entre les propriétés électroniques de RuO_2 et de ZnO . Par ailleurs, une tendance similaire a été mise en évidence pour la dégradation de MO. En outre, les nanocomposites RuO_2/ZnO ont pu être recyclés plusieurs fois sans diminution notable de l'activité photocatalytique ce qui démontre la stabilité chimique et photochimique des nanocomposites RuO_2/ZnO synthétisés. A notre connaissance, ce travail constitue le premier exemple de mise en évidence des potentialités des nanocomposites RuO_2/ZnO en photocatalyse.

Cette activité photocatalytique améliorée dans le cas des nanocomposites pour la décomposition de colorants organiques et la production de H_2 a été reliée à une meilleure séparation des charges résultant du champ électrique interne existant à l'interface des

hétérojonctions $\text{RuO}_2/\text{TiO}_2$ et RuO_2/ZnO . Le mécanisme de séparation de charge à l'interface est expliqué **Figure 7**. Lorsque l'oxyde de ruthénium aux propriétés de conductivité métallique est lié aux nanoparticules de TiO_2 ou de ZnO , les électrons migrent de TiO_2 ou ZnO vers RuO_2 afin de réaliser l'alignement des niveaux de Fermi des deux matériaux ce qui conduit à la formation d'une zone de déplétion à l'interface. Les charges formées à cette barrière Schottky conduisent à l'apparition d'un champ électrique interne à l'interface des hétérojonctions $\text{RuO}_2/\text{TiO}_2$ or RuO_2/ZnO . Sous irradiation UV, les électrons de la bande de valence de TiO_2 ou de ZnO sont excités vers la bande de conduction laissant des trous dans la bande de valence. Les paires électron-trou ainsi générées peuvent être séparées de manière efficace par le champ électrique interne existant à l'interface des deux oxydes. Cette séparation de charge efficace peut aussi augmenter la durée de vie des porteurs de charge et exalter l'efficacité du transfert de charge interfacial vers les substrats adsorbés sur les nanoparticules, et, ainsi, expliquer les activités photocatalytiques plus élevées observées dans le cas des nanocomposites $\text{RuO}_2/\text{TiO}_2$ et RuO_2/ZnO .

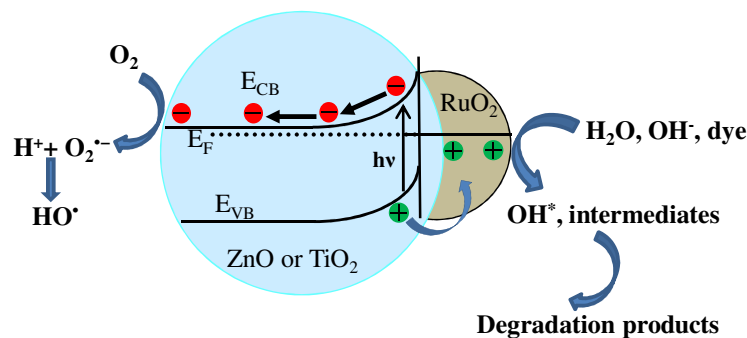


Figure 7: Représentation schématique des mécanismes de séparation des charges photogénérées dans les nanocomposites $\text{RuO}_2/\text{TiO}_2$ ou RuO_2/ZnO .

Enfin, des nanoparticules de TiO_2 pur et des hétérostructures p-n NiO/TiO_2 ont été synthétisées par voie sol-gel en utilisant le tétrabutoxyde de titane ($\text{Ti}(\text{OC}_4\text{H}_9)_4$) comme source de TiO_2 . Typiquement, une suspension colloïdale de nanoparticules de TiO_2 a été préparée par addition de n-butanol et d'acide acétique à du tétrabutoxyde de titane suivi d'addition d'eau sous agitation vigoureuse. Une quantité prédéterminée de nitrate de nickel hexahydrate a ensuite été ajoutée au sol de TiO_2 suivi par une agitation, un séchage et une calcination sous air à 500°C pour obtenir les composites de NiO/TiO_2 contenant différentes quantités de (0.1, 0.25, 0.5, 1, 2, 4 wt%) NiO .

Les pics observés dans le diffractogramme des rayons X de TiO_2 et 1 wt% NiO/TiO_2 séchés à 150°C confirment la formation exclusive de cristallites de TiO_2 anatase au cours de

la synthèse. Les analyses DRX et Raman des échantillons séchés et calcinés indiquent que le TiO_2 est sous forme anatase pure, aucun indice de la formation d'autres phases de TiO_2 (i.e. rutile ou brookite) ou de la présence d'impuretés n'étant détecté. Les images MET et HR-MET (**Figure 8**) indiquent que les poudres sol-gel de TiO_2 sont poreuses et que la taille des particules est d'environ 15 nm, ce qui est en excellent accord avec la taille moyenne des cristallites estimée à partir des diffractogrammes des rayons X et des spectres Raman.

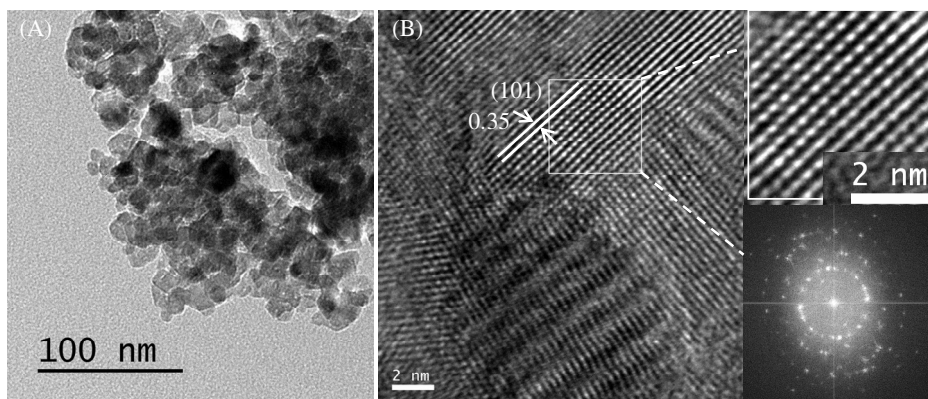


Figure 8: (A) Images MET et (B) HR-MET (en encart, agrandissement image HR-MET et profil SEAD) du nanocomposite 1 wt% NiO/ TiO_2 .

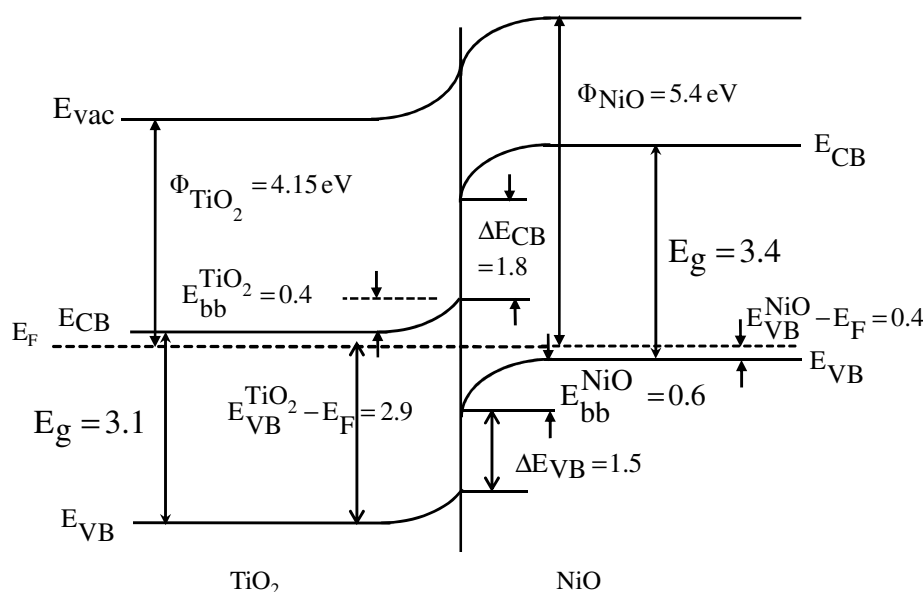


Figure 11: Représentation schématique de l'alignement des bandes d'énergie à l'interface entre TiO_2 et NiO. E_{CB} , E_{VB} , E_F , E_g sont les énergies du bas de la bande de conduction, du haut de la bande de valence, du niveau de Fermi et de la bande interdite, respectivement. $E_{bb}^{\text{TiO}_2}$ et E_{bb}^{NiO} correspondent à la courbure de bande à l'interface entre TiO_2 et NiO

Les valeurs d'énergie des bandes interdites de TiO_2 et NiO purs déterminées par spectroscopie UV-visible en réflexion diffuse ont été évaluées à 3,1 et 3,4 eV,

respectivement. Par ailleurs, le seuil d'absorption optique de l'hétérostructure NiO/TiO₂ est déplacé vers le visible du fait de l'introduction de NiO. L'alignement des bandes d'énergie dans l'hétérojonction p-n NiO/TiO₂ a été déterminé par XPS et UPS à partir des décalages des niveaux d'énergie de cœur. Un déplacement des niveaux de cœur Ti 2p_{3/2} et Ni 2p_{3/2} a été observé, respectivement de $0,4 \pm 0,1$ et $0,6 \pm 0,1$ eV, ce qui a été attribué à la courbure de bande à l'interface de l'hétérojonction NiO/TiO₂. Les décalages de bande de valence (ΔE_{VB}^{inter}) et de bande de conduction (ΔE_{CB}^{inter}) à l'interface ont été évalués à $1,5 \pm 0,1$ et $1,8 \pm 0,1$ eV, respectivement. L'alignement des bandes à l'interface représenté **Figure 11** permet d'expliquer le transfert de charge à l'hétérojonction NiO/TiO₂.

L'activité photocatalytique des nanoparticules à base d'hétérojonctions p-n NiO/TiO₂ a été étudiée dans la dégradation des colorants MB et MO. Les constantes de vitesse de dégradation déduites des pentes des courbes $\ln(C/C_0) = f(t)$ (Figure 10) indiquent que l'hétérojonction NiO/TiO₂ contenant 0.1 wt% de NiO possède une activité photocatalytique plus élevée que le TiO₂ sol-gel pur et le TiO₂ P25 pour la dégradation de MB et MO sous illumination UV. De plus, les photocatalyseurs à base d'hétérostructures NiO/TiO₂ ont pu être recyclés sans changement significatif de leur activité photocatalytique ce qui confirme la stabilité des nanomatériaux développés dans ce travail. En outre, l'activité photocatalytique des nanocomposites NiO/TiO₂ a également été évaluée pour la production de H₂ en solution aqueuse en présence de méthanol à température ambiante sous irradiation UV.

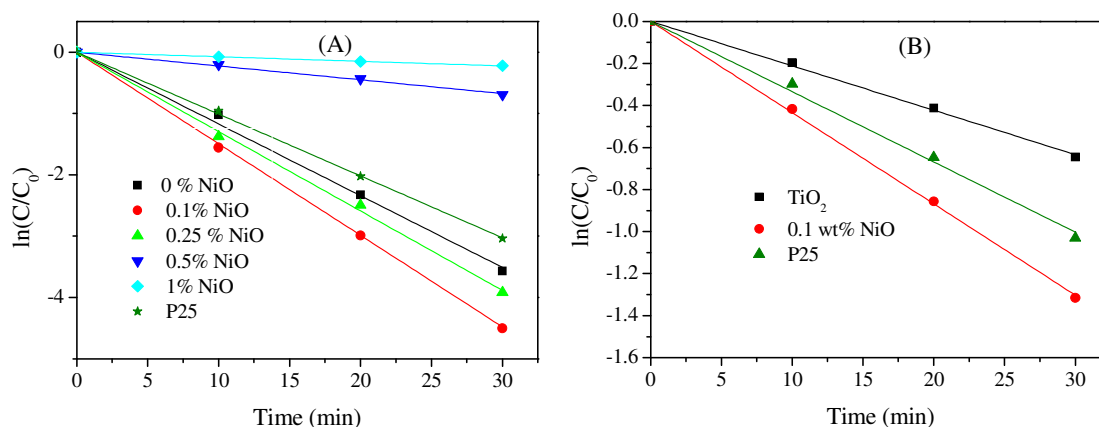


Figure 9: Cinétique du premier ordre pour la photodégradation de(A) MB et (B) MO. C_0 concentration initiale; C concentration au temps t .

La plus grande activité photocatalytique pour la production de H₂ a été obtenue pour l'ensemble de la gamme de teneur en NiO étudiée (**Figure 11A**). La quantité optimale en NiO a été trouvée à 1% en masse avec une vitesse de production moyenne de H₂ de 2693 μmol

$\text{h}^{-1}\text{g}^{-1}$ (**Figure 11B**). A notre connaissance, le nanocomposite 1 wt% NiO/TiO₂ développé par voie sol-gel dans ce travail constitue le système NiO/TiO₂ le plus efficace jamais rapporté pour générer du H₂.

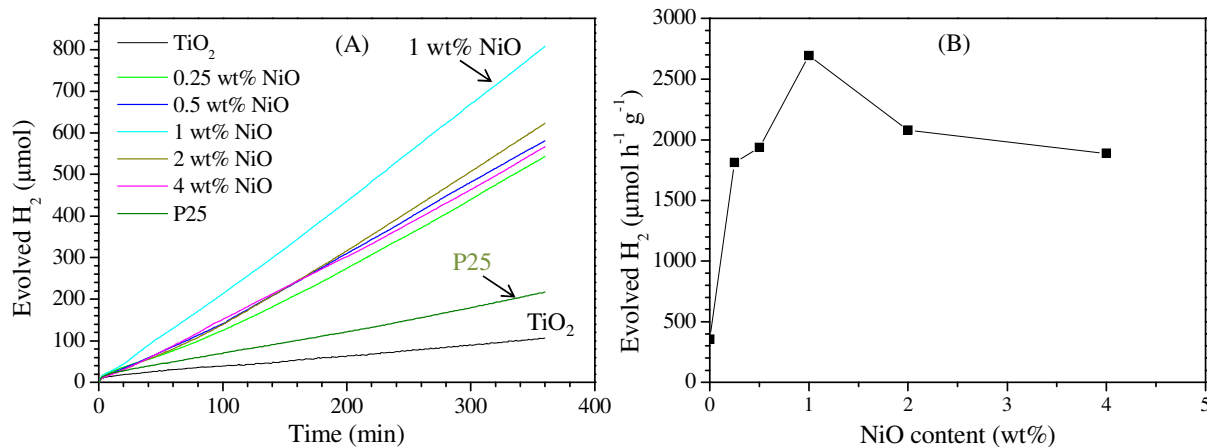


Figure 11: (A) Production photocatalytique de H₂ sur les photocatalyseurs TiO₂ et NiO/TiO₂ contenant différentes teneurs massiques de NiO et (B) effet du taux de NiO sur la production de H₂. Toutes les expériences ont été effectuées pendant 3 h dans des conditions identiques. Volume de solvant 10 mL (H₂O: méthanol = 1:1), quantité en photocatalyseur : 0.05 g.

Le mécanisme expliquant l'activité photocatalytique plus élevée des nanocomposites NiO/TiO₂ pour la dégradation de colorants organiques et la production de H₂ est présenté **Figure 12**. Le champ électrique interne existant à l'interface de l'hétérojonction p-n NiO/TiO₂ facilite le transfert des électrons photogénérés de la bande de conduction de NiO vers la bande de conduction de TiO₂ et, inversement, les trous photogénérés de la bande de valence de TiO₂ à la bande de valence de NiO, suggérant que les électrons et les trous photogénérés sont efficacement séparés. La séparation de charge efficace pourrait augmenter la durée de vie des porteurs de charge et améliorer l'efficacité de transfert de charge interfacial vers des substrats adsorbés, et, donc, expliquer la meilleure activité comparée aux matériaux purs NiO (semiconducteur de type p) et TiO₂ (semiconducteur de type n).

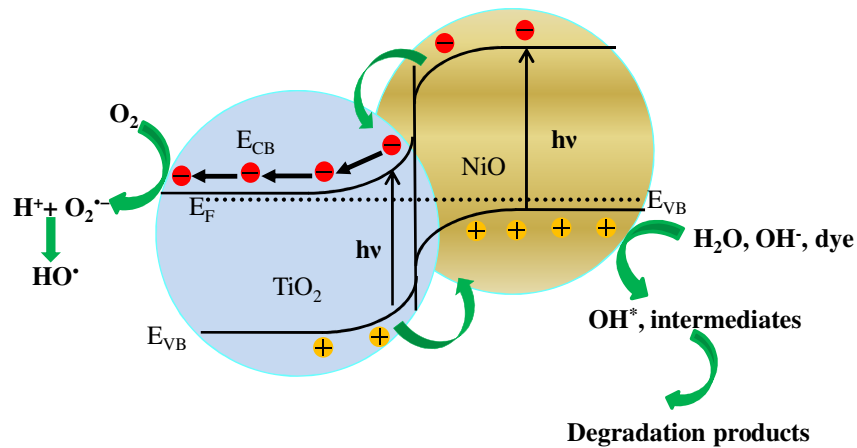


Figure 12: Représentation schématique des mécanismes de séparation des charges photogénérées dans les nanocomposites NiO/TiO₂.

En résumé, ce concept de photocatalyseurs à base d'hétérojonctions semiconductrices d'activité élevée a été interprété en termes d'alignement adéquat des bandes d'énergie des matériaux constituant ces composites. Par conséquent, cette technologie devrait à l'avenir trouver des débouchés industriels dans les domaines de l'élimination de l'environnement de composés organiques indésirables et de la production « verte » d'hydrogène.

L'activité photocatalytique du nanocomposite RuO₂/ZnO pour la production d'hydrogène mériterait d'être étudiée en détails puisque les niveaux du haut de la bande de valence et du bas de la bande de conduction de chaque constituant sont thermodynamiquement favorables pour réduire l'eau en hydrogène. Par ailleurs, l'efficacité photocatalytique peut être augmentée en piégeant les électrons photogénérés dans la bande de conduction du semi-conducteur. De plus, la formation de centres actifs pour l'activation et la réduction de l'eau en hydrogène peut aussi exalter l'efficacité catalytique pour la production d'hydrogène. Une des méthodes possibles est de déposer du platine (Pt) sur la surface de ZnO ou de TiO₂ dans les nanocomposites RuO₂/ZnO ou RuO₂/TiO₂ ce qui piège non seulement les électrons mais fournit aussi des centres actifs pour l'activation et la réduction de H₂O en H₂. Finalement, l'utilisation de polluants organiques comme donneurs d'électrons à la place du méthanol pourrait permettre de réduire les coûts de production de H₂ tout en permettant simultanément la production de H₂ et la dégradation de composés organiques indésirables. Les eaux usées contenant des polluants organiques tels que les colorants azo peuvent être considérées comme des donneurs adéquats pour cette application. La démonstration d'un tel concept pourrait avoir ainsi un impact industriel considérable.

Table of content

Chapter I : Introduction1

I.1. General introduction.....	2
I.2. Water Treatment.....	2
I.2.1. Conventional wastewater treatment technology and their drawbacks.....	4
I.2.2. Advanced oxidation processes (AOPs).....	4
I.2.3. Heterogeneous photocatalysis.....	6
I.2.3.1. Electronic structure of semiconductor photocatalysts	7
I.2.3.2. Basic principle of photocatalysis	8
I.2.3.3. Mechanism of generating oxidizing species.....	10
I.2.3.4. Photocalysts and its requirement for photocatalysis.....	12
I.3. Hydrogen production	14
I.3.1.1. Photocatalytic water splitting.....	16
I.3.1.2. Basic principle of photocatalytic hydrogen generation	16
I.4. Research objectives	18

Chapter II : Literature review25

II.1. Introduction.....	26
II.2. Approaches for efficient charge separation	26
II.2.1. Coupled semiconductors	26
II.2.2. Metal/semiconductor heterostructure nanocomposites	28
II.2.3. Scavenging of electrons and holes	29
II.2.4. Charge carrier trapping.....	30
II.3. Band bending	30
II.3.1. Band bending at metal/semiconductor contact.....	31
II.3.2. Band bending at p-n junction	32
II.3.3. Band bending at semiconductor/electrolyte interface	33
II.4. Heterostructure photocatalysts.....	35
II.4.1. Semiconductor/semiconductor heterostructure photocatalysts	35
II.4.1.1. SnO ₂ /TiO ₂ heterostructure photocatalysts.....	35
II.4.1.2. ZnO/TiO ₂ heterostructure photocatalysts	44
II.4.1.3. WO ₃ /TiO ₂ heterostructure photocatalysts	49

II.4.1.4. ZnO/SnO ₂ heterostructure photocatalysts	54
II.4.2. p-n heterojunction.....	60
II.4.3. Metal/semiconductor heterojunctions	64
II.4.3.1. RuO ₂ /TiO ₂ heterostructure photocatalysts	64
II.4.3.2. Ag/TiO ₂ heterostructure photocatalysts	66
II.4.3.3. Au/TiO ₂ heterostructure photocatalysts	71
II.4.3.4. Pt/TiO ₂ heterostructure photocatalysts	74
II.5. Conclusion	82

Chapter III : Nanostructured SnO₂/ZnO heterojunction

photocatalysts.....97

III.1. Introduction	98
III.2. Preparation method review	98
III.3. Result and discussion	102
III.3.1. Synthesis and particle characterization	102
III.3.2. Surface and interface analysis	107
III.3.3. Photocatalytic activity	111
III.4. Conclusion	116

Chapter IV : Metal/n-type semiconductor heterojunction

photocatalysts..... 119

IV.1. Introduction	120
IV.2. Nanostructured RuO ₂ /TiO ₂ heterojunction photocatalysts	123
IV.2.1. Preparation method review	123
IV.2.2. Results and discussions.....	124
IV.2.2.1. Synthesis and characterization of the nanocatalysts	124
IV.2.2.2. Interface analysis	133
IV.2.2.3. Photocatalytic activity.....	140
IV.2.2.3.1 Photocatalytic degradation of organic dyes	140
IV.2.2.3.2 Photocatalytic hydrogen production	145
IV.3. Nanostructured RuO ₂ /ZnO heterojunction photocatalysts.....	148
IV.3.1.1. Synthesis and characterization of the nanocatalysts	148
IV.3.1.2. Interface analysis	155

IV.3.1.3. Photocatalytic activity.....	159
IV.3.1.3.1. Photocatalytic degradation of organic dyes	159
IV.4. Conclusion.....	166
Chapter V : p-n NiO/TiO₂ heterojunction photocatalysts	173
V.1. Introduction	174
V.2. Preparation method review	175
V.3. Results and discussions	177
V.3.1. Synthesis and characterization of nanocomposites	177
V.3.2. Interface analysis.....	188
V.3.3. Photocatalytic activity	193
V.3.3.1. Photocatalytic degradation of organic dyes	193
V.3.3.2. Photocatalytic hydrogen production.....	199
V.4. Conclusions	202
General conclusion and perspectives.....	207
Chapter VI : Experimental section.....	215
VI.1. Chemicals used.....	216
VI.2. Synthesis of nanophotocatalysts.....	216
VI.2.1. Preparation of SnO ₂ /ZnO heterojunction photocatalysts	216
VI.2.2. Preparation of RuO ₂ /TiO ₂ heterojunction photocatalysts	217
VI.2.3. Preparation of RuO ₂ /ZnO heterojunction photocatalysts	217
VI.2.4. Preparation of NiO/TiO ₂ heterojunction photocatalysts	218
VI.3. Characterization methods	218
VI.3.1. Fourier transform infrared (FTIR)	218
VI.3.2. Raman spectroscopy	219
VI.3.3. X-ray powder diffraction (XRD)	219
VI.3.4. Transmission electron microscopy (TEM)	220
VI.3.5. Thermogravimetric analysis (TGA).....	221
VI.3.6. Nitrogen sorption measurement.....	221
VI.3.7. UV-Visible diffuse reflectance spectrometry (UV-Vis DRS)	222
VI.3.8. X-ray Photoelectron spectroscopy (XPS).....	223
VI.4. Photocatalytic Experiment	225

VI.4.1. Photocatalytic degradation of organic dyes	225
VI.4.2. Photocatalytic hydrogen production	225
Appendix	229

List of Figure

Figure I-1: Change of the electronic structure of a semiconductor compound as the number N of monomeric units present increases from unity to clusters of more than 2000 units.	8
Figure I-2: Schematic photoexcitation in a semiconductor photocatalyst followed by deexcitation pathways'	9
Figure I-3: Band position of commonly used semiconductors in aqueous electrolyte at pH 1.	13
Figure I-4: Photocatalytic hydrogen production from water using a powder photocatalyst. .	16
Figure I-5: (a) Basic principle of overall water splitting on a semiconductor particle (b) Processes involved in photocatalytic water splitting on a semiconductor particle	17
Figure II-1: Schematic energy band diagram of semiconductor heterojunctions.....	27
Figure II-2: Schematic illustration of charge transfer process in coupled heterostructure composites.....	28
Figure II-3: Energy band diagram at metal/n-type semiconductor heterojunction.	32
Figure II-4: Energy band diagram at the junction of TiO ₂ and NiO.....	33
Figure II-5: Space charge layer formation and band bending.	34
Figure II-6: Schematic representation of charge transfer process in heterostructure SnO ₂ /TiO ₂ photocatalysts.	36
Figure II-7: (a and b) Typical SEM images of the electrospun bicomponent SnO ₂ /TiO ₂ nanofibers calcined at 500 °C (c) Morphology of the hybrid nanofiber by scanning electron microscopy, with arrows showing the bead parts	39
Figure II-8: Schematic diagram of the charge-transfer process in the SnO ₂ /TiO ₂ composite film.....	41

Figure II-9: (A) SEM micrograph of pat-TiO ₂ /SnO ₂ /SL-glass after Ag photodeposition. (B) X-ray image of Ti for the same region as (A). (C) X-ray image of Ag for the same region as (A). (D) X-ray image of Ag for TiO ₂ /SnO ₂ /SL-glass.....	42
Figure II-10: Energy diagram for the SnO ₂ /TiO ₂ bilayer-type photocatalyst system	43
Figure II-11: Schematic diagram illustrating the charge-transfer process in the ZnO/TiO ₂ heterostructure under UV light irradiation.....	45
Figure II-12: UV-Vis reflectance spectra of nanoparticles synthesized with SDS and different Zn/Ti(OBu) ₄ molar ratio.	47
Figure II-13: (a) SEM cross-sectional images of aqueous solution growth ZnO nanorods (NRs), (b) ZnO/TiO ₂ CB nanostructures (the insert is a high magnification image and the scale bar is 200 nm)	48
Figure II-14: Energy band diagram and charge transfer process in WO ₃ /TiO ₂ heterostructure photocatalyst.	49
Figure II-15: The photoluminescence (PL) spectra of pure TiO ₂ and WO _x /TiO ₂ containing different mol% of WO _x	51
Figure II-16: Energy diagram for TiO ₂ and WO _x -Ti _{1-x} O ₂ systems.....	53
Figure II-17: Schematic band energy diagram of ZnO/SnO ₂ composite.	55
Figure II-18: SEM images of ZnO/SnO ₂ nanostructures obtained at different Zn ²⁺ /Sn ⁴⁺ molar ratios: (a) 2:1, (b) 1:1, (c) 4:1, (d) 1:2, (e) 0:1, and (f) 1:0, (g) CIL=0.1 g, Zn ²⁺ /Sn ⁴⁺ =1:1, (h) CIL=0.05 g, Zn ²⁺ /Sn ⁴⁺ =1:1; (a-f): CIL = 0.05 g.	57
Figure II-19: (a) TEM image of the as-synthesized SnO ₂ /ZnO heterojunction nanocatalyst (b) Energy-band diagram and photocatalytic mechanism of the as-synthesized SnO ₂ /ZnO heterojunction nanocatalyst. vac, vacuum level; E _f , Fermi level; CB, conduction band; VB, valence.	59
Figure II-20: Equilibration of semiconductor-metal nanocomposites with the redox couple before and after UV irradiation.....	64
Figure II-21: Interface charge-carrier transfer dynamics of anatase/rutile, Ag/ anatase and Ag/rutile within Ag/TiO ₂ composite thin films	67
Figure II-22: Photoinduced charge separation and charging of metal core in Ag@TiO ₂	69

Figure II-23: Stepwise Transfer of Electrons from TiO ₂ to Au to C ₆₀ following the excitation of TiO ₂ particles.....	71
Figure II-24: Schematic illustration for hydrogen evolution over Au/TiO ₂ photocatalysts under visible light irradiation.....	74
Figure II-25: Transition absorption spectra at 600 nm for TiO ₂ and Pt/TiO ₂ powder with 390 nm excitation.....	75
Figure II-26: Half-life mineralisation rates of 2000 g of carbohydrate carbon (as sucrose) and corresponding quantum efficiencies in ambient or oxygen-enriched suspensions by Degussa P25, FSP-made pure TiO ₂ (0Pt5) and Pt/TiO ₂ (XPt5, X = atom% Pt)	77
Figure II-27: Energy band positions of Pt/TiO ₂ -CO ₂ system	78
Figure II-28: Effect of sacrificial reagent type on photocatalytic H ₂ evolution activity of Pt/TiO ₂ (reaction condition: photocatalyst amount, 0.2 g; distilled water amount, 200 mL, sacrificial reagent amount, 20 mL, irradiation time, 5 h)	81
Figure II-29: Proposed photocatalytic reaction mechanism for Z-scheme water-splitting system using an IO ³⁻ /I redox mediator and a mixture of Pt/TiO ₂ -antase and TiO ₂ -rutile photocatalysts.....	82
Figure III-1: FTIR (A) and Raman (B) spectra of the as-synthesized photocatalysts after annealing in air at 500 ° C (a) SnO ₂ (b) SnO ₂ -ZnO, and (c) ZnO.....	102
Figure III-2: (A) XRD patterns of the as-synthesized photocatalysts annealed in air at 500 ° C and (B) XRD patterns of the SnO ₂ /ZnO photocatalyst annealed in air at different temperature. (a) SnO ₂ (b) SnO ₂ /ZnO, and (c) ZnO.	103
Figure III-3: TEM micrographs of the (a) dried SnO ₂ /ZnO heterostructure and (b) calcined SnO ₂ /ZnO photocatalyst. The inset SAED patterns reveal the occurrence of (a) crystalline SnO ₂ and (b) crystalline SnO ₂ and ZnO. HRTEM images (c, d) verify the crystallinity of both SnO ₂ and ZnO after calcination.	105
Figure III-4: (A) Nitrogen gas adsorption-desorption isotherms and (B) pore-size distribution of the SnO ₂ /ZnO photocatalyst.	106
Figure III-5: UV-Visible diffuse reflectance spectra (A) and plots of (F(R) hv) ² versus photon energy (hv) (B) of the as-synthesized materials after annealing in air at 500 ° C (a) SnO ₂ (b) SnO ₂ /ZnO, and (c) ZnO.	106

Figure III-6: XPS survey spectrum of the SnO ₂ /ZnO photocatalyst.	108
Figure III-7: XPS patterns of the SnO ₂ /ZnO photocatalyst (A) Sn 3d region; (B) Zn 2p region.	108
Figure III-8: XPS spectra of O1s region (full) of the SnO ₂ /ZnO photocatalyst with the corresponding fits for OH (dot), ZnO (dot-dash) and SnO ₂ (dash).	109
Figure III-9: (A) Core level Sn 3d _{5/2} spectra (B) VB spectra for the bulk SnO ₂ sample and (C) core level Zn 2p _{3/2} spectra (D) VB spectra for the bulk ZnO sample.....	110
Figure III-10: Band alignment diagram of the SnO ₂ /ZnO photocatalyst.	111
Figure III-11: Absorbance changes of MB solution after different irradiation times in the presence of the SnO ₂ /ZnO sample: initial (black), equilibrium (red), 10 min (blue), 20 min (green), 30 min (magenta), 40 min (brown) and 130 min (cyan).	112
Figure III-12: (A) Kinetic of the degradation of MB in the presence of UV only (square, dot), SnO ₂ /ZnO in the dark (triangle, dash), SnO ₂ /ZnO under UV (square, plain), SnO ₂ under UV (triangle, plain), and ZnO under UV (circle, plain). (B) ln (C/C ₀) as a function of the irradiation time for calcined SnO ₂ (triangle), SnO ₂ /ZnO (square) and ZnO (circle) photocatalysts.....	112
Figure III-13: (A) Cyclic runs in the photodegradation of MB using the SnO ₂ /ZnO photocatalyst under UV-light: 1st cycle (square), 2nd cycle (triangle), 3rd cycle (circle) and 4th cycle (diamond) (B) effect of pH on the photocatalytic activity of photocatalysts.....	114
Figure III-14: Schematic representation of the charge transfer process for the heterostructure SnO ₂ /ZnO photocatalyst.	115
Figure IV-1: FTIR (A) and Raman (B) spectra of as-synthesized photocatalysts calcined at 400 °C for 6h. (a) TiO ₂ , (b) 1 wt% RuO ₂ /TiO ₂ , (c) 2.5 wt% RuO ₂ /TiO ₂ , and (d) 5 wt% RuO ₂ /TiO ₂	124
Figure IV-2: XRD pattern of TiO ₂ and RuO ₂ /TiO ₂ in the 2θ region of 10-80 ° (A) and 26-66 ° (B). (a) TiO ₂ , (b) 0.5 wt% RuO ₂ /TiO ₂ , (c) 1 wt% RuO ₂ /TiO ₂ , (d) 2.5 wt% RuO ₂ /TiO ₂ , and (e) 5 wt% RuO ₂ /TiO ₂	126
Figure IV-3: TEM micrograph of (A) TiO ₂ and (B) and (C) 1 wt% RuO ₂ /TiO ₂ showing distribution of RuO ₂ by discrete contrast variation (D) SAED pattern of TiO ₂ (E-G) EDX elemental mapping of 1 wt% RuO ₂ /TiO ₂	127

Figure IV-4: EDX mapping of 1 wt% RuO ₂ /TiO ₂ photocatalysts.....	128
Figure IV-5: (A) TEM (B) STEM-BF (C) STEM-HAADF images and (D, E) EDX mapping of 5 wt% RuO ₂ /TiO ₂ nanoparticles.....	129
Figure IV-6: N ₂ adsorption–desorption isotherm and mesopore size distribution (inset) of as-synthesized TiO ₂ (A) and 1wt% RuO ₂ /TiO ₂ (B) photocatalysts.	130
Figure IV-7: UV-Visible diffuse reflectance spectra of as-synthesized nanoparticles. (a) TiO ₂ , (b) 1 wt% RuO ₂ /TiO ₂ , (c) 2.5 wt% RuO ₂ /TiO ₂ and (d) 5 wt% RuO ₂ /TiO ₂	131
Figure IV-8: (A) $(F(R) hv)^{1/2}$ vs. hv plot and (B) $(F(R) hv)^2$ vs. hv plot of as-synthesized nanoparticles. (a) TiO ₂ , (b) 1 wt% RuO ₂ /TiO ₂ , (c) 2.5 wt% RuO ₂ /TiO ₂ and (d) 5 wt% RuO ₂ /TiO ₂	132
Figure IV-9: XPS survey scan spectrum of heterostructure 1wt% RuO ₂ /TiO ₂ nanoparticles.	133
Figure IV-10: (A) High resolution XPS spectra of Ti 2p for 1 wt% RuO ₂ /TiO ₂ nanoparticles (B) High resolution XPS spectra of Ru 3d for (a) TiO ₂ and (b) 1 wt% RuO ₂ /TiO ₂ nanoparticles after spectral deconvolution.....	134
Figure IV-11: X-ray photoelectron survey spectra of (a) TiO ₂ substrate and (b) RuO ₂ thin film after a number of successive deposition sequences on TiO ₂ substrate.	134
Figure IV-12: X-ray photoelectron core level spectra of TiO ₂ recorded during stepwise deposition of RuO ₂ onto the TiO ₂ film. Spectra at the bottom (at 0 s) refer to the uncovered TiO ₂ film and the spectra at the top (after 300 s) refer to the saturated RuO ₂ film.	135
Figure IV-13: (A) Ultraviolet photoelectron spectra and (B) X-ray photoelectron spectra of the TiO ₂ film (a) and RuO ₂ film (b).....	136
Figure IV-14: (A) XP valence band spectra during stepwise deposition of RuO ₂ onto TiO ₂ film (B) evolution of the valence band position of TiO ₂ determined from core level binding energy: (A) the spectrum at bottom (at 0 s) refers to the uncovered TiO ₂ film and the spectrum at the top (after 300 s) refers to saturated RuO ₂ film.	137
Figure IV-15: Schematic band energy alignment at the interface of RuO ₂ and TiO ₂ . E _{CB} , E _{VB} , E _F , E _g are conduction band minimum, valence band maximum, Fermi level and energy gap, respectively. eV _{bb} refers to band bending at the interface of RuO ₂ and TiO ₂	138

Figure IV-16: X-ray photoelectron core level spectra of heterostructure RuO ₂ /TiO ₂ nanoparticles containing different wt% RuO ₂ . (a) TiO ₂ , (b) 1 wt% RuO ₂ /TiO ₂ , (c) 2.5 wt% RuO ₂ /TiO ₂ and 5 wt% RuO ₂ /TiO ₂	139
Figure IV-17: (A) UPS spectra of TiO ₂ (B) XP valence band spectra of TiO ₂ and RuO ₂ /TiO ₂ and (C) Evolution of XP valence band spectra with different content of RuO ₂ . (a) TiO ₂ , (b) 1 wt% RuO ₂ /TiO ₂ , (c) 2.5 wt% RuO ₂ /TiO ₂ and 5 wt% RuO ₂ /TiO ₂	139
Figure IV-18: Change of absorbance spectra of (A) MB and (B) MO solution after different irradiation times in the presence of 1 wt% RuO ₂ /TiO ₂	140
Figure IV-19: Kinetic of the degradation of MB (A) and MO (B); and plot of lnC/C ₀ against <i>t</i> for the photocatalytic degradation of MB (C) and MO (D) with the as-synthesized nanoparticles.	141
Figure IV-20: Cyclic runs in the photodegradation of MB employing 1 wt% RuO ₂ /TiO ₂ under UV light.	143
Figure IV-21: The effect of pH on the photocatalytic degradation of heterostructure 1 wt% RuO ₂ /TiO ₂ photocatalysts.....	143
Figure IV-22: Schematic diagram of photogenerated charge separation by internal electric field at RuO ₂ /TiO ₂ heterojunction and its photocatalytic process.	144
Figure IV-23: (A) photocatalytic evolution of H ₂ under different condition, photocatalytic evolution of gas (B) and H ₂ (C) over TiO ₂ and RuO ₂ /TiO ₂ photocatalysts and (D) effect of RuO ₂ loading on the H ₂ production. All the experiments were run for 3 h at identical condition.	146
Figure IV-24: (A) FTIR and (B) Raman spectra of as-synthesized photocatalysts. (a) ZnO, (b) 2 wt% RuO ₂ /ZnO, (c) 4 wt% RuO ₂ /ZnO, and (d) 6 wt% RuO ₂ /ZnO.....	149
Figure IV-25: XRD pattern of RuO ₂ /ZnO heterostructure recorded at different RuO ₂ content in the 2θ region of 10-80° (A) and 26-66° (B). (a) ZnO, (b) 2% RuO ₂ /ZnO, (c) 4% RuO ₂ /ZnO, (d) 6% RuO ₂ /ZnO.....	150
Figure IV-26: (A) TEM image and (B) HRTEM image of 4 wt% RuO ₂ /ZnO photocatalysts (C) EDX spectrum from part (A).....	151

Figure IV-27: (A) STEM secondary electron image (SEI) of 4 wt% RuO ₂ /ZnO and EDX maps of (B) Ru, (C) Zn and (D) Overlay (Ru and Zn). EDX mapping was carried out by scanning a region different from the region shown in (A).....	152
Figure IV-28: N ₂ adsorption–desorption isotherm and of as-synthesized ZnO (A) and 4 wt% RuO ₂ /ZnO (B) photocatalysts.....	153
Figure IV-29: UV-Vis diffused (A) absorption and (B) reflectance spectra of (a) ZnO, (b) 2 wt% RuO ₂ / ZnO, (c) 4 wt% RuO ₂ / ZnO and (d) 6 wt% RuO ₂ / ZnO.....	154
Figure IV-30: $(F(R) hv)^2$ versus hv plot for as-synthesized photocatalysts. (a) ZnO, (b) 2 wt% RuO ₂ / ZnO, (c) 4 wt% RuO ₂ / ZnO and (d) 6 wt% RuO ₂ / ZnO.....	155
Figure IV-31: (A) XPS survey spectra of ZnO (a) and 4 wt% RuO ₂ /ZnO (b). High-resolution spectra of 4 wt% RuO ₂ /ZnO sample: (B) Zn 2p spectra, (C) Ru 3d spectra and (D) O 1s spectra.....	156
Figure IV-32: Evolution of photoemission core level spectra of the heterostructure RuO ₂ /ZnO nanoparticles with different contents of RuO ₂ . (a) ZnO, (b) 2 wt% RuO ₂ /ZnO, (c) 4 wt% RuO ₂ /ZnO and 6 wt% RuO ₂ /ZnO.....	157
Figure IV-33: (A) UP spectrum of pure ZnO (B) XP valence band spectra of ZnO and RuO ₂ /ZnO with different amount of RuO ₂ . a) ZnO, (b) 2 wt% RuO ₂ /ZnO, (c) 4 wt% RuO ₂ /ZnO and 6 wt% RuO ₂ /ZnO.....	158
Figure IV-34: Schematic band energy alignment at the interface of RuO ₂ and ZnO. E _{CB} , E _{VB} , E _F , E _g are conduction band maximum, valence band maximum, Fermi level and energy gap, respectively. eV _{bb} refers to band bending at the interface of RuO ₂ and ZnO.....	159
Figure IV-35: UV-Visible spectra of (A) MB and (B) MO aqueous solutions as a function of reaction time in the presence of 4 wt% RuO ₂ /ZnO.....	160
Figure IV-36: Kinetic of the degradation of MB (A) and MO (B); plot of $\ln C/C_0$ against t for the photocatalytic degradation of MB (C) and MO (D) with as-synthesized nanoparticles..	160
Figure IV-37: (A) Cycling photodegradation of MB aqueous solution over 4 wt% RuO ₂ /ZnO (B) XRD patterns of the 4 wt% RuO ₂ /ZnO heterostructure before and after cycling photodegradation of MB.....	163
Figure IV-38: Effect of solution pH on MB degradation.....	164

Figure IV-39: schematic diagram showing the photogenerated charge separation mechanism of RuO ₂ /ZnO nanocomposites.	165
Figure V-1: TG curves of (a) TiO ₂ and (b) 1 wt% NiO/TiO ₂	178
Figure V-2: (A) FTIR spectra of (a) TiO ₂ (b) 1 wt% NiO/TiO ₂ dried at 150 °C and (b) FTIR spectra of (a) TiO ₂ (b) 0.1 wt% NiO/TiO ₂ (c) 0.25 wt% NiO/TiO ₂ (d) 0.5 wt% NiO/TiO ₂ and (e) 1 wt% NiO/TiO ₂ calcined at 500 °C.	178
Figure V-3: XRD of TiO ₂ and 1 wt% NiO/TiO ₂ dried at 150 °C for 2 h.	179
Figure V-4: (A) XRD pattern of the as-synthesized NiO/TiO ₂ nanocomposites with different content of NiO and (B) XRD pattern of the as-synthesized NiO/TiO ₂ nanocomposites in the 2θ region between 40 and 46° to show the peak of NiO (200).	179
Figure V-5: XRD pattern of the as-synthesized NiO nanoparticle.	180
Figure V-6: (A) Raman spectra of as-synthesized photocatalysts (B) enlarged region of Raman shift range 110-200 cm ⁻¹ . (a) TiO ₂ (b) 0.1 wt% NiO/TiO ₂ (c) 0.25 wt% NiO/TiO ₂ (d) 0.5 wt% NiO/TiO ₂ (e) 1 wt% NiO/TiO ₂	181
Figure V-7: (A) TEM and (B) HRTEM images (inset shows the SEAD pattern and enlarged view of HRTEM) of 1 wt% NiO/TiO ₂ nanocomposites.	183
Figure V-8: EDX elemental mapping of 1 wt% NiO/TiO ₂ nanocomposite.	183
Figure V-9: EDX elemental mapping of 4 wt% NiO/TiO ₂ nanocomposite.	184
Figure V-10: N ₂ adsorption-desorption isotherm of calcined (A) TiO ₂ and (B) 1 wt% NiO/TiO ₂	185
Figure V-11: UV-Vis diffuse absorption spectra of (A) as-synthesized photocatalysts; (a) TiO ₂ (b) 0.1 wt% NiO/TiO ₂ (c) 0.25 wt% NiO/TiO ₂ (d) 0.5 wt% NiO/TiO ₂ and (e) 1 wt% NiO/TiO ₂ and (B) NiO (inset: $(F(R) hv)^{1/2}$ vs $h\nu$ plot of NiO).	187
Figure V-12: $(F(R) hv)^{1/2}$ versus $h\nu$ for as-synthesized photocatalysts. (a) TiO ₂ (b) 0.1 wt% NiO/TiO ₂ (c) 0.25 wt% NiO/TiO ₂ (d) 0.5 wt% NiO/TiO ₂ and (e) 1 wt% NiO/TiO ₂	187
Figure V-13: A) XPS survey spectra of as-synthesized sample. High-resolution spectra of 1 wt% NiO/TiO ₂ sample: (B) Ti 2p spectra, (C) Ni 2p spectra and (D) O 1s spectra. (a) TiO ₂ and (b) 1 wt% NiO/TiO ₂	188

Figure V-14: Evolution of core level spectra (A) Ti 2p (B) O 1s (C) Ni 2p _{3/2} . (a) TiO ₂ (b) 0.1 wt% NiO/TiO ₂ (c) 0.25 wt% NiO/TiO ₂ (d) 0.5 wt% NiO/TiO ₂ (e) 1 wt% NiO/TiO ₂ (f) 4 wt% NiO/TiO ₂ (g) 25 wt% NiO/TiO ₂ (h) 50 wt% NiO/TiO ₂ (i) NiO.....	189
Figure V-15: Ultraviolet photoelectron spectra (HeI) of TiO ₂ and NiO.....	191
Figure V-16: (A) Valence band spectra of TiO ₂ and NiO (B) evolution of valence band position. (a) TiO ₂ (b) 0.1 wt% NiO/TiO ₂ (c) 0.25 wt% NiO/TiO ₂ (d) 0.5 wt% NiO/TiO ₂ (e) 1 wt% NiO/TiO ₂ (f) 4 wt% NiO/TiO ₂	191
Figure V-17: Band energy alignment at the heterojunction interface of n-type (TiO ₂) and p-type (NiO) semiconductor.....	192
Figure V-18: Typical absorbance spectra of (A) MB and (B) MO solution during the course of photodegradation.	193
Figure V-19: Kinetic of photodegradation of (A) MB (B) MO and pseudo-first order kinetic for the photodegradation of (C) MB and (D) MO.	194
Figure V-20: Recyclability of 0.1 wt% NiO/TiO ₂ photocatalysts for the degradation of MB.	196
Figure V-21: Effect of initial solution pH on the photocatalytic degradation of MB over 0.1 wt% NiO/TiO ₂	197
Figure V-22: Schematic representation of the photogenerated charge separation mechanism of NiO/TiO ₂ nanocomposites.....	198
Figure V-23: Photocatalytic evolution of H ₂ under different condition (A) photocatalytic evolution of gas (B) and H ₂ (C) over TiO ₂ and NiO/TiO ₂ photocatalysts and effect of NiO loading on the H ₂ production (D). All the experiments were run for 6 h at identical condition (photocatalyst, 0.05 g; water, 5 mL; methanol, 5 mL).	200
Figure VI-1: Schematic drawing of Darmstadt Integrated System for Fundamental research (DAISY-FUN).	224
Figure VI-2: Experiment set up for the photocatalytic production of hydrogen. (a) Waste (b) Ar/vacuum (c) thermostat outlet (d) thermostat inlet (e) thermostatically controlled reaction vessel (f) thermostat (g) pressure sensor.....	226

List of Table

Table I-1: Oxidation potential of some oxidants.....	5
Table II-1: Degradation of different organic pollutants with SnO ₂ /TiO ₂ heterostructure photocatalysts.....	37
Table II-2: Degradation of different organic pollutants with ZnO/TiO ₂ heterostructure phtocatalysts.....	46
Table II-3: Degradation of different organic pollutants with ZnO/SnO ₂ heterostructure photocatalysts.....	56
Table III-1: Nitrogen sorption porosimetry studies ^a of the as-synthesized SnO ₂ , ZnO and SnO ₂ /ZnO nanomaterials.	106
Table III-2: XPS binding energies of the core levels and VBM of SnO ₂ , ZnO and SnO ₂ /ZnO photocatalysts.....	111
Table III-3: Apparent (k_{app}) and normalized (k_{norm}) rate constants for the degradation of MB with the as-synthesized materials.....	113
Table IV-1: Crystallite size and textural properties of TiO ₂ and RuO ₂ /TiO ₂ catalysts.....	130
Table IV-2: Apparent reaction rate constant for the degradation of MB with as-synthesized nanoparticles.	142
Table IV-3: Crystallite size and textural properties of ZnO and RuO ₂ /ZnO photocatalysts.	154
Table IV-4: Apparent reaction rate constant for the degradation of MB with as-synthesized nanoparticles.	161
Table V-1: Mean particle size (in nm) of anatase TiO ₂ determined by XRD and Raman shift.	182
Table V-2: Nitrogen Sorption Porosimetry Studies of the as-synthesized TiO ₂ and NiO/TiO ₂ nanoparticles.	185
Table V-3: Apparent rate constant for the degradation of MB and MO with the as-synthesized photocatalysts.	195

List of abbreviation

AOP:	advanced oxidation process	h^+ :	hole
Ag:	Silver	HAADF:	high angle annular dark field
Au:	Gold	H ₂ O ₂ :	hydrogen peroxide
ATT:	Attapulgate	HRTEM:	high resolution transmission electron microscopy
BET:	Brunauer-Emmett-Teller	k:	degradation rate constant
BJH:	Barrett-Joyner-Halenda	L:	litre
BF:	bright field	LSPR:	localized surface plasmon resonance
C:	Concentration	M:	mol L ⁻¹
CTAB:	cetyl trimethyl ammonium Bromide	MB:	methylene blue
CdS:	cadmium sulphide	min:	minute
CO ₂ :	carbon dioxide	mL:	millilitre
CO:	carbon monoxide	mol:	mole
4-CP:	4-chlorophenol	MO:	methyl orange
CB:	conduction band	N ₂ :	nitrogen
CH ₄ :	Methane	NHE:	normal hydrogen electrode
CH ₃ OH:	methanol	Ni:	nickel
CN:	Cyanide	NiO:	nickel oxide
E _g :	band gap energy	OH:	hydroxyl group
E _{CB} :	conduction band energy	PCO:	photocatalytic oxidation
E _F :	Fermi energy	PCD:	photocatalytic degradation
E _{VB} :	valence band energy	Pd:	palladium
EDTA:	ethylenediaminetetraacetic acid	PL:	photoluminescence
EDX:	energy dispersive X-ray	ps:	picoseconds
eV _{bb} :	band bending	Pt:	Platinum
F(R):	remission function	R:	reflectance
fs:	Femtosecond	RhB:	rhodamine B
FTIR:	Fourier transform infrared	Ru:	ruthenium
FWHM:	full-width at half-maximum	RuCl ₃ :	ruthenium chloride
h:	Hour		

RuO ₂ :	ruthenium oxide	UV:	ultraviolet
s:	Second	VB:	valence band
SAED:	selected area electron diffraction	VBM:	valence band maximum
SPS:	surface photovoltage spectroscopy	Vis:	visible
S _{BET} :	BET specific surface area	WO ₃ :	tungsten trioxide
SnO ₂ :	tin dioxide	XRD:	X-ray diffraction
STEM:	scanning transmission electron microscopy	XPS:	X-ray photoelectron spectroscopy
TiO ₂ :	titanium dioxide	Zn(OAc) ₂ :	zinc acetate
t:	time	ZnO:	zinc oxide
TEM:	transmission electron microscopy	ZnS:	zinc sulphide
TGA:	thermogravimetric analysis	Φ_s :	work function of semiconductor
TNT:	TiO ₂ nanotube	Φ_m :	work function of metal
UPS:	ultraviolet photoelectron Spectroscopy	ν :	light frequency
		α :	absorption coefficient
		λ :	wavelength of light



Chapter I : Introduction

I.1. General introduction

As global population growth and economic development continue to ramp up, clean and sustainable energy production along with environmental concerns have emerged as the top issues and challenges for humanity over the past decade. Thus, the exponential growth of human population and the intensification of agricultural and industrial activities led to a continuous increase in the demand for earth's limited supply of freshwater. In this context, protection of natural water resources and development of new technologies for water and wastewater treatment became key environmental issues of the 21st century. On the other hand, the increasing awareness of the limited availability of Earth-abundant fossil raw materials currently stimulates numerous efforts to find benign and sustainable alternatives. Besides attempts to use more renewable as basic chemical feedstock, the sufficient supply of the growing energy demand of the world's population is one of the major challenges for science and engineering.¹ Therefore, the development of novel efficient processes to convert the energy from a renewable source is of utmost importance. Among the various resources for energy, hydrogen is of particular interest as it permits an efficient conversion of chemical energy into electrical energy using a fuel cell, while producing water as the only product.² Thus, a clear advantage of a hydrogen economy is the significant reduction in the emission of greenhouse gases.

Photocatalysis is a promising technology in the field of green technology. Photocatalysis is a catalytic process occurring at the surface of semiconductor materials under the irradiation of photons. It is an important chemical process that underpins the development of critical renewable energy and environmental technology such as photocatalytic water/air purification, hydrogen production from water splitting, and high efficiency/low cost solar cells. Currently the practical applications of this very attractive photocatalytic technique are, however, greatly restricted due to low separation probability of the photoinduced electron-hole pairs in the most stable semiconductor photocatalysts. Therefore, the big challenge for the researchers in the field of photocatalysis is to develop the photocatalysts that enhance the charge carriers separation providing industrial application for environment remediation and hydrogen production.

I.2. Water Treatment

Water is one of the most important natural resources on the planet upon which all life depends. About 75% of the earth's surface is covered by water. About 97% of the earth's

water is salt water in the oceans and 3% is fresh water contained in the poles (in the form of ice), ground water, lakes and rivers, which supply most of human and animal needs.³ Almost 69% from this tiny 3% of the world's fresh water is locked up in glaciers, icecaps, permanent snow cover of both poles, mountainous regions and in Greenland. Thirty percent of all fresh water is underground, most of it in deep, hard-to-reach aquifers. Only 0.25% of the freshwater on Earth is contained in river systems, lakes and reservoirs, which are the water we are most familiar with and the most accessible water source to satisfy human needs in our daily lives.³ Therefore, saving water to save the planet and to make the future of mankind safe constitutes a key issue for modern societies. Due to the rapid development of industrialization, population growth, society, science, technology our world is reaching to new high horizons but the cost which we are paying or will pay in near future is surely going to be too high. Rapid industrial growth and the worldwide population explosion have resulted in a large escalation of demand for fresh water, both for the household needs and for crops to produce adequate quantities of food. Besides other needs the demand for water has increased tremendously with agricultural, industrial and domestic sectors consuming 70%, 22% and 8% of the available fresh water, respectively and this has resulted in the generation of large amounts of wastewater containing a number of 'pollutants'.⁴ One of the important classes of the pollutants is dyes. Millions of various colored chemical substances have been generated within the last century or so, 10,000 of which are industrially produced.⁵ On a global scale, over 0.7 million tons of organic synthetic dyes are manufactured each year mainly for use in the textile, leather goods, industrial painting, food, plastics, cosmetics, and consumer electronic sectors.⁶ About 1–20% of the total global production of dyes is lost during the dyeing process and is released into the environment as textile effluent.^{5, 7} The impact of these dyes on the environment is a major concern because of the potentially carcinogenic properties of these chemicals. Besides this, weathering of these organic dyes through oxidation, hydrolysis, anaerobic decoloration or other chemical reactions occurring in the wastewater phase can produce potential carcinogens which impart adverse effect on animal and human health.⁸ The wastewater which is colored in the presence of these dyes can block both sunlight penetration and oxygen dissolution, which are essential for aquatic life. Thus there is a considerable need to treat efficiently these colored effluents before discharging them to various water bodies.

I.2.1. Conventional wastewater treatment technology and their drawbacks

Various approaches on handling and decontamination of effluents have been reported in the literature.⁹ The conventional method for treating these effluents can be divided into three categories: biological, chemical and physical. These conventional methods for treatment of effluents are ineffective because either they fail to achieve complete color removal or ineffectiveness on pollutants that are not readily adsorbable or volatile. Furthermore, they have further drawbacks since they simply transfer the pollutants to another phase which again creates disposal problems. Biological treatment requires large land area and is constrained by sensitivity toward diurnal variation as well as toxicity of some chemicals, and it shows less flexibility in design and operation.¹⁰ Although many organic molecules can be degraded by this way, many others are recalcitrant due to their complex chemical structure and synthetic organic origin.¹¹ On the other hand chemical methods use huge amount of chemicals and produce large volume of sludge which itself requires treatment. This method is very expensive too. Different physical methods such as membrane filtration processes (nanofiltration, reverse osmosis, electrodialysis, . . .) and adsorption techniques are widely used. The major disadvantage of the membrane processes is that they have a limited lifetime before membrane fouling occurs and the cost of periodic replacement must thus be included in any analysis of their economic viability. Liquid phase adsorption is one of the popular methods for the removal of pollutants from wastewater. Activated carbon is widely employed as adsorbent for the treatment of water and wastewater. However, the operating cost of activated carbon adsorption is high. Problems of regeneration and difficulty in separation from the wastewater after use are the two major concerns of using this material.

I.2.2. Advanced oxidation processes (AOPs)

It has been frequently observed that pollutants not amenable to biological treatments may also be characterized by high chemical stability and/or by strong difficulty to be completely mineralized. In these cases, it is necessary to adopt reactive systems much more effective than those adopted in conventional purification processes. As a response, the development of newer eco-friendly methods of destroying these pollutants became an imperative task. Thus, over the past decade, many research efforts have been devoted around the world to develop a newer, more powerful, and very promising technique called Advanced Oxidation Processes (AOPs) to treat the contaminants of drinking water and industrial effluents. AOPs are defined as “near ambient temperature and pressure water treatment

processes which involve the generation of hydroxyl radicals in sufficient quantity to effect water purification".¹² Although it is claimed that there are other species involved, the active species responsible for the destruction of contaminants in most cases seems to be the hydroxyl radical (OH^\bullet) which is unstable and quite reactive. Due to the instability of OH^\bullet radical, it must be generated continuously "in situ" through chemical or photochemical reactions.¹³

The hydroxyl radical (OH^\bullet) is a powerful, non-selective chemical oxidant, which acts very rapidly with most organic compounds. After fluorine, the hydroxyl radical is the second strongest known oxidant (see Table 1) having an oxidation potential of 2.8 V versus NHE (Normal Hydrogen Electrode).¹⁴ It is able to oxidize and mineralize almost every organic molecule, yielding CO_2 and inorganic ions.

Table I-1. Oxidation potential of some oxidants.¹⁴

Species	Oxidation potential (V) vs. NHE
Fluorine	3.03
Atomic oxygen	2.42
Ozone	2.07
Hydrogen peroxide	1.78
Perhydroxyl radical	1.70
Permanganate	1.68
Hypobromous acid	1.59
Chlorine dioxide	1.57
Hypochlorous acid	1.49
Hypoiodous acid	1.45
Chlorine	1.36
Bromine	1.09
Iodine	0.54

One of the mechanisms for the oxidation of organic molecules by hydroxyl radical is the abstraction of hydrogen from organic molecules (Eq. 1).¹⁴ This reaction generates organic radicals which by addition of molecular oxygen yield peroxy radicals (Eq. 2). These intermediates initiate thermal (chain) reactions of oxidative degradation, leading finally to carbon dioxide, water, and inorganic salts. Besides hydrogen abstraction, electron transfer to hydroxyl radicals (Eq. 3) constitutes another mechanism of oxidative degradation. Reaction (3) combined with a subsequent proton transfer can hardly be differentiated from Eq. 1.



The reaction scheme demonstrates clearly that rate and efficiency of oxidative degradation processes, which are primarily based on the production and the reactivity of radical intermediates, depend on the energy needed in order to homolyze a given chemical bond, and to a large extent on the concentration of dissolved molecular oxygen.¹⁴

AOPs can be classified into two main groups: (1) Non-photochemical AOPs and (2) Photochemical AOPs. Non-photochemical AOPs include cavitation,¹⁵ Fenton¹⁶ and Fenton-like processes,¹⁷ ozonation at high pH,¹⁸ ozone/hydrogen peroxide,¹⁹ wet air oxidation²⁰ etc. Photochemical oxidation processes include (i) homogenous processes such as vacuum UV photolysis,²¹ UV/H₂O₂,²² UV/O₃,²³ UV/ O₃/ H₂O₂,²⁴ photo-Fenton,²⁵ etc, and heterogeneous photocatalysis processes.²⁶

1.2.3. Heterogeneous photocatalysis

Among the AOPs, heterogeneous photocatalytic process utilizing the near UV radiation to photo-excite a semiconductor catalyst in the presence of oxygen has received considerable attention as a promising method for degrading both aquatic and atmospheric organic contaminants. This process involves the acceleration of photoreaction in the presence of semiconductor photocatalysts. The process is heterogeneous because there are two active phases, solid and liquid. Photocatalysis differs from other AOPs because it employs low energy UV-A light, and reusable catalysts, and it does not require addition of any other strong oxidants. This process can also be carried out utilizing the near part of solar spectrum (wavelength shorter than 380 nm) what transforms it into a good option to be used at big scale. One of the major applications of heterogeneous catalysis is photocatalytic oxidation to achieve partial or total mineralisation of gas phase or liquid phase contaminants to benign substances. The oxidizing species generated in photocatalytic process are either bound hydroxyl radicals or free holes. Even though degradation begins with a partial degradation, the term photocatalytic degradation usually refers to complete photocatalytic oxidation or photomineralisation, essentially to CO₂, H₂O, NO₃⁻, PO₄³⁻ and halide ions.²⁷ The advantages of heterogeneous photocatalysis process over other conventional methods can be summarized as follows: (i) the processes can be carried out under ambient condition (temperature and pressure); (ii) the process uses atmospheric oxygen as oxidant and no other

expensive oxidizing chemical is required; (iii) the oxidant is strong and less selective which leads to complete mineralization of almost all organic pollutants in wastewater; (iv) this process is known as green technology because degradation products (carbon dioxide, water and mineral acids) show moderate toxicity; (v) no residue of the original material remains and therefore no sludge requiring disposal to landfill is produced in this process; (vi) in addition, this process can be carried out at extremely low concentrations because the pollutants is strongly adsorbed on the surface of the catalyst, allowing sub part-per-million condition; (vii) the photocatalysts are cheap, non-hazardous, stable, biologically and chemically inert, insoluble under most conditions and reusable.

Summing up all these benefits and advantages, heterogeneous photocatalysis provides a cheap and effective alternative to clean water production and environmental remediation.

I.2.3.1. Electronic structure of semiconductor photocatalysts

For a better understanding of the subsequent discussions, it will be crucial to clarify a few fundamental definitions that are the most relevant to this context. An isolated atom exhibits discrete electronic energy states characterized by the quantum numbers n (shells), l (subshells), m_l (number of states in each subshell) and m_s (spin moment, $+1/2$ and $-1/2$). If two atoms are in close proximity, the electrons surrounding each atom start to interfere with each other, starting with the electrons of the outer shell. Each energy level will split into two due to the Pauli Exclusion Principle that states that each quantum state can be occupied by no more than one electron in an electron system such as an atom, molecule, or crystal. A solid is an assembly of a huge number N of atoms instead of the two atoms. As a consequence, when N atoms are brought close together, the energy levels that were identical in isolation split into N closely spaced but distinct energy levels.²⁸ Since the maximum and minimum energy allowed for each orbital is not dependent on the number of atoms but on nearest-neighbor interactions, the energy “width” over which these levels can split is limited. When N becomes large, the levels are so closely spaced that it is possible to consider them as a continuum of energetic states forming an “electronic energy band”. **Figure I-1** shows the change of the electronic structure of a semiconductor compound as the number N of monomeric units present increases from unity to clusters of more than 2000 units.²⁹ Thus, the electronic energy structure within a semiconductor consists of three distinguished regimes, i.e., the conduction band (CB), the valence band (VB) and the forbidden band. The forbidden band represents a region in which, for an ideal, undoped semiconductor, energy states do not exist. Energy

states only exist above and below this region. Taking the energy level of the electron in the vacuum as reference and as the uppermost level, the upper band is called the conduction band, and the lower one the valence band. In terms of energy, the difference between the upper edge of the valence band and the lower edge of the conduction band is called the band gap (E_g) of the semiconductor. The valence band is completely filled and the electrons cannot move along this band. On the other hand, conduction band is completely empty and has no electron to move. It requires applied energy to promote electron from valence band to conduction band, and since the band gap energy is different for different semiconductors, the required energy is also different for different semiconductors.

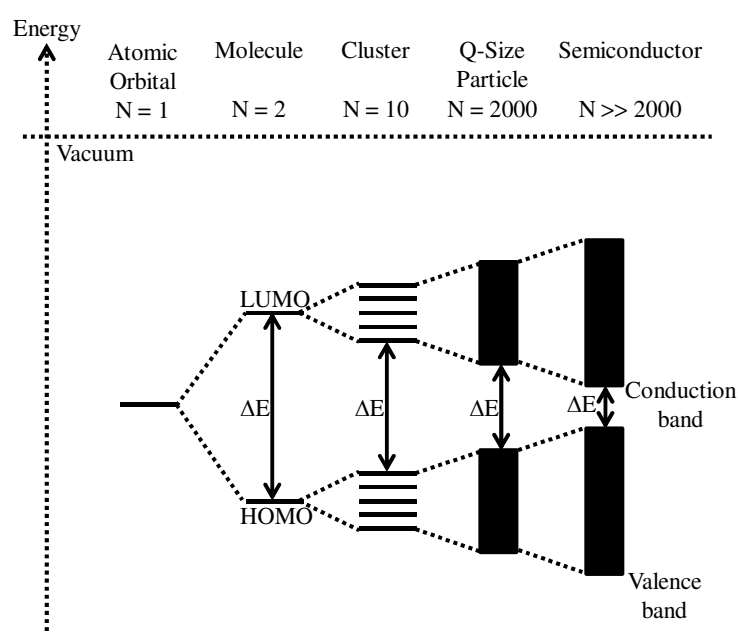


Figure I-1: Change of the electronic structure of a semiconductor compound as the number N of monomeric units present increases from unity to clusters of more than 2000 units.²⁹

The electron in the valence band can be excited thermally or optically. Under thermal excitation electrons are promoted from the valence band to the conduction band, with the concomitant formation of an equal number of holes in the valence band. In addition, light absorption by semiconducting materials lead to the generation of electron-hole pairs. The magnitude and the energy of the absorption process depend on the band structure of the semiconductor.

I.2.3.2. Basic principle of photocatalysis

In the photocatalytic oxidation process, organic pollutants are destroyed in the presence of semiconductor photocatalysts (e.g., TiO_2 , ZnO), an energetic light source, and an

oxidizing agent such as oxygen or air. The first step in the heterogeneous photocatalysis of organic and inorganic compounds is the interaction of semiconductor with light which results in the generation of electron-hole pairs in the semiconductor particles. When a semiconducting photocatalyst is illuminated with light the energy of which is equal to or greater than the band-gap energy, light is absorbed by the semiconductor and the valence band electrons are excited to the conduction band, leaving a positive hole in the valence band (Figure I-2).³⁰

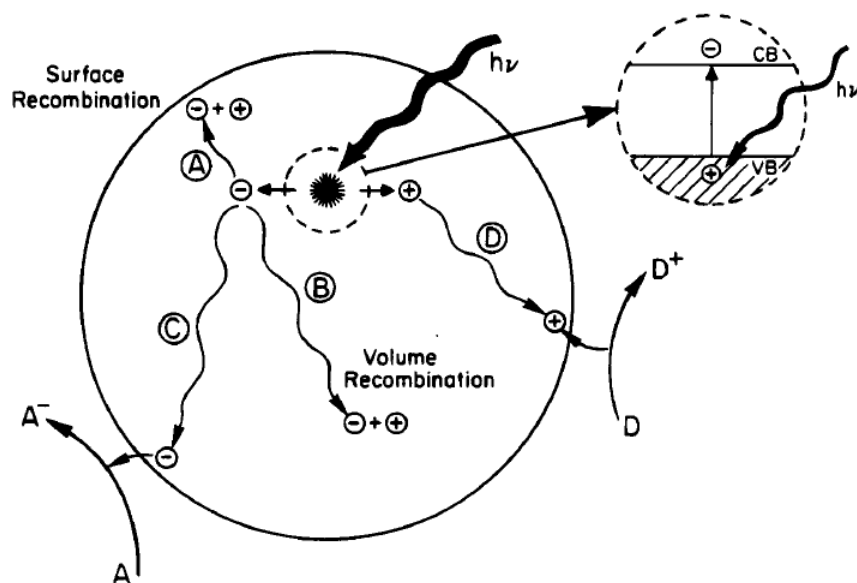


Figure I-2: Schematic photoexcitation in a semiconductor photocatalyst followed by deexcitation pathways.^{29, 31}

The excited state conduction-band electrons and valence-band holes can then follow several pathways. The photoinduced electrons transfer to adsorbed organic or inorganic species or to the solvent results from migration of electrons and holes to the semiconductor surface. The electron transfer process is more efficient if the species are pre-adsorbed on the surface.³² While at the surface the semiconductor can donate electrons to reduce an electron acceptor (usually oxygen in an aerated solution) (pathway C), a hole can migrate to the surface where an electron from a donor species can combine with the surface hole oxidizing the donor species (pathway D). The probability and rate of the charge transfer processes for electrons and holes depends on the respective positions of the band edges for the conduction and valence bands and the redox potential levels of the adsorbed species.

In competition with charge transfer to adsorbed species is electron and hole recombination. Recombination of the separated electron and hole can occur in the volume of

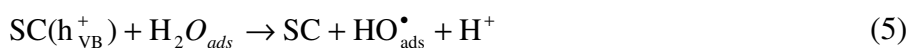
the semiconductor particle (pathway B) or at the surface (pathway A) with the simultaneous release of heat.

Oxygen is the usual electron acceptor employed in studies aimed at using of semiconductor photocatalysis for environmental cleaning; its role in these reactions has been the focus of attention of several theoretical and experimental studies.³³ It is generally admitted that photogenerated electrons can reduce molecular oxygen to $O_2^{\bullet-}$,³⁴ which can be subsequently transformed into other chemical species, such as HO_2^{\bullet} , HO_2^- , H_2O_2 , and possibly HO^{\bullet} radicals.^{31,35} These activated oxygen species may take part in the oxidation of the organic electron donor.^{35, 36} On the other hand, photogenerated holes can oxidize the electron donor (also referred to as the “hole scavenger”), either via the formation of reactive species such as surface-bound HO^{\bullet} radicals or through direct reaction with adsorbed organic molecules.³⁷ Together, these reactions can ultimately result in the complete photomineralization of the organic compounds to carbon dioxide, water, and mineral acids.

I.2.3.3. Mechanism of generating oxidizing species

The heterogeneous photocatalysis is a complex sequence of reactions. The oxidizing pathway is not yet fully understood. In classical heterogeneous photocatalytic process, the reaction itself occurs in the adsorbed phase and the overall process can be decomposed into five independent steps:³⁰ (i) mass transfer of the reactants in the liquid phase to the surface of catalyst; (ii) adsorption of the reactants onto the photon activated catalyst surface (i.e. surface activation by photon energy occurs simultaneously in this step); (iii) photocatalysis reaction for the adsorbed phase on the catalyst surface; (iv) desorption of the products from the catalyst surface; (v) desorption of the products from the surface of the catalysts.

There are two pathways through which OH radical can be formed. The valence band hole (h_{VB}^+) can either react with the adsorbed water or the adsorbed hydroxyl groups (OH^-) on the semiconductor photocatalysts (SC) as shown by Eq. (5) and Eq. (6), respectively.³⁸



To oxidize hydroxide ions or water, the oxidation potential for reaction (5) and (6) must lie above (i.e., be more negative than) the upper energy level position of the semiconductor valence band.

It is generally accepted that oxygen plays an important role in photocatalysis. Oxygen can trap conduction band electrons to form superoxide ion $O_2^{\bullet-}$ as shown in Eq. (7). These superoxide ions can react with hydrogen ions (formed by water splitting), forming HO_2^{\bullet} .



H_2O_2 could also be formed from HO_2^{\bullet} species according to the following reaction



The photogenerated hydrogen peroxide undergoes further decomposition to yield hydroxyl radicals.



It should be mentioned that it takes three electrons to produce one hydroxyl radical through the above pathway, but it takes only one hole to produce a hydroxyl radical from adsorbed water or hydroxyl group. Therefore, most of the hydroxyl radicals are generated through hole reactions. Nonetheless, the presence of electron scavengers (adsorbed oxygen) is vital for prolonging the recombination and successful functioning of the photocatalysis process. Eq. (7) depicts how the presence of oxygen prevents the recombination of electron-hole pairs, while allowing the formation of superoxide radicals. On the other hand, without the presence of water molecules, the highly reactive hydroxyl radicals could not be formed and impede the photodegradation of liquid phase organics. This was evidenced from a few reports that the photocatalytic reaction cannot proceed in the absence of water molecules.³⁹

The hydroxyl radical generated from the oxidation of adsorbed water where it is adsorbed as OH^- is the primary oxidant for the degradation of organic pollutants. Oxidation of organic compounds proceeds through a number of free radical reactions, producing a large number of intermediates, which in turn, undergo oxidative cleavage, ultimately resulting in

the formation of carbon dioxide, water and inorganic ions. In the photocatalytic degradation of pollutants, when the reduction process of oxygen and the oxidation of pollutants do not advance simultaneously, there is an electron accumulation in the CB, thereby causing an increase in the rate of recombination of e_{CB}^- and h_{VB}^+ .^{29,30}

I.2.3.4. Photocatalysts and its requirement for photocatalysis

The band edge position of the semiconductor is one of the most important and useful parameters that must be considered for using as photocatalyst. Knowledge of the band positions or flat band potentials is useful in as much as they indicate the thermodynamic limitations for the photoreactions that can be carried out with the charge carriers. The ability of a semiconductor to undergo photoinduced charge carrier transfer to adsorbed species on its surface is governed by the band energy positions of the semiconductor and the redox potentials of the adsorbed species. The energy level at the bottom of the conduction band is actually the reduction potential of photoelectrons and the energy level at the top of the valence band determines the oxidizing ability of photoholes, each value reflecting the ability of the system to promote reductions and oxidations, respectively.⁴⁰ The flatband potential which is fixed by the nature of the material and the proton exchange equilibria, determines the energy of the two charge carriers at the interface. From a thermodynamic point of view, adsorbed couples can be reduced photocatalytically by conduction band electrons if they have redox potentials more positive than the flat band potential of the conduction band and can be oxidized by valence band holes if they have redox potentials more negative than the flatband potential of the valence band.^{31,41} However, the primary criteria to get a good semiconductor photocatalysts for organic compound degradation are that the redox potential of the H_2O/OH^\bullet ($HO^- = OH^\bullet + e^-$, $E^0 = -2.8$ V) couple lies within the band gap domain of the material and that they are stable over prolonged periods of time.²⁹ An ideal photocatalyst should possess the following characteristics: (i) photoactive; (ii) have the ability to utilize visible and/or near-UV light; (iii) biologically and chemically inert; (iv) photostable (not prone to photoanodic corrosion); (v) inexpensive and (vi) non-toxic.⁴² The band edge positions of several commonly used semiconductors are presented in Figure I-3. It should be noted here that although bulk electronic structure of the semiconductors changes faintly with the pressure and temperature, the pH of the electrolyte used during the study influences the band edge position of the various semiconductors compared to the redox potentials for the adsorbate.

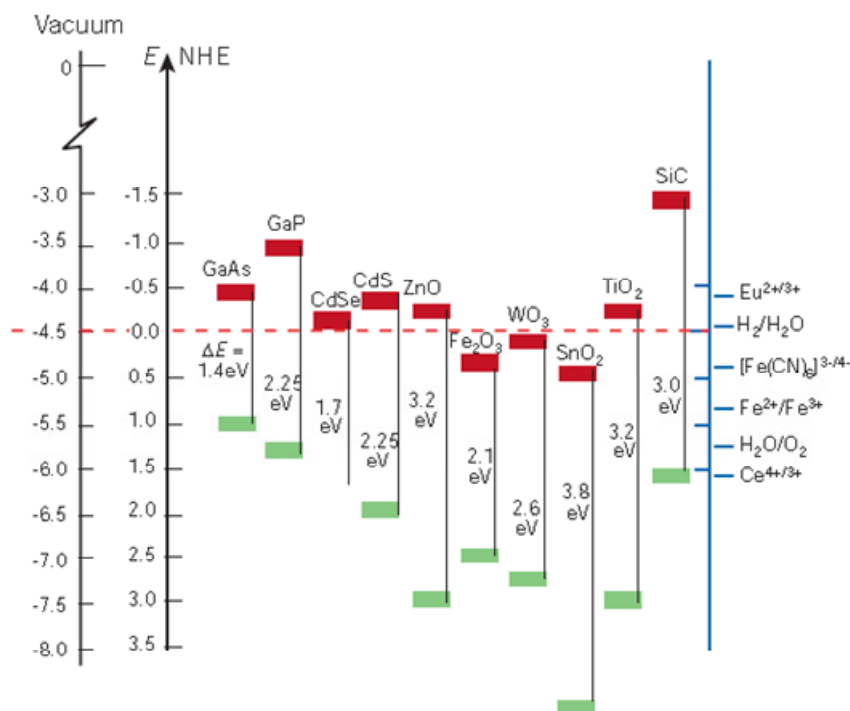


Figure I-3: Band position of commonly used semiconductors in aqueous electrolyte at pH 1.⁴³

In view of the utilization of energy (solar or UV light), semiconductors with lower band gap energy are more desired; however, the low band gap semiconductors usually suffer from serious stability problems. Such semiconductors show a tendency towards photoanodic corrosion. In the case of p-type semiconductor, the band gaps are too small and most suffer from seriously stability problems. As a result, p-type semiconductors are rarely used in semiconductor photocatalysis. It is generally found that only n-type semiconducting oxides are stable towards photoanodic corrosion, although such semiconductors usually have so large bandgaps that they can only absorb UV light.

Among the semiconductors shown in Figure I-3, some oxide and chalcogenides have enough band gap energies to be excited by UV or visible light, and the redox potentials of the edges of the valence band and conduction band can promote a series of oxidative and reductive reaction. Nonetheless, some of the candidates do not have long term stability in aqueous media. For example, the metal sulphide semiconductors, especially cadmium sulphide (CdS) and zinc sulphide (ZnS), are unstable since they undergo photoanodic corrosion, while hematite (α -Fe₂O₃), although absorptive in the visible region, is not a suitable semiconductor because of photocathodic corrosion.⁴⁴ Tungsten oxide (WO₃) can also be activated in the visible region but it is generally less photocatalytically active than titanium dioxide (TiO₂). However, TiO₂ is so far the most useful photocatalyst for widespread

environmental application, owing to its outstanding optical and electronic properties, chemical stability, non-toxicity and low cost.

TiO₂ exists mainly in three different crystalline forms: rutile (tetragonal), anatase (tetragonal) and brookite (orthorombic).⁴⁵ Rutile is the thermodynamically stable form, whereas anatase and brookite are metastable and are readily transformed to the thermodynamically stable rutile upon calcination at temperatures exceeding ~ 600 °C.⁴⁶

I.3. Hydrogen production

Energy production and environmental challenges are paramount issues in the 21st century. If the current birth rates remain at their current levels, the global population is predicted to reach 10 billion people by 2100, and primary energy consumption is projected to increase exponentially.⁴⁷ Total worldwide annual primary energy consumption was 532.8 exajoules (532.8×10^{18} joule) in 2008. It is expected to approach 770 exajoules by the year 2035 due to global production and population.⁴⁸ Fossil fuels such as oil, coal and natural gas play an important role to meet this huge demand in the development of global economy, providing all the energy for industry, agriculture, transportation and daily life. About 80 percent of the world total primary energy supply derived from the combustion of the fossil fuels. Thus, it is foreseeable that excessive exploration and over consumption of fossil fuels resulting from the rapid growth of world economy and the on-going increase of the world population will cause a depletion of limited fossil energy resources in near future. On the other hand, emission of pollutants, such as CO_x, NO_x, SO_x, soot, ash, droplets of tars, and other organic compounds resulting from the combustion of fossil fuels has caused enormous global climate problems, including the greenhouse effect, acid rain and other air pollution problems. To effectively address the depletion of fossil fuels and the serious environmental problem accompanying their combustion, modern society has been searching for a new form of energy that should, in principle, be a clean, renewable, cheap, safe, and viable alternative to fossil fuels and nuclear energy. So far, many forms of sustainable energy such as wind, geothermal, hydroenergy, and solar energy have been used. In particular, solar energy is one of the best sources of renewable energy as the energy from solar radiation accounts for a total of 5.457×10^{18} MJ annually.⁴⁹

One important clean fuel that has received a great deal of attention over the past few decades is hydrogen. Hydrogen is the simplest element and the most abundant gas in the universe. Hydrogen can be easily used in fuel cells for the generation of electricity without

emission of CO₂ emission. Moreover, H₂ molecules have higher energy content per weight than coal and gasoline.⁵⁰ The energy yield of hydrogen gas is as high as 122 kJg⁻¹, which is 2.75 times higher than that of hydrocarbon fuels, and 5 times higher than that of methanol and ethanol.⁵¹ Thus, hydrogen is considered as a viable alternative fuel and energy carrier for the future.

At present, about 95% of hydrogen consumed in the world is mainly produced from fossil fuels by steam reforming and thermal cracking of natural gas, coal gasification and electrolysis. The fossil resources are not feasible hydrogen resources since they cannot be replenished with the time scale of our lifetime and the additional emission of carbon dioxide from them will exceed the natural capacity and contribute to the global warming. Thus, the hydrogen produced in such ways cannot be regarded as a really environmentally benign fuel. Therefore, the best way of producing hydrogen is to utilize an alternative energy, such as hydropower, wind energy, and solar energy, to carry out the water-splitting reaction. Among these alternative energies, solar energy is the most promising approach since region-related limitations are less rigorous as compared to wind energy and hydropower. Hydrogen production via solar water splitting generally can be categorized into 3 types: (1) thermochemical water splitting; (2) photobiological water splitting, and (3) photocatalytic water splitting.⁵² Among these, photocatalytic water splitting is the most promising technology to produce “clean” hydrogen. In comparison with thermochemical and photobiological water-splitting techniques, it shows the following advantages: (1) reasonable solar-to-hydrogen efficiency; (2) low process cost; (3) the ability to achieve separate hydrogen and oxygen evolution during reaction; and (4) small reactor systems suitable for household applications, thus providing for a huge market potential.⁵²

Using a powdered photocatalyst for water splitting is the simplest method, as shown in **Figure I-4**. In a process that mimics photosynthesis, photocatalyst powders dispersed in water absorb solar energy and convert water into H₂ and O₂. Even though the separation of H₂ and O₂ evolved from the water splitting reaction is a disadvantage, the problem can be solved by using a Z-scheme photocatalyst system. Furthermore, powdered photocatalysts have an advantage for large-scale application of water splitting because of its simplicity. Therefore, H₂ from photocatalytic water splitting is a green and sustainable chemistry which can overcome energy and environmental issues resulting in an energy revolution.

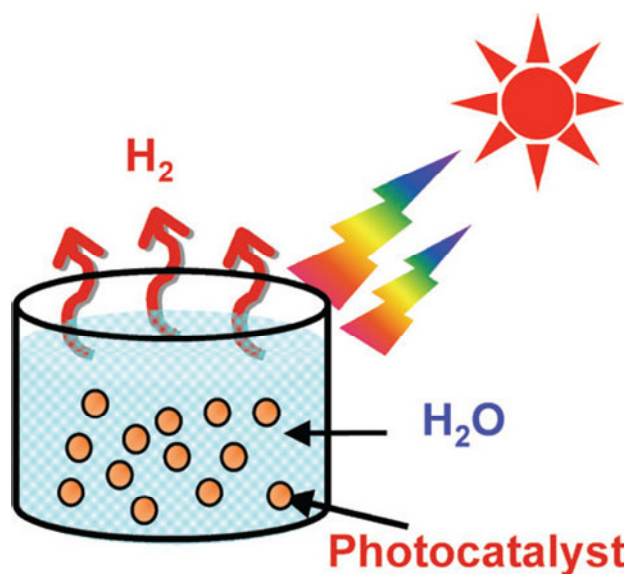
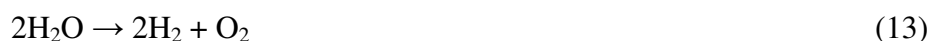


Figure I-4: Photocatalytic hydrogen production from water using a powder photocatalyst.

I.3.1.1. Photocatalytic water splitting

Catalytic splitting of pure water into H₂ and O₂ is a typical uphill reaction involving a large positive change in the Gibbs free energy ($\Delta G^\circ = +237 \text{ kJ mol}^{-1}$).



The half-reactions are described as follows



The water-splitting reaction is the conversion of photon energy into chemical energy accompanied with a largely positive change in the Gibbs free energy (Eq. 13). It mimics the photosynthesis of green plants. Therefore, photocatalytic water splitting has the perspective of an artificial photosynthesis in chemistry. Based on the Gibbs free energy change of uphill reactions, photocatalytic water splitting is distinguished from photocatalytic degradation reactions such as photo-oxidation of organic compounds using oxygen molecules that are generally downhill reactions.⁵³

I.3.1.2. Basic principle of photocatalytic hydrogen generation

The Honda–Fujishima effect of water splitting using a TiO₂ electrode was reported in the early 1970s, where TiO₂ electrode irradiated with UV light generated electrons and holes.⁵⁴ The photogenerated electrons reduced water to form H₂ on a platinum (Pt) counter electrode while holes oxidized water to form O₂ on the TiO₂ electrode with some external

bias by a power supply or pH difference between a catholyte and an anolyte. This concept, which emerged from the use of photoelectrochemical cells with semiconductor electrodes, was later applied by Bard to the design of a photocatalytic system using semiconductor particles or powders as photocatalysts.⁵⁵

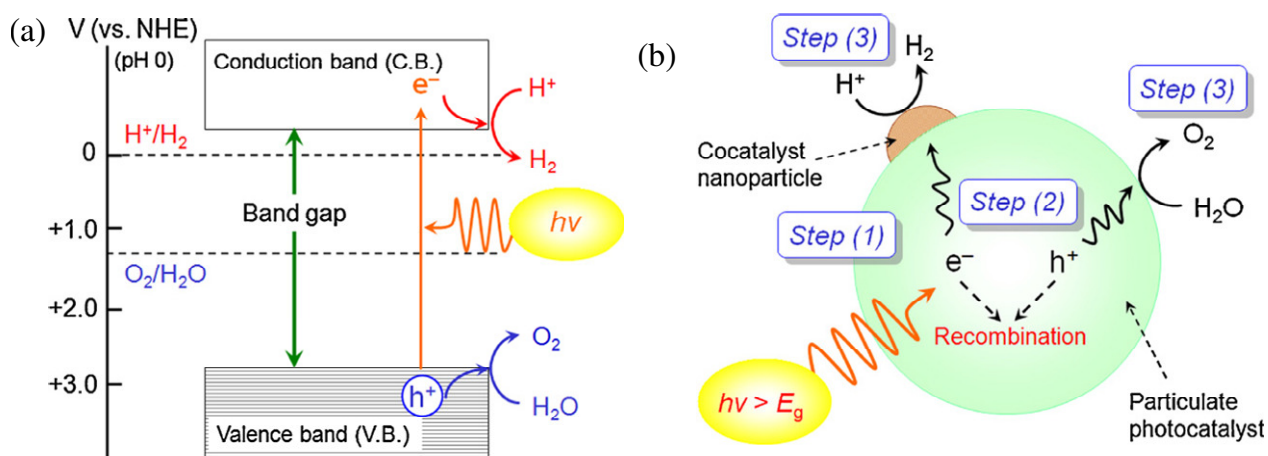


Figure I-5: (a) Basic principle of overall water splitting on a semiconductor particle⁵⁶ (b) Processes involved in photocatalytic water splitting on a semiconductor particle.⁵⁶

Figure I-5a shows a schematic illustration of the basic principles of overall water splitting on a semiconductor particle, which is essentially identical to a water-splitting PEC cell. Under irradiation with an energy equivalent to or greater than the band gap of the semiconductor photocatalyst, electrons in the valence band are excited into the conduction band, leaving holes in the valence band. The photogenerated electrons and holes cause redox reactions similarly to electrolysis. Water molecules are reduced by the electrons to form H_2 and are oxidized by the holes to form O_2 for overall water splitting. Important points in the semiconductor photocatalyst materials are the width of the band gap and levels of the conduction and valence bands. For H_2 evolution to happen, the conduction band potential of the semiconductor must be more negative than proton reduction potential of 0.0 V vs NHE at $\text{pH} = 0$ (-0.41 V at $\text{pH} = 7$). The potential of the valence band edge must be more positive than the oxidation potential of water of +1.23 V vs NHE at $\text{pH} = 0$ (+0.82 V at $\text{pH} = 7$).⁵⁷ Therefore, the minimum photon energy thermodynamically required to drive the reaction is 1.23 eV, which corresponds to a wavelength of ca. 1000 nm. However, there is an activation barrier in the charge transfer process between the photocatalyst and water molecules requiring photon energy greater than the band gap of the photocatalyst to drive the overall water-splitting reaction at a reasonable rate. In addition, the backward reaction, i.e., water formation from H_2 and O_2 , must be strictly inhibited, and the photocatalysts themselves must

be stable in the reaction. Figure I-5b shows the three processes involved in photocatalytic water splitting: (i) the electron/hole pairs are formed by excitation of the incident photon; (ii) the photogenerated charge carriers are separated and migrate to the surface of the photocatalysts; (iii) overall water splitting is achieved through the reduction of H^+ ions to H_2 by photogenerated electrons and the oxidation of H_2O to O_2 by holes, respectively. In this step, the surface sites and the state of the photocatalyst play key roles in achieving overall water splitting. Even when the potentials of the photogenerated electrons and holes are thermodynamically sufficient for water splitting, they may not be able to split water into H_2 and O_2 if the photocatalyst surface lacks active sites. Meanwhile, the reverse reaction to form water from the reaction between evolved H_2 and O_2 proceeds readily because of being downhill reaction. Therefore, some co-catalysts, such as platinum (Pt), palladium (Pd), ruthenium oxide (RuO_2) and nickel oxide (NiO_x), are usually loaded onto the photocatalyst surface as a dispersion of nanoparticles to introduce active sites for H_2 evolution.

The reaction of photogenerated H_2 and O_2 to form H_2O on the photocatalyst surface is normally called “surface back reaction”. It will inevitably have a negative effect on any enhancement of the photocatalytic activity, because it reduces the amount of H_2 emitted from the photocatalyst. Surface back reaction can be suppressed by adding sacrificial reagents or electron donor into the photocatalytic reaction environment. When the photocatalytic reaction is carried out in an aqueous solution including a reducing reagent, in other words, electron donors or hole scavengers, photogenerated holes irreversibly oxidize the reducing reagent instead of water. It enriches electrons in a photocatalyst and an H_2 evolution reaction is enhanced. Organic compounds (hydrocarbons) are widely used as electron donors for photocatalytic hydrogen production as they can be oxidized by valence band holes. The remaining strong reducing conduction band electrons can reduce protons to hydrogen molecules. Ethylenediaminetetraacetic acid (EDTA), methanol, ethanol, lactic acid and formaldehyde have been tested and proved to be effective to enhance hydrogen production.⁵⁸

I.4. Research objectives

Hydrogen produced from a renewable energy source such as water represents a green energy alternative capable of powering everything from laptops to submarines. On the other hand, the development of newer eco-friendly methods of destroying organic pollutants from air and wastewater streams became another imperative task. The technology of semiconductor-based photocatalytic water splitting to produce hydrogen and photocatalytic

degradation of organic pollutants can be considered as one of the most important approaches to solve both the world energy crisis and environment pollution. However, the main problem faced to industrialize this process is the recombination of photogenerated electron-hole pairs that result in low photocatalytic efficiency. The aim of the present work is to find a way of reducing the recombination of photogenerated charge carriers and its main objectives are:

1. To develop heterojunction photocatalyst by combining two different semiconducting metal oxides with suitable band edge position or by the combination of an oxide materials and a metal to define a vectorial charge separation.
2. To prepare heterostructure photocatalysts such as ZnO/SnO₂, RuO₂/TiO₂, RuO₂/ZnO and NiO/TiO₂ by different methods. The preparation routes used in the present study include sol-gel, precipitation and impregnation methods.
3. To perform physico-chemical characterizations of the obtained photocatalysts by FTIR, Raman spectroscopy, X-ray diffraction (XRD), nitrogen (N₂) sorption analysis, transmission electron microscopy (TEM), UV-Vis diffuse reflectance spectroscopy (DRS), X-ray photoelectron spectroscopy (XPS) and ultraviolet photoelectron spectroscopy (UPS) techniques.
4. To investigate the band energy alignment (valence band offset, conduction band offset and band bending) of the prepared heterostructures by photoemission spectroscopies (XPS, UPS) in order to prove the concepts of the approach proposed and to explain the charge transfer phenomena occurring at the interfaces in the different systems studied.
5. To investigate the photocatalytic activity of the prepared photocatalysts for the degradation of organic dyes (methylene blue and methyl orange) under UV light by varying different parameters including composition of the photocatalysts and pH. The stability and the recyclability of the prepared catalysts will also be investigated by cycling use.
6. To study the photocatalytic activity for hydrogen generation under UV light using methanol as sacrificial reagent.

- ¹ (a) Arakawa, H. *Chem. Rev.* **2001**, *101*, 953. (b) Schiermeier, Q.; Tollefson, J.; Scully, T.; Witze, A.; Morton, O. *Nature* **2008**, *454*, 816. (c) Armaroli, N.; Balzani, V. *Angew. Chem.* **2007**, *119*, 52. (d) Armaroli, N.; Balzani, V. *Angew. Chem. Int. Ed.* **2007**, *46*, 52.
- ² (a) Murray, M. L.; Seymour, E. H.; Pimenta, R. *Int. J. Hydrogen Energy* **2007**, *32*, 3223. (b) Lattin, W. C.; Utgikar, V. P. *Int. J. Hydrogen Energy* **2007**, *32*, 3230. (c) Crabtree, G. W.; Dresselhaus, M. S.; Buchanan, M. V. *Phys. Today* **2004**, *57*, 39.
- ³ Kalogirou, S. A. *Prog. Energy Combust. Sci.* **2005**, *31*, 242. (b) U. S. Geological Survey, **2009**.
- ⁴ (a) Shiklamov, I. "World Water Resources. A New Appraisal and Assessment for the 21st century." A Summary of the Monograph World Water Resources prepared in the Framework of the International Hydrological Programme, **1998**. (b) 4th UN World Water Development Report, **2012**.
- ⁵ Zollinger, H. *Color Chemistry, Syntheses, Properties and Applications of Organic Dyes and Pigments*, 2nd rev. ed., VCH, Weinheim, Germany, **1991**.
- ⁶ Rajeshwara, K.; Osugi, M. E.; Chanmanee, W.; Chenthamarakshan, C. R.; Zanoni, M. V. B. Kajitvichyanukul, P.; Ayer, R. K. *J. Photochem. Photobiol. C* **2008**, *9*, 171.
- ⁷ (a) Houas, A.; Lachheb, H.; Ksibi, M.; Elaloui, E.; Guillard, C.; Herrmann, J. M.; *Appl. Catal. B* **2001**, *31*, 145. (b) Rafols, C.; Barcelo, D. *J. Chromatogr. A* **1997**, *777*, 177. (c) Weber, E. J.; Stickney, V. C. *Water Res.* **1993**, *27*, 63.
- ⁸ (a) Prevot, A. B.; Baiocchi, C.; Brussino, M. C.; Pramauro, E.; Savarino, P.; Augugliaro, V.; Marci, G.; Palmisano, L. *Environ. Sci. Technol.* **2001**, *35*, 971. (b) O'Neill, C.; Lopez, A.; Esteves, S.; Hawkes, F. R.; Hawkes, D. L.; Wilcox, S. *Appl. Microbiol. Biotechnol.* **2000**, *53*, 249.
- ⁹ Robinson, T.; Marchant, R.; Nigam, P. *Bioresour. Technol.* **2001**, *77*, 247.
- ¹⁰ Bhattacharyya, K. G.; Sarma, A.; *Dyes Pigments*, **2003**, *57*, 211.
- ¹¹ Kumar, M. N. V. R.; Sridhari, T. R.; Bhavani, K. D.; Dutta, P. K. *Colorage*, **1998**, *45*, 25.
- ¹² Glaze, W. H.; Kang, J. W.; Chapin, D. H. *Ozone: Sci. Eng.* **1987**, *9*, 335.
- ¹³ Oliver, J. H.; Hyunook, K.; Chi, C. P.; *Crit. Rev. Environ. Sci. Technol.* **2000**, *30*, 499.
- ¹⁴ Legrini, O.; Oliveros, E.; Braun, A. M. *Chem. Rev.* **1993**, *93*, 671.
- ¹⁵ (a) Adewuyi, Y. G. *Ind. Eng. Chem. Res.* **2001**, *40*, 4681. (b) Hoffmann, M. R.; Hua, I.; Höchemer, R. *Ultrason. Sonochem* **1996**, *3*, S163. (c) Petrier, C.; Jiang, Y.; Lamy, M. F. *Env. Sci. Technol* **1998**, *32*, 1216. (d) Petrier, C.; Francony, A. *Wat. Sci. Tech.* **1997**, *35*, 175. (e) Cheung, H. M.; Bhatnagar, A.; Jansen, G. *Environ. Sci. Technol.* **1991**, *25*, 1510.
- ¹⁶ (a) Fenton, H. J. H. *J. Chem. Soc.* **1894**, *65*, 899. (b) Walling, C. *Acc. Chem. Res.* **1975**, *8*, 125. (c) Masarwa, A.; Calis, S. R.; Meyerstein, N.; Meyerstein, D. *Coord. Chem. Rev.* **2005**, *249*, 1937. (d) Chamarro, E.; Marco, A.; Esplugas, S. *Water Res.* **2001**, *35*, 1047. (e) Bouasla, C.; Samar, M. E. H.; Ismail, F. *Desalination* **2010**, *254*, 35. (f) Casero, I.; Sicilia, D.; Rubio, S.; Bendito, D. P.; *Water Res.* **1997**, *31*, 1985.

- ¹⁷ (a) Pignatello, J. J. *Environ. Sci. Technol.* **1992**, *26*, 944. (b) Ensing, B.; Buda, F.; Baerends, E. J. *J. Phys. Chem.* **2003**, *107*, 5722.
- ¹⁸ (a) Hoigne J., Chemistry of aqueous ozone and transformation of pollutants by ozonation and advanced oxidation processes. In: The handbook of environmental chemistry, Vol. 5, Part C. Hutzinger O. (ed.). Berlin, Springer-Verlag: **1998**. (b) Tehrani-Bagha, A. R.; Mahmoodi, N. M.; Menger, F.M. *Desalination*, **2010**, *260*, 34.
- ¹⁹ Ijpelaar, G. F.; Meijers, R. T.; Hopman, R.; Kruithof, J. C. *Ozone Sci. Eng.* **2000**, *22*, 607.
- ²⁰ (a) Baillod, C. R.; Lamparter, R. A.; Barna, B. A. *Chem. Eng. Prog.* **1985**, *81*, 51. (b) Mishra, V.; Mahajani, V.V.; Joshi, J.B. *Ind. Eng. Chem. Res.* **1995**, *24*, 2. (c) Dietrich, M. J.; Randall, T. L.; Canney, P. J. *Environ. Prog.* **1985**, *4*, 171. (d) Alaton, I. A.; Ferry, J.; *Dyes Pigm.* **2002**, *54*, 25.
- ²¹ (a) Gonzalez, M. G.; Oliveros, E.; Worner, M.; Braun, A. M. *J. Photochem. Photobiol. C* **2004**, *5*, 225. (b) Oppenländer, T.; Gliese, S. *Chemosphere*, **2000**, *40*, 15.
- ²² (a) Yang, Y.; Wyatt, D. T.; Bahorsky, M.; *Text. Chem. Color.* **1998**, *30*, 27. (b) Dein, A. M. E.; Libra, J. A.; Wiesmann, U. *Chemosphere*, **2003**, *52*, 1069. (c) Galindo, C.; Kalt, A. *Dyes Pigm.* **1998**, *40*, 27. (d) Shu, H. Y.; Huang, C. R.; Chang, M. C. *Chemosphere* **1994**, *29*, 2597.
- ²³ (a) Peyton, G. R.; Glaze, W. H. *Environ. Sci. Technol.* **1988**, *22*, 761.
- ²⁴ (a) Azbar, N.; Yonar, T.; Kestioglu, K. *Chemosphere*, **2004**, *55*, 35. (b) Perkowski, J.; Kos, L. *Fibres Text. East. Eur.* **2003**, *11*, 67. (c) Khan, H.; Ahmad, N.; Yasar, A.; Shahid, R. *Polish J. Environ. Stud.* **2010**, *19*, 83.
- ²⁵ (a) Bauer, R.; Fallmann, H. *Res. Chem. Intermed.* **1997**, *23*, 341. (b) Ruppert, G.; Bauer, R.; Heisler, G. J. *Chemosphere* **1994**, *28*, 1447. (c) Maciel, R.; Sant'Anna, Jr., G. L.; Dezotti, M. *Chemosphere* **2004**, *57*, 711. (d) Gernjak, W.; Krutzler, T.; Glaser, A.; Malato, S.; Caceres, J.; Bauer, R.; Alba, A. R. F. *Chemosphere*, **2003**, *50*, 71.
- ²⁶ (a) Howe, R. F. *Dev. Chem. Eng. Mineral Process.* **1998**, *6*, 55. (b) Chen, M. Sivakumar, M.; Ray, A. K. *Dev. Chem. Eng. Mineral Process.* **2000**, *8*, 505.
- ²⁷ Carp, O.; Huisman, C. L.; Reller, A. *Prog. Solid state Chem.* **2004**, *32*, 33.
- ²⁸ Callister, J. W. D. *Materials Science and Engineering – An Introduction*, 4th Edition. John Wiley & Sons, Inc., New York, **1997**.
- ²⁹ Hoffmann, M. R.; Martin, S. T.; Choi, W.; Bahnemann, D. W. *Chem. Rev.* **1995**, *95*, 69.
- ³⁰ Herrmann, J. M. *Catal. Today* **1999**, *53*, 115.
- ³¹ Linsebigler, A. L.; Lu, G.; Yates, J. T. *Chem. Rev.* **1995**, *95*, 735.
- ³² Matthews, R. W. *J. Catal.* **1988**, *113*, 549.
- ³³ (a) Schwitzgebel, J.; Ekerdt, J. G.; Gerischer, H.; Heller, A. *J. Phys. Chem.* **1995**, *99*, 5633. (b) Kesselman, J. M.; Shreve, G. A.; Hoffmann, M. R.; Lewis, N. S. *J. Phys. Chem.* **1994**, *98*, 13385. (c) Sukharev, V.; Kershaw, R.; *J. Photochem. Photobiol. A* **1996**, *98*, 65. (d) Ahmed, S.; Fonseca, S. M.;

- Kemp, T. J.; Unwin, P. R. *J. Phys. Chem. B* **2003**, *107*, 5892. (e) Fonseca, S. M.; Barker, A. L.; Ahmed, S.; Kemp, T. J.; Unwin, P. R. *Chem. Commun.* **2003**, 1002.
- ³⁴ (a) Remillard, J. T.; McBride, J. R.; Nietering, K. E.; Drews, A. R.; Zhang, X. *J. Phys. Chem. B* **2000**, *104*, 4440. (b) Ishibashi, K.; Fujishima, A.; Watanabe, T.; Hashimoto, K.; *J. Phys. Chem. B* **2000**, *104*, 4934. (12) Berger, T.; Sterrer, M.; Diwald, O.; Knozinger, E.; Panayotov, D.; Thompson, T.L.; Yates, J. T. *J. Phys. Chem. B* **2005**, *109*, 6061.
- ³⁵ (a) Henderson, M. A.; Epling, W. S.; Perkins, C. L.; Peden, C. H. F.; Diebold, U. *J. Phys. Chem. B* **1999**, *103*, 5328. (b) Nakamura, R.; Imanishi, A.; Murakoshi, K.; Nakato, Y.; *J. Am. Chem. Soc.* **2003**, *125*, 7443.
- ³⁶ Vinodgopal, K.; Stafford, U.; Gray, K. A.; Kamat, P.V. *J. Phys. Chem.* **1994**, *98*, 6797.
- ³⁷ (a) Rabani, J.; Yamashita, K.; Ushida, K.; StarkKira, A. J. *J. Phys. Chem. B* **1998**, *102*, 1689. (b) Micic, O. I.; Zhang, Y. N.; Cromack, K. R.; Trifunac, A. D.; Thurnauer, M. C. *J. Phys. Chem.* **1993**, *97*, 7277. (c) Micic, O. I.; Zhang, Y. N.; Cromack, K. R.; Trifunac, A. D.; Thurnauer, M. C. *J. Phys. Chem.* **1993**, *97*, 13284.
- ³⁸ Turchi, S. C.; Ollis, D. F. *J. Catal.* **1990**, *122*, 178.
- ³⁹ Chong, M. N.; Jin, Chow, C. W. K.; Saint, C. *Water Res.* **2010**, *44*, 2997.
- ⁴⁰ Serpone, N. *J. Photochem. Photobiol. A* **1997**, *104*, 1.
- ⁴¹ (a) Rajeswar, K. *J. Appl. Electrochem.* **1995**, *25*, 1067. (b) Bhatkhande, D. S.; Pangarkar, V. G.; Beenackers, A. J. *Chem. Technol. Biotechnol.* **2002**, *77*, 102.
- ⁴² Mills, A.; Hunte, S. L. *J. Photochem. Photobiol. A* **1997**, *108*, 1.
- ⁴³ Gratzel, M.; *Nature*, **2001**, *44*, 338.
- ⁴⁴ (a) Fox, M. A.; Dulay, M. T. *Chem. Rev.* **1993**, *93*, 341. (b) Pehkonen, S.; Siefert, R.; Webb, S.; Hoffmann, M. R. *Environ. Sci. Technol.* **1993**, *26*, 2056.
- ⁴⁵ Nolan, N. T.; Seery, M. K.; Pillai, S. C. *J. Phys. Chem. C* **2009**, *113*, 16151.
- ⁴⁶ Hu, Y.; Tsai, H. L.; Huangk, C. L. *Eur. Ceram. Soc.* **2003**, *23*, 691.
- ⁴⁷ World Population Prospects, United Nations Press Release, New York, **2011**, 1.
- ⁴⁸ Energy Information Administration, Annual Energy Outlook and International Energy Outlook, US Dept of Energy, Washington, DC, **2011**.
- ⁴⁹ Wakil, M. M. E. Powerplant technology, McGraw-Hill Education, Madison, **1984**.
- ⁵⁰ Wilhelm, E.; Fowler, M. A. *Bull. Sci. Technol. Soc.* **2006**, *26*, 235.
- ⁵¹ Xing, J.; Fang, W. Q.; Zhao, H. J.; Yang, H. G. *Chem. Asian J.* **2012**, *7*, 642.
- ⁵² Liao, C. H.; Huang, C. W.; Wu, J. C. S. *Catalysts* **2012**, *2*, 490.
- ⁵³ Kudo, A.; Miseki, Y. *Chem. Soc. Rev.* **2009**, *38*, 253.
- ⁵⁴ Fujishima, A.; Honda, K. *Nature* **1972**, *238*, 37.

⁵⁵ (a) Bard, A. J. *J. Photochem.* **1979**, *10*, 59. (b) Bard, A. J. *Science* **1980**, *207*, 139. (c) Bard, A. J. *J. Phys. Chem.* **1982**, *86*, 172.

⁵⁶ Maeda, K.; Domen, K.; *J. Phys. Chem. C* **2007**, *111*, 7851.

⁵⁷ Osterloh, F. E. *Chem. Mater.* **2008**, *20*, 35.

⁵⁸ (a) Bamwenda, G. R.; Tsubota, S.; Nakamura, T. ; Haruta, M. *J. Photochem. Photobiol. A* **1995**, *89*, 177. (b) Wu, N. L.; Lee, M. S. *Int. J. Hydrogen Energy* **2004**, *29*, 1601. (c) Li, Y. X.; Lu, G. X.; Li, S.B. *Chemosphere* **2003**, *52*, 843.

Chapter II : Literature review

II.1. Introduction

Semiconductor particles when subjected to the bandgap excitation behave as short-circuited electrodes, with both oxidation and reduction processes occurring on their surfaces.¹ Thus two critical processes determine the overall quantum efficiency for interfacial charge transfer. These are the competition between the recombination and the trapping of the charge carriers, followed by the competition between the recombination of the trapped charge carriers and the interfacial charge transfer. It is known that the charge separation/migration and recombination are two competitive processes, and the recombination of photogenerated electrons and holes is the major limitation in semiconductor photocatalysis as it reduces the overall quantum efficiency and hinders potential industrial applications.² When recombination occurs, the excited electron reverts to the valence band without reacting with adsorbed species non-radiatively or radiatively, dissipating the energy as light or heat.³

Recombination may occur either on the surface or in the bulk and is in general facilitated by impurities, defects or all factors which introduce bulk or surface imperfections into the crystal. Serpone *et al.*⁴ found that localization (trapping) of the electron as a Ti^{3+} species occurred with a time scale of about 30 ps and about 90% or more of the photogenerated electron/hole pairs recombined within 10 ns. The reduction of the recombination of photogenerated electrons and holes by accelerating their separation as well as the rapid charge transportation to their proper active sites for the redox reactions is essential for the achievement of high photocatalytic activity.

II.2. Approaches for efficient charge separation

A variety of approaches has been proposed to promote the charge separation and migration, thus resulting in reduced recombination and hence improved photocatalytic activity. The mostly used strategies are: (i) coupling of two semiconductors with different band gap energies making semiconductor/semiconductor heterostructure; (ii) surface modification by depositing redox couple or noble metal giving metal/semiconductor heterostructure; (iii) simultaneous scavenging of holes and electrons by surface adsorbed redox species; (iv) charge carrier trapping.

II.2.1. Coupled semiconductors

Coupling of two semiconductors with different band gap energies making a heterostructure semiconductor is an effective approach to promote charge separation and

minimize or inhibit charge-carrier recombination for improved photocatalytic activity. Many efforts have been made in the synthesis of different coupled semiconductors such as SnO₂-TiO₂,⁵ ZnO/TiO₂⁶ or CdS/TiO₂.⁷ The synthesized coupled semiconductors significantly enhance the photocatalytic efficiency by decreasing the recombination rate of the photogenerated electron-hole pairs and present potential application in water splitting, organic decomposition, and photovoltaic device.⁸ These composites were also considered as promising materials to develop a high efficiency photocatalyst activated with visible light. They can also compensate the disadvantages of the individual components and induce a synergistic effect such as an efficient charge separation and improvement of photostability.⁹

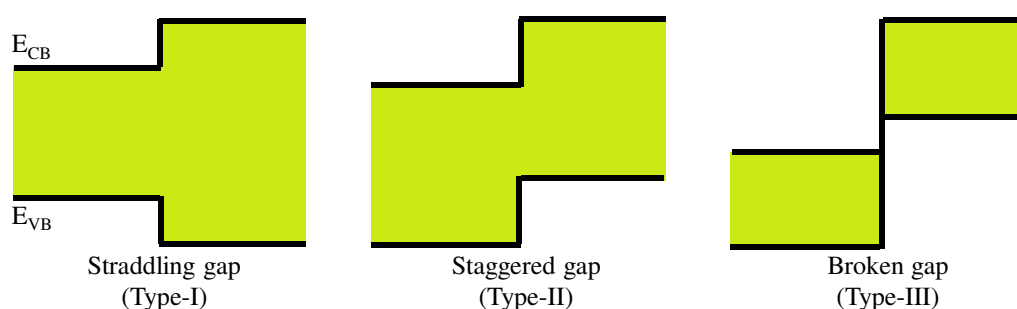


Figure II-1: Schematic energy band diagram of semiconductor heterojunctions.

According to the band alignment of the two semiconductors, the semiconductor heterostructure can be classified into three different types: straddling gap (type-I), staggered gap (type-II) and broken gap (type-III), as shown in **Figure II-1**. Considering a type-II band alignment, the energy gradient existing at the interface tends to spatially separate electrons and holes on the different sides of the heterojunctions, where electrons may be confined to one side and holes to the other side. The mechanism of the charge separation of the heterostructure photocatalysts are schematically described in **Figure II-2**. When a heterostructure photocatalyst is irradiated with UV light, electrons in the valence band (VB) are excited to the conduction band (CB) with the concomitant simultaneous generation of the same amount of holes in the valence band. Photogenerated electrons are then injected from the CB of the semiconductor with higher conduction band edge to the CB of the semiconductor with lower conduction band edge. In turn, the holes are injected in opposite direction, that increases the rate of charge separation and reduces the electron-hole pairs recombination. Depending upon the morphology, the heterostructure photocatalysts can be contact type or core/shell type. Although the charge separation mechanism in both contact type and core/shell type semiconductors is the same, the interfacial charge transfer is

significantly different.¹⁰ The charge transfer processes involved in contact type and core/shell type semiconductor systems are shown in **Figure II-2**. In contact type semiconductor system the two particles are in contact with each other and both holes and electrons are accessible for selective oxidation and reduction process on different particle surfaces. On the other hand, in core/shell type heterostructures the electrons get injected into the energy levels of the core semiconductor (if it has a conduction band potential which is lower than that of the shell). Therefore, only one charge carrier is accessible at the surface in a core/shell type semiconductor system, thus making selective charge transfer possible at the semiconductor electrolyte interface. The other charge carrier (here electron) gets trapped within the inner semiconductor particle and is not readily accessible for the reduction reaction. However, in the coupled heterostructure composite nanoparticles, no electric field is necessary, as the charge separation is achieved by the tunnelling of electrons.¹¹ It has been established that the interparticle electron transfer occurred within 500 fs-2 ps.¹²

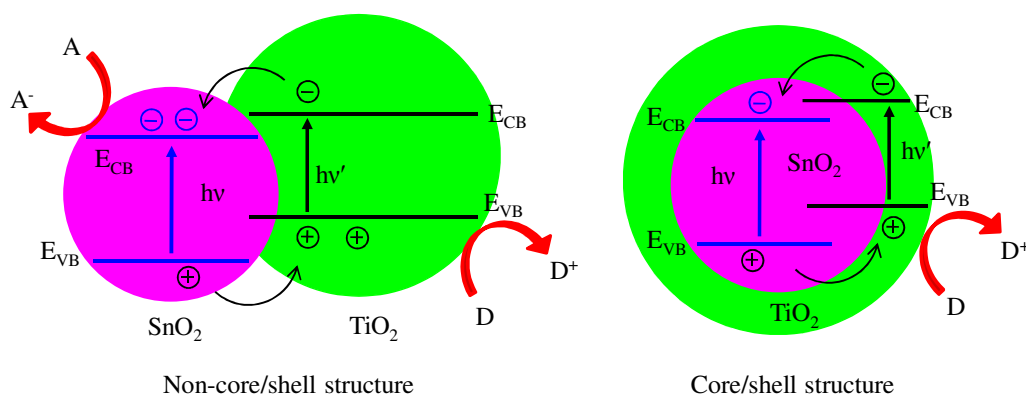


Figure II-2: Schematic illustration of charge transfer process in coupled heterostructure composites.

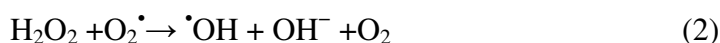
II.2.2. Metal/semiconductor heterostructure nanocomposites

Another effective method for increasing the life time of the photogenerated electron-hole pair and hence reducing their recombination is to deposit noble metals on the surface of semiconductors. Earlier investigation revealed that metal/semiconductor composites enhance the efficiency of the photocatalytic process, wherein metal deposits depending upon the work function serve as passive sink for electrons or holes, hindering the recombination. Due to different work function of the metal and semiconductor, a space charge region is created upon their contact and a built-in potential facilitate to drive the separation and transportation of photogenerated electron-hole pairs similar to that in the coupled semiconductors. The details mechanism of forming space charge region at metal/semiconductor interface will be discussed in the next section.

II.2.3. Scavenging of electrons and holes

Scavenging of photogenerated electrons or holes is another strategy to reduce the recombination and increase the photocatalytic efficiency. In the absence of suitable electron acceptor or donor, the recombination step is predominant and thus it limits the quantum yield. First of all, it is crucial to prevent the electron-hole recombination to ensure efficient photocatalysis. Dissolved molecular oxygen is generally used as an electron acceptor in heterogeneous photocatalytic reactions. Addition of external oxidant/electron acceptors into a semiconductor suspension has been shown to improve the photocatalytic degradation of organic contaminants (i) by reducing the electron-hole pairs recombination by accepting the conduction band electron; (ii) increasing the hydroxyl radical concentration and oxidation rate of intermediate compound; and (iii) generating more radicals and other oxidizing species to accelerate the degradation efficiency of intermediate compounds.¹³ Since hydroxyl radicals appear to play an important role in the photocatalytic degradation, several researchers have investigated the effect of addition of electron acceptors such as H₂O₂, potassium bromate (KBrO₃), and potassium persulfate (K₂S₂O₈) on the photocatalytic degradation of various pesticides and herbicides to enhance the formation of hydroxyl radicals as well as to inhibit the electron/hole pair recombination.^{13,14} In all cases the addition of oxidants has resulted in higher pollutant degradation rate compared to the molecular oxygen. For example, H₂O₂ can trap the photogenerated electron to stabilize the electron-hole pairs (reaction scheme 1).

Reaction scheme 1



Additional $\cdot\text{OH}$ radicals yielded via the reaction between H₂O₂ and e⁻ or O₂ \cdot (Eq. (1) and Eq. (2)) is expected to promote the degradation of pollutants. However, the excess H₂O₂ would trap the $\cdot\text{OH}$ radicals through Eq. (3) and Eq. (4).

On the other hand, adding electron donors (sacrificial reagents or hole scavengers) to react irreversibly with the photo-generated valence band holes can enhance the photocatalytic electron/hole separation resulting in higher quantum efficiency. By choosing a suitable hole scavenger the photogenerated electron can be selectively trapped in the surface states of the

semiconductor particles from which they undergo a photocatalytic reduction reaction with a dissolved reactant. Thus, in water-splitting reaction, oxygen is normally not desired in the photoreduction process as it competes with the substrate for the photogenerated electrons. Organic compounds (hydrocarbons) are widely used as electron donors for photocatalytic hydrogen production as they can be oxidized by valence band holes. The remaining strong reducing conduction band electrons can reduce protons to hydrogen molecules. EDTA, methanol, ethanol, cyanide ions (CN^-), lactic acid and formaldehyde have been tested as hole scavengers and proved to be effective to enhance hydrogen production.¹⁵ Photocatalytic decomposition of pollutants and photocatalytic production of clean hydrogen fuel can take place simultaneously when the pollutants are acted as electron donors.

II.2.4. Charge carrier trapping

Charge carrier trapping is associated with trapping the photogenerated electron, hole or both. Charge carrier trapping is an alternative technique to suppress recombination and increase the life time of electrons and holes to above a fraction of a nanosecond for efficient photocatalytic activity in a semiconductor.² During the preparation of colloidal and polycrystalline photocatalysts, surface and bulk irregularities naturally occur. The irregularities are associated with surface electron states which differ in their energy from the bands present in the bulk semiconductor. These electron states serve as charge carrier traps and may help to suppress the recombination of electrons and holes.² On the other hand, these defects may also be involved in the enhancement of recombination.

II.3. Band bending

When a semiconductor comes into contact with another phase (i.e. liquid, gas, or metal) exhibiting a different Fermi level or redox potential, electric charges at the interface are redistributed in order to equalize the chemical potential between the semiconductor and the second phase inducing the formation of a double layer.² The transfer of mobile charge carriers between the semiconductors and the contact phases or the trapping of charge carriers at surface states at the interface, produces a space charge layer which results in band bending of the semiconductor. The band bending effect influences the rate of photoinduced charge carrier separation and recombination and thus affects the photocatalytic efficiency. The electric field in the space charge region facilitates the special separation of photogenerated electron-hole pairs and depresses the recombination rate.¹⁶ Depending on the second phase, band bending can be classified as: (i) band bending at metal/semiconductor contact; (ii) band

bending at p-type semiconductor/n-type semiconductor heterojunction also called p-n junction; (iii) band bending at semiconductor/electrolyte interface; (iv) surface state induced band bending and (v) field-effect-induced band bending. Here in this section, the first three types will be discussed.

II.3.1. Band bending at metal/semiconductor contact

The interaction between two different materials with different work function can occur because of their different chemical potential. For example, the electrons can transfer from a material with lower work function (high Fermi level) to another material with high work function (low Fermi level) when they contact each other. The work function of an n-type semiconductor (Φ_s) is lower than that of the metal (Φ_m) such as Ag, Au, and Pt (**Figure II-3**). Hence, the electrons will transfer from the semiconductor to the metal until thermodynamic equilibrium is established between metal and semiconductor when they contact each other, that is, the Fermi level of the semiconductor ($E_{F,s}$) and metal ($E_{F,m}$) at the interface is the same. Under equilibrium, a double layer will be established at the metal/semiconductor interface, where the metal is negatively charged and the semiconductor is positively charged near its surface due to its electrostatic induction. As a result, the free charge carrier concentration near the semiconductor surface is depleted compared with the bulk. This region is called the space charge region and, hence, as the electron is depleted, it is also named depletion layer. If the semiconductor work function is higher than that of the metal, the electron will flow from the metal to the semiconductor and will accumulate in the space charge region. This region is called the accumulation layer. Due to built in potential between the semiconductor and metal the energy band edges in semiconductor are continuously shifted, and this phenomenon is called band bending. The energy bands bend upward toward the interface when $\Phi_m > \Phi_s$, while the edges bend downward toward the interface when $\Phi_m < \Phi_s$.

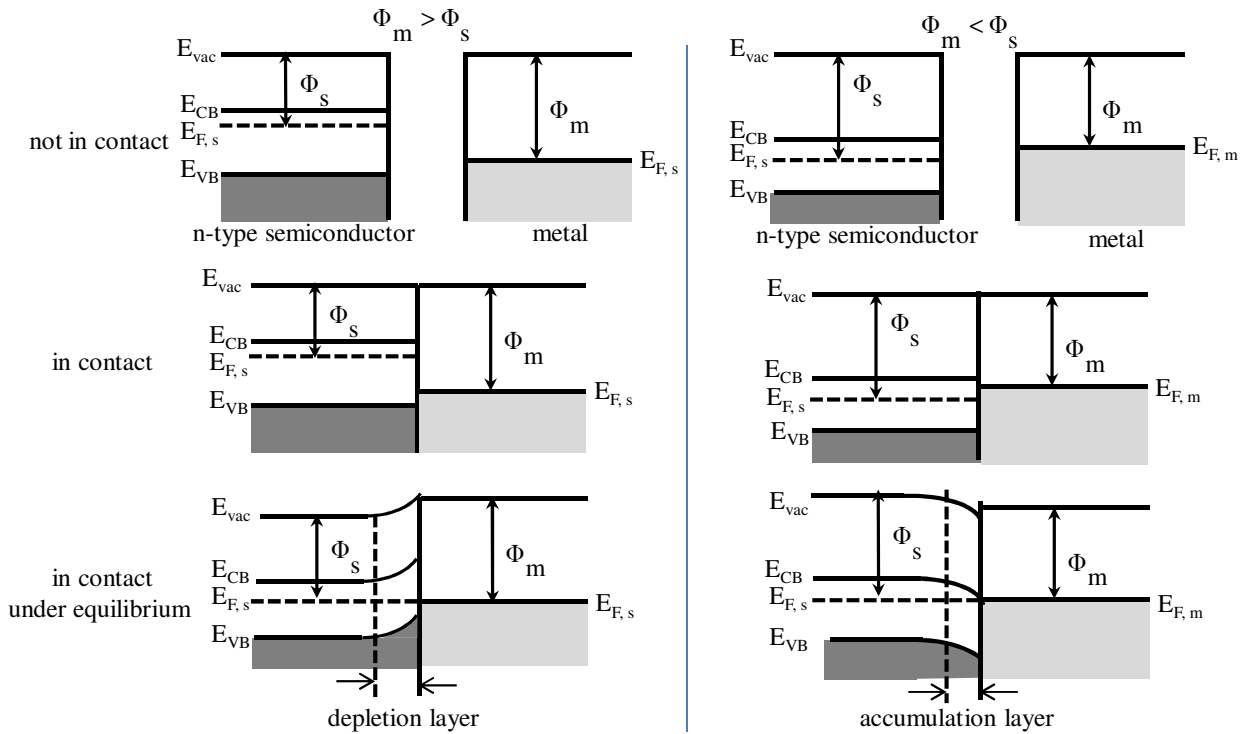


Figure II-3: Energy band diagram at metal/n-type semiconductor heterojunction.

II.3.2. Band bending at p-n junction

The Fermi level of a p-type semiconductor is lower than that of an n-type semiconductor. Thus, when they are placed into contact with each other, electrons will flow from the n-type semiconductor to p-type semiconductor and hole in the opposite direction. It causes the p-side of the junction to become negatively charged and the n-side to become positively charged, and thus to set up an electric field near the junction. Under equilibrium, the region near the junction is depleted of free carriers and a space charge configuration containing a high electric field is formed there. This space charge configuration is an electric dipole layer with positive charge toward junction of n-type semiconductor and negative charge toward the interface of p-type semiconductor. Thus, the bands of the n-type semiconductor bend upward and that of the p-type semiconductor bend downward. **Figure II-4** shows the band bending at the junction between p-type NiO and n-type TiO₂. When the p-n heterojunction is irradiated by ultraviolet (UV) light with an energy higher or equal to the band gaps of p-type and n-type semiconductor, the photogenerated electrons can move to the conduction band (CB) of the n-type semiconductors and the photogenerated holes to the valence band (VB) of the p-type semiconductor due to the formation of an inner electric field.¹⁷ Thus, the formation of a p-type/n-type semiconductor heterojunction might hinder the

recombination of the photogenerated electron-hole pairs and improve the photocatalytic efficiency.

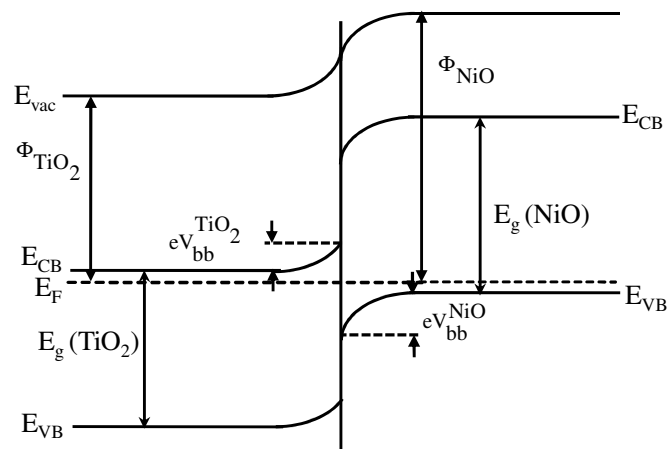


Figure II-4: Energy band diagram at the junction of TiO_2 and NiO .

II.3.3. Band bending at semiconductor/electrolyte interface

When a semiconductor is put into contact with an electrolyte (i.e. water containing organic pollutants), the electrochemical potential of the two phases must be the same. The electrochemical potential of the solution is determined by the redox potential of the electrolyte solution, and the redox potential of the semiconductor is determined by the Fermi level. If the redox potential of the solution and the Fermi level do not lie at the same energy level, a movement of charge between the semiconductor and the solution is required in order to equilibrate the two phases.¹⁸ If we assume that there is no ion diffusion through the electrode/electrolyte junction, the electrons are the only charge carriers capable to migrate through this interface in both directions. The transfer of electric charge produces a region on each side of the junction where the charge distribution differs from the bulk material, and this is known as the space charge region. Within the space charge region, an electric field is created which reflects the bending of the band edges. The mechanism of bending the band edges at the semiconductor/electrolyte interface is similar to that of the metal/semiconductor interface. Within the space charge layer, the valence and conduction bands are bent. The formation of space charge region and hence the bending of the band edges depend on the Fermi level position of the semiconductor with respect to the redox potential of the electrolyte.

Four types of situation of space charge layer for n-type semiconductor in contact with an electrolyte may be considered as shown in **Figure II-5**: (i) flat band situation (**Figure**

II-5a), where no space charge exists in the flat band region layer and the electrode is at the flat band potential. In this case, the semiconductor contains a uniform distribution of charge; (ii) accumulation layer (**Figure II-5b**), positive charges exist at the interface and electrons accumulate in the semiconductor close the surface, inducing an increase in the free electron density and a decrease in the free hole density. Band of the semiconductor bend down as one moves toward the surface as a result of the decrease of electron potential energy as one moves toward the positively charged outlayer; (iii) depletion layer (**Figure II-5c**), negative charges exist at the surface and positive charges accumulate near the surface, causing a decrease in the free electron density and an increase in the free hole density. The bands of the semiconductor then bend upward toward the surface; (iv) inversion layer (**Figure II-5d**), the depletion of the majority charge carriers extends far into the top of the valence band and the Fermi level decreases below the intrinsic level. The surface region of the semiconductor appears to be p-type while the bulk still exhibits n-type behavior.

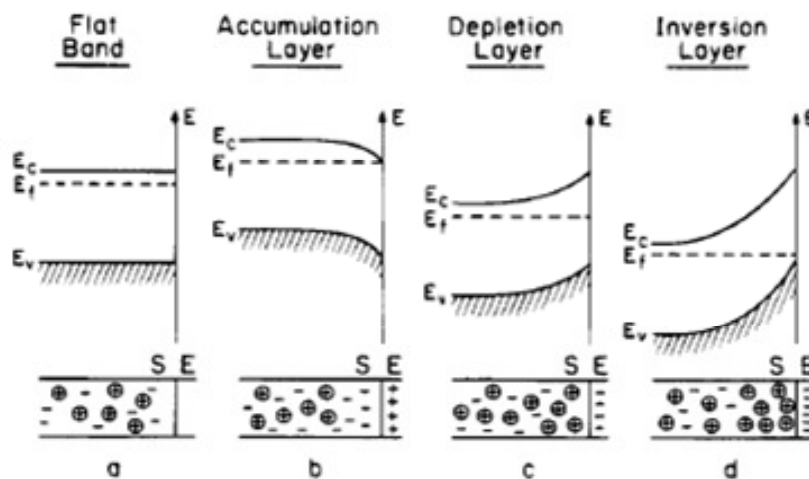


Figure II-5: Space charge layer formation and band bending.¹⁹

The depletion layer at the interface between a bulk semiconductor and a liquid medium plays an important role in light-induced charge separation. The local electrostatic field present in the space layer serves to separate the electron-hole pairs generated by irradiation of the semiconductor. For n-type semiconductor, the direction of the field is such that holes migrate to the interface where they undergo a chemical reaction and electrons move to the interior of the semiconductor.

II.4. Heterostructure photocatalysts

In contrast to single phase photocatalysts, heterojunction semiconductors or integrated multi-semiconductor systems possess significant advantages in promoting the separation of electron-hole pairs and keeping reduction and oxidation reactions at two different reaction sites. The aim of designing heterostructured photocatalysts is to promote the separation of photoexcited electron-hole pairs through various carrier-transfer pathways by combining suitable electronic structures in the same material. The efficient electron and/or hole transfer from one component to another with suitable band edge positions can greatly minimize the energy wasteful photoinduced electron-hole pairs recombination and increase the life time of charge carriers, thus promoting the photocatalytic efficiency. In this section, a wide range of recently developed heterojunction semiconductor photocatalysts, particularly TiO₂, ZnO and SnO₂ based heterojunctions will be discussed giving emphasis on the improvement of their photocatalytic performance for photocatalytic remediation of environment or hydrogen production. The physical phenomena behind the various ways to separate the electron-hole pairs will also be tentatively discussed.

II.4.1. Semiconductor/semiconductor heterostructure photocatalysts

II.4.1.1. SnO₂/TiO₂ heterostructure photocatalysts

Titanium oxide is a well-known photocatalyst working in the ultraviolet region of the electromagnetic spectrum. It is widely used for photocatalytic reactions like oxidation of organic pollutants in air and water as well as hydrogen generation from water. However, in order to increase the photocatalytic activity of TiO₂ for its practical use and commerce, it is crucial to decrease the recombination of photogenerated charge carriers. Coupling TiO₂ with another semiconductor with a suitable band edge position can effectively reduce the recombination by vectorial transfer of photogenerated electrons and holes. When TiO₂ is combined with another semiconductor whose conduction band is at a lower potential than TiO₂, the electrons present in the conduction band of TiO₂ can be transferred to the second semiconductor decreasing the recombination rate. Coupled SnO₂/TiO₂ system has recently attracted much attention due to enhanced charge separation and thus improved photocatalytic activity.²⁰

Both TiO₂ and SnO₂ are n-type semiconductors with band gap energies greater than 3.0 eV and exhibit a strong absorption threshold in the UV region. The conduction band

edges of TiO_2 and SnO_2 are located at $E_{\text{CB}}(\text{TiO}_2) = -0.5 \text{ V}$ and $E_{\text{CB}}(\text{SnO}_2) = 0 \text{ V}$ vs NHE at pH 7, respectively.^{20a} The valence band edge of SnO_2 [$E_{\text{VB}}(\text{SnO}_2) = 3.67 \text{ V}$] is much positive than that of anatase TiO_2 [$E_{\text{VB}}(\text{TiO}_2) = 2.87 \text{ V}$].^{20c} **Figure II-6** shows the charge transfer process in heterostructure $\text{SnO}_2/\text{TiO}_2$ photocatalysts. Upon band gap excitation, hole-electron pairs are generated in each semiconductor. Due to the lower conduction band edge of SnO_2 , electron will be injected into SnO_2 , while the hole will move in the opposite direction of the electron and accumulate on the TiO_2 particles, thereby making charge separation more efficient. Therefore, the interfacial charge transfer process can explain the higher photocatalytic activity of $\text{SnO}_2/\text{TiO}_2$ composites.

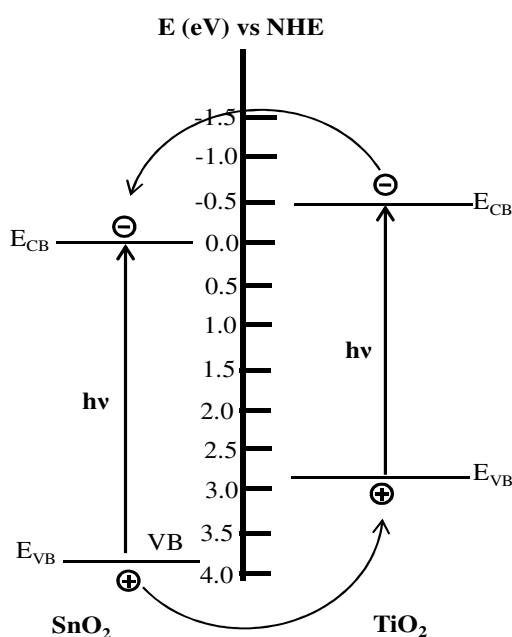


Figure II-6: Schematic representation of charge transfer process in heterostructure $\text{SnO}_2/\text{TiO}_2$ photocatalysts.

In recent years, coupling $\text{SnO}_2/\text{TiO}_2$ composites have been widely studied by many researchers for the degradation of organic pollutants and the composites showed higher photocatalytic activity than the single ones as shown in **Table II-1**. Shifu *et al.*²¹ prepared $\text{SnO}_2/\text{TiO}_2$ photocatalysts by ball milling using H_2O solution as disperser. The photocatalytic activities of $\text{SnO}_2/\text{TiO}_2$ photocatalysts prepared with or without ball milling with different content of doped SnO_2 were investigated by degrading an organophosphate insecticide monocrotophos.

Table II-1: Degradation of different organic pollutants with SnO₂/TiO₂ heterostructure photocatalysts

Pollutant	Dose g L ⁻¹	Reaction condition and efficiency	Synthesis method	Reference
Methylene blue (MB)	0.4	Under UV irradiation (355 nm). 125 mL of 5.35 x 10 ⁻⁵ mol/L MB. The composite with Ti/Sn = 28.2:1 showed higher degradation compared to TiO ₂	Flame synthesis method	Akurati <i>et al.</i> ^{20d}
Methylene blue (MB)	0.5	Under UV irradiation (30 W). 100 mL of 5.35 x 10 ⁻⁵ mol/L MB. Degradation efficiency of 5 wt% SnO ₂ /TiO ₂ after 20 min was 95% and that of TiO ₂ was 77%.	Solvothermal	Hou <i>et al.</i> ^{20e}
Active red X-3B	3.5	Under UV irradiation (300 W), 2000 mL of 50 mg/L X-3B. Degradation rate constant k, 0.13 min ⁻¹ for SnO ₂ /TiO ₂ composite with 18.4% loading of SnO ₂ and 0.06 min ⁻¹ for TiO ₂	Homogeneous precipitation	Shi <i>et al.</i> ²²
Acrylic acid	1	Under UV irradiation (9 W, 254 nm). 300 mL of 300 mg/L. after 6h, degradation efficiency of SnO ₂ /TiO ₂ with 15.1 mol% of SnO ₂ was 65% and that for TiO ₂ was 43%.	Sol-gel combined with super critical drying	Zhang <i>et al.</i> ²⁷
Methyl orange (MO)	0.5	Under UV irradiation (300 W, 365 nm). 450 mL of 20 mg/L MO. Degradation efficiency of SnO ₂ /TiO ₂ with molar ratio 0.15 was 94% and that of TiO ₂ was 30%.	Steric acid method	Yang <i>et al.</i> ²³
Rhodamine B (RhB)	0.25	Under UV irradiation. 40 mL of 2.5 x 10 ⁻⁵ M RhB. The TOC loss of 10 wt% SnO ₂ /TiO ₂ composites nanofiber was 61 % and than that of TiO ₂ was 21% after 40 min irradiation under UV.	Electrospinning	Hwang <i>et al.</i> ^{29b}
Rhodamine B (RhB)	1	Under UV irradiation (8W, 254nm). 2.5 x 10 ⁻⁵ mol/L RhB. Degradation rate constant k, 0.043 min ⁻¹ for SnO ₂ /TiO ₂ nanofiber with (3 mol% SnO ₂) and 0.013 min ⁻¹ for TiO ₂ .	Electrospinning	Zhang <i>et al.</i> ^{29c}
Rhodamine B (RhB)	0.2	Under UV irradiation (254 nm). 100 mL of 5 x 10 ⁻⁵ M RhB. Degradation rate constant k, 0.089 min ⁻¹ for SnO ₂ /TiO ₂ composite and 0.042 min ⁻¹ for TiO ₂	Electrospinning	Liu <i>et al.</i> ^{29a}
Rhodamine B (RhB)	0.1	Under UV irradiation (50 W, 315 nm). 450 mL of 20 mg/L MO. Degradation efficiency of SnO ₂ /TiO ₂ with Sn:Ti = 1:10 was 100% and that of TiO ₂ was 40%.nanocomposite after 1h.	Electrospinning combined hydrothermal	Wang <i>et al.</i> ²⁴
Rhodamine B (RhB)	1	Under UV irradiation. 100 mL of 1 x 10 ⁻⁵ mol/L RhB. Degradation rate constant k, 0.013 min ⁻¹ for SnO ₂ /TiO ₂ containing 10 mol% SnO ₂ and 0.007 min ⁻¹ for TiO ₂ .	Sol-gel	Messih <i>et al.</i> ²⁵

The SnO₂/TiO₂ photocatalysts containing 5 wt% SnO₂ and prepared with ball milling showed higher photocatalytic efficiency than that of SnO₂/TiO₂ prepared without ball milling. In fact, the efficiency of SnO₂/TiO₂ prepared without ball milling was lower than that of the pure TiO₂. The increased photocatalytic activity resulted from (i) an increased surface area obtained by ball milling; (ii) an efficient charge separation and (iii) a red shift of the absorption wavelength range (about 20 nm) along with an increased of the absorption intensity. Because of the absorption wavelength range red shift of about 20 nm and of the absorption intensity enhancement, the formation rate of electron–hole pairs at the photocatalyst surface also increases greatly, resulting in a higher photocatalytic activity for the SnO₂/TiO₂ photocatalyst. The reason for the absorption wavelength range red shift of the SnO₂/TiO₂ system could probably be attributed to the formation of defect energy level in the particles during high energy ball milling process. On the other hand, the stress and strains induced during the ball milling process result in lattice deformation of TiO₂ and SnO₂ with many defects possessing high lattice and surface energy. This lowers the activation energy for diffusion of elements allowing the atomic or ionic diffusion at room temperature. When the activation of the powder system is sufficiently high during the ball milling process, the collision between balls and grains of the powder will produce a rise in interface temperature which induces a strong coupling reaction and hence the better photocatalytic activity.²¹

The accumulation of recalcitrant, strongly bound reaction intermediates on the TiO₂ surface, deactivates the catalyst and influences the photocatalytic degradation rate. The modification of TiO₂ with SnO₂ could avoid the deactivation in photocatalytic reaction. In this context, Fresno *et al.*²⁶ studied the photocatalytic degradation of toluene over coupled SnO₂/TiO₂. The coupled photocatalysts gave higher degradation rate due to the absence of the deactivation process that occurs with the TiO₂ reference. In coupled photocatalyst, more water molecules adsorbed on the catalysts surface via weak hydrogen bonds instead of intermediates adsorption are responsible for catalyst deactivation.

The drying technique in the preparation of SnO₂/TiO₂ composites also strongly influences the photocatalytic activity. The SnO₂/TiO₂ nanocomposite photocatalysts prepared through supercritical fluid drying technique (SCFDT) showed enhanced photocatalytic activity in the degradation of acrylic acid as compared to pure TiO₂ or SnO₂/TiO₂ catalysts prepared by traditional drying.²⁷ The interfacial force of the solvent in traditional drying leads to collapse of the cavity structure and to aggregation of the particles, and therefore, increases the particle size and decreases the cavity volume. As a result, the surface area is reduced

resulting in lower photocatalytic activity. The SCFDT preparation method could remove this phenomenon by expanding the solvent alcohol in the pores rapidly without interfacial force. Thus, SCFDT preparation method reduced the aggregation of the nanoparticles giving smaller size composite particles which was attributed to the higher photocatalytic activity. After 6 h irradiation under UV, the degradation efficiency of the SnO₂/TiO₂ composite with 15.1 mol % SnO₂ prepared by SCFDT method was 65% while that of composite prepared by traditional drying method was 11%.

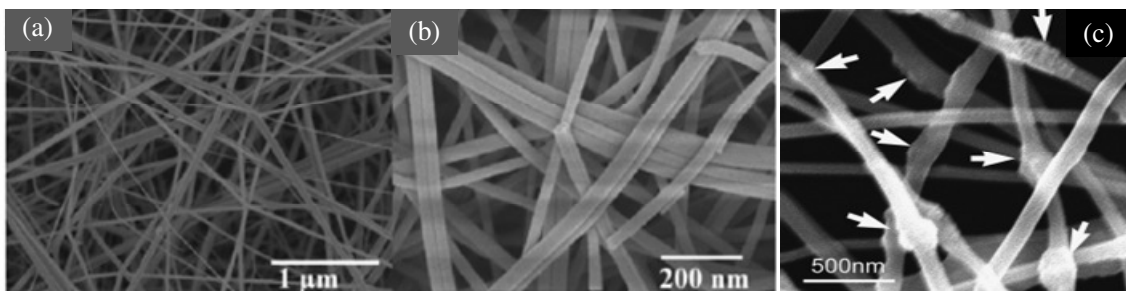


Figure II-7: (a and b) Typical SEM images of the electrospun bicomponent SnO₂/TiO₂ nanofibers calcined at 500 °C^{29a} (c) Morphology of the hybrid nanofiber by scanning electron microscopy, with arrows showing the bead parts.^{29c}

Nowadays the coupled SnO₂/TiO₂ systems are usually of a particle-like morphology, with a typical size of no larger than several hundred nanometers. It has to be conceded that eliminating the nanoscale catalyst particles from the reactants or productions is tremendously difficult and the particle photocatalyst itself might repollute the treated water and air. The particle photocatalyst might also show lower photocatalytic efficiency because of aggregation problems.²⁸ The SnO₂/TiO₂ nanofiber photocatalysts fabricated by electrospinning can solve the problem of separation because of its one-dimensional morphology.²⁹ The small diameter of nanofibers also provides a comparably large specific surface area as compared with nanoparticles, ensuring a high photocatalytic activity. Liu *et al.*^{29a} have prepared bicomponent SnO₂/TiO₂ nanofiber by a simple electrospinning process with a side-by-side dual spinneret method. The morphologies of the electrospun bicomponent nanofibers (shown in **Figure II-7a and b**) made it possible for both of the TiO₂ and SnO₂ components to be fully exposed at the surface promoting an increase in the charge separation of the photogenerated electrons and holes within the bicomponent system, allowing both of the photogenerated electrons and holes to participate in the overall photocatalytic reaction. The photocatalytic activity of the bicomponent SnO₂/TiO₂ nanofiber evidenced by degrading Rhodamine B (RhB) was much higher than that of pure TiO₂ as was expected from photoluminescence (PL) and surface photovoltage spectroscopy (SPS) measurement. In

another experiment, a necklace structured SnO₂/TiO₂ hybrid nanofiber photocatalyst has been prepared via the sol-gel electrospinning method which has been proven to be an excellent photocatalyst with a much higher photocatalytic activity than pure anatase nanofiber in the oxidation of RhB.^{29c}

Another approach to solve the problem of separation of the products, permitting reuse and recycling is the preparation of support-based photocatalysts. The SnO₂/TiO₂ hybrid oxide photocatalysts supported on attapulgite (ATT, or palygorskite, as it often called), were synthesized by depositing SnO₂/TiO₂ hybrid oxides on the surface of ATT to form a composite photocatalyst (denoted ATT-SnO₂/TiO₂) using an in situ sol-gel technique.³⁰ The photocatalytic activity of ATT-SnO₂/TiO₂ for the degradation of methyl orange or phenol was much higher than that of ATT-SnO₂, ATT-TiO₂ and Degussa P25.

In order to achieve significant improvements for industrial application and avoid the problem of separation of the nanophotocatalyst, many researchers prepared SnO₂/TiO₂ based thin films. Chen and his co-workers deposited a thin SnO₂/TiO₂ coating on foamed aluminium by plasma spraying technique.³¹ The SnO₂/TiO₂ coating containing 10 % SnO₂ exhibited higher photocatalytic activity for the degradation of gas-phase benzene. The high photocatalytic efficiency was attributed to reduced electron-hole recombination and higher content of hydroxyl group on SnO₂/TiO₂ coating. The surface photoactivity for a TiO₂ powder is proportional to the number of hydroxyl groups on its surface.³² With the increase of surface hydroxyl content, the opportunity to form more hydroxyl radical with photogenerated holes was increased resulting in improved photocatalytic activity. Liu and his co-workers also reported similar result where a SnO₂/TiO₂ composite thin films containing 10 mol% SnO₂ on soda-lime glass showed the highest photocatalytic efficiency for the degradation of methyl orange. The maximum rate of decolorization was about 60 % by the film with 10 mol% SnO₂ while that by the pure TiO₂ film was about 45 %.

A similar behavior has been reported for the degradation of Rhodamine B (RhB) by using SnO₂/TiO₂ composite films fabricated on transparent electro-conductive glass substrate.³³ Compared to TiO₂ films, the improved activity was attributed to the combined effects of low sodium content, better crystallization, appropriate phase composition of anatase (73.4%) and rutile (26.3%), and slower recombination rate of charge carriers. Upon UV illumination, electrons flew into the SnO₂ underlayer, while the hole diffused oppositely to the TiO₂ overlayer (**Figure II-8**). Consequently, more holes reached the TiO₂ surface to

cause oxidation reactions, while electrons were consumed for dioxygen reduction at the band edge of the SnO_2 film. The VB edge of TiO_2 inhibited the interfacial hole transfer from TiO_2 to SnO_2 , thereby increasing the hole density in the TiO_2 VB, and oxidized the organic contaminants.

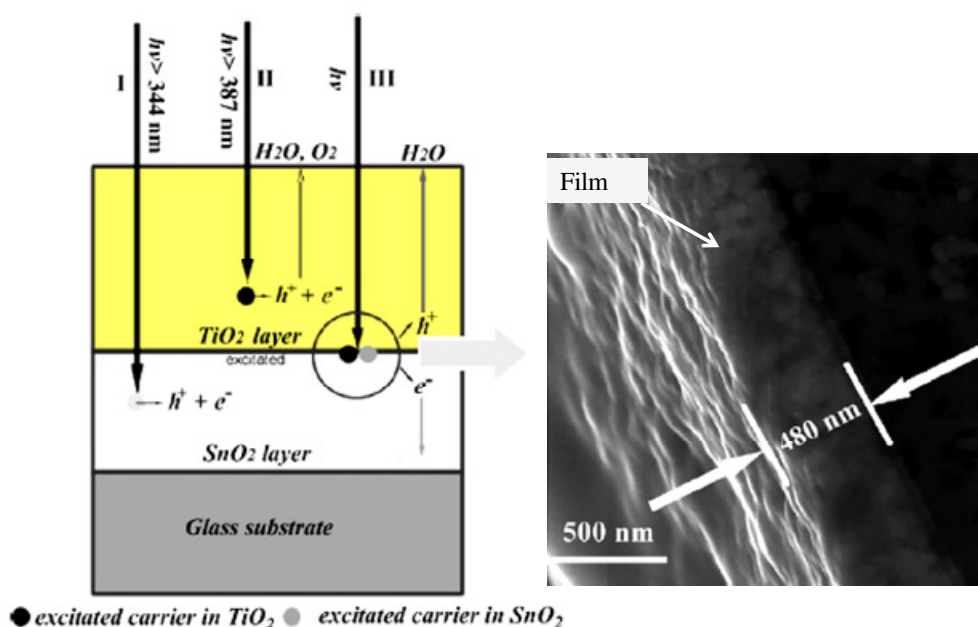


Figure II-8: Schematic diagram of the charge-transfer process in the $\text{SnO}_2/\text{TiO}_2$ composite film.³³

Vinodgopal and Kamat reported a very rapid decolorization of Acid Orange 7 using a coupled $\text{SnO}_2/\text{TiO}_2$ photoelectrode with mass ratio of $\text{SnO}_2:\text{TiO}_2 = 2:1$ under a bias potential.³⁴ They ascribed the enhanced degradation rate to the improved charge separation related to the good matching in the energy levels. The anodic bias potential was also reported to be responsible for the enhancement in photocatalytic activity by driving away the electrons into the conduction band of SnO_2 , thus promoting the oxidation of dye molecules on the TiO_2 surface where photogenerated holes were more abundant. Similar system was also reported for the improved photoelectrocatalytic degradation of naphthol blue black compared to pure TiO_2 .³⁵

Window glass (soda lime (SL) glass), an indispensable constituent of buildings and automobiles can be used as substrate for photocatalytic films which, from the practical point of view, can be used for the purification of air in the living space of human beings by utilizing of both solar and illuminating light as the excitation energy source. In order to fulfill this criterion, Tada and his co-workers fabricated bilayer-type patterned TiO_2 films on a SnO_2 film coated soda lime glass substrate by using an organically modified sol-gel method.³⁶ This

patterned bilayer-type photocatalyst (pat-TiO₂/SnO₂/glass) exhibited high photocatalytic activity as compared to non patterned sample for the gas phase decomposition of acetaldehyde resulting from efficient charge separation. Efficient interfacial electron transfer from the TiO₂ overlayer to the SnO₂ underlayer was demonstrated by labeling and visualizing the reduction sites with Ag particle as shown in **Figure II-9**.^{36a}

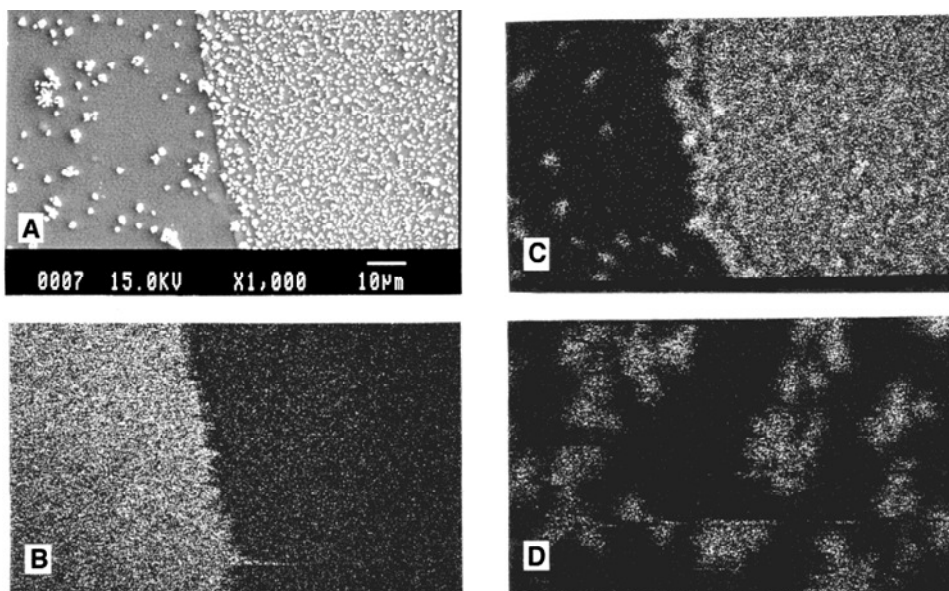


Figure II-9: (A) SEM micrograph of pat-TiO₂/SnO₂/SL-glass after Ag photodeposition. (B) X-ray image of Ti for the same region as (A). (C) X-ray image of Ag for the same region as (A). (D) X-ray image of Ag for TiO₂/SnO₂/SL-glass.^{36a}

Figure II-9A is a SEM photograph of pat-TiO₂/SnO₂/SL-glass after illumination; an X-ray image of Ti for the same region (**B**) revealed that the region at the left (light area) was covered with TiO₂ film, and the SnO₂ underlayer was exposed at the right (dark area). An X-ray image of Ag in the same region (**C**) demonstrated preferential deposition of Ag particles on the surface of SnO₂. A comparison of (**C**) and (**D**, X-ray image of Ag for TiO₂/SnO₂/SL-glass after photodeposition) indicated the enhancement of Ag photodeposition by patterned bilayer-type pat-TiO₂/SnO₂/SL-glass films. The excited electrons generated by the band gap transition of TiO₂ flew into SnO₂, where they are consumed by the reduction, indicating the specification of the reduction sites in the photocatalytic reaction. The result also showed that the activity of the non patterned TiO₂/SnO₂/SL-glass films decrease gradually due to the accumulation of electrons in the conduction band of SnO₂, because of SnO₂ being not directly in contact with reaction gas. Similar work is done in another investigation where a large area patterned TiO₂ film was formed on a SnO₂ coated soda lime glass using a gravure printing method.³⁷ Preferential deposition of Pt particles on the SnO₂ underlayer of pat-TiO₂/SnO₂

bilayer type photocatalysts showed a superior photocatalytic activity for the photocatalytic dehydrogenation of methanol.³⁸ The electrons flowing from TiO₂ to SnO₂ were trapped on its surface by Pt particles with large work function, providing active sites for the reduction of H⁺ generated during the oxidation reaction of H₂O and CH₃OH by the valence band holes to H₂.

Hattori and his co-workers^{20c} prepared double layered SnO₂/TiO₂-coupled films (as shown in **Figure II-10**) and studied their photocatalytic activity in both the oxidation of formic acid and 1,3,5,7-tetramethylcyclotetrasiloxane and the reduction of Ag⁺ and bis(2-dipyridyl)disulfide. By comparing the amount of CO₂ evolved, the photooxidation of formic acid on SnO₂/TiO₂-coupled films was confirmed to occur more efficiently than on pure TiO₂ films. The degradation of 1, 3, 5, 7-tetramethylcyclotetrasiloxane was also more efficient on the coupled SnO₂/TiO₂ films. On the other hand, photocatalytic reduction processes on SnO₂/TiO₂ couple were found to be less efficient than on pure TiO₂ films. These results are unanimously consistent with the vectorial charge carrier transfer as proposed earlier, the electrons transferred from TiO₂ into SnO₂ via the edges of the SnO₂ layer in contact with the electrolyte since the substrates are non-conducting.

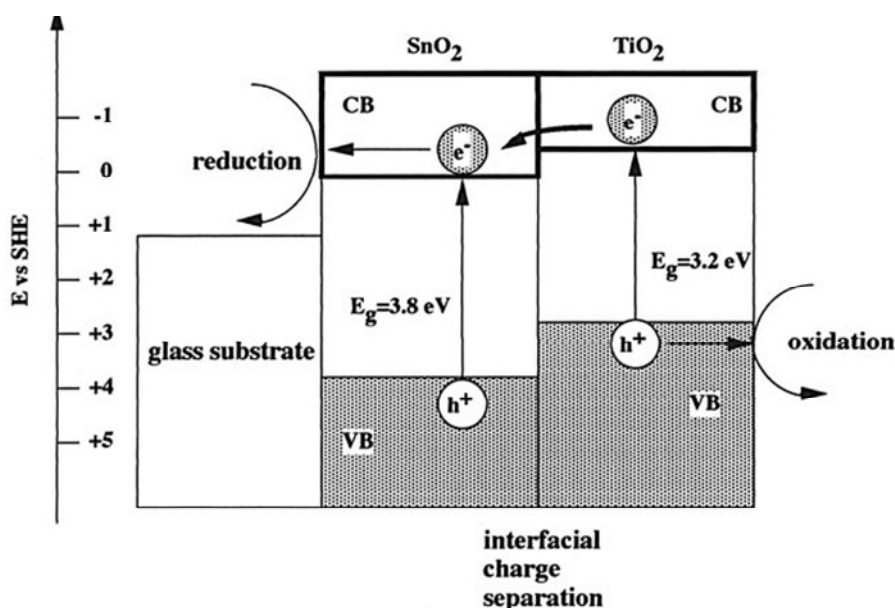


Figure II-10: Energy diagram for the SnO₂/TiO₂ bilayer-type photocatalyst system.^{20c}

Cao *et al.*³⁹ reported the similar finding where a double layered SnO₂/TiO₂ film was prepared by the plasma-enhanced chemical vapor deposition (PECVD) technique on glass slide with both of the two components exposed to the surface allowing both photogenerated electrons and holes to contribute to the photocatalytic reactions. The bilayer film showed higher catalytic activity for phenol degradation. The activity of this bilayer film was highest

when the deposition time of TiO₂ on a SnO₂ layer was 10 min and decreased thereafter. With an increase in the deposition time (30 min), electrons photogenerated on the SnO₂ film had little chance to contact with the absorbed oxygen molecules; thus, blocking the charge transfer between them and reducing the photocatalytic activity of the films. In other word, the photocatalytic activity of the composite film is similar to that of the one-component TiO₂ film.

The photocatalytic activity of SnO₂/TiO₂ bilayer film was also related to the thickness of the overlayer TiO₂. Shang *et al.*⁴⁰ studied the photocatalytic activity of glass/SnO₂/TiO₂ bilayer film with different thicknesses of TiO₂ layer on constant thickness of SnO₂ prepared by depositing anatase TiO₂ film on rutile SnO₂ film. The glass/SnO₂/TiO₂ bilayer film with optimum thicknesses of TiO₂ layer of 200 nm on constant thickness of SnO₂ of 120 nm showed much higher photocatalytic activity in the case of formaldehyde photodegradation compared with glass/TiO₂ film. The higher catalytic activity resulted from efficient interfacial charge separation via the process of electron transfer from TiO₂ to SnO₂. However, when the thickness of TiO₂ layer was beyond 200 nm, the photocatalytic activity of glass/SnO₂/TiO₂ film was nearly as same as glass/TiO₂ film. This was due to the fact that the photogenerated electrons in the coupled sample with thicker TiO₂ were far away from the SnO₂/TiO₂ interface and the distance traversed by the electrons to reach the interface of SnO₂/TiO₂ increased allowing the electrons to be trapped by holes before separation at the interface.

II.4.1.2. ZnO/TiO₂ heterostructure photocatalysts

Combining TiO₂ and ZnO has been well-established to remarkably enhance the separation efficiency of photoexcited charge carriers because of the formation of heterojunction structure between them, thus boosting quantum efficiency and photostability of the composite photocatalyst. Although the binding energies of ZnO and TiO₂ are analogous to each other, notably, potentials of the conduction band and the valence band of ZnO are still a bit more negative than those of TiO₂.⁴¹ In the photocatalytic process, the electron transfers from the conduction band of ZnO to the conduction band of TiO₂ under illumination and, conversely, the hole transfers from the valence band of TiO₂ to the valence band of ZnO, decreasing the pairs' recombination rate.⁴² This charge separation effectively increases the lifetime of the charge carriers and enhances the efficiency of the interfacial charge transfer to adsorbed substrates. **Figure II-11** describes the charge-transfer process in the ZnO/TiO₂ heterostructure under UV light irradiation.

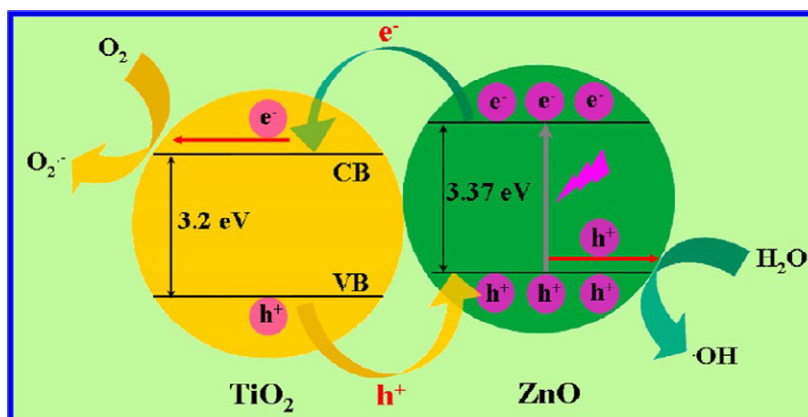


Figure II-11: Schematic diagram illustrating the charge-transfer process in the ZnO/TiO₂ heterostructure under UV light irradiation.^{41a}

Many attempts have been made to prepare ZnO/TiO₂ heterostructures which showed superior photocatalytic activity for the degradation of organic pollutants (**Table II-2**), such as methyl orange (MO),⁴³ methylene blue (MB),⁴⁴ rhodamine dye,⁴⁵ malachite green,⁴⁶ azo dye,⁴⁷ sodium methyl red,⁴⁸ phenol and its derivatives.⁴⁹ Ge and his co-workers^{43d} reported higher photocatalytic efficiency of ZnO/TiO₂ composites synthesized by using the solvothermal method and ultrasonic precipitation followed by heat treatment in the photocatalytic degradation of methyl orange. The degradation efficiency by the as-synthesized heterostructured photocatalysts was found to be the best at pH 2.0 in the experimental condition used showing 98.13% degradation efficiency after 30 min and complete mineralization after 60min. The higher degradation efficiency resulted from the vectorial charge separation at the ZnO/TiO₂ interface. They also investigated that the intermediates produced during photocatalytic degradation were unstable and decomposed within about 60 min at pH 2.0.

A hollow sphere composed of mixed metal oxides (ZnO-TiO₂) was prepared by a facile approach involving coating of functionalized polystyrene template beads with the successive layers of ZnO and TiO₂ nanoparticles, respectively, followed by calcination of resulting PS/ZnO-TiO₂ core shell composite particles at elevated temperature.^{45a} The fabricated ZnO-TiO₂ hollow spheres showed superior photocatalytic activity for the degradation of rhodamine 6G compared with those of ZnO and TiO₂ hollow spheres. In order to overcome the problem of pollution of treated water with nanoparticle and decreasing the photocatalytic activity, ZnO/TiO₂ composite nanofibers with diameters in the range of 85-200 nm were fabricated via the electrospinning technique using cellulose acetate as the fiber template.^{45b} The promoted charge separation of electrons and holes due to the coupling effect

of ZnO and TiO₂ in the composite nanofiber reduced the recombination of the electron-hole pairs resulting in higher photocatalytic efficiency of the ZnO/TiO₂ composite nanofiber containing 15.8 wt% ZnO than the pure nanofiber in degrading Rhodamine B or phenol.

Table II-2: Degradation of different organic pollutants with ZnO/TiO₂ heterostructure photocatalysts

Pollutant	Dose g L ⁻¹	Reaction condition and efficiency	Synthesis method	Reference
Cyanide (CN ⁻) detoxification	0.33	Under visible light. 75 mL of 10 mM cyanide. Photocatalytic efficiency of composite was higher than that of TiO ₂ P25.	Modified ammonia evaporation-induced	Karunakaran <i>et al.</i> ^{45c}
Methyl orange (MO)	10	Under UV irradiation. 100 mL of 0.1-1 g/L MO. Degradation ratio D after 5 h, 72% for composite and 50% for TiO ₂ .	Sol-gel	Liao <i>et al.</i> ^{43a}
Methyl orange (MO)	2.5	Under UV irradiation (1250 W, λ=365 nm), 50 mL of 20 mg/L of MO. Degradation rate constant k, 0.085 min ⁻¹ for composite and 0.07 min ⁻¹ for TiO ₂	Homogeneous hydrolysis	Zhang <i>et al.</i> ^{43f}
Methylene blue (MB)	10	Under sun light, 50 mL of 20 mg/L of MB. Degradation efficiency of ZnO/TiO ₂ with Ti/Zn = 1:1 was 99% and that for TiO ₂ was 94%.	Precipitation	Jiang <i>et al.</i> ^{44a}
Rhodamine B (RhB)	0.5	Under UV irradiation (12 W). 10 mL of 8 mg/L RhB. Degradation rate for composite was 0.75 mg/(L h) and that for TiO ₂ was 0.57 mg/(L h)	Electrospinning	Liu <i>et al.</i> ^{45b}
Rhodamine 6G	0.86	Under UV irradiation. 70 mL of 1 x 10 ⁻⁵ M. The rate of degradation with ZnO/TiO ₂ composites was much higher than that of TiO ₂ .	Template assisted	Agrawal <i>et al.</i> ^{45a}
Phenol	1.6	Under UV irradiation (355 nm). 80 mL of 20 mg/L phenol. Degradation rate constant k, 0.071 min ⁻¹ for composite and 0.061 min ⁻¹ for ZnO at pH 6.7.	Mechanical mixing	Serpone <i>et al.</i> ^{42a}
Phenol	0.5	Under UV irradiation (12 W). 10 mL of 20 mg/L phenol. Degradation rate for composite was 1.833 mg/(L h) and that for TiO ₂ was 1.13 mg/(L h)	Electrospinning	Liu <i>et al.</i> ^{45b}
Phenol	0.4	Under UV irradiation (< 340 nm). 400 mL of 100 mg/L MO. The ZnO/TiO ₂ nanocomposite showed enhanced degradation efficiency compared to TiO ₂	Vapor hydrolysis method	Zhang <i>et al.</i> ^{49a}

In order to determine the influence of morphology on the photocatalytic activity, different shapes of ZnO/TiO₂ composite nanoparticles, including spherical and cubic nanoparticles, hexagonal nanorods, and nanobelts with different sizes, were prepared by adjusting the precursors molar ration, i. e. Zn : Ti(OBu)₄ ratio and the nature of the surfactant

employed.^{43b} Spherical ZnO/TiO₂ composite nanoparticles were obtained by using sodium dodecyl benzene sulfonate (DBS) while cubic ZnO/TiO₂ nanoparticles (Zn/Ti(OBu)₄ = 0.5:1), hexagonal nanorods (Zn/Ti(OBu)₄ = 0.25:1), and nanobelts (Zn/Ti(OBu)₄ = 0.17:1) were obtained by using sodium dodecyl sulfonate (SDS). The hexagonal nanorods showed the highest photocatalytic activity for the degradation of methyl orange. This enhanced activity was attributed to the higher surface to volume ratio of the nanorods than that of the nanosphere with similar dimension that would provide higher density of active sites available for surface reaction as well as a higher interfacial charge transfer rate. Another reason of the improved photocatalytic properties was the red shift in the UV-Vis light reflectance, as shown in **Figure II-12**. Nanorods, with their increased surface area, provided surface states within the band gap that effectively reduce the band gap.

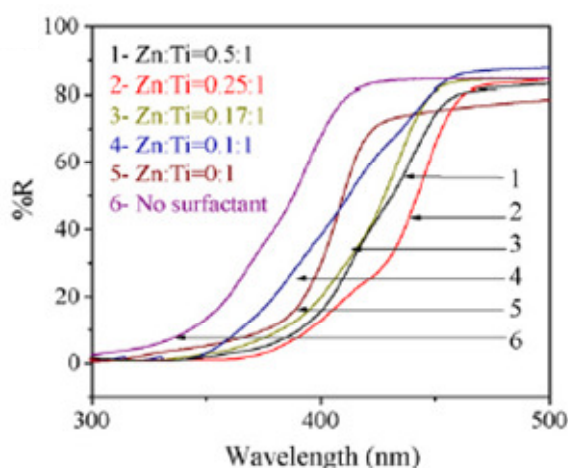


Figure II-12: UV-Vis reflectance spectra of nanoparticles synthesized with SDS and different Zn/Ti(OBu)₄ molar ratio.^{43b}

Many researchers reported that ZnO/TiO₂ composite films lead to higher photocatalytic efficiency due to the suppression of charge carrier recombination.⁵⁰ Composite films made of ZnO particles or nanorods along with TiO₂ nanotube showed higher photocatalytic efficiency compared to ZnO films and TiO₂ films.^{51, 41a, 47c} Recently, Xiao^{41a} fabricated three-dimensional ZnO-functionalized TiO₂ nanotube arrayed (ZnO/TNTs) heterostructure via a facile two-step anodization associated with a pyrolysis step, by which in situ formed ZnO nanocrystals were uniformly anchored in the framework of TNTs due to intimate interfacial contact between the polar TiO₂ surface and the ZnO precursor. The resulting ZnO/TNTs heterostructure film deposited on Ti foil manifested superior photocatalytic performances for the degradation of Rhodamine B (RhB) to its counterparts of pure ZnO, TNTs, and commercial TiO₂ (Degussa P25) nanoparticulate film. The enhanced

photocatalytic activities of the heterostructure was attributed to the large exposed surface area of TNTs to surrounding medium and formation of heterojunction structure in the interface between ZnO and TNTs which greatly promotes efficient separation of photogenerated electron-hole charge carriers. The higher photocatalytic activity of ZnO/TNTs heterostructure resulting from efficient charge separation was confirmed by transient photocurrent response and EIS results. The photocurrent response of the ZnO/TNTs heterostructure was nearly 2-fold higher than that of blank TNTs and the impedance arc radius of the ZnO/TNTs heterostructure was smaller than that of TNTs, indicating more efficient separation of photoexcited electron-hole pairs when compared with TNTs.^{41a} In another experiment, Zhang *et al.*^{47c} reported that the ZnO nanorods embedded in highly ordered TiO₂ nanotubes arrays (ZnO NR /TiO₂ NTs) electrode showed higher photocatalytic activity in degrading methyl orange as compared with TiO₂ NTs electrode. The electrode was fabricated through electrosynthesis of TiO₂ NTs array in HF solution by anodization method followed by cathodic electrodeposition of ZnO embedded in the TiO₂ nanatube arrays.

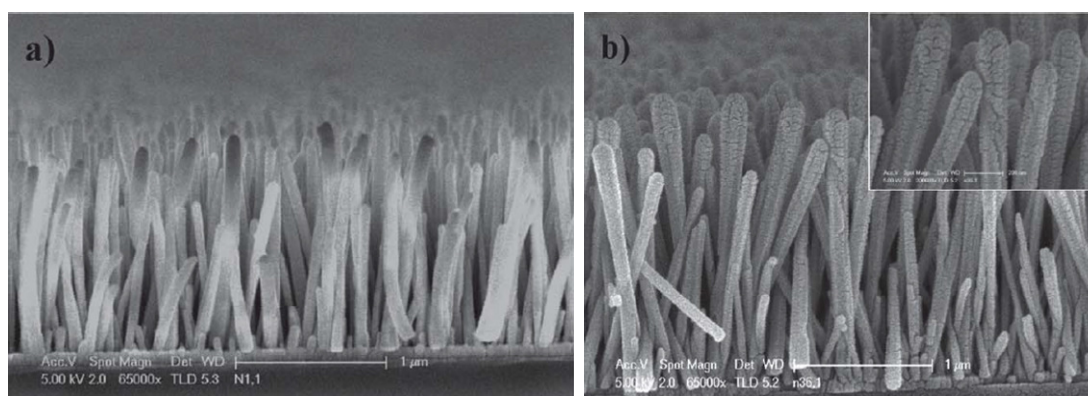


Figure II-13: (a) SEM cross-sectional images of aqueous solution growth ZnO nanorods (NRs), (b) ZnO/TiO₂ CB nanostructures (the insert is a high magnification image and the scale bar is 200 nm).⁵³

Taking into account the easy aggregation of spherical nanocomposites, Chen *et al.*⁵² fabricated a coupled biocomponent composites consisting of TiO₂ nanoparticles and ZnO 1D nanorods by using a one-step hydrothermal method. The photoanode of the synthesized ZnO-TiO₂ composite prepared on the FTO glass showed higher photocatalytic activity for the degradation of methylene blue and enhanced photocurrent with several orders of magnitude higher intensities than that of the mere TiO₂ nanoparticles or ZnO nanorods. The enhancement of the photocurrent and photocatalytic activities resulted from the increased surface area, which can raise the light harvesting and the ability of generating photoinduced electron-hole pairs of active sites, and the favorable electron-transfer properties of the

heterojunctions ZnO/TiO₂ in the coupled ZnO-TiO₂ nanocomposites. Heterostructure ZnO/TiO₂ core-brush nanostructures showing the single crystal ZnO nanorod as the core and polycrystalline TiO₂ nanowires as the brush-like outer layer (shown in **Figure II-13**) were synthesized on glass substrates by a combination of aqueous solution growth and magnetron sputtering method.⁵³ The photocatalytic activity of the ZnO/TiO₂ core-brush nanostructure evaluated by the decomposition reaction of Bromopyrogallol Red dye under UV (245 nm) and visible-light (450 nm) irradiation was much higher than that of a TiO₂ film and a ZnO/TiO₂ composite film. The photocatalytic activity enhancement of the ZnO/TiO₂ core-brush was attributed to the interaction effect, lower band gap energy and its unique core-brush feature which can lower the recombination rate of electron-hole pairs, extend the absorption range and provide a high density of active sites.

II.4.1.3. WO₃/TiO₂ heterostructure photocatalysts

It is known that band gaps of WO₃ and TiO₂ are 2.8 and 3.2 eV, respectively.⁵⁴ Both the upper edge of the valence band and the lower edge of the conduction band of WO₃ are lower (i. e. more positive) than those of TiO₂.⁵⁴ TiO₂ can be excited by photons with wavelengths under 387 nm, which produces photogenerated electron-hole pairs.

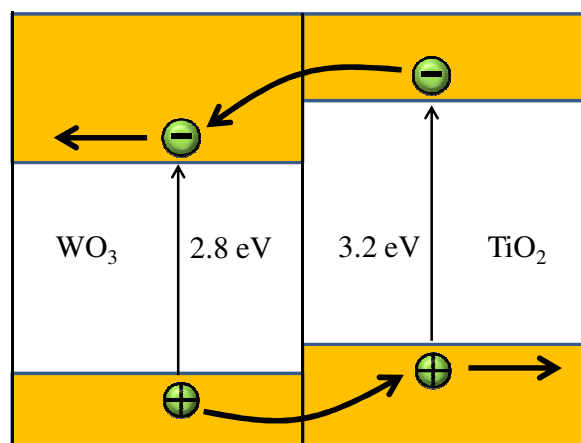


Figure II-14: Energy band diagram and charge transfer process in WO₃/TiO₂ heterostructure photocatalyst.

Figure II-14 shows the charge transfer process at the interface of WO₃/TiO₂ nanocomposites. For WO₃, theoretically, it can be excited by photons with wavelengths under 443 nm, but it shows only low photocatalytic activity under UV light irradiation. When WO₃ and TiO₂ form a coupled photocatalyst, TiO₂ and WO₃ can be excited simultaneously under UV illumination. As the conduction band of WO₃ is lower than that of TiO₂, the former can

act as a sink for the photogenerated electrons. The photogenerated electrons of the TiO_2 conduction band will be transferred to the conduction band of WO_3 . Since the holes move in the opposite direction from the electrons, photogenerated holes might be trapped within the TiO_2 particle, which makes charge separation more efficient. This spatial charge separation limits the recombination of photogenerated charges and thus increases the photocatalytic activity.

To date, the WO_3/TiO_2 nanocomposites have been prepared by several methods like sol-gel,⁵⁵ hydrothermal,⁵⁶ incipient wetness method,⁵⁷ impregnation,⁵⁸ flame-spray pyrolysis,⁵⁹ ultrasonic spray pyrolysis,⁶⁰ pulsed laser deposition,⁶¹ ball milling,⁶² precipitation,⁶³ electrosynthesis,⁶⁴ template synthesis⁶⁵ or physical mixing.⁶⁶ Saepurahman *et al.*^{58d} prepared tungsten-loaded TiO_2 and studied the effect of TiO_2 modification with tungsten trioxide, WO_3 , on the photocatalytic activity. The result showed that tungsten loading stabilized the anatase phase of TiO_2 from transforming into inactive rutile phase giving more stability with higher tungsten loading as compared to the unmodified TiO_2 . Similar conclusion were drawn by other authors.^{55f, 55h, 56e, 67} The photocatalytic activity of tungsten-loaded TiO_2 was superior to that of unmodified TiO_2 with a 2-fold increase in degradation rate of methylene blue, and equally effective for the degradation of different class of dyes such as methyl violet and methyl orange at 1 mol% WO_3 loading. The photocatalytic activity decreased with WO_3 loading higher than 2 mol%, while at lower than 0.6 mol% WO_3 loading, no significant enhancement in the photocatalytic activity was observed. Higher photocatalytic efficiency of WO_3/TiO_2 prepared by sol-gel process for the degradation of formic acid has been reported at W/Ti molar ratio of 3%.^{55h} Shifu *et al.*⁶² also described the superior photocatalytic activity of the coupled WO_3/TiO_2 photocatalysts prepared by ball milling containing optimum percentage of 3% WO_3 for the degradation of organophosphate insecticide monocrotophos. The WO_3/TiO_2 photocatalysts containing 3 mol% WO_3 prepared by microwave assisted hydrothermal method showed higher photocatalytic activity for the degradation of Rhodamine B under visible light.^{56e} The maximum improvement of MB degradation by flame-made WO_3/TiO_2 has been reported at 3.6 mol%,⁵⁹ while others have reported only 40–50% increment at 3mol% WO_3/TiO_2 .^{58e} However, the photocatalytic activity of WO_3/TiO_2 was maximized when the surface is covered with WO_3 with monolayer thickness, theoretically at 3.2 mol% WO_3 , with the degradation of aqueous dichlorobenzene enhanced by 2.5-fold, and benzene and 2-propanol degradation in the gas phase enhanced by 3.6- and 5.9-fold, respectively.^{58e}

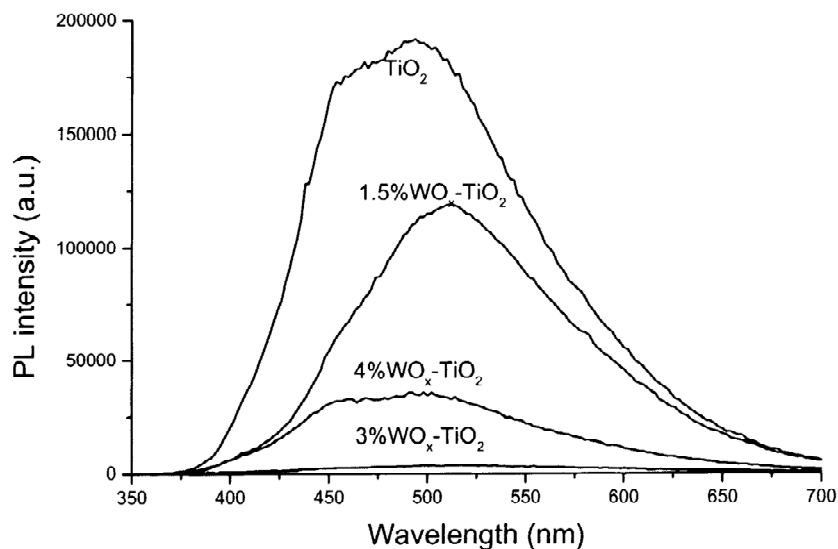


Figure II-15: The photoluminescence (PL) spectra of pure TiO_2 and WO_x/TiO_2 containing different mol% of WO_x .^{55a}

Li *et al.*^{55a} reported that coupled WO_3/TiO_2 photocatalysts prepared by a sol-gel method can form stoichiometric solid solution of $\text{W}_x\text{Ti}_{1-x}\text{O}_2$. Solid solution of $\text{W}_x\text{Ti}_{1-x}\text{O}_2$ can produce a tungsten impurity energy level and depend on the amount of WO_3 . When the content of WO_3 is lower than an optimum ratio, tungsten impurity energy level would be a separation center. On the contrary, when the content of WO_3 is higher than an optimum ratio, tungsten impurity energy level would be a recombination center as evidenced by photoluminescence (PL) spectra (**Figure II-15**). So, the activity of the photocatalyst raises with the increase in the amount of doped- WO_3 ; but it will decrease drastically when WO_3 content is higher than a given value. The highest activity for WO_x/TiO_2 prepared using sol gel method for degradation of MB under visible lamp was at 3 mol% WO_3 .^{55a} Song *et al.*⁶⁷ observed similar result where the rate of MB degradation increased initially with increasing the impurity fraction of WO_x in TiO_2 and then decreased when the molar content of WO_x exceeded 1%.

The beneficial effect of WO_3 on photocatalytic activity can also be explained by the loading of electron-accepting species on the TiO_2 surface, which is a good way of slowing down electron-hole recombination.^{56d, 68} Since W^{6+} can be easily reduced to W^{5+} ,⁶⁹ the photoexcited electrons in the conduction band of TiO_2 can be easily accepted by WO_3 , following the scheme $\text{W}^{6+} + e^-(\text{TiO}_2)_{\text{CB}} \rightarrow \text{W}^{5+}$. In this case, WO_3 helps in trapping of photogenerated electrons. This has also been confirmed in the literature⁷⁰ by charge transfer measurements using UV-Vis diffuse reflectance spectroscopy of photoproducted electrons

from TiO_2 to W^{6+} ; this charge transfer increased as the WO_3 content raised. But, on the other hand, it must be taken into account that excessively loaded WO_3/TiO_2 catalysts could act as recombination centers for electron-hole pairs, according to the scheme $\text{W}^{6+} + e^-(\text{TiO}_2)_{\text{CB}} \rightarrow \text{W}^{5+}$ but $\text{W}^{5+} + e^-(\text{TiO}_2)_{\text{VB}} \rightarrow \text{W}^{6+}$. Therefore, an optimum in WO_3 content is necessary to optimize its ability to trap the photogenerated electron trapping.

Another origin of the higher photocatalytic efficiency of WO_3/TiO_2 is its higher adsorption affinity toward electrolytes or organic molecules compared to the case with pure TiO_2 , due to its high surface Lewis acidity.^{58e} WO_3 is indeed more acidic than TiO_2 . Hence, the Lewis surface acidity of WO_3/TiO_2 will be increased with increasing WO_3 concentration, until the entire TiO_2 surface is covered with WO_3 . The surface acidity of WO_3/TiO_2 measured as a function of WO_3 content increased steadily, until it reached a plateau level at approximately 3 mol% of WO_3 in WO_3/TiO_2 indicating that at least 3 mol% of WO_3 is needed to cover the TiO_2 surface completely. A further increase in WO_3 concentration did not have any influence on the acidity of WO_3/TiO_2 composite particles. The photocatalytic activity also followed the same hysteresis as the acidity dependence. The increased acidity generates a higher affinity of WO_3/TiO_2 for species with unpaired electrons. Because of this, this material can absorb more OH^- or H_2O , which is a prerequisite for the hydroxyl radical formation necessary for photooxidation reactions. At the same time, the catalyst is able to more easily adsorb organic reactants with polarized functional groups having high affinity with acidic surfaces.

The coupling of WO_3 to titania also allows for extending absorption into the visible range and targeting solar photocatalysis applications, due to 2.8 eV band gap energy falling within the solar spectrum.^{55a, 57a, 68, 71, 72} When WO_3 ($E_g = 2.8$ eV) and TiO_2 ($E_g = 3.2$ eV) form a coupled photocatalyst, WO_3 can be excited by photons under visible illumination, TiO_2 remaining unexcited. Upon visible excitation, an electron from WO_3 may be promoted from the valence band to the conduction band, leaving behind a hole in the valence band. As the valence band of WO_3 is lower than that of TiO_2 , the later can act as a hole receiver. The photo-generated holes of the WO_3 valence band will be transferred to the valence band of TiO_2 while photogenerated electrons remain in the conduction of WO_3 causing charge separation to become more efficient. The positive holes in the valence band of TiO_2 can be trapped by OH^- or H_2O species adsorbed on the surface of the catalyst, producing reactive hydroxylradicals in aqueous media.

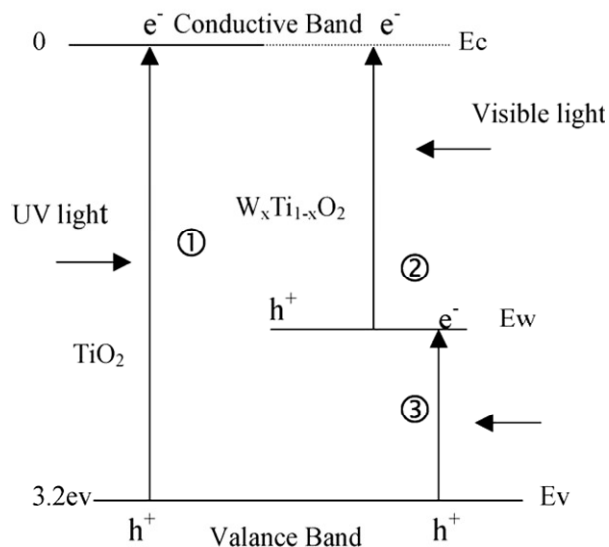


Figure II-16: Energy diagram for TiO₂ and WO_x-Ti_{1-x}O₂ systems.⁶⁷

The shift in the absorption spectrum of WO₃/TiO₂ to the visible region has been observed for such heterostructure prepared by the sol gel route,⁶⁷ ball milling method,⁶² or hydrothermal method.^{56b} Saupurahman *et al.*^{58d} reported that XPS analysis of 3 mol% WO₃/TiO₂ showed the existence of W⁶⁺, W⁵⁺ and W⁴⁺ where the first two are predominant species. It was suggested that W⁴⁺ can substitute Ti⁴⁺ due to the similarity in ionic radius, forming the non-stoichiometric solid solution W_xTi_{1-x}O₂ that could produce a tungsten impurity energy level. The light absorption band of TiO₂ changed from the near UV to the visible light range because of the tungsten impurity energy level as shown in **Figure II-16**. Optical absorption measurement revealed shifting of the absorption spectrum to the visible region by tungsten doping, even though no clear absorption edge was observed. In another study, the WO_x/TiO₂ prepared by sol mixing method showed the optimum tungsten loading at 1 mol%.⁶⁷ However, the XPS analysis of 1 mol% WO₃/TiO₂ similarly showed the existence of W⁴⁺, W⁵⁺, and W⁶⁺, with the first two as predominant species, and the absorption spectrum of W-doped TiO₂ was found shifted to the visible light. Impregnation method also shifted the absorption spectrum of TiO₂ where the shift was possibly caused by the impurity energy level within the band gap of TiO₂ as the metal was spread over the surface, and not incorporated into the TiO₂ framework.⁷³

Higher photocatalytic activity of the WO₃/TiO₂ composite film has also been reported for the degradation of organic pollutant under both UV and visible light.^{71, 74} It has been reported by Miyauchi *et al.*⁵⁴ that by having TiO₂ facing the incident UV light instead of WO₃

leads to enhanced photocatalysis. The photoinduced hydrophilicity of TiO₂ films with underlying WO₃ layers (TiO₂/WO₃ layered thin film) and the photocatalytic activity for the oxidation of methylene blue were increased resulting from efficient charge transfer between the TiO₂ and WO₃ layers. Similar effects were observed by Somasundaram *et al.*⁷⁵ when they studied the photoaction of TiO₂/WO₃ composite films. It has also been reported by Irie *et al.*⁷⁶ that the interfacial area between the TiO₂ layer and WO₃ layer played an important role in charge separation, thus affecting the photocatalytic activity. By increasing the contact area between the TiO₂ and WO₃ surfaces, more separated electron-hole pairs can live longer due to the charge separation effect. In addition, the crystal phase of both the TiO₂ and WO₃ layers plays a key role in the overall photocatalytic performance. Higashimoto *et al.*⁷⁷ has reported that a two-layer TiO₂/WO₃ system yielded higher efficiency in photoelectrochemical experiments with the TiO₂ layer being crystalline and the WO₃ phase being amorphous than with both layers being crystalline. The explanation for this effect is that the amorphous WO₃ has its conduction band level closer to that of TiO₂ and thus allows for easier charge carrier transfer. Fuerte *et al.*⁷⁸ observed continuously enhanced photocatalytic activity in toluene degradation by TiO₂/WO₃ when the tungsten concentration was enhanced. They ascribed the effect to the creation of W-related trapping centers on the catalyst surface and intraband electronic states. Needle-like TiO₂/WO_{3-x} composite thin films achieved by atmospheric pressure chemical vapour deposition demonstrated enhanced photocatalytic activity in the degradation of stearic acid under different irradiation conditions in the UV range.⁷⁹ The increase in activity of films was rationalized in terms of an effective vectorial charge separation at the interface of the two oxide semiconductors. In another report, multilayer TiO₂/WO₃ thin films, containing 5% WO₃ layers deposited on silicon and quartz glass substrate by pulsed laser deposition (PLD) method showed the best photocatalytic response to the decomposition of methylene blue in aqueous solution.⁶¹

II.4.1.4. ZnO/SnO₂ heterostructure photocatalysts

Zinc oxide (ZnO) is an n-type semiconductor of wurtzite structure with a direct energy wide band gap of 3.2–3.3 eV at room temperature.⁸⁰ SnO₂ is another n-type semiconductor with band gap energy ($E_g = 3.5\text{--}3.6$ eV) higher than that of ZnO.⁸¹ But, the conduction band (CB) position of SnO₂ is lower than that of ZnO and the valence band (VB) of ZnO is positioned between the VB and CB of SnO₂ and the CB of ZnO is positioned above the CB of SnO₂.⁸² As shown in **Figure II-17**, when the ZnO/SnO₂ heterojunction is irradiated by UV light with the photon energy higher or equal to the band gaps of ZnO and SnO₂, the

photogenerated electron in the conduction band of ZnO can easily transfer to the conduction band of SnO₂. At the same time, the holes in the valence band of SnO₂ can transfer to the valence band of ZnO. As a result, the formation of the ZnO/SnO₂ heterojunction by coupling two semiconductors could hinder the charge recombination and improve the photocatalytic efficiency.

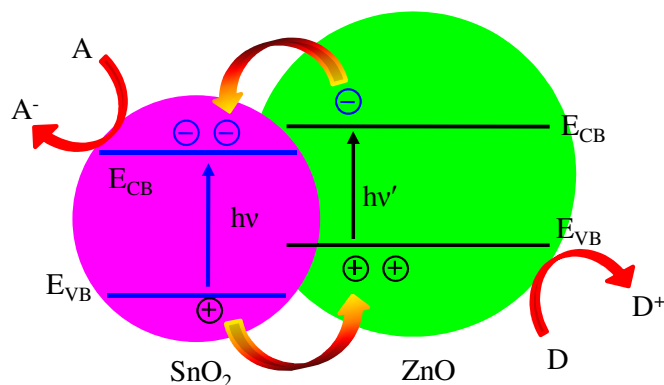


Figure II-17: Schematic band energy diagram of ZnO/SnO₂ composite.

ZnO/SnO₂ heterostructure photocatalysts have been synthesized by a variety of different processes, including hydrothermal method,^{83, 81} sol-gel route,⁸⁴ co-precipitation method⁸⁵ and mechanochemical process.⁸⁶ The ZnO/SnO₂ photocatalysts fabricated by all the above mentioned processes showed superior photocatalytic activity for the degradation of organic pollutants. **Table II-3** summarizes the degradation of different organic pollutants by ZnO/SnO₂ heterostructure photocatalysts prepared through different methods.

Kowsari and Ghelzelbash studied the effect of morphology on the photocatalytic activity for the degradation of methyl orange.^{83a} The ZnO/SnO₂ nanostructured photocatalysts was prepared by hydrothermal route in the presence of the chiral ionic liquid (CIL) ditetrabutylammonium tartrate. A regular morphology of the ZnO/SnO₂ nanostructure was obtained by controlling the morphology of the precursor with CIL and Zn²⁺/Sn⁴⁺ molar ratio as shown in **Figure II-18**. However, the ZnO/SnO₂ nanosheets (**Figure II-18 g**) showed the highest photocatalytic activity compared to ZnO/SnO₂ of other morphologies.

Table II-3: Degradation of different organic pollutants with ZnO/SnO₂ heterostructure photocatalysts.

Pollutant	Dose g L ⁻¹	Reaction condition and efficiency	Synthesis method	Reference
Methylene blue (MB)	0.5	Under UV irradiation (365 nm). 3 L of 10mg/L MB. Degradation rate constant k, 0.018 min ⁻¹ for coupled ZnO/SnO ₂ and 0.003 min ⁻¹ for SnO ₂ .	Co-precipitation	Lin & Chiang ^{85a}
Rhodamine B (RhB)	1	Under UV irradiation (200 W). 10 mL of 4.79 mg/L RhB. Degradation rate constant k, 0.19% min ⁻¹ for composite and 0.013% min ⁻¹ for SnO ₂ .	Hydrothermal	Wen <i>et al.</i> ^{83b}
Rhodamine B (RhB)	1.67	Under UV irradiation (250 W, λ=365 nm), 3 mL of 1.2 x 10 ⁻⁵ M of RhB. Composites of ZnO/SnO ₂ showed 20% better efficiency than that of P25.	Sol-gel	Davis <i>et al.</i> ^{84a}
Methyl orange (MO)	0.5	Under UV irradiation. 50 mL of 20 mg/L MO. Photocatalytic activity of ZnO/SnO ₂ was higher than that of SnO ₂ or ZnO.	Hydrothermal	Wang <i>et al.</i> ⁸¹
Methyl orange (MO)	1.25	Under UV irradiation (253.7 nm). 80 mL of 20 mg/L MO. Coupled ZnO/SnO ₂ with Zn ²⁺ /Sn ⁴⁺ = 1:1 gave higher photocatalytic efficiency compared to ZnO and SnO ₂ .	Hydrothermal	Kowsari and Ghezlbash ^{83a}
Methyl orange (MO)	1.33	Under UV irradiation (365 nm). 150 mL of 20mg/L MO. The ZnO/SnO ₂ composite calcined at 700 °C with a molar ration of Zn:Sn of 2:1 exhibited best photocatalytic efficiency.	Co-precipitation	Yang <i>et al.</i> ^{85b}
Methyl orange (MO)	2.5	Under UV irradiation (365 nm). 100 mL of 20mg/L MO. Photocatalytic activity of ZnO/SnO ₂ was 21.3 times higher than that of SnO ₂ .	Co-precipitation	Wang <i>et al.</i> ^{85c}
Methyl orange (MO)	2.5	Under UV irradiation (300W). 100 mL of 20mg/L MO. Rate constant for ZnO/SnO ₂ , Degussa P25, ZnO, SnO ₂ were 0.0865, 0.0822, 0.0335, 0.0124 min ⁻¹ , respectively.	Co-precipitation	Zhang <i>et al.</i> ^{85d}
Methyl orange (MO)	2.5	Under UV irradiation (365 nm). 100 mL of 20mg/L MO. Rate constant for ZnO/SnO ₂ , ZnO, and SnO ₂ were 0.5657 0.3406, 0.0215, and 0.0124 min ⁻¹ , respectively.	Co-precipitation	Cun <i>et al.</i> ^{85f}
4-chlorophenol (4-CP)	1.2	Under UV irradiation (8 W). 3 L of 2 x 10 ⁻⁴ M 4-CP. Rate constant for ZnO/SnO ₂ , ZnO were 0.612, 0.347, h ⁻¹ , respectively, at pH 7.	Physical mixing	Ou <i>et al.</i> ⁸⁷

The enhanced photocatalytic efficiency of nanosheet heterostructure was attributed to higher BET surface area. The BET surface area of nanosheet was 78.6 m²/g while that of other

morphology shown in **Figure II-18 (a-f)** were 20.6, 22.14, 24.30, 25.45, and 37.40 78.6 m²/g, respectively.

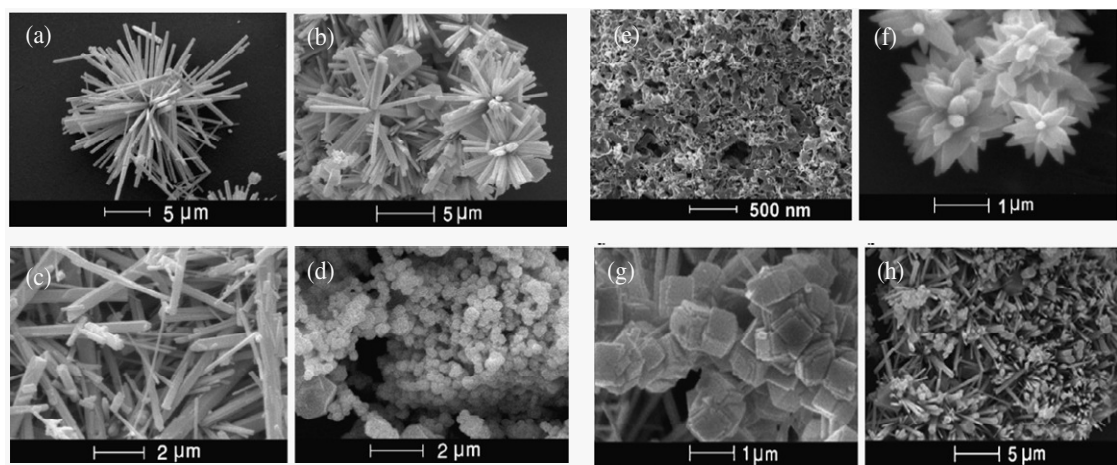


Figure II-18: SEM images of ZnO/SnO₂ nanostructures obtained at different Zn²⁺/Sn⁴⁺ molar ratios: (a) 2:1, (b) 1:1, (c) 4:1, (d) 1:2, (e) 0:1, and (f) 1:0, (g) CIL=0.1 g, Zn²⁺/Sn⁴⁺=1:1, (h) CIL=0.05 g, Zn²⁺/Sn⁴⁺=1:1; (a-f): CIL = 0.05 g.^{83a}

In another report, ZnO/SnO₂ hollow spheres and hierarchical nanosheets were synthesized using an aqueous solution containing ZnO rods, SnCl₄, and NaOH by using a simple hydrothermal method.⁸¹ The ZnO/SnO₂ hollow spheres were obtained by hydrothermal treatment at 160 °C. The morphology of the ZnO/SnO₂ hollow spheres changed to hierarchical nanosheets when the temperature was increased from 160 °C to 200 °C. Both composites showed higher photocatalytic activities in the degradation of methyl orange than that of ZnO rods or SnO₂ nanomaterials. The increased charge separation by ZnO/SnO₂ composites resulted in the higher photocatalytic efficiency. Aerogel nanocomposites of ZnO/SnO₂ were prepared through a facile, sol-gel method without the use of a template or a supporting matrix.⁸⁴ The photocatalytic efficiency of this composite was 20% better than that of commercial TiO₂ (Degussa P25) and was related to a high internal surface area, a small crystallite size and a porous network preserved even after annealing.

Due to high specific surface areas and length to diameter ratios, fiber-shaped photocatalysts showed improved behaviors compared to the particle form as far as the recycling and aggregation issues are concerned. Zhang *et al.*⁸⁸ have synthesized one-dimensional ZnO/SnO₂ nanofibers by a simple combination method of sol-gel process and electrospinning technique using a precursor solution obtained by dissolving ZnCl₂ and SnCl₂·2H₂O in dimethylformamide and then adding polyvinylpyrrolidone (PVP) to the above solution. The diameter of the resulted nanofiber was ranged from 100 to 150 nm and the

length was several micrometers. The photocatalytic activity of ZnO/SnO₂ nanofibers for the degradation of Rhodamine B (RhB) was much higher than that of electrospun ZnO and SnO₂ nanofibers, which could be attributed to the formation of a ZnO/SnO₂ heterojunction in the ZnO/SnO₂ nanofibers and the high specific area of the ZnO-SnO₂ nanofibers. They explained the charge separation mechanism with the help of band bending at the interface of ZnO/SnO₂ heterojunction. The work function of SnO₂ is higher than that of ZnO. In the ZnO/SnO₂ heterojunction, the electrons from SnO₂ transfer to ZnO in order to equalise the Fermi level at thermal equilibrium. Therefore, a built in potential develop which results in the band bending at the interface. Due to this band bending, the photogenerated hole and electron transfer in the opposite direction leading to reduced recombination of charge carriers. Liu *et al.*⁸⁹ also studied the photocatalytic activity of ZnO/SnO₂ nanofibers prepared by electrospinning method using Zn(OAc)₂ and SnCl₄·5H₂O as precursors and cellulose acetate as the fiber template in the mixed solvent of N,N-dimethylformamide/acetone (1:1, V:V) followed by calcination at 500 °C. The maximum photocatalytic activity was shown for composite nanofibers with the molar ratio of Zn:Sn = 2:1, more or less Zn:Sn ratios lowered the photocatalytic efficiency. The enhancement of the photocatalytic activity was attributed to the high BET surface areas, high efficiency in the light utilization and high efficient separation of photogenerated electron/hole pairs. Wang *et al.*⁹⁰ investigated the effect of mesoporous structure on the photocatalytic properties based on ZnO-SnO₂ coupled nanofibers. The result showed that the higher photocatalytic activity was obtained by mesoporous ZnO-SnO₂ (M-Z-S) coupled nanofibers in contrast to that of the ZnO-SnO₂ (M-S) coupled nanofibers. The improved photocatalytic activity of the M-Z-S nanofibers stemmed from the high specific surface area and the mesoporous texture. The large surface area provided more active adsorption sites and photocatalytic reaction centers. On the other hand, the mesoporous structure in the (M-Z-S) coupled nanofibers M-Z-S nanofibers makes them more efficient light harvesters which resulted in a higher photocatalytic activity.

A network-structured SnO₂/ZnO heterojunction photocatalyst (**Figure II-19a**) synthesized through a simple two step solvothermal method, in which solvothermally fabricated ZnO nanorods were used as seeds, and SnO₂ subsequently grew on their surfaces, exhibited excellent photocatalytic activity for the degradation of methyl orange.⁹¹ The photocatalytic activity of mesoporous network-structured SnO₂/ZnO was superior to the solvothermally synthesized SnO₂ and ZnO samples which was attributed to the SnO₂/ZnO heterojunction, the pore structure, and higher Brunauer-Emmett-Teller (BET) surface area of

the sample: (1) The SnO₂/ZnO heterojunction improved the separation of photogenerated electron-hole pairs due to the potential energy differences between SnO₂ and ZnO, thus enhancing the photocatalytic activity. The charge separation mechanism shown in **Figure II-19b** was similar as described elsewhere.⁸⁸ (2) The SnO₂/ZnO sample might possess more surface reaction sites and adsorb and transport more dye molecules due to the higher BET surface area and many pore channels, also leading to higher photocatalytic activity

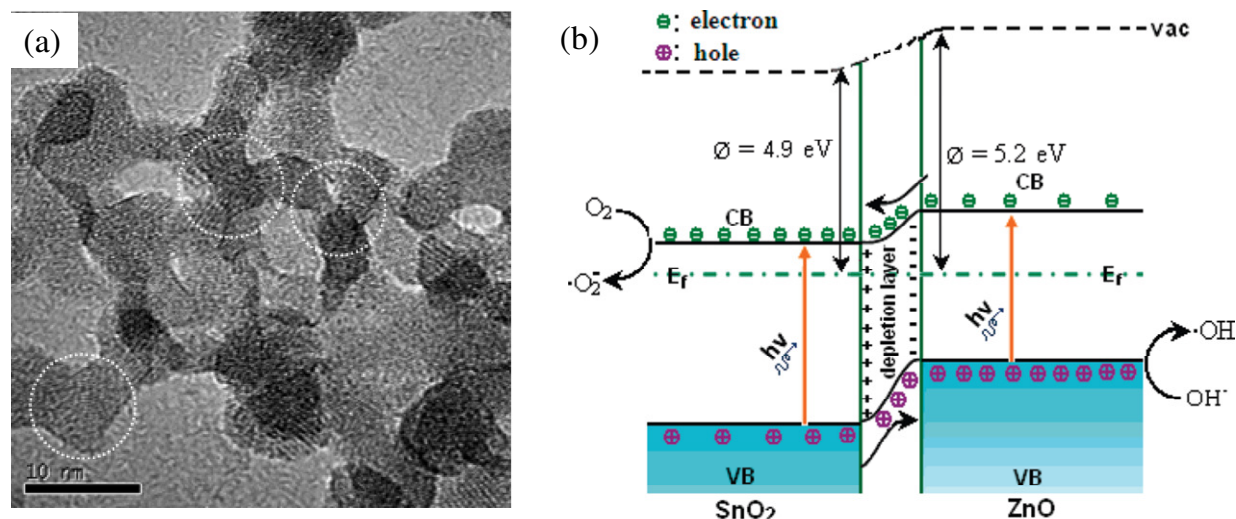


Figure II-19:(a) TEM image of the as-synthesized SnO₂/ZnO heterojunction nanocatalyst (b) Energy-band diagram and photocatalytic mechanism of the as-synthesized SnO₂/ZnO heterojunction nanocatalyst. vac, vacuum level; E_f, Fermi level; CB, conduction band; VB, valence.⁹¹

As for the other systems, the photocatalytic activity of ZnO/SnO₂ films for the degradation of organic pollutants was also investigated. Thin films of the mixed ZnO/SnO₂ system were obtained by the sol-gel technique, involving the mixture of zinc oxide and tin oxide precursor solutions that was deposited by the dip coating method on glass substrates.⁹² The films of the mixed ZnO/SnO₂ system with a Zn:Sn = 4:1 ratio and sintered at 500 °C, showed a higher photocatalytic activity for the degradation of methylene blue than the pure SnO₂ or ZnO films. This was attributed to an increase in the superficial area. Furthermore, Zhu *et al.*⁹³ investigated the photocatalytic activity of SnO₂/ZnO/chitosan films for the degradation of methyl orange under visible light irradiation. The SnO₂/ZnO quantum dots (3-5 nm diameters) heterojunction immobilized on cross linked chitosan films (SnO₂/ZnO/chitosan films) were fabricated by a co-precipitation technique combined with solution casting method. The SnO₂/ZnO/chitosan films exhibited efficient decolorization of azo dyes during the photocatalytic reaction under visible light irradiation.

II.4.2. p-n heterojunction

It has already been mentioned in **section II.3.2** that the fabrication of an actual p-n heterojunction in various composites photocatalysts constitutes another approach to achieve efficiently electron-hole pairs separation because of the existence of an internal electric field from the n-type semiconductor to the p-type semiconductor.⁹⁴ It is known that NiO is a p-type semiconductor,⁹⁵ and TiO₂ is an n-type semiconductor. When p-type NiO and n-type TiO₂ are put into contact, a p-n junction will be formed between p-NiO and n-TiO₂ particles. Theoretically, when p-type semiconductor NiO and n-type semiconductor TiO₂ form p-n junctions, an inner electric field will be formed at the interface. At the equilibrium, the inner electric field forms because the p-type semiconductor NiO region carries negative charge, while TiO₂ region gets the positive charge. According to the energy band diagram of p-n NiO/TiO₂ junction shown in **Figure II-4**, as the p-n junction is irradiated by photons, the photogenerated holes will flow to the valence band of NiO nanoparticles (negative side), while the electrons flow to the conduction band of TiO₂ (positive side). As a result, the photogenerated electrons and holes are separated efficiently, and the photocatalytic activity is enhanced.

Currently, NiO-loaded TiO₂, acting as a model nano-p-n junction photocatalyst, is being extensively investigated to improve the photocatalytic activity of TiO₂. Among various methods available for the synthesis of photocatalytic active nanocomposites, sol-gel is considered to be the most successful one in creating nanoparticulate systems with controlled pore structure. Shifu *et al.*⁹⁶ fabricated the p-n junction NiO/TiO₂ photocatalyst by sol-gel method. The photocatalytic activity of the p-n junction NiO/TiO₂ with optimum 0.5 % doped-NiO (mole ration of Ni/Ti) was much higher than that of TiO₂ on the photocatalytic reduction of Cr₂O₇²⁻ owing to the effective charge separation by the inner electric field. However, such process was not favourable in the photocatalytic oxidation of rhodamine B. on the other hand, Chen *et al.*⁹⁷ reported higher degradation efficiency of methylene blue with 0.5 wt% NiO/TiO₂. Similarly, the photocatalytic preferential oxidation of CO with O₂ in the presence of H₂ was found to proceed efficiently on NiO/TiO₂ containing 0.5 wt% NiO.⁹⁸ To get deeper insight in this system, Ku *et al.*⁹⁹ investigated the effect of NiO amount on both texture and structure of the NiO/TiO₂ photocatalysts prepared by the sol-gel route. Coupling of NiO retarded the phase transformation of TiO₂ and hindered the aggregation of particles resulting in a slight increase in the surface area. The heterostructure catalyst exhibited higher response of surface photovoltage and higher photocatalytic activity for the reduction of hexavalent

chromium than pure TiO₂ indicating that the recombination of photogenerated electron-hole pairs was delayed by the inner electric field caused by the p-n junction region. Higher photocatalytic degradation of methylene blue was obtained by mesoporous NiO/TiO₂ nano-mixed oxides containing 5 mol% NiO with definite particle size and controlled pore structure synthesized by sol-gel route using cetyltrimethylammonium bromide template.¹⁰⁰ The higher photocatalytic activity of the samples was attributed to reduction in particle size, the increasing in surface area, the photoelectron/hole separation efficiency and the extension of the wavelength range of photoexcitation. Finally, it is also worth mentioning that the mesoporous-assembled TiO₂/NiO mixed oxide nanocrystals containing 25 mole% NiO synthesized by a sol-gel process with the aid of a structure-directing surfactant under mild condition showed a higher photocatalytic activity for the degradation of methyl orange.¹⁰¹

Iwaszuk *et al.*¹⁰² studied the origin of the visible-light response of surface modified TiO₂ with NiO cluster. The results showed that NiO clusters were deposited on TiO₂ surfaces with large adsorption energies ranging from -3.18 to -6.15 eV, with metallic Ni-Ti bonds leading to extra stabilization on rutile (110) compared with anatase (001). The deposited clusters narrowed the TiO₂ band gap, which pushed the photoactivity into the visible region due to the presence of NiO states at the top of the valence band of TiO₂. The NiO/TiO₂ exhibited a high level visible-light activities for 2-naphthol and p-cresol degradations concurrently with enhanced UV-light activity. The enhanced photocatalytic activity was attributed both to the charge separation due to the excitation from the Ni 3d surface sub-band to the TiO₂ conduction band and the action of the NiO species as a mediator for the electron transfer from the TiO₂ conduction band to O₂. Jin *et al.*¹⁰³ proposed a similar explanation for narrowing the band gap of the surface modified TiO₂ with NiO that caused a high visible-light activity and a significant increase in the UV-light activity for the degradation of 2-naphthol. p-n junction heterostructure TiO₂ nanobelts produced by assembling NiO nanoparticles on TiO₂ nanobelts also exhibited much enhanced photocatalytic activity under visible light for the degradation of methyl orange through the separation of holes and electrons produced at the p-n junction.¹⁰⁴ Sim *et al.*¹⁰⁵ investigated the photocatalytic decomposition of methylene blue under solar light with p-n junction NiO/TiO₂ nanotubes. NiO/TiO₂ samples showed higher degradation efficiency compared to that of TiO₂ nanotubes.

Sreethawong *et al.*¹⁰⁶ prepared mesoporous NiO/TiO₂ composites using the sol-gel process in the presence of a suitable template. The as-synthesized NiO/TiO₂ demonstrated higher photocatalytic activities for H₂ evolution from aqueous methanol solutions. The

optimum level of NiO loading was 1.5 wt%. Elouali *et al.*¹⁰⁷ prepared a porous ceramic wafer photocatalyst disc from several commercially available titanias. The wafers were coated on one face with Pt and a NiO co-catalyst on the reverse side. The activities of the ceramic wafer were tested for hydrogen and oxygen evolution from aqueous sacrificial systems. Loading with NiO was found to greatly increase photo-oxidation activity by 677% at the expense of a 67% reduction in the hydrogen production rate. Guo *et al.*¹⁰⁸ demonstrated the synthesis of TiO₂ nanotube arrays based on a Ti substrate by a facile and effective two-electrode anodization process in an aqueous electrolyte. The NiO/TiO₂ junction electrode was fabricated by employing electroless plating and annealing which resulted in TiO₂ nanotube arrays coated with a layer of NiO nanoparticles. The resulting NiO/TiO₂ junction electrode enabled to obtain an enhanced photocurrent (3.05 mA cm⁻²) as compared with a TiO₂ electrode based on TiO₂ nanotube arrays (0.92 mA cm⁻²) under AM 1.5 G (100 mw cm⁻²) at a bias of 0.65V resulting from reduced recombination of photogenerated charge carriers. Furthermore, the NiO/TiO₂ junction electrode exhibited a considerable and sustained water splitting behavior demonstrating a 2:1 volume ratio of hydrogen and oxygen.

Other n-type semiconductors as ZnO or SnO₂ can also be used in combination with NiO to build p-n heterostructure photocatalysts. Thus, the p-n NiO/ZnO heterojunctions also exhibit high photocatalytic activity in degradation of organic pollutants compared with pure ZnO resulting from suppression of the recombination of photogenerated electron-hole pairs by the mutual transfer of photogenerated electrons or holes in the heterojunctions. Zhang *et al.*¹⁰⁹ investigated the photocatalytic activity of one-dimensional electrospun nanofibers of NiO/ZnO heterojunctions synthesized by using a sol-gel process and electrospinning technology. The results showed that the NiO/ZnO heterojunction nanofibers with the Ni/Zn molar ratio of 1 possessed higher photocatalytic activity than the pure NiO and ZnO nanofibers for the degradation of rhodamine B dye under UV light irradiation due to the enhanced separation efficiency of the photogenerated electron-hole pairs from the *p-n* heterojunctions. The PL spectra and SPS measurement confirmed the enhanced charge separation. In addition, these nanofibers could be easily recycled without a decrease in the photocatalytic activity due to their one-dimensional nanostructure properties. Hameed *et al.*¹¹⁰ also reported the higher catalytic efficiencies of NiO/ZnO nanocomposites synthesized by co-precipitation/co-gel formation techniques using potassium hydroxide (KOH), sodium carbonate (Na₂CO₃) and oxalic acid (H₂C₂O₄) as precipitating agents. All the three synthesized nanocomposites showed appreciable activity for the decolorization of methyl

orange and methylene blue for both dyes being observed with KOH derived NiO/ZnO nanocomposites. Shifu *et al.*¹¹¹ observed higher photocatalytic reduction of $\text{Cr}_2\text{O}_7^{2-}$ and lower photocatalytic oxidation of methylene blue with p-n junction NiO/ZnO photocatalysts compared with pure ZnO.

This system is also efficient to achieve water reduction under visible light as investigated by Belhadi *et al.*¹¹² The best performance was obtained in basic media on 4% NiO loaded NiO/ZnO composite using $\text{S}_2\text{O}_3^{2-}$ as sacrificial agent with hydrogen evolution rate of $435 \mu\text{mol h}^{-1}$. The best performance was attributed to the effective dispersion of NiO over the support that led to enhance the photoactivity. The electrons generated upon visible light in the conduction band of NiO, anchored uniformly on ZnO, diffuse to the interface for achieving the water reduction. These properties found recently interesting application in sensing of dilute hydrogen sulfide (H_2S) gas. Thus, Xu *et al.*¹¹³ reported enhanced sensitivity with hierarchical NiO@ZnO gas sensor compared with the pure ZnO, NiO, and the ZnO/NiO mixed gas sensors.

Examples with SnO_2 are rare. However, it is worthwhile to mention that Mohamed and Aazam investigated the photocatalytic oxidation of CO over NiO/ SnO_2 photocatalyst synthesized by coprecipitation method under UV irradiation.¹¹⁴ Compared with pure SnO_2 , the 33.3 mol% NiO/ SnO_2 composite led to a twentyfold enhancement of the photocatalytic oxidation of CO resulting from efficient interface electron transfer.

In another report, the p-n junction p-ZnO/ TiO_2 photocatalyst was prepared by ball milling of TiO_2 in H_2O solution doped with p-ZnO. The p-n junction photocatalyst p-ZnO/ TiO_2 exhibited higher photocatalytic reduction activity for the reduction of $\text{Cr}_2\text{O}_7^{2-}$, but lower photocatalytic oxidation activity for the oxidation of methyl orange.^{43c} The higher photocatalytic performance of p-ZnO/ TiO_2 was attributed to the inner electric field assisted charge separation at the junction interfaces between the p-ZnO and TiO_2 semiconductors, which consequently favors an effective photoexcited electron-hole separation. On the other hand, ZnO could trap the hole ($\text{ZnO} + 2\text{h}^+ \rightarrow \text{Zn}^{2+} + 1/2\text{O}_2$) enriching electrons in the interface to react with $\text{Cr}_2\text{O}_7^{2-}$ adsorbed on the photocatalysts surface, thus increasing photocatalytic reduction activity and lowering photocatalytic oxidation activity. Similar result was also obtained for the photocatalytic reduction of $\text{Cr}_2\text{O}_7^{2-}$ by single-step synthesized ZnO/ TiO_2 nanoparticles by microwave radiation.^{44c}

II.4.3. Metal/semiconductor heterojunctions

Modification of semiconductor with noble metals, such as Ag, Au, Pd, Pt nanoparticles is a profound way to enhance the photocatalytic activity by increasing the lifetime of the electron-hole pairs and allows the extension of the light absorption of wide band gap semiconductor to the visible region due to the surface plasmon resonance (SPR) effect of noble metals.¹¹⁵ The metal nanoparticles often act as electron scavengers improving charge separation within the semiconductor-metal photocatalyst system.¹¹⁶ The electron accumulation on the metal deposits shifts the Fermi level of metal to more negative potentials, and the resulting Fermi level of the composites shifts closer to the CB of the semiconductor (**Figure II-20**).¹¹⁷

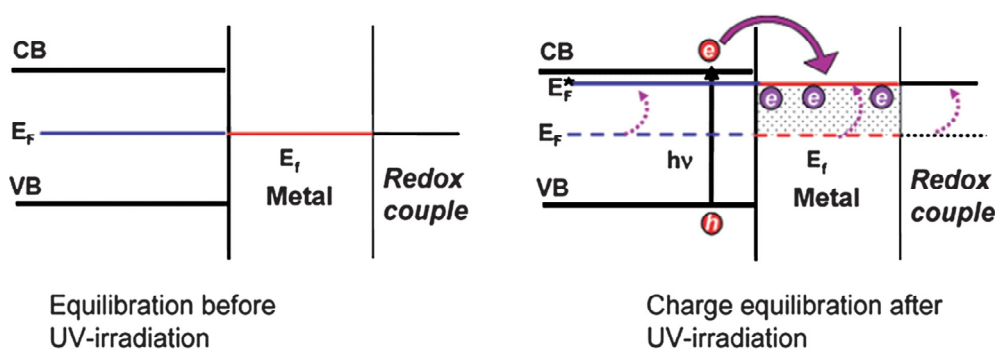


Figure II-20: Equilibration of semiconductor-metal nanocomposites with the redox couple before and after UV irradiation.¹¹⁷

The negative shift in the Fermi level reveals the better charge separation and the more reductive power of the composite system. Thus, the metal particles distributed on the surface of the semiconductors could greatly enhance the overall photocatalytic efficiency. Furthermore, metallic nanoclusters located on the semiconductor surface can act as effective cocatalysts to reduce the overpotential for surface electrochemical reactions or gas evolution processes.

II.4.3.1. RuO₂/TiO₂ heterostructure photocatalysts

Adequate RuO₂ homogeneously distributed on the surface of TiO₂ particles can serve as a shallow trap of holes to favour the separation of electron-hole pairs and delay the recombination of holes with electron, thus improving the photodegradation efficiency. The RuO₂ has a high work function located in the band gap above the valence band of TiO₂.¹¹⁸ When they are put into contact, electron will be transferred from TiO₂ to RuO₂ in order to equalize the Fermi level at the thermal equilibrium. As a consequence an upward bending of

the energy bands is expected from TiO₂ to RuO₂ which favours an efficient charge separation at the RuO₂/TiO₂ interface under illumination. Another important beneficial effect of RuO₂ loading on TiO₂ is the increase in conductivity, which ultimately allows a more efficient charge transfer within the photocatalyst and makes it kinetically faster when it is involved in the redox processes.¹¹⁹

Several studies have shown that TiO₂ decorated with RuO₂ particles or films could catalyze the oxygen production by improving the efficiency of charge separation at the metal oxide/semiconductor interface.¹²⁰ Ohno *et al.*^{120c} found that Ru-doped TiO₂ materials exhibit a photocatalytic activity under visible light due to the formation of an impurity energy level which then modifies the band gap of TiO₂. Housekova *et al.*^{120b} prepared nanocrystalline titania particles doped with ruthenium oxide by homogeneous hydrolysis of TiOSO₄ in aqueous solution in the presence of urea. The resulting composites showed an enhanced photocatalytic activity for the decomposition of acetone in the gaseous phase under visible light. The RuO₂ caused the anatase to rutile transformation to occur at lower temperatures, resulting in a decrease in the band gap. Amama *et al.*¹²¹ reported a higher photocatalytic activity of TiO₂/RuO₂ prepared by the impregnation method compared to that of TiO₂/RuO₂ prepared by the slurry precipitation method for the photocatalytic oxidation of trichloroethylene. The enhanced activity was obtained with an optimum amount of 0.4 wt% RuO₂. Liquid-phase cyclohexene epoxidation with H₂O₂ over RuO₂-loaded sol-gel (SG)-derived mesoporous-assembled TiO₂ nanocrystals was also examined.¹²² It was found that the 1 mol% RuO₂/TiO₂ synthesized by single-step sol-gel method showed a higher catalytic activity with satisfactorily high cyclohexene conversion and cyclohexene oxide selectivity.

A porous TiO₂ films were also modified with RuO₂ by the impregnation and dropping methods.¹²³ Modification with an appropriate amount of RuO₂ improved the titania photocatalytic performance in the degradation of Eosin Y by retarding the recombination of holes with electrons. RuO₂-modified TiO₂ prepared by the impregnation method showed better photocatalytic performance than that of the materials obtained by the dropping method because of the uniform distribution of RuO₂ formed by the impregnation method. Yao *et al.*¹²⁴ deposited RuO₂/TiO₂ films on float pearls (FP) by the sol-gel dipping method. The photocatalytic activity of RuO₂/TiO₂/FP was evaluated through the degradation of beta-cypermethrin (BEC) under UV light or visible light. The photocatalytic degradation of BEC was experimentally demonstrated to follow the Langmuir-Hinshelwood kinetic model. It was

also found that the RuO₂/TiO₂/FP system was particularly efficient in the photocatalytic degradation of BEC under visible light.

Ismail *et al.*¹²⁵ investigated the photocatalytic activity of mesoporous RuO₂/TiO₂ nanocomposites prepared through one step sol-gel method by choosing the photocatalytic CH₃OH oxidation to HCHO as test reaction under UV and visible light. It was observed that RuO₂ promoted the photocatalytic activity for the formaldehyde formation under visible light and photonic efficiency was enhanced by doping RuO₂ into TiO₂. The maximum photonic efficiency was obtained at 0.5 wt% RuO₂/TiO₂ and then gradually decreased when the amount of RuO₂ was raised above 0.5 wt%. The incorporation of Ru⁴⁺ into the anatase TiO₂ lattice led to photocatalytic activity in the visible spectral range. The photonic efficiency stemmed from the enhanced interfacial charge transfer of the photogenerated charge carriers to the surface species.

II.4.3.2. Ag/TiO₂ heterostructure photocatalysts

Silver (Ag) nanoparticles were also widely used for surface modification of TiO₂ to enhance the photocatalytic activity of TiO₂-based materials under UV and visible light and to improve antibacterial properties.¹²⁶ Ag-modified TiO₂ showed a higher photocatalytic activity than pure TiO₂ due to some different physical and chemical mechanisms that may act separately or simultaneously. First of all, when TiO₂ and Ag are put into contact, electron will transfer from the TiO₂ to the metallic Ag particles due to the higher Fermi level of TiO₂ than that of Ag, resulting in a space charge layer at the boundaries between Ag and TiO₂. The electric field drives the photogenerated electrons to the interior to achieve the separation of the photogenerated electron-hole pairs and to inhibit their recombination. Thus, the valence band photogenerated holes are free to react with OH⁻ adsorbed onto the TiO₂ to create hydroxyl radicals (•OH), which are able to decompose the pollutant, so a higher catalytic activity is obtained.¹²⁷ Secondly, plasmon resonance effects in metallic Ag nanoparticles can also be responsible for a local enhancement of the electric field, facilitating electron-hole pair production.¹²⁸ Lastly, Ag can improve the quantum yield by accelerating the removal and transfer of electrons from the catalyst particles to the molecular oxygen.¹²⁹

A variety of synthetic approaches have been developed to prepare silver-deposited titania materials. Widely used methods include precipitation deposition,¹³⁰ incipient wet impregnation,¹³¹ sol-gel,¹³² and photoreduction.¹³³ Suh *et al.*¹³⁴ investigated the photocatalytic degradation of rhodamine B (RhB) with Ag-deposited TiO₂ prepared by the peptization

method under visible and UV light irradiation. The Ag/TiO₂ significantly enhanced the RhB photodegradation under visible light irradiation whereas the RhB photodegradation under UV irradiation was slightly enhanced. The significant enhancement in the Ag/TiO₂ photoactivity under visible light irradiation can be ascribed to simultaneous effects of Ag deposits by both acting as electron traps and enhancing the RhB adsorption on the Ag/TiO₂ surface. More RhB molecules are adsorbed on the surface of Ag/TiO₂ than on the TiO₂ surface, enhancing the photoexcited electron transfer from the visible-light sensitized RB to the conduction band of TiO₂ and subsequently increasing the electron transfer to the adsorbed O₂. Wodka *et al.*¹³⁵ reported significantly higher photocatalytic activity of Ag/TiO₂ (P25) composites than that of pure P25 for the degradation of oxalic acid, formic acid and humic acid under artificial solar light (ASL) and UV light irradiation. In the degradation reaction of oxalic acid under ASL irradiation, Ag/TiO₂ composites were several times more active than pure P25.

Photocatalytic activity of TiO₂ modified by Ag was tested by degrading many organic compounds such as methylene blue (MB),^{130, 132a, 133, 136} methyl orange (MO),¹³⁷ astrazone orange G,¹³⁸ and rhodamine B (RhB).¹³⁴ Kim *et al.*^{136b} reported higher photocatalytic activity of Ag-containing TiO₂/carbon Nanofibers (Ag–TiO₂/CNF) composites in the degradation of MB under visible light illumination. This photocatalyst degraded MB 17 times faster than TiO₂/CNF without silver particles after 3 h. The Ag nanoparticles acted as electron acceptors and trapped the photogenerated electrons immediately, which caused an increase in the photodegradation rate and reduced electron–hole pair recombination.

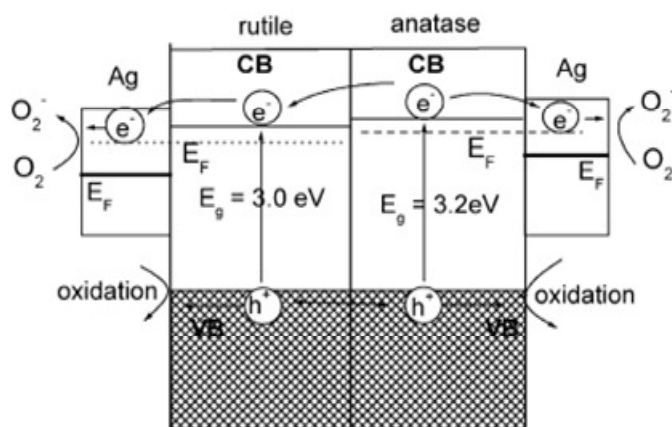


Figure II-21: Interface charge-carrier transfer dynamics of anatase/rutile, Ag/ anatase and Ag/rutile within Ag/TiO₂ composite thin films.^{137b}

This system has also been developed as film by liquid phase deposition method (LPD) and was investigated by decomposing MO.^{137b} The photocatalytic activity of Ag/TiO₂ multiphase

nanocomposite thin films exceeded that of pure TiO₂ thin films by a factor of more than 6.3. The multiphase was obtained by controlling the concentration of AgNO₃ precursor. The Ag⁺ ions promoted the formation of brookite phase and also reduced the anatase to rutile phase transition temperature. The enhanced photocatalytic activity was attributed to the fact that there were many hetero-junctions, for example anatase/rutile, anatase/brookite, Ag/anatase, Ag/rutile and so on, present in the Ag/TiO₂ multiphase nanocomposite films, that facilitates rapid separation of the photogenerated electron-hole pairs as shown in **Figure II-21**.

In most of the photocatalytic studies, Ag nanoparticles are dispersed on the TiO₂ surface. Such a catalyst structure, though effective, results in exposing both metal to reactants and the surrounding medium. The corrosion, dissolution and reaction of metals during the photocatalytic reaction limited the efficacy and the stability of the photocatalysts, especially for long-term working. To improve the catalytic performance of oxide-metal composites, core-shell nanoparticles with Ag cores and TiO₂ shells have attracted a considerable attention recently.^{132a,b,139} The Ag@TiO₂ core-shell nanoparticles prepared by the hydrazine reduction of Ag⁺/Ni²⁺ ions and the subsequent sol-gel coating of TiO₂ in an aqueous solution of CTAB demonstrated significantly higher photocatalytic activities in the degradation of rhodamine B than TiO₂ nanoparticles in the visible light region.^{132b} The enhance photocatalytic activity was attributed to the formation of Schottky barrier at the core-shell interface as well as to the excitation of the photogenerated electrons from the surface of Ag cores to the conduction band of TiO₂ shells. In contrast, the Ag@TiO₂ nanoparticles showed lower photocatalytic activities than TiO₂ nanoparticles under UV light illumination. This could be attributed to the lower TiO₂ content as well as the transfer of photogenerated electrons from TiO₂ shells to Ag cores, where the photoinduced electrons might recombine with holes and hence lead to a decrease in the photocatalytic activity. In the absence of electron scavengers, Ag has the ability to store the photogenerated electrons, as shown in **Figure II-22**. The transfer of electrons from TiO₂ shells to Ag cores continues until a Fermi level equilibrium is established between Ag and TiO₂.^{139a,b,140} The stored electrons can be readily estimated by titrating with a known redox couple such as thionine or C₆₀. Another convenient way to probe the electron storage in metal nanoparticles is by monitoring its plasmon frequency. The addition of electrons to silver nanoparticles or nanorods causes a blue shift in the absorption spectrum due to the increasing surface plasmon frequency of the electron gas.^{139a} The shift in the surface plasmon resonance band can be used to estimate the number of electrons stored in the Ag core, with about 66 electrons per Ag/TiO₂ core/shell structure.^{139a} The stored electrons

can be discharged when an electron acceptor such as O_2 , thionine, or C_{60} is introduced into the system. This electron storage ability shows the importance of such structures in photon energy conversion by storing electrons during excitation and delivering them back in the dark. However, their photocatalytic activity is limited as indicated by a $C_{60}/C_{60}^{\bullet-}$ probe under UV irradiation.

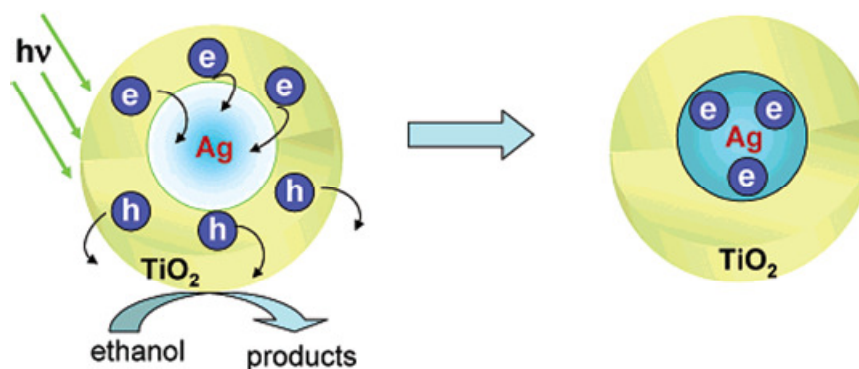


Figure II-22: Photoinduced charge separation and charging of metal core in $Ag@TiO_2$.^{139b}

Recently, TiO_2 nanoparticles were introduced as possible photocatalysts in the destruction of bacteria. Ag or Ag complex-doped TiO_2 were found to be significantly more photocatalytically and antimicrobially active than uncoated TiO_2 nanoparticles under light.¹⁴¹ For instance, Zhang *et al.*¹⁴² demonstrated that Ag/TiO_2 synthesized by a triblock copolymer induced reduction of $[Ag(NH_3)_2]^+$ ions in ethanol showed enhanced photocatalytic and bactericidal activities compared to the uncoated TiO_2 . Wu *et al.*¹⁴³ reported the montmorillonite supported Ag/TiO_2 composites, which exhibited high photocatalytic activity and good recycling performance in the degradation of *E. Coli* under visible light. The improved photocatalytic properties were ascribed to the increase surface active centers and the localized surface Plasmon effect of the Ag nanoparticles. The catalyst $AgBr/TiO_2$ was found to be highly photocatalytic in the destruction of bacteria in water under visible light.¹⁴⁴ Hu *et al.*¹⁴⁵ synthesized visible-light-active $Ag/AgBr/TiO_2$ nanoparticles by a deposition-precipitation process and demonstrated their enhanced photocatalytic activity in destroying bacteria. Elahifard *et al.*¹⁴⁶ reported that $Ag/AgBr/TiO_2$ -covered apatite had a high ability for adsorbing bacteria in the dark and exhibited a significantly improved antibacterial activity under visible light. Recently, higher photocatalytic activity of a ternary $Ag/AgBr/TiO_2$ nanotube array has been assessed via the inactivation of *Escherichia coli* under visible light irradiation.¹⁴⁷

Photocatalytic reduction has also been studied employing Ag/TiO₂ nanocomposite powders with very small Ag clusters (diameter ~1.5 nm) and low Ag loading (~0.24 wt%) prepared by a photo-assisted deposition method.¹⁴⁸ The composite showed very high efficiency in the photocatalytic reduction of nitrobenzene and bis(2-dipyridyl)disulfide. The Ag(0) nanoclusters attracting the photoelectrons from the TiO₂ CB worked as selective adsorption/reduction sites for nitrobenzene and bis(2-dipyridyl)disulfide, while the TiO₂ surface with trapped photogenerated holes served as oxidation sites. The high efficiency of such reactions was explained by the combined effects of selective adsorption and rectified charge separation. Photoactivity enhancement was also observed in the photoreduction of selenate ions by Ag/TiO₂.^{133g} Without Ag, the selenate was firstly reduced by photoelectrons to Se(0). Then, upon the exhaustion of the selenate in the solution, the as-formed Se(0) was further reduced to H₂Se. In the presence of Ag, the selenate was directly reduced to H₂Se. The photoelectrons were thought to be transferred from TiO₂ to Se(0) via Ag. The accumulation of electrons in Se⁰ before the exhaustion of Se(VI) led to the reduction of Se(0) to Se²⁻.

Zhang *et al.*^{136c} investigated the effects of chemical states of Ag on the photoelectrochemical (PEC) properties of Ag(0)/TiO₂ and Ag(I)/TiO₂ composites prepared by photoreduction-thermal treatment (PRT) method. Only the Ag(0) containing samples showed notable photocurrent under visible light. It was also demonstrated that Ag(0) was photoexcited because of plasmon resonance in the visible light region, and charge separation was accomplished by the transport of photoexcited electrons from Ag(0) to the TiO₂ conduction band with the simultaneous formation of Ag(I), which could be partially reduced to the initial active Ag(0) state under the following UV light irradiation. However, Ag(0)-TiO₂ showed poorer photocatalytic activity than Ag(I)-containing ones in degrading methylene blue (MB) under visible light. It was proposed that photoexcited Ag(I) rather than Ag(0) acted as active sites that were responsible for the enhanced photocatalytic abilities, whereas Ag(0) might contribute to the stability of the photocatalysts. Recently, Ag(0)/TiO₂ obtained by thermal treatment was considered to be inactive in the destruction of azodyes¹⁴⁵ and *E. coli*¹⁴⁶ under visible light, whereas Ag(I) (mainly Ag₂O) was demonstrated to play an important role in photocatalysis by promoting efficient separation of the generated electrons and holes.^{126a} Xin *et al.*¹⁴⁹ reported three types of silver species, including Ag₂O, AgO and Ag(0), in the Ag/TiO₂ composites prepared by a sol-gel method. At lower Ag loadings (< 0.3 mol%), silver mainly exists as Ag₂O and AgO, whereas at higher loadings (up to 5 mol%), all

three types exist with Ag(0) being the dominant one. The improved photocatalytic degradation of Rhodamine B by Ag/TiO₂ indicates that both oxidized and metallic silver can effectively capture the photogenerated electrons and enhance the photoactivity of TiO₂.

II.4.3.3. Au/TiO₂ heterostructure photocatalysts

Gold nanoparticles have good electron-storing properties and have the ability to act as electron transfer sites on nanostructures due to their higher work function. In this context, Subramanian *et al.*¹¹⁷ have probed the transfer of electrons to Au by exciting TiO₂ nanoparticles under steady-state and laser pulse excitation. Using the C₆₀/C₆₀⁻ redox couple as a probe to determine the Fermi level of the Au/TiO₂ composite system (C₆₀⁻ is stable in N₂ atmosphere and is readily monitored from its absorption maximum at 1075 nm), the size-dependent shift in the apparent Fermi level of the Au/TiO₂ composite (20 mV for 8-nm diameter and 40 mV for 5-nm and 60 mV for 3-nm gold nanoparticles) showed the ability of Au nanoparticles to influence the energetics by improving the photoinduced charge separation. The negative shift in the Fermi level was an indication of better charge separation and more reductive power for the composite system than the pristine TiO₂. The greater shift in Fermi energy with small Au particles indicated that the apparent Fermi level of the composite system can be tuned by controlling the size of the metal nanoparticle.

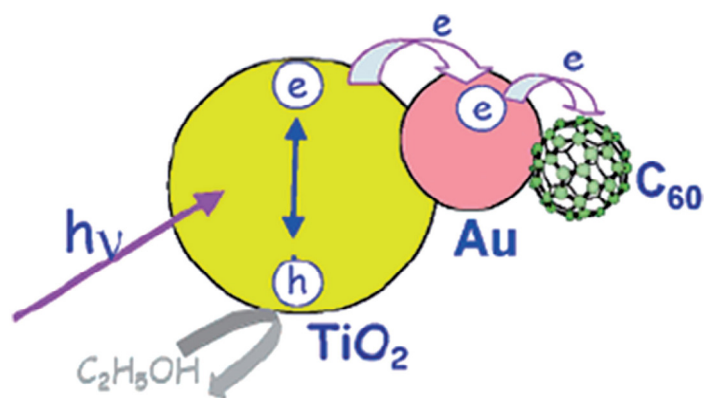


Figure II-23: Stepwise Transfer of Electrons from TiO₂ to Au to C₆₀ following the excitation of TiO₂ particles.¹¹⁷

Isolation of individual charge-transfer steps from UV-excited TiO₂ → Au → C₆₀ provided mechanistic and kinetic information on the role of metal in semiconductor-assisted photocatalysis and size dependent catalytic activity of metal-semiconductor nanocomposites is shown in **Figure II-23**. Upon UV excitation of TiO₂ colloid in deaerated ethanol-toluene, the photogenerated electrons get trapped at Ti⁴⁺ as confirmed by blue coloration of the TiO₂

suspension. After addition of Au nanoparticles with controlled size, the trapped electrons were then transferred to Au, as indicated by the decreased blue coloration. Once C_{60} was introduced, the electrons trapped at the Au electrons were further transferred to reduce C_{60} to C_{60}^- as was confirmed by the increased absorption at 1075 nm.

Gold nanoparticles can respond to visible light due to the localized surface plasmon resonance (LSPR), which is produced by the collective oscillation of the surface electrons, exhibiting great potential for extending the light absorption range of wide band semiconductors.¹⁵⁰ Some works have been reported that the immobilization of Au NPs on TiO_2 led to visible induced photocatalysis for the degradation of dyes,¹⁵¹ various volatile organic compounds,¹⁵² and toxic persistent organic pollutants.¹⁵³ In this case, the visible light generated the photoexcited electrons of the gold nanoparticles due to the surface plasmon resonance and the excited electrons are injected to the conduction band of TiO_2 . Furube *et al.*¹⁵⁴ investigated the dynamics of the charge separation of electrons and holes generated at Au-NP-loaded TiO_2 nanoparticles with femtosecond transient absorption spectroscopy. These results showed a charge-transfer mechanism in which the Plasmon-induced charge in the Au-NP transfers an electron to the TiO_2 conduction band due to the localization of the electromagnetic field by LSPR excitation. The electron injection from gold nanoparticles to TiO_2 occurred within 240 fs with an electron injection yield of about 40%. The charge recombination kinetics within 1 ns indicated that most of the injected electrons finally recombine to gold nanoparticles. The charge recombination decay strongly depends on the particles size of TiO_2 nanoparticles. Larger TiO_2 particles resulted in longer charge recombination times because of the longer diffusion length of electrons in those TiO_2 particles.¹⁵⁵ Kowalska *et al.*¹⁵⁶ reported that particle sizes of TiO_2 and Au are the key factors for high level activity. However, a possible reason for the high level of activity to their samples with larger Au particle size is the wider wavelength range, leading to a larger number of absorbed photons.

Recently, Nishijima *et al.*¹⁵⁷ demonstrated plasmonic photocurrent generation from visible to near-infrared wavelengths without affecting photoelectric conversion using electrodes in which gold nanorods (Au-NRs) are elaborately arrayed on the surface of a TiO_2 single crystal. On the other hand, Tian *et al.*¹⁵⁸ observed plasmon-enhanced photocurrent generation and photocatalytic oxidation of ethanol and methanol in TiO_2 films loaded with gold nanoparticles (Au-NPs). Lu *et al.*¹⁵⁹ reported higher photocatalytic degradation of 2,4-dichlorophenol under visible light by a light harvesting photocatalyst fabricated by infiltrating

Au nanoparticles into TiO₂ photonic crystals (TiO₂ PC/Au NPs). Some research groups reported that chemical reactions such as oxidation of aromatic alcohols¹⁶⁰ and oxidation of 2-propanol to acetone.¹⁶¹ On the other hand, others have reported the higher photocatalytic activity of Au/TiO₂ under UV light for the oxidation of methanol to formaldehyde,¹⁶² degradation of organic dyes,¹⁶³ and phenol.¹⁶⁴ In each case, the increased photocatalytic activities of Au/TiO₂ nanoparticles were attributed to the Au/TiO₂ heterointerfaces.

These systems were also studied for H₂ production since Au particles serve as an active site for H₂ production, on which the trapped photogenerated electrons are transferred to protons to produce H₂. The H⁺ ions reduction to H₂ over the Au metal surface is easier and more efficient than over TiO₂. Higher photocatalytic production of H₂ has been reported via photocatalytic reforming of methanol used as sacrificial agent on Au/TiO₂ photocatalysts.¹⁶⁵ Chiarello *et al.*^{165b} reported 30 times higher hydrogen production upon gold addition to TiO₂. Furthermore, a 30% higher reaction rate was attained with the vapour phase reactor, i.e. in the absence of liquid-phase mass transfer rate limitations, ensuring the production of up to 10.2 mmol of H₂ h⁻¹ g_{cat}⁻¹, with an apparent photon efficiency of 6.3%. Ruiz *et al.*¹⁶⁶ investigated the photocatalytic hydrogen production from methanol water splitting with Au/TiO₂ catalysts prepared by deposition-precipitation with urea. The Au/TiO₂ nanoparticle containing 0.5 wt% Au showed highest production of hydrogen. The mechanism was explained as follows: (i) the excitation of TiO₂ by UV-Vis light forming the hole–electron pair ; (ii) these induces the split of water molecules to oxygen and hydrogen ions; (iii) the electrons generated on the TiO₂ surface are transferred to the metallic particle and reduce these hydrogen ions to hydrogen gas. Finally, methanol might present a direct oxidation on the holes (h⁺) generating hydrogen ions and aldehydes. Wu *et al.*^{165d} investigated the effect of size of Au particle on the hydrogen production via photocatalytic reforming of methanol on Au/TiO₂ catalyst. The rate of hydrogen production was greatly increased when the gold particle size was reduced from 10 nm to 3 nm. The negative shift in the Fermi level induced by smaller gold particles enhanced charge separation and reductive power for the photocatalyst, resulting in a higher photocatalytic activity of Au/TiO₂.

Excitation of surface plasmon resonance (SPR) on gold nanoparticles can also contribute significantly to the photocatalytic hydrogen evolution of Au/TiO₂ nanoparticles under visible light as some of the energetic electrons from SPR excitation have sufficient potential to drive water reduction.¹⁶⁷ Recently, Fang *et al.*¹⁶⁸ reported that Au/TiO₂ nanocomposites prepared co-polymer assisted sol-gel route exhibited remarkable visible-light

activity for H₂ evolution from photocatalytic water reduction in the presence of ascorbic acid as the electron donor.

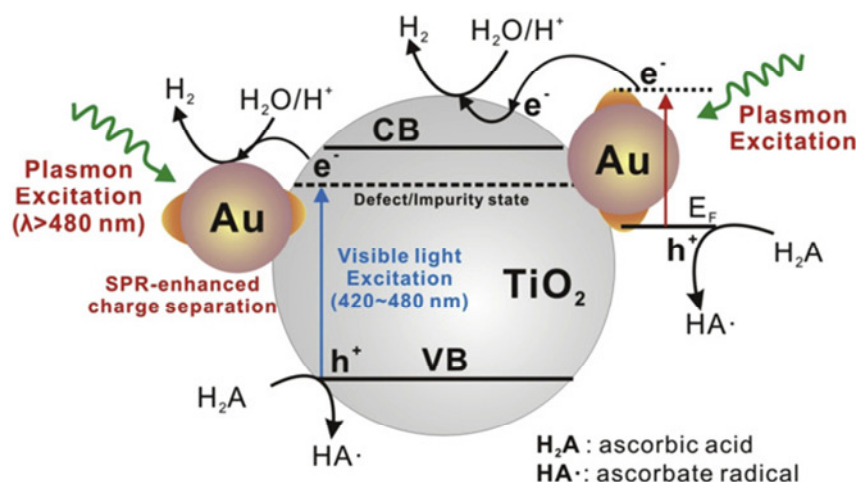


Figure II-24: Schematic illustration for hydrogen evolution over Au/TiO₂ photocatalysts under visible light irradiation.¹⁶⁸

This visible-light-driven photocatalytic activity was attributed to three major reasons as shown in **Figure II-24**. First, the defect/impurity states in the TiO₂ matrix led to weak visible-light absorption near 420 nm; Second, the plasmon-excitation of gold nanoparticles at longer wavelengths enhanced this weak visible light excitation through strong localized electric field and improves charge separation on TiO₂; Third, some plasmon-excited electrons with sufficient high energy could transfer from Au nanoparticles to the contacting TiO₂ to generate hydrogen by reducing water.

II.4.3.4. Pt/TiO₂ heterostructure photocatalysts

The modification of titania with platinum (Pt) is another way to enhance the photocatalytic activity of titania as platinum acts as an electron acceptor and a Schottky barrier is formed at the interface between TiO₂ and Pt.¹⁶⁹ Platinum also provides catalytic sites for adsorbed species and reaction intermediates.¹⁷⁰ However, the reported Pt effects have not been always positive¹⁷¹ and the role of Pt deposits in photocatalytic reaction mechanism seems to be far more complex than being a simple electron sink.

TiO₂ photocatalysts loaded with Pt deposits have been widely applied to the remediation of contaminated water and air with high degrees of photocatalytic conversion.¹⁷² As time-resolved pump-probe spectroscopy is a powerful method to investigate the dynamics of the charge carriers such as trapping, recombination and charge transfer processes with high

time resolution, Furube *et al.*¹⁷³ exploited this method to study the trapping of photoexcited electrons in Pt/TiO₂ systems. As shown in **Figure II-25**, in addition to the normal decay of the transient absorption of the trapped CB electrons in TiO₂ at 600 nm due to the electron/hole recombination following 390 nm excitation, a new decay component lasting a few picoseconds was observed and interpreted as the photoelectron migration from TiO₂ to Pt. Concerning their decay profiles, a fast decay of 5 ps was observed at 600 nm for Pt-loaded TiO₂ while almost no decay was observed up to a few tens ps for non-loaded TiO₂.

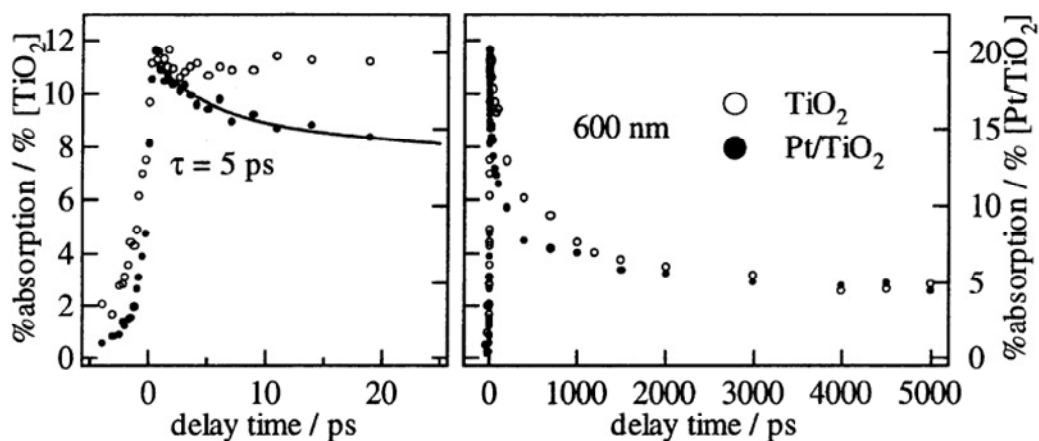


Figure II-25: Transition absorption spectra at 600 nm for TiO₂ and Pt/TiO₂ powder with 390 nm excitation.¹⁷³

Moreover, the decay of Pt-loaded TiO₂ became slower than that of the non-loaded one after several hundred ps. The PL emission spectra are also useful to disclose the efficiency of charge carrier trapping, immigration, and transfer, and to understand the fate of electron-hole pairs in semiconductor particles since PL emission results from the recombination of free carriers. In this context, Li and Li¹⁷⁴ reported that the PL intensity of the Pt/TiO₂ nanoparticles prepared by photoreduction process was significantly lower than that of the pure TiO₂. The less PL intensity of the Pt/TiO₂ indicated a lower radiation recombination of the photogenerated electrons and holes. The lower recombination can be explained in the following manner. Firstly, the Pt deposited on the TiO₂ surface produced the highest Schottky barrier at the interface that facilitated the electron capture. XPS studies revealed the presence of Pt⁴⁺ as PtO₂ on the surface of TiO₂ and the formation of Ti³⁺ resulting from the interaction between Pt and TiO₂ matrix occurred during photoreduction. Thus, secondly, Pt⁴⁺ species trapped the electrons, which migrated to adsorbed O₂. Thirdly, Ti³⁺ could enhance the oxygen chemisorption and promote the excited electrons trapped by O₂.

The Pt effects in photocatalysis are substrate specific and depend on the Pt-substrate interaction as well as the properties of Pt deposits. The photocatalytic degradation (PCD) of a specific substrate are often contradictory. For example, Zhao *et al.*¹⁷⁵ reported that the PCD of Rhodamine B (RhB) on Pt/TiO₂ was 3 times faster than its PCD on naked TiO₂, whereas Muradov¹⁷⁶ observed that the platinization of TiO₂ did not change the PCD rate of RhB significantly. Enhanced PCDs of phenolic compounds on Pt/TiO₂ have not been observed in many studies.¹⁷⁷ Reported experimental results about the PCD of trichloroethylene (TCE) on Pt/TiO₂ were contradictory as well. Chen *et al.*¹⁷⁸ reported that the platinization of TiO₂ drastically reduced the PCD rate of TCE, and Driessen *et al.*¹⁷⁹ observed a similar phenomenon. On the contrary, Crittenden *et al.*¹⁸⁰ reported that such a significant retardation in PCD of TCE was not observed with Pt/TiO₂. Lee and Choi¹⁸¹ have studied the effects of Pt speciation on TiO₂ on the photocatalytic degradation of a few chlorinated organic compounds (trichloroethylene (TCE), perchloroethylene (PCE), dichloroacetate (DCA), 4-chlorophenol (4-CP)). The results showed that TiO₂ with oxidized Pt species (Pt_{ox}/TiO₂) was less reactive than TiO₂ with metallic Pt (Pt(0)/TiO₂) for all the substrates tested. In particular, Pt_{ox}/TiO₂ strongly inhibited the PCD of TCE and PCE whereas it was more reactive than pure TiO₂ for the PCD of other compounds. The photocurrents obtained with the Pt_{ox}/TiO₂ electrode were lower than those measured for the Pt(0)/TiO₂ electrode, which was ascribed to the role of Pt_{ox} species as a recombination center. Sano *et al.*¹⁸² reported similar lower acetaldehyde degradation rate and CO₂ production rate of Pt_{ox}/TiO₂ than that of Pt(0)/TiO₂ suggesting higher activity of metal Pt as co-catalyst for acetaldehyde degradation with TiO₂. The oxidation of noble metal serves the recombination center resulting in reduction of the charge separation efficiency.

The beneficial effect of Pt deposits depends to a large extent on the loading. For example, the rate of photooxidation of 2-propanol and (*S*)-lysine, which was negligible without Pt, increased drastically with Pt loading up to ca. 0.3 wt % and then slightly decreased.^{169b} Teoh *et al.*¹⁸³ investigated the effect of loading of Pt in Pt/TiO₂ photocatalyst prepared by the flame spray pyrolysis (FSP) method on the photocatalytic degradation of sucrose. The optimum performance was obtained at 0.5 atom% Pt loading (**Figure II-26**). At loadings higher than optimum, holes recombination with negatively charged Pt deposits may decrease the adsorption of negatively charged oxidants and light shielding effects may also hinder the process. A detrimental effect on photocatalytic activity of TiO₂ was observed at very low Pt loadings (0.1 atom%) due to very small of the deposit size that does not allow for establishing

sufficient contact with sucrose molecules. This was confirmed by high photocurrent density at the Pt surface, thereby increasing electron-hole recombination and decreasing the overall mineralization rates. The Pt effects could also be influenced by the light intensity. Park *et al.*¹⁸⁴ reported that the Pt effect was positive at high light intensity for the photocatalytic degradation of trichloroethylene (TCE), but was negative at low light intensity. This effect was confirmed by photocurrent collection in the Pt/TiO₂ suspension with polyoxometalate (POM) used as an electron shuttle. The negative effect at low light intensity was attributed to the photochemical interactions between the Pt surface and reactive intermediates (TCE radical anions and reduced POM anions) inducing a null reaction.

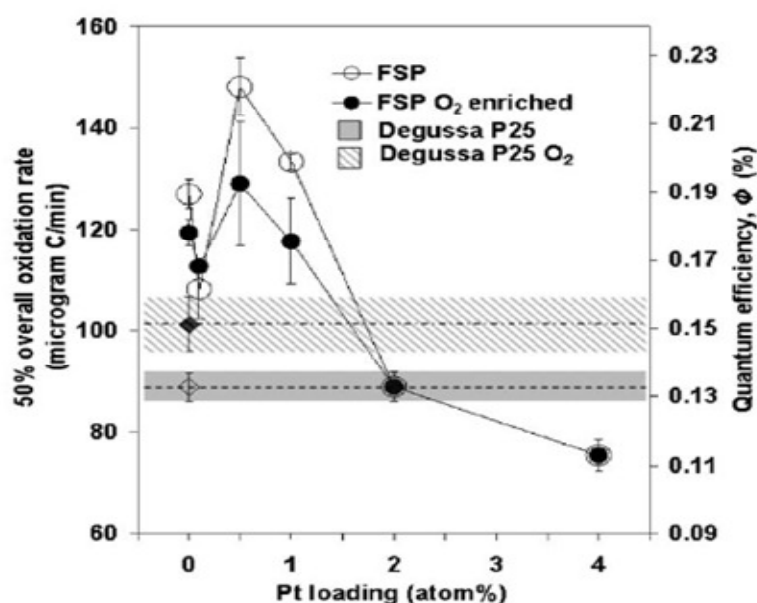


Figure II-26: Half-life mineralisation rates of 2000 g of carbohydrate carbon (as sucrose) and corresponding quantum efficiencies in ambient or oxygen-enriched suspensions by Degussa P25, FSP-made pure TiO₂ (0Pt5) and Pt/TiO₂ (XPt5, X = atom% Pt).¹⁸³

Biswas and co-workers¹⁸⁵ investigated the effect of size of Pt in Pt/TiO₂ nanostructured films, which contained one dimensional structured TiO₂ single crystals coated with Pt nanoparticles, prepared by using versatile gas-phase deposition methods on the photocatalytic reduction of CO₂ to CH₄. The size of Pt nanoparticles was controlled by changing the time for Pt deposition, and the mean sizes of Pt nanoparticles of 0.5–2 nm were obtained as the deposition time changed from 5–60 s. The Pt/TiO₂ nanofilms exhibited very high efficiencies for photocatalytic reduction of CO₂ with H₂O vapour in a continuous flow reactor to CH₄ under UV-light irradiation. The highest rate of CH₄ formation was obtained at a mean Pt particle size of 1nm with quantum yield of 2.41%. Both smaller and bigger Pt cocatalysts displayed lower activities for CH₄ formation. It is proposed that the smaller Pt

nanoparticles possibly have higher energy band separation due to quantum confinement, preventing electron transfer from the TiO₂ conduction band to Pt as shown in **Figure II-27**. On the other hand, when the size of Pt nanoparticles became larger, their property may approach that of bulk Pt, capturing both photoexcited electrons and holes and acting as charge recombination centers. Thus, it is concluded that the optimal size of Pt nanoparticles is that with energy bands positioned between -4.4 eV (the lower energy level of TiO₂ conduction band) and -5.65 eV (the work function of bulk Pt).

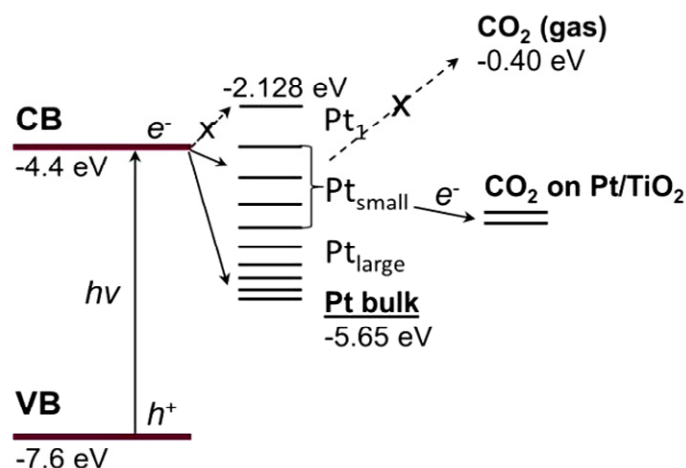


Figure II-27: Energy band positions of Pt/TiO₂-CO₂ system.¹⁸⁵

Platinized TiO₂ has also been investigated for its thermal and photocatalytic activity for CO oxidation. Thermal oxidation of CO on Pt/TiO₂ at ambient temperatures has been reported but its activity is much lower than that of Au/TiO₂. As for the photocatalytic activity, Vorontsov *et al.*¹⁸⁶ have reported that the quantum yield of CO oxidation on photoplatinized TiO₂ (1.2%) is higher than that of naked TiO₂ (0.6%) and that the photocatalytic oxidation (PCO) activity increases with lowering of Pt oxidation state (highest with Pt(0)/TiO₂). Gan *et al.*¹⁸⁷ found that both TiO₂ surface structure and Pt nanoclusters size have deep effects on CO surface chemistry and that the CO adsorption energy is enhanced on smaller Pt nanoparticles. Einaga *et al.*¹⁸⁸ observed that Pt/TiO₂ was active for the oxidation of CO to CO₂ in the dark after UV illumination was turned off and concluded that photo-generated oxidant species O⁻ and O₃⁻ remain stabilized on the Pt surface to initiate CO oxidation. On the other hand, since the enhanced photocatalytic oxidation of CO on Pt/TiO₂ was not observed at low temperature (105 K), Linsebigler *et al.*¹⁸⁹ concluded that the Pt enhancement effect in CO oxidation is ascribed not to the Schottky-barrier electron trapping in metal deposits, but to the thermal catalytic effects. Pt photodeposited on TiO₂ demonstrated

higher photooxidation rate of CO compared to naked TiO₂ samples.^{172d} The photoconversion of CO to CO₂ was quantitative in presence of O₂ and strongly inhibited in its absence or in the presence of alternative oxidants such as N₂O. The addition of water vapor in the presence of O₂ slightly affected the CO oxidation kinetics indicating that hydroxyl radical did not play a significant role in CO photooxidation and the main oxidant was O₂. The active oxygen species generated on illuminated Pt/TiO₂ surface were stable enough to survive for several minutes even in a dark period taking part in a successive photooxidation reaction. Pt nanoparticles deposited on TiO₂ enhanced the photooxidation by providing surface sites on which active oxygen species photogenerated from adsorbed O₂ were stabilized.

Platinum has also been widely used as the co-catalyst in photocatalytic hydrogen production over TiO₂.¹⁹⁰ It has been shown to greatly enhance the photocatalytic activity for hydrogen evolution. The Pt nanoparticles function as co-catalyst by providing active centres for the activation and reduction of H₂O to H₂ or the activation and reduction of CO₂ to CO and organic compounds such as CH₄, CH₃OH in the presence of H₂O, while the oxidation of H₂O or a sacrificial reagent occurs at different sites on the semiconductor or another co-catalyst for oxidation reaction. Mogyorosi *et al.*¹⁹¹ compared the photocatalytic activities for the production of H₂ of noble metal (Pt, Au, Ag) loaded TiO₂ using different sacrificial agents. The metal was deposited on the TiO₂ (P25) by photoreduction method. In the presence of methanol, the order of the catalytic efficiency for H₂ production was found to be Pt/TiO₂>>Au/TiO₂>Ag/TiO₂>>P25. The Pt/TiO₂ demonstrated highest hydrogen production rate also in the presence of oxalic acid and formic acid as compared to other two noble metals. The higher H₂ production rate from aqueous solution of ethanol was also found with Pt/TiO₂ when compared with other metal (Rh, Pd, Ni) loaded TiO₂ showing quantum yield (38% at 380 nm) 40 times higher than that for TiO₂ alone (0.9%).¹⁹² When noble metals contact with n-type semiconductor TiO₂, the excited electrons of TiO₂ move into noble metals. These systems cause Schottky-diode behaviors in noble metal contacts on TiO₂. Under these conditions, Pt nanoparticles shows more effective electron-acceptor properties because of the larger work function of Pt (Pt; 5.65 eV, Au; 5.1, Ag; 4.26, Pd; 5.12 eV, Rh; 4.98 eV).¹⁹³ As a result, Pt nanoparticles can effectively restrict the recombination of electrons and holes and Pt/TiO₂ photocatalysts show a highest activity.

Bamwenda *et al.*^{15a} investigated the effect of deposition method for Pt/TiO₂ and Au/TiO₂ photocatalysts on the H₂ production from water/methanol solution. The co-catalysts were loaded by four preparation methods, i.e., deposition–precipitation (DP), impregnation

(IMP), photodeposition (FD) and, in the case of Au, by physical mixing with colloidal gold suspension (MIX). The activity of the Pt-loaded samples was generally about 30% higher than that of the Au-loaded samples. For both series of the samples, the samples prepared by the photodeposition method showed higher activity than those prepared by other preparation methods. The activities of the platinum samples were decreased in the order Pt/TiO₂-FD > Pt/TiO₂-DP ≈ Pt/TiO₂-IMP. During photochemical deposition, the deposition of gold and platinum particles occurred at or near the site of photoexcitation. This facilitated the efficient transport of photogenerated electrons from TiO₂ to the metal particles resulting in higher H₂ production. The higher overall activity of Pt samples was probably due to a more effective trapping and pooling of photogenerated electrons by Pt and/or because platinum sites had a higher capability for the reduction reaction. The optimum loading amounts were 0.3-1 wt% for Pt-loaded samples. The exposed surface area of the co-catalyst had only a small influence on the hydrogen production rate. It was suggested that the active sites for the reaction may be the metal surface close to the TiO₂ and the TiO₂ surface around the perimeter of the metal nanoparticles. The reason why the activity decreased on the samples with higher loading amount of co-catalyst was rationalized as follows: the metal particles may block the photoabsorption by TiO₂ to decrease the surface concentration of the electrons and holes, or the deposited metal particles may act as recombination centers for the photogenerated electrons and holes.

Photoefficiency of the Pt/TiO₂ system for H₂ was improved by using sacrificial agents or electron donors. Their main task is to prohibit rapid recombination of photogenerated electrons and holes by reacting irreversibly with the photogenerated holes. A large variety of organic compounds have been selected for electron donors during photocatalytic H₂ production with Pt/TiO₂ system including alcohol (methanol, ethanol, isopropanol etc),^{15a, 190d,f, 194} organic acids (formic acid, acetic acid, oxalic acid, etc)^{191, 195} aldehydes (formaldehyde, acetaldehyde, etc.),¹⁹⁶ EDTA,^{190f, 197} biomass,¹⁹⁸ and pollutants.¹⁹⁹ Sreethawong *et al.*²⁰⁰ investigated the effect of various sacrificial reagents on photocatalytic H₂ evolution with mesoporous Pt/TiO₂ photocatyst. The result shown in **Figure II-28** revealed that the alcohol series showed a considerably higher activity than others among the sacrificial reagent investigated. This might be attributable to the ease in donating lone-pair electrons to the valence band hole upon the photocatalyst excitation, as compared to other types of sacrificial reagents. Among the alcohol series itself, methanol was found to be the most effective and the strongest sacrificial reagent to yield the highest photocatalytic H₂

evolution activity. It appears that compounds possessing very high polarity,^{95b} such as acids and ketones, are unable to effectively suppress the electron–hole recombination, probably due to their stable electronic configuration. In another study, Blount *et al.*²⁰¹ showed that hydrogen formed on Pt/TiO₂ for all the organics with H bonded to the carbon in a –C–O– group. When only alkyl group were bonded to the carbon in a –C–O– group, alkanes are formed but not H₂. Abstraction of a hydrogen atom appeared to be the first step in PCD of alcohols, acids, and esters. Alcohols react to form the corresponding aldehyde and either H₂ or alkanes. Acids and esters react similarly through two parallel pathways, and one pathway extracted lattice oxygen.

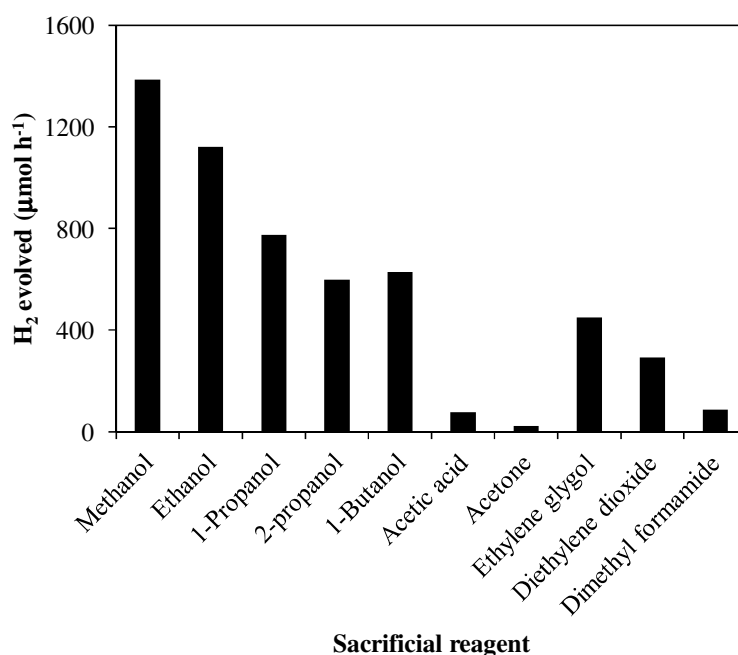


Figure II-28: Effect of sacrificial reagent type on photocatalytic H₂ evolution activity of Pt/TiO₂ (reaction condition: photocatalyst amount, 0.2 g; distilled water amount, 200 mL, sacrificial reagent amount, 20 mL, irradiation time, 5 h).²⁰⁰

The use of organic wastes and pollutants in water as electron donors produce H₂, with simultaneous removal of environmental pollutants. In order to evaluate photocatalytic H₂ production performance using organic pollutants as sacrificial agents, Yu *et al.*²⁰² examined the photocatalytic activity of Pt/TiO₂ nanosheets with exposed (001) facets using glycerol, triethanolamine, and glucose as model electron donors or scavengers; the photocatalytic H₂ production rates of these systems were 169.1, 140.2, and 133.6 μmol h⁻¹, respectively, indicating the usefulness of these pollutants as sacrificial agents. Similarly higher hydrogen production rate with simultaneous degradation of organic pollutants¹⁹⁹ and reforming of

biomass^{190g, 198} were reported by Pt/TiO₂ photocatalyst resulting from decreased rates of electron-hole recombination and oxygen-hydrogen back reaction.

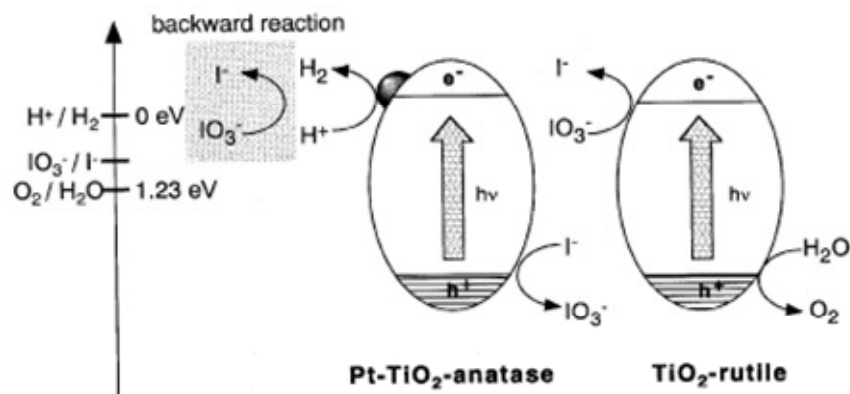


Figure II-29: Proposed photocatalytic reaction mechanism for Z-scheme water-splitting system using an IO₃⁻/I⁻ redox mediator and a mixture of Pt/TiO₂-anatase and TiO₂-rutile photocatalysts.²⁰³

Abe *et al.*²⁰³ designed a two-step photoexcitation system for overall water splitting into H₂ and O₂. It was composed of an IO₃⁻/I⁻ redox shuttle and two different photocatalysts: Pt-loaded anatase TiO₂ for H₂ evolution and rutile TiO₂ for O₂. Under UV irradiation, simultaneous gas evolution of H₂ (180 μmol/h) and O₂ (90 μmol/h) was observed from a basic (pH = 11) NaI aqueous suspension of these two different TiO₂ photocatalysts. The proposed photocatalytic reaction mechanism for water-splitting is shown in **Figure II-29**. The overall water splitting proceeded by the redox cycle between IO₃⁻ and I⁻ under basic conditions as follows: (a) water reduction to H₂ and I⁻ oxidation to IO₃⁻ over Pt-TiO₂-anatase and (b) IO₃⁻ reduction to I⁻ and water oxidation to O₂ over TiO₂-rutile. In another experiment, a stoichiometric decomposition of water into H₂ and O₂ (H₂/O₂ = 2) took place when a suspension of Pt-TiO₂ in aqueous NaNO₂ was irradiated with UV light and the activity and stability were promoted by the addition of Na₂CO₃ to the NaNO₂ solution.²⁰⁴ Some researchers reported photocatalytic hydrogen production over Pt/TiO₂ under UV irradiation by using different type of sensitizers such as merocyanine dye,²⁰⁵ Eosin Y,²⁰⁶ and heteropoly blue.^{190e} Abe *et al.*^{206b} reported that the Eosin Y-fixed Pt/TiO₂ exhibited high efficiency and quite steady H₂ production from aqueous TEA solution under visible-light irradiation for long periods, the quantum yield at 520 nm being about ~10%.

II.5. Conclusion

The semiconductor-based photocatalytic water splitting to produce hydrogen and photocatalytic degradation of organic pollutants from water and air have been proved as one of the most important technology to solve both of the world energy crisis and environment

pollution. Among the wide spectrum of metal oxide semiconductors, TiO_2 has attracted significant attention over the past decades due to its excellent performance as a photocatalyst under UV light irradiation. However, the main drawback of recombination of the photogenerated charge carriers hinders the industrial application of this technology. In this literature review, different strategies as, for instance, the coupling of two semiconductors with different energy band gap, metal deposition on the surface of semiconductor to reduce the charge carrier recombination have been discussed. Special attention has been paid to the heterostructure metal oxide nano composite related to TiO_2 , ZnO and SnO_2 . The heterostructure junction with built-in potential effectively drive the separation and transportation of photogenerated electron-hole pairs. The incorporation of noble metal as a co-catalyst on the semiconductor surface especially on TiO_2 is an effective way for photocatalytic hydrogen generation. The metal deposition also extends the absorption to the visible region allowing the use of solar light to achieve the photocatalytic process. Although heterostructure photocatalysts enhance photocatalytic efficiency, other factors such as specific surface area, porosity and the band position of the semiconductors also strongly influence the photocatalytic efficiencies. Specially, band alignment determination at the interface is still unexplored in most of the studies. Therefore, there is enough room to investigate in detail the reason behind the enhanced photocatalytic efficiency.

-
- ¹ Kamat, P. V. *Chemtech* **1995**, 25, 22.
- ² Linsebigler, A. L.; Lu, G.; Yates Jr, J. T. *Chem. Rev.* **1995**, 95, 735.
- ³ (a) Chen, X.; Mao, S. S. *Chem. Rev.* **2007**, 107, 2891. (b) Liqiang, J.; Yichun, Q.; Baiqi, W.; Shudan, L.; Baojiang, J.; Libin, Y.; Wei, F.; Honggang, F.; Jiazhong, S. *Sol. Energy Mater. Sol. Cells* **2006**, 90, 1773.
- ⁴ Serpone, N.; Lawless, D.; Khairutdinov, R.; Pelizzetti, E. *J. Phys. Chem.* **1995**, 99, 16655.
- ⁵ Vinodgopal, K.; Kamat, P. V. *Environ. Sci. Technol.* **1995**, 29, 841. (b) Shifu, C.; Lie, C.; Shen, G.; Gengyu, C. *Mater. Chem. Phys.* **2006**, 98, 116.
- ⁶ (a) Wang, H.; Wu, Z.; Liu, Y.; Sheng, Z. *J. Mol. Catal. A: Chem.* **2008**, 287, 176. (b) Liu, R.; Huiyan Ye, H.; Xiong, X.; Liu, H. *Mater. Chem. Phys.* **2010**, 121, 432.
- ⁷ Wu, L.; Yu, J. C.; Fu, X. *J. Mol. Catal. A: Chem.* **2006**, 244, 25.
- ⁸ (a) Kamat, P. V. *J. Phys. Chem. C* **2008**, 112, 18737 (b) Jum, S. J.; Hyun, G. K.; Upendra, A. J.; Ji, W. J.; Jae, S. L. *Int. J. Hydrogen Energy* **2008**, 33, 5975. (c) Leshkies, K. S.; Duvakar, R.; Basu, J.; Pommer, E. E.; Boercker, J. E.; Carter, C. B.; Kortshagen, U. R.; Norris, D. J.; Aydil, E. S. *Nano Letters* **2007**, 7, 1793.
- ⁹ Hagfeldt, A.; Gratzel, M. *Chem. Rev.* **1995**, 95, 49.
- ¹⁰ Bedja, I.; Kamat, P. V. *J. Phys. Chem.* **1995**, 99, 9182.
- ¹¹ Henglein, A. *Ber. Bunsen Ges. Phys. Chem.* **1997**, 101, 1562.
- ¹² Evans, J. E.; Springer, K. W.; Zhang, J. H. *J. Chem. Phys.* **1994**, 101, 6222.
- ¹³ (a) Bahnemann, W.; Muneer, M.; Haque, M. M. *Catal. Today* **2007**, 124, 133. (b) Singh, H. K.; Saquib, M.; Haque, M.; Muneera, M.; Bahnemann, D. *J. Mol. Catal. A: Chem.* **2007**, 264, 66. (c) Rahman, M. A.; Muneer, M. *Desalination* **2005**, 181, 161.
- ¹⁴ Wei, L.; Shifu, C.; Wei, Z.; Sujuan, Z. *J. Hazard. Mater.* **2009**, 164, 154.
- ¹⁵ (a) Bamwenda, G. R.; Tsubota, S.; Nakamura, T.; Haruta, M. *J. Photochem. Photobiol. A* **1995**, 89, 177. (b) Lee, S. G.; Lee, S. W.; Lee, H. I. *Appl. Catal. A* **2001**, 207, 173. (c) Li, Y. X.; Lu, G. X.; Li, S. B. *Chemosphere* **2003**, 52, 843. (d) Wu, N. L.; Lee, M. S. *Int. J. Hydrogen Energy* **2004**, 29, 1601. (e) Nada, A. A.; Barakat, M. H.; Hamed, H. A.; Mohamed, N. R.; Veziroglu, T. N. *Int. J. Hydrogen Energy* **2005**, 30, 687.
- ¹⁶ Zhang, Z.; Yates Jr, J. T. *Chem. Rev.* **2012**, 112, 5520.
- ¹⁷ Zhang, Z.; Shao, C.; Li, X.; Wang, C.; Zhang, M.; Liu, Y. *ACS Appl. Mater. Interfaces* **2010**, 2, 2915.
- ¹⁸ Bott, A. W. *Curr. Sep.* **1998**, 17, 87.
- ¹⁹ Gratzel, M. *Heterogeneous Photochemical Electron Transfer*; CRC Press: Boca Raton, **1989**.
- ²⁰ (a) Vinodgopal, K.; Kamat, P. V. *Environ. Sci. Technol.* **1995**, 29, 841. (b) Zhou, M.; Yu, J.; Liu, S.; Zhai, P.; Jiang, L. *J. Hazard. Mater.* **2008**, 154, 1141. (c) Hattori, A.; Tokihisa, Y.; Tada, H.; Ito,

- S. J. Electrochem. Soc.* **2000**, *147*, 2279. (d) Akurati, K. K.; Vital, A.; Hany, R. Bommer, B.; Graule, T.; Winterer, M. *Int. J. Photoenergy*, **2005**, *7*, 153. (e) Hou, L. R.; Yuan, C. Z.; Peng, Y. *J. Hazard. Mater. B* **2007**, *139*, 310.
- ²¹ Shifu, C.; Lei, C.; Shen, G.; Gengu, C. *Mater. Chem. Phys.* **2006**, *98*, 116.
- ²² Shi, L.; Li, C.; Gu, H.; Fang, D. *Mater. Chem. Phys.* **2000**, *62*, 62.
- ²³ Yang, J.; Li, D.; Wang, X.; Yang, X.; Lu, L. *J. Solid State Chem.* **2002**, *165*, 193.
- ²⁴ Wang, C.; Shao, C.; Zhang, X.; Liu, Y. *Inorg. Chem.* **2009**, *48*, 7261.
- ²⁵ Messih, M. F. A.; Ahmed, M. A.; Syhed, A. S. E. *J. Photochem. Photobiol. A* **2013**, *260*, 1.
- ²⁶ Fresni, F.; Alonso, M. D. H.; Tudela, D.; Coronado, J. M.; Soria, J. *Appl. Catal. B* **2008**, *84*, 598.
- ²⁷ Zhang, J.; Feng, L.; Wei, J.; Gou, X.; Cao, W. *Chinese Sci. Bull.* **2006**, *51*, 2050.
- ²⁸ Rachel, A.; Subrahmanyam, M.; Boule, P. *Appl. Catal. B* **2002**, *37*, 301.
- ²⁹ (a) Liu, Z.; Sun, D. D.; Guo, P.; Leckie, J. O. *Nano Lett.* **2007**, *7*, 1081. (b) Hwang, S. H.; Kim, C.; Jang, J. *Catal. Commun.* **2011**, *12*, 1037. (c) Zhang, R.; Wu, H.; Lin, D.; Pan, W. *J. Am. Ceram. Soc.* **2009**, *92*, 2463. (d) Zhang, R.; Wu, H.; Lin, D.; Pan, W. *J. Am. Ceram. Soc.* **2010**, *93*, 605.
- ³⁰ (a) Zhang, L.; Lv, F.; Zhang, W.; Li, R.; Zhong, H.; Zhao, Y.; Zhang, Y.; Wang, X. *J. Hazard. Mater.* **2009**, *171*, 294. (b) Zhang, L.; Liu, J.; Tang, C.; Lv, J.; Zhong, H.; Zhao, Y.; Wang, X. *Appl. Clay Sci.* **2011**, *50*, 68.
- ³¹ Chen, H.; Lee, S. W.; Kim, T. H.; Hur, B. Y. *J. Eur. Ceram. Soc.* **2006**, *26*, 2231.
- ³² Pelizzetti, E.; Minero, C. *Electrochi. Acta*, **1993**, *38*, 47.
- ³³ Zhou, M.; Yu, J.; Liu, S.; Zhai, P.; Jiang, L. *J. Hazard. Mater.* **2008**, *154*, 1141.
- ³⁴ Vinodgopal, K.; Kamat, P. V. *Environ. Sci. Technol.* **1995**, *29*, 841.
- ³⁵ Vinodgopal, K.; Bedja, I.; Kamat, P. V. *Chem. Mat.* **1996**, *8*, 2180.
- ³⁶ (a) Tada, H.; Hattori, A.; Tokihisa, Y.; Imai, K.; Tohge, N.; Ito, S. *J. Phys. Chem. B* **2000**, *104*, 4585. (b) Hattori, A.; Tokihisa, Y.; Tada, H.; Tohge, N.; Ito, S.; Hongo, K.; Shiratsuchi, R.; Nogami, G. *J. Sol-Gel Sci. Technol.* **2001**, *22*, 53.
- ³⁷ Kawahara, T.; Doushita, K.; Tada, H. *J. Sol-Gel Sci. Technol.* **2003**, *27*, 301.
- ³⁸ Tada, H.; Konishi, Y.; Kokubu, A.; Ito, S. *Langmuir* **2004**, *20*, 3816.
- ³⁹ Cao, Y.; Zhang, X.; Yang, W.; Du, H.; Bai, Y.; Li, T.; Yao, J. *J. Chem. Mater.* **2000**, *12*, 3445.
- ⁴⁰ Shang, J.; Yao, W.; Zhu, Y.; Wu, N. *Appl. Catal. A* **2004**, *257*, 25.
- ⁴¹ (a) Xiao, F. X. *ACS Appl. Mater. Interfaces* **2012**, *4*, 7055. (b) Guo, J.; Li, J.; Yin, A.; Fan, K.; Dai, W. *Chin. J. Chem.* **2010**, *28*, 2144.
- ⁴² (a) Serpone, N.; Maruthamuthu, P.; Pichat, P.; Pelizzetti, E.; Hidaka, H. *J. Photochem. Photobiol. A* **1995**, *85*, 247. (b) Sukharev, V.; Kershaw, R. *J. Photochem. Photobiol. A* **1996**, *98*, 165.
- ⁴³ (a) Liao, S.; Donggen, H.; Yu, D.; Su, Y.; Yuan, G. *J. Photochem. Photobiol. A* **2004**, *168*, 7. (b) Liao, D. L.; Badour, C. A.; Liao, B. Q. *J. Photochem. Photobiol. A* **2008**, *194*, 11. (c) Shifu, S.; Wei,

- Z.; Wei, L.; Sujuan, Z. *Appl. Surf. Sci.* **2008**, 255, 2478. (d) Ge, M.; Guo, C.; Zhu, X.; Ma, L.; Han, Z.; Hu, W.; Wang, Y. *Front. Environ. Sci. Engin. China* **2009**, 3, 271. (e) Tian, J.; Chen, L.; Yin, Y.; Wang, X.; Dai, J.; Zhu, Z.; Liu, X.; Wu, P. *Surf. Coat. Technol.* **2009**, 204, 205. (f) Zhang, M.; An, T.; Liu, X.; Hu, X.; Sheng, G.; Fu, J. *Mater. Lett.* **2010**, 64, 1883. (g) Mani, J.; Sakeek, H.; Habouti, S.; Dietze, M.; Souni, M. E. *Catal. Sci. Technol.* **2012**, 2, 379.
- ⁴⁴ (a) Jiang, Y.; Sun, Y.; Liu, H.; Zhu, F.; Yin, F. *Dyes Pigm.* **2008**, 78, 77. (b) Chen, D.; Zhang, H.; Hu, S.; Li, J. *J. Phys. Chem. C* **2008**, 112, 117. (c) Arin, J.; Thongtem, S.; Thongtem, T. *Mater. Lett.* **2013**, 96, 78.
- ⁴⁵ (a) Agrawal, M.; Gupta, S.; Pich, A.; Zafeiropoulos, N.E.; Stamm, M. *Chem. Mater.* **2009**, 21, 5343. (b) Liu, R.; Ye, H.; Xiong, X.; Liu, H. *Mater. Chem. Phys.* **2010**, 121, 432. (c) Karunakaran, C.; Biramasundari, G.; Gomathisankar, P.; Manikandan, G.; Anandi, V. *Mater. Res. Bull.* **2011**, 46, 1586. (d) Xiao, F. X. *ACS Appl. Mater. Interfaces* **2012**, 4, 7055.
- ⁴⁶ (a) Bansal, P.; Bhullar, N.; Sud, D. *Desalin. Water Treat.* **2009**, 12, 108. (b) Stoyanova, A.; Hitkova, H.; Nedelcheva, A. B.; Iordanova, R.; Ivanova, N.; Sredkova, M. *J. Chem. Technol. Metal.* **2013**, 48, 2, 154.
- ⁴⁷ (a) Kostedt, W. L.; Ismail, A. A.; Mazyck, D. W. *Ind. Eng. Chem. Res.* **2008**, 47, 1483. (b) Darzi, S. J.; Mahjoub, A. R. *J. Alloys Compd.* **2009**, 486, 805. (c) Zhang, Z.; Yuan, Y.; Liang, L.; Cheng, Y.; Shi, G.; Jin, L. *J. Hazard. Mater.* **2008**, 158, 517.
- ⁴⁸ Sartori, A.; Visentin, F.; Habra, N. E.; Zorzi, C. D.; Natali, M.; Garoli, D.; Gerbasi, R.; Casarin, M.; Rossetto, G. *Cryst. Res. Technol.* **2011**, 46, 885.
- ⁴⁹ (a) Zhang, Q.; Fan, W.; Gao, L. *Appl. Catal. B* **2007**, 76, 168. (b) Shaogui, Y.; Xie, Q.; Xinyong, L.; Yazhi, L.; Shuo, C.; Guohua, C. *Phys. Chem. Chem. Phys.* **2004**, 6, 659.
- ⁵⁰ (a) Zhang, Z.; Yuan, Y.; Fang, Y.; Liang, L.; Ding, H.; Jin, L. *Talanta*, **2007**, 73, 523. (b) Shaogui, Y.; Xie, Q.; Xinyong, L.; Yazhi, L.; Shuo, C.; Guohua, C. *Phys. Chem. Chem. Phys.* **2004**, 6, 659. (c) Sukharev, V.; Kershaw, R. *J. Photochem. Photobiol. A* **1996**, 98, 165. (d) Mani, J.; Sakeek, H.; Habouti, S.; Dietze, M.; Souni, M. E. *Catal. Sci. Technol.* **2012**, 2, 379. (e) Kim, D. W.; Lee, S.; Jung, H. S.; Kim, J. Y.; Shin, H.; Hong, K. S. *Int. J. Hydrogen Energy*, **2007**, 32, 3137. (f) Deguchi, T.; Imai, K.; Matsui, H.; Iwaski, M.; Tada, H.; Ito, S. *J. Mater. Sci.* **2001**, 36, 4723.
- ⁵¹ (a) Qiu, J.; Jin, Z.; Liu, Z.; Liu, X.; Liu, G.; Wu, W.; Zhang, X.; Gao, X. *Thin Solid Films*, **2007**, 515, 2897. (b) Kim, S. S.; Na, S. I.; Nah, Y. C.; *Electrochimica Acta* **2011**, 58, 503.
- ⁵² Chen, D.; Zhang, H.; Hu, S.; Li, J. *J. Phys. Chem. C* **2008**, 112, 117.
- ⁵³ Yan, X.; Zou, C.; Gao, X.; Gao, W. *J. Mater. Chem.* **2012**, 22, 5629.
- ⁵⁴ Miyauchi, M.; Nakajima, A.; Watanabe, T.; Hashimoto, K. *Chem. Mater.* **2002**, 14, 4714.
- ⁵⁵ (a) Li, X. Z.; Li, F. B.; Yang, C. L.; Ge, W. K. *J. Photochem. Photobiol. A* **2001**, 141, 209. (b) Yang, H.; Shi, R.; Zhang, K.; Hu, Y.; Tang, A.; Li, X. *J. Alloys Compd.* **2005**, 398, 200. (c) Yang, H.;

- Zhang, D.; Wang, L. *Mater. Lett.* **2002**, *57*, 674. (d) Sajjad, A. K. L.; Shamaila, S.; Tian, B. Z.; Chen, F.; Zhang, J. L. *Appl. Catal. B* **2009**, *91*, 397. (e) Delgado, N. A. R.; Reyes, L. H.; Mar, I. L. G.; Pinilla, M. A. G.; Ramirez, A. H. *Catal. Today* **2013**, <http://dx.doi.org/10.1016/j.cattod.2012.11.011>. (f) Hathway, T.; Rockafellow, E. M.; Oh, Y. C.; Jenks, W. S. *J. Photochem. Photobiol. A* **2009**, *207*, 197. (g) Piszcz, M.; Tryba, B.; Grzmil, B.; Morawski, A. M. *Catal. Lett.* **2009**, *128*, 190. (h) Riboni, F.; Bettini, L. G.; Bahnemann, D. W.; Selli, E. *Catal. Today*, **2013**, *209*, 28.
- ⁵⁶ (a) Puddu, V.; Mokaya, R.; Puma, G. L. *Chem. Commun.* **2007**, 4749. (b) Ke, D.; Liu, H. Peng, T.; Liu, X.; Dai, K. *Mater. Lett.* **2008**, *62*, 447. (c) Leghari, S. A. K.; Sajjad, S.; Chen, F.; Zhang, J. *Chem. Eng. J.* **2007**, *166*, 906. (d) Yamin, Y.; Keller, N.; Keller, V. *J. Photochem. Photobiol. A* **2012**, *245*, 43. (e) Ren, G.; Gao, Y.; Yin, J.; Xing, A.; Liu, H.; *J. Chem. Pak.* **2011**, *33*, 666.
- ⁵⁷ (a) Lin, C. F.; Wu, C. H.; Onn, Z. N. *J. Hazard. Mater.* **2008**, *154*, 1033. (b) Do, Y. R.; Lee, W.; Dwight, K.; Wold, A. *J. Solid State Chem.* **1994**, *108*, 198. (c) Song, K. Y.; Park, M. K.; Kwon, Y. T.; Lee, H. W.; Chung, W. J.; Lee, W. I. *Chem. Mater.* **2001**, *13*, 2349.
- ⁵⁸ (a) Tryba, B.; Piszcz, M.; Morawski, A. W. *Int. J. photoenergy* **2009**, *2009*, 1. (b) Yamazoe, S.; Masutani, Y.; Teramura, K.; Hitomi, Y.; Shishido, T.; Tanaka, T. *Appl. Catal. B* **2008**, *83*, 123. (c) Grandcolas, M.; Cottineau, T.; Louvet, A.; Keller, N.; Keller, V. *Appl. Catal. B* **2013**, *138-139*, 128. (d) Saepurahman, Abdullah, M. A.; Chong, F. K. *J. Hazard. Mater.* **2010**, *176*, 451. (e) Kwon, T. Y.; Song, K. Y.; Lee, W. I.; Choi, G. J.; Do, R. Y. *J. Catal.* **2000**, *191*, 192.
- ⁵⁹ Akurati, K. K.; Vital, A.; Dellemann, J. P.; Michalow, K.; Graule, T.; Ferri, D.; Baiker, A. *Appl. Catal. B* **2008**, *79*, 53.
- ⁶⁰ Yang, J.; Zhang, X.; Liu, H.; Wang, C.; Liu, S.; Sun, P. *Catal. Today*, **2013**, *201*, 195.
- ⁶¹ Shinguu, H.; Bhuiyan, M. M. H.; Ikegami, T.; Ebihara, K. *Thin Solid Films* **2006**, *506-507*, 111.
- ⁶² Shifu, C.; Lei, C.; Shen, G.; Gengyu, C. *Powder Technol.* **2005**, *160*, 198.
- ⁶³ Wang, F.; Chen, X.; Hu, X.; Wong, K. S.; Yu, J. C. *Sep. Purif. Technol.* **2012**, *91*, 67.
- ⁶⁴ Georgieva, J.; Armyanov, S.; Valova, E.; Poullos, I.; Sotiropoulos, S. *Electrochem. Commun.* **2007**, *9*, 365.
- ⁶⁵ (a) Lv, K.; Li, J.; Qing, X.; Li, W.; Chen, Q. *J. Hazard. Mater.* **2011**, *189*, 329 (b) Yang, E. I.; Shi, J. J.; Liang, H. C.; Cheuk, W. K. *Chem. Eng. J.* **2011**, *174*, 539.
- ⁶⁶ Singh, S. A.; Madras, G. *Sep. Purif. Technol.* **2013**, *105*, 79.
- ⁶⁷ Song, H.; Jiang, H.; Liu, X.; Meng, G. *J. Photochem. Photobiol. A* **2006**, *181*, 421.
- ⁶⁸ Bosc, F.; Wdwards, D.; Keller, N.; Keller, V.; Ayral, A. *Thin Solid Films*, **2006**, *495*, 272.
- ⁶⁹ Tennakone, K.; Heperuma, O. A.; Bandara, J. M. S.; Kiridena, W. C. B. *Semicon. Sci. Technol.* **1992**, *7*, 423.
- ⁷⁰ Martin, C.; Palmisano, L.; Rives, V.; Sclafani, A. *Catal. Lett.* **1997**, *49*, 235.
- ⁷¹ Rampaul, A.; Parkin, I. P.; O'Neill, S. A.; DeSouza, J.; Mills, A.; Elliott, N. *Polyhed.* **2003**, *22*, 35.

- ⁷² Keller, N.; Barraud, E.; Bosc, F.; Edwards, D.; Keller, V. *Appl. Catal. B* **2007**, *70*, 423.
- ⁷³ Paola, A. D.; Marci, G.; Palmisano, L.; Schiavello, M.; Uosaki, K.; Ikeda, S.; Ohtani, B. *J. Phys. Chem. B* **2002**, *106*, 637.
- ⁷⁴ (a) Keller, V.; Bernhardt, P.; Garin, F. *J. Catal.* **2003**, *215*, 129. (b) Puddu, V.; Mokaya, R. Puma, G. L. *Chem. Commun.* **2007**, 4749. (c) Stojadinovic, S.; Radic, N.; Vasilic, R.; Petkovic, M.; Stefanov, P.; Zekovic, L.; Grbic, B. *Appl. Catal. B* **2012**, *126*, 334. (d) Smith, W.; Zhao, Y. *J. Phys. Chem.* **2008**, *112*, 19635.
- ⁷⁵ Somasundaram, S.; Tacconi, N.; Chenthamarakshan, C. R.; Rajeshwar, K.; Tacconi, N. R. *J. Electroanal. Chem.* **2005**, *577*, 167.
- ⁷⁶ Irie, H.; Mori, H.; Hashimoto, K. *Vacuum* **2004**, *74*, 625.
- ⁷⁷ (a) Higashimoto, S.; Ushiroda, Y.; Azuma, M. *Top. Catal.* **2008**, *47*, 148. (b) Higashimoto, S.; Kitahata, N.; Mori, K.; Azuma, M. *Catal. Lett.* **2004**, *101*, 49.
- ⁷⁸ Fuerte, A.; Alonso, M. D. H.; Maira, A. J.; Arias, A. M.; Garcia, M. F.; Conesa, J. C.; Soria, J.; Munuera, G. *J. Catal.* **2002**, *212*, 1.
- ⁷⁹ Cabrera, R. Q.; Latimer, E. R.; Kafizas, A.; Blackman, C. S.; Carmalt, C. J.; Parkin, I. P. *J. Photochem. Photobiol. A* **2012**, *239*, 60.
- ⁸⁰ Gupta, T. K. *J. Am. Ceram. Soc.* **1990**, *73*, 1817.
- ⁸¹ Wang, W. W.; Zhu, Y. J.; Yang, L. X. *Adv. Funct. Mater.* **2007**, *17*, 59.
- ⁸² Grätzel, M. *Nature* **2001**, *414*, 338.
- ⁸³ (a) Kowsari, E. Ghezelbash, M. R. *Mater. Lett.* **2012**, *68*, 17. (b) Wen, Z.; Wang, G.; Lu, W.; Wang, Q.; zhang, Q.; Li, J. *Cryst. Growth Des.* **2007**, *9*, 1722.
- ⁸⁴ Davis, M.; Hikal, W. M.; Gümeçi, C.; Weeks, L. J. H. *Catal. Sci. Technol.* **2012**, *2*, 922.
- ⁸⁵ (a) Lin, C. C.; Chiang, Y. J. *Chem. Eng. J.* **2012**, *181-182*, 196. (b) Yang, Z.; Lv, L.; Dai, Y.; Xv, Z.; Qian, D.; *Appl. Surf. Sci.* **2010**, *256*, 2898. (c) Cun, W.; Wang, X.; Xu, B. Q.; Zhao, J.; Mai, B.; Peng, P.; Sheng, G.; Fu, J. *J. Photochem. Photobiol. A* **2004**, *168*, 47. (d) Zhang, M.; An, T.; Hu, X.; Wang, C.; Sheng, G.; Fu, J. *Appl. Cat. A* **2004**, *260*, 215. (e) Zhang, M.; Sheng, G.; Fu, J.; An, T.; Wang, X.; Hu, X. *Mater. Lett.* **2005**, *59*, 3641. (f) Cun, W.; Jincui, Z.; Xinming, W.; Bixian, M.; Guoying S., Ping'an, P.; Jiamo, F. *Appl. Cat. B* **2002**, *39*, 269. (g) Wang, H.; Baek, S.; Lee, J.; Lim, S. *Chem. Eng. J.* **2009**, *146*, 355.
- ⁸⁶ Dodd, A.; McKinley, A. Saunders, M.; Tsuzuki, T. *Nanotechnol.* **2006**, *17*, 692.
- ⁸⁷ Ou, H. H.; Lo, S. L.; Wu, C. H. *J. Hazard. Mater.* **2006**, *B137*, 1362.
- ⁸⁸ Zhang, Z.; Shao, C.; Li, X.; Zhang, L.; Xue, H.; Wang, C.; Liu, Y. *J. Phys. Chem.* **2010**, *114*, 7920.
- ⁸⁹ Liu, R.; Huang, Y.; Xiao, A.; Liu, H. *J. Alloys Compd.* **2010**, *503*, 103.
- ⁹⁰ Wang, Z.; Li, Z.; Zhang, H.; Wang, C. *Catal. Cummun.* **2009**, *11*, 257.

- ⁹¹ Zheng, L.; Zheng, Y.; Chen, C.; Zhan, Y.; Lin, X.; Zheng, Q.; Wei, K.; Zhu, J. *Inorg. Chem.* **2009**, *48*, 1819.
- ⁹² Martínez, D. Y. T.; Pérez, R. C.; Delgado, G. T.; Ángel, O. Z. *J. Photochem. Photobiol. A* **2012**, *235*, 49.
- ⁹³ Zhu, H. Y.; Xiao, L.; Jiang, R.; Zeng, G. M.; Liu, L. *Chem. Eng. J.* **2011**, *172*, 746.
- ⁹⁴ Gaun, M. L.; Ma, D. K.; Hu, S. W.; Chen, Y. J.; Huang, S. M. *Inorg. Chem.* **2011**, *50*, 800.
- ⁹⁵ (a) Sato, H.; Minami, T.; Takata, S.; Yamada, T. *Thin Solid Films* **1993**, *236*, 27. (b) Hameeda, A.; Gondal, M.A. *J. Mol. Catal. A: Chem.* **2005**, *233*, 35.
- ⁹⁶ Shifu, C.; Sujuan, Z.; Wei, L. Wei, Z. *J. Hazard. Mater.* **2008**, *155*, 320.
- ⁹⁷ Chen, C. J.; Liao, C. H.; Hsu, K. C.; Wu, Y. T.; Wu, J. C. S. *Catal. Commun.* **2011**, *12*, 1307.
- ⁹⁸ Kamegawa, T.; Kim, T. H.; Morishima, J.; Matsuoka, M.; Anpo, M. *Catal. Lett.* **2009**, *129*, 7.
- ⁹⁹ Ku, Y.; Lin, C. N.; Hou, W. M. *J. Mol. Catal. A: Chem.* **349**, 349, 20.
- ¹⁰⁰ Ahmed, M. A. *J. Photochem. Photobiol. A* **2012**, *238*, 63.
- ¹⁰¹ Sreethawong, T.; Ngamsinlapasathian, S.; Yoshikawa, S. *Chem. Eng. J.* **2012**, *192*, 292.
- ¹⁰² Iwaszyk, A.; Nilan, M.; Jin, Q.; Fujishima, M.; Tada, H. *J. Phys. Chem. C* **2013**, *117*, 2709.
- ¹⁰³ Jin, Q.; Ikeda, T.; Fujishima, M.; Tada, H. *Chem. Commun.* **2011**, *47*, 8814.
- ¹⁰⁴ Lin, J.; Shen, J.; Wang, R.; Cui, J.; Zhou, W.; Hu, P.; Liu, D.; Liu, H.; Wang, J.; Boughton, R. I.; Yue, Y. *J. Mater. Chem.* **2011**, *21*, 5106.
- ¹⁰⁵ Sim, L. C.; Ng, K. W.; Ibrahim, S.; Saravanan, P. *Int. J. Photoenergy* **2013**, article ID 659013.
- ¹⁰⁶ Sreethawong, T.; Suzuki, Y.; Yoshikawa, S. *Int. J. Hydrogen Energy* **2005**, *30*, 1053.
- ¹⁰⁷ Elouali, S.; Mills, A.; Parkin, I. P.; Bailey, E.; McMillan, P. F.; Darr, J. A. *J. Photochem. Photobiol. A* **2010**, *216*, 110.
- ¹⁰⁸ Gou, J.; Fu, W.; Yang, H.; Yu, Q.; Zhao, W.; Zhao, X.; Sui, Y.; Ding, J.; Li, Y.; Cheng, S.; Li, M. *J. Phys. D: appl. Phys.* **2010**, *43*, 245202.
- ¹⁰⁹ Zhang, Z.; Shao, C.; Li, X.; Wang, C.; Zhang, M.; Liu, Y. *ACS Appl. Mater. Interfaces* **2010**, *2*, 2915.
- ¹¹⁰ Hameed, A.; Montini, T.; Gombac, V.; Fornasiero P. *Photochem. Photobiol. Sci.* **2009**, *8*, 677.
- ¹¹¹ Shifu, C.; Wei, Z.; Wei, L.; Sujuan, Z. *J. Sol-Gel Sci. Technol.* **2009**, *50*, 387.
- ¹¹² Belhadi, A.; Boumaza, S.; Trari, M. *Appl. Energy*, **2011**, *88*, 4490.
- ¹¹³ Xu, L.; Zheng, R.; Liu, S.; Song, J.; Chen, J.; Dong, B.; Song, H. *Inorg. Chem.* **2012**, *51*, 7733.
- ¹¹⁴ Mohamed, R. M.; Aazam, E. S. *J. Nanotechnol.* **2012**, Article ID 794874.
- ¹¹⁵ (a) Sakthivel, S.; Shankar, M. V.; Palanichamy, M.; Arabindoo, B.; Bahnemann, D. W.; Murugesan, V. *Water Res.* **2004**, *38*, 3001. (b) Jakob, M.; Levanon, H.; Kamat, P. V. *Nano. Lett.* **2003**, *3*, 353. (c) Dawson, A.; Kamat, P. V. *J. Phys. Chem. B* **2001**, *105*, 960. (d) Kubo, W.; Tatsuma,

- T. *J. Mater. Chem.* **2005**, *15*, 3104. (e) Iliev, V.; Tomova, D.; Bilyarska, A.; Eliyas, A.; Petrov, L. *Appl. Catal. B* **2006**, *63*, 266.
- ¹¹⁶ Kamat, P. V. *J. Phys. Chem. B* **2002**, *106*, 7729.
- ¹¹⁷ Subramanian, V.; Wolf, E. E.; Kamat, P. V. *J. Am. Chem. Soc.* **2004**, *126*, 4943.
- ¹¹⁸ Schafranek, R.; Schaffner, J.; Klein, A. *J. Eur. Ceram. Soc.* **2010**, *30*, 187.
- ¹¹⁹ Blondeel, J.; Harriman, A.; Poter, G.; Urwin, D.; Kiwi, J. *J. Phys. Chem.* **1983**, *87*, 2629.
- ¹²⁰ (a) Amouyal, E.; Keller, P.; Moradpour, A. *J. Chem. Soc., Chem. Commun.* **1980**, 1019-1023. (b) Houskova, V.; Stengl, V.; Bakardjieva, S.; Murafa, N.; Tyrpekl, V. *Appl. Catal. B* **2009**, *89*, 613. (c) Ohno, T.; Tanigawa, F.; Fujihara, K.; Izumi, S.; Matsumura, M. *J. Photochem. Photobiol. A* **1999**, *127*, 107. (d) Blondeel, G.; Harriman, A.; Porter, G.; Urwin, D.; Klwl, J. *J. Phys. Chem.* **1983**, *87*, 2629. (e) Sakata, T.; Hashimoto, K.; Kawai, T. *J. Phys. Chem.* **1984**, *88*, 5214.
- ¹²¹ Amama, P. B.; Ito, K.; Murabayashi, M. *J. Mater. Sci.* **2004**, *39*, 4349.
- ¹²² Woragamon, K.; Jongpatiwut, S. *Catal. Lett.* **2010**, *136*, 249.
- ¹²³ Liu, P.; Li, W. *J. Mater. Res.* **2011**, *26*, 1532.
- ¹²⁴ Yao, B. H.; Wang, L. M.; Wang, C.; Wang, Y. X.; Zhao, G. Y. *Chin. J. Chem. Phys.* **2007**, *20*, 789.
- ¹²⁵ Ismail, A. A.; Robben, L.; Bahnemann, D. W. *ChemPhysChem* **2011**, *12*, 982.
- ¹²⁶ (a) Arabatzis, I. M.; Stergiopoulos, T.; Bernard, M. C.; Labou, D.; Noephytides, S. G.; Falaras, P. *Appl. Catal. B* **2003**, *42*, 187. (b) Zhang, D. Q.; Li, G. S.; Yu, J. C. *J. Mater. Chem.* **2010**, *20*, 4529. (c) Ji, Z.; Ismail, M. N.; Callahan, D. M., Jr.; Pandowo, E.; Cai, Z.; Goodrich, T. L.; Ziemer, K. S.; Warzywoda, J.; Sacco, A., Jr. *Appl. Catal. B* **2011**, *102*, 323. (d) Stathatos, E.; Lianos, P.; Falaras, P.; Siokou, A. *Langmuir* **2000**, *16*, 2398. (e) Smirnova, N.; Vorobets, V.; Linnik, O.; Manuilov, E.; Kolbasov, G.; Eremenko, A. *Surf. Interface Anal.* **2010**, *42*, 1205. (f) Liu, S. X.; Qu, Z. P.; Han, X. W.; Sun, C. L. *Catal. Today* **2004**, *93-95*, 877. (g) Dobosz, A.; Sobczykński, A. *Water Res.* **2003**, *37*, 1489.
- ¹²⁷ Serpone, N. *J. Photochem. Photobiol. A* **1997**, *104*, 1.
- ¹²⁸ Zhao, G.; Kozuka, H.; Yoko, T. *Thin Solid Films* **1996**, *277*, 147.
- ¹²⁹ Gerischer, H.; Heller, A. *J. Electrochem. Soc.* **1992**, *139*, 113.
- ¹³⁰ Logar, M.; Jancar, B.; Sturm, S.; Suvorov, D. *Langmuir* **2010**, *26*, 12215.
- ¹³¹ (a) Shie, J. L.; Lee, C. H.; Chiou, C. S.; Chang, C. T.; Chang, C. C.; Chang, C. Y. *J. Hazard. Mater.* **2008**, *155*, 164. (b) Halasi, G.; Kecskemeti, A.; Solymosi, F. *Catal. Lett.* **2010**, *135*, 16.
- ¹³² (a) Chin, S. F.; Pang, S. C.; Dom, F. E. I. *Mater. Lett.* **2011**, *65*, 2673. (b) Chuang, H. Y.; Chen, D. H. *Nanotechnol.* **2009**, *20*, 105704. (c) Moonsiri, M.; Rangsunvigit, P.; Chavadej, S.; Gulari, E. *Chem. Eng. J.* **2004**, *97*, 241. (d) Yun, H. J.; Lee, H.; Kim, N. D.; Yi, J. *Electrochem. Commun.* **2009**, *11*, 363.

- ¹³³ (a) Sun, L.; Li, J.; Wang, C.; Li, S.; Lai, Y.; Chena, H.; Lin, C. *J. Hazard. Mater.*, **2009**, *171*, 1045. (b) Anandan, S.; Kumar, P.S.; Pugazhenthiran, N.; Madhavan, J.; Maruthamuthu, P. *Sol. Energy Sol. Cells* **2008**, *92*, 929. (c) Bansal, A.; Madhavi, S.; Tan, T. T. Y.; Lim, T. M. *Catal. Today*, **2008**, *131*, 250. (d) Lin, Y. C.; Lin, C. H. *Environ. Prog.* **2008**, *27*, 496. (e) Liu, Y.; Wang, X.; Yang, F.; Yang, X. *Microporous Mesoporous Mater.* **2008**, *114*, 431. (f) Li, C. H.; Hsieh, Y. H.; Chiu, W. T.; Liu, C. C.; Kao, C. L. *Sep. Purf. Technol.* **2007**, *58*, 148. (g) Tan, T. T. Y.; Yip, C. K.; Beydoun, D.; Amal, R. *Chem. Eng. J.* **2003**, *95*, 179.
- ¹³⁴ Suh, H. M. S.; Choi, J. R.; Hah, H. J.; Koo, S. M.; Bae, Y. C. *J. Photochem. Photobiol. C* **2004**, *163*, 37.
- ¹³⁵ Wodka, D.; Bielanska, E.; Socha, R. P. ; Wodka, M. E.; Gurgul, J.; Nowak, P.; Warszynski, P.; Kumakiri, I. *ACS Appl. Mater. Interface* **2010**, *2*, 1945.
- ¹³⁶ (a) Liu, J.; Li, X.; Zuo, S.; Yu, Y. *Appl. Clay Sci.* **2007**, *37*, 275. (b) Kim, C. H.; Kim, B. H.; Yang, K. S. *Synth. Met.* **2011**, *161*, 1068. (c) Zhang, H.; Wang, G.; Chen, D.; Lv, X.; Li, J. *Chem. Mater.* **2008**, *20*, 6543.
- ¹³⁷ (a) You, X.; Chen, F.; Zhang, J.; Anpo, M. *Catal. Lett.* **2005**, *102*, 247. (b) Yu, J.; Xiong, J.; Cheng, B.; Liu, S. *Appl. Catal. B* **2005**, *60*, 211. (c) Zhang, X.; Zhou, M.; Lei, L. *Mater. Chem. Phys.* **2005**, *91*, 73. (d) Arabatzis, I. M.; Stergiopoulos, T.; Bernard, M. C.; Labou, D.; Neophytides, S. G.; Falaras, P. *Appl. Catal. B*, **2003**, *42*, 187.
- ¹³⁸ Sökmen, M.; Özkan, A. *J. Photochem. Photobiol. A* **2002**, *147*, 77.
- ¹³⁹ (a) Hirakawa, T.; Kamat, P. V. *J. Am. Chem. Soc.* **2005**, *127*, 3928. (b) Hirakawa, T.; Kamat, P. V. *Langmuir*, **2004**, *20*, 14. (c) Cheng, B.; Le, Y.; Yu, J. *J. Hazard. Mater.* **2010**, *177*, 971.
- ¹⁴⁰ Takai, A.; Kamat, P. V. *ACS Nano*, **2011**, *9*, 7369.
- ¹⁴¹ (a) Kubacka, A.; Cerrada, M. L.; Serrano, C.; Garcia, M. F.; Ferrer, M.; Garcia, M. F. *J. Phys. Chem. C* **2009**, *113*, 9182. (b) Messaoud, M.; Chadeau, E.; Brunon, C.; Ballet, T.; Rappenne, L.; Roussel, F.; Leonard, D.; Oulahal, N.; Langlet, M. *J. Photochem. Photobiol. A* **2010**, *215*, 147. (c) Pan, X.; Ramirez, I. M.; Mernaugh, R.; Liu, J. *Colloids Surf. B* **2010**, *77*, 82 (d) Akhavan, O. *J. Colloid Interface Sci.* **2009**, *336*, 117 (e) Keleher, J.; Bashant, J.; Heldt, N.; Johnson, L.; Li, Y. *World J. Microbiol. Biotechnol.* **2002**, *18*, 133.
- ¹⁴² Zhang, L.; Yu, J. C.; Yip, H. Y.; Li, Q.; Kwong, K. W.; Xu, A. W.; Wong, P. K. *Langmuir*, **2003**, *19*, 10372.
- ¹⁴³ Wu, T. S.; Wang, K. X.; Li, G. D.; Sun, S. Y.; Sun, J.; Chen, J. S. *ACS Appl. Mater. Interfaces* **2010**, *2*, 544.
- ¹⁴⁴ Lan, Y.; Hu, C.; Hu, X.; Qu, J. *Appl. Catal. B* **2007**, *73*, 354.
- ¹⁴⁵ Hu, C.; Lan, Y. Q.; Qu, J. H.; Hu, X. X.; Wang, A. M. *J. Phys. Chem. B* **2006**, *110*, 4066.

- ¹⁴⁶ Elahifard, M. R.; Rahimnejad, S.; Haghghi, S.; Gholami, M. R. *J. Am. Chem. Soc.* **2007**, *129*, 9552.
- ¹⁴⁷ Hou, Y.; Li, X.; Zhao, Q.; Chen, G.; Raston, C. *Environ. Sci. Technol.* **2012**, *46*, 4042.
- ¹⁴⁸ (a) Tada, H.; Teranishi, V.; Inubushi, Y.; Ito, S. *Langmuir*, **2000**, *16*, 3304. (b) Tada, H.; Ishida, T.; Takao, A.; Ito, S. *Langmuir* **2004**, *20*, 7898. (c) Tada, H.; Teranishi, K.; Ito, S. *Langmuir* **1999**, *15*, 7084.
- ¹⁴⁹ Xin, B.; Jing, L.; Ren, Z.; Wang, B.; Fu, H. *J. Phys. Chem. B* **2005**, *109*, 2805.
- ¹⁵⁰ (a) Naya, S. I.; Inoue, A.; Tada, H. *J. Am. Chem. Soc.* **2010**, *132*, 6292. (b) Ide, Y.; Matsuoka, M.; Ogawa, M. *J. Am. Chem. Soc.* **2010**, *132*, 16762. (c) Wang, H.; Faria, J. L.; Dong, S.; Chang, Y. *Mater. Sci. Eng.* **2012**, *177*, 913. (d) Ruiz, H.; Gomez, R.; Lopez, R.; Cordillo, A. H.; Avella, J. A. P.; Moctezuma, E.; Perez, E. *Catal. Commun.* **2012**, *21*, 72. (e) Zhu, S.; Liang, S.; Gu, Q.; Xie, L.; Wang, J.; Ding, Z.; Liu, P. *Appl. Catal. B* **2012**, *119-120*, 146.
- ¹⁵¹ (a) Zhu, H. Y.; Chen, X.; Zheng, Z. F.; Ke, X. B.; Jaatinen, E.; Zhao, J. C.; Guo, C.; Xie, T. F.; Wang, D. *J. Chem. Commun.* **2009**, 7524. (b) Uddin, M. J.; Cesano, F.; Scarano, D.; Bonino, F.; Agstini, G.; Spoto, G.; Bordiga, S.; Zecchina, A. *J. Photochem. Photobiol. A* **2008**, *199*, 64. (c) Zhang, N.; Liu, L.; Fu, X.; Xu, Y. *J. Phys. Chem. C* **2011**, *115*, 9136.
- ¹⁵² (a) Chen, X.; Zhu, H. Y.; Zhao, J. C.; Zheng, Z. F.; Gao, X. P. *Angew. Chem., Int. Ed.* **2008**, *47*, 5353. (b) Cojocar, B.; Neatu, S.; Pârvulescu, E. S.; Lévy, F.; Pârvulescu, V. I.; Garcia, H. *Appl. Catal. B* **2011**, *107*, 140. (d) Wu, X. F.; Song, H. Y.; Yoon, J. M.; Yu, Y. T.; Chen, Y. F. *Langmuir* **2009**, *25*, 6438.
- ¹⁵³ (a) Gonzalez, V. R.; Zanella, R.; Angel, G. D.; Gomez, R. *J. Mol. Catal. A: Chem.* **2008**, *281*, 93. (b) Alvaro, M.; Cojocar, B.; Ismail, A. A.; Petrea, N.; Ferrer, B.; Harraz, F. A.; Parvulescu, V. I.; Garcia, H. *Appl. Catal. B* **2010**, *99*, 191.
- ¹⁵⁴ Furube, A.; Du, Luchao, Hara, K.; Katoh, R.; Tachiya, M. *J. Am. Chem. Soc.* **2007**, *129*, 14852.
- ¹⁵⁵ Du, L.; Furube, A.; Yamamoto, K.; Hara, K.; Katoh, R.; Tachiya, M. *J. Phys. Chem. C* **2009**, *113*, 6454.
- ¹⁵⁶ Kowalska, E.; Abe, R.; Ohtani, B. *Chem. Commun.* **2009**, 241.
- ¹⁵⁷ Nishijima, Y.; Ueno, K.; Yokota, Y.; Murakoshi, K.; Misawa, H. *J. Phys. Chem. Lett.* **2010**, *1*, 2031.
- ¹⁵⁸ (a) Tian, Y.; Tatsuma, T. *J. Am. Chem. Soc.* **2005**, *127*, 7632. (b) Tian, Y.; Tatsuma, T. *Chem. Commun.* **2004**, 1810.
- ¹⁵⁹ Lu, Y.; Yu, H.; Chen, S.; Quan, X.; Xhao, H. *Environ. Sci. Technol.* **2012**, *46*, 1724.
- ¹⁶⁰ Naya, S.; Teranishi, M.; Isobe, T.; Tada, H. *Chem. Commun.* **2010**, *46*, 815.
- ¹⁶¹ Kowalska, E.; Mahaney, O. O. P.; Abe, R.; Ohtani, B. *Phys. Chem. Chem. Phys.* **2010**, *12*, 2344.

- ¹⁶² (a) Ismail, A. A.; Bahnemann, D. W.; Bannat, I.; Wark, M. *J. Phys. Chem. C* **2009**, *113*, 7429. (b) Pradhan, S.; Ghosh, D.; Chen, S. *ACS Appl. Mater. Interfaces* **2009**, *9*, 2060.
- ¹⁶³ (a) Arabatzis, I. M.; Stergiopoulos, T.; Andreeva, D.; Kitova, S.; Neophytides, S. G.; Falaras P. *J. Catal.* **2003**, *220*, 127. (b) Li, J.; Zeng, H. C. *Chem. Mater.* **2006**, *18*, 4270. (c) Liu, Y.; Chen, L.; Hu, J.; Li, J.; Richards, J. J. *J. Phys. Chem. C* **2010**, *114*, 1641. (d) Jung, J. M.; Wang, M.; Kim, E. J.; Hahn, S. H. *Vacuum*, **2008**, *82*, 827. (e) Fu, X.; Liu, J.; Yang, H.; Sun, J.; Li, X.; Zhang, X.; Jia, Y. *Mater. Chem. Phys.* **2011**, *130*, 334.
- ¹⁶⁴ (a) Li, H.; Bian, Z.; Zhu, J.; Huo, Y.; Li, H.; Lu, Y. *J. Am. Chem. Soc.* **2007**, *129*, 4538. (b) Su, R.; Tiruvalam, R.; He, Q.; Dimitratos, N.; Kesavan, L.; Hammond, C.; Sanchez, J. A. L.; Bechstein, R.; Kiely, C. J.; Hutchings, G. J. Besenbacher, F. *ACS Nano*, **2012**, *6*, 6284.
- ¹⁶⁵ (a) Chiarello, G. L.; Aguirre, M. H.; Selli, E. *J. Catal.* **2010**, *273*, 182 (b) Chiarello, G. L.; Forni, L.; Selli, E. *Catal. Today*. **2009**, *144*, 69. (c) Chiarello, G. L.; Selli, E.; Forni, L. *Appl. Catal. B* **2008**, *84*, 332. (d) Wu, G.; Chen, T.; Su, W.; Zhou, G.; Zong, X.; Lei, Z.; Li, C. *Int. J. Hydrogen Energy* **2008**, *33*, 1243.
- ¹⁶⁶ Ruiz, S. O.; Zanella, R.; Lopez, R.; Gordillo, A. H.; Gomez, R. *J. Hazard. Mater.* **2013**, <http://dx.doi.org/10.1016/j.jhazmat.2013.03.057>.
- ¹⁶⁷ (a) Linic, S.; Christopher, P.; Ingram, D. B.; *Nat. Mater* **2011**, *10*, 911. (b) Matos, J.; Marino, T.; Molinari, R.; Garcia, H. *Appl. Catal. A* **2012**, *417-418*, 263.
- ¹⁶⁸ Fang, J.; Cao, S. W.; Wang, Z.; Shahjamali, M. M.; Loo, S. C. J.; Barber, J.; Xue, C. *Int. J. Hydrogen Energy* **2012**, *37*, 17853.
- ¹⁶⁹ (a) Kiwi, J.; Grätzel, M.; *J. Phys. Chem.* **1984**, *88*, 1302. (b) Ohtani, B.; Iwai, K.; Nishimoto, S. I.; Sato, S. *J. Phys. Chem. B* **1997**, *101*, 3349. (c) Kenedy III, J. C.; Datye, A. K. *J. Catal.* **1998**, *179*, 375. (d) Chen, J.; Ollis, D. F.; Rulkens, W. H.; Bruning, H. *Water Res.* **1999**, *33*, 661 (e) Lee, J.; Choi, W. *J. Phys. Chem. B* **2005**, *109*, 7399. (f) Vorontsov, A. V.; Stoyanova, I. V.; Kozlov, D. V.; Simagina, V. I.; Savinov, E. N.; *J. Catal.* **2000**, *189*, 360.
- ¹⁷⁰ Haick, H.; Paz, Y. *J. Phys. Chem. B* **2003**, *107*, 2319.
- ¹⁷¹ (a) Klare, M.; Scheen, J.; Vogelsang, K.; Jacobs, H.; Broekaert, J. A. C. *Chemosphere* **2000**, *41*, 353. (b) Einaga, H.; Futamura, S.; Ibusuki, T. *Environ. Sci. Technol.* **2001**, *35*, 1880. (c) Sun, B.; Vorontsov, V.; Smirniotis, P. G. *Langmuir* **2003**, *19*, 3151. (d) Chen, J.; Ollis, D. F.; Rulkens, W. H.; Bruning, H. *Water Res.* **1999**, *33*, 661.
- ¹⁷² (a) Mills, A.; Hunte, S. L. *J. Photochem. Photobiol. A* **1997**, *108*, 1. (b) Kim, S.; Choi, W. *J. Phys. Chem. B* **2002**, *106*, 13311. (c) Kraeutler, B.; Bard, A. J. *J. Am. Chem. Soc.* **1978**, *100*, 4317. (d) Hwang, S.; Lee, M. C.; Choi, W. *Appl. Catal. B* **2003**, *46*, 49. (e) Bae, E.; Choi, W. *Environ. Sci. Technol.* **2003**, *37*, 147. (f) Lee, J.; Park, H.; Choi, W. *Environ. Sci. Technol.* **2002**, *36*, 5462.
- ¹⁷³ Furube, A.; Asahi, T.; Masuhara, H.; Yamashita, H.; Anpo, M. *Chem. Phys. Lett.* **2001**, *336*, 424.

- ¹⁷⁴ Li, F. B.; Li, X. Z. *Chemosphere*, **2002**, *48*, 1003.
- ¹⁷⁵ Zhao, W.; Chen, C.; Li, X.; Zhao, J.; Hidaka, H.; Serpone, N. *J. Phys. Chem. B* **2002**, *106*, 5022.
- ¹⁷⁶ Muradov, N. Z. *Solar Energy* **1994**, *52*, 283.
- ¹⁷⁷ (a) Hufschmidt, D.; Bahnemann, D.; Testa, J. J.; Emilio, C. A.; Litter, M. I. *J. Photochem. Photobiol. A* **2002**, *148*, 223. (b) Sun, B.; Vorontsov, V.; Smirniotis, P. G. *Langmuir* **2003**, *19*, 3151. (c) Trillas, M.; Peral, J.; Domenech, X. *Appl. Catal. B* **1995**, *5*, 37.
- ¹⁷⁸ Chen, J.; Ollis, D. F.; Rulkens, W. H.; Bruning, H. *Water. Res.* **1999**, *33*, 661.
- ¹⁷⁹ Driessen, M. D.; Grassian, V. H. *J. Phys. Chem. B* **1998**, *102*, 1418.
- ¹⁸⁰ Crittenden, J. C.; Liu, J.; Hand, D. W.; Perram, D. L. *Water Res.* **1997**, *31*, 429.
- ¹⁸¹ Lee, J.; Choi, W. *J. Phys. Chem. B* **2005**, *109*, 7399.
- ¹⁸² Sano, T.; Negishi, N.; Uchino, K.; Tanaka, J.; Matsuzawa, S.; Takeuchi, K. *J. Photochem. Photobiol. A* **2003**, *160*, 93.
- ¹⁸³ Teoh, W. Y.; Madler, L.; Beydoun, D.; Pratsinis, S. E.; Amal, R. *Chem. Eng. Sci.* **2005**, *60*, 5852.
- ¹⁸⁴ Park, H.; Lee, J.; Choi, W. *Catal. Today* **2006**, *111*, 259.
- ¹⁸⁵ Wang, W. N.; An, W. J.; Ramalingam, B.; Mukherjee, S.; Niedzwiedzki, D. M.; Gangopadhyay, S.; Biswas, P. *J. Am. Chem. Soc.* **2012**, *134*, 11276.
- ¹⁸⁶ Vorontsov, A. V.; Savinov, E. N.; Zhensheng, J.; *J. Photochem. Photobiol. A* **1999**, *125*, 113.
- ¹⁸⁷ Gan, S.; Liang, Y.; Baer, D. R.; Sievers, M. R.; Herman, G. S.; Peden, C. H. F. *J. Phys. Chem. B* **2001**, *105*, 2412.
- ¹⁸⁸ Einaga, H.; Ogata, A.; Futamura, S.; Ibusuki, T.; *Chem. Phys. Lett.* **2001**, *338*, 303.
- ¹⁸⁹ Linsebigler, A.; Rusu, C.; Yates, J.T.; Jr. *J. Am. Chem. Soc.* **1996**, *118*, 5284.
- ¹⁹⁰ (a) Abe, T.; Suzuki, E.; Nagoshi, K.; Miyashita, K.; Kaneko, M. *J. Phys. Chem. B* **1999**, *103*, 1119. (b) Bamwenda, G. R.; Tsubota, S.; Nakamura, T.; Haruta, M. *J. Photochem. Photobiol. A* **1995**, *89*, 177. (c) Chen, T.; Feng, Z.; Wu, G.; Shi, J.; Ma, G.; Ying, P.; Li, C. *J. Phys. Chem. C* **2007**, *111*, 8005. (d) Daskalaki, V. M.; Panagiotopoulou, P.; Kondarides, D. I. *Chem. Eng. J.* **2011**, *170*, 433. (e) Fu, N.; Lu, G. *Catal. Lett.* **2009**, *127*, 319. (f) Galinska, A.; Walendziewski, *J. Energy Fuels* **2005**, *19*, 1143. (g) Kondarides, D. I.; Daskalaki, V. M.; Patsoura, A.; Verykios, X. E. *Catal. Lett.* **2008**, *122*, 26. (h) Lee, K.; Nam, W. S.; Han, G. Y. *Int. J. Hydrogen Energy* **2004**, *29*, 1343. (i) Maruyama, T.; Nishimoto, T. *Ind. Eng. Chem. Res.* **1991**, *30*, 1634. (j) Nemoto, J.; Gokan, N.; Ueno, H.; Kaneko, M. *J. Photochem. Photobiol. A* **2007**, *185*, 295.
- ¹⁹¹ Mogyorosi, Kmetyko, A.; Czirbus, N.; Vereb, G.; Dombi, A. *React. Kinet. Catal. Lett.* **2009**, *98*, 215.
- ¹⁹² Y. Mizukoshi, Y. Makise, T. Shuto, J. Hu, A. Tominaga, S. Shironita and S. Tanabe, *Ultrason. Sonochem.* **2007**, *14*, 387.
- ¹⁹³ B. Herbert, J. Michaelson, *J. Appl. Phys.* **1977**, *48*, 4728.

- ¹⁹⁴ (a) Chen, T.; Feng, Z. Wu, G.; Shi, J.; Ma, G.; Ying, P.; Li, C. *J. Phys. Chem. C* **2007**, *111*, 8005. (b) Chiarello, G. L.; Ferri, D.; Selli, E. *J. Catal.* **2011**, *280*, 168. (c) Liu, H.; Yuan, J.; Shangguan, W. *Energy Fuels* **2006**, *20*, 2289. (d) Sreethawong, T.; Suzuki, Y.; Yoshikawa, S. *C. R. Chimie* **2006**, *9*, 307. (e) Sreethawong, T.; Yoshikawa, S. *Int. J. Hydrogen Energy* **2006**, *31*, 786. (f) Strataki, N.; Bekiari, V.; Kondarides, D. I.; Lianos, P. *Appl. Catal. B* **2007**, *77*, 184. (g) Daskalaki, V. M.; Kondarides, D. I. *Catal. Today* **2009**, *144*, 75 (g) Zou, J. J.; Liu, C. J.; Yu, K. L.; Cheng, D. G.; Zhang, Y. P.; He, F.; Du, F.; Cui, L. *Chem. Phys. Lett.* **2004**, *400*, 520. (h) Zou, J. J.; Chen, C.; Liu, C. J.; Zhang, Y. P.; Han, Y.; Cui, L. *Mater. Lett.* **2005**, *59*, 3437.
- ¹⁹⁵ (a) Li, Y.; Lu, G.; Li, S. *Appl. Catal. A* **2001**, *214*, 179. (b) Li, Y.; Lu, G.; Li, S. *Chemosphere* **2003**, *52*, 843. (c) Zheng, X. J.; Wei, L. F.; Zhang, Z. H.; Jiang, Q. J.; Wei, Y. J.; Xie, B.; Wei, M. B. *Int. J. Hydrogen Energy* **2009**, *34*, 9033.
- ¹⁹⁶ (a) Chowdhury, P.; Malekshoar, G.; Ray, M. B.; Zhu, J.; Ray, A. K. *Ind. Eng. Chem. Res.* **2013**, *52*, 5023. (b) Patsoura, A.; Kondarides, D. I. Verykios, X. E. *Catal. Today* **2007**, *124*, 94.
- ¹⁹⁷ Liu, H.; Yuan, J.; Shangguan, W. *Energy Fuels* **2006**, *20*, 2289.
- ¹⁹⁸ (a) Xu, Q.; Ma, Y.; Zhang, J.; Wang, X.; Feng, Z.; Li, C. *J. Catal.* **2011**, *278*, 329. (b) Fu, X.; Long, J.; Wang, X.; Leung, D. Y. C.; Ding, Z.; Wu, L.; Zhang, Z.; Li, Z.; Fu, X. *Int. J. Hydrogen Energy* **2008**, *33*, 6484.
- ¹⁹⁹ Patsoura, A.; Kondarides, D.; I.; Verykios, X.E. *Catal. Today* **2007**, *124*, 94.
- ²⁰⁰ Sreethawong, T.; Puangpetch, T. Chavadej, S.; Yoshikawa, S. *J. Power Sources* **2007**, *165*, 861.
- ²⁰¹ Blount, M. C.; Buchholz, J. A.; Falconer, J. L. *J. Catal.* **2001**, *197*, 303.
- ²⁰² Yu, J.; Qi, L.; Jaroniec, M. *J. Phys. Chem. C* **2010**, *114*, 13118.
- ²⁰³ Abe, R.; Sayama, K.; Domen, K.; Arakawa, H. *Chem. Phys. Lett.* **2001**, *344*, 339.
- ²⁰⁴ Sayama, K.; Abe, R.; Arakawa, H.; Sugihara, H. *Catal. Commun.* **2006**, *7*, 96.
- ²⁰⁵ Abe, R.; Sayama, K.; Arakawa, H. *Chem. Phys. Lett.* **2002**, *362*, 441.
- ²⁰⁶ (a) Sreethawong, T.; Junbua, C.; Chavadej, S. *J. Power Sources* **2009**, *190*, 513. (b) Abe, R.; Hara, K.; Sayama, K.; Domen, K.; Arakawa, H. *J. Photochem. Photobiol. A* **2000**, *137*, 63.

**Chapter III : Nanostructured SnO₂/ZnO heterojunction
photocatalysts**

III.1. Introduction

As previously discussed in the second chapter, the coupling of SnO₂ and ZnO increases the photocatalytic efficiency due to suitable conduction and valence band potentials where SnO₂ acts as an electron sink. Several works associating SnO₂ with ZnO have been reported for achieving an efficient charge separation and improving the photocatalytic properties of both oxides. However, even though it has been reported that the enhanced photocatalytic properties found with SnO₂/ZnO heterostructures were related to improved charge separation, no determination of the band alignment in such system has been reported so far to confirm this feature, the photocatalytic activity of SnO₂/ZnO systems still remaining largely unexplored. On the other hand, there are some synthetic issues that have to be addressed for further investigations. Thus, one-pot synthesis combined with annealing at high temperature can lead to crystalline impurities as Zn₂SnO₄¹ that requires the development of alternative preparation procedures.

As a consequence, we herein report on the characterization and the photocatalytic properties of SnO₂/ZnO materials prepared by a simple two-step procedure. Nanosized SnO₂ particles were first prepared by homogeneous precipitation coupled with hydrothermal treatment and, then, reacted with zinc acetate in acidic medium followed by calcination in air to grow ZnO particles. The photocatalytic activity and recycling ability of the resulting SnO₂/ZnO heterostructure were investigated by the degradation of methylene blue (MB) dye under UV irradiation and compared to those of SnO₂ and ZnO nanopowders. To gain a deeper insight in the relationship between the electronic properties and the photocatalytic activity, the band alignment of the SnO₂/ZnO photocatalyst was carefully determined by UV-Visible diffuse reflectance and X-ray Photoelectron spectroscopies. The enhanced photocatalytic properties of the SnO₂/ZnO photocatalysts were rationalized in terms of a better charge separation related to the effective semiconductor heterojunction.

III.2. Preparation method review

Various strategies have been investigated to produce SnO₂/ZnO heterostructures including hydrothermal method,² sol-gel method,³ co-precipitation method,^{1,4} mechanochemical process.⁵ Wang *et al.*^{2c} reported a hydrothermal method for the preparation of SnO₂/ZnO hollow structures and hierarchical nanosheets by using ZnO rods as a starting material. ZnO rods were prepared by heating a solution of Zn(NO₃)₂ · 6H₂O and NaOH

dissolved in distilled water in an oil bath at 50 °C for 90 min. Centrifugation, washing and drying at 60 °C in vacuum then produced the expected nanoparticles. The SnO₂/ZnO photocatalyst was prepared by hydrothermally treating a suspension of cetyltrimethylammonium bromide (CTAB), SnCl₄ · 5H₂O, and ZnO rods in 30 mL of NaOH aqueous solution in a Teflon-lined stainless-steel autoclave at a temperature between 100 and 200 °C for different times. Hydrothermal treatment at 160 °C for 30 min gave cubes, spheres and other irregular shapes with a wide size distribution, whereas increasing hydrothermal treatment time to 12 h led to the formation of SnO₂/ZnO hollow spheres with diameter ranging from 400 to 600 nm and a shell thickness of about 200 nm. On the other hand, hydrothermal treatment at 200 °C gave hierarchical nanosheets of SnO₂/ZnO.

In another experiment, mesoporous SnO₂ doped with a low concentration of ZnO (SnO₂/ZnO) was prepared through a hydrothermal method by using CTAB as a structure-directing agent.^{2b} In a typical synthesis procedure, tin chloride pentahydrate (SnCl₄ · 5H₂O) and zinc chloride (ZnCl₂) were slowly added to a solution of CTAB and sodium hydroxide in a mixed solvent of alcohol and water. The resultant suspension was then heated in an autoclave at 160 °C for 15 h followed by washing with distilled water and drying at 60 °C. The doping of ZnO into mesoporous SnO₂ enhanced the surface area from 156.7 to 200.5 m² g⁻¹ and stabilizing the mesoporous structure. A regular morphology of the SnO₂/ZnO nanostructures was obtained by hydrothermal route controlling the morphology of the precursor with the chiral ionic liquid (CIL) ditetrabutylammonium tartrate.^{2a} The morphology changed from flower-like nanostructures to irregular rod-shaped nanostructures with increasing concentrations of Zn²⁺ in the presence of Sn⁴⁺ maintaining CIL at 0.05 g, while SnO₂/ZnO nanosheets were obtained by increasing the amount of CIL from 0.05 to 0.1 g, keeping other reaction conditions constant.

A network-structured SnO₂/ZnO heterojunction photocatalyst was synthesized through a simple two step solvothermal method.⁶ In a typical procedure, a mixed solution of Zinc acetate and NaOH in 30 mL of ethanol was heated in an autoclave which was put in an oven at 160 °C for 24 h (first step). After adding an aqueous solution of SnCl₄ into the above solution, the autoclave was heated again at 160 °C for another 24 h (second step). The final products were filtered, washed with deionized water and ethanol and finally dried in the air at 80 °C for 10 h. The BET surface area of the obtained SnO₂/ZnO sample was 168 m²/g, which was much higher than those of pure SnO₂ (94 m²/g) and ZnO (23 m²/g).

Davis *et al.*³ prepared aerogel nanocomposites containing ZnO and SnO₂ through sol-gel method without the use of a template or supporting matrix. In a typical procedure, a colorless solution was prepared by dissolving Zn(NO₃)₂·6H₂O and SnCl₄·5H₂O with a molar ratio 1:1 in 3 mL 2-propanol with stirring. Subsequently, 10 equivalents of propylene oxide was quickly added, shaken and set aside to gel undisturbed. Highly stable gel network was formed in ~ 1 min. The monolith obtained after washing and drying was annealed at 500 °C to induce the desired metal oxide phases. The average particle size of SnO₂ was found to be ~7 nm and the surface area for the as-synthesized and annealed aerogels were determined to be 475 m² g⁻¹ and 92 m² g⁻¹, respectively.

In another report, Zhang *et al.*⁷ synthesized one-dimensional SnO₂/ZnO nanofibers by a simple combination method of sol-gel process and electrospinning technique using a precursor solution obtained by dissolving ZnCl₂ and SnCl₂·2H₂O with molar ratio of Zn²⁺ to Sn⁴⁺ equal to 1 in dimethylformamide and subsequently adding polyvinylpyrrolidone (PVP) to the above solution. The composite nanofibers were then calcined at 550 °C for 2h. The diameter of the resulted nanofibers was ranging from 100 to 150 nm and the length was several micrometers. The average grain size of ZnO nanoparticles (42 nm) in SnO₂/ZnO nanofibers was a bit larger than that of ZnO nanoparticles (30 nm) in ZnO nanofibers. However, the grain size of SnO₂ nanoparticles (13 nm) in SnO₂/ZnO nanofibers was much smaller than that of SnO₂ nanoparticles (31 nm) in SnO₂ nanofibers. The BET surface area of the SnO₂/ZnO nanofibers was 45.5 m²/g, which was much larger than that of pure ZnO (17.3 m²/g) and SnO₂ (27.6 m²/g). Wang *et al.*⁸ also fabricated mesoporous ZnO-SnO₂ (M-Z-S) coupled nanofibers by electrospinning technique using a solution prepared by dissolving SnCl₂·2H₂O and pluronic P-123 in a mixed solvent of N, N-dimethylformamide/ethanol in a glove box under vigorous stirring for 6 h and subsequently adding ZnCl₂ and of PVP into the above solution. The diameter of M-Z-S coupled nanofibers after calcinations at 600 °C for 4 h in air was 80-150 nm. BET analysis showed higher surface area (156 m²/g) of M-Z-S coupled nanofiber with narrow pore size distribution than that (57 m²/g) of Z-S coupled nanofibers.

Similarly, Liu *et al.*⁹ also prepared mesoporous ZnO/SnO₂ composite nanofibers by electrospinning method using Zn(OAc)₂ and SnCl₄·5H₂O as precursors and cellulose acetate (CA) as the fiber template in the mixed solvent of N, N-dimethylformamide/acetone (1:1, v:v) followed by calcination at 500 °C. Then the mesoporous ZnO/SnO₂ composite nanofibers were prepared by calcinations of Zn(OH)₂/SnO₂/cellulose composite nanofibers, which was

obtained from the hydrolysis of $\text{Zn}(\text{OAc})_2/\text{SnO}_2/\text{CA}$ composite nanofibers in a base solution. Without hydrolysis, the calcination of $\text{Zn}(\text{OAc})_2/\text{SnO}_2/\text{CA}$ composite nanofibers at $500\text{ }^\circ\text{C}$ in air generated sheet-particle instead of nanofibers. The CA component in the $\text{Zn}(\text{OAc})_2/\text{SnO}_2/\text{CA}$ composite nanofibers melts upon heating due to its thermoplasticity, resulting in transformation from fiber to molten CA which is decomposed on increasing heat leaving behind ZnO/SnO_2 sheet-like particles. On the other hand, hydrolysis converted CA into thermoplastic cellulose which acted as fiber template. The average crystallite size of SnO_2 and ZnO in the SnO_2/ZnO composite nanofibers was slightly smaller than that of pure SnO_2 and pure ZnO nanofibers.

Cun *et al.*^{1a, b} prepared nanosized coupled ZnO/SnO_2 photocatalysts by using co-precipitation method. In a typical procedure, the pH of solution of $\text{SnCl}_4 \cdot 5\text{H}_2\text{O}$ and $\text{ZnSO}_4 \cdot 7\text{H}_2\text{O}$ dissolved in a minimum amount of deionized water was adjusted by adding 4 mol/L of NaOH solution. The precipitate obtained was filtered and washed with deionized water followed by drying at $100\text{ }^\circ\text{C}$ in air. The dried powder was then annealed at different temperature to obtain the nanosized coupled ZnO/SnO_2 photocatalysts. The mean grain sizes of the SnO_2 and the ZnO increased with increasing calcination temperature and an inverse spinel-type Zn_2SnO_4 phase was formed at $700\text{ }^\circ\text{C}$ and continued at $900\text{ }^\circ\text{C}$. Similarly, coupled ZnO/SnO_2 photocatalyst was prepared employing $\text{NH}_3 \cdot \text{H}_2\text{O}$ as the precipitant.^{1c} Lin and Chiang⁴ prepared $\text{Zn}(\text{OH})_2/\text{Sn}(\text{OH})_4$ photocatalysts by pumping two aqueous solution of $\text{ZnSO}_2/\text{SnCl}_4$ and NaOH into a rotary packed bed, where co-precipitation occurred to form $\text{Zn}(\text{OH})_2/\text{Sn}(\text{OH})_4$. The coupled ZnO/SnO_2 photocatalysts was then obtained by annealing these precursors at $600\text{ }^\circ\text{C}$ for 10 h. Zhang *et al.*^{1d} also prepared ZnO/SnO_2 photocatalysts by homogeneous co-precipitation method using $\text{Zn}(\text{NO}_3)_2$ and Na_2SnO_3 as the starting materials and ethyl acetate as the precipitating agent. In a typical procedure, a transparent solution was prepared by adding dropwise 10 mol/L aqueous solution of NaOH into 100 mL of 0.5 mol/L $\text{Zn}(\text{NO}_3)_2$ under vigorous stirring followed by addition of 100 mL of 0.5 mol/L Na_2SnO_3 and certain volume of water. Subsequently, 200 ml of H_2O , CH_3COCH_3 and $\text{CH}_3\text{COOC}_2\text{H}_5$ mixture solution with 3:3:2 volume ratio was added into the above mixture solution at room temperature under vigorous stirring, and the resulting solution was subjected to precipitation by the hydrolysis of ethyl acetate until the reaction mixture attained a pH value between 9 and 10. The precipitant obtained was then washed, dried and calcined in the air at different temperature. In another study, SnO_2/ZnO composite oxides with various molar ratios of Sn:Zn have been synthesized at different calcination temperatures via a facile

cetyltrimethylammonium bromide (CTAB)-assisted co-precipitation method with $\text{Zn}(\text{NO}_3)_2 \cdot 6\text{H}_2\text{O}$ and $\text{SnCl}_4 \cdot 5\text{H}_2\text{O}$ as starting materials and NaOH as precipitating agent.^{1f} The sample with the molar ratio of Sn:Zn of 1:2 calcined at 600 °C was composed of uniform spherical particles with sizes of ca. 50 nm while cubes with side lengths of about 200-300 nm was observed when the calcination temperature was raised to 700 °C.

III.3. Result and discussion

III.3.1. Synthesis and particle characterization

The heterostructure SnO_2/ZnO photocatalyst with a molar ration of Sn : Zn 1:1 was prepared through a two-steps procedure, first SnO_2 was prepared by homogenous precipitation method using urea as precipitant followed by hydrothermal treatment and, then, zinc acetate ($\text{Zn}(\text{OAc})_2 \cdot 2\text{H}_2\text{O}$) was added to the as-synthesized SnO_2 particle suspension followed by calcination at 500 °C to yield the SnO_2/ZnO heterostructure . Precipitation of SnO_2 was observed when a clear solution of SnCl_4 and urea was reacted at 90 °C in aqueous medium. The pH of the solution increased gradually due to the progressive decomposition of urea into NH_3 and CO_2 , leading to the nucleation and growth of uniformly nanosized particles.¹⁰ The molar ration of Sn to Zn was confirmed by microanalysis (Sn : Zn 0.9 ± 0.1 : 1).

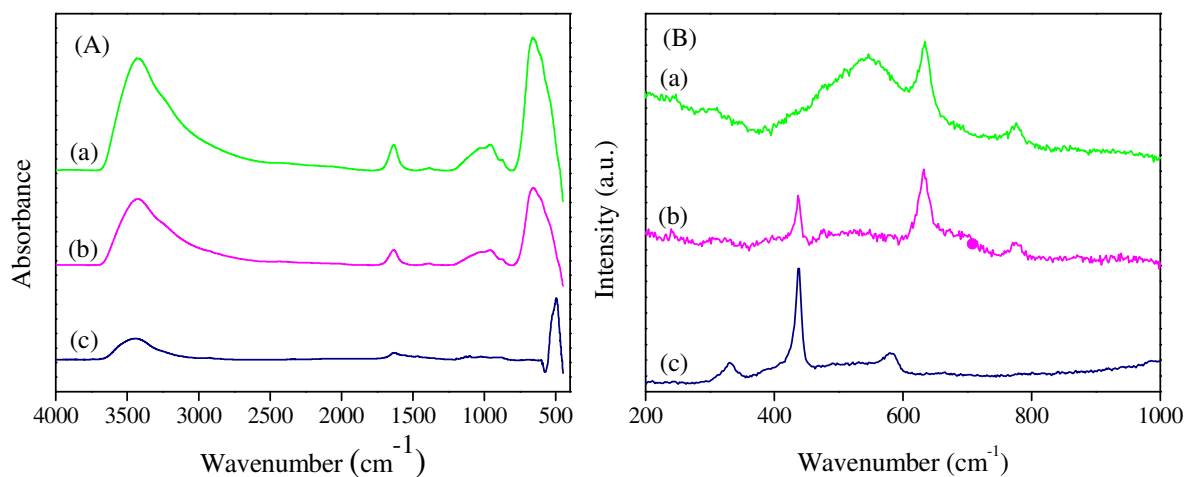


Figure III-1: FTIR (A) and Raman (B) spectra of the as-synthesized photocatalysts after annealing in air at 500 °C (a) SnO_2 (b) $\text{SnO}_2\text{-ZnO}$, and (c) ZnO .

After annealing in air at high temperature, FTIR studies revealed the complete elimination of the undesirable organics and the formation of metal oxide species (**Figure III-1A**). Thus, above 2000 cm^{-1} , a very broad absorption around 3430 cm^{-1} ascribed to OH stretching

vibration modes is observed for each sample.¹¹ Key features observed below 2000 cm^{-1} include a band at 1634 cm^{-1} due to the bending vibrations of absorbed molecular water, and wide bands at 659 cm^{-1} assigned to Sn-O stretching modes of Sn-O-Sn (**Figure III-1Aa and 1Ab**)¹² and at 555 cm^{-1} due to Zn-O stretching modes (**Figure III-1Aa and 1Ac**).¹³ Furthermore, the Raman spectrum of the as-synthesized SnO₂/ZnO photocatalyst showed three main features at 438, 632 and 776 cm^{-1} which could be assigned to the vibration modes E_2 for wurtzite ZnO¹⁴ as well as A_{1g} and B_{2g} for cassiterite SnO₂.¹⁵ Bands at 332 (second-order vibration originating from the zone boundary phonons)¹⁶ and $585 (E_1(LO))\text{ cm}^{-1}$ were observed for the pure ZnO sample but were found to be very weak for the heterostructure. It is also worthwhile to mention that the broad resonance observed in the SnO₂ spectrum at 552 cm^{-1} , a feature that could be related to surface modes,¹⁷ has collapsed after reaction with zinc acetate and further calcination. As a consequence, the signature of both wurtzite ZnO and cassiterite SnO₂ appeared in the Raman spectrum of the SnO₂/ZnO photocatalyst. This was confirmed by the XRD patterns of the materials calcined at $500\text{ }^\circ\text{C}$ (**Figure III-2A**).

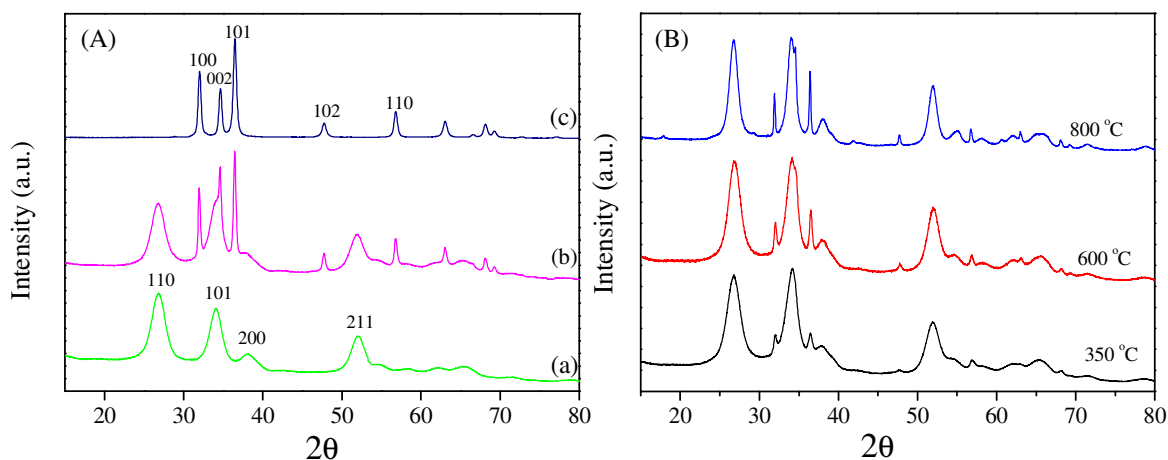


Figure III-2: (A) XRD patterns of the as-synthesized photocatalysts annealed in air at $500\text{ }^\circ\text{C}$ and (B) XRD patterns of the SnO₂/ZnO photocatalyst annealed in air at different temperature. (a) SnO₂ (b) SnO₂/ZnO, and (c) ZnO.

All the diffraction lines in **Figure III-2Aa** and **III-2Ac** were those expected for the standard rutile-like, i.e. cassiterite, crystalline structure of SnO₂ (space group: $P4_2/mmm$, JCPDS file no. 41-1445) and the standard hexagonal wurtzite ZnO (space group: $P6_3/mc$, JCPDS file no. 36-1451), respectively. The diffraction peaks of pure SnO₂ (**Figure III-2Aa**) were considerably broadened revealing a small mean crystallite size which was estimated to be $5 \pm 0.5\text{ nm}$. On the other hand, the diffraction peaks of ZnO (**Figure III-2Ac**) were rather

sharp indicating a better crystallized sample, with an average crystallite size of about 18 ± 1 nm. ZnO seemed to calcine more easily and, thus, tends to have larger grain size than SnO₂. Furthermore, **Figure III-2Ab** shows two sets of diffraction peaks for the SnO₂/ZnO sample ascribed to hexagonal wurtzite ZnO and cassiterite SnO₂. No additional peaks related to ZnSnO₄ were observed in this sample that confirmed that the sample only contained nanocrystalline ZnO and SnO₂ particles. The full-width half-maximum (FWHM) for SnO₂ in SnO₂/ZnO photocatalyst is slightly larger than that found for pure SnO₂ showing that the size of the SnO₂ crystallite, i.e. 4.5 ± 0.5 nm, in the SnO₂/ZnO photocatalyst was smaller than that in pure SnO₂. On the other hand, the crystallite size of ZnO, i.e. 27 ± 1 nm, in SnO₂/ZnO was larger than that of pure ZnO. As previously reported for similar heterostructures,^{1a} the presence of SnO₂ causes an increase in the crystallite size of ZnO whereas that of ZnO restrains the growth of SnO₂ nanocrystals. In order to see the effect of calcination temperature on the crystallite size, the heterostructure SnO₂/ZnO was calcined at different temperatures. **Figure III-2B** shows the XRD patterns of the heterostructure SnO₂/ZnO calcined at different temperatures. As seen in **Figure III-2B**, the phase of the as-synthesized heterostructure SnO₂/ZnO photocatalysts calcined at different temperature were the couple of SnO₂ and ZnO, but the diffraction peaks became continuously sharper with increasing temperature which indicated that the size of crystallite increased with temperature. The size of SnO₂ crystallite calculated by the Scherrer's equation at temperature 350 °C, 600 °C and 800 °C were 4, 4.7, and 6.5 nm and that of ZnO were 7.4, 18.0 and 34.4 nm, respectively.

Figure III-3 shows TEM images of SnO₂/ZnO heterostructures dried at 90 °C (**Figure III-3a**) and calcined at 500°C (**Figure III-3b**). Moreover, HRTEM micrographs of the calcined materials are shown to verify the crystallinity of both SnO₂ and ZnO after the heat treatment (**Figure III-3c, d**). The shape of the pure SnO₂ nanoparticles was spherical and of uniform size. It is worth mentioning that the diameter of the pure SnO₂ was about 5 nm which was in good agreement with the crystallite size deduced from the XRD patterns. The dried SnO₂/ZnO heterostructure was composed of amorphous ZnO and nanocrystalline SnO₂, while upon hydrothermal treatment both phases were crystalline, as confirmed by the Selected Area Electron Diffraction (SAED) pattern shown in **Figure III-3b**. According to the TEM bright field images, the SnO₂/ZnO photocatalyst was composed of aggregated ZnO particles of approximately 100 nm in diameter and nanosized SnO₂ particles, as also shown in the HRTEM images in **Figure III-3c** and **d**. These results were consistent with those inferred from the above XRD analysis. Furthermore, a large number of small pores were observed

between the nanoparticles suggesting that the SnO₂/ZnO photocatalyst is mesoporous. This feature was then assessed by N₂ sorption analyses.

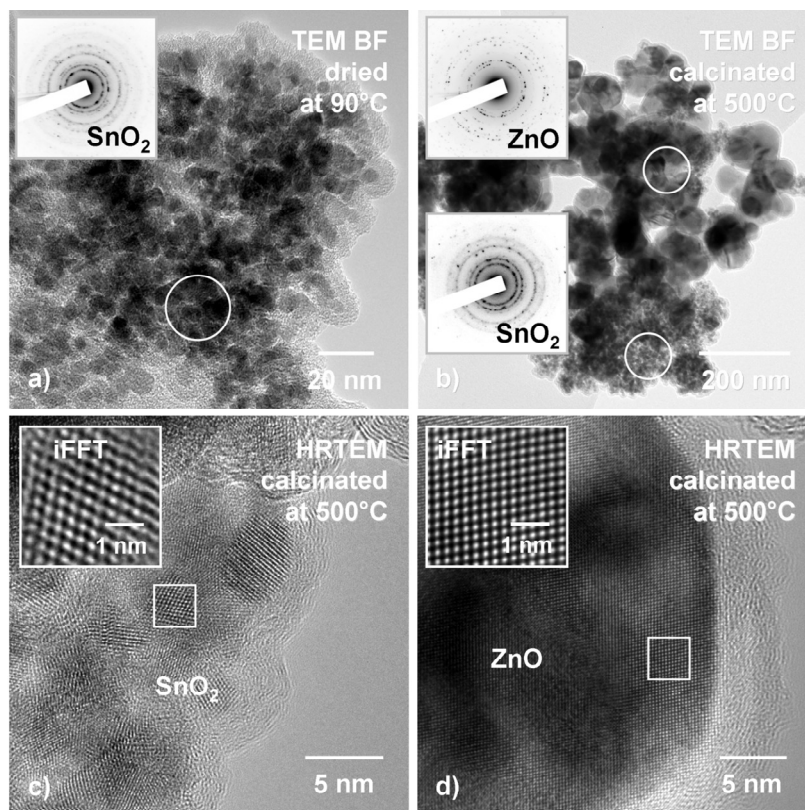


Figure III-3: TEM micrographs of the (a) dried SnO₂/ZnO heterostructure and (b) calcined SnO₂/ZnO photocatalyst. The inset SAED patterns reveal the occurrence of (a) crystalline SnO₂ and (b) crystalline SnO₂ and ZnO. HRTEM images (c, d) verify the crystallinity of both SnO₂ and ZnO after calcination.

The N₂ adsorption-desorption isotherm of the SnO₂/ZnO heterostructure exhibited a type IV-like behavior including a type H2 hysteresis loop (**Figure III-4a**) which is typical of mesoporous materials according to the IUPAC classification.¹⁸ The H2-hysteresis loop indicated the presence of pores of non-uniform sizes and shapes, characteristic of solids consisting of particles crossed by nearly cylindrical channels or made by aggregates (consolidated) or agglomerates (unconsolidated) of spheroidal particles being fully consistent with the TEM data.¹⁹ The BET surface area and pore volume for this system were estimated to be 77 m².g⁻¹ and 0.26 cm³.g⁻¹, respectively, these values lay between those of pure SnO₂ and ZnO analogues (**Table III-1**). Furthermore, the pore size distribution for the SnO₂/ZnO photocatalyst was rather large with an average pore diameter of 14 ± 1 nm (**Figure III-4b**). As a consequence, all these data were consistent with the formation of mesoporous SnO₂/ZnO nanocatalyst.

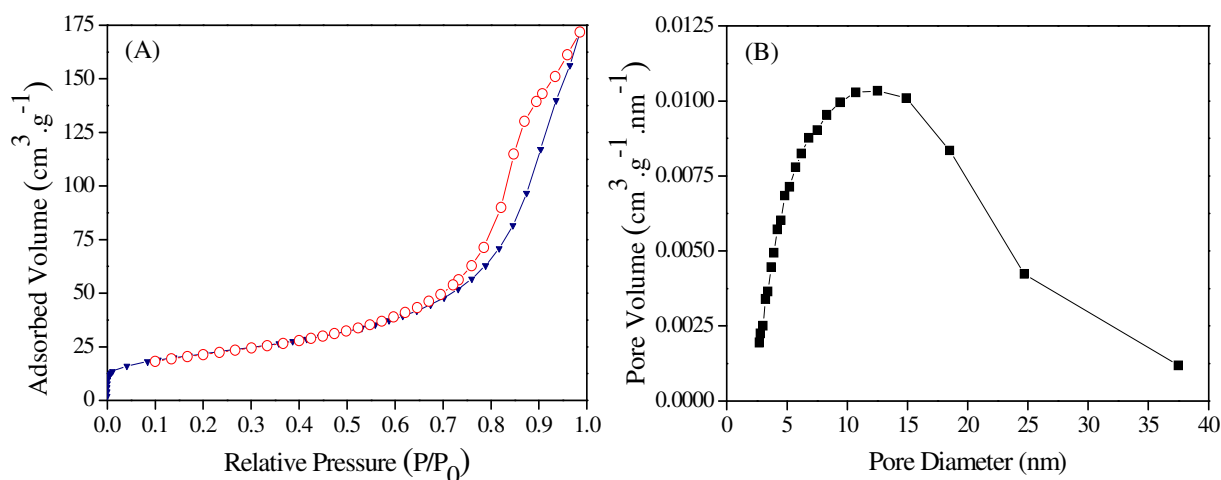


Figure III-4: (A) Nitrogen gas adsorption-desorption isotherms and (B) pore-size distribution of the SnO₂/ZnO photocatalyst.

Table III-1: Nitrogen sorption porosimetry studies^a of the as-synthesized SnO₂, ZnO and SnO₂/ZnO nanomaterials.

Sample	S_{BET} (m ² g ⁻¹)	Pore volume (cm ³ g ⁻¹)	Pore size (nm)
SnO ₂	90 ± 2.5	0.22 ± 0.02	9.8 ± 0.5
ZnO	45 ± 1.5	0.29 ± 0.02	26.5 ± 1
SnO ₂ /ZnO	77 ± 2.0	0.26 ± 0.02	14 ± 0.5

^a Surface areas were determined by BET, mean pore diameters by BJH theory (applied to the adsorption branch), and pore volumes by single-point analysis.

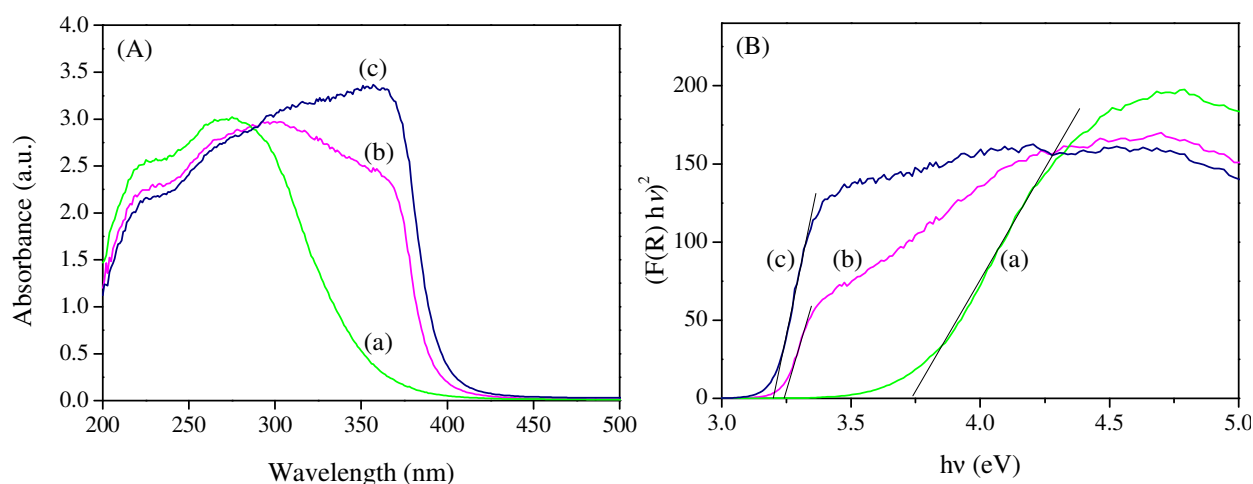


Figure III-5: UV-Visible diffuse reflectance spectra (A) and plots of $(F(R) hv)^2$ versus photon energy ($h\nu$) (B) of the as-synthesized materials after annealing in air at 500 °C (a) SnO₂ (b) SnO₂/ZnO, and (c) ZnO.

The optical properties of the various samples prepared were then investigated by UV-Visible diffuse reflectance. The absorption edge for the SnO₂/ZnO photocatalyst was

estimated to be about 390 nm, which was shifted toward visible region compared to pure SnO₂ sample (**Figure III-5A**). The absorption edges of ZnO and SnO₂ were determined to be 394 and 355 nm, respectively. Compared to the SnO₂ sample, the SnO₂/ZnO photocatalyst showed an obvious absorption edge increment of ca. 35 nm. The absorption edge at higher wavelengths revealed that the heterostructure photocatalysts could more efficiently utilize light for the photocatalytic purpose.²⁰ Nonetheless, it was close to that of ZnO due to the 1:1 composition of the heterostructure, since, to some extent, the absorption edge of the heterostructure should be the combined contribution of each component in the SnO₂/ZnO composite.²¹ Furthermore, it has been shown for a crystalline direct semiconductor that the optical absorption near the band edge follows the equation $\alpha(h\nu) = A(h\nu - E_g)^{1/2}$ where α , ν , E_g , and A are the absorption coefficient, light frequency, band gap energy, and a constant, respectively.²² It is generally admitted that the absorption coefficient (α) can be replaced by the remission function $F(R)$. The later can be written in terms of diffused reflectance (R) according to the Kubelka-Munk theory: $\alpha/s = F(R) = (1-R)^2/(2R)$ where s is scattering coefficient.²³ The band gap energies (E_g values) of the as-synthesized samples can thus be estimated from a plot of $((F(R)h\nu)^2 = f(h\nu)$, the intercepts of the tangents yielding the band gap energies of the as-synthesized samples (**Figure III-5B**). The estimated band gap energies of the resulting samples were therefore about 3.7, 3.23 and 3.2 eV for SnO₂, SnO₂-ZnO, and ZnO, respectively. The values for ZnO and SnO₂ are in good agreement with those reported by others.²⁴

III.3.2. Surface and interface analysis

To gain a better insight into the surface composition and the band alignment in the SnO₂/ZnO photocatalyst, X-ray Photoelectron Spectroscopy studies were performed on the SnO₂, ZnO and SnO₂/ZnO samples annealed at 500 °C in air. As shown in the survey spectrum of **Figure III-6**, the SnO₂/ZnO heterostructure only shows emissions of Sn, O, and Zn elements with only a very weak C line, the different peaks observed being assigned to Sn 3*d*, Sn 3*p*, Sn 4*d*, Zn 2*p*, Zn 3*s*, and Zn 3*p* core levels and to Sn *MNN*, Zn *LMM* and O *KLL* Auger features.

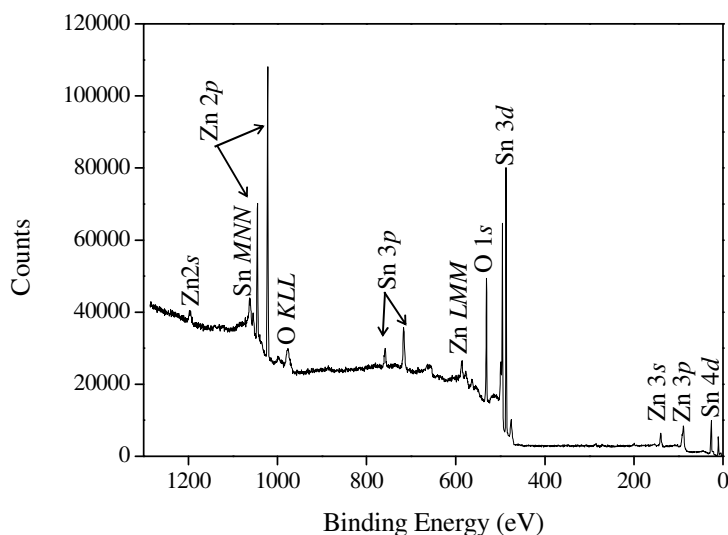


Figure III-6: XPS survey spectrum of the SnO₂/ZnO photocatalyst.

The high resolution XPS spectra for Sn 3d (**Figure III-7A**) reveals the spin orbital splitting of the Sn 3d_{5/2} and Sn 3d_{3/2} core level states of tin centered at 486.8 and 495.2 eV, respectively, which were symmetric and were assigned to the lattice tin oxide. The separation between the Sn 3d_{5/2} and Sn 3d_{3/2} level (8.41 eV) corresponds to the standard spectrum of Sn²⁵ and of commercial SnO₂ reported in the literature.²⁶ The measured emission lines also correspond to a binding energy of Sn⁴⁺ ion in SnO₂.²⁵ **Figure III-7B** shows the pronounced splitting of the Zn 2p emission into two symmetric peaks. The peak centered at 1021.8 eV was attributed to the Zn 2p_{3/2} and the other one at 1044.9 eV to Zn 2p_{1/2}, indicating a normal oxidation state of Zn²⁺ in the SnO₂/ZnO photocatalyst.

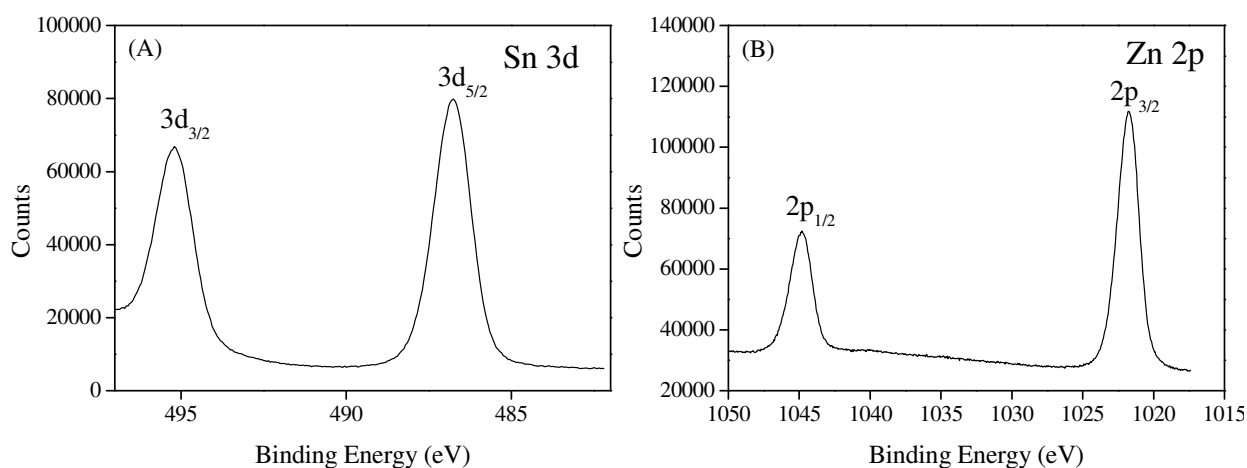


Figure III-7: XPS patterns of the SnO₂/ZnO photocatalyst (A) Sn 3d region; (B) Zn 2p region.

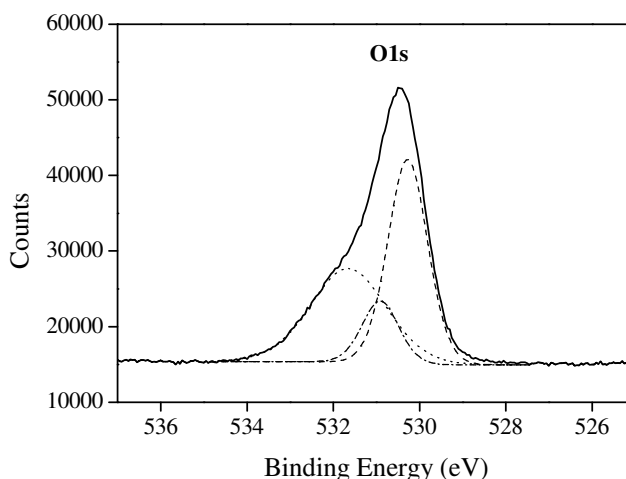


Figure III-8: XPS spectra of O1s region (full) of the SnO₂/ZnO photocatalyst with the corresponding fits for OH (dot), ZnO (dot-dash) and SnO₂ (dash).

Figure III-8 shows the XPS high resolution spectrum of oxygen. The shape of the spectrum is asymmetric which indicates that there are several chemical states according to the measured binding energy. Thus, the region of O 1s could be deconvoluted into three peaks centered at 530.3, 530.8 and 531.5 eV. The lower binding energy peak at 530.3 eV was attributed to oxygen in SnO₂,^{27,28} while the peak centered at 530.8 eV is due to the Zn-O binding.²⁹ The peak at 531.5 could be ascribed to adsorbed hydroxyl species.^{25, 28, 30} The results confirmed that the SnO₂/ZnO photocatalyst was actually composed of SnO₂ and ZnO entities.

The valence band offset (VBO) ΔE_V of the heterostructure SnO₂/ZnO was calculated according to Eq. (1)

$$\Delta E_V = (E_{Zn\cdot 2p} - E_{V\cdot ZnO})_{bulk}^{ZnO} - (E_{Sn\cdot 3d} - E_{V\cdot SnO_2})_{bulk}^{SnO_2} - \Delta E_{CL} \quad (1)$$

where $\Delta E_{CL} = (E_{Zn\cdot 2p} - E_{Sn\cdot 3d})_{heterostructure}$ is the energy difference between Zn 2p and Sn 3d core levels (CLs), which were measured in the SnO₂/ZnO sample. $E_{Zn\cdot 2p}$ and $E_{Sn\cdot 3d}$ are the binding energies in the bulk of ZnO and SnO₂, respectively; $E_{V\cdot ZnO}$ and $E_{V\cdot SnO_2}$ are the valence band maxima in the bulk of ZnO and SnO₂, respectively. In order to determine the band alignment of the SnO₂/ZnO nanocatalyst, the core level positions and the valence band maximum (VBM) positions of bulk SnO₂ and bulk ZnO were also determined. **Figure III-9A** and **C** show the experiment results of bulk SnO₂ and bulk ZnO, respectively. The VBM positions in the VB spectra were determined by linear extrapolation of the leading edges of the VB spectra of the bulk SnO₂ and ZnO samples to the base lines (**Figure III-9B, D**). The

energy difference of the Sn $3d_{5/2}$ CL peak to VBM, $(E_{Sn3d} - E_{V,SnO_2})_{bulk}^{SnO_2}$, was determined to be 483.4 ± 0.05 eV while that of Zn $2p_{3/2}$ to ZnO VBM, $(E_{Zn2p} - E_{V,ZnO})_{bulk}^{ZnO}$, was 1019.05 ± 0.05 eV. The energy difference of Sn $3d_{5/2}$ and Zn $2p_{3/2}$ CLs, ΔE_{CL} in the SnO₂/ZnO heterostructure was evaluated to be 535.0 ± 0.05 eV. All the parameters obtained from the XPS spectrum are summarized in **Table III-2**. According to equation (1), the resulting valence band offset (VBO), ΔE_V , was calculated to be 0.7 eV.

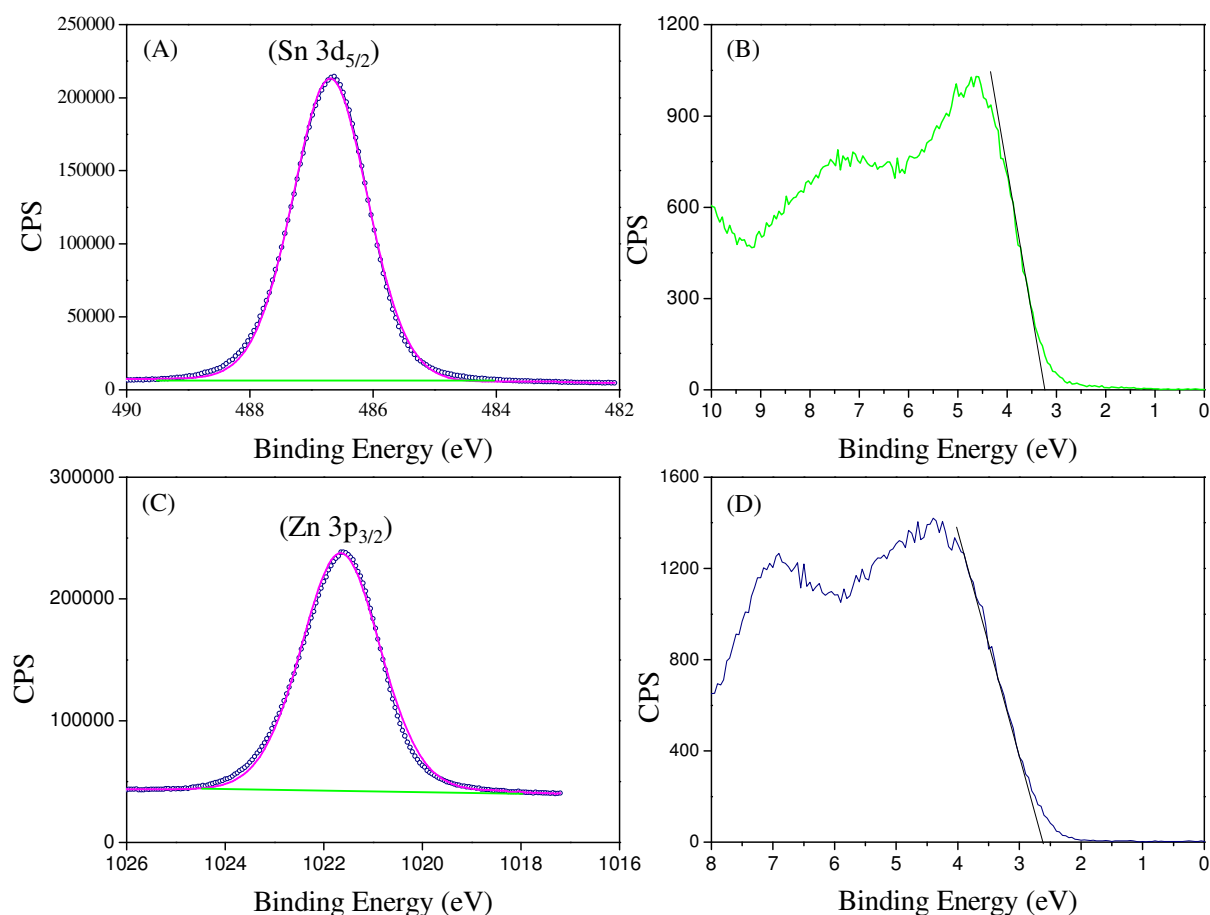
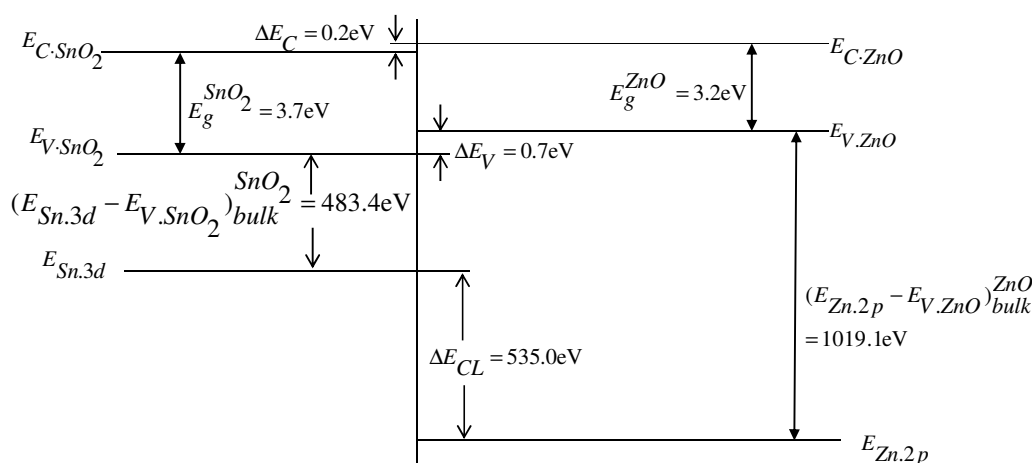


Figure III-9: (A) Core level Sn $3d_{5/2}$ spectra (B) VB spectra for the bulk SnO₂ sample and (C) core level Zn $2p_{3/2}$ spectra (D) VB spectra for the bulk ZnO sample.

Finally the conduction band offset (CBO) was estimated by the formula $\Delta E_C = \Delta E_V + E_g^{ZnO} - E_g^{SnO_2}$, where E_g^{ZnO} and $E_g^{SnO_2}$ are the optical band gap of ZnO and SnO₂, respectively. Using the band gap of SnO₂ (3.7 eV) and ZnO (3.2 eV) determined by UV-Visible diffuse reflectance spectroscopy (**Figure III-5B**), the ΔE_C was calculated to be 0.2 ± 0.05 eV that led to the proposed energy band diagram for the SnO₂/ZnO sample shown in **Figure III-10**. This experimentally determined energy diagram is fully consistent with the formation of mesoporous SnO₂/ZnO type II heterojunction nanomaterials.

Table III-2: XPS binding energies of the core levels and VBM of SnO₂, ZnO and SnO₂/ZnO photocatalysts.

Sample	State	Binding energy (eV)
SnO ₂	Sn 3d _{5/2}	486.70 ± 0.05
	VBM	3.30 ± 0.05
ZnO	Zn 2p _{3/2}	1021.70 ± 0.05
	VBM	2.60 ± 0.05
SnO ₂ /ZnO	Sn 3d _{5/2}	486.80 ± 0.05
	Zn 2p _{3/2}	1021.80 ± 0.05

**Figure III-10:** Band alignment diagram of the SnO₂/ZnO photocatalyst.

III.3.3. Photocatalytic activity

To evidence the photocatalytic activities of the as-synthesized SnO₂/ZnO nanomaterials, the photocatalytic decomposition of methylene blue (MB) was performed as a test reaction according to the literature.³¹ As depicted in **Figure III-11**, the maximum absorption peaks of MB at 664 nm diminished gradually and disappeared completely under UV light irradiation for 80 min in the presence of the SnO₂/ZnO nanocatalyst. Meanwhile, the color of the solution changed gradually, suggesting that the chromophoric structure of MB was decomposed. Furthermore, blank experiments in the absence of irradiation with the photocatalyst or in the presence of irradiation without the photocatalyst, as well as similar experiments with pure SnO₂ and ZnO samples were carried out to rationalize the photocatalytic activity of the as-synthesized SnO₂/ZnO photocatalyst. The degradation efficiency of the as-synthesized samples was defined as C/C_0 , where C_0 is the initial concentration of MB, after equilibrium adsorption, and C its concentration during the reaction. Both blank experiment results showed that MB could not be decomposed without

the photocatalyst and/or UV irradiation (**Figure III-12A**). In contrast, the degradation efficiency of the SnO₂/ZnO photocatalyst after 20 min was of about 88%, whereas values of about 72% and 50% were found after 20 min for the SnO₂ and ZnO samples, respectively (**Figure III-12**). As a result, the mesoporous SnO₂/ZnO heterojunction nanomaterial showed the fastest decomposition rate of MB that validates the concept developed in this study.

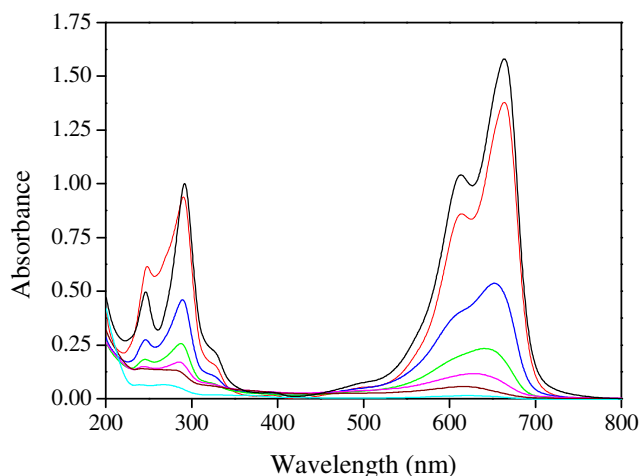


Figure III-11: Absorbance changes of MB solution after different irradiation times in the presence of the SnO₂/ZnO sample: initial (black), equilibrium (red), 10 min (blue), 20 min (green), 30 min (magenta), 40 min (brown) and 130 min (cyan).

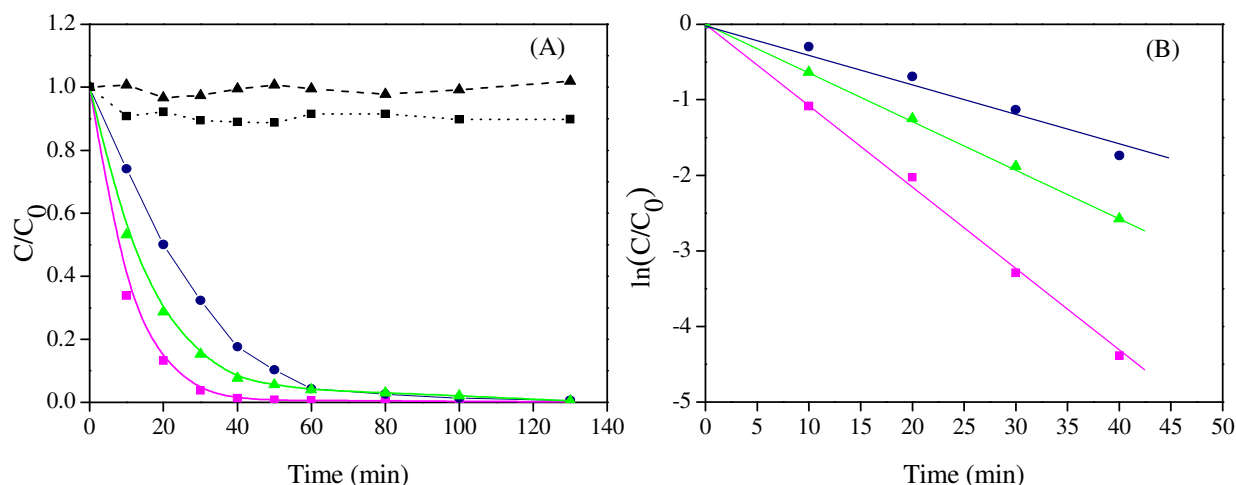


Figure III-12: (A) Kinetic of the degradation of MB in the presence of UV only (square, dot), SnO₂/ZnO in the dark (triangle, dash), SnO₂/ZnO under UV (square, plain), SnO₂ under UV (triangle, plain), and ZnO under UV (circle, plain). (B) $\ln(C/C_0)$ as a function of the irradiation time for calcined SnO₂ (triangle), SnO₂/ZnO (square) and ZnO (circle) photocatalysts.

For a better understanding of the photocatalytic efficiency of the as-synthesized samples, the kinetic analysis of MB degradation is discussed in the following. It is generally assumed that reaction kinetics can be described in terms of Langmuir–Hinshelwood model, which can be expressed following Eq. (2):³²

$$-\frac{dC}{dt} = k_r \frac{K_a C}{1 + K_a C} \quad (2)$$

where $(-dC/dt)$ is the degradation rate of MB, C is the concentration of MB, t is the reaction time, k_r is a reaction rate constant, and K_a is the adsorption coefficient of the reactant. As the initial concentration of MB is very low ($C_0 = 10$ mg/L in the as-described experiments), $K_a C$ is negligible and Eq. (2) can be described as first-order kinetics. Setting Eq. (2) at the initial conditions of the photocatalytic procedure, when $t = 0, C = C_0$, it can be described as

$$\ln \frac{C}{C_0} = -k_{app} t \quad (3)$$

where k_{app} is the apparent rate constant, used as the basic kinetic parameter for different photocatalysts, since it enables one to determine a photocatalytic activity independent of the previous adsorption period in the dark, and the concentration of the remaining dye in solution.

Table III-3: Apparent (k_{app}) and normalized (k_{norm}) rate constants for the degradation of MB with the as-synthesized materials^a.

Photocatalysts	k_{app} (min ⁻¹)	k_{norm} g/(m ² .min)	R^2
SnO ₂ /ZnO	0.093	12.1×10^{-4}	0.98
SnO ₂	0.063	7.1×10^{-4}	0.99
ZnO	0.040	8.9×10^{-4}	0.98

^a k_{norm} calculated from k_{app} and the BET surface area given in Table 1

This model was then applied to the present data (**Figure III-12B**) and the apparent first-order rate constants, before and after normalization by the BET surface area, is reported in **Table III-3**. First of all, the degradation of MB followed a first order kinetic rate for all samples. Furthermore, the mesoporous SnO₂/ZnO heterojunction nanomaterial was clearly a much more effective photocatalyst than the SnO₂ and ZnO analogues with an apparent MB degradation rate constant reaching 0.093 min⁻¹.

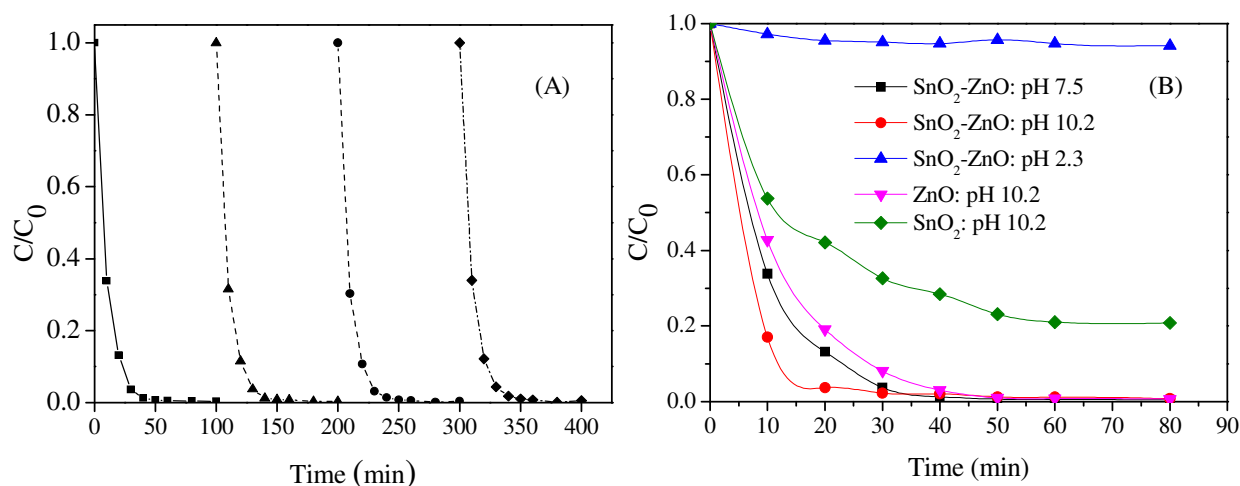


Figure III-13: (A) Cyclic runs in the photodegradation of MB using the SnO₂/ZnO photocatalyst under UV-light: 1st cycle (square), 2nd cycle (triangle), 3rd cycle (circle) and 4th cycle (diamond) (B) effect of pH on the photocatalytic activity of photocatalysts.

The as-synthesized heterojunction nanocatalyst can be recycled and reused several times without significant loss of efficiency, which is a key requirement for a possible industrial application. Thus, the photocatalytic efficiency of the SnO₂/ZnO heterojunction photocatalyst for the 4 cycling reuse were 99.3, 99.2, 99.3 and 99.0% after 50 min of reaction time, respectively (**Figure III-13A**). No significant change in the catalytic efficiency of the degradation of MB dye by the photocatalysts after successive cycles of use under UV irradiation indicated the stability and reproducibility of the catalysts.

Finally, pH, in photocatalysis systems, can be considered as one of the most important parameters that can greatly affect the photo-oxidation process. The photocatalytic efficiency SnO₂/ZnO in the degradation of MB as a function of solution pH is shown in **Figure III-13B**. it is also worth mentioning that the photocatalytic activity collapsed in acidic solution and was improved in basic medium, the SnO₂/ZnO photocatalyst being always the most efficient. Considering the positive charge of cationic MB dye in solution, the effect of pH on the photocatalytic degradation of MB can be rationalized on the basis of electrostatic adsorption model where cations are more readily accumulated at the negative sites on heterostructure SnO₂/ZnO. This can be explained on the basis of the point of zero charge (pHpzc) of SnO₂/ZnO particle. At lower pH, the surface of the catalyst is positively charged, but at higher pH it becomes negatively charged. Since MB is a cationic dye, high pH favors adsorption on the catalyst surface which results in high degradation efficiency. On the other hand, at lower pH the electrostatic repulsion between the MB cations and positively charged

oxide surface greatly reduces the adsorption of the MB dye resulting drastic decrease in degradation rate.

Scheme 1: Proposed mechanism for the degradation of MB under UV-irradiation in the presence of the SnO₂/ZnO photocatalyst.

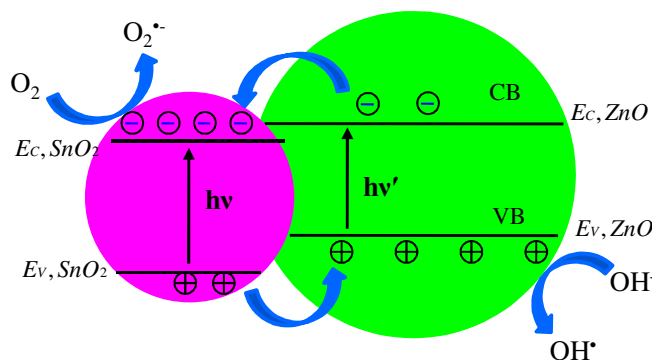
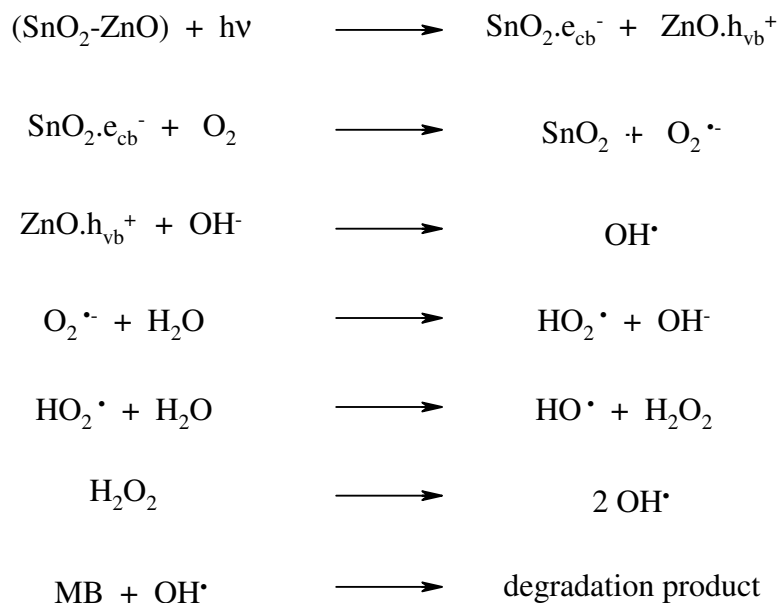


Figure III-14: Schematic representation of the charge transfer process for the heterostructure SnO₂/ZnO photocatalyst.

In summary, the improved photocatalytic activity found for the SnO₂/ZnO heterostructure can be rationalized on the basis of the above-determined band alignment as follows (**Figure III-14** and **Scheme 1**). Upon UV illumination, electrons in the VB could be excited to the CB of both oxides, with the concomitant formation of the same amount of holes in the VB. According to the type II band alignment and the heterojunction formed, the electrons were collected by the SnO₂ nanosized particles and the holes by the ZnO particles as they are transferred to a more stable electronic state, that is, downward for electron transfer from ZnO to SnO₂, upward corresponding to a more stable bonding situation for holes from

SnO₂ to ZnO (Comparison between **Figure III-10** and **Figure III-14**). The resulting charge carrier separation (electrons preferentially on the SnO₂ particle, holes preferentially at the ZnO particle) leads to increased carrier lifetime because of reduced charge recombination. As a consequence, the formation of hydroxyl OH[•] radicals by reaction of holes with surface hydroxyl groups or physisorbed water molecules at the zinc oxide surface is enhanced. On the other side, also the reaction of electrons with dissolved oxygen molecules to give superoxide radical anions, O₂^{•-}, yielding hydroperoxy radicals HO₂[•] on protonation and finally OH[•] radicals will be more efficient. OH[•] radicals are a strong oxidizing agent well-known to decompose organic substrates as MB dye.³³ As a result, the enhanced charge separation related to the SnO₂/ZnO heterojunction favors the interfacial charge transfer to physisorbed species forming OH[•] radicals and reduce possible back reactions, and therefore accounts for the higher activity of the SnO₂/ZnO nanomaterials.

III.4. Conclusion

Mesoporous SnO₂/ZnO heterojunction photocatalysts have been successfully prepared using a two-step solution route involving the synthesis of nanosized SnO₂ particles by homogenous precipitation combined with an hydrothermal treatment that were further reacted with zinc acetate followed by calcination. The UV-VIS diffuse reflectance studies showed that the band gap energy of the heterostructure SnO₂/ZnO photocatalyst was red-shifted compared to that of pure SnO₂ and ZnO. A careful examination of the band alignment by XPS revealed a type-II band alignment with VBO of $\Delta E_V = 0.7 \pm 0.05$ eV and CBO of $\Delta E_C = 0.2 \pm 0.05$ eV for the SnO₂/ZnO heterojunction photocatalyst. This heterojunction photocatalyst showed higher photocatalytic activity than the pure SnO₂ and ZnO nanocatalysts for the degradation of MB dye under UV light irradiation in neutral and basic media due to improved separation of photogenerated electrons and holes. Furthermore, the heterostructure photocatalysts could be easily recycled without significant change in the catalytic activity which evidenced the stability of the catalysts and the reproducibility of the approach. This concept of semiconducting heterojunction nanocatalysts with high photocatalytic activity should find industrial application in the future to remove undesirable organics from the environment.

- ¹ (a) Cun, W.; Jincai, Z.; Xinming, W.; Bixian, M.; Guoying, S.; Ping'an, P.; Jiamo, F. *Appl. Catal. B: Environ.* **2002**, *39*, 269. (b) Cun, W.; Wang, X.; Xu, B.; Zhao, J.; Mai, B.; Ping'an, P.; Sheng, G.; Jiamo, F. *J. Photochem. Photobiol. A: Chem.* **2004**, *168*, 47. (c) Zhang, M.; An, T.; Hu, X.; Wang, C.; Sheng, G.; Fu, J. *Appl. Catal. A: Gen.* **2004**, *260*, 215. (d) Zhang, M.; Sheng, G.; Fu, J. An, T.; Wang, X.; Hu, X. *Mater. Lett.* **2005**, *59*, 3641. (e) Wang, H.; Baek, S.; Lee, J.; Lim, S. *Chem. Eng. J.* **2009**, *146*, 355. (f) Yang, Z.; Lv, L.; Dai, Y.; Xu, Z.; Qian, D. *Appl. Surf. Sci.* **2010**, *256*, 2898.
- ² (a) Kowsari, E. Ghezalbash, M. R. *Mater. Lett.* **2012**, *68*, 17. (b) Wen, Z.; Wang, G.; Lu, W.; Wang, Q.; Zhang, Q.; Li, J. *Cryst. Growth Des.* **2007**, *9*, 1722. (c) Wang, W. W.; Zhu, Y. J.; Yang, L. X. *Adv. Funct. Mater.* **2007**, *17*, 59.
- ³ Davis, M.; Hikal, W.M.; Gümeçi, C.; Weeks, L. J. H. *Cat. Sci. Technol.* **2012**, *2*, 922.
- ⁴ Lin, C. C.; Chiang, Y. J. *Chem. Eng. J.* **2012**, *181-182*, 196.
- ⁵ Dodd, A.; McKinley, A. Saunders, M.; Tsuzuki, T. *Nanotechnol.* **2006**, *17*, 692.
- ⁶ Zheng, L.; Zheng, Y.; Chen, C.; Zhan, Y.; Lin, X.; Zheng, Q.; Wei, K.; Zhu, J. *Inorg. Chem.* **2009**, *48*, 1819.
- ⁷ Zhang, Z.; Shao, C.; Li, X.; Zhang, L.; Xue, H.; Wang, C.; Liu, Y. *J. Phys. Chem.* **2010**, *114*, 7920.
- ⁸ Wang, Z.; Li, Z.; Zhang, H.; Wang, C. *Catal. Commun.* **2009**, *11*, 257.
- ⁹ Liu, R.; Huang, Y.; Xiao, A.; Liu, H. *J. Alloys Compd.* **2010**, *503*, 103.
- ¹⁰ Song, K. C.; Kang, Y. *Mater. Lett.* **2000**, *42*, 283.
- ¹¹ Sibin, C. P.; Kumar, S. R.; Mukundan, P.; Warriar, K. G. K. *Chem. Mater.* **2002**, *14*, 2876.
- ¹² Chen, D.; Gao, L. *J. Colloid Inter. Sci.* **2004**, *279*, 137.
- ¹³ Ismail, H. M. *J. Anal. Appl. Pyrolysis* **1991**, *21*, 315.
- ¹⁴ (a) Damen, T. C.; Porto, S. P. S.; Tell, B. *Phys. Lett.* **1966**, *144*, 570. (b) Khan, A.; Kordesch, M. E. *Mater. Lett.* **2008**, *62*, 230.
- ¹⁵ (a) Scott, J. F. *J. Chem. Phys.* **1970**, *53*, 852. (b) Kumar, V.; Govind, A.; Nagarajan, R. *Inorg. Chem.* **2011**, *50*, 5637.
- ¹⁶ Xu, C. X.; Sun, X. W.; Zhang, X. H.; Ke, L.; Chua, S. J. *Nanotechnol.* **2004**, *15*, 856.
- ¹⁷ Loridant, S. *J. Phys. Chem. B* **2002**, *106*, 13273.
- ¹⁸ Sing, K. S. W.; Everett, D. H.; Haul, R. A. W.; Moscou, L.; Pierotti, R. A.; Rouquerol, J.; Siemieniewska, T. *Pure Appl. Chem.* **1985**, *57*, 603.
- ¹⁹ Leofanti, G.; Padovan, M.; Tozzola, G.; Venturelli, B. *Catal. Today* **1998**, *41*, 207.
- ²⁰ Shifu, C.; Lei, C.; Shen, G.; Gengyu, C. *Powder Technol.* **2005**, *160*, 198.
- ²¹ Liu, R.; Ye, H.; Xiong, X.; Liu, H. *Mater. Chem. Phys.* **2010**, *121*, 432.
- ²² Davis E. A.; Mott, N. F. *Phil. Mag.* **1970**, *22*, 903.
- ²³ Jahan, F.; Islan, M. H.; Smith, B. E. *Sol. Energy Mater. Sol. Cells* **1995**, *37*, 383.

- ²⁴ (a) A. Hagfeldt, M. Gratzel, *Chem. Rev.* **1995**, *95*, 49. (b) Lin, C. F.; Wu, C. H.; Onn, Z. N. *J. Hazard. Mater.* **2008**, *154*, 1033. (c) Memming, R. *Electrochim. Acta*, **1980**, *25*, 77. (d) Vogel, R.; Hoyer, P.; Weller, H. *J. Phys. Chem.* **1994**, *98*, 3183.
- ²⁵ Moulder, J. F.; Sticke, W. F.; Sobol, K. P. E.; Bomben, D. in *Handbook of X-ray photoelectron spectroscopy*, United State of America, **1995**, 127.
- ²⁶ Babar, A. R.; Shinde, S. S.; Moholkar, A. V.; Rajpure, K. Y. *J. Alloys Compd.* **2010**, *505*, 743.
- ²⁷ Chang, S. T.; Leu, I. C.; Hon, M. H. *J. Cryst. Growth*, **2004**, *273*, 195.
- ²⁸ Li, G.; Leung, M. K. H. *J. Sol-Gel Sci. Technol.* **2010**, *53*, 499.
- ²⁹ Ballerini, G.; Ogle, K.; Labrousse, M. G. B. *Appl. Surf. Sci.* **2007**, *253*, 6860.
- ³⁰ Mu, J.; Shao, C.; Guo, Z.; Zhang, Z.; Zhang, M.; Zhang, P.; Chen, B.; Liu, Y. *ACS Appl. Mater. Interfaces* **2011**, *3*, 590.
- ³¹ (a) Guo, Y.; Wang, H.; He, C.; Qiu, L.; Cao, X. *Langmuir* **2009**, *25*, 4678. (b) Logar, M.; Jancar, B.; Sturm, S.; Suvorov, D. *Langmuir* **2010**, *26*, 12215. (c) Hirose, Y.; Mori, T.; Morishita, Y.; Itadani, A.; Kudoh, T.; Ohkubo, T.; Matsuda, T.; Kittaka, S.; Kuroda, Y. *Inorg. Chem.* **2011**, *50*, 9948. (d) Kang, J.; Kuang, Q.; Xie, Z.-X.; Zheng, L. S. *J. Phys. Chem. C* **2011**, *115*, 7874.
- ³² Burch, R.; Breen, J. P.; Meunier, F. C. *Appl. Catal. B: Environ.* **2002**, *39*, 283.
- ³³ (a) Tayade, R. J.; Sivakumar, T. S.; Bajaj, H. C. *Ind. Eng. Chem. Res.* **2009**, *48*, 10262. (b) Zhang, L.; Yin, L.; Wang, C.; Lun, N.; Qi, Y. *ACS Appl. Mater. Interfaces* **2010**, *2*, 1769.

**Chapter IV : Metal/n-type semiconductor heterojunction
photocatalysts**

IV.1. Introduction

Since the pioneer works of Fujishima and Honda in 1972 who succeeded in splitting water into hydrogen and oxygen under light irradiation employing TiO_2 as anode material,¹ enormous research activities have been carried out over the past two decades to develop semiconductor photocatalysts with high activities for purifying various environmental pollutants in water and air.² Among the various metal oxide semiconductors, TiO_2 has been widely used as a photocatalyst because of its relatively high photocatalytic activity, biological and chemical stability, low cost, non-toxicity and long-term stability against photocorrosion and chemical corrosion.² However, the high recombination rate of the photoinduced electron–hole pairs formed in photocatalytic processes limits the application of TiO_2 . Therefore, determining how to modify TiO_2 to prepare a photocatalyst with higher photocatalytic activity has become the key point studied by many scholars.

While TiO_2 is widely employed as an efficient photocatalyst, Zinc oxide (ZnO), a direct wide band-gap semiconductor, has been considered as a suitable alternative to TiO_2 due to its similar band-gap energy, and thus similar photocatalytic mechanism and capacity. However, some studies have confirmed that ZnO exhibits better efficiency than TiO_2 in photocatalytic degradation of some dyes, even in aqueous solution in some cases.³ Moreover, ZnO photocatalysts on the nanometer-scale have become more and more attractive because of their unique physical and chemical properties different from the bulk.⁴ However, rapid recombination of photoexcited electrons and holes also weakens its photocatalytic efficiency. To address these issues, the design and modification of ZnO photocatalysts with high sensitivity and reactivity has attracted much attention. It was found that the photocatalytic performance of ZnO can be greatly improved by developing ZnO -based heterostructures or composites.⁵ For example, ZnO -based coupled semiconductor systems such as ZnO-TiO_2 ,⁶ ZnO-SnO_2 ,⁷ ZnO-WO_3 ,⁸ have shown high photocatalytic efficiency for increasing the charge separation and extending the energy range of photoexcitation.

On the other hand, among different approaches, surface modification by depositing noble metal on the TiO_2 ,⁹ and ZnO ¹⁰ has been reported as an effective method to reduce electron-hole recombination in the photocatalytic process. Depending on the alignment of the energy levels, the deposits act as electron sinks or holes accumulators, favouring separation of the photogenerated charge carriers and enhancing the oxidation and reduction reactions required for organic degradation and photocatalytic hydrogen production from water. This is

due to the possible induced band bending effect when a metal comes into contact of a semiconductor; a Schottky barrier is created which facilitates the transfer of electrons or holes from the semiconductor to the metal depending upon the work function of the metal.¹¹

Apart from noble metals (Au, Ag, Pt, ...), other metallic compounds can also be associated with TiO₂ or ZnO to enhance its photocatalytic performances. Thus, ruthenium oxide (RuO₂) belongs to the family of transition metal oxides with rutile structure showing an interesting variety of properties. Because of its high chemical stability, electrical (metallic) conductivity and excellent diffusion barrier properties, RuO₂ based nanomaterials have been used for various technological applications such as supercapacitors, electrodes for chlorine electrogeneration,¹² water splitting into hydrogen or oxygen,¹³ CO oxidation in sensors,¹⁴ or catalysts for CO₂ methanation,¹⁵ and HCl oxidation.¹⁶ RuO₂ exhibits an excellent metallic conductivity related to its partially filled metal (d)-oxygen (p) π^* band in RuO₂.¹⁷ Sakat *et al.*¹⁸ showed that RuO₂ is an efficient hole and electron transfer catalyst on TiO₂ and seems to improve the efficiency of charge separation at the metal/semiconductor interface, when deposited in small amounts, because an excess amount is capable of acting as a recombination center. In addition, RuO₂ has a high work function,¹⁹ situated in the band gap above the valence band of TiO₂ or ZnO. When they are put into contact, electrons will transfer from TiO₂ (or ZnO) to RuO₂ in order to equalize the Fermi level at thermal equilibrium. As a consequence an upward bending of energy bands is expected from TiO₂ (or ZnO) to RuO₂ which favours an efficient charge carrier separation at the RuO₂/TiO₂ (or RuO₂/ZnO) interface under illumination. Another important beneficial effect of RuO₂ loading on TiO₂ (or ZnO) is the increase in conductivity, which ultimately allows more efficient charge transfer within the photocatalyst and makes it kinetically faster when it is involved in the redox processes.²⁰ To the best of our knowledge, the photocatalytic properties of RuO₂/TiO₂ in aqueous phase for the degradation of organic dye as well as the production of hydrogen remain largely unexplored although a few studies focused on RuO₂/TiO₂.²¹ On the other hand, as far as we know, there is no direct evidence for studying the effect of RuO₂ modification of ZnO on the photocatalytic performance. In addition, the interfacial band energy alignment determination to explain the charge carriers separation mechanism at the interfaces of both RuO₂/TiO₂ and RuO₂/ZnO systems have not been reported yet. This prompted us to prepare RuO₂/TiO₂ and RuO₂/ZnO nanoparticles and systematically perform interface analysis for the determination of the interfacial band energy alignment.

As a consequence, we hereafter report on the characterization and the photocatalytic properties of RuO₂/TiO₂ and RuO₂/ZnO nanomaterials prepared by impregnation methods, along with a thorough interface analysis. The photocatalytic activity and recycling ability of as-synthesized samples were investigated by the degradation of methylene blue (MB) and methyl orange (MO) dyes under UV irradiation and compared to those of commercial TiO₂ (Degussa P25) nanopowder. The photocatalytic activity of the as-synthesized RuO₂/TiO₂ system was also evaluated by producing hydrogen in the presence of methanol as sacrificial reagent under UV light irradiation. To gain a deeper insight on the relationship between the electronic properties and the photocatalytic activity, the band bending at the interfaces of RuO₂/TiO₂ and RuO₂/ZnO systems was carefully determined by X-ray Photoelectron spectroscopies (XPS), Ultraviolet Photoelectron spectroscopies (UPS) and UV-Visible diffuse reflectance spectroscopy. The enhanced photocatalytic properties were rationalized in terms of a better charge separation related due to band bending at the RuO₂/TiO₂ or RuO₂/ZnO interface.

IV.2. Nanostructured RuO₂/TiO₂ heterojunction photocatalysts

IV.2.1. Preparation method review

Very few studies have been performed on the preparation and investigation of photocatalytic performances of the RuO₂/TiO₂ photocatalysts. The RuO₂/TiO₂ photocatalysts reported so far were mainly synthesized by sol-gel,²² hydrolysis,²³ and impregnation²⁴ techniques. Recently, Ismail *et al.*²¹ prepared hexagonal RuO₂/TiO₂ mesoporous nanocomposites through simple one-step sol-gel reactions of tetrabutyl orthotitanate (TBOT) with ruthenium(III) acetylacetonate in the presence of a F127 triblock copolymer as a structure-directing agent. Results showed that the composite contained rutile phase TiO₂ that increased with increasing the RuO₂ content for the samples containing more than 1 wt% RuO₂. The specific surface area of undoped TiO₂ of 180 m²/g decreased slightly after adding 10 %wt RuO₂ to 156 m²/g, which suggested that high RuO₂ content blocked the TiO₂ mesopore structures. In another study, Woragamon *et al.*²⁵ has synthesized mesoporous RuO₂/TiO₂ by a single-step sol-gel method. In a typical synthesis procedure, a 0.1 M solution of laurylamine hydrochloride (LAHC) was added to a mixture of acetylacetone (ACA) and tetraisopropyl orthotitanate (TIPT) in a 1:1 molar ration to obtain a molar ratio of TIPT:LAHC = 4:1. Subsequently, ruthenium chloride hydrate (RuCl₃.xH₂O) was added to the resulting yellow sol and aged for 2 days at 80 °C followed by calcination at different temperature to get the final RuO₂/TiO₂ nanocomposites. The resulting catalysts calcined at 400 °C for 4 h was anatase with crystallite size of 8.7 nm and specific surface area of 126 m²/g. Furthermore, Yae *et al.*^{22b} prepared TiO₂ sol by adding glacial acetic acid and ethanol in water into a mixture of tetra-n-butyl titanate and ethanol with a molar ration of 0.185:1.2 followed by the addition of polyethylene glycol and acetylacetone in the above sol solution. Subsequently, RuO₂/TiO₂ sol was prepared by slowly adding (NH₄)₂[Ru(H₂O)Cl₆] solution into TiO₂ sol. The resulting sol was used to make a film on float pearls followed by calcination at 500 °C for 120 min. The result showed that the amorphous RuO₂ was highly dispersed on the anatase TiO₂.

On the other hand, RuO₂/TiO₂ was prepared by homogeneous hydrolysis of ruthenium chloride (RuCl₃) and titanium oxosulphate (TiOSO₄) in the presence of urea at 100 °C for 8 h maintaining a solution pH of 2 with sulfuric acid.^{23a} Then, the RuO₂/TiO₂ powder was obtained by washing, drying at 105 °C in a furnace followed by calcinations at 600 °C for 2 h. The resulting RuO₂/TiO₂ powder contained both the anatase and rutile phase TiO₂. The

sizes of the crystallite of anatase, rutile TiO_2 and RuO_2 were about 21, 37, and 55 nm, respectively. The particle size of anatase also decreased with increasing the RuO_2 content. In contrast, BET surface area of $\text{RuO}_2/\text{TiO}_2$ composites increased from 57.3 to 82.1 m^2g^{-1} when the RuO_2 content was increased from 0.019 to 2.878 mol%.

Finally, the simplest method appeared to be an impregnation method. Thus, commercial TiO_2 was impregnated by aqueous solution of RuCl_3 under vigorous stirring at room temperature.^{24a, c} Then, elimination of solvent followed by calcination at different temperature yielded the expected $\text{RuO}_2/\text{TiO}_2$ nanoparticles.

IV.2.2. Results and discussions

IV.2.2.1. Synthesis and characterization of the nanocatalysts

First of all, TiO_2 nanoparticles were prepared by a sol-gel route involving the hydrolysis condensation of titanium tetraisopropoxide followed by a hydrothermal post-treatment. The resulting nanoparticulate powder was then impregnated with a solution of different amounts of ruthenium (III)- 2, 4-pentanedionate followed by calcination at 400 °C that allow for obtaining $\text{RuO}_2/\text{TiO}_2$ nanocomposites containing 0.5, 1, 2.5, 5, 10 and 20 wt% RuO_2 and hereafter named as 0.5 wt% $\text{RuO}_2/\text{TiO}_2$, 1 wt% $\text{RuO}_2/\text{TiO}_2$, 2.5 wt% $\text{RuO}_2/\text{TiO}_2$, 5 wt% $\text{RuO}_2/\text{TiO}_2$, 10 wt% $\text{RuO}_2/\text{TiO}_2$ and 20 wt% $\text{RuO}_2/\text{TiO}_2$.

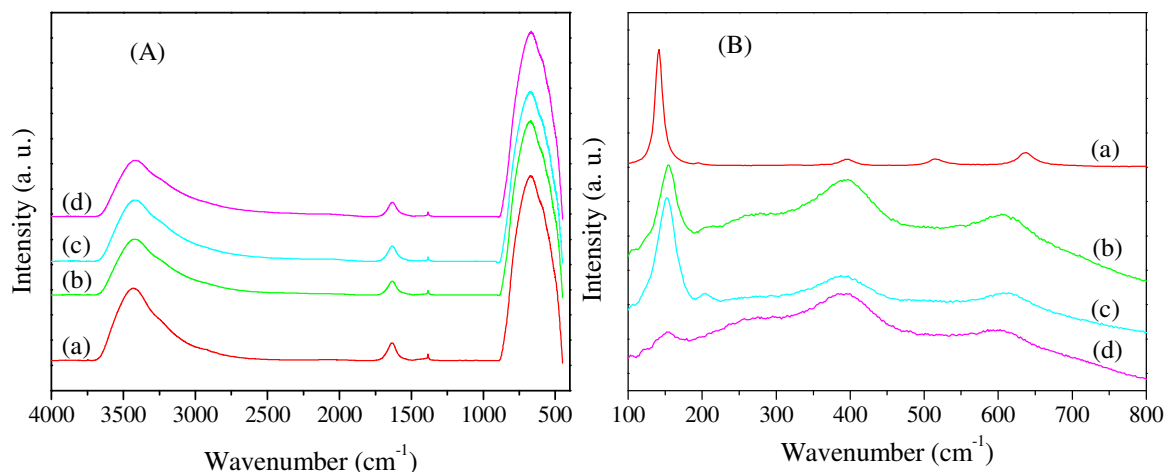


Figure IV-1: FTIR (A) and Raman (B) spectra of as-synthesized photocatalysts calcined at 400 °C for 6h. (a) TiO_2 , (b) 1 wt% $\text{RuO}_2/\text{TiO}_2$, (c) 2.5 wt% $\text{RuO}_2/\text{TiO}_2$, and (d) 5 wt% $\text{RuO}_2/\text{TiO}_2$.

Whatever the RuO_2 content, heterostructure RuO_2 nanoparticles showed the same features by FTIR spectroscopy (**Figure IV-1A**) as the as-synthesized TiO_2 : (i) a broad band centered at 3433 cm^{-1} resulting from an overlapping of the stretching vibration bands (O-H)

of surface hydroxyl groups or adsorbed water molecules;²⁶ (ii) a resonance at 1636 cm^{-1} assigned to $\delta(\text{OH})$ of water molecules;²⁷ (iii) a broad and prominent band centered at 700 cm^{-1} attributed to Ti-O and Ti-O-Ti vibrations.²⁶ It is worth mentioning that the existence of surface hydroxyl groups is very essential for the photocatalytic reactions since they can react with photoexcited holes generated on the catalyst surface and produce hydroxyl radicals.

Furthermore, both the anatase and rutile phases of TiO_2 can be sensitively identified by Raman spectroscopy based on their Raman spectra. Thus, according to factor group analysis, anatase has six Raman active modes ($A_{1g} + 2B_{1g} + 3E_g$). According to the Raman spectrum of an anatase single crystal, Arsov *et al.*²⁸ have reported that the six allowed modes appeared at 144 cm^{-1} (E_g), 197 cm^{-1} (E_g), 399 cm^{-1} (B_{1g}), 516 cm^{-1} (A_{1g}), 516 cm^{-1} (B_{1g}), and 639 cm^{-1} (E_g). RuO_2 has a rutile structure, which is tetragonal with two RuO_2 molecules per primitive unit cell. According to the factor group analysis, there are 15 optical modes of RuO_2 , among which four modes are Raman active with symmetries A_{1g} , B_{1g} , B_{2g} and E_g .²⁹ The three major Raman features of a rutile single crystal RuO_2 , namely the E_g , A_{1g} , and B_{2g} are located at 528 , 646 and 716 cm^{-1} , respectively.³⁰ **Figure IV-1B** displays the Raman spectra of as-synthesized TiO_2 and heterostructure $\text{RuO}_2/\text{TiO}_2$ nanoparticles containing different percentages of RuO_2 calcined at $400\text{ }^\circ\text{C}$ with excitation lines at 514.5 nm . All the spectra show the characteristic peaks of anatase TiO_2 . The Raman peaks observed at 143 , 195 , 397 , 515 and 637 cm^{-1} in **Figure IV-1Ba** are assigned as the E_g , E_g , B_{1g} , $A_{1g} + B_{1g}$, and E_g modes of anatase TiO_2 , respectively. These results are in good agreement with those reported in literature.³¹ **Figure IV-1B(b-d)** shows the Raman spectra of heterostructure $\text{RuO}_2/\text{TiO}_2$ nanoparticles containing various percentages of RuO_2 . The figures show an increase background with increasing RuO_2 which might be due to surface plasmon absorption related to RuO_2 . Comparing these spectra with the spectra of TiO_2 , it is clear that the Raman bands at lower frequency for heterostructure $\text{RuO}_2/\text{TiO}_2$ shifted towards higher wavenumber and the bands broaden with increasing RuO_2 content. This Raman shift can be explained in the following way: in spite of the stable rutile structure of RuO_2 , the ionic radii of Ti^{4+} and Ru^{4+} are very close and these ions are in sixfold coordination which resulted in an incorporation of Ru^{4+} into the anatase structure of TiO_2 without any geometrical constraints. The large Raman shift was due to the big difference in atomic weight of ruthenium and titanium.³²

The crystalline phases in pure TiO_2 and heterostructure $\text{RuO}_2/\text{TiO}_2$ nanoparticles containing different wt % (0.5, 1.0, 2.5, and 5.0) of RuO_2 were investigated using XRD

analysis (**Figure IV-2**). Regardless of the wt% of RuO₂, the main diffraction peaks could be indexed as the (101), (004), (200), (105), (211) and (204) diffraction lines corresponding to the anatase phase of TiO₂ (**Figure IV-2A**). Peaks corresponding to RuO₂ were not seen clearly. In order to identify the crystalline phase of RuO₂ and the presence of other phases of TiO₂, the XRD patterns of all the samples were plotted with enhanced intensity in the region 2θ from 26 to 66° as shown in **Figure IV-2B**. A small broad peak at 2θ = 31.32° could be ascribed to brookite TiO₂ traces, the presence of which having been previously reported in the literature for TiO₂ particles prepared by a similar method.³³ **Figure IV-2B(b-e)** also showed the presence of two extra peaks of the RuO₂/TiO₂ samples at 28.1° and 35.5° which could be indexed to RuO₂ (110) and (101) planes, respectively. The intensities of these peaks corresponding to RuO₂ increased with increasing RuO₂ contents. The crystallite sizes of TiO₂ estimated from the line broadening of anatase (101) diffraction peak using the Scherrer formula are presented in **Table IV-1**. The crystallite size of the pure TiO₂ was about 18 nm and that of the RuO₂ in RuO₂/TiO₂ samples were 10 ± 1 nm. In the case of RuO₂ loaded TiO₂, the crystallite sizes of TiO₂ remained almost unchanged, and were also of about 18 nm.

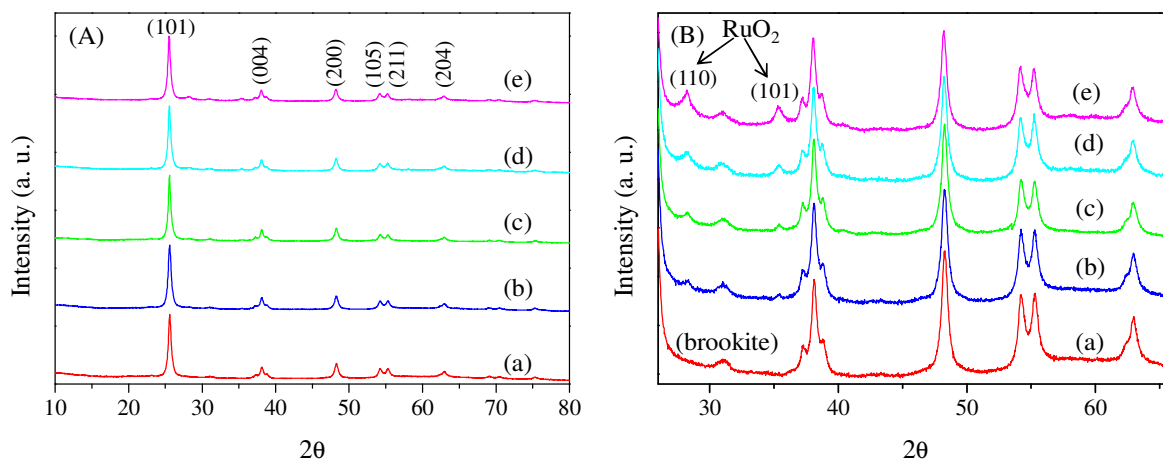


Figure IV-2: XRD pattern of TiO₂ and RuO₂/TiO₂ in the 2θ region of 10-80 ° (A) and 26-66 ° (B). (a) TiO₂, (b) 0.5 wt% RuO₂/TiO₂, (c) 1 wt% RuO₂/TiO₂, (d) 2.5 wt% RuO₂/TiO₂, and (e) 5 wt% RuO₂/TiO₂.

The particle size and the morphology were confirmed by TEM analysis. **Figure IV-3A** shows the TEM micrograph of TiO₂ nanoparticle calcined at 400 °C for 6 h. The shapes of the pure TiO₂ nanoparticles were cube and rhombohedra of uniform nanoscale size. It is worth mentioning that the diameter of the pure TiO₂ was about 17 nm which was in good agreement with the crystallite size deduced from the XRD patterns.

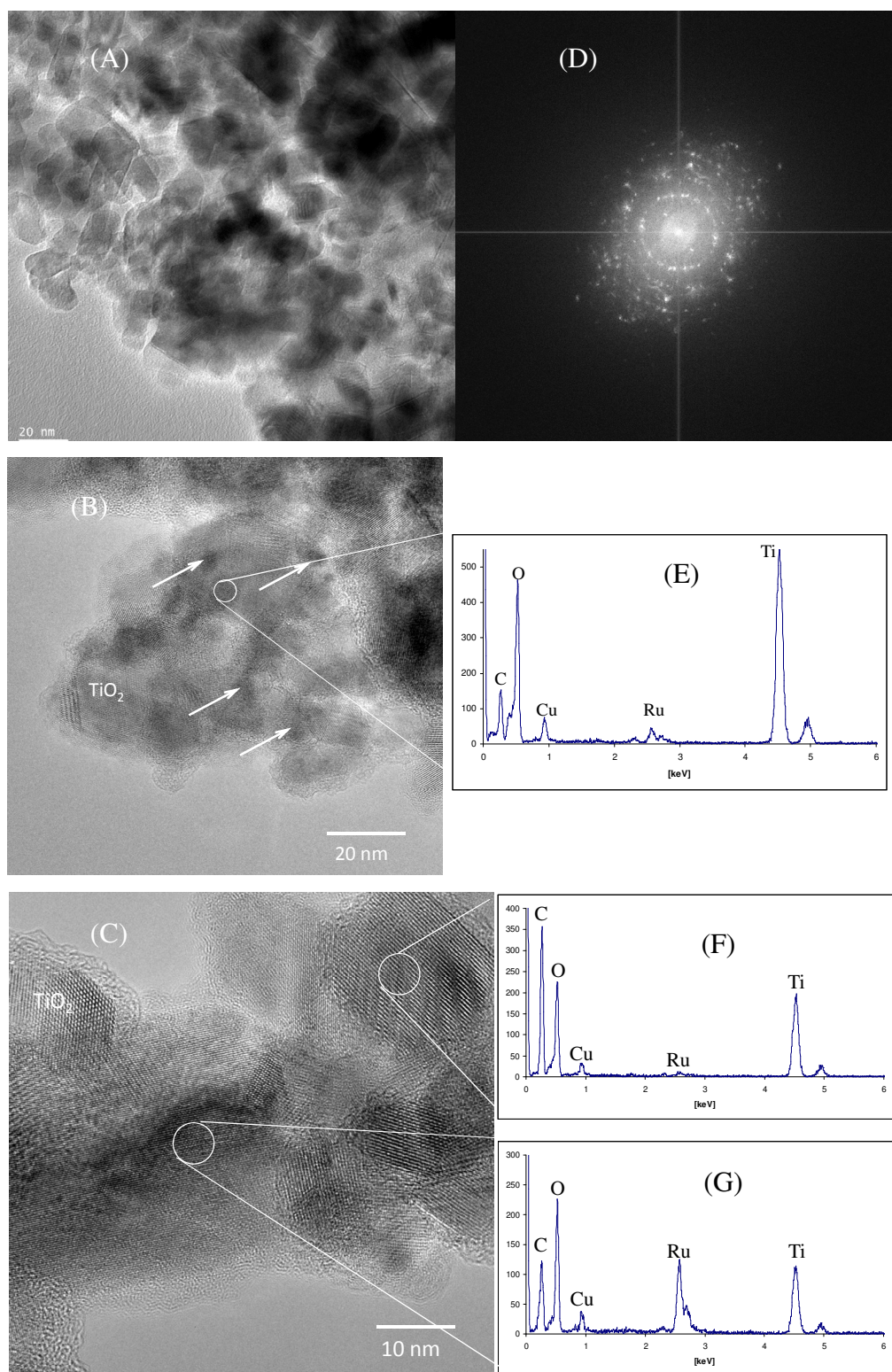


Figure IV-3: TEM micrograph of (A) TiO₂ and (B) and (C) 1 wt% RuO₂/TiO₂ showing distribution of RuO₂ by discrete contrast variation (D) SAED pattern of TiO₂ (E-G) EDX elemental mapping of 1 wt% RuO₂/TiO₂.

The formation of nanocrystallite of TiO₂ was confirmed by selected area electron diffraction (SAED) pattern as shown in **Figure IV-3D**. The first ring associated with the diffraction

arising from the (101) plane of anatase TiO_2 correspond to interplanar distance of 0.35 nm. **Figure IV-3(B, C)** shows the distribution of RuO_2 in 1wt% $\text{RuO}_2/\text{TiO}_2$ nanocomposites. As shown in the **Figure IV-3(B, C)**, the RuO_2 is inhomogeneously distributed, visible by discrete contrast variations as shown by arrows. The peaks corresponding to Ti, Ru and O were observed in the EDX (Energy dispersive X-ray spectroscopy) pattern (**Figure IV-3(E-G)**), revealing the formation of $\text{RuO}_2/\text{TiO}_2$ composite. The spatial distribution of RuO_2 in heterostructure was confirmed by the EDX elemental mapping as shown in **Figure IV-4**. The EDX elemental mapping obviously showed the formation of RuO_2 particles on TiO_2 . The crystallite size of TiO_2 and RuO_2 were observed in the range of 15-18 nm and 5-10 nm, respectively (**Figure IV-3(B, C)**) which were in good agreement with the values obtained by XRD.

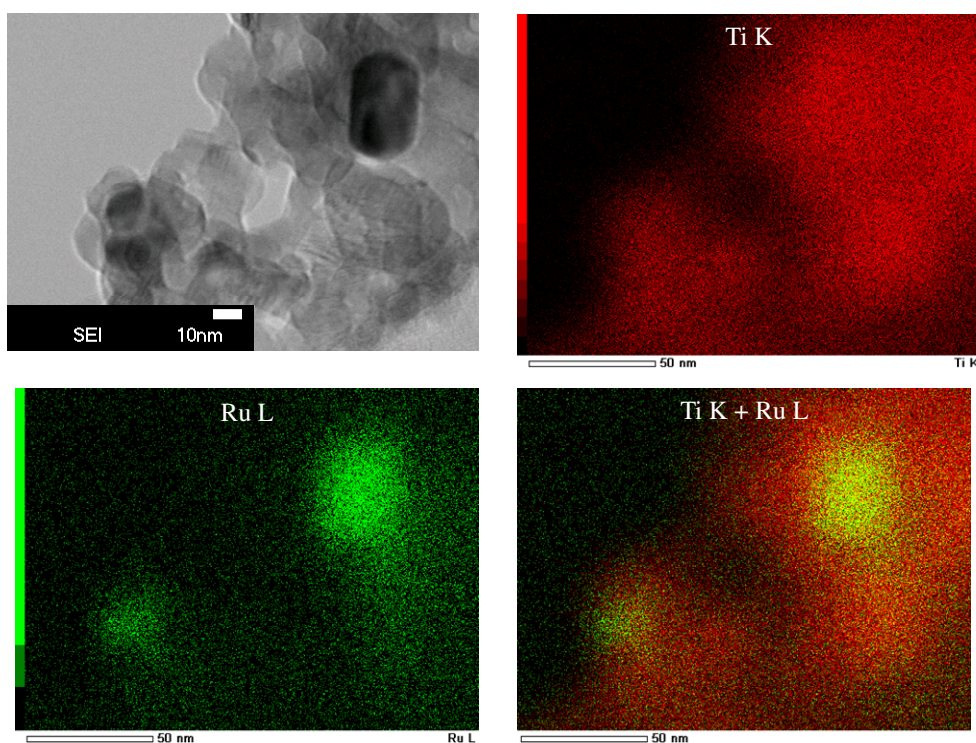


Figure IV-4: EDX mapping of 1 wt% $\text{RuO}_2/\text{TiO}_2$ photocatalysts.

To confirm the deposition of RuO_2 on the surface of TiO_2 , scanning transmission electron (STEM) bright field (BF) and high angle annular dark field (HAADF) experiments were performed. First of all, the TEM image of $\text{RuO}_2/\text{TiO}_2$ sample containing 5 wt% RuO_2 was measured. It can be seen that the RuO_2 is deposited as cluster on the surface of TiO_2 nanoparticles (**Figure IV-5A**). The BF image (**Figure IV-5B**) shows the presence of RuO_2 nanoparticles with a clear contrast in STEM-HAADF image (**Figure IV-5C**) indicating the

deposition of RuO₂ on TiO₂ surface. Contrast variation was seen between RuO₂ and TiO₂ nanoparticles, because the contrast variation in STEM images is Z-related and due to the higher atomic number of Ru, those particles are brighter in HAADF images. EDX analysis performed on the sample (**Figure IV-5E**) further confirmed the presence of RuO₂ deposited on the surface of TiO₂.

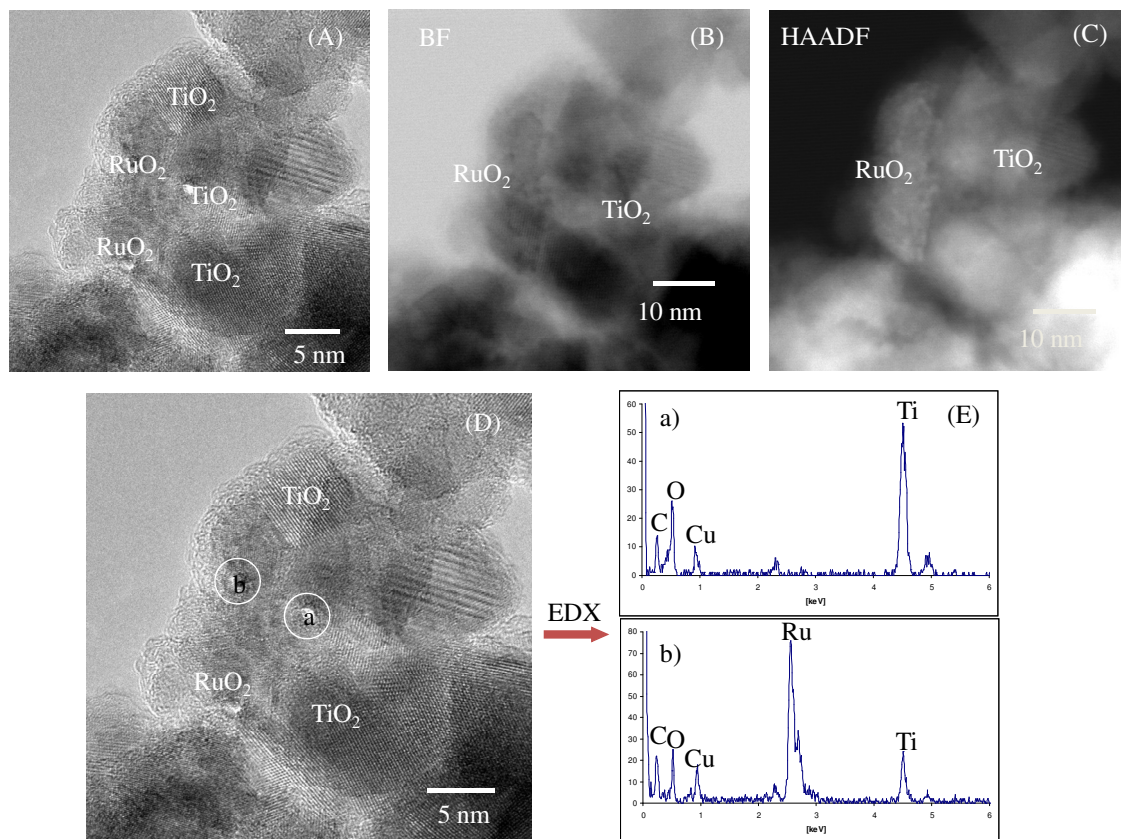


Figure IV-5: (A) TEM (B) STEM-BF (C) STEM-HAADF images and (D, E) EDX mapping of 5 wt% RuO₂/TiO₂ nanoparticles.

The N₂ adsorption–desorption measurement at liquid N₂ temperature was used to study the mesoporosity and the textural properties of the TiO₂ and RuO₂/TiO₂ catalysts. **Figure IV-6** shows the N₂ adsorption–desorption isotherm and pore size distribution of the as-synthesized TiO₂ photocatalyst, compared with the isotherms of 1 wt% RuO₂/TiO₂. The isotherm of the synthesized TiO₂ in **Figure IV-6A** revealed a type IV sorption behavior including a type H2 hysteresis loop which is typical of mesoporous materials according to the IUPAC classification. The H2-hysteresis loop indicated the presence of pores of non-uniform sizes and shapes that was characteristic of solids consisting of particles crossed by nearly cylindrical channels or made by aggregates (consolidated) or agglomerates (unconsolidated) of spheroidal particles.³⁴ The 1 wt% RuO₂/TiO₂ (**Figure IV-6B**) as well as all other TiO₂

samples containing different percentages of RuO₂ (Figures not shown) also exhibited this IUPAC type IV sorption isotherms characteristic of mesoporous solids. The pore size distributions for TiO₂ and 1 wt% RuO₂/TiO₂ nanoparticles (BJH model applied to the adsorption branch of the sorption isotherm) were rather large, i. e. from 4 to 35 nm, with an average pore diameter of 16.5 ± 0.5 nm (*inset, Figure IV-6*).

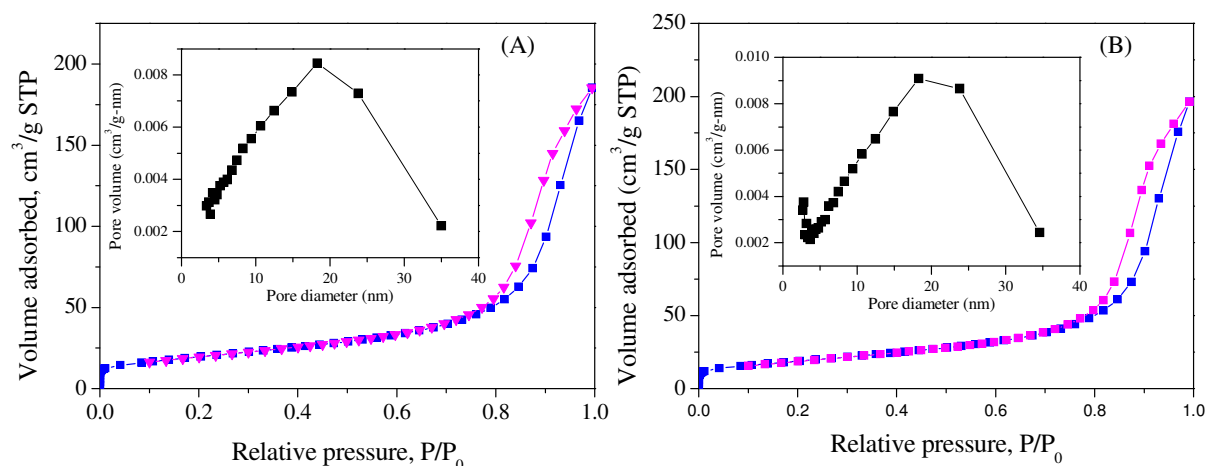


Figure IV-6: N₂ adsorption–desorption isotherm and mesopore size distribution (inset) of as-synthesized TiO₂ (A) and 1wt% RuO₂/TiO₂ (B) photocatalysts.

Table IV-1: Crystallite size and textural properties of TiO₂ and RuO₂/TiO₂ catalysts.

Samples	Crystallite size (nm)	BET Surface area (m ² /g)	Mean pore diameter (nm)	Total pore volume (cm ³ /g)
TiO ₂	18.0 ± 0.5	68 ± 2	17.5 ± 0.5	0.31 ± 0.02
1% RuO ₂ -TiO ₂	17.5 ± 0.5	67 ± 2	17.0 ± 0.5	0.30 ± 0.02
2.5% RuO ₂ -TiO ₂	18.0 ± 0.5	69 ± 2	16.0 ± 0.5	0.28 ± 0.02
5% RuO ₂ -TiO ₂	18.0 ± 0.5	63 ± 2	16.0 ± 0.5	0.26 ± 0.02
P25	-	47 ± 1	11.5 ± 0.5	0.13 ± 0.02

The textural properties, namely BET surface area, mean pore diameter, and total pore volume, of the as-synthesized mesoporous TiO₂, RuO₂ loaded TiO₂ and Degussa P-25 catalysts are given for comparison in **Table IV-1**. The mesoporous TiO₂ catalyst possesses

BET surface area of $68 \pm 2 \text{ m}^2/\text{g}$ with mean pore diameter and total pore volume of 17.5 ± 0.5 (within the mesopore region) and $0.31 \pm 0.02 \text{ cm}^3/\text{g}$, respectively. When RuO_2 were loaded onto the mesoporous TiO_2 , aiming at improving the catalytic performance, it was seen that the BET surface area, the mean pore diameter, and the total pore volume remained almost unchanged upon increasing the wt% of RuO_2 up to 5% (**Table IV-1**). Thus, the 5 wt% $\text{RuO}_2/\text{TiO}_2$ photocatalysts only showed a slight decrease in BET surface area, i. e. $63 \pm 2 \text{ m}^2/\text{g}$ to be compared with $67 \pm 2 \text{ m}^2/\text{g}$ for the 1 wt% $\text{RuO}_2/\text{TiO}_2$ photocatalysts that could stem from the blockage of the mesopores with deposited RuO_2 particles.³⁵ As a consequence, the as-synthesized catalysts could be reliably considered as nanocrystalline mesoporous material according to N_2 adsorption–desorption and XRD data.

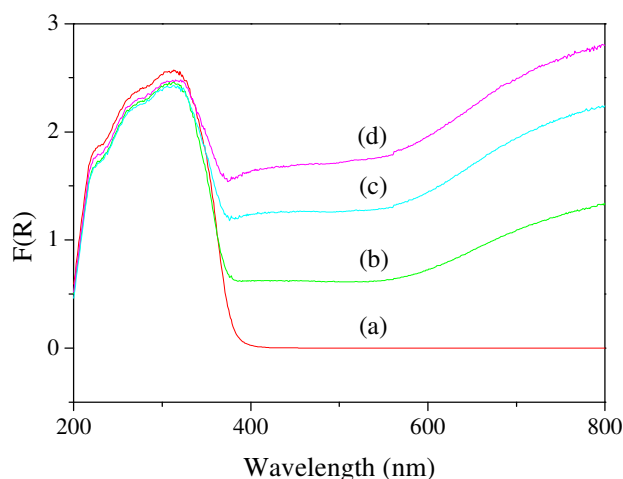


Figure IV-7: UV-Visible diffuse reflectance spectra of as-synthesized nanoparticles. (a) TiO_2 , (b) 1 wt% $\text{RuO}_2/\text{TiO}_2$, (c) 2.5 wt% $\text{RuO}_2/\text{TiO}_2$ and (d) 5 wt% $\text{RuO}_2/\text{TiO}_2$.

The optical properties of the various samples prepared were then investigated by UV–Visible diffuse reflectance (UV-Vis DR). The UV-Vis DR spectra of the as-synthesized samples are shown in **Figure IV-7**. The as-synthesized pure TiO_2 sample exhibited the characteristic spectrum of TiO_2 with its fundamental sharp edge around 385 nm. By contrast, along with the absorption edge in the Near-UV region assigned to the TiO_2 nanoparticles, the $\text{RuO}_2/\text{TiO}_2$ nanocomposites exhibit a continuous absorption in the visible range, the intensity of which increases with RuO_2 content. As a result, the heterostructure $\text{RuO}_2/\text{TiO}_2$ nanocomposites absorb light in the whole visible region, which might suggest that the obtained photocatalyst could be active in the visible light region. Absorption of the visible light by this composite can be attributed to the surface plasmon resonance effect (SPR) that is related to excitation of collective electron oscillations in the metallic RuO_2 nanoparticle by the electric field of the electromagnetic wave.

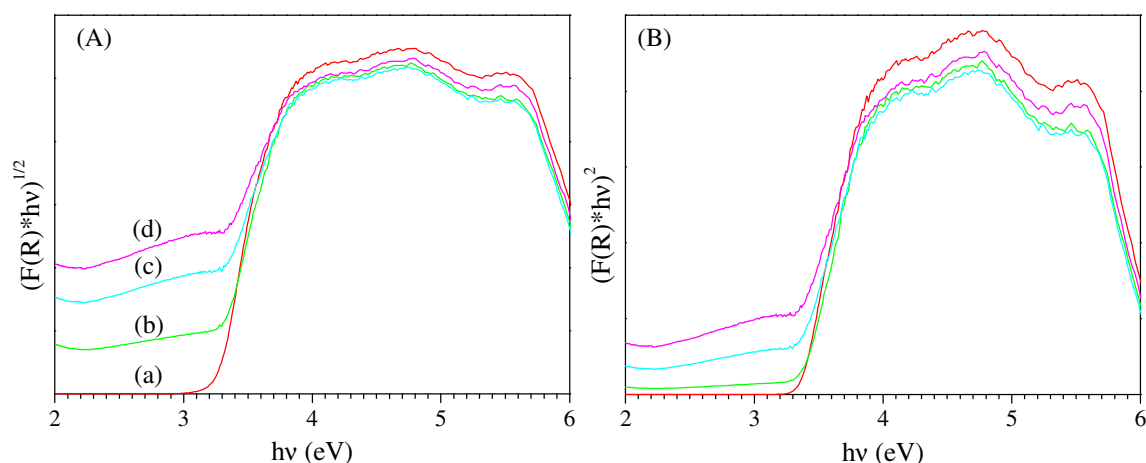


Figure IV-8: (A) $(F(R) hv)^{1/2}$ vs. hv plot and (B) $(F(R) hv)^2$ vs. hv plot of as-synthesized nanoparticles. (a) TiO_2 , (b) 1 wt% $\text{RuO}_2/\text{TiO}_2$, (c) 2.5 wt% $\text{RuO}_2/\text{TiO}_2$ and (d) 5 wt% $\text{RuO}_2/\text{TiO}_2$.

Based on their absorption spectra, the band gap energy (E_g) of the as-synthesized nanoparticles was calculated from the following equation, $\alpha(h\nu) = A(h\nu - E_g)^n$ where α , ν , E_g , and A are the absorption coefficient, light frequency, band gap energy, and a constant, respectively.³⁶ Among them, n is determined by the type of optical transition of a semiconductor ($n = 1/2$ for direct transition and $n = 2$ for indirect transition). The energy of the band gap was calculated by extrapolating a straight line to the abscissa axis, where α is zero, for $E_g = h\nu$.³⁷ It is generally admitted that the absorption coefficient (α) can be replaced by the remission function, $F(R)$. The latter can be written in terms of reflectance (R) according to the Kubelka-Munk theory: $\alpha/s = F(R) = (1-R)^2/(2R)$, where s is the scattering coefficients.³⁸ The optical band gap energies (E_g values) of the as-synthesized samples for direct transition can thus be estimated from the plot of $(F(R) hv)^2$ vs. hv and that for indirect transition can be estimated from the plot of $(F(R) hv)^{1/2}$ vs. hv , the intercepts of the tangents yielding the band gap energies of the as-synthesized samples. To establish the type of band-to-band transition in these synthesized particles, the absorption data were fitted to equations for both indirect and direct band gap transitions. **Figure IV-8A** presents $(F(R) hv)^{1/2}$ vs. hv plot for the as-synthesized TiO_2 and $\text{RuO}_2/\text{TiO}_2$ samples used to determine their band gap energy associated with an indirect transition. The band gap of as-synthesized pure anatase TiO_2 nanopowder as calculated from the extrapolation of the absorption edge onto the energy axis was 3.23 eV which was consistent with the results of **Figure IV-7**. It can be observed that the indirect band gap energy decreased gradually with increasing the RuO_2 amount. The band gap energies decreased from 3.23 eV for pure TiO_2 to 3.19, 2.98 and 2.85 eV for 1 wt% $\text{RuO}_2/\text{TiO}_2$, 2.5 wt% $\text{RuO}_2/\text{TiO}_2$ and 5 wt% $\text{RuO}_2/\text{TiO}_2$, respectively. To evaluate the band

gap energy of the nanoparticles associated to their direct transition, $(F(R) hv)^2$ vs. hv was plotted for each sample (**Figure IV-8B**). The estimated band gap values are larger than those associated with indirect transitions

IV.2.2.2. Interface analysis

To distinguish the existing form of ruthenium cations and the chemical composition of the as-synthesized $\text{RuO}_2/\text{TiO}_2$ nanoparticles, X-ray photoelectron spectroscopy (XPS) studies were carried out. Apart from a C 1s peak located around 285 eV which might be attributed to adventitious carbon-based contaminant, only titanium, oxygen and ruthenium related emissions were detected in the survey spectrum of $\text{RuO}_2/\text{TiO}_2$ nanoparticles after calcination (**Figure IV-9**). The high resolution XPS spectra for Ti 2p showed two peaks in the Ti 2p region, the first one centered at 459.37 eV assigned to the Ti 2p_{3/2} and the other one centered at 465.11 eV corresponding to Ti 2p_{1/2} (**Figure IV-10A**). The peak separation between Ti 2p_{3/2} and Ti 2p_{1/2} was 5.74 eV, which was consistent with the expected oxidation state of Ti^{4+} in the as-synthesized $\text{RuO}_2/\text{TiO}_2$ nanoparticles.³⁹ No indication of a high contribution of reduced Ti^{3+} was found in the spectrum.

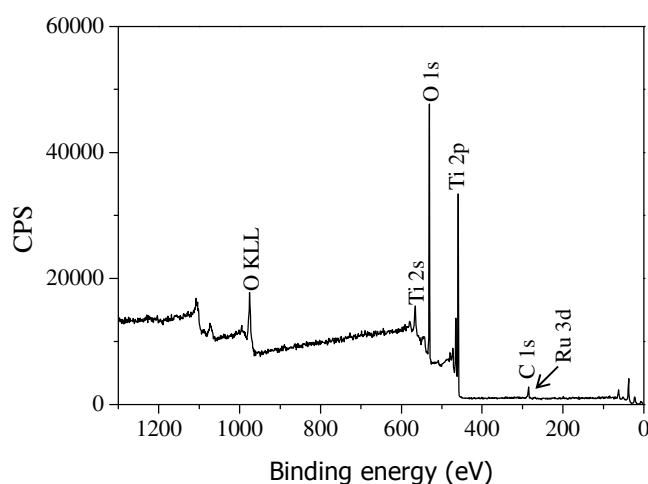


Figure IV-9: XPS survey scan spectrum of heterostructure 1wt% $\text{RuO}_2/\text{TiO}_2$ nanoparticles.

Figure IV-10B displayed the high resolution XPS emission line of Ru 3d. The binding energy of Ru 3d_{3/2} was unfortunately overlapped with that of C 1s, thus the Ru oxidation state was evaluated from the Ru 3d_{5/2} emission line. The Ru 3d_{5/2} peak was located at 280.63 eV which indicates the existence of Ru^{4+} ruthenium cation, as expected for RuO_2 .^{39a, 40} These results further confirmed that the $\text{RuO}_2/\text{TiO}_2$ nanoparticles contain RuO_2 and TiO_2 .

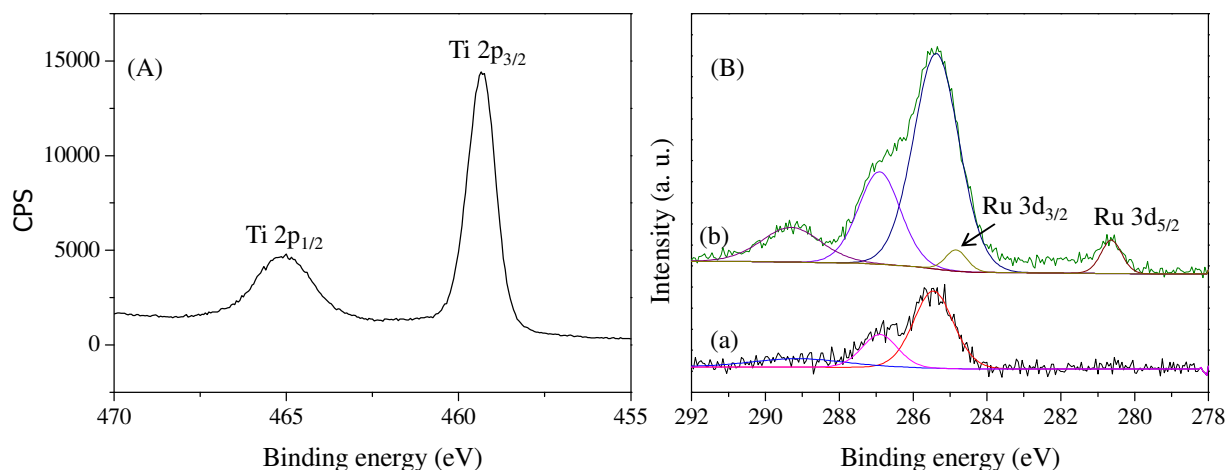


Figure IV-10: (A) High resolution XPS spectra of Ti 2p for 1 wt% RuO₂/TiO₂ nanoparticles (B) High resolution XPS spectra of Ru 3d for (a) TiO₂ and (b) 1 wt% RuO₂/TiO₂ nanoparticles after spectral deconvolution.

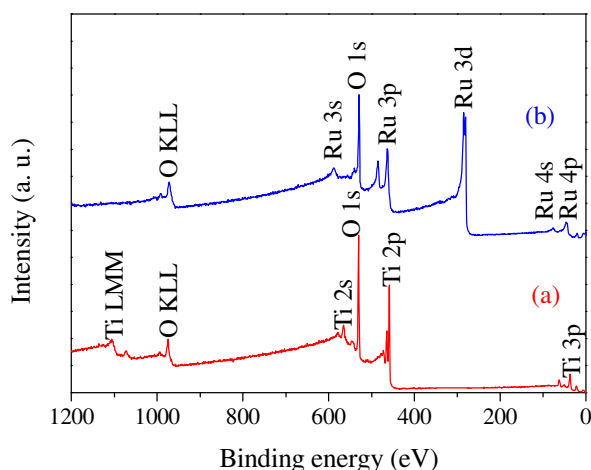


Figure IV-11: X-ray photoelectron survey spectra of (a) TiO₂ substrate and (b) RuO₂ thin film after a number of successive deposition sequences on TiO₂ substrate.

To get an in depth understanding of the interface properties of the RuO₂/TiO₂ heterojunction, an in-situ interface experiment was carried out by successive deposition of a RuO₂ thin layer on the TiO₂ substrate and consequently the band bending at the interface between RuO₂ and TiO₂ was determined from the core level binding energy shifts. RuO₂ films were formed step by step to a desired amount until the bulk property of RuO₂ was obtained. Photoelectron spectra were recorded at each stage of the RuO₂ deposition. **Figure IV-11** shows the survey spectra of the TiO₂ substrate and stepwise deposited RuO₂ film after the saturation of spectral changes has been attained. In the case of the TiO₂ film only emissions from Ti and O were present. The absence of C 1s emission due to adsorbed hydrocarbon expected at a binding energy of around 284.8 eV shows that the TiO₂ film

surface was free of contaminations. The RuO₂ film also showed the emission lines of only Ru and O which also confirmed the absence of carbon contamination in the course of RuO₂ deposition.

Figure IV-12 shows the evolution of Ti 2p, O 1s and Ru 3d emissions recorded in the course of RuO₂ deposition. During stepwise deposition of RuO₂, the attenuation of substrate emission of Ti as well as the growth of the Ru emission was observed with increasing thickness of RuO₂. The shape of Ti 2p_{3/2} emission line did not change with increasing RuO₂ thickness, but that of Ti 2p_{1/2} emission line changed due to a growing Ru 3p_{1/2} emission line superimposing at a binding energy of ~464 eV.

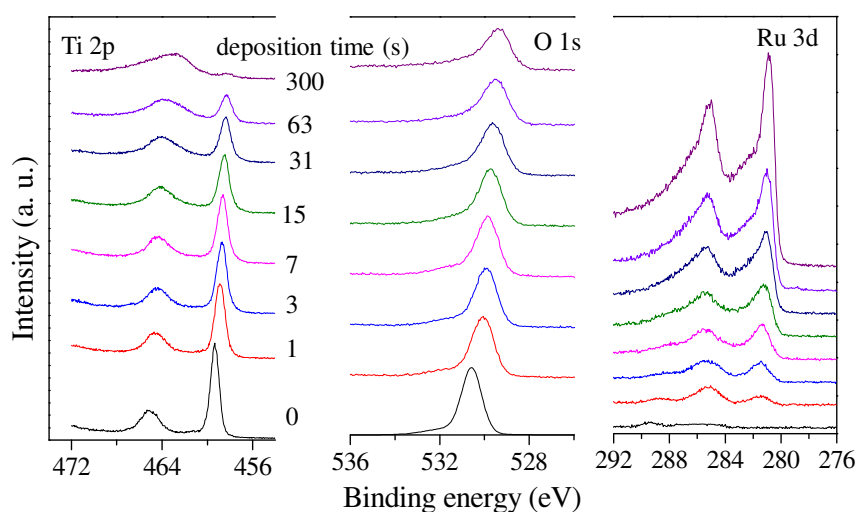


Figure IV-12: X-ray photoelectron core level spectra of TiO₂ recorded during stepwise deposition of RuO₂ onto the TiO₂ film. Spectra at the bottom (at 0 s) refer to the uncovered TiO₂ film and the spectra at the top (after 300 s) refer to the saturated RuO₂ film.

The form of the O emission changed gradually with increasing thickness of RuO₂ from a symmetric line form to a shape with an asymmetry at higher binding energies. This change in O 1s emission line shape is due to the metallic character of RuO₂.⁴¹ It was found that both Ti 2p_{3/2} and O 1s lines were shifted towards the lower binding energy by 1.22 and 1.25 eV, respectively, from their original values. The slightly higher shift observed from the O 1s line than the Ti 2p_{3/2} line may be due to an overlap of O 1s emission from both RuO₂ and TiO₂. We consider a rather parallel shift of both Ti 2p_{3/2} and O 1s emission lines ignoring this slight difference in peak shift. The almost unchanged Ti 2p_{3/2} emission line shape as well as the parallel shift of both Ti 2p_{3/2} and O 1s emissions in the course of RuO₂ deposition suggested no interfacial decomposition reaction between RuO₂ and TiO₂. The Ru 3d_{5/2} emission line is also shifted to lower binding energy by an amount of 0.65 eV and changes in its spectral

shape from a rather broad emission line at higher binding energy to a sharp line followed by a shake-up satellite due to free electrons excitation as typically found for metallic transition metal compounds which is due to bulk RuO_2 .⁴²

UPS measurements of the clean TiO_2 film as well as the as-deposited RuO_2 film were performed to determine the work-function. The work-functions of the films were calculated using Eq. (1).⁴³

$$\Phi = h\nu - E_{\text{cutoff}} \quad (1)$$

where, $h\nu$ (21.2 eV), and E_{cutoff} are incoming photon energy from He I source, and the secondary electron cutoff energy, respectively.

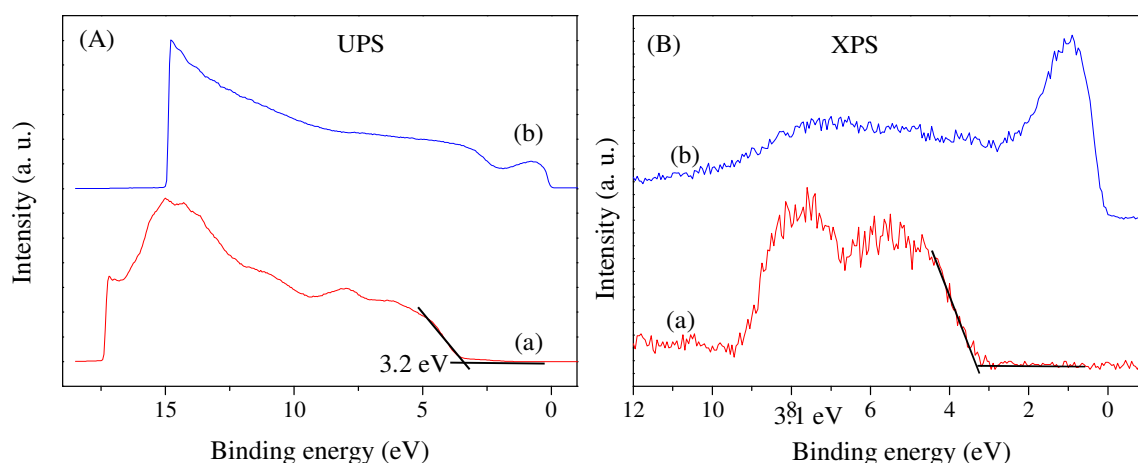


Figure IV-13: (A) Ultraviolet photoelectron spectra and (B) X-ray photoelectron spectra of the TiO_2 film (a) and RuO_2 film (b).

From Eq. 1 and the UPS spectra shown in **Figure IV-13A**, the work-functions of TiO_2 film before deposition of the RuO_2 and that of RuO_2 film after being saturated were calculated. The TiO_2 film showed a work-function value of 3.8 ± 0.1 eV. This value of work function is close to the work function of 3.9 eV of TiO_2 film on ITO substrate cited in the literature.⁴⁴ The work-function of the RuO_2 film gives a value of 6.2 ± 0.1 eV. Yun *et al.*⁴⁵ showed that the work function of RuO_2 is changed with the crystallinity of RuO_2 when deposited on SiO_2 . The improvement of crystallinity by annealing at high temperature decreased the defect or lattice misfits of the RuO_2 film surface resulting in an increased electron density of RuO_2 film at the surface region. As a result, the work function of the RuO_2 films annealed at 300 °C was 5.17 eV while the work function of the RuO_2 films decreased to 5.03 eV after the annealing process at 500 °C. However, the work function of RuO_2 films deposited at room temperature

was always found very close to 6.1 ± 0.05 eV as measured by UPS.^{118, 46} **Figure IV-13** shows the UPS and XPS valence band region of the uncovered TiO_2 film and the saturated RuO_2 film. As shown in **Figure IV-13A**, the UPS valence band spectra of TiO_2 consisted of mainly two peaks at ~ 6 and ~ 8 eV, corresponding to π (non bonding) and σ (bonding) O 2p bands, respectively.⁴⁷ The valence band maximum (VBM) of TiO_2 was determined by linearly extrapolating the low binding energy edge of the valence band intersecting with the background. The VBM of TiO_2 is determined to be 3.1 ± 0.1 eV and 3.2 ± 0.1 eV measured by XPS and UPS, respectively. These numbers suggested that the TiO_2 was an n-type semiconductor. A slightly higher binding energy position of valence band maximum deduced from UPS could be related to the energy-dependence of the photoionization cross-section and different surface sensitivity of UPS and XPS.⁴⁶ Sample charging could also account for a higher VBM position measured with UPS. The RuO_2 spectra show an intense line just below the Fermi edge ($E_B = 0$) which belongs to the occupied Ru 4d-d* states just below the Fermi level which are followed by the O 2p band emission.

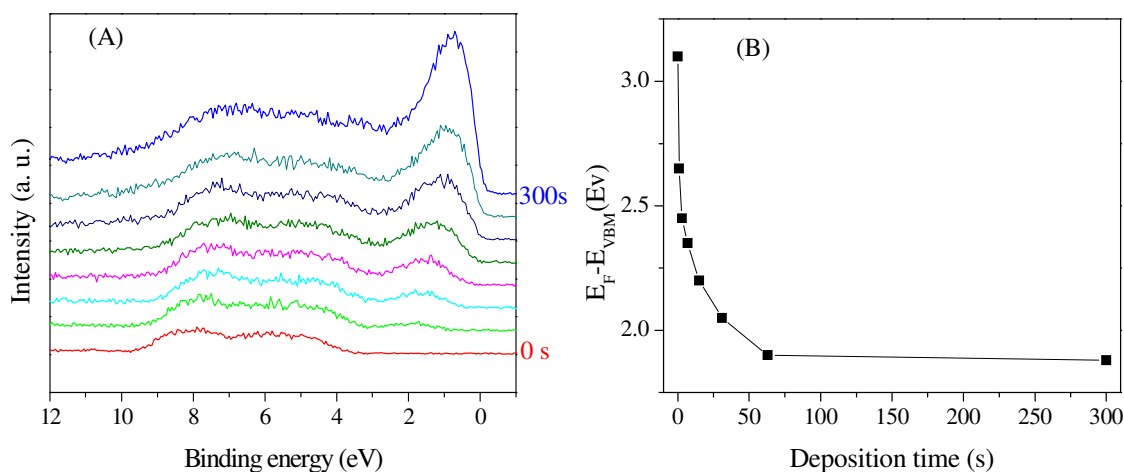


Figure IV-14: (A) XP valence band spectra during stepwise deposition of RuO_2 onto TiO_2 film (B) evolution of the valence band position of TiO_2 determined from core level binding energy: (A) the spectrum at bottom (at 0 s) refers to the uncovered TiO_2 film and the spectrum at the top (after 300 s) refers to saturated RuO_2 film.

Figure IV-14A shows the evolution of the XP valence band spectra during the stepwise deposition of RuO_2 onto TiO_2 film. The overall valence band spectra gradually shifts toward lower binding energy with increasing amount of RuO_2 deposition. For a better visibility of the shift of the valence band maximum of TiO_2 with respect to Fermi level due to the superimposing of the valence of TiO_2 and RuO_2 , the valence band shift was determined from the core level binding energy shift of Ti $2p_{3/2}$ during the interface experiment. As shown in **Figure IV-14B**, the valence band position rapidly shifts to the lower binding energies, and

then approached to a saturation value as the deposition proceeded. The valence band position with respect to Fermi level, $E_F - E_{VBM}$ shifted from 3.1 eV for the uncovered TiO₂ film to 1.88 eV for the saturated RuO₂ film.

This energy shift of ~1.22 of the VBM of TiO₂ as determined by the Ti 2p_{3/2} core level line can be attributed to the band bending of TiO₂ developed at the interface of RuO₂/TiO₂ due to the initially different Fermi level position of RuO₂ and TiO₂ film. The overall work function difference of 2.4 eV leads to a band bending of 1.22 eV in TiO₂ and to an additional dipole potential drop of 1.18 eV at the interface of RuO₂/TiO₂. A schematic band energy alignment at the RuO₂/TiO₂ heterojunction as deduced from these results is shown in **Figure IV-15**.

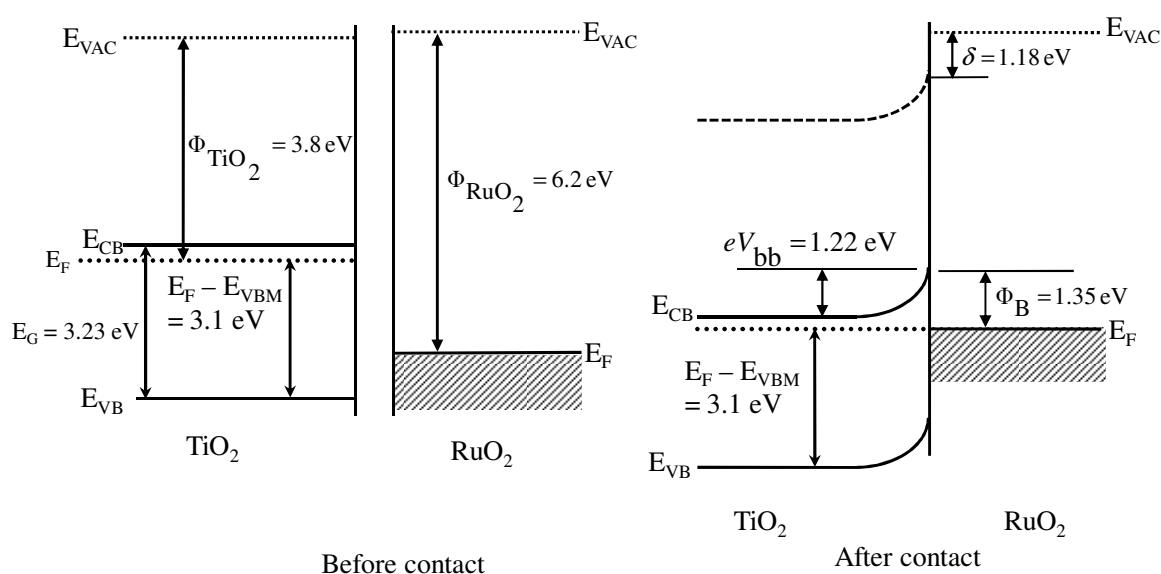


Figure IV-15: Schematic band energy alignment at the interface of RuO₂ and TiO₂. E_{CB} , E_{VB} , E_F , E_g are conduction band minimum, valence band maximum, Fermi level and energy gap, respectively. eV_{bb} refers to band bending at the interface of RuO₂ and TiO₂.

Now we will return to the surface analysis of the RuO₂/TiO₂ nanoparticles. The X-ray photoelectron Ti 2p, O 1s and Ru 3d core level spectra of the heterostructure RuO₂/TiO₂ nanoparticles containing different wt% of RuO₂ are shown in **Figure IV-16**. According to this figure, the shift of the core level peaks observed for the nanoparticles is small when compared to those of the bulk material as seen during the interface experiment. It is found that both Ti 2p_{3/2} and O 1s peaks are only shifted towards lower binding energy by 0.2 ± 0.05 and 0.1 eV, respectively, from their original values.

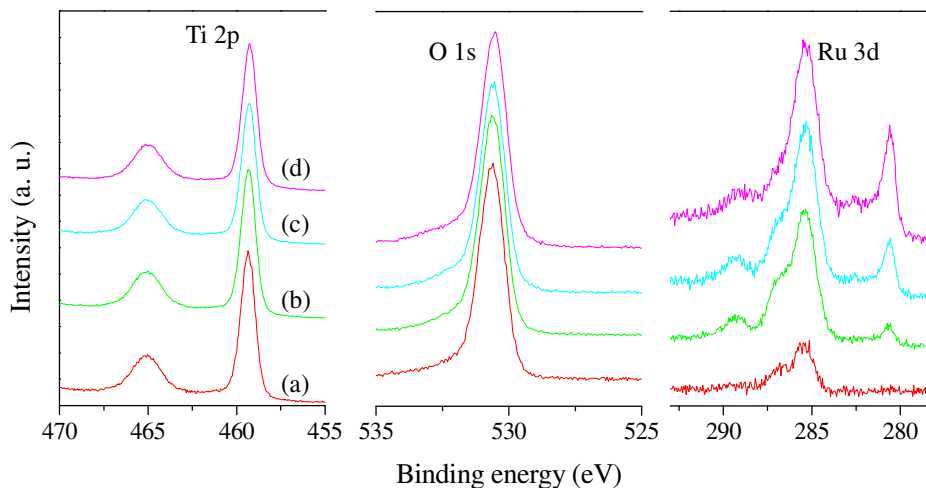


Figure IV-16: X-ray photoelectron core level spectra of heterostructure $\text{RuO}_2/\text{TiO}_2$ nanoparticles containing different wt% RuO_2 . (a) TiO_2 , (b) 1 wt% $\text{RuO}_2/\text{TiO}_2$, (c) 2.5 wt% $\text{RuO}_2/\text{TiO}_2$ and 5 wt% $\text{RuO}_2/\text{TiO}_2$.

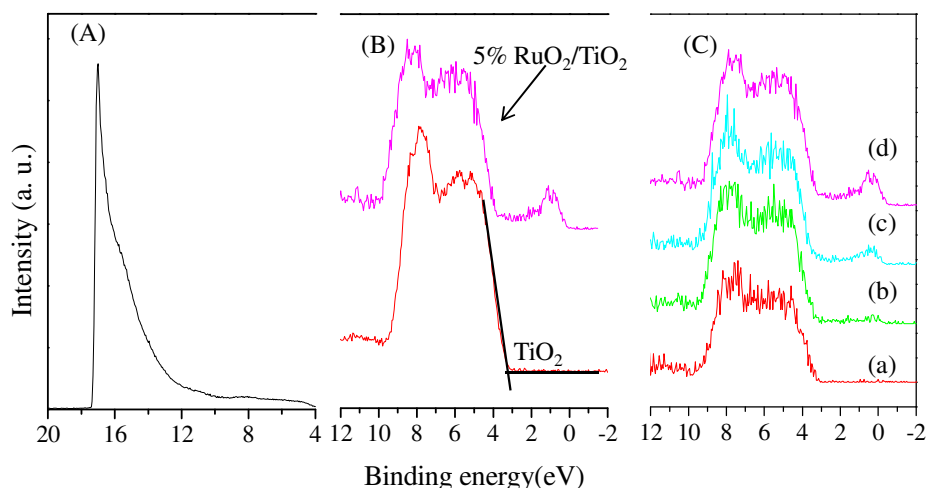


Figure IV-17: (A) UPS spectra of TiO_2 (B) XP valence band spectra of TiO_2 and $\text{RuO}_2/\text{TiO}_2$ and (C) Evolution of XP valence band spectra with different content of RuO_2 . (a) TiO_2 , (b) 1 wt% $\text{RuO}_2/\text{TiO}_2$, (c) 2.5 wt% $\text{RuO}_2/\text{TiO}_2$ and 5 wt% $\text{RuO}_2/\text{TiO}_2$.

The unparallel shift of both $\text{Ti } 2p_{3/2}$ and $\text{O } 1s$ can be related to interfacial reaction between RuO_2 and TiO_2 forming Ti-O-Ru bond. **Figure IV-17** show the UPS spectra and the evolution of XP valence band spectra. The work function of pure TiO_2 determined by UPS was 3.9 eV. The valence band maximum for pure TiO_2 nanoparticle was determined to be 3.15 eV and the position of the VBM shifted to lower binding energy with increasing content of RuO_2 . The shift of the valence band position (0.2 ± 0.05 eV) with respect to Fermi level, $E_F - E_{VBM}$ was determined by the core level shift of $\text{Ti } 3p_{3/2}$ and was attributed to band bending at the interface of $\text{RuO}_2/\text{TiO}_2$ nanoparticles which was small as compared to the

planar semiconductor. The difference in the PES results in heterostructure alignment can be related to two effects: i) in the composite systems the barrier below the RuO₂ coverage in the TiO₂ substrate is shielded from analysis; ii) for the formation of a complete space charge layer the diameter of the TiO₂ particles must exceed the depletion layer width.

IV.2.2.3. Photocatalytic activity

IV.2.2.3.1 Photocatalytic degradation of organic dyes

To evidence the photocatalytic efficiency of the as-synthesized RuO₂/TiO₂ nanomaterials, experiments of the photocatalytic decomposition of methylene blue (MB) and methyl orange (MO) were performed as a test reaction according to the literature.⁴⁸

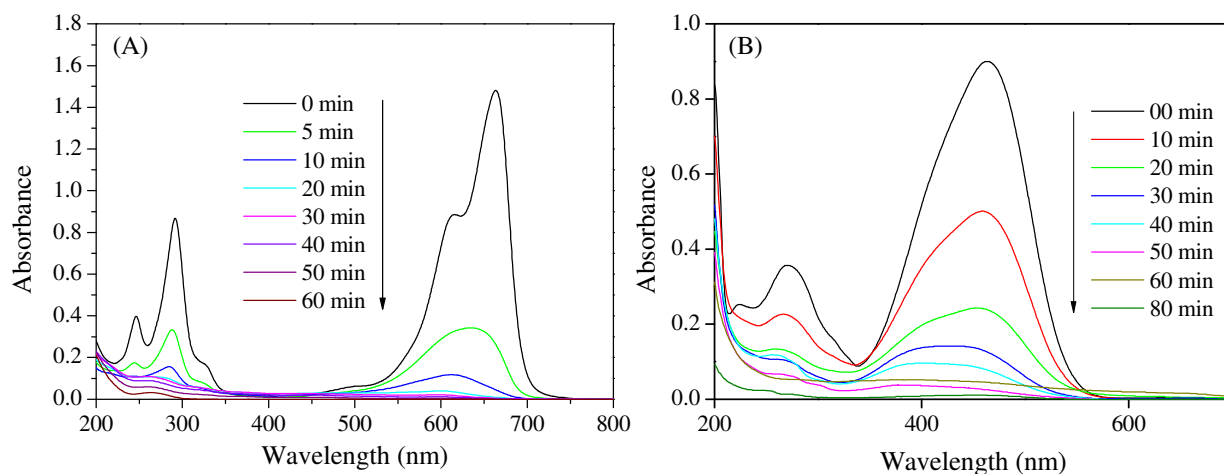


Figure IV-18: Change of absorbance spectra of (A) MB and (B) MO solution after different irradiation times in the presence of 1 wt% RuO₂/TiO₂.

As depicted in **Figure IV-18A**, the maximum absorption peaks of MB at 664 nm diminished gradually and disappeared completely under UV light irradiation for 60 min in the presence of the RuO₂/TiO₂ nanocatalyst. Meanwhile, the color of the solution changed gradually, suggesting that the chromophoric structure of MB was decomposed. A similar trend was also observed for the decomposition of MO (**Figure IV-18B**). Furthermore, blank experiments in the presence of irradiation without the photocatalyst were carried out to rationalize the photocatalytic activity of the as-synthesized RuO₂/TiO₂ photocatalyst. The degradation efficiency of the as-synthesized samples was defined as C/C_0 , where C_0 and C are the initial concentration after equilibrium adsorption and the concentration of MB during the reaction time, respectively. Blank experiment results showed that MB could not be decomposed without the photocatalyst under UV irradiation.

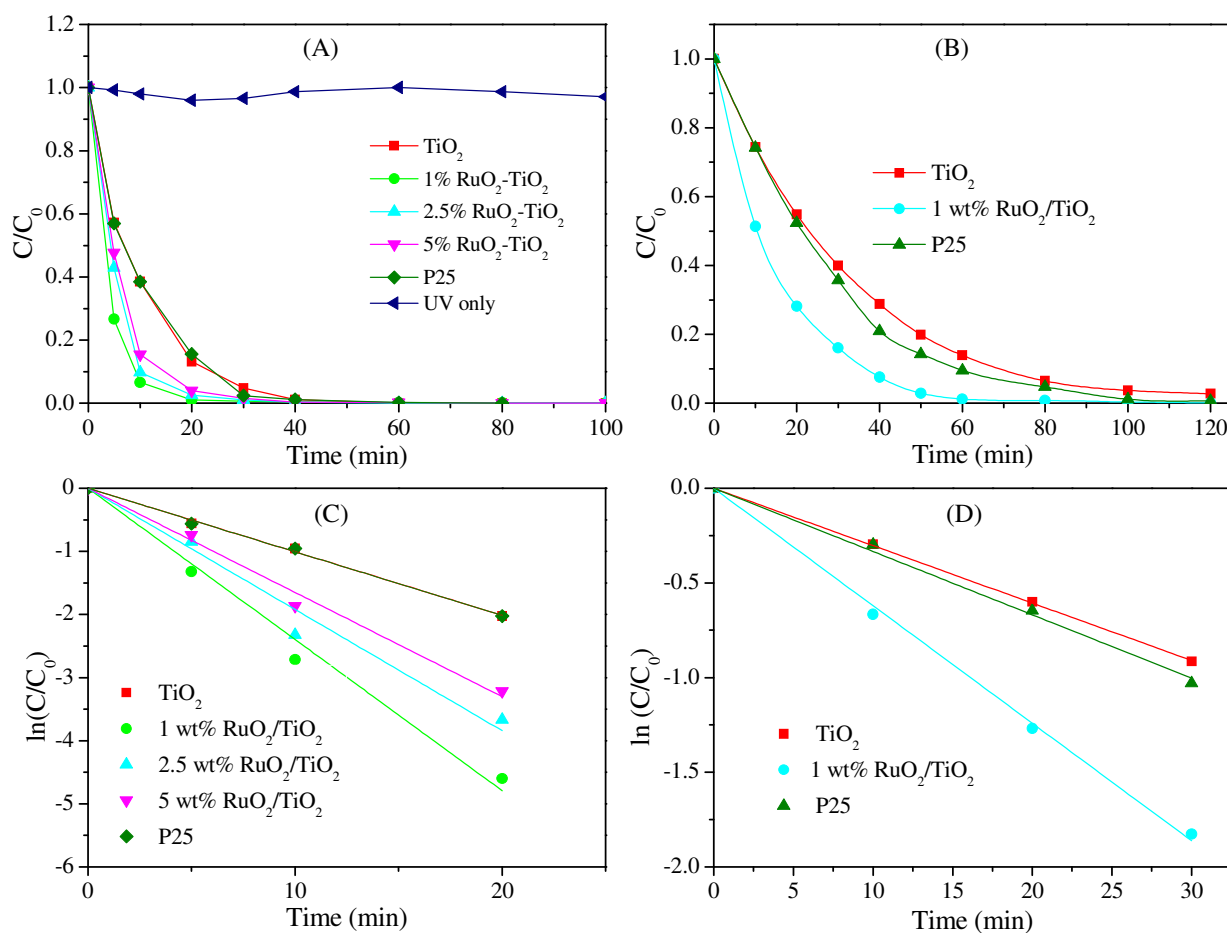


Figure IV-19: Kinetic of the degradation of MB (A) and MO (B); and plot of $\ln C/C_0$ against t for the photocatalytic degradation of MB (C) and MO (D) with the as-synthesized nanoparticles.

In order to elucidate the effect of wt% of RuO_2 on the photocatalytic activity of $\text{RuO}_2/\text{TiO}_2$ photocatalyst, a set of parallel experiments were conducted with $\text{RuO}_2/\text{TiO}_2$ photocatalysts containing different wt% of RuO_2 . **Figure IV-19A** shows the effect of wt% of RuO_2 on the photocatalytic degradation of MB. As seen in **Figure IV-19**, $\text{RuO}_2/\text{TiO}_2$ composite nanoparticles had a higher photocatalytic activity than pure TiO_2 . The heterostructure $\text{RuO}_2/\text{TiO}_2$ nanoparticle with 1 wt% RuO_2 was a superior catalyst with the degradation efficiency of 94% after 10 min irradiation of UV light. By contrast, values of about 62, 90 and 85% were found for the TiO_2 , 2.5 wt% $\text{RuO}_2/\text{TiO}_2$ and 5 wt% $\text{RuO}_2/\text{TiO}_2$ samples, respectively. Similarly, 1 wt% $\text{RuO}_2/\text{TiO}_2$ also showed higher photocatalytic performance for the degradation of MO as compared to pure TiO_2 and commercial TiO_2 (Degussa P25) (**Figure IV-19B**). As a result, the mesoporous $\text{RuO}_2/\text{TiO}_2$ heterojunction nanomaterials showed the faster decomposition rate of MB as well as that of MO that validates the concept of improved minority charge carrier separation developed in this study. For a better understanding of the photocatalytic efficiency of the as-synthesized samples, the

kinetic analysis of MB and MO degradation was discussed. It is well accepted that the photocatalytic decomposition of organic pollutants follows with a pseudo first-order kinetic. A plot of $\ln(C/C_0)$ against reaction time t yields a straight line whose slope gives the apparent reaction constant, k_{app} . **Figure IV-19C** and **D** show the plots of $\ln(C/C_0)$ against t for different as-synthesized photocatalysts for the degradation of MB and MO, respectively. The apparent reaction rate constants, BET surface area (S_{BET}) of catalysts and the normalized rate constant k_{norm} defined as $k_{norm} = k_{app}/S_{BET}$ for the degradation of MB and MO using different as-synthesized photocatalysts are summarized in **Table IV-2**. As shown in **Table IV-2**, the RuO_2/TiO_2 nanocomposite had a higher photocatalytic activity than the pure TiO_2 nanoparticles, as evidenced by the larger value of k_{app} . The RuO_2/TiO_2 nanocomposite with 1 wt% RuO_2 showed the highest photocatalytic activity with an apparent degradation rate constant reaching 0.239 and 0.062 min^{-1} for the degradation of MB and MO, respectively, values 2.4 and 2 times higher than those measured with commercial TiO_2 P25, respectively.

Table IV-2: Apparent reaction rate constant for the degradation of MB with as-synthesized nanoparticles.

Photocatalysts	Dye	k_{app}, min^{-1}	$S_{BET}, m^2/g$	$k_{norm}, g/(m^2 \cdot min)$	R^2
TiO_2	MB	0.101	67.5	1.49×10^{-3}	0.997
1 wt% RuO_2-TiO_2	MB	0.239	67.2	3.56×10^{-3}	0.99
2.5 wt % RuO_2-TiO_2	MB	0.192	69.6	2.75×10^{-3}	0.97
5 wt% RuO_2-TiO_2	MB	0.165	62.8	2.63×10^{-3}	0.989
P25	MB	0.101	47	2.14×10^{-3}	0.998
TiO_2	MO	0.03	67.5	0.44×10^{-3}	0.999
1 wt% RuO_2-TiO_2	MO	0.062	67.2	0.92×10^{-3}	0.999
P25	MO	0.033	47	0.7×10^{-3}	0.999

In addition, this nanocatalyst can be recycled and reused several times without significant loss of efficiency, which is a key requirement for a possible industrial application. Thus, the photocatalytic efficiency of the RuO_2/TiO_2 heterojunction photocatalyst for the 4

cycling reuse were 99.6, 99.5, 99.2 and 99.4% after 30 min of reaction time, respectively (**Figure IV-20**).

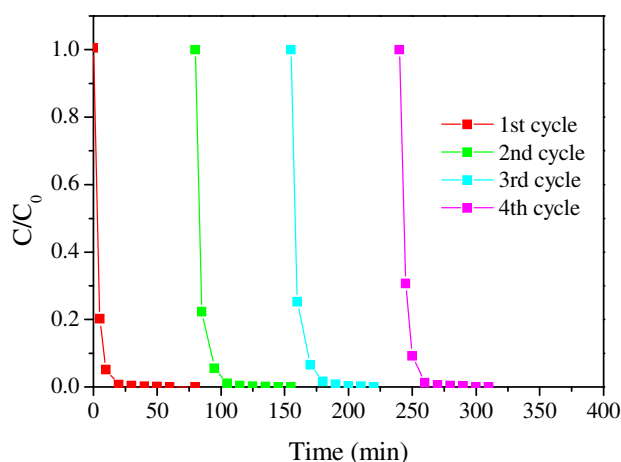


Figure IV-20: Cyclic runs in the photodegradation of MB employing 1 wt% RuO₂/TiO₂ under UV light.

As the photodegradation process is greatly affected by pH, the effect of pH on the efficiency of photocatalytic degradation of MB was examined at the pH = 2, 7 and 10.2. The photocatalytic degradation efficiency of MB solution as a function of pH is shown in **Figure IV-21**. The results showed that the pH of the solution had a direct influence on the heterogeneous photocatalysis process.

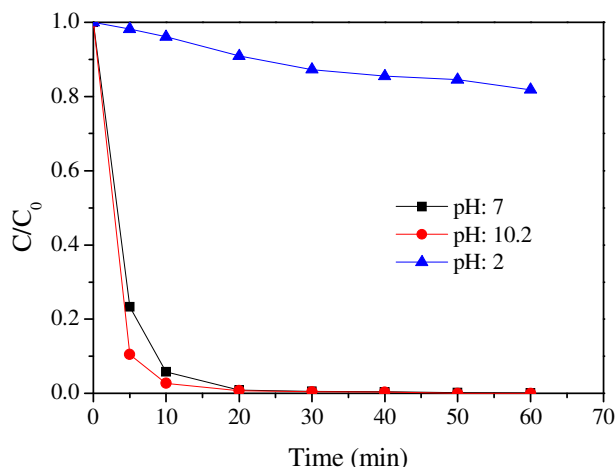


Figure IV-21: The effect of pH on the photocatalytic degradation of heterostructure 1 wt% RuO₂/TiO₂ photocatalysts.

As observed in **Figure IV-21**, the efficiency was higher in alkaline solutions than that in acidic solutions. This is indicative of the significant role of the surface properties of the heterostructure RuO₂/TiO₂ photocatalyst; the variation of solution pH changes the surface

charge of the photocatalysts and shifts the potentials of catalytic reactions. As a result, the adsorption of dye on the surface is altered thereby causing a change in the reaction rate. Considering the positive charge of cationic MB dye in solution, the effect of pH on the photocatalytic degradation of MB can be rationalized on the basis of an electrostatic adsorption model where cations are more readily accumulated at the negative sites on the heterostructure the $\text{RuO}_2/\text{TiO}_2$. This can be explained on the basis of the point of zero charge (pHzpc) of $\text{RuO}_2/\text{TiO}_2$ particle. At lower pH, the surface of the catalyst is positively charged, but at higher pH it becomes negatively charged. Since MB is a cationic dye, high pH favors adsorption on the catalyst surface which results in high degradation efficiency. On the other hand, at lower pH the electrostatic repulsion between the MB cations and positively charged oxide surface greatly reduces the adsorption of the MB dye resulting in a drastic decrease in degradation rate.

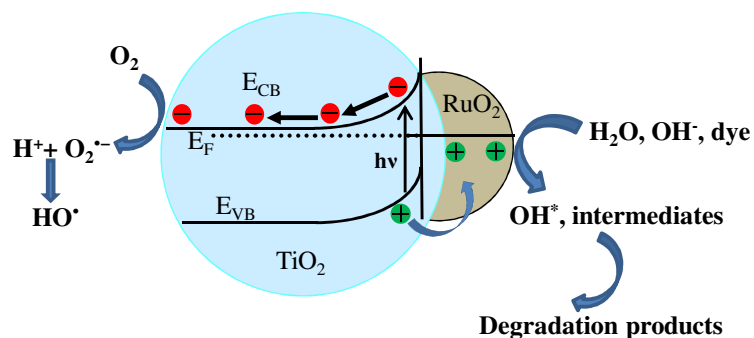


Figure IV-22: Schematic diagram of photogenerated charge separation by internal electric field at $\text{RuO}_2/\text{TiO}_2$ heterojunction and its photocatalytic process.

The higher photocatalytic activity of heterostructure $\text{RuO}_2/\text{TiO}_2$ nanoparticles is related to the role of RuO_2 on the surface of TiO_2 nanoparticles. **Figure IV-22** shows in detail the mechanism of photogenerated charge separation at the interface of heterojunction $\text{RuO}_2/\text{TiO}_2$ nanoparticles and its photocatalytic process. As we have seen from the surface analysis the Fermi level of TiO_2 is higher than that of RuO_2 , hence, for contact formation the electrons are transferred from the TiO_2 to RuO_2 until thermodynamic equilibrium is established between the two when they come into contact to each other. As a consequence, the Fermi level of the semiconductor and metal like RuO_2 at the interface is the same that results in the formation of an electron depletion region and surface upward-bent band in the semiconductor. This electron depletion region formed at these Schottky barrier leads to an internal electric field at the interface of the heterojunction $\text{RuO}_2/\text{TiO}_2$ nanoparticles at thermal equilibrium. Under UV light irradiation, the electron in the VB of TiO_2 is excited to

the CB by leaving a hole in the VB. The photogenerated electron-hole pairs can be separated effectively by the internal electric field developed at RuO₂/TiO₂ interface. The generated electrons tend to move to the positive side of the internal electric field; the electrons are transferred to the semiconductor side and take part in the reduction of dissolved oxygen forming superoxide radical anions, O₂^{•-}, yielding hydroperoxy radicals HO₂[•] on protonation and finally OH[•] radicals. At the same time, the photogenerated holes transferred to RuO₂ particles oxidize the surface hydroxyl groups or physisorbed water molecules, forming activated hydroxyl species OH^{*}, that activated hydroxyl species are strong oxidizing agent well-known to decompose organic substrates as MB or MO dye. In addition a hole transfer to the HOMO states of the dye which leads to a direct oxidation process of the dye can also not be neglected. Thus, an internal electric field caused the vectorial charge transport and transfer of electrons and holes into different directions and then retarded the photogenerated electron-hole pairs recombination, resulting in a better photocatalytic activity.

IV.2.2.3.2 Photocatalytic hydrogen production

Photocatalytic activity of the as-synthesized heterostructured photocatalysts was also quantified by photocatalytic hydrogen (H₂) evolution from the suspension of the photocatalysts with different RuO₂ content in an aqueous methanol solution under UV light irradiation using 1.6 W Hg vapour light source. Experimental procedure for the production of H₂ is described in detailed in the experiment section. **Figure IV-23A** shows photocatalytic H₂ production in the absence of photocatalyst or sacrificial agent (methanol) and in the presence of both the photocatalyst and methanol. The H₂ production under UV irradiation for 3 h was only 20.4 mL with no photocatalyst adding into the photoreactor, while in the absence of methanol but in the presence of catalysts, H₂ production was 24.5 mL. In contrast, the H₂ production was increased more than 77 times in the present of photocatalyst (5 wt% RuO₂/TiO₂) and methanol. These results indicated that both the photocatalysts and the sacrificial agent are essential for photocatalytic H₂ production. **Figure IV-23B** shows the time course of the photocatalytic gas evolution over TiO₂ and RuO₂/TiO₂ containing different amount of RuO₂. The amount of the evolved gas almost linearly increased with increasing irradiation time. The evolved gas was analyzed with gas chromatography. We identified CO₂, in an amount of 0.31 wt%, in the gas mixture. No O₂ and CH₄ was detected in the evolved gas mixture. **Figure IV-23C** shows the hydrogen production over the as-synthesized photocatalysts. Irrespective of the amount of RuO₂, the yield of H₂ over heterostructure

RuO₂/TiO₂ photocatalysts was higher than that of pure TiO₂ and commercial TiO₂ P25. Therefore, the presence of RuO₂ played an important role in photocatalytic H₂ production. It was found that the 5 wt% RuO₂/TiO₂ gave the highest rate of hydrogen production of 618 μmol/h. In order to obtain efficient RuO₂/TiO₂, effect of RuO₂ loading on the photocatalytic H₂ production were studied (shown in **Figure IV-23D**).

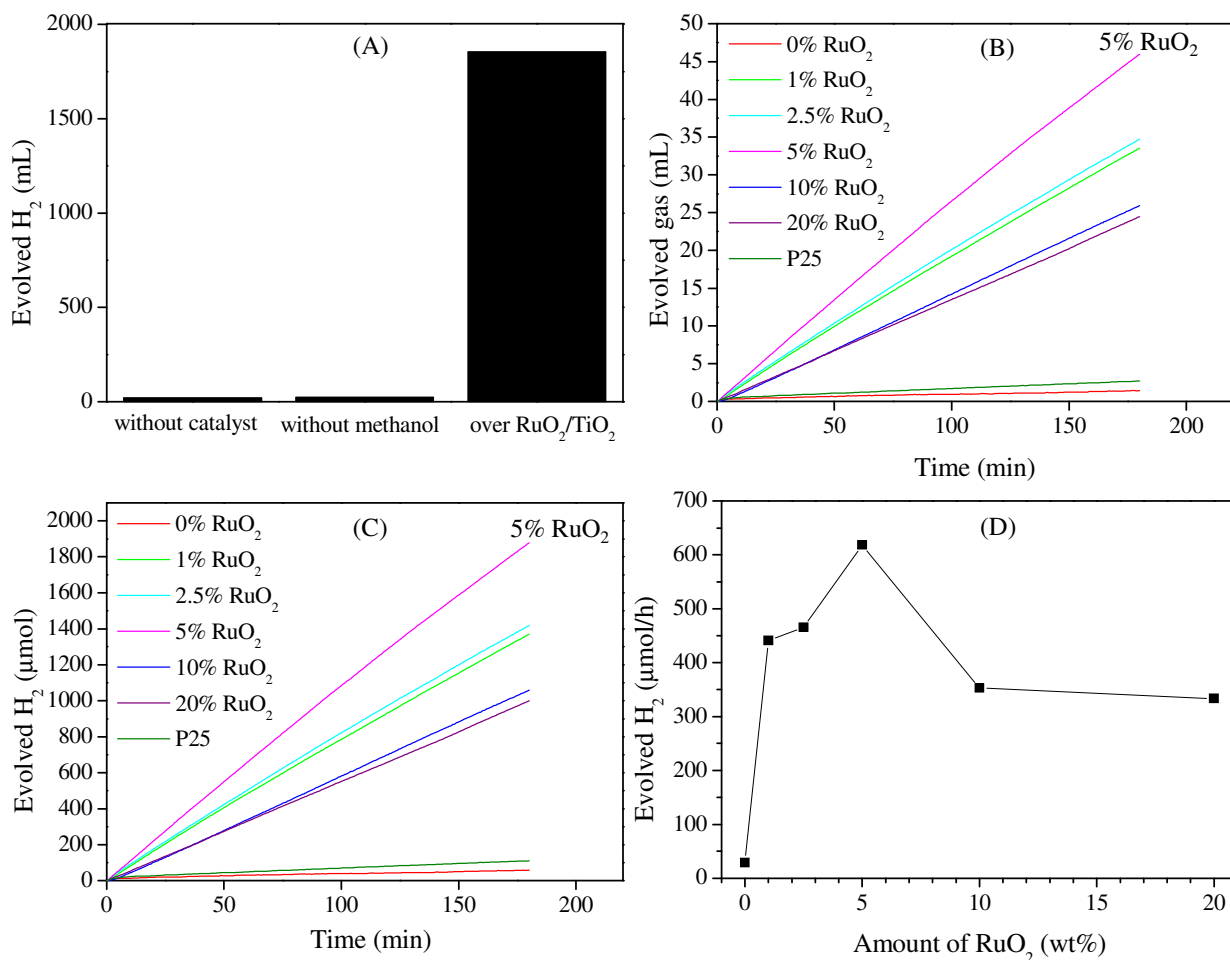


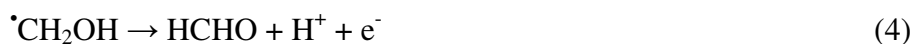
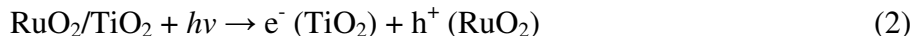
Figure IV-23: (A) photocatalytic evolution of H₂ under different condition, photocatalytic evolution of gas (B) and H₂ (C) over TiO₂ and RuO₂/TiO₂ photocatalysts and (D) effect of RuO₂ loading on the H₂ production. All the experiments were run for 3 h at identical condition.

It was seen that the rate of H₂ production increased initially with increasing RuO₂ content, reached a maximum and then started to decrease once the RuO₂ content was increased beyond a certain point. With an increase in RuO₂ content, from 1 wt% to 5 wt%, the rate of H₂ increased from 441 μmol/h to 618 μmol/h. In contrast, with further increase in RuO₂ content from 5 wt% to 10 wt%, the H₂ production rate dropped rapidly from 618 μmol/h to 353 μmol/h. The photocatalytic activity of RuO₂/TiO₂ was influenced by the Schottky barriers developed at the interface between RuO₂ and TiO₂. When RuO₂ content was below 5 wt%, the number of Schottky barriers at RuO₂/TiO₂ interface was enhanced with increment

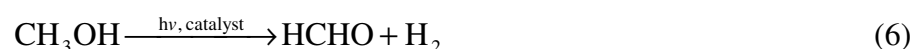
of RuO₂ loading, consequently resulting in an increase in photocatalytic activity. However, when the RuO₂ loading was above the optimum loading, the active sites on the TiO₂ surface that were available for absorption of light and electron donors were covered by excessive RuO₂ particles. Another explanation is that, at higher metal loadings, the deposited metal particles may act as recombination centres for photogenerated electrons and holes. As a result, the photocatalytic activity of RuO₂/TiO₂ was remarkably decreased due to inefficient excitation.

In the absence of oxygen and presence of sacrificial species such as methanol, the holes generated by the light (Eq. (2)) react with methanol (CH₃OH) to produce $\cdot\text{CH}_2\text{OH}$ radical. The $\cdot\text{CH}_2\text{OH}$ radical possesses sufficiently negative oxidation potential (-0.74 V) and could further react to produce H⁺, electron and HCHO ((Eq. (4)).⁴⁹ On the other hand, electrons in the conduction band of the particle will simultaneously reduce water or protons in the solution to form gaseous H₂ as shown by Eq. (5). These reactions proceed competitively with the recombination of the photoinduced electrons and holes

On the basis of the above results, following photoreactions on the photocatalysts could be proposed as



The overall reaction is



The product, formaldehyde (HCHO), could be further oxidized to methanoic acid HCOOH and subsequently to CO₂ together with hydrogen generation via eqs



So far an idealized mechanistic scheme of electron-hole pair separation of a well defined planar metal-semiconductor contact has been described. However, it is evident from the comparison of the model experiments to the analysis of predeposited nanostructured

RuO₂/TiO₂ heteroparticles changes in morphology and size dependent electronic properties must also be taken into account. The observed band bending shift in the RuO₂/TiO₂ nanocatalysts is smaller than on the film heterointerface for two reasons. First of all the smaller size of the TiO₂ and RuO₂ particles does not allow to saturate the band bending as the standard space charge layers thickness will exceed the size of the particles (an effect which depend on doping). In addition, the RuO₂ at small concentration ratio has not completely formed its bulk electronic structure (as is evident from the observed size dependent changes in the spectral feature). Furthermore, the spatial distribution of the RuO₂ deposits on the TiO₂ substrates are not yet optimized as is also suggested from TEM data. For optimization of carrier separation a well defined anisotropy must be obtained in the synthesis of the photocatalyst.

IV.3. Nanostructured RuO₂/ZnO heterojunction photocatalysts

IV.3.1.1. Synthesis and characterization of the nanocatalysts

As no preparation method of RuO₂/ZnO nanocomposites was reported so far, a two-step procedure was established to prepare them. At first, nanosized ZnO particles were prepared by homogeneous precipitation method using zinc acetate and urea as the precursor and precipitating agent, respectively. Precipitation of Zn(OH)₂ was observed when a clear solution of zinc acetate and urea was reacted at 90 °C in aqueous medium. The pH of the solution increased gradually due to the progressive decomposition of urea into NH₃ and CO₂, leading to the nucleation and growth of uniformly nanosized particles which were calcined at 350 °C. Subsequently, the RuO₂/ZnO systems containing 2, 4 and 6 wt% of RuO₂ were prepared by impregnating the resulting ZnO nanoparticles with a solution containing the desired amount of ruthenium (III) chloride hydrate (RuCl₃ · xH₂O) followed by calcination at 350 °C in air. After annealing in air at high temperature, FTIR studies revealed the complete elimination of the undesirable organics and the formation of metal oxide species (**Figure IV-24A**). Irrespective of the RuO₂ content, each spectrum showed a broad absorption band centered at 3434 cm⁻¹ due to the presence of OH groups. Furthermore, the band at 1631 cm⁻¹ was due to bending vibration of molecular water, whereas the intense absorption band at 505 cm⁻¹ was assigned to the stretching vibration mode of ZnO bonds in zinc oxides.⁵⁰

Furthermore, Raman scattering spectroscopy was used to extract nanostructural information of the samples. The technique is capable of elucidating the photocatalyst

structural complexity as peaks from each material are clearly separated in frequency, and therefore the phases are easily distinguishable. Thermodynamically stable ZnO crystallite possesses a wurtzite (hexagonal) structure and belongs to the space group of C_{6v}^4 . Group theory predicts that the materials with C_{6v}^4 space group are expected to have $A_1 + 2B_1 + E_1 + 2E_2$ optical phonon modes near the center of the Brillouin zone. Among these optical phonon modes, A_1 and E_1 modes are both Raman and infra-red active. Moreover, these A_1 and E_1 modes are polar which split into transverse optical (TO) and longitudinal optical (LO) phonons. E_2 mode consists of two modes of low- and high-frequency phonons which are Raman active only and B_1 modes are silent.⁵¹ The bands in the Raman spectra can be entirely explained on the basis of published data for c-ZnO:^{51b, 52} E_2 (low) at 101 cm^{-1} , E_2 (high) at 437 cm^{-1} , A_1 (TO) at 380 cm^{-1} , E_1 (TO) at 407 cm^{-1} , A_1 (LO) at 574 cm^{-1} , and E_1 (LO) at 583 cm^{-1} . The rest of the vibrations are usually labeled as second order vibrations.⁵³ RuO₂ has a rutile structure, which is tetragonal with two RuO₂ molecules per primitive unit cell. According to the factor group analysis, there are 15 optical modes of RuO₂, among which four modes are Raman active with symmetries A_{1g} , B_{1g} , B_{2g} and E_g .⁵⁴ The three major Raman features of a rutile single crystal RuO₂, namely the E_g , A_{1g} , and B_{2g} are located at 528 , 646 and 716 cm^{-1} , respectively.⁵⁵

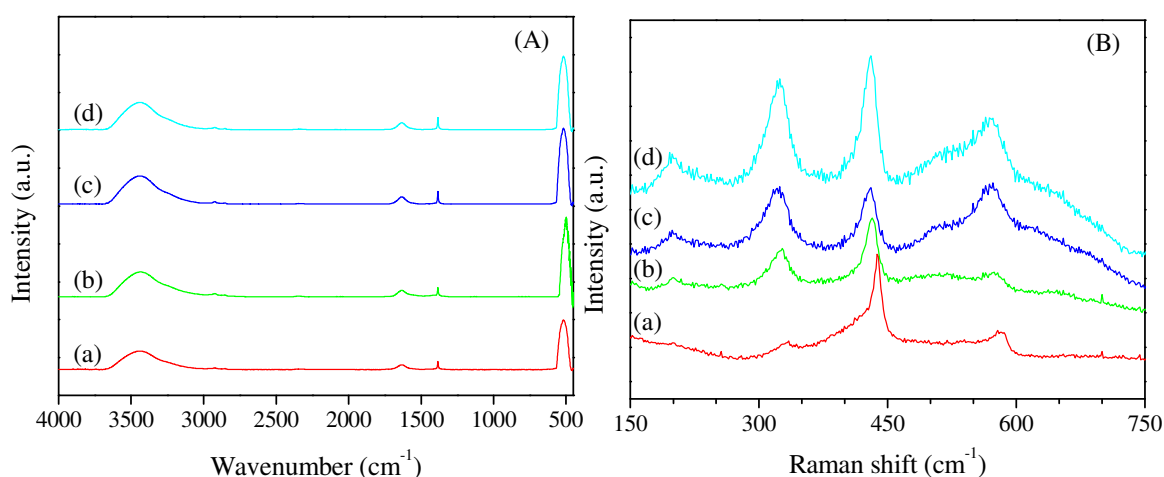


Figure IV-24: (A) FTIR and (B) Raman spectra of as-synthesized photocatalysts. (a) ZnO, (b) 2 wt% RuO₂/ZnO, (c) 4 wt% RuO₂/ZnO, and (d) 6 wt% RuO₂/ZnO.

Figure IV-24B shows the Raman spectra of ZnO nanoparticles and RuO₂-ZnO nanocomposites. The main dominant sharp peak labeled as E_2 at 438 cm^{-1} is known as Raman active phonon mode, which was characteristic of the Wurtzite hexagonal phase of ZnO (**Figure IV-24Ba**). A very weak shoulder at 410 cm^{-1} in pure ZnO corresponded to the mode

of $E_1(\text{TO})$.⁵⁶ The peaks that appeared at 205 cm^{-1} and 335 cm^{-1} could be assigned as second order modes.⁵⁷ The frequency of the first-order Raman peak at 585 cm^{-1} could be ascribed to the longitudinal optical (LO) phonons of E_1 . It is obvious for **Figure IV-24B(b-d)** that the intensity of Raman peaks for $\text{RuO}_2\text{-ZnO}$ nanocomposites was enhanced as compared to pure ZnO with increasing the amount of RuO_2 on the surface of ZnO nanocatalysts. This enhancement was predominant for the first order LO phonon mode. In addition, the red shift of both E_2 mode and LO phonon could also be observed. The presence of an electric field can enhance the scattering by Raman active optical phonons due to polarization by the field of the excitonic states. This scattering is proportional to the electric field and goes through a maximum. The transfer of electrons from ZnO to RuO_2 leads to the formation of interfacial electric field between ZnO and RuO_2 due to different work functions. This local electric field increases the electron-phonon coupling, which led to the enhancement of the Raman intensity of ZnO. Otherwise, more phonon modes of ZnO have been activated in $\text{RuO}_2\text{-ZnO}$ nanocomposites compared to ZnO nanocatalysts.

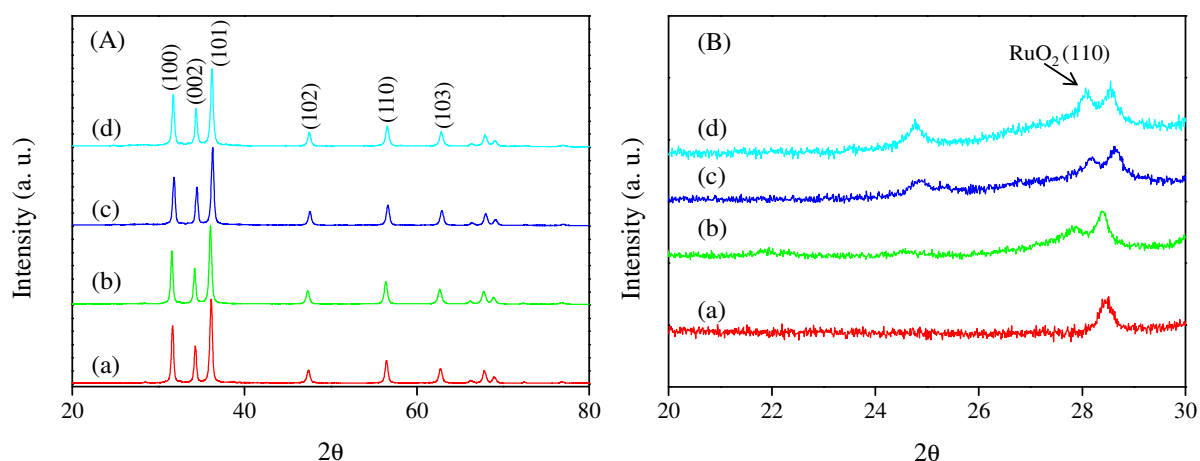


Figure IV-25: XRD pattern of RuO_2/ZnO heterostructure recorded at different RuO_2 content in the 2θ region of $10\text{-}80^\circ$ (A) and $26\text{-}66^\circ$ (B). (a) ZnO, (b) 2% RuO_2/ZnO , (c) 4% RuO_2/ZnO , (d) 6% RuO_2/ZnO .

The crystalline phases of the catalysts were further confirmed by using XRD analysis (**Figure IV-25**). Irrespective of the RuO_2 content, all the diffraction peaks could be readily indexed as hexagonal Wurtzite structure for ZnO for both pure ZnO and RuO_2/ZnO in well agreement with the reported data (JCPDS File No. 36-1451). The peaks at 2θ of 31.7° , 34.3° , 36.2° , 47.5° and 56.5° , corresponded to the crystal planes (100), (002), (101), (102), and (110) of crystalline ZnO, respectively. Peaks corresponding to RuO_2 were not seen clearly. In order to identify the crystalline phase of RuO_2 , the XRD pattern of all the samples were

plotted with enhanced intensity in the region 2θ from 20 to 30 as shown in **Figure IV-25B**. A close view in the 2θ range of 20-30° showed an extra peak at 2θ of 28° that could be indexed to RuO_2 (110).⁵⁸ The intensity of RuO_2 peaks in the nanocomposite samples increased with the increase in the amount of RuO_2 content indicating the formation of RuO_2 along with ZnO . Moreover, the average crystal size of ZnO was estimated from line broadening of (101) diffraction peak using the Scherrer formula as shown **Table IV-3**. Compared to the average crystal size of 25 nm for the pure ZnO , it seems that there was no appreciable change in the average crystal size of as-synthesized RuO_2/ZnO heterostructure containing different RuO_2 content.

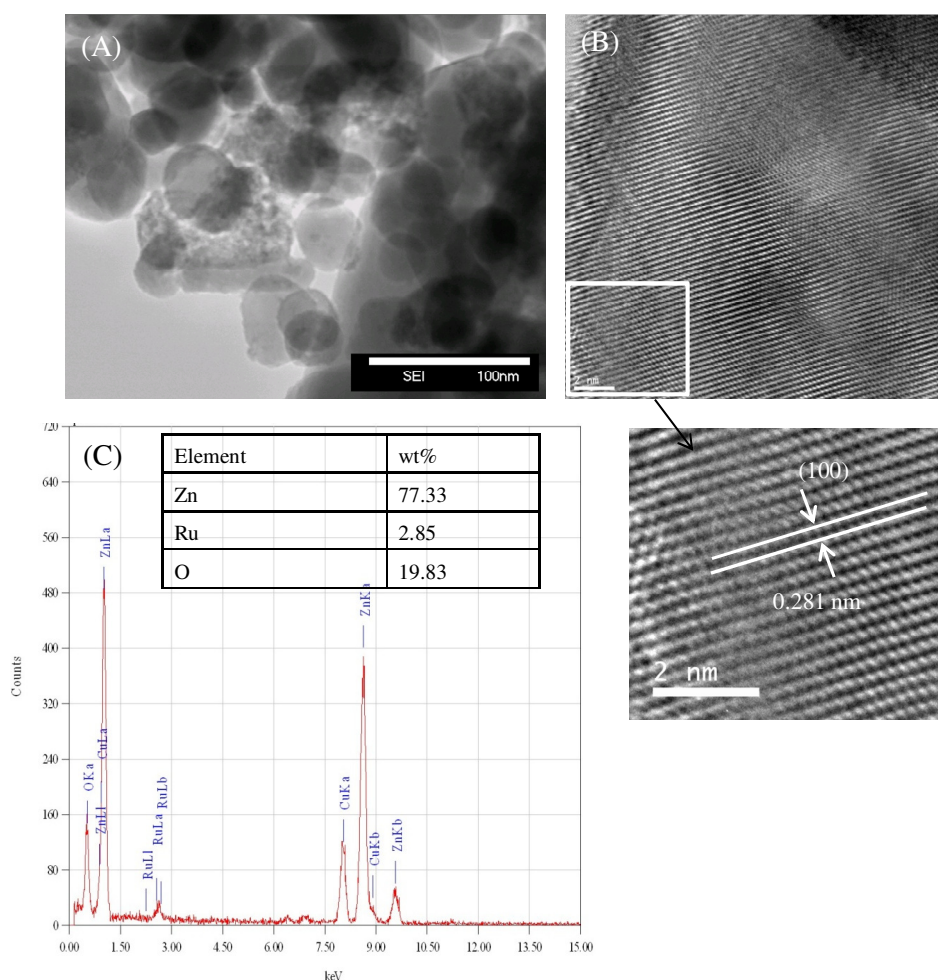


Figure IV-26: (A) TEM image and (B) HRTEM image of 4 wt% RuO_2/ZnO photocatalysts (C) EDX spectrum from part (A).

In order to obtain detailed information about the microstructure and morphology of the as-synthesized samples, TEM observations were carried out. **Figure IV-26A, B** show the TEM images of the as-synthesized sample with a RuO_2 content of 4 wt%. A low magnified

TEM image of this sample demonstrated the formation of nanocrystalline ZnO aggregates composed of spherical nanoparticles. The observed ZnO particle size in the range of 25-30 nm agreed well with the crystallite size estimated from the XRD analysis.

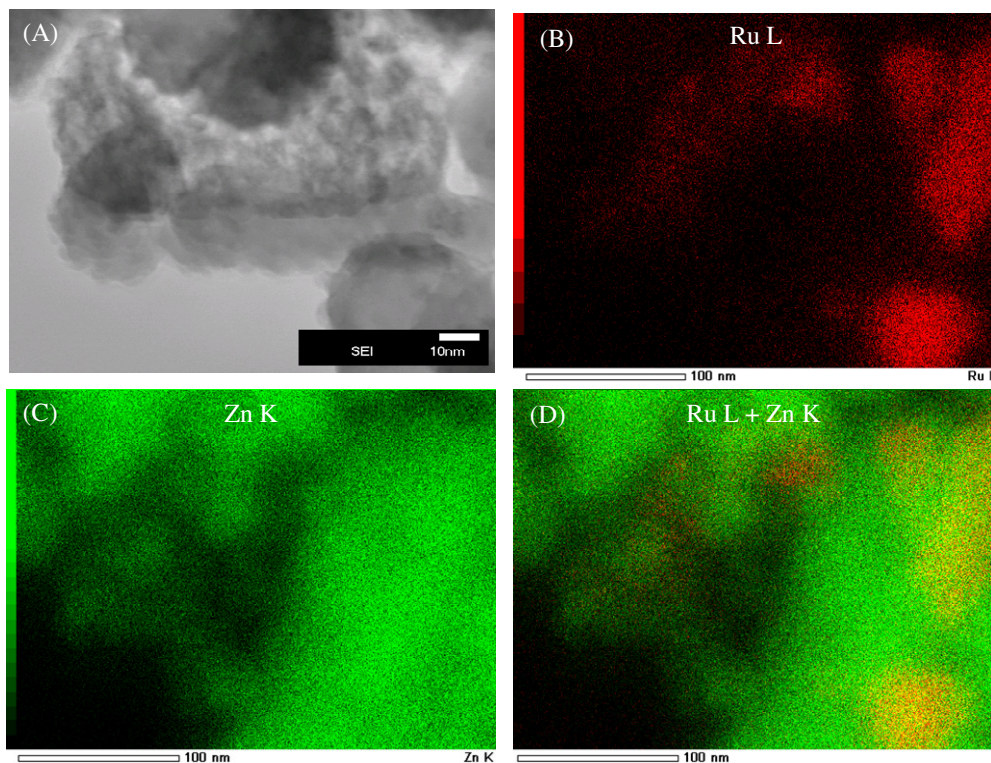


Figure IV-27: (A) STEM secondary electron image (SEI) of 4 wt% RuO₂/ZnO and EDX maps of (B) Ru, (C) Zn and (D) Overlay (Ru and Zn). EDX mapping was carried out by scanning a region different from the region shown in (A).

In order to obtain the microstructure of the samples, high-resolution transmission electron microscopy (HRTEM) observations were carried out, and the corresponding results are shown in **Figure IV-26B**. The interplanar distance of 0.28 nm is consistent with the lattice spacing of the (100) plane expected for the hexagonal wurtzite ZnO. The composition and the presence of RuO₂ of the as-synthesized samples were confirmed by energy dispersive X-ray (EDX) analysis and the results are shown in **Figure IV-26C**. All of the peaks in the curves were ascribed to Zn, Ru, O, and Cu, and no peaks of other elements are observed. The copper signal is from the sample holder. Therefore, it can be concluded that the as-synthesized samples were composed of Zn, Ru and O, which was in good agreement with the above XRD results. In addition, EDX analysis revealed the elemental compositions of the as-synthesized samples (listed in **Figure IV-26C**) and the calculated weight percentage of RuO₂ was 3.75 wt% which was close to the theoretical value (4.0 wt %). EDX maps shown in **Figure IV-27** further confirmed that RuO₂ was deposited on ZnO as cluster.

The textures of the as-synthesized photocatalysts were then analyzed by the N₂ adsorption isotherm technique. **Figure IV-28** shows N₂ adsorption-desorption isotherms for the pure ZnO and 4 wt% RuO₂/ZnO samples. According to the IUPAC classification,⁵⁹ type-II sorption isotherms were found for both samples which are typical of materials including large mesopores and/or macropores. The porosity detected, with average pore size diameter between 14 and 23 nm, can be attributed to the intercrystallite space that can be observed as evidenced by the TEM images (**Figure IV-27**). Indeed, the grains consist in a network of aggregated nanoparticles, the voids between the nanoparticles accounting for the porosity detected by N₂ sorption measurements.

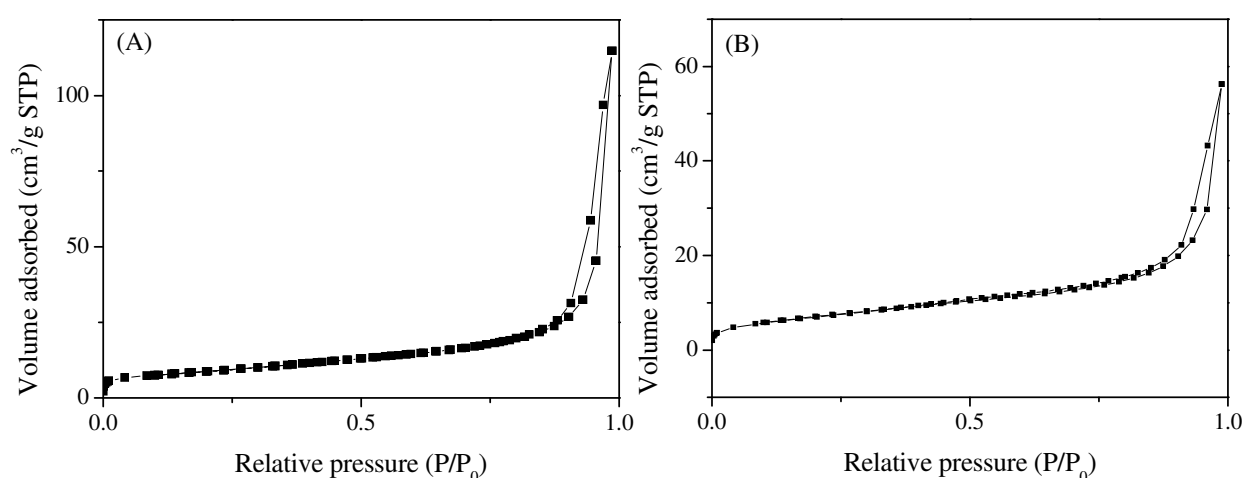


Figure IV-28: N₂ adsorption–desorption isotherm and of as-synthesized ZnO (A) and 4 wt% RuO₂/ZnO (B) photocatalysts.

The textural properties, namely BET surface area, mean pore diameter, and total pore volume, of the as-synthesized mesoporous ZnO and RuO₂ loaded ZnO catalysts are given for comparison in **Table IV-3**. The ZnO catalyst possessed BET surface area of 31 m²/g with mean pore diameter and total pore volume of 22.9 (within mesopore region) and 0.18 cm³/g, respectively. When RuO₂ were loaded onto the ZnO, aiming to improve the catalytic performance, it was seen that the BET surface area, mean pore diameter, and total pore volume as shown in **Table IV-3** were slightly decreased with increasing the wt% of RuO₂. The BET surface area, mean pore diameter, and total pore volume for 4 wt% RuO₂/ZnO were 25 m²/g, 14 nm and 0.09 cm³/g, respectively. The decrease in BET surface area could result from the blocking of mesopore dimension when RuO₂ particles were deposited.

Table IV-3: Crystallite size and textural properties of ZnO and RuO₂/ZnO photocatalysts.

Samples	Crystallite size (nm)	BET Surface area (m ² /g)	Mean pore diameter ^a (nm)	Total pore volume (cm ³ /g)
ZnO	25 ± 1	31 ± 1	23 ± 0.5	0.18 ± 0.02
2% RuO ₂ -ZnO	25 ± 1	29 ± 1	19 ± 0.5	0.14 ± 0.02
4% RuO ₂ -ZnO	26 ± 1	25 ± 1	14 ± 0.5	0.09 ± 0.02
6% RuO ₂ -ZnO	25 ± 1	22 ± 1	15 ± 0.5	0.08 ± 0.02

^a: Adsorption average pore diameter ($4V/A$ by *BET*)

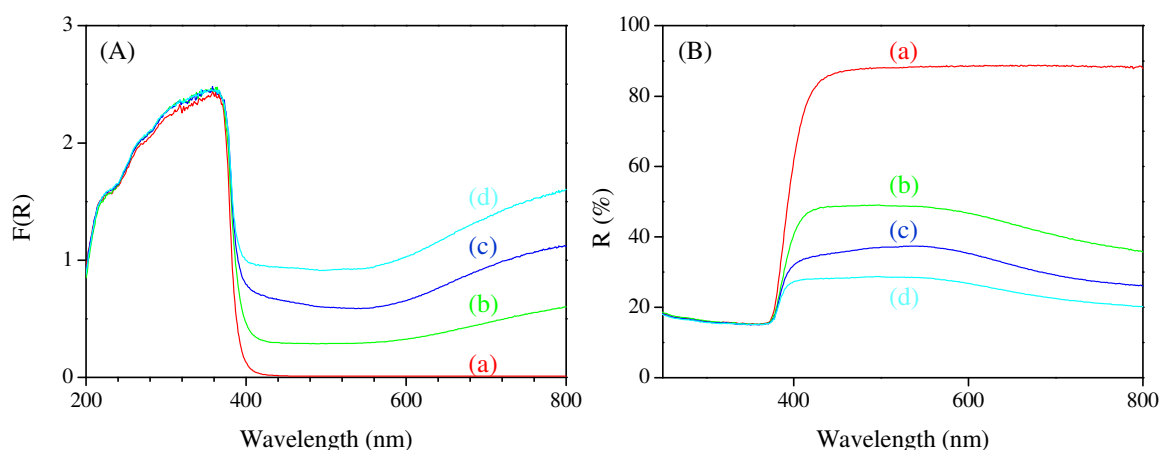


Figure IV-29: UV-Vis diffused (A) absorption and (B) reflectance spectra of (a) ZnO, (b) 2 wt% RuO₂/ZnO, (c) 4 wt% RuO₂/ZnO and (d) 6 wt% RuO₂/ZnO.

The optical property such as the band gap of the as-synthesized nanoparticles was determined by means of the optical absorption spectrum.⁶⁰ **Figure IV-29A** shows the UV-Vis diffuse absorption spectra of as-synthesized ZnO and RuO₂/ZnO nanocomposite photocatalysts containing different weight percentage of RuO₂. For all the samples, a significant increase in the absorption at wavelength shorter than 400 nm could be assigned to the intrinsic band gap absorption of ZnO. The RuO₂ loading obviously influenced visible light absorption of ZnO. Compared to pure ZnO (**Figure IV-29Aa**), the absorption spectra of all RuO₂/ZnO samples (**Figure IV-29A(b-d)**) showed an enhanced absorption in the visible-light region. In addition, the absorption increased with raising the RuO₂ content. The

absorption in the visible region could be clarified in more detail from UV-Vis diffused reflectance spectra as shown in **Figure IV-29B**. Pure ZnO reflected about 89 % visible light and absorbed about 85 % UV light (**Figure IV-29Ba**). In contrast, the reflectance of RuO₂/ZnO nanocomposites was lower than that of pure ZnO in all the wavelength range of 400-800 nm. However, in the UV region, it is not obvious because of the very high absorption of UV light for pure ZnO. The enhancement of visible-light absorption was due to the fact that the incident photon frequency was resonant with the collective excitations of the conduction electrons of RuO₂ nanoparticles called localized surface plasmon resonance (LSPR). To take into account that ZnO is a direct band gap semiconductor, the optical band gap was calculated from the Kubelka-Munk relation by extrapolating the linear portion of the plot of $(F(R) hv)^2$ versus hv to $F(R) = 0$ (**Figure IV-30**). The calculated band gap energy for pure ZnO was found to be 3.23 eV from the extrapolation of the corresponding plot. The calculated band gap for ZnO was in good agreement with the literature.⁶¹ On the other hand, the estimated band gap energies decreased from 3.23 eV for pure ZnO to 3.14 eV, for 6 wt% RuO₂/ZnO.

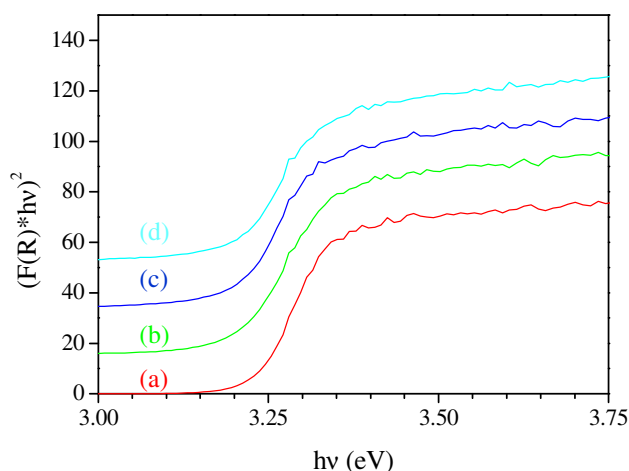


Figure IV-30: $(F(R) hv)^2$ versus hv plot for as-synthesized photocatalysts. (a) ZnO, (b) 2 wt% RuO₂/ZnO, (c) 4 wt% RuO₂/ZnO and (d) 6 wt% RuO₂/ZnO.

IV.3.1.2. Interface analysis

To clarify the elemental and chemical state of the as-synthesized samples, XPS measurements were conducted on pure ZnO and RuO₂/ZnO composites with different RuO₂ contents. Apart from the C 1s peak located at 284.4 eV from hydrocarbon contaminants, all of the peaks in the survey spectra of pure ZnO and 4 wt% RuO₂/ZnO (**Figure IV-31A**) can be ascribed to Zn, O and Ru without any further peak characteristic of other elements. Thus, there was no Ru emission for pure ZnO (**Figure IV-31Aa**) and the RuO₂/ZnO was formed by

Zn, O and Ru. The results were in good agreement with the XRD and EDX results discussed above.

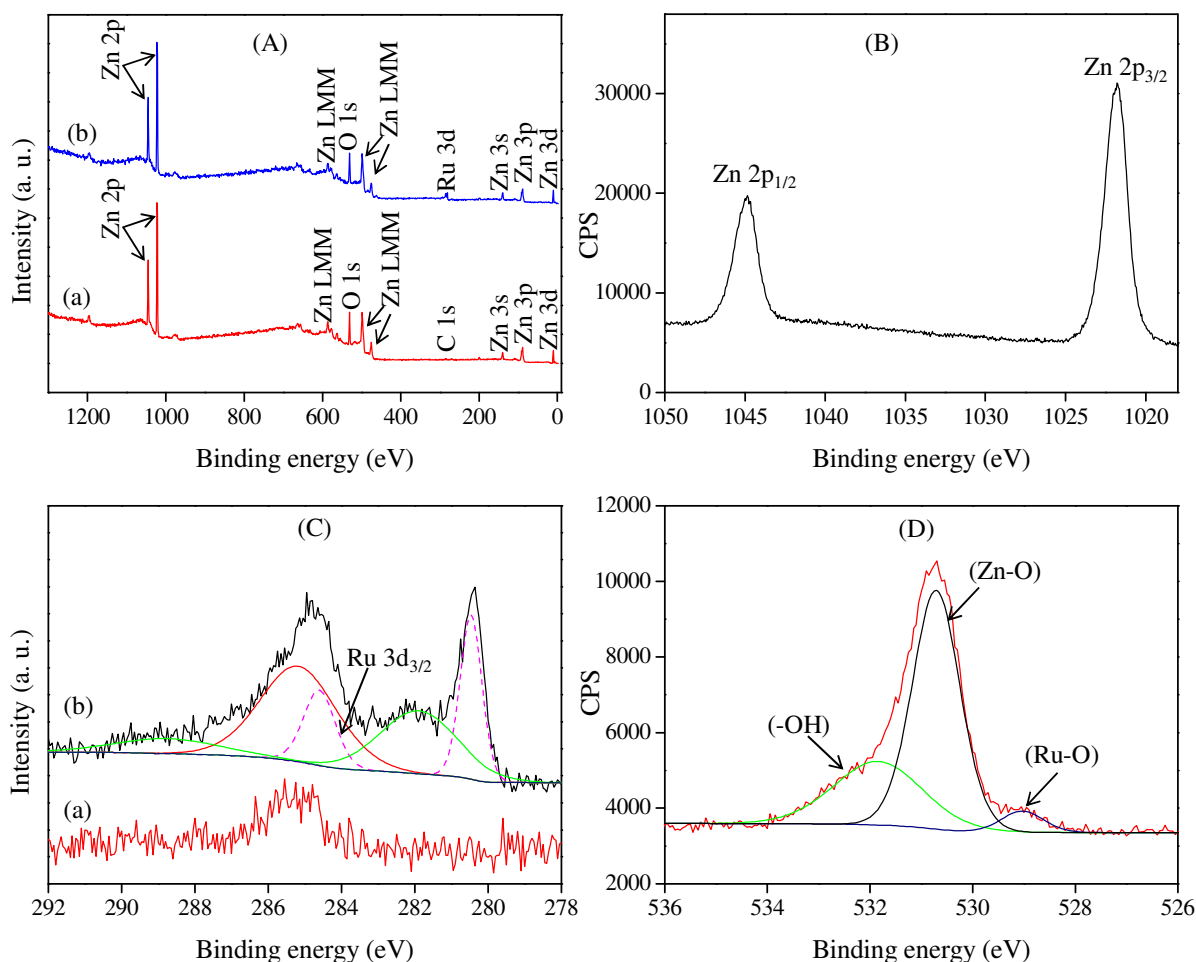


Figure IV-31: (A) XPS survey spectra of ZnO (a) and 4 wt% RuO₂/ZnO (b). High-resolution spectra of 4 wt% RuO₂/ZnO sample: (B) Zn 2p spectra, (C) Ru 3d spectra and (D) O 1s spectra.

The high-resolution spectra of Zn, Ru, and O species are shown in **Figure IV-31(B-D)**, respectively. The emission line appearing in **Figure IV-31B** is symmetric and centered at 1021.83 and 1044.92 eV, which were attributed to Zn 2p_{3/2} and Zn 2p_{1/2}, respectively. Thus, it could be confirmed that Zn mainly forms Zn²⁺ chemical state in the as-synthesized samples.⁶² **Figure IV-31C** provides high-resolution XPS spectra of Ru 3d in the 4 wt% RuO₂/ZnO sample. C 1s peaks overlap with Ru 3d_{3/2} or the satellite peak, thus the later can not be clearly recognized. The Ru 3d signal shows two different binding states of ruthenium atoms and exhibit asymmetric lineshapes. The deconvoluted peaks were identified as Ru 3d_{5/2} and 3d_{3/2} at 280.45 eV and 284.60 eV, respectively, and were attributed to the Ru⁴⁺ chemical state of Ru and it existed as RuO₂ in the as-synthesized samples. The deconvolution of the XPS spectra revealed another additional feature with broader line width at 281.9 eV for the Ru

$3d_{5/2}$ line higher than the major peak by 1.45 eV. The origin of these satellite peaks which was also observed on oxidized Ru metal surface is still controversial in the literature, where it has been claimed to be related to excitation of the RuO_2 plasmon,⁶³ the surface species of Ru high bonding states,⁶⁴ or due to the final-state screening effect.⁶⁵

Figure IV-31D shows the O 1s peaks for 4 wt% RuO_2/ZnO sample. It can be seen that the O 1s emission line was asymmetric, suggesting that there were more than one kind of species in the samples. The peak could be fitted into three symmetrical peaks centered at 529.03, 530.70, and 531.84 eV. The first peak at 529.03 eV was attributed to the lattice oxygen in RuO_2 . The second peak at 530.70 eV was assigned to the lattice oxygen of ZnO .⁶⁶ The higher binding energy at 531.8 eV was attributed to the oxygen of surface hydroxyl group of RuO_2 and ZnO ,⁶⁷ which was fully consistent with the FTIR result. As suggested by FTIR, the presence of surface hydroxyl group is confirmed, these groups play an important role in the photocatalytic property of semiconductor by capturing photoinduced holes to produce hydroxyl radical, leading to better photocatalytic property.^{2b, 68}

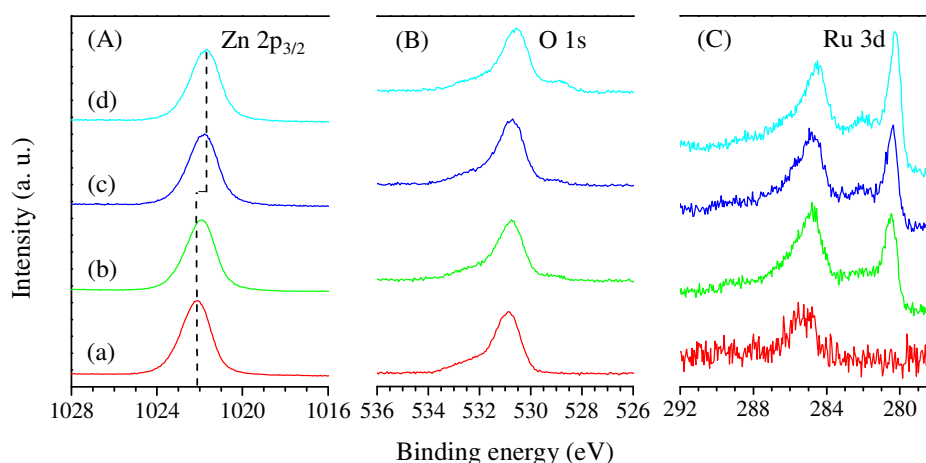


Figure IV-32: Evolution of photoemission core level spectra of the heterostructure RuO_2/ZnO nanoparticles with different contents of RuO_2 . (a) ZnO , (b) 2 wt% RuO_2/ZnO , (c) 4 wt% RuO_2/ZnO and 6 wt% RuO_2/ZnO .

Band bending developed at the interface of RuO_2/ZnO was also determined by XPS and UPS from the core level binding energy shifts. **Figure IV-32** shows the evolution of the core level spectra of RuO_2/ZnO nanocomposites containing different amount of RuO_2 . The $\text{Zn } 2p_{3/2}$ line shape did not change with increasing RuO_2 content as shown in **Figure IV-32A**. On the other hand, the O 1s emission was changed gradually to lower binding energies with the RuO_2 content resulting from the metallic character of RuO_2 . The intensity of the $\text{Ru } 3d_{5/2}$ emission line increased with increasing RuO_2 content as shown in **Figure IV-32C**. However,

it was found that both Zn $2p_{3/2}$ and O 1s peaks were shifted to lower binding energies with the increasing RuO₂ content. The binding energy shift for Zn $2p_{3/2}$ was estimated from the difference between the values of pure ZnO and ZnO containing 6 wt% RuO₂. The Zn $2p_{3/2}$ and O 1s peaks were shifted to lower binding energies by 0.40 ± 0.05 and 0.45 ± 0.05 eV, respectively, from their original values. A slightly higher shift observed from O 1s peak than Zn $2p_{3/2}$ peak might be due to contribution from both ZnO and RuO₂. We consider a rather parallel shift of both Ti $2p_{3/2}$ and O 1s emission lines ignoring this slight difference in peak shift. The Ru $3d_{5/2}$ emission line was also shifted to lower binding energy by an amount of 0.25 ± 0.05 eV and changes its spectral shape from a rather broad emission line at higher binding energy to a sharp line followed by a shake-up satellite due to free electrons excitation as typically found for metallic transition metal compounds which is due to bulk RuO₂.

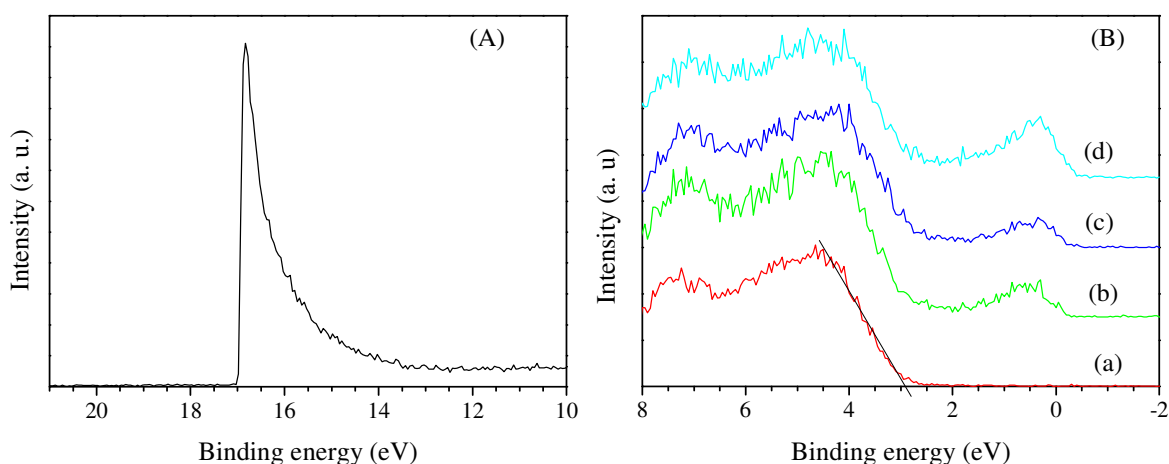


Figure IV-33: (A) UPS spectrum of pure ZnO (B) XP valence band spectra of ZnO and RuO₂/ZnO with different amount of RuO₂. a) ZnO, (b) 2 wt% RuO₂/ZnO, (c) 4 wt% RuO₂/ZnO and 6 wt% RuO₂/ZnO.

The work function of ZnO was determined by ultraviolet photoelectron spectroscopy (UPS). **Figure IV-33A** shows the secondary electron cutoff recorded with UPS using HeI and the work function for pure ZnO was calculated to be about 4.2 eV. This value agreed well with the work function for n-type ZnO in the literature.⁶⁹ **Figure IV-33B** shows the evolution of the valence band spectra of ZnO containing different amount of RuO₂: the valence band maximum (VBM) shifted toward lower binding energy with increasing RuO₂ content. The VBM was deduced by linearly extrapolating the low binding energy edge of the valence band intersecting with the background. The calculated VBMs were 2.90 ± 0.05 , 2.75 ± 0.05 , 2.60 ± 0.05 and 2.5 ± 0.05 eV for ZnO, 2 wt% RuO₂/ZnO, 4 wt% RuO₂/ZnO and 6 wt% RuO₂/ZnO, respectively. These values suggested that as-synthesized ZnO is a n-type semiconductor. The

shift of the VBM was 0.4 ± 0.05 eV, which was consistent with the shifts observed in Zn $2p_{3/2}$ and O 1s core levels shown above. These shifts can be attributed to a minimum band bending of ZnO at the interface. As a result, all these data allowed for proposing the energy band diagram of RuO_2/ZnO heterojunction showing the band bending at the interface between RuO_2 and ZnO as presented in **Figure IV-34**.

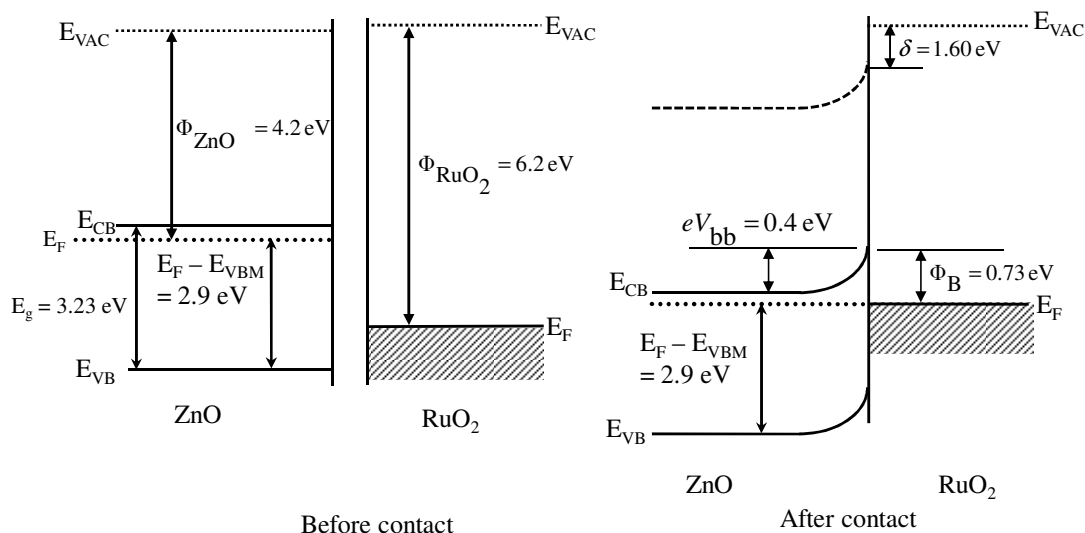


Figure IV-34: Schematic band energy alignment at the interface of RuO_2 and ZnO. E_{CB} , E_{VB} , E_F , E_g are conduction band maximum, valence band maximum, Fermi level and energy gap, respectively. eV_{bb} refers to band bending at the interface of RuO_2 and ZnO.

IV.3.1.3. Photocatalytic activity

IV.3.1.3.1. Photocatalytic degradation of organic dyes

The photocatalytic performance of RuO_2/ZnO was evaluated by using MB and MO as representative organic pollutants. In the experiments, the commercial TiO_2 (Degussa P-25) was used as a photocatalytic reference to qualitatively understanding the photocatalytic activity of RuO_2/ZnO catalysts. The evolution of the spectral changes with the photodegradation of MB and MO over the fresh RuO_2/ZnO nanocomposites is shown in **Figure IV-35**. The MB and MO dyes initially showed major absorption band at 664 nm and 464 nm, respectively, while a gradual decrease in the absorption with a slight shift of the band to shorter wavelength was observed with UV light irradiation through the aqueous solution of MB and MO. The color of the MB solution eventually disappeared within 50 min (**Figure IV-35A**) which is consistent with the facile destruction of the chromophoric structure of the MB, while it took more than 80 min to disappear the color of MO (**Figure IV-35B**) suggesting that the degradation rate of MB was higher than that of MO.

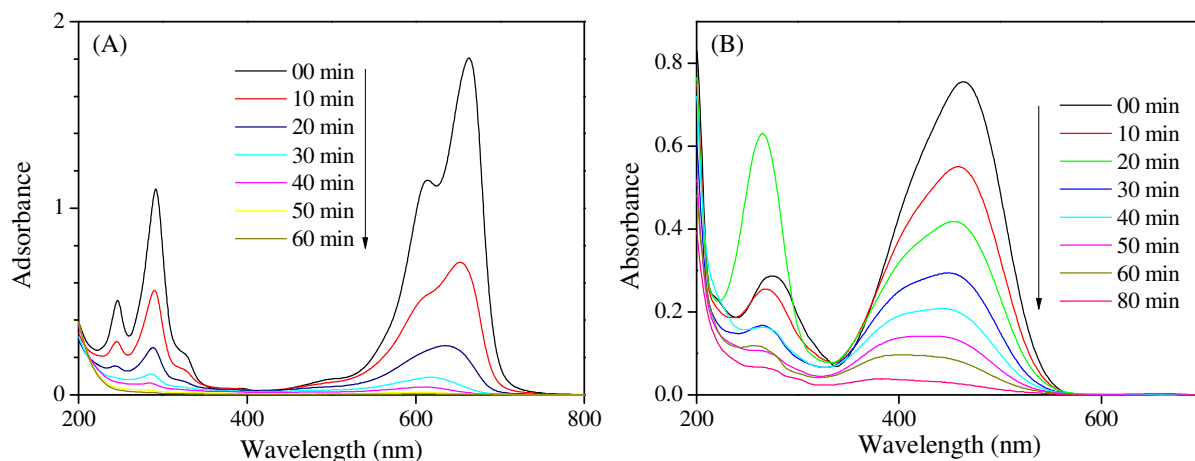


Figure IV-35: UV-Visible spectra of (A) MB and (B) MO aqueous solutions as a function of reaction time in the presence of 4 wt% RuO₂/ZnO.

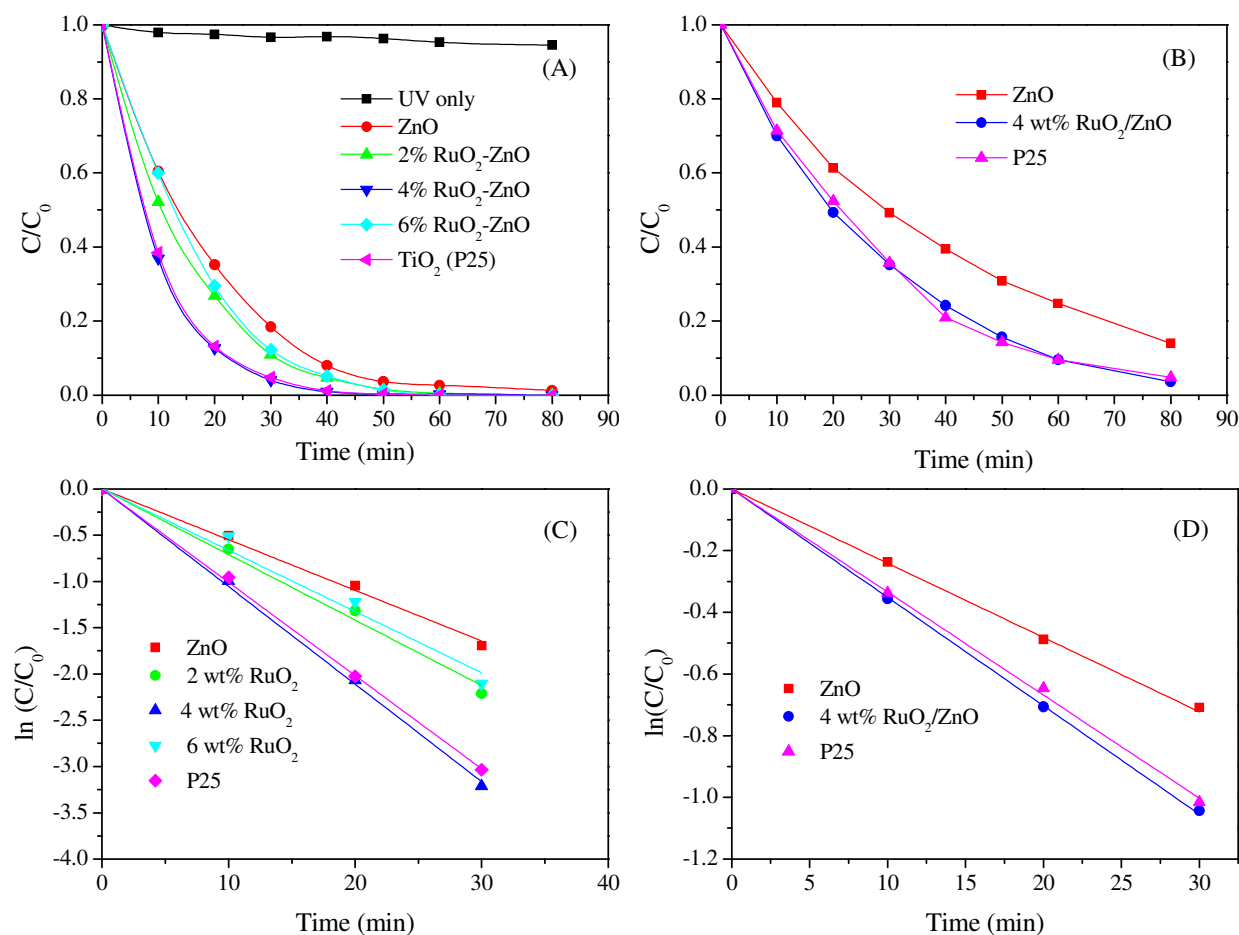


Figure IV-36: Kinetic of the degradation of MB (A) and MO (B); plot of $\ln(C/C_0)$ against t for the photocatalytic degradation of MB (C) and MO (D) with as-synthesized nanoparticles.

The photocatalytic activities of the as-synthesized samples with different RuO₂ contents and Degussa P-25 are shown in **Figure IV-36**. C_0 and C in **Figure IV-36** represent the initial concentration after the adsorption–desorption equilibrium for 0.5 h and the real-time

concentration of MB, respectively. As it can be seen, without any catalyst, no significant decrease in the concentration of MB was observed under UV irradiation. The addition of catalysts resulted in obvious degradation of MB, and all the RuO₂/ZnO heterostructures actually exhibited an enhanced photocatalytic activity in contrast with pure ZnO. In addition, the RuO₂ content clearly defined the photocatalytic performance of RuO₂/ZnO heterostructure nanocomposites. Thus, the photocatalytic activities of RuO₂/ZnO samples first increased with increasing RuO₂ content up to 4 wt% RuO₂ and then decreased with further increasing of RuO₂ to 6 wt% (**Figure IV-36A**). The photodegradation efficiency of MB was about 65%, 73%, 88%, 71% and 87% for ZnO, 2 wt% RuO₂/ZnO, 4 wt% RuO₂/ZnO, 6 wt% RuO₂/ZnO and P25, respectively, when the reaction was performed under UV light for 20 min. Therefore, 4% RuO₂ was found to be the optimum concentration, and the higher content of RuO₂ could be unfavorable to photocatalytic efficiency.

Table IV-4: Apparent reaction rate constant for the degradation of MB with as-synthesized nanoparticles.

Photocatalysts	Dye	k_{app}, min^{-1}	$S_{BET}, m^2/g$	$K_{norm}, g/(m^2 \cdot min)$	R^2
ZnO	MB	0.054	31	1.74×10^{-3}	0.995
2%RuO ₂ -ZnO	MB	0.071	29	2.44×10^{-3}	0.992
4% RuO ₂ -ZnO	MB	0.106	25	4.24×10^{-3}	0.998
6% RuO ₂ -ZnO	MB	0.066	22	3.03×10^{-3}	0.981
TiO ₂ (Degussa P25)	MB	0.101	47	2.14×10^{-3}	0.998
ZnO	MO	0.024	31	0.77×10^{-3}	0.998
4 wt% RuO ₂ /ZnO	MO	0.035	25	1.4×10^{-3}	0.999
P25	MO	0.033	47	0.7×10^{-3}	0.997

Similarly, 4 wt% RuO₂/ZnO nanocomposites also showed higher photocatalytic degradation efficiency for the degradation of MO when compared with that of pure TiO₂ and commercial P25 (**Figure IV-36B**). For a better and quantitative understanding of the photocatalytic efficiency of the as-synthesized samples, the kinetic analysis of MB and MO degradation was

discussed. As shown in **Figure IV-36C** and **D**, the photodegradation of MB and MO by RuO₂/ZnO nanocomposites followed a first-order rate law, $\ln(C/C_0) = -k_{app}t$, where k_{app} is apparent rate constant of the degradation. The apparent reaction rate constants, *BET* surface area (S_{BET}) of catalysts and the normalized rate constant k_{norm} defined as $k_{norm} = k_{app}/S_{BET}$ for the degradation of MB and MO using different as-synthesized photocatalysts are summarized in **Table IV-4**. It is obvious from the table that the reaction rates of RuO₂/ZnO nanocomposite samples were much higher than that of as-synthesized ZnO. Especially, 4% RuO₂/ZnO sample showed the highest catalytic activity with a rate constant $k_{app} = 0.106 \text{ min}^{-1}$ for MB degradation that was about 2 times higher than that of pure ZnO (0.0054 min^{-1}) and was comparable with that of commercial TiO₂ (Degussa P25) (0.101 min^{-1}).

It is known that the activity of photocatalyst is related to many factors, such as the size and the *BET* surface areas of materials. The *BET* surface areas for 2 wt% RuO₂/ZnO, 4 wt% RuO₂/ZnO and 6 wt% RuO₂/ZnO were 29, 25, and 22 m²/g, respectively. For pure ZnO and Degussa P25, the *BET* surface area values were 31 and 47 m²/g, respectively. From these results, we found that the pure ZnO and Degussa P25 had higher surface area than RuO₂/ZnO composites. It is indicated that the high *BET* surface area is favorable for the improvement of the photocatalytic activity. Thus, in our study, the better performance of RuO₂/ZnO photocatalyst than that of P25 and ZnO particles was not due the *BET* factors, but was contributed to the synergistic action of RuO₂ and ZnO particles.

On the other hand, it has been well-established that ZnO generally suffers from photocorrosion for photocatalytic applications.⁷⁰ Hence, it is of prime importance to probe the photostability of the RuO₂/ZnO heterostructures. To this end, cyclic photodegradation experiments and XRD were combined to access the evaluation. **Figure IV-37A** displays cycling experiments of the RuO₂/ZnO nanostructure for photodegradation of MB under irradiation of UV light. The results indicated that no noticeable change was observed even the photocatalyst went through four successive recycles, suggesting the RuO₂/ZnO heterostructures were stable during the course of photodegradation. Moreover, XRD patterns (**Figure IV-37B**) of the used and fresh samples revealed intact crystalline phase of the RuO₂/ZnO heterostructure after successive use.

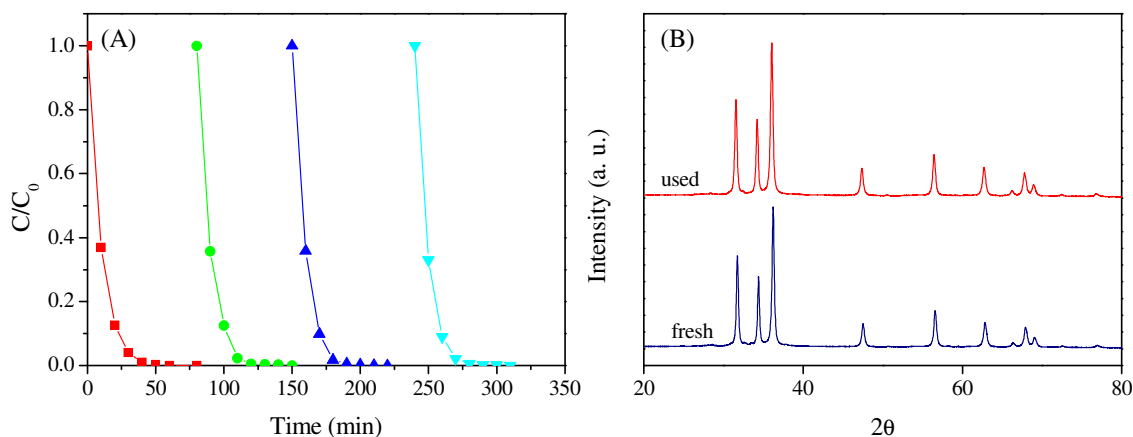
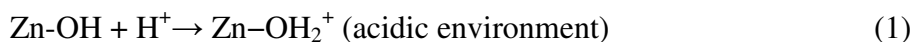


Figure IV-37: (A) Cycling photodegradation of MB aqueous solution over 4 wt% RuO₂/ZnO (B) XRD patterns of the 4 wt% RuO₂/ZnO heterostructure before and after cycling photodegradation of MB.

Organic compounds in wastewater differ greatly in several parameters, particularly in their speciation behaviour, solubility in water and hydrophobicity. While some compounds are uncharged at common pH conditions typical of natural water or wastewater, other compounds exhibit a wide variation in speciation (or charge) and physico-chemical properties. At pH below its pK_a value, an organic compound exists as a neutral species. Above this pK_a value, organic compound attains a negative charge. Some compounds can exist in positive, neutral, as well as negative forms in aqueous solution. On the other hand, pH also determines the surface charge of the photocatalyst and the size of aggregates it forms. This variation can also significantly influence their photocatalytic degradation behaviour. The surface charge of photocatalyst and ionization or speciation (pK_a) of an organic pollutant can be profoundly affected by the solution pH. Electrostatic interaction between semiconductor surface, solvent molecules, substrate and charged radicals formed during photocatalytic oxidation is strongly dependent on the pH of the solution. Therefore the pH of the solution can play a key role in the adsorption and photocatalytic oxidation of pollutants. Primarily, ZnO becomes hydroxylated in the presence of water to form hydroxide layers (Zn-OH).⁷¹ The zinc hydroxide surface (Zn-OH) can become charged by reacting with H⁺ (acidic environment) or OH⁻ (basic environment) ions due to surface amphoteric reactions (Eq. 1, 2).⁷²



At low pH hydroxide surfaces adsorb protons to produce positively charged surfaces. At high pH they lose protons to produce negatively charged surfaces [39]. The zero point charge of ZnO (pH_{zpc}) has been reported to be 7.5-9.8.⁷³ Therefore, the surface functional groups of ZnO can be $ZnOH_2^+$, $ZnOH$, and ZnO^- at $pH < pH_{zpc}$, pH_{zpc} and $pH > pH_{zpc}$, respectively. On the other hand, MB dye ($pK_a \approx 3.8$) at high pH ($pH \geq pK_a$), exist as a cation in aqueous solution. The effect of pH on the efficiency of photocatalytic degradation of MB was examined at the $pH = 2.5, 7.5$ and 9.9 and the results are shown in **Figure IV-38**. After 20 min irradiation, the percentages of MB degradation were 87, 79 and 60% at $pH 9.9, 7.5$ and 2.5 , respectively. The enhanced photodegradation of MB at higher pH was attributed to the favourable adsorption of the cationic MB dye on the negatively charged oxide surface. On the other hand, at lower pH the electrostatic repulsion between the MB cations and positively charged oxide surface greatly reduces the adsorption of the MB dye resulting in a drastic decrease in degradation rate.

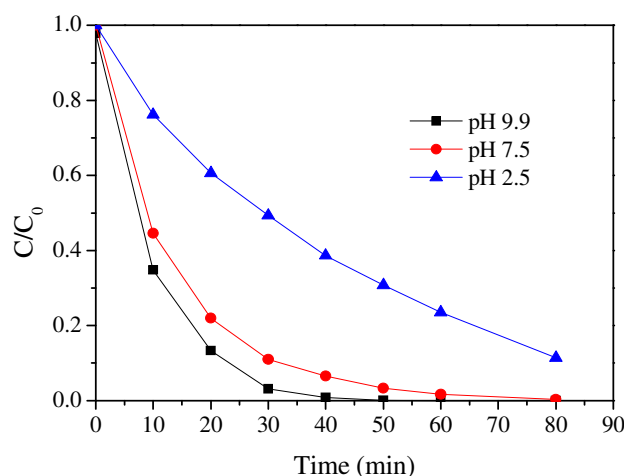


Figure IV-38: Effect of solution pH on MB degradation.

It has also been reported that in a slightly alkaline solution ($pH 8-9$), hydroxyl radicals are more easily generated by oxidizing the available OH^- on the photocatalyst surface.⁷⁴ Thus, generally, the photodegradation efficiency is expected to be enhanced with increasing pH due to the ready availability of hydroxyl radicals for the reaction.

The enhanced photocatalytic activity of heterostructure RuO_2/ZnO nanoparticles was related to the role of RuO_2 on the surface of TiO_2 nanoparticles. The photogenerated charge separation and the photocatalytic mechanism of the heterostructured RuO_2/TiO_2 nanocomposite system is represented in a schematic diagram as shown in **Figure IV-39**.

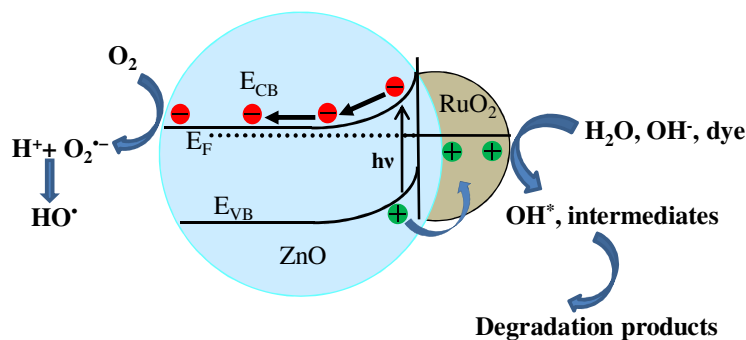
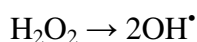
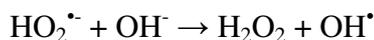
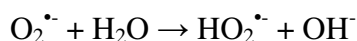
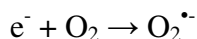
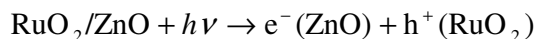


Figure IV-39: schematic diagram showing the photogenerated charge separation mechanism of RuO₂/ZnO nanocomposites.

It is known that the work function of RuO₂ (6.2 eV) is larger than that of ZnO (4.2 eV). The Fermi energy level of ZnO is higher than that of RuO₂ due to its smaller work function. Accordingly, when the metallic RuO₂ are attached to ZnO nanoparticles, the electrons will migrate from ZnO to RuO₂ in order to achieve the Fermi level equilibration. Meanwhile, an electrostatic field is built in the discontinuity interface of ZnO and RuO₂ because of electron transfer, which could lead to an upward bending of the energy bands of ZnO. When the heterostructure RuO₂/ZnO nanocomposites are illuminated by UV light with photon energy higher or equal to the band gap of ZnO, electrons in the valence band (VB) can be excited to the CB with simultaneous generation of the same amount of holes in the VB. As the Fermi energy level of RuO₂ is just above the valence band band maximum of ZnO, the holes in the valence band of ZnO can transfer from ZnO nanoparticles to RuO₂ nanoparticles driven by the built in potential at the interface, suggesting that the photogenerated electrons and holes were efficiently separated. The efficient charge separation can also increase the lifetime of the charge carriers and enhance the efficiency of the interfacial charge transfer to adsorbed substrates, and then account for the higher activity of the RuO₂/ZnO nanocomposites.

The photocatalytic reaction process can be proposed as follows





The electrons in the conduction band of ZnO react with molecular oxygen adsorbed on the surface of ZnO to generate superoxide radicals anion ($O_2^{\bullet-}$). The $O_2^{\bullet-}$ radicals further react with H_2O to produce OH^{\bullet} radicals. On the other hand, holes migrated to RuO_2 react with surface-bound hydroxyl groups (or H_2O) to produce activated hydroxyl species (OH^*) which is an extremely strong oxidant for the mineralization of organic substrates as dyes (MB or MO). In addition, photogenerated holes transferred to RuO_2 surface can also directly oxidize the organic dyes through the formation of intermediates.

IV.4. Conclusion

In summary, mesoporous heterostructure RuO_2/TiO_2 nanoparticles photocatalysts have been successfully prepared by impregnation of TiO_2 nanoparticles, synthesized by the sol-gel process, in a ruthenium acetylacetonate solution and, then, thermal annealing at 400 °C. The UV-Vis diffuse reflectance studies showed that the band gap energy of the heterostructure RuO_2/TiO_2 photocatalyst was red-shifted compared to that of TiO_2 . An interface experiment to model the junction was carried out by stepwise deposition of RuO_2 on the TiO_2 film by XPS and UPS and a shift of Ti $2p_{3/2}$ and O 1s core level spectra were determined to be 1.22 and 1.25 eV, respectively which was ascribed to the band bending at the interface of the heterojunction RuO_2/TiO_2 . The heterojunction 1 wt% RuO_2/TiO_2 photocatalyst showed higher photocatalytic activity than the pure TiO_2 and reference commercial TiO_2 P25 for the degradation of MB and MO dyes under UV light irradiation in neutral and basic media. Furthermore, the heterostructure photocatalysts could be easily recycled without significant change in the catalytic activity which evidenced the stability of the catalysts and the reproducibility of the approach. The photocatalytic activity for the production of H_2 was carried out under UV in the presence of methanol as a hole scavenger. The 5 wt% RuO_2/TiO_2 photocatalysts showed higher catalytic activity with average hydrogen production rate of $618 \mu\text{mol h}^{-1}$. Without RuO_2 the production rate decreased dramatically to $29 \mu\text{mol h}^{-1}$ that points out the key role of RuO_2 for efficient hydrogen production.

In addition, heterostructured RuO_2/ZnO photocatalysts were prepared in two steps. Nanosized ZnO particles were first prepared by homogeneous precipitation technique using urea as precipitating agent followed by calcination, and, then, RuO_2/ZnO systems were prepared by impregnating the ZnO in ruthenium (III) chloride hydrate ($RuCl_3 \cdot xH_2O$) solution followed by calcination in air. UV-Vis diffuse reflectance studies showed enhanced light

absorption in the visible region due to surface plasmon resonance. An energy band diagram of RuO₂/ZnO nanocomposites was also determined by XPS and UPS from the shift of Zn 2p_{3/2} and O 1s core level spectra. A shift of Zn 2p_{3/2} and O 1s core level spectra were determined to be at least 0.40 ± 0.05 and 0.45 ± 0.05 eV, respectively, which was ascribed to the band bending at interface of heterojunction RuO₂/ZnO nanoparticles. The investigation of photocatalytic ability indicated that the RuO₂/ZnO nanocomposites possessed a higher photocatalytic activity than the pure ZnO for the degradation of MB and MO dyes under UV light irradiation. Furthermore, like RuO₂/TiO₂ heterojunction photocatalyst, the RuO₂/ZnO nanocomposites could also be easily recycled without decrease of photocatalytic activity confirming the stability of the as-synthesized RuO₂/ZnO photocatalysts.

This higher photocatalytic activity for degrading organic dyes and producing H₂ was related to the higher charge probability resulting from the internal electric field developed at the interface of RuO₂/TiO₂ or RuO₂/ZnO heterojunctions. Therefore, the semiconducting heterojunction photocatalysts might be promising alternatives in the future for environmental remediation and for production of clean and renewable energy source as H₂.

- ¹ Fujishima, A.; Honda, K. *Nature*, **1972**, 238, 37.
- ² (a) Fujishima, A.; Rao, T. N.; Tryk, D. A. *J. Photochem. Photobiol. C* **2000**, 1, 1. (b) Hoffmann, M. R.; Martin, S. T.; Choi, W.; Bahnemann, D. W. *Chem. Rev.* **1995**, 95, 69. (c) Uddin, M. T.; Nicolas, Y.; Olivier, C.; Toupance, T.; Servant, L.; Müller, M. M.; Kleebe, H. J.; Ziegler, J.; Jaegermann, W. *Inorg. Chem.* **2012**, 51, 7764.
- ³ (a) Khodja, A. A.; Sehili, T.; Pilichowski, J. F.; Boule, P. *J. Photochem. Photobiol. A* **2001**, 141, 231. (b) Daneshvar, N.; Salari, D.; Khataee, A. R. *J. Photochem. Photobiol. A* **2004**, 162, 317. (c) Gouvea, C. A. K.; Wypych, F.; Moraes, S. G.; Duran, N.; Nagata, N.; Peralta-Zamora, P. *Chemosphere* **2000**, 40, 433. (d) Dindar, B.; Icli, S. *J. Photochem. Photobiol. A* **2001**, 140, 263.
- ⁴ (a) Hariharan, C. *Appl. Catal. A* **2006**, 304, 55. (c) Zheng, Y.; Chen, C.; Zhan, Y.; Lin, X.; Zheng, Q.; Wei, K.; Zhu, J.; Zhu, Y. *Inorg. Chem.* **2007**, 46, 6675.
- ⁵ (a) He, Y. J.; Yu, X. Y.; Li, T. L.; Yan, L. Y.; Yang, B. L. *Powder Technol.* **2006**, 166, 72. (b) Kim, C.; Doha, S. J.; Lee, S. G.; Lee, S. J.; Kima, H. Y. *Appl. Catal. A* **2007**, 330, 127. (c) Wang, C.; Wang, X. M.; Xu, B. Q.; Zhao, J. C.; Mai, B. X.; Peng, P. A.; Sheng, G. Y.; Fu, J. M. *J. Photochem. Photobiol. A* **2004**, 168, 47. (d) Zhang, M. L.; An, T. C.; Hu, X. H.; Wang, C.; Sheng, G. Y.; Fu, J. M. *Appl. Catal. A* **2004**, 260, 215.
- ⁶ (a) Liao, S.; Donggen, H.; Yu, D.; Su, Y.; Yuan, G. *J. Photochem. Photobiol. A* **2004**, 168, 7. (b) Liao, D. L.; Badour, C. A.; Liao, B. Q. *J. Photochem. Photobiol. A* **2008**, 194, 11. (c) Shifu, S.; Wei, Z.; Wei, L.; Sujuan, Z. *Appl. Surf. Sci.* **2008**, 255, 2478. (d) Ge, M.; Guo, C.; Zhu, X.; Ma, L.; Han, Z.; Hu, W.; Wang, Y. *Front. Environ. Sci. Engin. China* **2009**, 3, 271. (e) Tian, J.; Chen, L.; Yin, Y.; Wang, X.; Dai, J.; Zhu, Z.; Liu, X.; Wu, P. *Surf. Coat. Technol.* **2009**, 204, 205. (f) Zhang, M.; An, T.; Liu, X.; Hu, X.; Sheng, G.; Fu, J. *Mater. Lett.* **2010**, 64, 1883. (g) Mani, J.; Sakeek, H.; Habouti, S.; Dietze, M.; Souni, M. E. *Catal. Sci. Technol.* **2012**, 2, 379.
- ⁷ (a) Lin, C. C.; Chiang, Y. J. *Chem. Eng. J.* **2012**, 181-182, 196. (b) Yang, Z.; Lv, L.; dai, Y.; Xv, Z.; Qian, D.; *Appl. Surf. Sci.* **2010**, 256, 2898. (c) Cun, W.; Wang, X.; Xu, B. Q.; Zhao, J.; Mai, B.; Peng, P.; Sheng, G.; Fu, J. *J. Photochem. Photobiol. A* **2004**, 168, 47. (d) Zhang, M.; An, T.; Hu, X.; Wang, C.; Sheng, G.; Fu, J. *Appl. Catal. A* **2004**, 260, 215. (e) Zhang, M.; Sheng, G.; Fu, J.; An, T.; Wang, X.; Hu, X. *Mater. Lett.* **2005**, 59, 3641. (f) Cun, W.; Jincai, Z.; Xinming, W.; Bixian, M.; Guoying S., Ping'an, P.; Jiamo, F. *Appl. Catal. B* **2002**, 39, 269. (g) Wang, H.; Baek, S.; Lee, J.; Lim, S. *Chem. Eng. J.* **2009**, 146, 355.
- ⁸ (a) Li, D.; Haneda, H.; Ohashi, N.; Hishita, S.; Yoshikawa, Y. *Catal. Today*, **2004**, 93-95, 895. (b) Li, D.; Haneda, H. *J. Photochem. Photobiol. A* **2003**, 160, 203.
- ⁹ (a) Yun, H. J.; Lee, H.; Kim, N. D.; Yi, J. *Electrochem. Commun.* **2009**, 11, 363. (b) Bowker, M.; James, D.; Stone, P.; Bennett, R.; Perkins, N.; Millard, L.; Greaves, J.; Dickinson, A. *J. Catal.* **2003**, 217, 427. (c) Liu, C. H.; Hong, M. H.; Zhou, Y.; Chen, G. X.; Saw, M. M.; Hor, A. T. S. *Phys. Scr.*

- 2007**, *TI29*, 326. (d) Li, C. H.; Hsieh, Y. H.; Chiu, W. T.; Liu, C. C.; Kao, C. L. *Sep. Purif. Technol.* **2007**, *58*, 148. (e) Tan, T. T. Y.; Yip, C. K.; Beydoun, D.; Amal, R. *Chem. Eng. J.* **2003**, *95*, 179. (f) Yang, J. C.; Kim, Y. C.; Shul, Y. G.; Shin, C. H.; Lee, T. K. *Appl. Surf. Sci.* **1997**, *121/122*, 525. (g) Li, X. Z.; Li, F. B. *Environ. Sci. Tech.* **2001**, *35*, 238.
- ¹⁰ (a) Jing, L.; Wang, D.; Wang, B.; Li, S.; Xin, B.; Fu, H.; Sun, J. *J. Mol. Catal. A: Chem.* **2006**, *244*, 193. (b) Gouvea, C. A. K.; Wypych, F.; Moraes, S. G.; Duran, N.; Zamora, P. P. *Chemosphere* **2000**, *40*, 427. (c) Height, M. J.; Pratsinis, S. E.; Mekasuwandumrong, O.; Praserttham, P. *Appl. Catal. B: Environ.* **2006**, *63*, 305. (d) Zhou, G., Deng, J. *Mater. Sci. Semicond. Proc.* **2007**, *10*, 90. (e) Chen, T.; Zheng, Y.; Lin, J. M.; Chen, G. *J. Am. Soc. Mass. Spectrom.* **2008**, *19*, 997. (f) Subramanian, V.; Wolf, E. E.; Kamat, P. V. *J. Phys. Chem.* **2003**, *B 107*, 7479.
- ¹¹ Dalven, R. *Physics of Metal–Semiconductor and Metal–Insulator–Semiconductor Junctions, Introduction to Applied Solid State Physics*, 2nd ed., Plenum Press, New York, London, **1990**.
- ¹² Trasatti, S. *Electrochim. Acta*, **1991**, *36*, 225.
- ¹³ (a) Koetz, E. R.; Stucki, S. *J. Appl. Electrochem.* **1987**, *17*, 1190 (b) Mills, A.; Duckmanton, P. A.; Reglinski, J. *Chem. Commun* **2010**, *46*, 2397.
- ¹⁴ (a) Li, G.; Fan, Y.; Zhang, T.; Ge, T. Hou, H. *J. Coord. Chem.* **2008**, *61*, 540. (b) Reuter, K.; Scheffler, M. *Phys. Rev. B: Condens. Matter Mater. Phys.* **2006**, *73*, 045433.
- ¹⁵ Abe, T.; Tanizawa, M.; Watanabe, K.; Taguchi, A. *Energy Environ. Sci.* **2009**, *2*, 315.
- ¹⁶ (a) Lopez, N.; Segura, J. G.; Marin, R. P.; Ramirez, J. P. *J. Catal.* **2008**, *255*, 29. (b) Mondelli, C.; Amrute, A. P.; Krumeich, F.; Schmidt, T.; Ramirez, J. P. *ChemCatChem*, **2011**, *3*, 657.
- ¹⁷ Riga, J.; Noel, C. T.; Pireaux, J. J.; Caudano, R.; Verbist, J. J.; Gobillon, Y. *Phys. Scr.* **1977**, *16*, 351.
- ¹⁸ Sakata, T.; Hashimoto, K.; Kawai, T. *J. Phys. Chem.* **1984**, *88*, 5214.
- ¹⁹ Schafranek, R.; Schaffner, J.; Klein, A. *J. Eur. Ceram. Soc.* **2010**, *30*, 187.
- ²⁰ Blondeel, J.; Harriman, A.; Poter, G.; Urwin, D.; Kiwi, J. *J. Phys. Chem.* **1983**, *87*, 2629.
- ²¹ (a) Ismail, A. A.; Robben, L.; Bahnemann, D. W. *ChemPhysChem* **2011**, *12*, 98. (b) Chueh, Y. L.; Hsieh, C. H.; Chang, M. T.; Chou, Li. J.; Lao, C. S.; Song, J. H.; Gan, J. Y.; Wang, Z. L. *Adv. Mater.* **2007**, *19*, 143. (c) Osman, J. R.; Crayston, J. A.; Pratt, A.; Richens, D. T. *Mater. Chem. Phys.* **2008**, *110*, 256.
- ²² (a) Woragamon, K.; Jongpatiwut, S.; Sreethawong, T. *Cat. Lett.* **2010**, *136*, 249. (b) Yao, B. H.; Wang, L. M.; Wang, C.; Wang, Y. X.; Zhao, G. Y. *Chin. J. Chem. Phys.* **2007**, *20*, 789.
- ²³ (a) Houskova, V.; Stengl, V.; Bakardjieva, S.; Murafa, N.; Tyrpekl, V. *Appl. Catal. B* **2009**, *89*, 613. (b) Blondeel, G.; Harriman, A.; Porter, G.; Urwin, D.; Kiwi, J. *J. Phys. Chem.* **1983**, *87*, 2629.

- ²⁴ (a) Amama, P. B.; Ito, K.; Murabayashi, M. *J. Mater. Sci.* **2004**, *39*, 4349. (b) Liu, P.; Li, W. *J. Mater. Res.* **2011**, *26*, 1532. (c) Ohno, T.; Tanigawa, F.; Fujihara, K.; Izumi, S.; Matsumura, M. *J. Photochem. Photobiol. A* **1999**, *127*, 107.
- ²⁵ Woragamon, K.; Jongpatiwut, S.; Sreethawong, T. *Cat. Lett.* **2010**, *136*, 249.
- ²⁶ Chen, Y.; Kang, K. S.; Yoo, K. H.; Jyoti, N.; Kim, J. *J. Phys. Chem. C* **2009**, *113*, 19753.
- ²⁷ Nagaveni, K.; Hegde, M. S.; Ravishankar, N.; Subbanna, G. N.; Madras, G. *Langmuir* **2004**, *20*, 2900.
- ²⁸ Arsov, L. D.; Kormann, C.; Plieth, W. *J. Raman Spectrosc.* **1991**, *22*, 573.
- ²⁹ Korotcov, A. V.; Huang, Y. S.; Tiong, K. K.; Tsai, D. S. *J. Raman Spectrosc.* **2007**, *38*, 737.
- ³⁰ Huang, Y. S.; Liao, P. C. *Sol. Energy Mater. Sol. Cells* **1998**, *55*, 179.
- ³¹ Gupta, S. K.; Desai, R.; Jha, P. K.; Sahoo, S.; Kirin, D. *J. Raman Spectrosc.* **2010**, *41*, 350.
- ³² Ismail, A. A.; Robben, L.; Bahnemann, D. W. *ChemPhysChem*, **2011**, *12*, 982.
- ³³ Tebby, Z.; Babot, O.; Toupance, T.; Park, D.; Campet, G.; Delville, M. H. *Chem. Mater.* **2008**, *20*, 7260.
- ³⁴ Leofanti, G.; Padovan, M.; Tozzola, G.; Venturelli, B. *Catal. Today*, **1998**, *41*, 207.
- ³⁵ Sreethawong, T.; Yamadab, Y.; Kobayashi, T.; Yoshikawa, S. *J. Mol. Catal. A: Chem.* **2006**, *248*, 226.
- ³⁶ Davis, E. A.; Mott, N. F. *Phil. Mag.* **1970**, *22*, 903.
- ³⁷ Sanchez, E.; Lopez, T. *Mater. Lett.* **1995**, *25*, 271.
- ³⁸ Jahan, F.; Islan, M. H.; Smith, B. E. *Sol. Ener. Mater. Solar Cells* **1995**, *37*, 283.
- ³⁹ (a) Moulder, J. F.; Sticke, W. F.; Sobol, P. E.; Bomben, D. Hand book of X-ray photoelectron spectroscopy, United State of America, **1995**. (b) Liu, G.; Jaegermann, W.; He, J.; Sundström, V.; Sun, L. *J. Phys. Chem. B* **2002**, *106*, 5814.
- ⁴⁰ Sarma, D. D.; Rao, C. N. R. *J. Electron Spectrosc. Relat. Phenom.* **1980**, *20*, 25.
- ⁴¹ Donaich, S.; Sunjic, M. *J. Phys. C: Solid State Phys.* **1970**, *3*, 285.
- ⁴² Over, H.; Seitsonen, A. P.; Lundgren, E.; Smedh, M.; Andersen, J. N. *Surf. Sci.* **2002**, *504*, L196.
- ⁴³ (a) Ishii, H.; Sugiyama, K.; Ito, E.; Seki, K.; *Adv. Mater.* **1999**, *11*, 605 (b) Braun, S.; Salaneck, W. R.; Fahlman, M. *Adv. Mater.* **2009**, *21*, 1450.
- ⁴⁴ Li, C. Y.; Wen, T. C.; Lee, T. H.; Guo, T. F.; Huang, J. C. A.; Lin, Y. C.; Hsu, Y. J. *J. Mater. Chem.* **2009**, *19*, 1643.
- ⁴⁵ Yun, D. J.; Ra, H.; Jo, S. B.; Maeng, W.; Lee, S.; Park, S.; Jang, J. W.; Cho, K.; Rhee, S. W. *ACS Appl. Mater. Interfaces* **2012**, *4*, 4588.
- ⁴⁶ Chen, F.; Schafrank, R.; Wu, W.; Klein, A. *J. Phys. D: Appl. Phys.* **2011**, *44*, 255301.
- ⁴⁷ (a) Sanjinés, R.; Tang, H.; Berger, H.; Gozzo, F.; Margaritono, G.; Lévy, F. *J. Appl. Phys.* **1994**, *75*, 2945. (b) Orendorz, A.; Wüsten, J.; Ziegler, C.; Gnaser, H. *Appl. Surf. Sci.* **2005**, *252*, 85.

- ⁴⁸ (a) Guo, Y.; Wang, H.; He, C.; Qiu, L.; Cao, X. *Langmuir* **2009**, *25*, 4678. (b) Logar, M.; Jancar, B.; Sturm, S.; Suvorov, D. *Langmuir* **2010**, *26*, 12215. (c) Hirose, Y.; Mori, T.; Morishita, Y.; Itadani, A.; Kudoh, T.; Ohkubo, T.; Matsuda, T.; Kittaka, S.; Kuroda, Y. *Inorg. Chem.* **2011**, *50*, 9948. (d) Kang, J.; Kuang, Q.; Xie, Z. X.; Zheng, L. S. *J. Phys. Chem. C* **2011**, *115*, 7874.
- ⁴⁹ Perissinotti, L. L.; Brusa, M. A.; Grela, M. A. *Langmuir* **2001**, *17*, 8422.
- ⁵⁰ (a) Kwon, Y. J.; Kim, K. H.; Lim, C. S.; Shim, K. B.; *J. Ceram. Proc. Res.* **2002**, *3*, 146. (b) Silva, R. F.; Zaniquelli, M. E. D.; *Colloid. Surface A* **2002**, *198-200*, 551.
- ⁵¹ (a) Umar, A.; Karunagaran, B.; Suh, E. K.; Hahn, Y. B. *Nanotechnol.* **2006**, *17*, 4072. (b) Khan, A.; Kordesch, M. E. *Mater. Lett.* **2008**, *62*, 230. (c) Cheng, A. J.; Tzeng, Y.; Xu, H.; Alur, S.; Wang, Y.; Park, M.; Wu, T. H.; Shannon, C. L.; Kim, D. J.; Wang, D. *J. Appl. Phys.* **2009**, *105*, 073104.
- ⁵² Damen, T. C.; Porto, S. P. S.; Tell, B.; *Phys. Rev.* **1966**, *144*, 570.
- ⁵³ Xu, C. X.; Sun, X. W.; Zhang, X. H.; Ke, L.; Chua, S. J. *Nanotechnol.* **2004**, *15*, 856.
- ⁵⁴ Korotcov, A. V.; Huang, Y. S.; Tjong, K. K.; Tsai, D. S. *J. Raman Spectrosc.* **2007**, *38*, 737.
- ⁵⁵ Huang, Y. S.; Liao, P. C. *Sol. Energy Mater. Sol. Cells*, **1998**, *55*, 179.
- ⁵⁶ Alim, K. A.; Fonoberov, V. A.; Balandin, A. A. *J. Appl. Phys. Lett.* **2005**, *86*, 053103.
- ⁵⁷ (a) Tzolov, M.; Tzenov, N.; Malinowska, D. D.; Pizzuto, C.; Vitali, G.; Zollo, G.; Ivanov, I. *Thin Solid Films* **2000**, *379*, 28. (b) Exarhos, G. J.; Rose, A.; Windish, C. F. Jr. *Thin Solid Films* **1997**, *308*, 56. (c) Rajalakshmi, M.; Arora, A. K. *J. Appl. Phys.* **2000**, *87*, 2445.
- ⁵⁸ Colomer, M. T.; Jurado, J. R. *Chem. Mater.* **2000**, *12*, 923.
- ⁵⁹ (a) Sing, K. S. W.; Everett, D. H.; Haul, R. A. W.; Moscou, L.; Pierotti, R. A.; Rouquerol, J.; Siemieniewska, T. *Pure Appl. Chem.* **1985**, *57*, 603. (b) Kruk, M.; Jaroniec, M. *Chem. Mater.* **2001**, *13*, 3169.
- ⁶⁰ Essick, J.; Mather, R. *Am. J. Phys.* **1993**, *61*, 646.
- ⁶¹ Vinod, R.; Sajan, P.; Achary, S. R.; Tomas, C. M.; Sanjose, V. M.; Bushiri, M. J. *J. Phys. D: Appl. Phys.* **2012**, *45*, 425103.
- ⁶² Dwivedi, V. K.; Srivastava, P.; Prakash, G. V. *J. Semicond.* **2013**, *34*, 033001.
- ⁶³ Over, H.; Seitsonen, A. P.; Lundgren, E.; Smedh, M.; Andersen, J. N. *Surf. Sci.* **2002**, *504*, L196.
- ⁶⁴ Reuter, K.; Scheffler, M. *Surf. Sci.* **2001**, *490*, 20.
- ⁶⁵ Cox, P. A.; Goodenough, J. B.; Travener, P. J.; Telles, D.; Egdell, R. G. *J. Solid State Chem.* **1986**, *62*, 360.
- ⁶⁶ Teng, X. M.; Fan, H. T.; Pan, S. S.; Ye, C.; Li, G. H. *J. Appl. Phys.* **2006**, *100*, 053507.
- ⁶⁷ Bai, S.; Guo, T.; Li, D.; Luo, R.; Chen, A.; Liu, C. C. *Sens. Actuators, B* **2013**, *182*, 747.
- ⁶⁸ Linsebigler, A. L.; Lu, G.; Yates, J. Y. *Chem. Rev.* **1995**, *95*, 735.
- ⁶⁹ Kalblein, D.; Weitz, R. T.; Bottcher, H. J.; Ante, F. Zschieschang, U.; Kern, K.; Klauk, H. *Nano Lett.* **2011**, *11*, 5309.

⁷⁰ (a) Spatish, P.; Poullos, I. *Corros. Sci.* **1995**, *37*, 673. (b) Hoffman, A. J.; Carraway, E. R.; Hoffmann, M. R. *Environ. Sci. Technol.* **1994**, *28*, 776. (c) Dijken, A. V.; Janssen, A. H.; Smitsmans, M. H. P.; Vanmaekelbergh, D.; Meijerink, A. *Chem. Mater.* **1998**, *10*, 3513.

⁷¹ Sakthivel, S.; Neppolian, B.; Shankar, M. V.; Arabindoo, B.; Palanichamy, M.; Murugesan V. *Solar Energ. Mater. Solar Cells* **2003**, *77*, 65.

⁷² Degen, A.; Kosec, M. *J. Eur. Ceram. Soc.* **2000**, *20*, 667.

⁷³ (a) Rao, S. R.; Finch, J. A. *Int. J. Miner. Process.* **2003**, *69*, 251. (b) Music, S.; Dragcevic, D.; Maljkovic, M.; Popovic, S. *Mater. Chem. Phys.* **2002**, *77*, 521.

⁷⁴ (a) Shukla, G. *Appl. Phys. A: Mater. Sci. Process.* **2009**, *97*, 115 (b) Li, G.; Zhu, M.; Chen, J.; Li, Y.; Zhang, X. *J. Environ. Sci.* **2011**, *23*, 744.

Chapter V : p-n NiO/TiO₂ heterojunction photocatalysts

V.1. Introduction

As pointed out in chapters I and IV, although TiO_2 has been widely used as a photocatalyst due to its biological and chemical stability, low cost and non-toxic nature, the fast recombination of photogenerated electron-hole pairs is still an obstacle for practical applications. Therefore, improving photocatalytic activity by modification has become a hot topic among researchers in the last decade. Many studies, especially noble metal deposition and forming composite photocatalysts from different semiconductors, have been devoted to the improvement of the TiO_2 photocatalytic activity by retarding the recombination of photogenerated electron-hole pairs.

It is known that the n-n type composite photocatalysts, such as ZnO/TiO_2 ,¹ SnO_2/ZnO ,² $\text{SnO}_2/\text{TiO}_2$,³ or WO_3/TiO_2 ,⁴ have been investigated extensively. The results showed that almost all the n-n junction composite semiconductors had higher photocatalytic activity than single ones. In the meantime, another novel and promising concept of establishing a p-n junction at the interfacial contact between an n-type TiO_2 semiconductor and a p-type semiconductor has been proposed as an effective way to suppress the electron-hole pair recombination and prolong the electron's lifetime.⁵ Theoretically, the p-n junction is formed at the interface as a space charge region when p-type (hole-rich) and n-type (electron-rich) semiconductors are contacted. Electron and hole carriers are transferred to the p-type and n-type semiconductor, respectively, in forming electronic equilibrium. The inner electric field is established at equilibrium and then acts as a potential barrier to prevent the recombination of electron and hole. The potential related to the electric field enhances the movement of free electrons from p-type to n-type semiconductors and the movement of free holes from n-type to p-type semiconductors. Therefore, the photogenerated electron-hole pairs excited by UV irradiation are efficiently separated by the inner electric field to minimize the recombination.

Nickel oxide (NiO) is a p-type semiconductor frequently used as a cocatalyst loaded with various n-type semiconductors because of its high p-type concentration, high hole mobility, and cost effectiveness.⁶ Thus, NiO can be efficiently employed to form a p-n junction with the n-type TiO_2 semiconductor. A few research groups have investigated the photocatalytic performances of the p-n junction NiO/TiO_2 photocatalysts.^{5a, 7} Most of the work reported in the literature mainly focused on the photocatalytic oxidation of organics. To our knowledge, there is little information regarding photocatalytic hydrogen production using

NiO/TiO₂ nanocomposites.⁸ In addition, no actual determination of the band bending at the NiO/TiO₂ interface has been achieved so far allowing for rationalizing the enhanced charge separation concept mentioned above. This prompted us to synthesize and to investigate the photocatalytic performance of NiO/TiO₂ nanocomposites for the photocatalytic degradation of organic dyes and production of hydrogen.

Herein, the p-n junction NiO/TiO₂ photocatalyst was synthesized by a simple, easy and one pot sol-gel route using titanium butoxide, n-butanol and nickel nitrate as starting materials. The p-n junction NiO/TiO₂ photocatalyst was then characterized by FTIR, X-ray powder diffraction (XRD), Raman, UV-vis diffuse reflection spectroscopy, N₂ adsorption-desorption isotherm, transmission electron microscopy (TEM) and X-ray photoelectron spectroscopy (XPS). The band energy alignment at the NiO/TiO₂ interface was determined by X-ray Photoelectron spectroscopies (XPS) and Ultraviolet Photoelectron spectroscopy (UPS). The photocatalytic activity of the photocatalysts was evaluated by photocatalytic oxidation of methylene blue (MB), methyl orange (MO) and photocatalytic production of hydrogen. The possible mechanisms of p-n junction formation and separation of photogenerated electron and hole were also discussed.

V.2. Preparation method review

So far, Several methods have been applied to synthesize NiO/TiO₂ p-n junction heterostructures, such as sol-gel,^{5b, 7d-e, 8a, 9} incipient wetness impregnation,^{7a-c} electroless plating,¹⁰ chemical-solution-deposition-decomposition^{7h} or evaporation-induced method.¹¹ Among the various methods available for the synthesis of photocatalytic nanocomposites, sol-gel is considered to be the most successful one in creating nanoparticulate systems with controlled pore structure. Thus, Ahmed^{7e} synthesized mesoporous NiO/TiO₂ nanoparticles by the sol-gel route using titanium chloride and nickel acetylacetonate as precursors and cetyltrimethylammonium bromide as controlling template to tune the porous structure. In a typical procedure, cetyltrimethylammonium bromide surfactant dissolved in ethanol was added at a level just below its critical micelle concentration to a solution of titanium chloride and nickel acetylacetonate dissolved in ethanol followed by dropwise addition of an aqueous solution of ammonia. After aging for 48 h, the resultant sol was filtered, washed and dried at 100 °C followed by calcination at 800 °C to obtain the final product. XRD studies showed that TiO₂ in NiO/TiO₂ nanocomposites containing up to 5 mol% NiO was anatase, where as pure TiO₂ calcined at 800 °C was a mixture of anatase and rutile phase, indicating that the

NiO stabilized the metastable anatase phase and impeded its transformation to rutile. The NiO/TiO₂ nanocomposites were highly porous and the specific surface area of the NiO/TiO₂ nanocomposites containing 5 mol% NiO was 138 m²/g. Sreethawong *et al.*^{8a} also prepared NiO/TiO₂ photocatalyst via a combined sol-gel route involving a surfactant-assisted templating mechanism, where a 0.1 M solution of laurylamine hydrochloride (LAHC) of pH 4 was added to an equimolar solution of acetylacetone and tetraisopropyl orthotitanate (TIPT) to obtain a molar ratio of TIPT to LAHC 4. After stirring at 40 °C for 10 h, nickel methoxypropylate was added to the resulting yellow sol and aged for 5 days at 40 °C followed by drying at 80 °C and calcination at 500 °C to obtain the desired photocatalyst. The crystallite size of the resulting 1.5 wt% NiO/TiO₂ photocatalyst was 10.5 nm and the specific surface area was about 80 m²/g. In another study, a colloidal solution of NiO/TiO₂ with different Ni/Ti molar ratio was prepared by adding dropwise a solution of nickel nitrate hydrate (Ni(NO₃)₂·6H₂O) in ethanol and dilute nitric acid to a solution of tetrabutyl titanate dissolved in n-butanol.^{5b} The NiO/TiO₂ powder was obtained by drying the colloid followed by calcination in air at different temperatures between 400 and 700 °C. The average diameter of anatase particle in the 0.5 mol% NiO/TiO₂ catalyst was 14 nm and the NiO loading inhibited the crystal growth of TiO₂.

Sim *et al.*^{7a} prepared p-n junction NiO/TiO₂ nanotubes by the incipient wetness impregnation method. In a typical procedure, titanium nanotubes (TNTs) synthesized by an anodization method were immersed overnight in nickel nitrate solution with various molar concentrations followed by calcination at 450 °C. The crystallite size of the resulting NiO/TNTs was around 34 nm. Similarly, Chen *et al.*^{7b} have prepared NiO/TiO₂ photocatalyst by adding dropwise the desired amount of nickel nitrate dissolved in a minimum amount of deionized water into the desired amount of TiO₂ powder prepared by sol-gel route followed by calcination at 350 °C. The as-synthesized titania mainly contained anatase phase with traces of rutile phase.

Guo *et al.*¹⁰ synthesized NiO/TiO₂ junction electrode by electroless plating. At first, self-organized TiO₂ nanotube arrays were prepared by anodizing, in which a pure Ti sheet served as the anodic electrode and graphite plate as the cathode and an aqueous solution of 1 M NaH₂PO₄ and 0.5 wt% HF as electrolyte. Subsequently, the NiO/TiO₂ junction electrode was prepared by putting the TiO₂ nanotube arrays into a solution of NaC₆H₅O₇·2H₂O, NH₄Cl, NiSO₄·6H₂O and NaH₂PO₂ at a pH of 9 adjusting by NH₄OH followed by annealing at 600 °C. The inner pore diameter of the resulting TiO₂ nanotube arrays was 60–90 nm with a wall

thickness approximately of 15 nm and a length of 600 nm while the particle size of NiO on TiO₂ was 20-40 nm.

In another study, NiO/TiO₂ nanoparticles were prepared by an evaporation-induced synthetic method, in which a coating of the Ni(NH₃)₆²⁺ complex cation over TiO₂ was obtained in-situ by adding ammonia to TiO₂ P25, suspended in the required volume of millimolar Ni²⁺ solution under vigorous stirring, to reach a pH of 14.¹¹ Then, the ammonia was evaporated to convert the ammonia complex to hydroxide and eventually, NiO/TiO₂ nanoparticles were obtained by annealing the later at 450 °C. The sample contained both anatase and rutile phases of TiO₂ with average crystallite size of about 23 nm and a BET specific surface area of 65 m² g⁻¹.

In the present study, p-n junction NiO/TiO₂ nanocomposites were synthesized by the sol-gel route as this method allows for preparing more easily pure anatase TiO₂.

V.3. Results and discussions

V.3.1. Synthesis and characterization of nanocomposites

Pure TiO₂ and heterostructure NiO/TiO₂ photocatalysts were synthesized by the sol-gel process using titanium butoxide (Ti(OC₄H₉)₄) as the TiO₂ source. In a typical procedure, a colloidal solution of TiO₂ was prepared by adding n-butanol and acetic acid to titanium butoxide followed by the addition of water under vigorous stirring. The predetermined amount of nickel nitrate hexahydrate Ni(NO₃)₂·6H₂O was added into the TiO₂ sol followed by stirring, drying and calcination at 500 °C in air to obtain NiO/TiO₂ nanocomposites with different content of NiO (0.1, 0.25, 0.5, 1, 2, 4 wt% NiO). Most of the organic carbon coming from the precursors was removed after calcination which as confirmed by thermogravimetric (TG) analysis (**Figure V-1**). A total mass loss of only 1.6% for pure TiO₂ and 0.28 % for 1 wt% NiO/TiO₂ indicated that the organic precursors were completely decomposed by high temperature sintering. The negligible mass loss could be attributed to the loss of water adsorbed from environment. To confirm the complete removal of the organics during the thermolysis, the experiments were carried out under argon and the species evolved were analyzed by mass spectrometry (MS). No fragment peaks were observed by mass spectrometry (MS) evidencing the complete removal of the organics. This was further confirmed by FTIR.

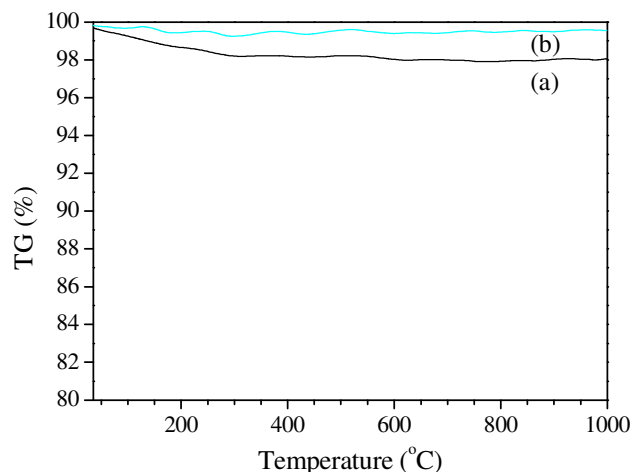


Figure V-1: TG curves of (a) TiO_2 and (b) 1 wt% NiO/TiO_2 .

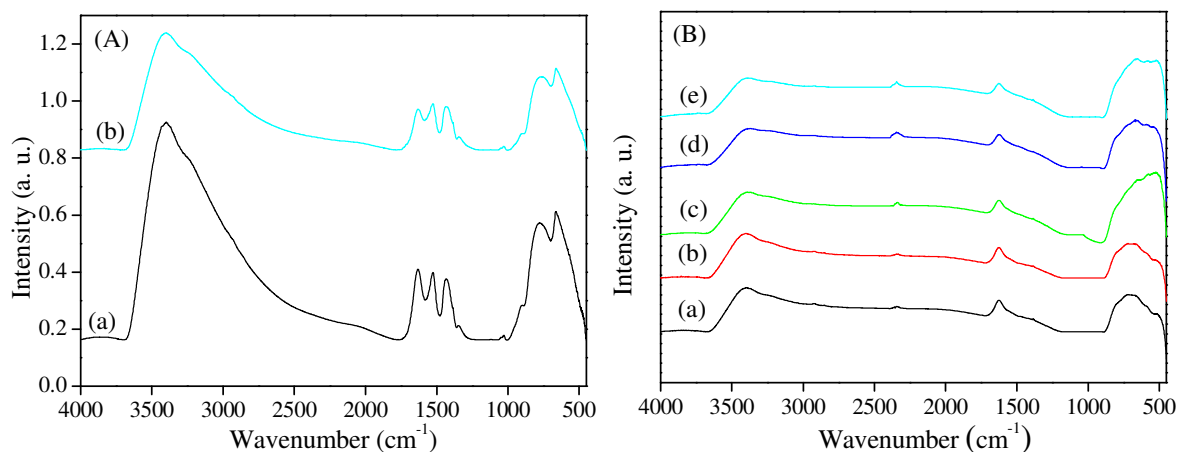


Figure V-2: (A) FTIR spectra of (a) TiO_2 (b) 1 wt% NiO/TiO_2 dried at 150 °C and (B) FTIR spectra of (a) TiO_2 (b) 0.1 wt% NiO/TiO_2 (c) 0.25 wt% NiO/TiO_2 (d) 0.5 wt% NiO/TiO_2 and (e) 1 wt% NiO/TiO_2 calcined at 500 °C.

FTIR spectra recorded for the TiO_2 and NiO/TiO_2 dried at 150 °C and calcined at 500 °C are shown in **Figure V-2**. The FTIR spectrum of the powder TiO_2 and 1 wt% NiO/TiO_2 samples dried at 150°C shows absorption bands at about 3400, 1630, 1530, 1430, 817, and 620 cm^{-1} (**Figure V-2A**). The spectrum displayed two characteristics broad band centered at 3400 and 1630 cm^{-1} which were ascribed to the stretching and bending modes of vibrations of physisorbed water or owing to the existence of surface hydroxyl groups (Ti-OH).¹² The bands at 1530 cm^{-1} were assigned to the asymmetric stretching vibration of COO (acetate) groups bonded to titanium.¹³ The band at 1430 cm^{-1} was ascribed to the bending modes of C-H bonds which come from the residual butyl group in the as-synthesized TiO_2 .¹⁴ The low-frequency region of the spectrum (below 900 cm^{-1}) was attributed to stretching vibrations involving metal-oxygen bands (e.g., Ti-O, Ti-O-Ti and, Ti-O-Bu) suggesting the formation of

TiO₂ at low temperature. After calcination of the samples, all the peaks resulting from the organic groups have disappeared (**Figure V-2B**). The remaining very broad peak between 450-900 cm⁻¹ centered at 720 cm⁻¹ could be assigned to the Ti-O lattice vibration, which indicated that TiO₂ grains had grown after calcination of TiO₂ prepared by sol-gel route.¹⁵ These peaks for NiO/TiO₂ samples were shifted to lower wavenumber with increasing the NiO amount.

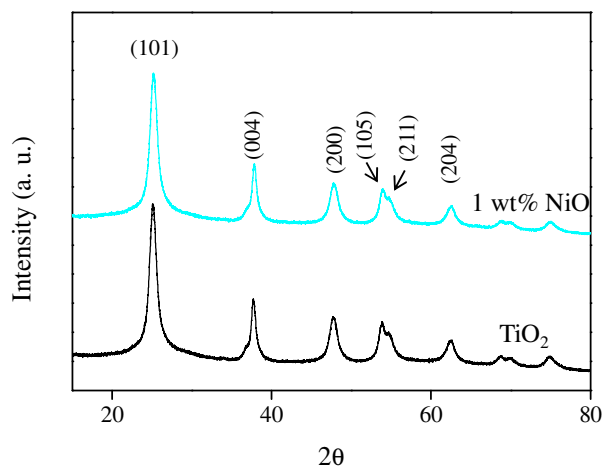


Figure V-3: XRD of TiO₂ and 1 wt% NiO/TiO₂ dried at 150 °C for 2 h.

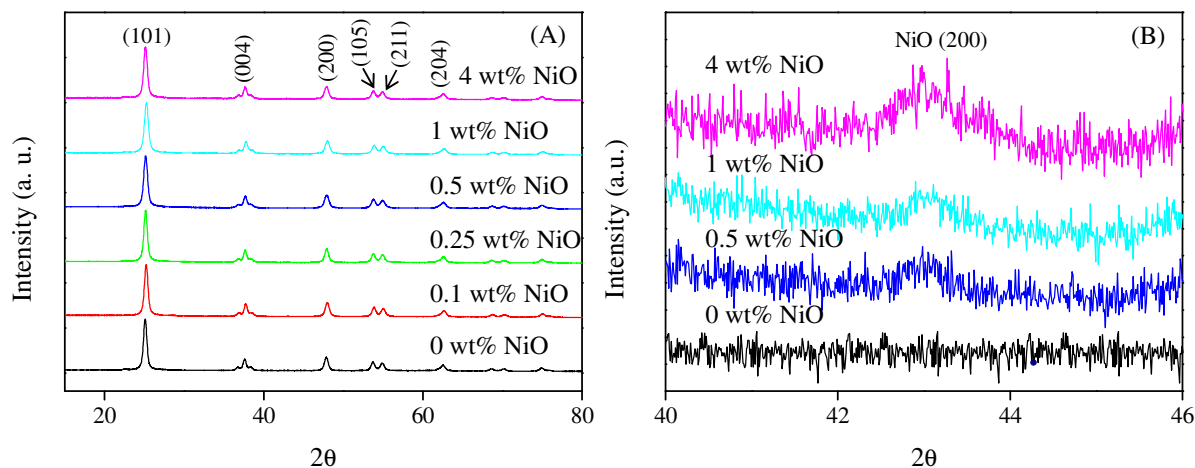


Figure V-4: (A) XRD pattern of the as-synthesized NiO/TiO₂ nanocomposites with different content of NiO and (B) XRD pattern of the as-synthesized NiO/TiO₂ nanocomposites in the 2 θ region between 40 and 46° to show the peak of NiO (200).

To characterize the crystal structure of the as-synthesized samples, XRD measurements were carried out on TiO₂ nanoparticles and NiO/TiO₂ nanocomposites with various NiO contents. The XRD patterns of TiO₂ nanoparticles and NiO/TiO₂ nanocomposites with various NiO contents shown in **Figure V-3** revealed clear peaks which can be indexed to pure anatase TiO₂. The crystallite size for dried TiO₂ and 1 wt% NiO/TiO₂ was 7.5 and 7.3 nm, respectively. This

clearly confirmed that anatase phase TiO_2 was developed during the synthetic procedure at room temperature followed by drying at $150\text{ }^\circ\text{C}$. The XRD patterns of the as-synthesized NiO/TiO_2 nanocomposites calcined at $500\text{ }^\circ\text{C}$ are shown in **Figure V-4**. The pure TiO_2 showed several dominant peaks at 2θ of 25.2° , 37.7° , 48° , 53.8° , 55.1° and 62.6° which could be indexed as (101), (004), (200), (105), (211) and (204) planes of pure anatase phase of TiO_2 (JCPDS 78-2486), respectively. It is also worth mentioning that no other diffraction peaks corresponding to other phase of TiO_2 (i.e. rutile and brookite) or any crystalline impurity were observed from the XRD pattern. The predominant existence of pure anatase phase TiO_2 implied the successful role of sol-gel route for the efficient synthesis of TiO_2 photocatalyst modified by NiO . The absence of the rutile phase was beneficial to the photocatalytic activity of the composite catalysts, owing to higher photocatalytic activity of anatase than that of rutile.¹⁶ Moreover, the route employed in this chapter, that involved the hydrolysis-condensation of $\text{Ti}(\text{O}^i\text{Bu})_4$ followed by calcination in air, appeared to be more efficient to get pure anatase than the process developed in the previous chapter (based on hydrolysis-condensation of $\text{Ti}(\text{O}^i\text{Pr})_4$ followed by hydrothermal treatment) that always gave small amount of brookite TiO_2 .¹⁷ Furthermore, as seen in **Figure V-4A**, all NiO/TiO_2 samples exhibited quite similar XRD diffractograms. Thus, in all cases, the diffraction peaks of NiO were not clearly identified, illustrating that NiO was highly dispersed in the bulk phase of the catalysts.

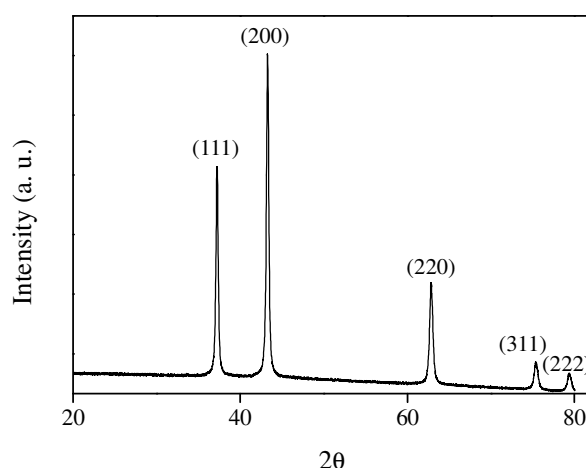


Figure V-5: XRD pattern of the as-synthesized NiO nanoparticle.

Another reason of the missing NiO signal might be the combination of its low content and its small particle size, being less than 5 nm due the low sensitivity of the XRD analysis. However, we plotted the XRD pattern in the 2θ region between 40 and 46° (**Figure V-4B**) to

examine the appearance of any peak corresponding to NiO, as the most intense peak of NiO is seen at 2θ of 43.3° . As seen, a fairly weak peak was observed which could be assigned to the (200) plane of NiO. In addition, for the composite catalysts, there was no observation of new diffraction peaks other than TiO_2 , especially NiTiO_3 phase, indicating the absence of crystalline mixed oxides. The possibly formed phase of NiO was examined by using XRD of pure NiO prepared by the similar procedure described above but without titanium precursor (**Figure V-5**). The peaks positions appearing at 2θ of 37.24° , 43.30° , 62.83° , 75.40° and 79.35° can be readily indexed as (111), (200), (220), (311), and (222) crystal planes of NiO, respectively. All these diffraction peaks can be perfectly indexed to the face-centered cubic (FCC) crystalline structure of NiO, which was in accordance with that of the standard spectrum (JCPDS, No. 04-0835). The average crystallite size of TiO_2 in the as-synthesized photocatalysts estimated from the line broadening of the anatase (101) diffraction peak using the Scherrer formula is shown in **Table V-1**. The calculated crystallite size of TiO_2 prepared by the sol-gel method was in the range of 13-16 nm and the crystallite size of TiO_2 slightly decreased with increasing the NiO content which was also supported by Raman results.

The crystalline phase and the size of crystallite of as-synthesized photocatalysts were further confirmed by Raman investigation. Raman spectroscopy is a powerful method to investigate the structural properties of nanoparticles, monitoring the unusual band broadening and shifts of Raman bands associated with particle size. Thus, it is possible to determine the size of the nanoparticles from a measurement of the maximum of the low frequency Raman band.¹⁸

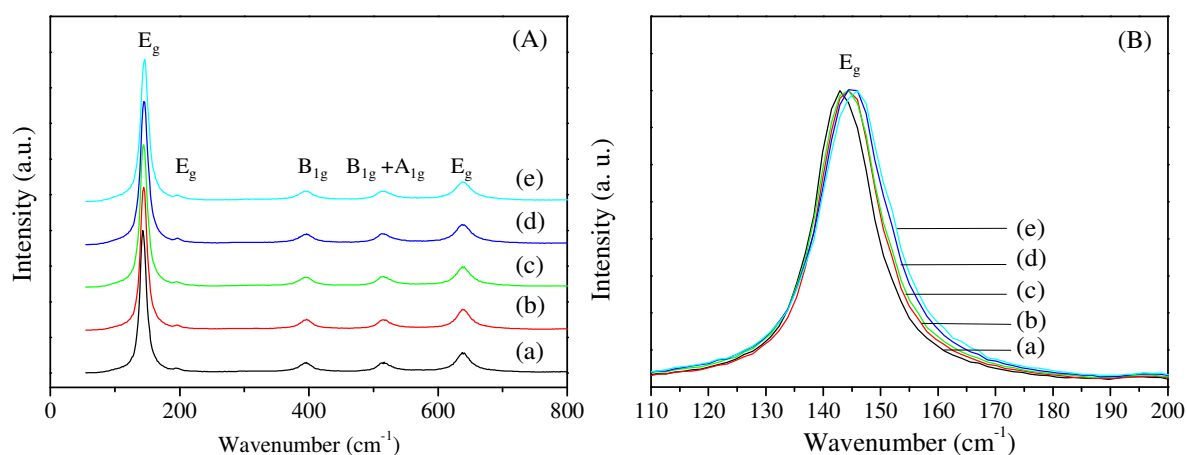


Figure V-6: (A) Raman spectra of as-synthesized photocatalysts (B) enlarged region of Raman shift range $110\text{-}200\text{ cm}^{-1}$. (a) TiO_2 (b) 0.1 wt% NiO/ TiO_2 (c) 0.25 wt% NiO/ TiO_2 (d) 0.5 wt% NiO/ TiO_2 (e) 1 wt% NiO/ TiO_2 .

The Raman spectra of the as-synthesized photocatalysts are depicted in **Figure V-6A**. According to the group theory, anatase has six Raman-active modes ($A_{1g} + 2B_{1g} + 3E_g$).¹⁹ Ohsaka reported the Raman spectrum of an anatase single crystal where six allowed modes appeared at 144 (E_g), 197 (E_g), 399 (B_{1g}), 513 (A_{1g}), 519 (B_{1g}), and 639 cm^{-1} (E_g).²⁰ From the Raman spectra, it seems evident that both the pure and NiO-modified TiO_2 only included the anatase phase. There was no apparent impurity-related mode in the Raman spectra of heterostructure NiO/ TiO_2 samples, which is in agreement with the above discussed XRD results. For pure TiO_2 , the high intensity lower frequency E_g mode was observed at 143 cm^{-1} , which was well in agreement with the values reported in the literature.²¹ In order to highlight the difference between the spectra, the position of the E_g mode near 143 cm^{-1} is presented in **Figure V-6B** in the enlarged region of range 110-200 cm^{-1} in which the intensity of the Raman spectra was normalized. With increasing the NiO amount, the position of the Raman bands, in particular the E_g mode shifted towards higher wavenumbers. This observation could be attributed to the reduction of the particle size of TiO_2 with increasing the NiO content. When the grain size decreases to a nanometer scale, the vibrational properties of materials are greatly influenced. Mainly, a volume contraction occurs within the nanoparticles due to size-induced radial pressure, which lead to an increase in the force constants because of the decrease in the interatomic distances. In vibrational transitions, the wavenumber varies approximately in proportion to the square root of force constant. Consequently, the Raman bands shift towards a higher wavenumber due to the increasing force constants. The crystallite size of the as-synthesized photocatalyst were determined from the shift of low frequency E_g mode and the calculated crystallite size is presented in **Table V-1**. The average size of the crystallites was well agreed with that determined by XRD.

Table V-1: Mean particle size (in nm) of anatase TiO_2 determined by XRD and Raman shift.

Sample	E_g mode position, (cm^{-1})	Crystallite size (XRD), (nm)	Crystallite size (Raman) ^a , (nm)
TiO_2	143.0	16.0 ± 0.5	17.0 ± 0.5
0.1 wt% NiO- TiO_2	144.3	15.5 ± 0.5	15.5 ± 0.5
0.25 wt% NiO- TiO_2	144.6	14.2 ± 0.5	16.0 ± 0.5
0.5 wt% NiO- TiO_2	145.5	14.0 ± 0.5	13.6 ± 0.5
1 wt% NiO- TiO_2	146.0	13.0 ± 0.5	13.0 ± 0.5

^a Crystallite size was determined by the Raman shift of E_g mode of anatase TiO_2 according to the model (shown in appendix, **Figure A-1**) proposed by Balaji *et al.*²²

Transmission electron microscopy (TEM) was used to further examine the crystallite/particle size, the crystallinity and the morphology of the as-synthesized samples derived by the sol-gel route. **Figure V-7** shows the TEM and HRTEM images of the 1 wt% NiO/TiO₂ nanocomposite.

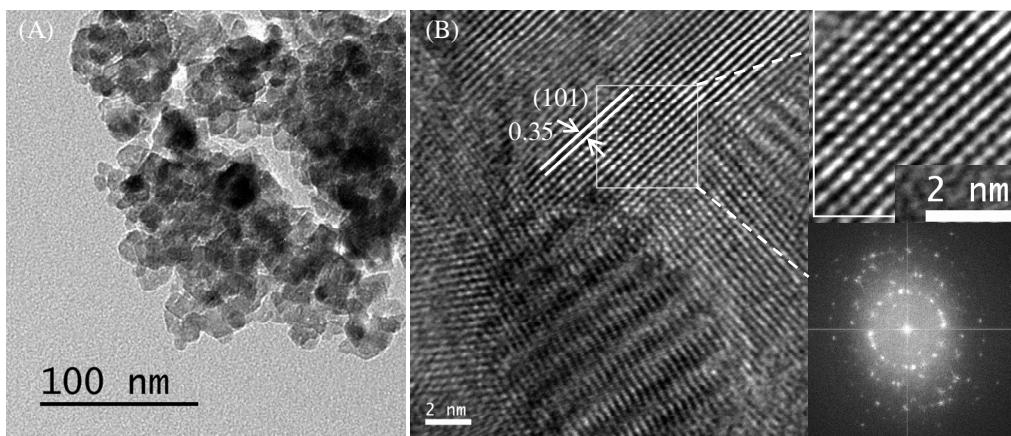


Figure V-7: (A) TEM and (B) HRTEM images (inset shows the SEAD pattern and enlarged view of HRTEM) of 1 wt% NiO/TiO₂ nanocomposites.

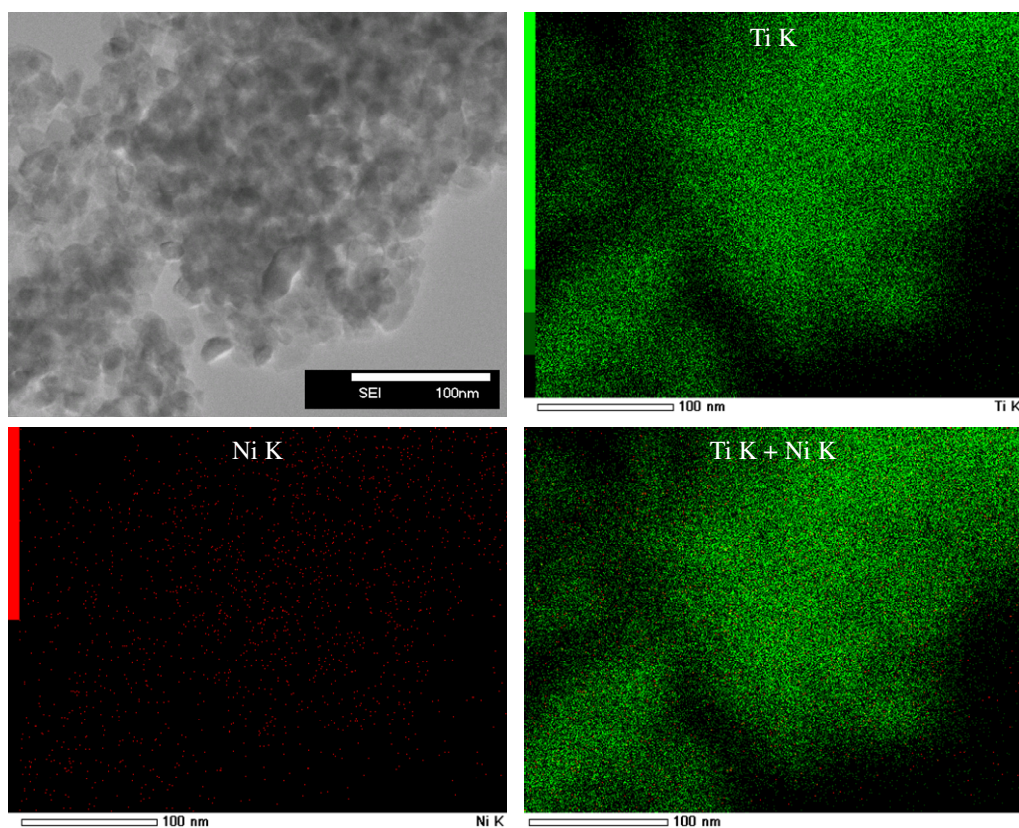


Figure V-8: EDX elemental mapping of 1 wt% NiO/TiO₂ nanocomposite.

It was found that the as-synthesized NiO/TiO₂ sample (**Figure V-7A**) was porous in nature and the average size of the primary particles was around 15 nm, which was in good agreement with the average crystallite values determined by XRD and Raman spectroscopy. Moreover, as shown in the inset of **Figure V-7B**, the lattice fringe observed corresponds to distances of 0.35 nm which agreed well with the distance of the (101) lattice plane of TiO₂. The selected area diffraction pattern (SAED) shown in the inset of **Figure V-7B** also confirmed the crystalline anatase phase, in agreement with the X-ray diffraction data. In order to confirm the presence of NiO in the nanocomposites, the elemental mapping using energy dispersive X-ray (EDX) analysis was carried out on samples of the NiO/TiO₂ coupled photocatalysts. As shown in **Figure V-8**, the elemental mapping of titanium and nickel in the 1 wt% NiO/TiO₂ sample showed that nickel was uniformly dispersed throughout the coupled catalyst indicating the presence of very small NiO particles. The uniform dispersion of NiO in the nanocomposites was further confirmed by EDX analyses of NiO/TiO₂ materials containing higher weight percentage of NiO (4 wt%) as shown in **Figure V-9**.

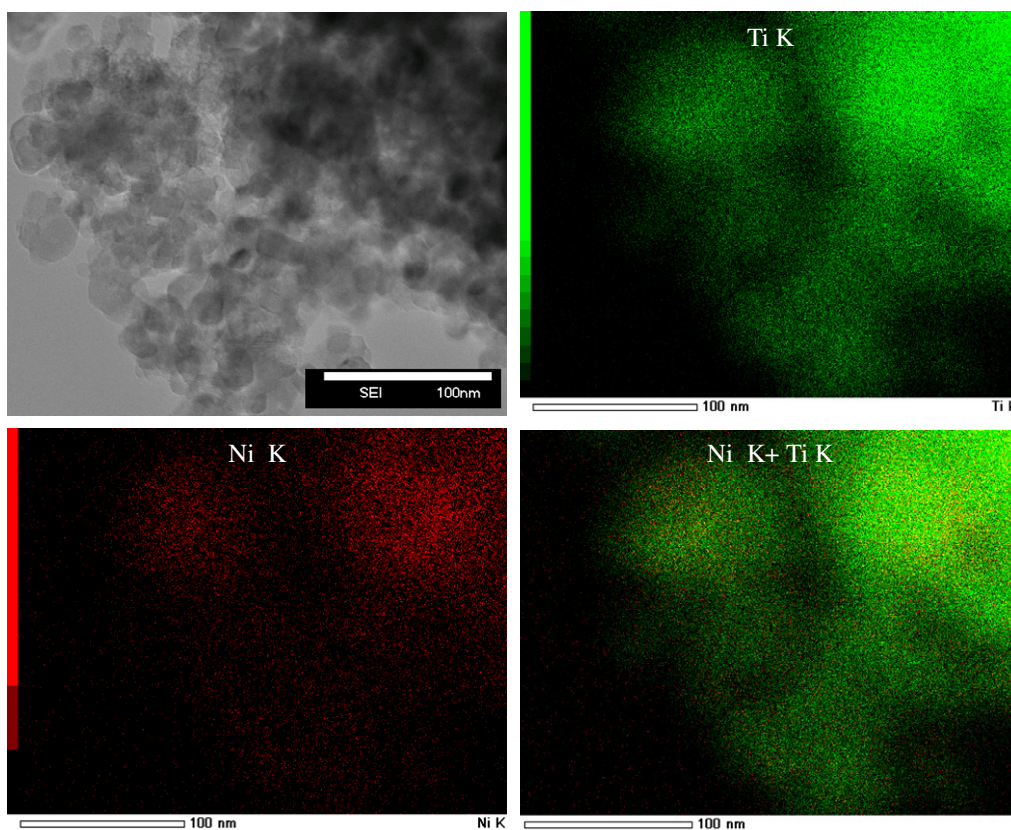


Figure V-9: EDX elemental mapping of 4 wt% NiO/TiO₂ nanocomposite.

Then, the texture of the as-synthesized photocatalysts was analyzed by nitrogen sorption measurements. N₂ adsorption-desorption isotherms of the as-synthesized TiO₂

nanoparticles (**Figure V-10A**) and NiO/TiO₂ nanocomposites (**Figure V-10B**) containing 1 wt% NiO exhibited a typical IV-type sorption behavior with hysteresis loop, which was a marked characteristic of mesoporous materials, according to the IUPAC classification.²³ The well-defined hysteresis loop with a sloping adsorption branch and a relatively steep desorption branch belonged to the H2 type. The abrupt increase in adsorbed N₂ volume at high pressure can be attributed to the capillary condensation of N₂ inside the mesopores. The H2-type hysteresis loop is generally attributed to a difference in mechanisms between condensation and evaporation processes of gaseous N₂ molecules occurring either in narrow-neck and wide-body pores (often referred to as ink-bottle pores) or in the inter nanoparticle void space that can be observed in the TEM images. The pore size distributions of mesopores in the as-synthesized samples were analyzed by BJH methods and the results are illustrated in the inset of **Figure V-10**. A narrow monomodal pore size distribution, centered at a pore diameter of 8.5 ± 0.5 nm, implied relative uniform channels in the mesoporous region.

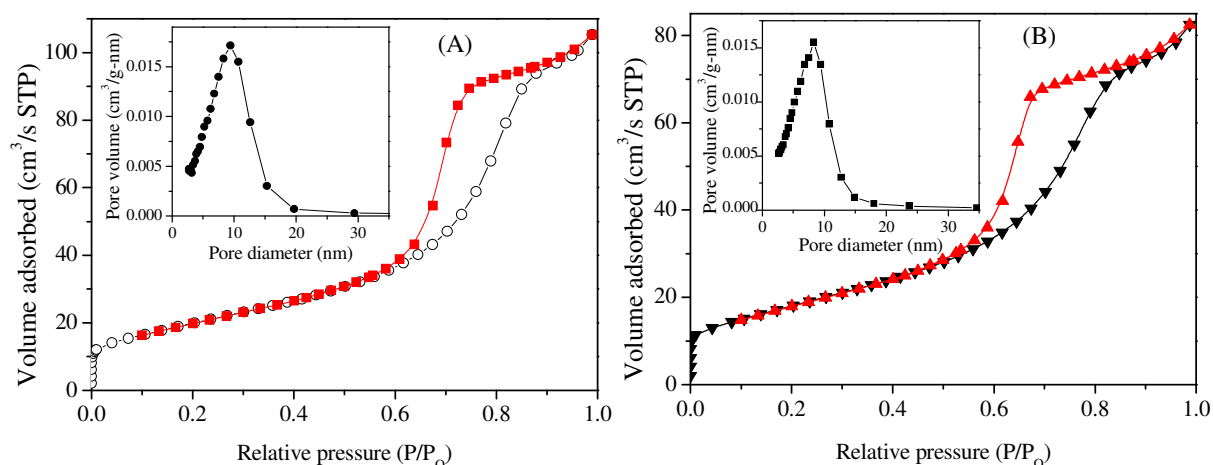


Figure V-10: N₂ adsorption-desorption isotherm of calcined (A) TiO₂ and (B) 1 wt% NiO/TiO₂.

The textural properties, i.e. Brunauer-Emmett-Teller (BET) specific surface areas, mean mesopore diameter and pore volumes of the as-synthesized photocatalysts are summarized in **Error! Not a valid bookmark self-reference..** The BET surface areas of pure TiO₂ calculated from the linear part of the Brunauer-Emmett-Teller (BET) plot was 72 m² g⁻¹. The surface area of the NiO/TiO₂ nanocomposites significantly decreased from 70 to 43 m² g⁻¹ with increasing the amount of NiO loading from 0.1 up to 4 wt%. As the change in density of the NiO/TiO₂ nanocomposites is negligible in the 0.1-4 wt% NiO range, the decrease in S_{BET} could be related to pore blocking due to NiO deposition.

Table V-2: Nitrogen Sorption Porosimetry Studies of the as-synthesized TiO₂ and NiO/TiO₂ nanoparticles.

Sample	Crystallite size (nm)	S _{BET} (m ² g ⁻¹)	Pore volume (cm ³ g ⁻¹)	Pore size (nm)
TiO ₂ (dry)	7.5 ± 0.5	250 ± 2	0.27 ± 0.02	4.3 ± 0.5
1 wt% NiO/TiO ₂ (dry)	7.3 ± 0.5	251 ± 2	0.27 ± 0.02	4.3 ± 0.5
TiO ₂	16.0 ± 0.5	72 ± 2	0.16 ± 0.02	9.0 ± 0.5
0.1 wt% NiO/TiO ₂	15.5 ± 0.5	70 ± 2	0.13 ± 0.02	7.5 ± 0.5
0.5 wt% NiO/TiO ₂	14.2 ± 0.5	67 ± 2	0.14 ± 0.02	9.0 ± 0.5
1 wt% NiO/TiO ₂	14.0 ± 0.5	65 ± 2	0.13 ± 0.02	7.5 ± 0.5
4 wt% NiO/TiO ₂	13.0 ± 0.5	43 ± 2	0.09 ± 0.02	8.5 ± 0.5

In order to estimate the energy band gap of the catalyst particles, the optical property of the as-synthesized nanoparticles was studied by UV-Vis diffuse reflectance spectra as shown in **Figure V-11**. Pure TiO₂ exhibited a steep absorption edge located at ca. 385 nm (**Figure V-11Aa**) indicating the excitation of electrons from valence band (O 2p states) to conduction band (Ti 3d states). The absorption edges of composite photocatalysts were found to shift towards visible region with the presence of NiO. Moreover, the extended red-shift absorption edge revealed the good contact between NiO and TiO₂ as consequence of the inter-dispersion of the two oxides. A possible explanation is that the valence band of TiO₂ is mainly formed by overlapping oxygen 2p orbitals (O pπ states), whereas its conduction band is mainly constituted by 3d orbitals (t_{2g} bands) of the Ti⁴⁺ cation.²⁴ In the junction region, the electronic contact between NiO and TiO₂ may lead to a charge transfer transition from the NiO valence band to the conduction band of TiO₂ to enable visible light to be absorbed.^{24, 25} Bokhimi *et al.*²⁶ also reported that the UV-vis diffuse reflectance spectra of CuO/TiO₂ exhibited an extension of absorption edge to the visible region related to a transition from the valence band of the nanocrystalline CuO to the conduction band of nanocrystalline TiO₂ because of a good contact between CuO and TiO₂ crystals.

As mentioned in different reports and evidenced in chapter IV, anatase TiO₂ can be considered as an indirect semiconductor.²⁷ **Figure V-12** shows the plots of $(F(R) hv)^{1/2}$ versus hv for as-synthesized photocatalysts, where $F(R)$ is the Kubelka-Munk function and hv is the photon energy. The indirect energy band gap of pure TiO₂ estimated from the extrapolation of the tangent to the abscissa was 3.1 eV. This obtained band gap value of pure TiO₂ is in good agreement with the reported values.²⁸ On the other hand, the reported optical

energy band-gap of NiO ranges from 3.4 eV²⁹ to 4.0 eV,³⁰ depending on how the location of the band edge is defined: by the location of the first absorption feature, midpoint of the first rise, or where the maximum slope of absorption extrapolates to zero.³⁰ However, some strong absorption in the visible range occurred (**Figure V-11B**), which could be assigned to intra-3d transitions of Ni²⁺ in the cubic crystal field of NiO.³¹ As NiO is a direct band gap semiconductor,³² the band gap energy of the NiO was estimated from a plot of $(F(R) hv)^2$ versus hv . The band gap of NiO was estimated to be of 3.4 eV (**Figure V-11B**, inset), in rather good agreement with literature values.³³

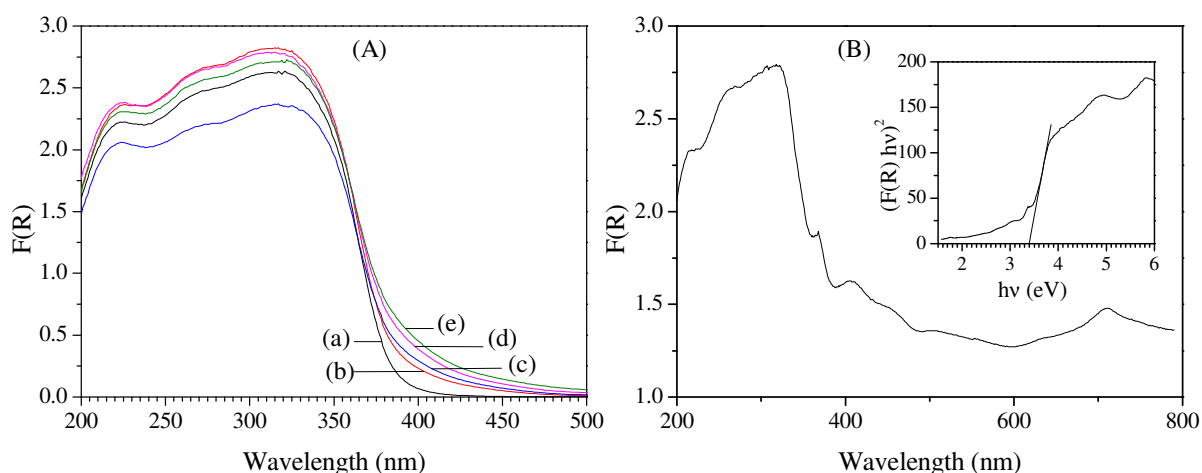


Figure V-11: UV-Vis diffuse absorption spectra of (A) as-synthesized photocatalysts; (a) TiO₂ (b) 0.1 wt% NiO/TiO₂ (c) 0.25 wt% NiO/TiO₂ (d) 0.5 wt% NiO/TiO₂ and (e) 1 wt% NiO/TiO₂ and (B) NiO (inset: $(F(R) hv)^{1/2}$ vs hv plot of NiO).

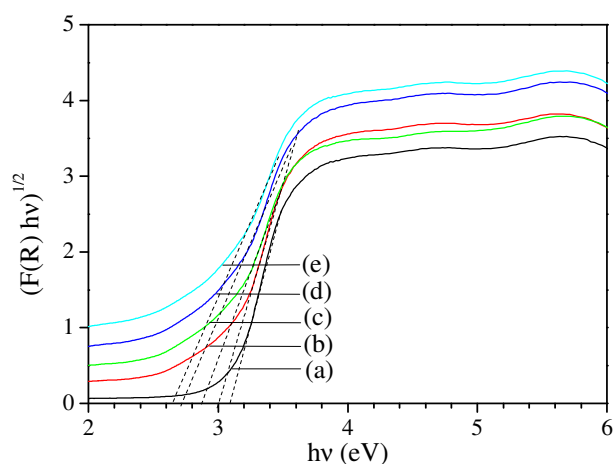


Figure V-12: $(F(R) hv)^{1/2}$ versus hv for as-synthesized photocatalysts. (a) TiO₂ (b) 0.1 wt% NiO/TiO₂ (c) 0.25 wt% NiO/TiO₂ (d) 0.5 wt% NiO/TiO₂ and (e) 1 wt% NiO/TiO₂.

In contrast, a significant decrease of the band gap energies for the NiO/TiO₂ nanocomposites was observed with a gap value shifting from 3.0 eV to 2.65 eV when the

NiO content was increased from 0.1 to 1 wt% (**Figure V-12(b-e)**). As mentioned above, the electronic interaction of the conduction band of the Ti 3d orbitals of titanium oxide and the Ni 3d orbitals of NiO might explain the decrease in energy gap between the Ti d and O p orbitals of TiO₂. Such a phenomenon would lead visible light absorption.

V.3.2. Interface analysis

To further illuminate the surface composition and chemical state of the elements existing in NiO/TiO₂ samples, X-ray photoelectron spectroscopy (XPS) analysis was performed on the as-synthesized samples. As shown in **Figure V-13A**, the survey spectra of 1 wt% NiO/TiO₂ confirmed the presence of Ti, Ni, and O and no peak of any other elements was detected. In contrast, the survey scan of pure TiO₂ only shows the presence of Ti and O elements. Hence, the XPS spectra confirmed that TiO₂ was composed of only two elements, Ti, O, and NiO/TiO₂ was formed by Ti, O and Ni. The results were in good agreement with the XRD and EDX results discussed above.

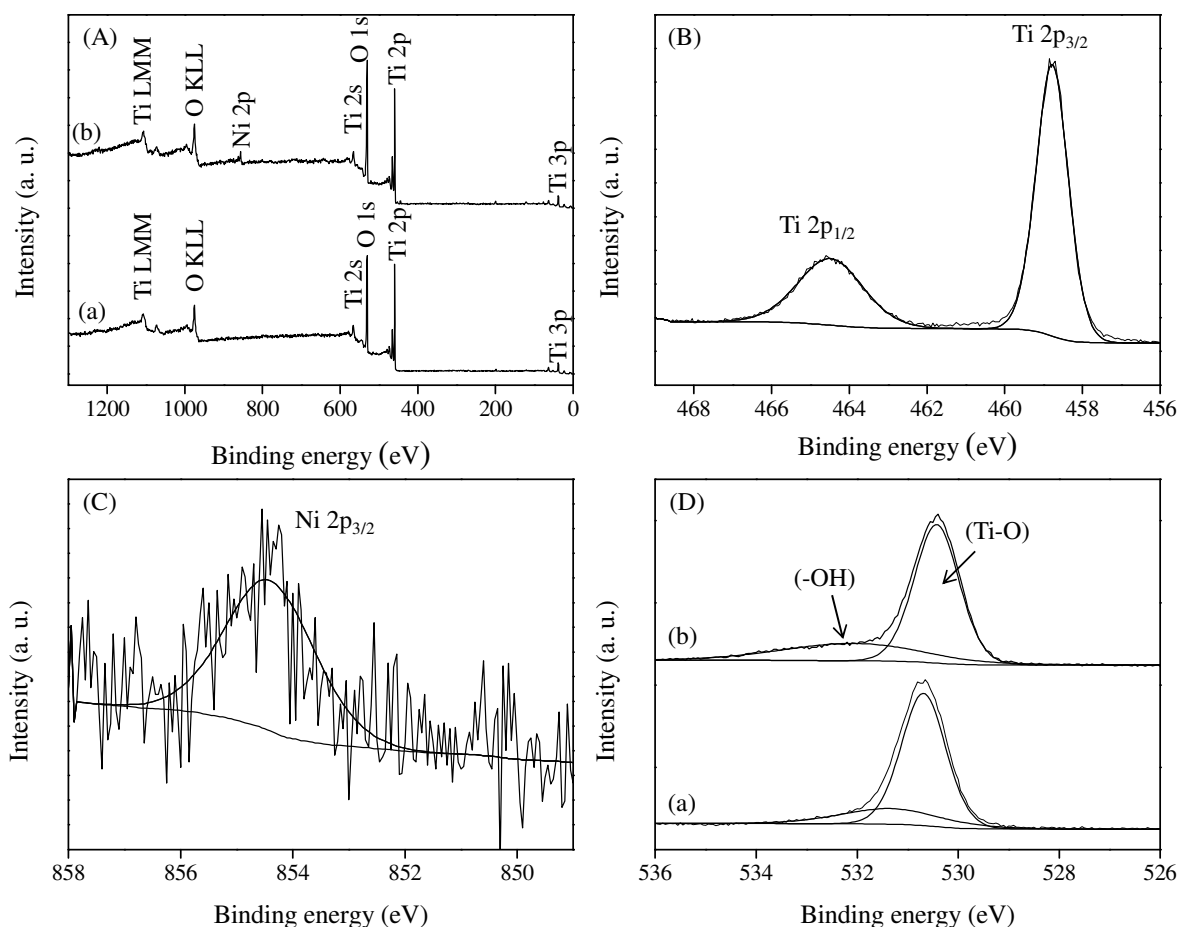


Figure V-13: A) XPS survey spectra of as-synthesized sample. High-resolution spectra of 1 wt% NiO/TiO₂ sample: (B) Ti 2p spectra, (C) Ni 2p spectra and (D) O 1s spectra. (a) TiO₂ and (b) 1 wt% NiO/TiO₂.

Figure V-13B shows the high resolution XPS spectra of the Ti 2p core level of the NiO/TiO₂ sample containing 1 wt% NiO. Peak fitting to the spectra was applied using Gaussian-Lorentzian peak shape after subtraction of Shirley background. The Ti 2p spectrum shows two symmetric peaks, the peak centered at 458.8 eV corresponded to the Ti 2p_{3/2} and another one centered at 464.5 eV was assigned to Ti 2p_{1/2}. The typical binding energy of Ti 2p_{3/2} was reported to be in the range of 458.5-459.7 eV.³⁴ The symmetric peak of Ti 2p_{3/2} at 458.8 eV indicated the formal oxidation state of Ti⁴⁺ in the as-synthesized NiO/TiO₂ nanocomposites.³⁵ Furthermore, the Ni 2p_{3/2} photoemission line for the 1 wt% NiO/TiO₂ sample was located at 854.4 eV (**Figure V-13C**) which indicated the existence of nickel cation as Ni²⁺, as expected for NiO.³⁶ These data therefore definitely evidenced the presence of NiO species in the 1 wt% NiO/TiO₂ photocatalyst.

As illustrated in **Figure V-13D**, the O 1s XPS spectrum of 1 wt% NiO/TiO₂ was wide and asymmetric at higher binding energy, showing that there were at least two forms of O binding states. The O 1s spectrum was deconvoluted into two main components. The emission line at 530.4 eV was attributed to the O lattice of TiO₂ (O 1s-Ti states, TiO₂) while the peak at 531.9 eV was ascribed to the hydroxyl group in the water molecules adsorbed on the particle surface. The O 1s peak for NiO was reported to be 529.3 eV, thus the O 1s peak related to NiO overlaps with O 1s of TiO₂.

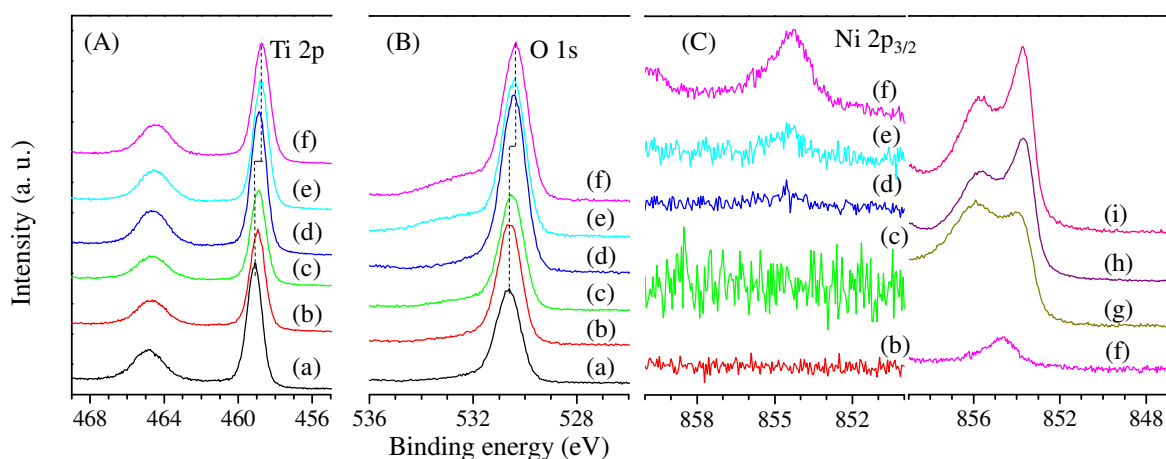


Figure V-14: Evolution of core level spectra (A) Ti 2p (B) O 1s (C) Ni 2p_{3/2}. (a) TiO₂ (b) 0.1 wt% NiO/TiO₂ (c) 0.25 wt% NiO/TiO₂ (d) 0.5 wt% NiO/TiO₂ (e) 1 wt% NiO/TiO₂ (f) 4 wt% NiO/TiO₂ (g) 25 wt% NiO/TiO₂ (h) 50 wt% NiO/TiO₂ (i) NiO.

In order to investigate the electronic properties, we determined the band energy alignment at the interfaces of NiO/TiO₂ nanocomposites by XPS and UPS from the core level binding energy shifts. **Figure V-14A** shows the evolution of the core level spectra of Ti 2p of

NiO/TiO₂ nanocomposites containing different amount of NiO. Starting with the pure TiO₂, the Ti 2p_{3/2} spectrum shows a peak at a binding energy of 459.1 eV. The spectral line shape and the peak position of the Ti 2p_{3/2} core level for the pure TiO₂ were in good agreement with the earlier studies of anatase TiO₂.³⁷ The emission lines were shifted to lower binding energy (BE) with increasing NiO content. This shift in BE of TiO₂ core levels with the increase in NiO loading may indicate the formation of a space charge layer (band bending) at the interface of NiO/TiO₂ nanocomposite.³⁸ The Ti 2p_{3/2} line for NiO/TiO₂ nanocomposite with 4 wt% NiO was at a binding energy of 458.7 eV, a shift to lower BE of 0.4 ± 0.1 eV, which can be ascribed to the down ward shift of E_F possibly induced by band bending in the TiO₂ particles. Core level photoemission can also distinguish the bonding environment of surface and near-surface atoms and changes induced by the adsorption of molecules on the surface. The formation of covalent or ionic bonds due to surface reactions should result in chemically shifted components.³⁹ Apart from a slight broadening of all peaks, there were no significant changes in the spectral line shape of the TiO₂ core level (**Figure V-14A**) feature following NiO loading which implied that no chemical interface reaction occurs between TiO₂ nanoparticles and NiO entities.

Figure V-14B shows the evolution of the core level O 1s emission lines of NiO/TiO₂ nanocomposites with different content of NiO. The form of the O emission line was symmetric and there was no significant change in the line shape when the NiO content was lower than 0.5 wt%. Above 0.5 wt% content, the form of the O spectra was changed gradually with increasing NiO content from a symmetric line form to a shape with an asymmetry at higher binding energies. This change of O 1s emission line most probably results from the contribution of adsorbed OH⁻ species.⁴⁰ The O 1s peak was also shifted to the low binding energy by 0.35 ± 0.1 eV.

Turning to the Ni 2p_{3/2} core level photoemission spectra shown in **Figure V-14C**, we observed an increase in the intensity of Ni 2p_{3/2} core level signal. The Ni 2p_{3/2} signals were shifted to lower binding energy with increasing the NiO content. The Ni 2p_{3/2} emission lines were found at binding energies of 854.5, 854.35, and 853.75 eV for 1 wt% NiO/TiO₂, 4 wt% NiO/TiO₂ and NiO, respectively. The shift of the Ni 2p_{3/2} emission line for 1 wt% NiO/TiO₂ was $\sim 0.6 \pm 0.1$ eV.

Then, as previously done for the other heterostructures (e. g. RuO₂/TiO₂ in Chapter IV) studied in this thesis, the work function ϕ of the NiO or the TiO₂ sample was determined

from the secondary electron cutoff observed in the ultraviolet photoelectron spectrum (UPS) recorded using He-I excitation (**Figure V-15**). The secondary electron onset on the left side of the spectrum was determined to be 17.05 and 15.8 eV for TiO₂ and NiO, respectively. The work function was then calculated to be 4.15 ± 0.1 and 5.4 ± 0.1 eV for TiO₂ and NiO, respectively, by subtracting the secondary electron onset position of the UPS spectrum from the excitation energy (21.2 eV).

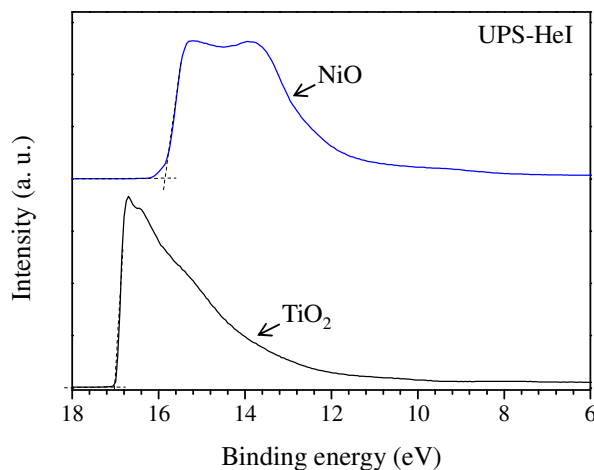


Figure V-15: Ultraviolet photoelectron spectra (HeI) of TiO₂ and NiO.

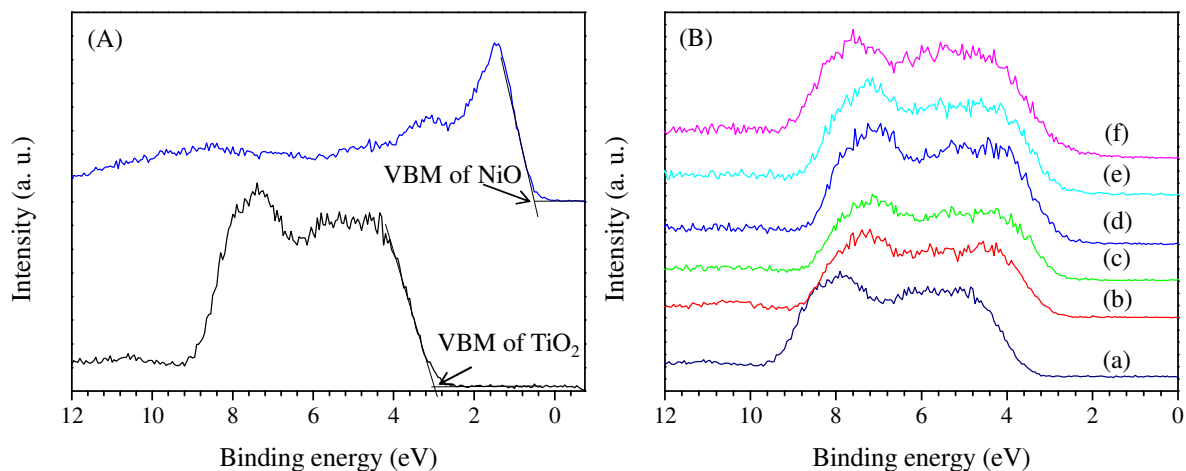


Figure V-16: (A) Valence band spectra of TiO₂ and NiO (B) evolution of valence band position. (a) TiO₂ (b) 0.1 wt% NiO/TiO₂ (c) 0.25 wt% NiO/TiO₂ (d) 0.5 wt% NiO/TiO₂ (e) 1 wt% NiO/TiO₂ (f) 4 wt% NiO/TiO₂.

Figure V-16A shows the valence band spectrum of TiO₂ and NiO, respectively. The valence band maximum (VBM) was determined by linearly extrapolating the low binding energy edge of the valence band intersecting with the background. The calculated value of 2.9 ± 0.1 eV was obtained as the VBM energy position for the TiO₂, while a value of 0.4 ± 0.1 eV was obtained for NiO, which indicated that the as-synthesized TiO₂ and NiO were n-

type and p-type semiconductors, respectively. **Figure V-16B** shows the evolution of VB spectra of NiO/TiO₂ nanocomposites containing different amount of NiO. It is obvious that the VBM shifted toward lower binding energy with increasing NiO loading. The valence band was shifted by $\sim 0.43 \pm 0.1$ eV, which was consistent with the Ti 2p_{3/2} core level shift.

Photoemission spectra from a heterojunction interface may be used to extract the band energy profile at the interface. The valence band offset (ΔE_{VB}^{inter}) and the conduction band offset (ΔE_{CB}^{inter}) at the interface are calculated from:

$$\Delta E_{VB}^{inter} = (E_{VB}^{TiO_2} - E_{VB}^{NiO})^{bulk} - (|E_{bb}^{TiO_2}| + |E_{bb}^{NiO}|) \quad (1) \quad \text{and}$$

$$\Delta E_{CB}^{inter} = \Delta E_{VB}^{inter} + (E_g^{NiO} - E_g^{TiO_2}) \quad (2)$$

Here, inter and bulk designate interface and bulk, respectively. A value of $(E_{VB}^{TiO_2} - E_{VB}^{NiO})^{bulk}$ could be determined by calculating the difference of VBM between pure TiO₂ and NiO. The quantities, $E_{bb}^{TiO_2}$ and E_{bb}^{NiO} , referring to the band bending in n-type semiconductor (TiO₂) and p-type semiconductor (NiO), respectively, were estimated by the core level shifts, these numbers were obtained above. For example the valence band offset is calculated, $\Delta E_{VB}^{inter} = (2.9 \pm 0.1 - 0.4 \pm 0.1) - (1 \pm 0.1) = 1.5 \pm 0.1$ eV based on the VBM values of TiO₂ and NiO determined previously.

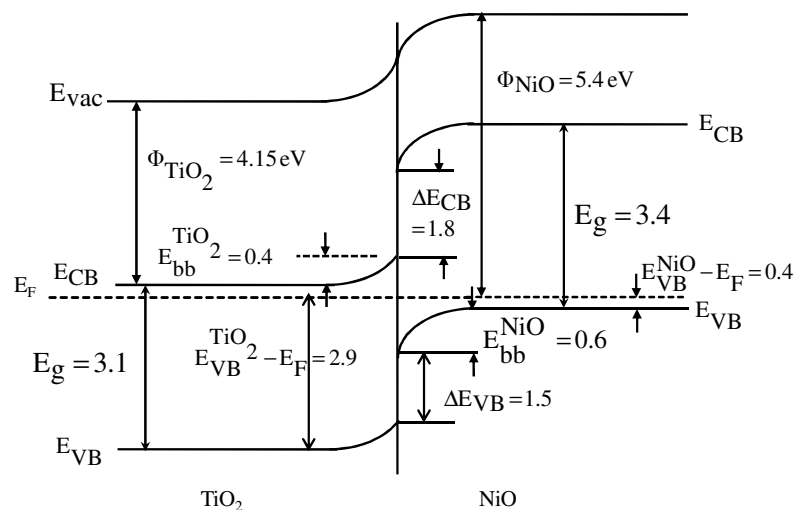


Figure V-17: Band energy alignment at the heterojunction interface of n-type (TiO₂) and p-type (NiO) semiconductor.

The band gap energies determined by UV-Vis diffuse spectroscopy for TiO₂ and NiO were 3.1 and 3.4 eV, respectively. According to Eq. (2) the conduction band offset (ΔE_{CB}^{inter}) was

thus obtained to be 1.8 ± 0.1 eV. As a consequence, the resulting band energy alignment at the interface for a heterojunction NiO/TiO₂ nanocomposite is shown in **Figure V-17**

V.3.3. Photocatalytic activity

V.3.3.1. Photocatalytic degradation of organic dyes

The photocatalytic activity of the pure TiO₂ and as-synthesized NiO/TiO₂ nanocomposites were investigated by decomposing methylene blue (MB) and methyl orange (MO) after checking that there was no degradation with photocatalysts in the absence of light irradiation or under UV irradiation in the absence of photocatalyst. By contrast, both MB and MO can be decolorized efficiently in aqueous NiO/TiO₂ dispersions by UV light irradiation. The change in the absorbance spectra of the MB and MO solutions during the reaction was monitored with initial 10 mg/L dye concentration and 1 g/L catalyst loading and the results are shown in **Figure V-18**.

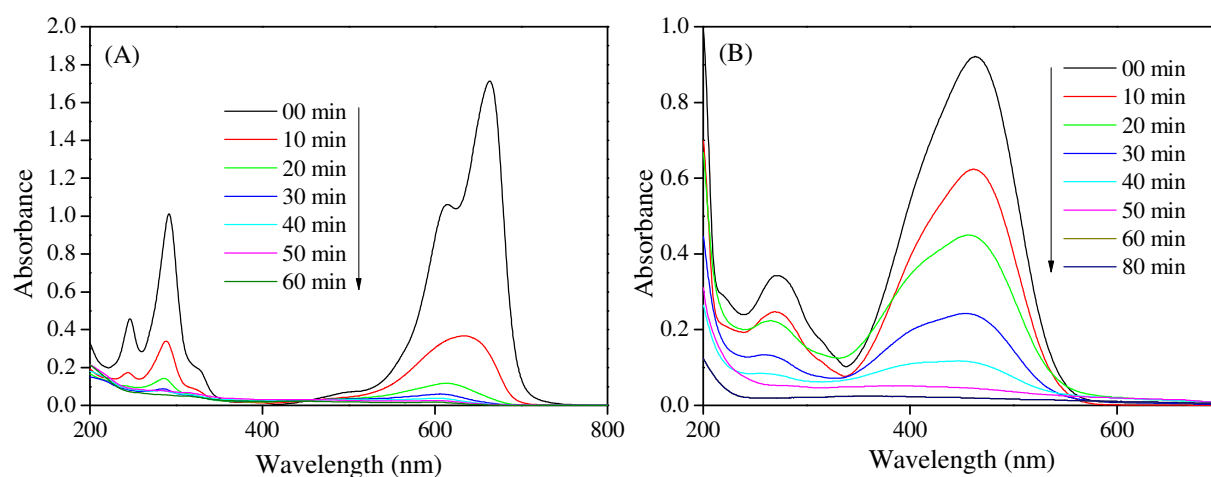


Figure V-18: Typical absorbance spectra of (A) MB and (B) MO solution during the course of photodegradation.

The MB shows a maximum absorption peak at 664 nm and the decolorization efficiency was recorded with respect to the change in intensity of the absorption peak at 664 nm. As shown in **Figure V-18A**, the intensity of the characteristic absorption peak has been found to decrease gradually with increasing the exposure time indicating the photocatalytic degradation of the dye in the presence of NiO/TiO₂ nanocomposites. On the other hand, the decrease in the absorbance under 300 nm was also a strong indication of the degradation of dye. After UV light irradiation for 1 h, the maximum absorption peaks around 664 nm has completely disappeared. The absorbance of MO was similarly decreased with increasing irradiation time (**Figure V-18B**).

The photocatalytic activity of NiO/TiO₂ nanocomposites with different NiO contents for the degradation of MB and MO is reported in **Figure V-19**. It can be seen that NiO/TiO₂ nanocomposite containing 0.1 and 0.25 wt% NiO displayed higher photocatalytic activity for the degradation of MB compared to TiO₂ (**Figure V-19A**). The NiO/TiO₂ heterostructure catalysts with NiO content of 0.1 wt% showed the highest photocatalytic activity. However, when the NiO content exceeded 0.1 wt%, the photocatalytic activity of the NiO/TiO₂ heterostructure decreased with an increase in the NiO content. A similar trend was obtained for the degradation of MO over the as-synthesized NiO/TiO₂ photocatalysts resulting in higher degradation efficiency with the 0.1 wt% NiO/TiO₂ photocatalyst (**Figure V-19B**). The above results indicated that the optimum NiO content in NiO/TiO₂ mixtures as obtained in the experiments for the degradation of organic dyes was about 0.1 wt%.

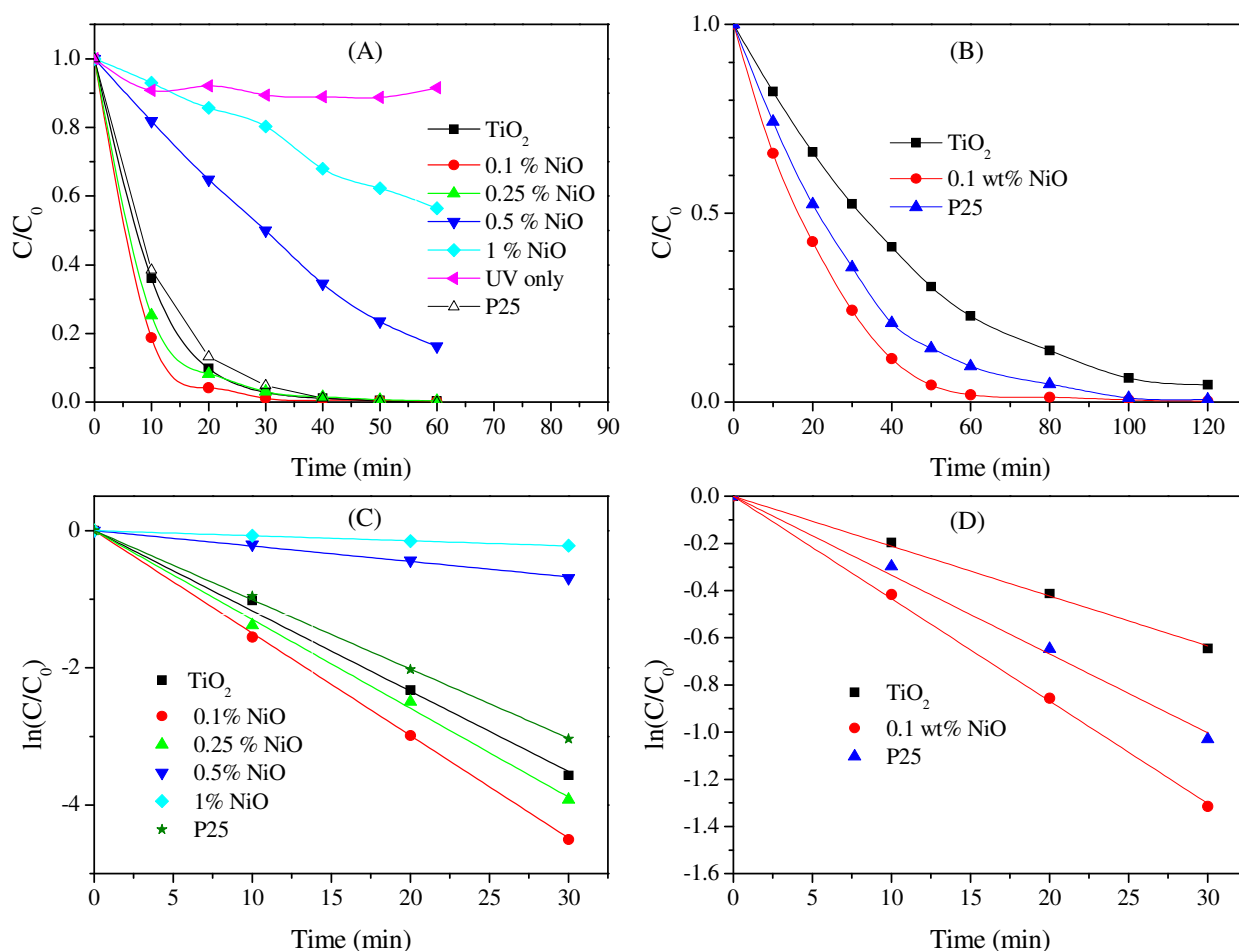


Figure V-19: Kinetic of photodegradation of (A) MB (B) MO and pseudo-first order kinetic for the photodegradation of (C) MB and (D) MO.

To quantitatively understand the reaction kinetics of the MB and the MO degradation in our experiments, a pseudo-first order model expressed by the equation $\ln(C/C_0) = -k_{app}t$ was used, which can be generally admitted for photocatalytic degradation if the initial

concentration of the pollutant is low. C_0 and C are the concentrations of dye in the solution at time 0 and t , respectively, and k_{app} is the pseudo-first order apparent rate constant. Plotting $\ln(C/C_0)$ versus t gives the apparent rate constant (k_{app}) for the degradation of dyes, from the slope of the curve fitting line and the intercept is equal to zero. **Figure V-19C and D** show that the photodegradation of MB and MO by the heterostructure NiO/TiO₂ nanocomposites obeyed the pseudo-first order reaction kinetics. The apparent rate constants obtained from the slope of the plot of $\ln(C/C_0)$ vs t and the normalized rate constant (k_{norm}) defined as $k_{norm} = k_{app}/S_{BET}$ for the degradation of MB and MO are shown in **Table V-3**. A good correlation with pseudo-first order reaction kinetics ($R^2 > 0.99$) was found. The reaction rate constant, k_{app} was found to be 0.117, 0.149, 0.129, 0.022, 0.007 and 0.101 min⁻¹ for TiO₂, 0.1 wt% NiO/TiO₂, 0.25 wt% NiO/TiO₂, 0.5 wt% NiO/TiO₂, 1 wt% NiO/TiO₂ and P25, respectively, for the degradation of MB. It is clear that the reaction rate of 0.1 wt% NiO/TiO₂ nanocomposite samples was higher than that of as-synthesized TiO₂. Especially, the nanocomposite photocatalytic activity of the heterostructure 0.1 wt% NiO/TiO₂ nanocomposite was even higher than that of commercial P25. Similarly, the rate constant of 0.1 wt% NiO/TiO₂ (0.048 min⁻¹) was about 2.3 times higher than that of the as-synthesized TiO₂ (0.021 min⁻¹) for the degradation of MO. Finally, regardless of the photocatalysts studied, the degradation rate of MB was faster than that of MO.

Table V-3: Apparent rate constant for the degradation of MB and MO with the as-synthesized photocatalysts.

Photocatalysts	Dye	k_{app} , min ⁻¹	S_{BET} , m ² /g	K_{norm} , g/(m ² .min)	R^2
TiO ₂	MB	0.117	72	1.63 x 10 ⁻³	0.999
0.1 wt% NiO/TiO ₂	MB	0.149	70	2.14 x 10 ⁻³	0.999
0.25 wt% NiO/TiO ₂	MB	0.129	69	1.87 x 10 ⁻³	0.992
0.5 wt% NiO/TiO ₂	MB	0.022	67	0.32 x 10 ⁻³	0.995
1 wt% NiO/TiO ₂	MB	0.007	65	0.11 x 10 ⁻³	995
TiO ₂ (Degussa P25)	MB	0.101	47	2.12 x 10 ⁻³	0.999
TiO ₂	MO	0.021	72	0.29 x 10 ⁻³	0.998
0.1 wt% NiO/TiO ₂	MO	0.048	70	0.65 x 10 ⁻³	0.993
TiO ₂ (Degussa P25)	MO	0.033	47	0.70 x 10 ⁻³	0.995

One of today's main industrial wastewater treatment strategies is focused on the development of green technologies and management practices for environmental benefit. Then, the recycling of used photocatalysts can be foreseen as a good practice for sustainable wastewater treatment. Consequently, it is necessary to demonstrate whether, after a photocatalytic treatment, the catalyst can be reused. The NiO/TiO₂ catalyst with 0.1 wt% NiO content was used and recycled for consecutive reuse on MB degradation; the process was repeated up to four times. The recyclability of the NiO/TiO₂ nanocomposites with 0.1 wt% NiO content was investigated by performing recycling experiments and the efficiency of the photodegradation process was evaluated and compared between the reuse cycles. **Figure V-20** shows the performance of a recycled NiO/TiO₂ sample measured under identical conditions over four recycle tests. There was no noticeable change in the photocatalytic activity of the recycled catalyst after four cycles under UV light irradiation, which indicated that the as-synthesized photocatalysts displayed a high stability, recyclability and an efficient photoactivity for degradation of the organic pollutants under UV light irradiation.

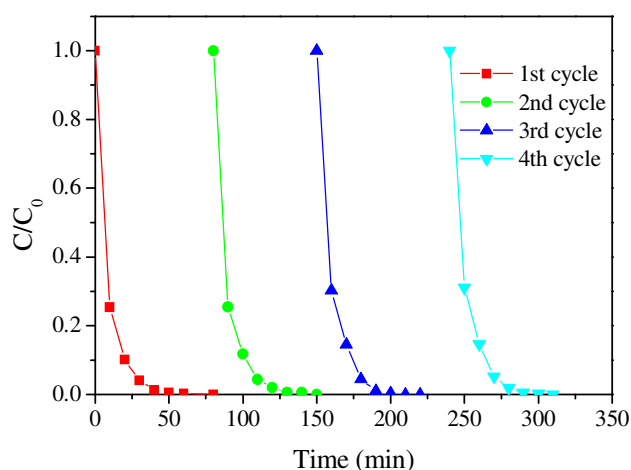
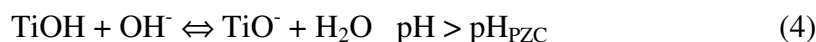
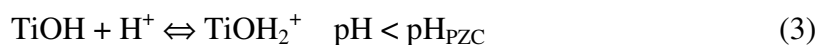


Figure V-20: Recyclability of 0.1 wt% NiO/TiO₂ photocatalysts for the degradation of MB.

In order to investigate the effect of solution pH on the photocatalytic degradation of MB, experiments were carried out at pH 2.5, 7.2 and 10.1. The results are depicted in **Figure V-21**. It can be seen that the best photocatalytic activity was obtained in alkaline medium. The photocatalytic degradation efficiencies were 94%, 81% and 3% at pH 10.1, 7.2 and 2.5, respectively, after 10 min of irradiation. In fact, the dye was completely mineralized within 30 min at a pH above 7. On the other hand, only 12% of dyes were decomposed in acidic medium even after 80 min. As the NiO content in the NiO/TiO₂ composite was low, we could explain the higher photocatalytic activity of the as-synthesized photocatalysts by the

amphoteric behaviour of semiconducting titanium dioxide and the change of the surface charge properties of TiO_2 with the changes of pH around its point of zero charge (pH_{PZC}) according to the following reaction:



pH changes can thus influence the adsorption of dye molecules onto the catalysts surface, an important step for the photocatalytic oxidation to take place. Ku *et al.*⁴¹ found that the pH_{PZC} of NiO/TiO_2 nanocomposites containing NiO in the range of 0.1 to 5% to be of 5.6-6.7. On the other hand, MB in aqueous solution of pH higher than 3.8 exists as cation as the pK_a value of MB is 3.8 already mentioned in Chapter IV. The surface of NiO/TiO_2 would be negatively charged in the alkaline media ($\text{pH} > 6.7$) and adsorb cationic MB easily as a result of electrostatic attraction of the negatively charged NiO/TiO_2 with the cationic MB dye. Under acidic conditions, it is difficult for cationic MB dye to adsorb onto the positively charged catalyst surface

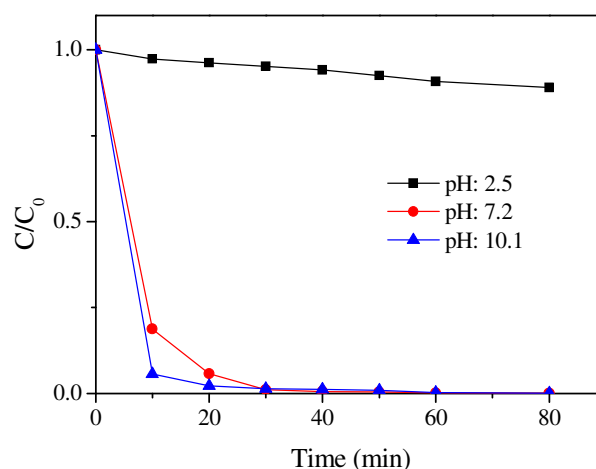


Figure V-21: Effect of initial solution pH on the photocatalytic degradation of MB over 0.1 wt% NiO/TiO_2 .

The enhanced photocatalytic activity of heterostructure NiO/TiO_2 nanocomposites was related to the role of NiO on the surface of TiO_2 nanoparticles. The photogenerated charge separation and the photocatalytic mechanism of the heterostructured NiO/TiO_2 nanocomposite system are depicted in the schematic diagrams as shown in **Figure V-17** and **Figure V-22**.

We have found that that the works function of NiO (5.4 eV) is larger than that of TiO₂ (4.15 eV). The Fermi energy level of TiO₂ is higher than that of NiO due to its smaller work function. When the p-type NiO and n-type TiO₂ formed the p-n heterojunction, the electron transfer occurred from TiO₂ to NiO while the hole transfer occurred from NiO to TiO₂ until the system attained equilibration due to the carrier transfer between the NiO and TiO₂. Meanwhile, an inner electric field was built up at the interface between NiO and TiO₂ because of electron and hole transfer. When the p-type NiO and n-type TiO₂ heterojunction was excited by UV light with a photon energy higher or equal to the band gaps of NiO and TiO₂, the electrons in the VB could be excited to the CB with simultaneous generation of the same amount of holes in the VB. From the energy band structure diagram of the p-type NiO and n-type TiO₂ heterojunction (**Figure V-22**), it can be inferred that the photogenerated electron transfer occurred from the CB of NiO to the CB of TiO₂ and, conversely, the photogenerated hole transfer could take place from the VB of TiO₂ to the VB of NiO, suggesting that the photogenerated electrons and holes were efficiently separated. Alternatively also an electron (of TiO₂)/hole (of NiO) recombination may take place at the heterojunction interface (Z-scheme). The efficient charge separation could increase the lifetime of the charge carriers and enhance the efficiency of the interfacial charge transfer to adsorbed substrates and then account for the higher activity of the p-type NiO and n-type TiO₂ heterojunction nanocomposites.

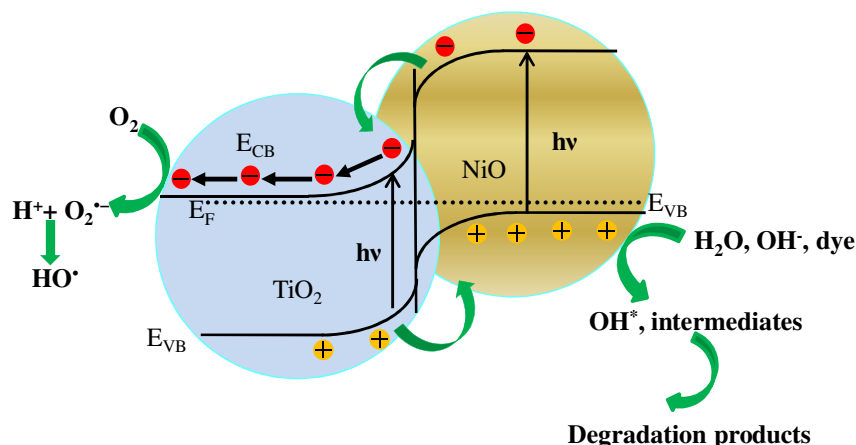
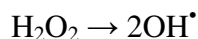
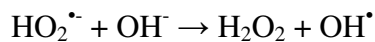
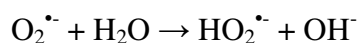
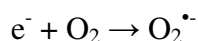
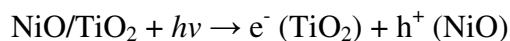


Figure V-22: Schematic representation of the photogenerated charge separation mechanism of NiO/TiO₂ nanocomposites.

As a consequence, the following photocatalytic reaction process can be proposed which is similar to those described in the previous chapters for RuO₂/TiO₂ and RuO₂/ZnO systems.



Under UV light irradiation, the photogenerated electrons moved to the TiO₂ side; meanwhile, the photogenerated holes moved to the NiO side. Subsequently, the electrons in the conduction band of TiO₂ react with molecular oxygen adsorbed on the surface of TiO₂ to generate superoxide radicals anion (O₂^{•-}). The O₂^{•-} radicals further react with H₂O to produce OH[•] radicals, which was a strong oxidizing agent for decomposing the organic dye. In contrast, holes on the NiO surface take part in the oxidation reaction with surface adsorbed dye molecules leading to the final degradation products.

V.3.3.2. Photocatalytic hydrogen production

The photocatalytic activity of the as-synthesized NiO/TiO₂ heterojunction photocatalysts was also investigated by the photocatalytic hydrogen production from the suspension of the photocatalysts containing different amount of NiO (0.25-4 wt%) in a deaerated aqueous methanol solution (v:v 1:1) under UV light irradiation for 6 h using 1.6 W Hg vapour light source. Blank experiment revealed that there was no significant production of hydrogen (H₂) in the absence of catalyst or methanol as shown in **Figure V-23A**. Moreover, water alone did not show any evidence of H₂ evolution upon the irradiation. However, the irradiation of NiO/TiO₂ suspensions containing methanol led to the observable evolution of H₂ gas (**Figure V-23A**) indicating that both the photocatalysts and the sacrificial agent are essential for photocatalytic H₂ production.

Typical representations of the photocatalytic evolution of gas as a function of time for the NiO/TiO₂ samples with various NiO loading are shown in **Figure V-23B**. It was found that the amount of evolved gas was increased linearly over the experimental irradiation time of 6 h indicating that the as-synthesized photocatalyst was stable. This finding was fully consistent with the good recycling of this photocatalyst evidenced for the photocatalytic

degradation of MB. In addition, the evolved gas was analyzed by gas chromatography to know the composition of the obtained gas. The results showed negligible amount of CO_2 , CO and CH_4 in the evolved gas and most of the product was H_2 . The calculated amount of H_2 production after subtracting the gas evolved in the blank experiment are shown in **Figure V-23C**. Regardless of the amount of NiO loading, the NiO/TiO₂ photocatalysts showed higher photocatalytic production of H_2 compared to pure TiO₂ or commercial TiO₂ (Degussa P25).

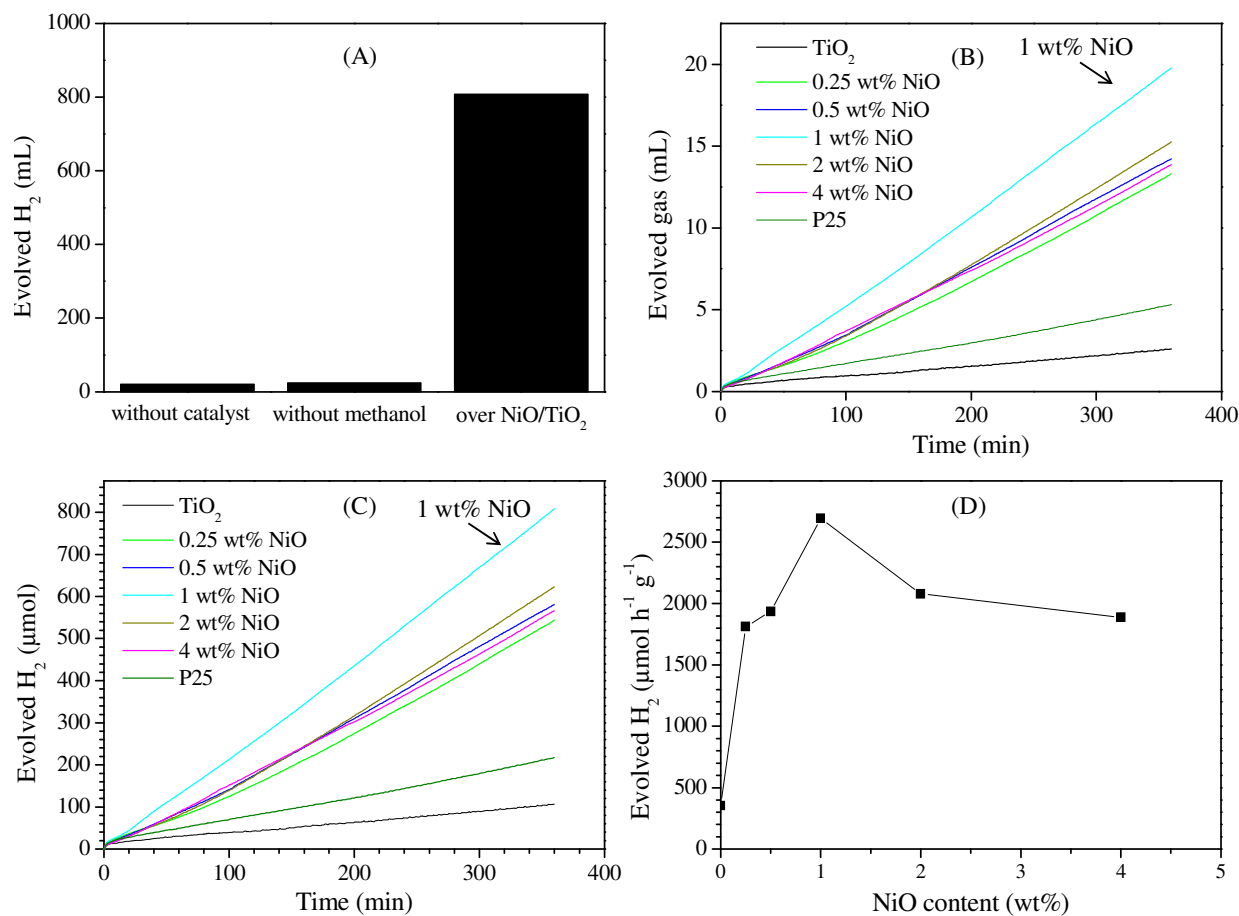


Figure V-23: Photocatalytic evolution of H_2 under different condition (A) photocatalytic evolution of gas (B) and H_2 (C) over TiO₂ and NiO/TiO₂ photocatalysts and effect of NiO loading on the H_2 production (D). All the experiments were run for 6 h at identical condition (photocatalyst, 0.05 g; water, 5 mL; methanol, 5 mL).

After 6 h irradiation, the H_2 production in the presence of pure TiO₂ was 106.5 μmol , while it was 808 μmol when 1 wt% NiO/TiO₂ was used as catalyst. To get a deeper understanding in the process involved, the H_2 evolution rate was plotted as a function of the NiO loading (**Figure V-23D**). It was seen that the activity towards H_2 production increased with

increasing NiO content up to about 1 wt% NiO and then decreased thereafter. A similar trend was observed for RuO₂/TiO₂ system discussed in chapter IV. With an increase in NiO content from 0.25 wt% to 1 wt%, the H₂ production rate gradually increased from 1812 μmol h⁻¹g⁻¹ to 2693 μmol h⁻¹g⁻¹. In contrast, with further increase in NiO content from 1 wt% to 4 wt%, the H₂ production rate dropped from 2693 μmol h⁻¹g⁻¹ to 1888 μmol h⁻¹g⁻¹. This suggested that the optimum loading of NiO was about 1 wt%. It can be proposed that, when the NiO content was lower than its optimum value, the trapping sites of carriers increased with the increase of the amount of NiO, which prolonged the lifetime of carriers, thus improving the photocatalytic activity. Therefore, the photoreduction activity increased. But when the amount of NiO was higher than its optimum value, the decrease in the photocatalytic activity might be attributed to the excess of NiO nanoparticles on the photosensitive TiO₂ surface, which caused the decrease in the light absorption capability and accordingly lower the photogenerated electrons. In addition, when the loading of NiO was higher than the optimum value, the depth of penetration of the light to the TiO₂ became extremely small, scattering was much increased, and a detrimental effect on the reaction rate was developed.

The as-synthesised NiO/TiO₂ nanocomposites prepared by sol-gel process in this study showed a higher photocatalytic activity for the production of hydrogen than that reported in the literature. Recently, Elouali *et al.*^{8b} reported the H₂ production rate of platinumized commercial TiO₂ (Inorganic PC50) in suspension to be 263.3 μmol h⁻¹g⁻¹ which was almost identical to an equal weight of a PC50 ceramic wafer coated one side with Pt. However, loading of NiO as co-catalyst lowered the hydrogen production rate to 85.5 μmol h⁻¹g⁻¹ and increased the oxygen production rate. In another study, Shreethawong *et al.*^{8a} investigated the sacrificial hydrogen production of mesoporous TiO₂ supported NiO photocatalyst from an aqueous methanol solution using 300 W high pressure Hg lamp as UV light source. The highest H₂ production rate obtained was 811 μmol h⁻¹g⁻¹, which is much

lower than the maximum H₂ production rate reached in the present study, i. e. 2693 μmol h⁻¹ g⁻¹.

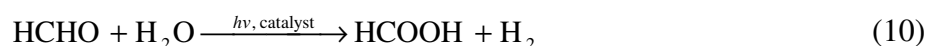
On the basis of the above results and as proposed for the RuO₂/TiO₂ system in chapter IV, the possible photoreactions on the photocatalysts are the following



The overall reaction is



The product, formaldehyde (HCHO), could be further oxidized to methanoic acid HCOOH and subsequently to CO₂ together with hydrogen generation via eqs



In the absence of oxygen, the photogenerated holes react with sacrificial agent methanol (CH₃OH) to produce $\cdot\text{CH}_2\text{OH}$ radical (Eq. (6)). The $\cdot\text{CH}_2\text{OH}$ radical possesses sufficiently negative oxidation potential (-0.74 V) and could further react to produce H⁺, electron and HCHO ((Eq. (7)).⁴² On the other hand, electrons in the conduction band of the particle will simultaneously reduce water or protons in the solution to form gaseous H₂ as shown by Eq. (8). These reactions proceed competitively with the recombination of the photoinduced electrons and holes

V.4. Conclusions

Mesoporous heterostructure NiO/TiO₂ nanoparticles photocatalysts have been successfully prepared by a single-step sol-gel route using titanium n-butoxide and nickel nitrate as precursors followed by calcination at 500 °C. XRD analysis showed that the as-synthesized TiO₂ was completely anatase phase with no trace of any other phase, which was confirmed by Raman spectroscopy. The UV-Vis diffuse reflectance studies showed that the band gap energy of the heterostructure NiO/TiO₂ photocatalyst was red-shifted compared to

that of TiO₂. XPS and UPS have been used to determine the energy level line up at the interface of p-n NiO/TiO₂ heterojunction nanoparticle from the shift of Ti 2p_{3/2} and Ni 2p_{3/2} core level spectra. A shift of Ti 2p_{3/2} and Ni 2p_{3/2} core level spectra were observed to be 0.4 ± 0.1 and 0.6 ± 0.1 eV, respectively, which were ascribed to band bending at the interface of heterojunction NiO/TiO₂ nanoparticles. The investigation of the photocatalytic ability indicated that the p-n NiO/TiO₂ heterojunction nanoparticles containing 0.1 wt% NiO possessed higher photocatalytic activity than the pure TiO₂ and commercial TiO₂ P25 for the degradation of MB and MO dyes under UV light irradiation due to the enhanced separation efficiency of photogenerated electron-hole pairs from the p-n heterojunctions. In addition, the heterostructure photocatalysts could be easily recycled without any significant change in the catalytic activity which evidenced the stability of the catalysts and the reproducibility of the approach. The photocatalytic activity of the as-synthesized NiO/TiO₂ heterojunction nanoparticles was also investigated by the production of H₂ in an aqueous solution of methanol at ambient temperature under UV irradiation. The greater photocatalytic activity for H₂ evolution was obtained for the entire investigated range of NiO loading. The optimum level of NiO was found at 1 wt% with average H₂ production rate of $2693 \mu\text{mol h}^{-1}\text{g}^{-1}$. To the best of our knowledge, the sol-gel 1 wt% NiO/TiO₂ nanocomposite developed in this work is the most efficient NiO/TiO₂ system ever reported to generate hydrogen. This higher photocatalytic activity for degrading organic dye and producing H₂ was related to the higher charge separation resulting from internal electric field developed at the interface of the NiO/TiO₂ heterojunction. Thus, the enhanced photocatalytic activities of heterojunction photocatalysts resulting from reduced charge recombination will allow us to use these systems in various applications such as photocatalytic water/air purification and photocatalytic hydrogen production.

¹ (a) Liao, S.; Donggen, H.; Yu, D.; Su, Y.; Yuan, G. *J. Photochem. Photobiol. A* **2004**, *168*, 7. (b) Liao, D. L.; Badour, C. A.; Liao, B. Q. *J. Photochem. Photobiol. A* **2008**, *194*, 11. (c) Shifu, S.; Wei, Z.; Wei, L.; Sujuan, Z. *Appl. Surf. Sci.* **2008**, *255*, 2478. (d) Ge, M.; Guo, C.; Zhu, X.; Ma, L.; Han, Z.; Hu, W.; Wang, Y. *Front. Environ. Sci. Engin. China* **2009**, *3*, 271. (e) Tian, J.; Chen, L.; Yin, Y.; Wang, X.; Dai, J.; Zhu, Z.; Liu, X.; Wu, P. *Surf. Coat. Technol.* **2009**, *204*, 205. (f) Zhang, M.; An, T.; Liu, X.; Hu, X.; Sheng, G.; Fu, J. *Mater. Lett.* **2010**, *64*, 1883. (g) Mani, J.; Sakeek, H.; Habouti, S.; Dietze, M.; Souni, M. E. *Catal. Sci. Technol.* **2012**, *2*, 379.

² (a) Lin, C. C.; Chiang, Y. J. *Chem. Eng. J.* **2012**, *181-182*, 196. (b) Yang, Z.; Lv, L.; Dai, Y.; Xv, Z.; Qian, D.; *Appl. Surf. Sci.* **2010**, *256*, 2898. (c) Cun, W.; Wang, X.; Xu, B. Q.; Zhao, J.; Mai, B.; Peng, P.; Sheng, G.; Fu, J. *J. Photochem. Photobiol. A* **2004**, *168*, 47. (d) Zhang, M.; An, T.; Hu, X.; Wang, C.; Sheng, G.; Fu, J. *Appl. Catal. A* **2004**, *260*, 215. (e) Zhang, M.; Sheng, G.; Fu, J.; An, T.; Wang, X.; Hu, X. *Mater. Lett.* **2005**, *59*, 3641. (f) Cun, W.; Jincai, Z.; Xinming, W.; Bixian, M.; Guoying, S.; Pingan, P.; Jiamo, F. *Appl. Catal. B* **2002**, *39*, 269. (g) Wang, H.; Baek, S.; Lee, J.; Lim, S. *Chem. Eng. J.* **2009**, *146*, 355.

³ (a) Vinodgopal, K.; Kamat, P. V. *Environ. Sci. Technol.* **1995**, *95*, 841. (b) Zhou, M.; Yu, J.; Liu, S.; Zhai, P.; Jiang, L. *J. Hazard. Mater.* **2008**, *154*, 1141. (c) Hattori, A.; Tokihisa, Y.; Tada, H.; Ito, S. *J. Electrochem. Soc.* **2000**, *147*, 2279. (d) Akurati, K. K.; Vital, A.; Hany, R. Bommer, B.; Graule, T.; Winterer, M. *Int. J. Photoenergy*, **2005**, *7*, 153. (e) Hou, L. R.; Yuan, C. Z.; Peng, Y. *J. Hazard. Mater. B* **2007**, *139*, 310. (f) Shifu, C.; Lei, C.; Shen, G.; Gengu, C. *Mater. Chem. Phys.* **2006**, *98*, 116.

⁴ (a) Li, X. Z.; Li, F. B.; Yang, C. L.; Ge, W. K. *J. Photochem. Photobiol. A* **2001**, *141*, 209. (b) Yang, H.; Shi, R.; Zhang, K.; Hu, Y.; Tang, A.; Li, X. *J. Alloys Compd.* **2005**, *398*, 200. (c) Yang, H.; Zhang, D.; Wang, L. *Mater. Lett.* **2002**, *57*, 674. (d) Sajjad, A. K. L.; Shamaila, S.; Tian, B. Z.; Chen, F.; Zhang, J. L. *Appl. Catal. B* **2009**, *91*, 397. (e) Delgado, N. A. R.; Reyes, L. H.; Mar, I. L. G.; Pinilla, M. A. G.; Ramirez, A. H. *Catal. Today* **2013**, <http://dx.doi.org/10.1016/j.cattod.2012.11.011>. (f) Hathway, T.; Rockafellow, E. M.; Oh, Y. C.; Jenks, W. S. *J. Photochem. Photobiol. A* **2009**, *207*, 197. (g) Piszcz, M.; Tryba, B.; Grzmil, B.; Morawski, A. M. *Catal. Lett.* **2009**, *128*, 190.

⁵ (a) Cavas, M.; Gupta, R. K.; Al-Ghamdi, A. A.; Serbetci, Z.; Gafer, Z. H.; El-Tantawy, F.; Yakuphanoglu, F. *J. Electroceram.* **2013**, DOI: 10.1007/s10832-013-9822-z. (b) Shifu, C.; Sujuan, Z.; Wei, L. Wei, Z. *J. Hazard. Mater.* **2008**, *155*, 320. (c) Lee, Y. M.; Hsu, C. H.; Chen, H. W. *Appl. Surf. Sci.* **2009**, *255*, 4658.

⁶ Zhang, Z.; Shao, C.; Li, X.; Wang, C.; Zhang, M.; Liu, Y. *ACS Appl. Mater. Interfaces* **2010**, *2*, 2915.

⁷ (a) Sim, L. C.; Ng, K. W.; Ibrahim, S.; Saravanan, P. *Int. J. Photoenergy* **2013**, article ID 659013. (b) Chen, C. J.; Liao, C. H.; Hsu, K. C.; Wu, Y. T.; Wu, J. C. S. *Catal. Commun.* **2011**, *12*, 1307. (c)

- Kamegawa, T.; Kim, T. H.; Morishima, J.; Matsuoka, M.; Anpo, M. *Catal. Lett.* **2009**, *129*, 7. (d) Ku, Y.; Lin, C. N.; Hou, W. M. *J. Mol. Catal. A: Chem.* **2011**, *349*, 20. (e) Ahmed, M. A. *J. Photochem. Photobiol. A* **2012**, *238*, 63. (f) Iwaszyk, A.; Nilan, M.; Jin, Q.; Fujishima, M.; Tada, H. *J. Phys. Chem. C* **2013**, *117*, 2709. (g) Jin, Q.; Ikeda, T.; Fujishima, M.; Tada, H. *Chem. Commun.* **2011**, 47, 8814. (h) Lin, J.; Shen, J.; Wang, R.; Cui, J.; Zhou, W.; Hu, P.; Liu, D.; Liu, H.; Wang, J.; Boughton, R.I.; Yue, Y. *J. Mater. Chem.* **2011**, *21*, 5106.
- ⁸ (a) Sreethawong, T.; Suzuki, Y.; Yoshikawa, S. *Int. J. Hydrogen Energy* **2005**, *30*, 1053. (b) Elouali, S.; Mills, A.; Parkin, I. P.; Bailey, E.; McMillan, P. F.; Darr, J. A. *J. Photochem. Photobiol. A* **2010**, *216*, 110.
- ⁹ Sreethawong, T.; Ngamsinlapasathian, S.; Yoshikawa, S. *Chem. Eng. J.* **2012**, *192*, 292.
- ¹⁰ Gou, J.; Fu, W.; Yang, H.; Yu, Q.; Zhao, W.; Zhao, X.; Sui, Y.; ding, j.; Li, Y.; Cheng, S.; Li, M. *J. Phys. D: Appl. Phys.* **2010**, *43*, 245202.
- ¹¹ Chockalingam, K.; Ganapathy, A.; Paramasivan, G.; Govindasamy, M.; Viswanathan, A. *J. Am. Ceram. Soc.* **2011**, *94*, 2499.
- ¹² (a) Nakayama, T. *J. Electrochem. Soc.* **1994**, *141*, 237. (b) Suda, Y.; Morimoto, T. *Langmuir* **1987**, *3*, 786. (c) Tanaka, K.; White, J. M. *J. Phys. Chem.* **1982**, *86*, 4708. (d) Sanchez, E.; Lopez, T.; Gomez, R.; Bokhimi; Morales, A.; Novaro, O. *J. Solid State Chem.* **1996**, *122*, 309.
- ¹³ Parra, R.; Góes, M. S.; Castro, M. S.; Longo, E.; Bueno, P. R.; Varela, J. A. *Chem. Mater.* **2008**, *20*, 143.
- ¹⁴ Wang, D.; Xiao, L.; Luo, Q.; Li, X.; An, J.; Duan, Y. *J. Hazard. Mater.* **2011**, *192*, 150.
- ¹⁵ Yu, B.; Jiang, X.; Yin, J.; *Nanoscale*, **2013**, *5*, 5489.
- ¹⁶ Zhou, W.; Zhou, Y.; Tang, S. *Mater. Lett.* **2005**, *59*, 3115.
- ¹⁷ Tebby, Z.; Babot, O.; Toupance, T.; Park, D. H.; Campet, G.; Delville, M. H. *Chem. Mater.* **2008**, *20*, 7260
- ¹⁸ (a) Dogan, G.; Tomkiewicz, M. *J. Phys. Chem.* **1993**, *97*, 12651. (b) Zhu, Z.; Tsung, L. Y.; Tomkiewicz, M. *J. Phys. Chem.* **1995**, *99*, 15945, 15950.
- ¹⁹ Popa, M.; Diamandescu, L.; Vasiliu, F.; Teodorescu C. M.; Cosoveanu, V.; Baia, M.; Feder, M.; Baia, L.; Danciu, V. *J. Mater. Sci.* **2009**, *44*, 358.
- ²⁰ Ohsaka, T. *J. Phys. Soc. Jpn* **1980**, *48*, 1661.
- ²¹ (a) Gupta, S. K.; Desai, R.; Jha, P. K.; Sahoo, S.; Kirin, D. *J. Raman Spectrosc.* **2010**, *41*, 350. (b) Stengl, V.; Grygar, T. M. *Int. J. Photoenergy* **2011**, ID 685935.
- ²² Balaji, S.; Djaoued, Y.; Robichaud, J. *J. Raman Spectrosc.* **2006**, *37*, 1416.
- ²³ Sing, K. S. W.; Everett, D. H.; Haul, R. A. W.; Moscou, L.; Pierotti, R. A.; Rouquerol, J.; Siemieniowska, T. *Pure Appl. Chem.* **1985**, *57*, 60.

- ²⁴ Guo, J.; Fu, W. Y.; Yang, H. B.; Yu, Q. J.; Zhao, W. Y.; Zhou, X. M.; Sui, Y. M.; Ding, J.; Li, Y. G.; Cheng, L. S.; Li, M. H. *J. Phys.D: Appl. Phys.* **2010**, *43*, 245202.
- ²⁵ Mor, G. K.; Prakasam, H. E.; Varghese, O. K.; Shankar, K.; Grimes, C. A. *Nano Lett.* **2007**, *7*, 2356.
- ²⁶ Bokhimi, X.; Morales, A.; Novaro, O. *Chem. Mater.* **1997**, *9*, 2616.
- ²⁷ (a) Wang, Z.; Helmersson, U.; Käll, P. O. *Thin Solid Films* **2002**, *405*, 50. (b) Sen, S.; Mahanty, S.; Roy, S.; Heintz, O.; Bourgeois, S.; Chaumont, D. *Thin Solid Films* **2005**, *474*, 245. (c) Coronado, D. R.; Gattorno, G. R.; Pesqueira, M. E. E.; Cross, R. D.; Oskam, G. *Nanotechnol.* **2008**, *19*, 145605.
- ²⁸ (a) Iwaszuk, A.; Nolan, M.; Jin, Q.; Fujishima, M.; Tada, H. *J. Phys. Chem. C* **2013**, *117*, 2709. (b) Kavan, L.; Stato, T.; Gratzel, M.; Fitzmaurice, D.; Shklover, V. *J. Phys. Chem.* **1993**, *97*, 9493.
- ²⁹ Patil, P. S.; Kadam, L. D.; *Appl. Surf. Sci.* **2002**, *199*, 211.
- ³⁰ Hufner, S. *Adv. Phys.* **1994**, *43*, 183.
- ³¹ (a) Adler, D.; Feinlieb, J. *Phys. Rev. B* **1970**, *2*, 3112. (b) Tsuboi, T.; Kleeman, W. *J. Phys.: Condens. Matter* **1994**, *6*, 8625. (c) Boschloo, G.; Hagfeldt, A. *J. Phys. Chem. B* **2001**, *105*, 3039.
- ³² Gupta, R. K.; Ghosh, K.; Kahol, P. K. *Physica E* **2009**, *41*, 617.
- ³³ (a) Zhang, Z.; Shao, C.; Li, X.; Wang, C.; Zhang, M.; Liu, Y. *ACS Appl. Mater. Interfaces* **2010**, *2*, 2915. (b) Manikandan, A.; Vijaya, J. J.; Kennedy, L. J. *Physica E* **2013**, *49*, 117.
- ³⁴ Yoshitake, M.; Thananan, A.; Aizawakia, T.; Yoshihara, K. *Surf. Interface Anal.* **2002**, *34*, 698.
- ³⁵ Cao, X.; Jing, W.; Xing, W.; Fan, Y.; Kong, Y.; Dong, J. *Chem. Commun.* **2011**, *47*, 3457.
- ³⁶ Xu, L.; Zheng, R.; Liu, S.; Song, J.; Chen, J.; Dong, B.; Song, H. *Inorg. Chem.* **2012**, *51*, 7733.
- ³⁷ (a) Zabova, H.; Sobek, J.; Cirkva, V.; Solcova, O.; Kment, S.; Hajek, M. *J. Solid State Chem.* **2009**, *182*, 3387. (b) Bullock, E. L.; Patthey, L.; Steinemann, S. G. *Surf. Sci.* **1996**, *352*, 504. (c) Takahashi, I.; Payne, D. J.; Palgrave, R. G.; Egdell, R. G. *Chem. Phys. Lett.* **2008**, *454*, 314.
- ³⁸ Liu, G.; Schulmeyer, T.; Brotz, J.; Klein, A.; Jaegermann, W. *Thin Solid Films*, **2003**, *431-432*, 477.
- ³⁹ Evans, D. A.; Steiner, H. J.; Roberts, A. R. V.; Dhanak, V.; Cabailh, G.; O'Brien, S.; McGovern, I. T.; Braun, W.; Kampen, T. U.; Park, S.; Zahn, D. R. T. *Appl. Surf. Sci.* **2003**, *212-213*, 417.
- ⁴⁰ M. C.; Payne, B. P.; Biesinger, Lau, L. W. M.; Gerson, A.; Smart, R. S. C. *Surf. Interface Anal.* **2009**, *41*, 324.
- ⁴¹ Ku, Y.; Lin, C. N.; Hou, W. M. *J. Mol. Catal. A: Chem.* **2011**, *349*, 20.
- ⁴² Perissinotti, L. L.; Brusa, M. A.; Grela, M. A. *Langmuir* **2001**, *17*, 8422.

General conclusion and perspectives

It is now well-established that energy production and environmental challenges constitute paramount issues for the 21st century. Thus, limited fossil fuel resources and strict environmental regulations motivate the search for sustainable, efficient and environmentally friendly energy sources. For instance, hydrogen produced from renewable sources has great potential as a future energy carrier. On the other hand, acute problems related to hazardous organic waste remediation have emerged as an international priority. In this context, photocatalytic processes over semiconducting oxide surfaces have attracted significant attention in recent years as potentially efficient, environmentally friendly, and low cost methods for water/air purification as well as for renewable hydrogen production. However, the recombination of photogenerated electron-hole pairs that result in low photocatalytic efficiency has hampered the industrialization of this technology. To elaborate new perspectives in this field, this work deals with the improvement of the efficiency of the photocatalytic process by reducing the recombination via vectorial charge transfer. In this aim, new heterostructure photocatalysts were developed by depositing metallic oxide on the surface of semiconductors or by coupling two semiconductors with suitable band edge position.

First of all, the theory and background necessary to understand semiconductor photocatalysis were detailed, with a peculiar emphasis laid on the electronic and optical properties of the bulk and nanoparticulate semiconducting materials. This was followed by the discussion of the basic principles of semiconductor photocatalysis and the thermodynamics that governs the photocatalytic performance. In the second chapter, heterostructure photocatalyst systems based on titanium dioxide (TiO₂), zinc oxide (ZnO) and tin dioxide (SnO₂) were reviewed with a particular focus on the strategies to improve the photocatalytic activity. Electronic modification of the catalyst by deposition of metal particles or other semiconductor particles showed a strong effect on the photoactivity of the system resulting from the efficient electron-hole pair separation and the dynamics of interfacial charge transfer. However, a systematic study of the effect of various parameters such as specific surface area, porosity and energy band alignment in such systems was still largely unexplored.

To draw new prospects in this field, three different kinds of heterostructure system such as n-type/n-type semiconductor (SnO₂/ZnO), metal/n-type semiconductor (RuO₂/TiO₂ and RuO₂/ZnO) and p-type/n-type semiconductor (NiO/TiO₂) heterojunction photocatalysts were synthesized, characterized and their photocatalytic activities were investigated for the

degradation of organic dyes and the production of hydrogen. These catalysts are individually discussed below with highlight to the charge separation mechanism at the interface of the heterostructure that resulted in enhanced photocatalytic efficiency for the degradation of methylene blue (MB), methyl orange (MO) and the production of hydrogen. For each system, we described a powerful tool based on a combination of XPS/UPS studies with UV-Visible absorption data to determine accurately the energy band alignment allowing for the rationalization of the photocatalytic properties.

In a first step, the SnO₂/ZnO system was studied as a model heterostructure n-type/n-type semiconductor heterojunction photocatalyst in order to establish the general scientific methodology followed in this work. Mesoporous SnO₂/ZnO heterojunction photocatalyst was successfully prepared using a two-step solution route involving the synthesis of nanosized SnO₂ particles by the homogeneous precipitation combined with an hydrothermal treatment that were further reacted with zinc acetate followed by calcination. The UV-Visible diffuse reflectance (DRS) studies showed that the band gap energy of the heterostructure SnO₂/ZnO photocatalyst was red shifted compared to pure SnO₂ and ZnO. Special emphasis was given on the determination of band alignment at the interface of SnO₂/ZnO heterojunction. XPS was used as a direct method to measure the VBO of the heterostructure SnO₂/ZnO photocatalyst. A type-II band alignment with valence band offset (VBO) of $\Delta E_V = 0.7 \pm 0.05$ eV and conduction band offset (CBO) of $\Delta E_C = 0.2 \pm 0.05$ eV was obtained. The heterostructure SnO₂/ZnO photocatalyst showed higher photocatalytic activity than pure SnO₂ and ZnO for the degradation of MB dye under UV light irradiation. The degradation rate constant normalized with respect to BET specific surface area for heterostructure SnO₂/ZnO nanocomposite was 1.7 times higher than that of SnO₂ and was around 1.4 times higher than that of ZnO. The enhanced degradation rate was attributed to vectorial transfer of photogenerated electrons and holes resulting from the band discontinuity at the interface of the SnO₂/ZnO nanocomposites confirmed from band alignment. Furthermore, the heterostructure photocatalysts could be easily recycled without any significant change in the catalytic activity which indicated the stability and reproducibility of the catalysts. In addition, the high pH favoured the adsorption of cationic MB dye on the catalyst surface which resulted in high degradation efficiency. Finally, a mechanism was proposed for the photocatalytic degradation of MB.

In the next step, we focused our attention on developing heterostructure metal/n-type semiconductor RuO₂/TiO₂ photocatalysts, the ruthenium oxide being expected to act as a

quasi-metallic material. The target heterostructure was prepared by impregnation of TiO₂ nanoparticles, synthesized by the sol-gel process, in a ruthenium (III) acetylacetonate solution followed by annealing at 400 °C. Regardless of the RuO₂ amount, the as-synthesized nanocatalyst was made of a mesoporous network of aggregated TiO₂ anatase nanoparticles modified with RuO₂ according to N₂ sorption and transmission electron microscopy (TEM) studies. DRS showed that the heterostructure RuO₂/TiO₂ nanocomposites absorb light in the whole visible range which was attributed to surface plasmon resonance effect (SPR) suggesting that the obtained photocatalyst could be active in the visible region. In order to clarify the charge separation at the interface of the RuO₂/TiO₂ heterojunction, an energy band alignment was determined by XPS and UPS. At first, a model interface experiment was carried out by stepwise deposition of RuO₂ on the TiO₂ film. *In-situ* XPS measurement showed a shift of Ti 2p_{3/2} core level spectra toward lower binding energy of 1.22 eV which was ascribed to upward band bending at the interface of the RuO₂/TiO₂ heterojunction. The evident band bending for the heterostructure RuO₂/TiO₂ nanocomposites was determined to be 0.2 ± 0.05 eV. The photocatalytic decomposition of MB and MO in solution under UV light irradiation revealed that the heterostructure 1 wt% RuO₂/TiO₂ catalyst led to higher activities than pure anatase TiO₂ and reference commercial TiO₂ P25 nanoparticles. The degradation rate constant normalized with respect to BET specific surface area was 1.7 and 1.3 times higher than that of P25 for the degradation of MB and MO, respectively. In addition, recycling of the as-synthesized photocatalysts with no appreciable change in degradation rate constant confirmed the stability of the catalysts. Furthermore, the production of H₂ under UV irradiation in the presence of methanol as a hole scavenger was also achieved with this system. Irrespective of RuO₂ content, the hydrogen production rate over RuO₂/TiO₂ photocatalysts was higher than that of pure sol-gel TiO₂ and commercial P25 TiO₂. The 5 wt% RuO₂/TiO₂ photocatalysts showed higher catalytic activity with average hydrogen production rate of 618 μmol/h. This higher photocatalytic activity for the decomposition of organic dyes and producing H₂ was related to the higher charge separation efficiency resulting from the built-in potential developed at the interface of the RuO₂/TiO₂ heterojunction.

As the band gap energy and the photocatalytic mechanism of ZnO is similar to that of TiO₂, we have also developed an original heterostructure including both ZnO and RuO₂ by using a two-step procedure similar to that described for the RuO₂/TiO₂ nanocomposite: preparation of ZnO by homogenous precipitation method and subsequently RuO₂/ZnO by

impregnating ZnO in ruthenium (III) chloride hydrate solution followed by annealing. As for the RuO₂/TiO₂ system, the RuO₂/ZnO nanocomposite also showed light absorption in the visible region. An energy band diagram of RuO₂/ZnO nanocomposites was determined by XPS and UPS from the shift of the core level spectra. A shift of Zn 2p_{3/2} core level spectra was determined to be 0.42 ± 0.05 eV which was assigned to band bending at the interface of heterojunction RuO₂/ZnO nanoparticles. 4 wt% RuO₂/ZnO showed higher photocatalytic performance under UV illumination for the decomposition of MB and MO when compared with the pure ZnO and commercial TiO₂ P25. The degradation rate constants normalized with BET surface area of 4 wt% RuO₂/ZnO nanocomposite for the degradation of MB were 2.4 and 2 times higher than that of pure ZnO and P25, respectively, suggesting that the better photocatalytic performance of heterostructure RuO₂/ZnO nanocomposite was not due to surface area, but contributed to the synergistic action of RuO₂ and ZnO. A similar trend was also observed for the degradation of MO. The upward band bending of ZnO toward the interface facilitated to transfer the photogenerated electron to ZnO and hole to RuO₂ allowing vectorial charge separation that resulted in higher photocatalytic efficiency. Furthermore, the RuO₂/ZnO nanocomposites could also be easily recycled without any decrease of the photocatalytic activity evidencing the stability of the as-synthesized RuO₂/ZnO photocatalysts. To the best of our knowledge, this work constitutes the first evidence of the potentialities of RuO₂/ZnO nanocomposites in photocatalysis.

Finally, heterostructure p-type/n-type semiconductor NiO/TiO₂ photocatalyst was successfully prepared at room temperature by a single-step sol-gel route using titanium n-butoxide as the precursor followed by calcination at 500 °C. XRD analysis showed that the as-synthesized TiO₂ was completely anatase phase and no other phase was observed which was confirmed by the Raman spectroscopy. XRD analysis also revealed a crystallite size of TiO₂ dried at 150 °C of about 7.5 nm suggesting that the anatase TiO₂ nanoparticle was developed during synthesis at low temperature. The UV-Vis DRS studies revealed that the absorption edge of the coupled NiO/TiO₂ photocatalyst was shifted towards the visible region due to the introduction of NiO. The energy level line up at the p-n NiO/TiO₂ heterointerface was determined by XPS and UPS from the core level energy shift. A shift of Ti 2p_{3/2} and Ni 2p_{3/2} core level spectra were observed to be 0.4 ± 0.1 and 0.6 ± 0.1 eV, respectively, which were ascribed to band bending at the interface of heterojunction NiO/TiO₂ nanoparticles. The valence band offset (ΔE_{VB}^{inter}) and the conduction band offset (ΔE_{CB}^{inter}) at the interface were calculated to be of 1.5 ± 0.1 and 1.8 ± 0.1 eV, respectively. The band alignment at the

interface could explain the charge transfer at the NiO/TiO₂ heterojunction. It was found that the p-n NiO/TiO₂ heterojunction containing 0.1 wt% NiO possessed higher photocatalytic activity for the degradation of MB and MO than pure TiO₂ and P25. The photocatalytic activity of the as-synthesized NiO/TiO₂ heterojunction nanoparticles was also investigated by the production of H₂ in an aqueous solution of methanol at ambient temperature under UV irradiation. A greater photocatalytic activity for H₂ evolution was obtained for the entire investigated range of NiO loading. The optimum level of NiO was found at 1 wt% with average H₂ production rate of 135 μmol/h. This higher photocatalytic activity for degrading organic dye and producing H₂ was related to the higher charge separation efficiency resulting from the internal electric field developed at the interface of the NiO/TiO₂ heterojunction.

In summary, the concept of semiconducting heterojunction nanocatalysts with high photocatalytic activity has been rationalized in terms of energy band alignment. As a consequence, this technology should find industrial application in the future to remove undesirable organics from the environment and to produce renewable H₂.

The potential levels of the valence band and the conduction band edges play a vital role in predicting the type of reactions that can occur at the surface of the semiconductor photocatalysts. To achieve H₂ production, the conduction band potential of the semiconductor must be more negative than proton reduction potential of 0.0 V vs NHE at pH = 0 (-0.41 V at pH = 7). Meanwhile, the potential of valence band edge must be more positive than the oxidation potential of water of +1.23 V vs NHE at pH = 0 (+0.82 V at pH = 7).¹ As the conduction band position of ZnO is thermodynamically favourable to reduce water to hydrogen, the photocatalytic activity of RuO₂/ZnO nanocomposites for the production of hydrogen should be investigated in the future.

Furthermore, the main role of RuO₂ in RuO₂/ZnO or RuO₂/TiO₂ nanocomposites was to accept the holes from the valence band of the TiO₂ or ZnO and subsequently to accelerate the transfer of the holes to the electron donors. On the other hand, the photogenerated electrons take part in reduction reactions at the surface of TiO₂ or ZnO nanocrystallites. The photocatalytic efficiency can be increased by trapping the photogenerated electrons in the conduction band of semiconductor. In addition, providing active centres for the activation and reduction of H₂O to H₂ can also increase the catalytic efficiency for the production of hydrogen. One of the possible ways would consist in depositing noble metal cocatalysts which not only accept the electron but also provide active centres for the activation and

reduction of H_2O to H_2 . Thus, it is well known that Pt nanoparticles show very fast electron take-up from semiconductor conduction band electrons upon light excitation. It also provides favourable adsorption sites for the reactants allowing the reduction reaction with the electrons easy and fast. Noble metal Pt particles deposited on the ZnO or TiO_2 surface of RuO_2/ZnO or $\text{RuO}_2/\text{TiO}_2$ nanocomposites could therefore behave as a short-circuited micro photoelectrochemical cell in which Pt would be the cathode and RuO_2 the anode. This system could increase the photocatalytic efficiency for the decomposition of organic pollutant and hydrogen production even further. Band gap excitation produces an electron-hole pairs in the ZnO or TiO_2 particles. The electrons would subsequently be channelled to Pt sites where hydrogen evolution would occur or electrons would react with oxygen in case of organic decomposition. On the other hand, holes produced in the valence band of the photocatalysts would transfer to the RuO_2 and oxidize electron donors or water to oxygen. Thus, modification of ZnO or TiO_2 particles with Pt and RuO_2 could increase in the efficient charge separation and improved photocatalytic activity. Particularly, the presence of Pt and RuO_2 significantly reduces the overpotential for H_2 and O_2 production, respectively. Among various methods available for platinum deposition, photoplatinization should be an effective method to deposit Pt selectively on ZnO or TiO_2 surfaces.

Finally, methanol was used as an electron donor in this study, the role of which was to react irreversibly with the photogenerated holes and/or oxygen thereby suppressing the electron/hole recombination and/or the reverse reaction between H_2 and O_2 and thus increasing the rate of hydrogen production. Organic pollutants can perform the role of electron donors, thereby can reduce the hydrogen production costs while at the same time can serve the dual role of hydrogen production as well as organic degradation. The chosen sacrificial agent should be inexpensive compared to the hydrogen produced to make the process a feasible one. Wastewater containing organic pollutants such as azo dyes can be considered as suitable electron donor for this purpose. The proof of such a concept could have a huge impact for industrial purpose.

¹ Osterloh, F.E. *Chem. Mater.*, **2008**, *20*, 35

Chapter VI : Experimental section

VI.1. Chemicals used

Anhydrous tin tetrachloride (Acros Organic), sodium bicarbonate (Alfa Aesar), ruthenium (III) 2, 4-pentanedionate (Alfa Aesar), ruthenium chloride hydrate (Sigma Aldrich), nickel nitrated hexahydrate (Alfa Aesar), titanium (IV) isopropoxide (Sigma Aldrich), titanium (IV) butoxide (Sigma Aldrich), zinc acetate dihydrate (Alfa aesar), urea (Sigma Aldrich), propan-2-ol (Acros organics), ethanol (Aldrich), 1-butanol (Sigma Aldrich), acetic acid (Acros Organics), tetrahydrofuran (Sigma Aldrich), sodium hydroxide (Acros Organics), hydrochloric acid (Sigma Aldrich), methylene blue (MB) (Alfa Aesar), methyl orange (MO) (Alfa Aesar). All chemicals were used as received. P25 TiO₂ nanoparticles were provided by Degussa. Deionised water purified by a Millipore (Milli-Q) water purification system was used in all experiments.

VI.2. Synthesis of nanophotocatalysts

VI.2.1. Preparation of SnO₂/ZnO heterojunction photocatalysts

Anhydrous tin tetrachloride, zinc acetate dihydrate, sodium bicarbonate and urea of analytical grade were used without further purification. Nanocrystalline SnO₂ colloids were first prepared by homogeneous precipitation using a procedure adapted from the literature.¹ In a typical experiment, 2.08 g (0.04 M) of anhydrous SnCl₄ and 14.4 g (1.2 M) of urea, used as the precipitant, were mixed in 200 mL of deionized water. The solution was then heated at 90 °C for 4 h. The resulting precipitates were filtered and washed with distilled water. The solids obtained were then dispersed in 100 mL aqueous solution of acetic acid (pH 2) and subjected to hydrothermal treatment in an autoclave at 240 °C for 16 h. The resulting suspension was then condensed to a final SnO₂ concentration of 10-15 wt% by a rotary evaporator. The latter suspension was then divided into two parts. The first one was dried at 90 °C overnight and then calcined in air at 500 °C for 2 h. To prepare the SnO₂/ZnO heterostructure with a 1:1 molar ratio, 0.437 g of Zn(CH₃COO)₂·2H₂O was added to 5 g of the 12 wt% SnO₂ aqueous suspension. After stirring for 12 h, the resulting mixture was dried at 90 °C overnight and then annealed in air at 500 °C for 2 h to yield the hereafter named SnO₂/ZnO photocatalyst. Finally, ZnO was prepared by precipitation method:² to a solution of 5.5 g of Zn(CH₃COO)₂·2H₂O in distilled water (100 mL), and under continuous stirring, was added an aqueous solution of sodium bicarbonate until reaching a neutral pH. After filtration of the precipitate, the latter was dried at 110 °C overnight and subsequently calcined at 500 °C in air

for 2h to give the hereafter named ZnO photocatalyst. The different powders prepared were crushed with pestle and mortar before further characterization and photocatalytic experiments.

VI.2.2. Preparation of RuO₂/TiO₂ heterojunction photocatalysts

The heterostructure RuO₂/TiO₂ photocatalyst was prepared in two steps. First, TiO₂ was prepared by a sol-gel process according to a procedure described elsewhere.³ A solution of 19 g of tetra(propan-2- oxy)titanium in 20 mL of propan-2-ol was progressively added to 91 mg of glacial acetic acid in 26.8 mL deionized water under strong stirring (pH 3). The solution was stirred for 15 h at room temperature, and then the volatiles (acetic acid and propan-2-ol) were eliminated by heating at 120 °C. The resulting powder was then mixed with about 20 mL of deionized water and heated at 250 °C in an autoclave for 13 h. The resulting powder was dried at 300 °C for 30 min and then bleached under UV irradiation for 3 h to yield 5.3 g of titanium dioxide as a white powder. Heterostructure RuO₂/TiO₂ was prepared in the second step by impregnation method. In a typical procedure, a desired amount of ruthenium (III) 2, 4-pentanedionate was dissolved into 50 mL tetrahydrofuran. TiO₂ powder (0.3 g) was then dispersed into the solution. After the solutions were stirred vigorously for 4 h at room temperature, the solvents were evaporated at 80 °C. Subsequently, the loaded TiO₂ was dried in an oven at 70 °C overnight and finally calcined at 400 °C in air for 6 h to achieve the desired RuO₂/TiO₂ catalyst. The content of RuO₂ in RuO₂/TiO₂ powder was controlled by changing the concentration of the ruthenium (III) 2, 4-pentanedionate solution. The heterostructure RuO₂/TiO₂ nanocomposites containing 1, 2.5, 5, 10, and 20 wt% of RuO₂ were obtained by adding 0.91×10^{-2} , 2.30×10^{-2} , 4.70×10^{-2} , 9.98×10^{-2} and 22.45×10^{-2} g of ruthenium (III) 2, 4-pentanedionate, respectively, to tetrahydrofuran.

VI.2.3. Preparation of RuO₂/ZnO heterojunction photocatalysts

ZnO nanoparticle was first prepared by homogeneous precipitation method from a solutions of zinc acetate dihydrate, Zn(CH₃COO)₂ · 2H₂O using urea as a precipitant. In a typical procedure, 1.62 g (0.037 M) of zinc acetate dehydrate was dissolved in 200 mL of deionized water containing 6 g (0.5 M) of urea. The solution was magnetically stirred at room temperature in a round bottomed flask until a homogeneous solution was obtained. The solution was then heated at a temperature of 90 °C for 4 h. Upon completion of the reaction, a white precipitate obtained was centrifuged at 5000 rpm for 10 min and washed with deionized water till it was neutral. The resulting precipitate was then dried at 110 °C

overnight followed by calcination at 350 °C in air for 2 h to obtain ZnO nanoparticle powder. Heterostructure RuO₂/ZnO was prepared by impregnation method already discussed for the preparation of heterostructure RuO₂/TiO₂ photocatalyst. In a typical procedure, a desired amount of ruthenium (III) chloride hydrate was dissolved into 50 mL deionized water. ZnO nanopowder (0.3 g) was then dispersed into the solution and was vigorously stirred for 8 h. The amounts of ruthenium (III) chloride hydrate dissolved into water to obtain RuO₂/ZnO catalysts containing 2, 4 and 6 wt% RuO₂ were 1.83×10^{-2} , 3.74×10^{-2} and 5.73×10^{-2} g, respectively. The solvent was then removed by evaporation followed by drying at 110 °C overnight. Subsequently, the loaded ZnO was finally calcined at 350 °C in air for 2 h to achieve the desired RuO₂/ZnO photocatalysts.

VI.2.4. Preparation of NiO/TiO₂ heterojunction photocatalysts

The heterostructure NiO/TiO₂ photocatalyst was prepared at room temperature by the sol-gel route. Titanium butoxide was used as the precursor for TiO₂. A mixture of 4.3 mL n-butanol and 2.6 mL acetic acid was added into 4 mL of titanium butoxide. Subsequently, a colloid solution of TiO₂ was obtained by adding dropwise 4 mL of water to the above solution and stirred vigorously for 8 h. For the preparation of heterostructure NiO/TiO₂ photocatalyst, nickel nitrate hexahydrate (Ni(NO₃)₂ · 6H₂O) was used as the precursor for NiO. Predetermined amount of nickel nitrate hexahydrate was added to the colloid of TiO₂ and stirred vigorously overnight. The amounts of nickel nitrate hexahydrate to obtain NiO/TiO₂ photocatalysts containing 0.1, 0.25, 0.5, 1, 2, 4 and 25 wt% of NiO were 0.35×10^{-2} , 0.89×10^{-2} , 1.79×10^{-2} , 3.61×10^{-2} , 7.31×10^{-2} , 14.92×10^{-2} and 1.19 g, respectively. The colloidal solution obtained was then dried at 150 °C for 2 h, and the resulting powder was annealed in air at 500 °C for 2 h. The pure TiO₂ was prepared under the same conditions used for the NiO/TiO₂ samples. The calcined NiO/TiO₂ or TiO₂ samples were ground into fine particles prior to characterization and further application for photocatalysis.

VI.3. Characterization methods

VI.3.1. Fourier transform infrared (FTIR)

Infrared radiation interacts with chemical bonds to cause stretches, bends and various other atomic vibrations. For a vibration to give rise to absorption of infrared radiation, it must cause a change in the dipole moment of the molecule. The larger this change the more intense the absorption band will be.

In this dissertation, all IR spectra were recorded using a Perkin-Elmer spectrum 100 FTIR spectrophotometer. Samples were recorded as a KBr disc with 2 wt% sample, using 16 scans per sample over the range 4000-450 cm^{-1} .

VI.3.2. Raman spectroscopy

Raman spectroscopy is used in condensed matter physics and chemistry to study vibrational, rotational, and other low-frequency modes in a system. It relies on inelastic scattering, or Raman scattering of monochromatic light, usually from a laser used to polarize electrons in molecular bonds. The polarization process can result in a loss of energy (Raman effect) that is characteristic of the energy of a probed molecular bond. The amount of the polarizability change will determine the Raman scattering intensity, whereas the Raman shift is equal to the vibrational level that is involved. Raman spectroscopy is commonly used in chemistry, since vibrational information is very specific for the chemical bonds in molecules. Therefore, Raman spectroscopy as a powerful method can be used to investigate the structural properties of nanoparticles because the vibration in Raman spectra with decrease in particle size can be easily detected.⁴ It is also possible to determine the size of nanoparticles by using phonon confinement effect.⁵ The technique is complimentary to IR spectroscopy, because only molecular vibrations that are polarizable produce Raman shifted photons.

In this study, all Raman scatterings were measured at room temperature using Horiba Jobin Yvon (Labram HR 800) spectrometer with Ar^+ laser as excitation source operating at 514.5 nm. Typically, a small amount of powdered sample was mounted on a glass slide using a spatula tip. Using the attached microscope and camera, the instrument was focused on the powder sample through the objective lens. One scan was recorded with a detector exposure time of 2 sec.

VI.3.3. X-ray powder diffraction (XRD)

Powder XRD is one of the primary non-destructive techniques used to characterize solid-state materials. It can provide valuable information about the crystalline phase because each crystalline solid has a unique XRD pattern. The structure of a crystal is analyzed by the X-ray diffraction patterns. When X-ray light with a wavelength λ is incident on a crystal, a diffraction peak occurs if the Bragg condition is satisfied:

$$n\lambda = 2d \sin\theta \quad (1)$$

where d is the lattice spacing of the crystal and θ is the angle of incidence. The Cu $K\alpha$ emission ($\lambda = 1.5418 \text{ \AA}$) from a copper target is the most common X-ray source for the diffraction measurement. Furthermore, a powder XRD pattern is also used to determine the average crystallite size of the nanoparticles. From the resulting diffractogram the crystallite size (D , nm) can be estimated using the Scherrer equation.⁶

$$D = \frac{0.9\lambda}{\beta \cos\theta} \quad (2)$$

where D is the average nanocrystallite size (nm), λ is the X-ray wavelength (1.542 \AA), β is the full-width at half-maximum (FWHM) intensity (in radians), and θ is the Bragg angle of the peak of interest.

In our study, the X-ray diffraction (XRD) measurement was carried out by X-ray diffractometer (Bruker AXS, D2 PHASER A26-X1-A2B0D3A) using Cu $K\alpha$ radiation. A continuous scan mode was used to collect 2θ data from $10\text{-}80^\circ$ with a 0.1 sampling pitch and a 2° min^{-1} scan rate. Fine powdered samples were spread onto a quartz glass sample holder for measuring XRD.

VI.3.4. Transmission electron microscopy (TEM)

Transmission electron microscopy (TEM) is utilized to obtain high (atomic) resolution images of materials. TEM transmits a focused, high-energy electron beam through a sample. The electrons scatter off the nuclei of atoms in the sample and are projected onto a fluorescent screen. Through this process, atomic scale images can be collected. In addition, a selected area electron diffraction (SAED) pattern can be obtained from single nanostructures, to analyze the orientation of crystallographic planes. By combining the information gained from atomic scale imaging and diffraction patterns, the surface crystallographic planes of a material can be identified. Scanning Transmission Electron Microscopy (STEM) can be combined with the high-angle annular dark field (HAADF) imaging technique to provide Z-contrast images which can distinguish particles of different atomic number. The image brightness is approximately dependent on the square of the atomic number (Z^2) of the atoms present and very useful for particles with a great difference in atomic mass and not so useful for particles with similar atomic masses.

The elemental composition of a sample can be determined by Energy-Dispersive X-ray Spectroscopy (EDX). EDX is the more commonly used technique and involves ionization

of the sample from the X-rays of the microscope. The X-ray emissions from this ionization event are then analyzed with a solid-state energy dispersive detector. Each element gives out a unique pattern of X-ray lines from the K, L, and M shells which allows for straightforward analysis. This technique is also useful for constructing elemental maps to characterize the microstructural composition and elemental distribution of multicomponent catalysts on the nanometer scale.

In this study, TEM was performed using a Jeol JEM 2100F (Jeol, Tokyo, Japan) operating at an acceleration voltage of 200 kV (wavelength $\lambda = 2.51$ pm) equipped with a Schottky-type FEG and an EDX system (Oxford, Wiesbaden, Germany). For transmission electron microscopy (TEM) sample preparation, the photocatalysts were dispersed in ethanol using an ultrasonic bath (high purity methanol 99.8%, Sigma–Aldrich Co.) and a small droplet of the suspension was placed on holey carbon (Cu) grid. Upon drying, the samples were lightly coated with carbon to avoid charging under the electron beam.

VI.3.5. Thermogravimetric analysis (TGA)

TGA is an important thermal technique and is widely used for the characterization of solid materials including polymer, organic, inorganic and composite materials. TGA can determine: (1) moisture/liquid content and the presence of volatile species, (2) decomposition temperatures, and (3) the rate of degradation. In this dissertation, TGA-MS studies were performed on a Netzsch STA409 simultaneous analyzer coupled with a Thermostat GSD 300T3 Balzers Instruments mass spectrometer. Thermogravimetry (TG) curves were recorded in the 30-1000 °C temperature range with a heating rate of 5 °C min⁻¹ under an air flow.

VI.3.6. Nitrogen sorption measurement

The textural characterization, such as surface area, pore volume and the pore size distribution of the as-synthesized photocatalysts were obtained by N₂ sorption isotherm measurement using an ASAP2010 micrometric equipment. Samples were outgassed at 150 °C in vacuum for a time interval long enough to reach a constant pressure (<10 μm Hg). The nitrogen adsorption-desorption isotherms were measured at liquid nitrogen temperature (77 K) taken P/P₀ from 0 to 0.99. The specific surface areas were calculated by the BET method (S_{BET}) between 0.1 and 0.3 relative pressure. Pore size distributions were evaluated by the Barrett-Joyner-Halenda (BJH) method for mesopores.⁷

VI.3.7. UV-Visible diffuse reflectance spectrometry (UV-Vis DRS)

Electronic excitations of electrons from filled bands to empty bands are typically induced by electromagnetic radiation in the UV and visible light range (UV-Vis spectroscopy). Wavelengths of these types of radiation are on the order of 200 to 800 nm. With the Planck constant h and the speed of light c , the wavelength λ can be converted into excitation energy according to the following equation:

$$E = \frac{hc}{\lambda} \quad (3)$$

Depending on the energy gap between valence band maximum (VBM) and conduction band minimum (CBM) photons with wavelengths too long to excite an electron into the empty bands will pass through, while photons with sufficient amounts of energy will be absorbed and based on the electronic selection rules create an electron in the excited state. UV-Vis spectroscopy is therefore suitable to determine important information about the electronic structure and can be used to estimate band gap values.

The optical properties of all the as-synthesized nanoparticles were investigated by diffuse reflectance spectra. Diffuse reflectance spectra of the powder photocatalysts were measured by placing the samples in 1 mm quartz cell using an UV-Vis-NIR spectrometer (Lambda 900) at room temperature in the wavelength range of 200-800 nm. Pure powdered BaSO₄ was used as a reference sample.

The original coordinates of the spectra, reflectance (R) vs. wavelength (λ), were transformed to Kubelka-Munk function $F(R)$ vs. photon energy ($h\nu$). The reflectance data were converted to the absorption coefficient $F(R)$ values according to the Kubelka–Munk equation (Eq. (4)), i.e.:

$$F(R) = \frac{(1 - R)^2}{2R} \quad (4)$$

where $F(R)$ is equivalent to the absorption coefficient. The band gap energy (E_g) of as-synthesized nanoparticles was calculated from the following equation, $\alpha(h\nu) = A(h\nu - E_g)^n$ where α , ν , E_g , and A are the absorption coefficient, light frequency, band gap energy, and a constant, respectively.⁸ Among them, n is determined by the type of optical transition of a semiconductor ($n = 1/2$ for direct transition and $n = 2$ for indirect transition). For a semiconductor material, a plot of $(\alpha h\nu)^{1/n}$ against $h\nu$ should show a linear region just above

the optical absorption edge. The band gap energy was calculated by extrapolating a straight line to the abscissa axis, where α is zero, for $E_g = h\nu$.⁹ According to the Kubelka-Munk theory the diffuse reflectance is related to the absorption coefficient as

$$\frac{\alpha}{s} = F(R) = \frac{(1-R)^2}{2R} \quad (5)$$

where s is the scattering coefficient. The optical energy band gap (E_g values) for direct transition can thus be estimated from a plot of $(F(R) h\nu)^2$ vs. $h\nu$ and that for indirect transition can be estimated from the plot of $(F(R) h\nu)^{1/2}$ vs. $h\nu$, the intercepts of the tangents to the abscissa axis yielding the band gap energies of the semiconductors.

VI.3.8. X-ray Photoelectron spectroscopy (XPS)

XPS is a quantitative spectroscopic technique that measures the elemental composition, and the chemical and electronic states of the elements that exist within a material. X-ray photoelectron spectroscopy (XPS) utilizes a monochromatic X-ray source to excite electrons from core levels of the atoms near the surface (~1-10 nm) of a solid sample into vacuum. The electrons ejected from the sample are collected by a hemispherical electron energy analyzer which measures the kinetic energy of the ejected electrons. The kinetic energy measured can then be used to determine the binding energy (BE) of the electron from the following equation:

$$E_{BE} = h\nu - E_{kin} - \phi \quad (6)$$

Where h is Planck's constant, ν is the frequency of the exciting energy source, and ϕ is the work function of the spectrometer.¹⁰ Each ejected electron from an element has a characteristic binding energy and the position of this binding energy is used to identify the element and core level of the electron that can be found by consulting binding energy tables.¹¹ The peak intensities can be used to quantitatively determine the elemental composition and the peak positions can be used to determine oxidation states for the elements. In this dissertation, XPS was used to analyze the chemical state of as-synthesized photocatalysts. In addition, the band alignment at the interface of the heterostructure photocatalysts was also determined by XPS technique.

The interface experiments for the model were performed at the Darmstadt Integrated System for Material research (DAISY-MAT), which combines a Physical Electronics PHI 5700 multitechnique surface analysis system with several deposition chambers via an

ultrahigh vacuum sample transfer. X-ray photoelectron (XP) spectra were recorded using monochromatic Al $K\alpha$ (1486.6 eV) radiation with an energy resolution of ≈ 0.4 eV as determined from the broadening of the Fermi edge of a sputter cleaned Ag sample. Ultraviolet photoelectron (UP) spectra were measured in normal emission with HeI excitation. RuO_2 was deposited by reactive direct current magnetron sputtering from a metallic Ru target. The substrates were held at room temperature during deposition. A pressure of 1 Pa, a substrate to target distance of 10 cm and an Ar/ O_2 ratio of 92.5/7.5 were used. The deposition conditions were chosen to guarantee the formation of fully oxidized RuO_2 .

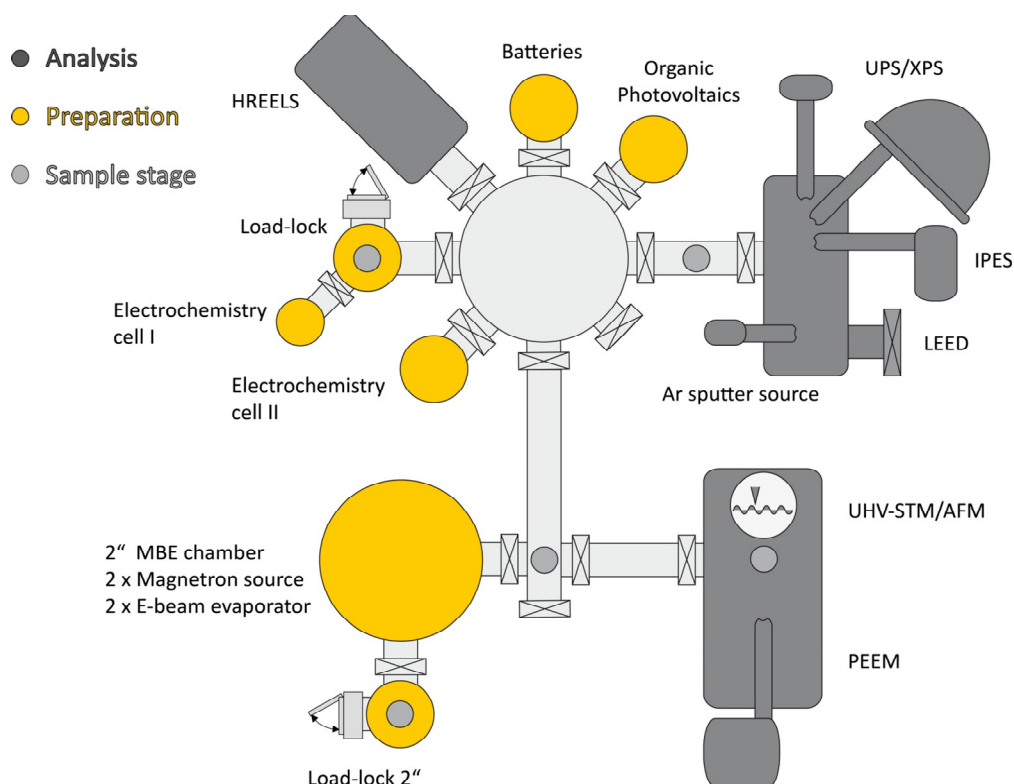


Figure VI-1: Schematic drawing of Darmstadt Integrated System for Fundamental research (DAISY-FUN).

The interface experiment for heterostructure $\text{RuO}_2/\text{TiO}_2$ nanoparticles was performed at Darmstadt Integrated System for Fundamental research (DAISY-FUN) (**Figure VI-1**), the XPS spectra were recorded using a PHOIBOS 225 (Specs GmbH) spectrometer. Monochromatized X-ray ($K\alpha$: 1486.6 eV) from an Al anode was used for excitation. The charge effect was evaluated using the main component of the C 1s peak, associated with adventitious hydrocarbons with a binding energy of 284.8 eV as reference for calibration. The base pressure in the sample during the measurements was less than 3×10^{-8} mbar.

VI.4. Photocatalytic Experiment

VI.4.1. Photocatalytic degradation of organic dyes

Photocatalytic activities of as-synthesized samples were evaluated by the degradation of methylene blue (MB) and methyl orange (MO) dyes. All the experiments were conducted at room temperature open to air. In each experiment, 0.1 g photocatalyst was dispersed in 100 mL of MB or MO solution (10 mg/L) to obtain the concentration of the catalyst at 1.0 g/L. The experiments were carried out in a pyrex beaker illuminated with a 125 W high pressure mercury lamp (Philips, HPL-N 125 W/542 E27), emitting UV light. The UV lamp was positioned above the solution beaker. Prior to irradiation, the suspension was stirred in the dark for 30 min to reach adsorption/desorption equilibrium. The solutions were continuously stirred during the experiments. At given irradiation time intervals, 4 mL of the suspensions were collected, and then centrifuged (4000 rpm, 10 min) to separate the photocatalyst particles. The concentrations of MB and MO were measured by UV-Vis Spectrophotometer (Shimadzu, UV-1650 pc) scanning from 200 nm to 800 nm monitoring the absorption at λ_{\max} = 664 and 464 nm, respectively. A calibration plot based on Beer–Lambert’s law was established by relating the absorbance to the concentration. In each case, blank experiments were also conducted with the catalysts in the absence of light and without the catalysts when the solution containing the dissolved dye was illuminated. In some cases, repetitive photodegradation of MB during four consecutive cycles was performed with 1.0 g/ L of catalyst at 10 mg/ L dye concentration in order to investigate the stability of the photocatalysts. After each cycle, the catalyst was washed with distilled water and a fresh solution of MB was added before each photocatalytic run.

VI.4.2. Photocatalytic hydrogen production

The catalytic experiments were carried out in an argon atmosphere and under exclusion of air. Solvents were distilled under an argon atmosphere, or degassed via standard procedures prior to use and stored under argon. The used UV light source of wavelength in the range of 320 to 400 nm was Hg vapor light source (LUMATEC SUPERLITE 400). The input power of the light source was 1.6 W.

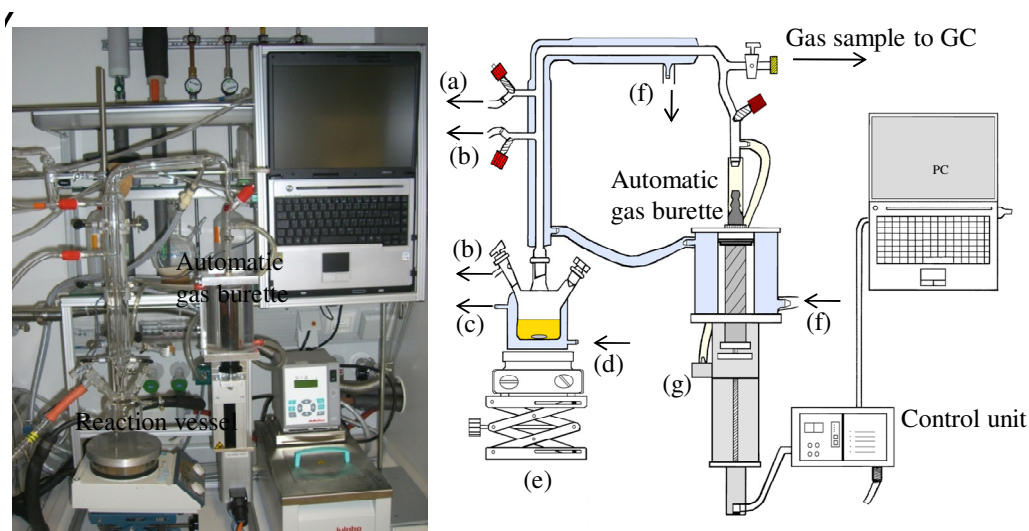


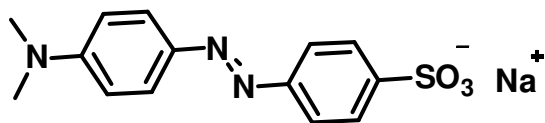
Figure VI-2: Experiment set up for the photocatalytic production of hydrogen. (a) Waste (b) Ar/vacuum (c) thermostat outlet (d) thermostat inlet (e) thermostatically controlled reaction vessel (f) thermostat (g) pressure sensor.

Figure VI-2 shows the experimental set up for the photocatalytic production of hydrogen at LIKAT, Rostock, Germany. The photocatalytic experiments were conducted in a double walled thermostatically controlled reaction vessel (under a constant temperature of 25.0°C) which was connected via a condenser to an automatic gas burette. In a typical reaction, the double-walled reaction vessel connected to the automatic gas burette was evacuated and flushed with argon three times to remove any other gases. The photocatalysts were introduced as a powder and the mixture of methanol/H₂O (1:1, 10 mL) was added, and the temperature was maintained at 25°C by a thermostat. The mixture was stirred (300 rpm) for 5 min to reach thermal equilibrium. The photocatalytic reaction was started by irradiating the reaction vessel with light. The volumes of the evolved gases were determined by an automatic gas burette. The gas burette was equipped with a pressure sensor. Evolving gas during the reaction causes a pressure increase in the closed system, which is compensated by volume increase of the burette syringe by an automatic controlling unit. The gas evolution curves are collected by a PC. After each reaction a gas sample was taken and quantitatively analyzed by gas chromatography (HP6890N, carboxen 1000, thermal conductivity detector (TCD) and methanizer/flame ionization detector (FID), external calibration). The variance of the volumes for reproduction of experiments was between 1–15%.

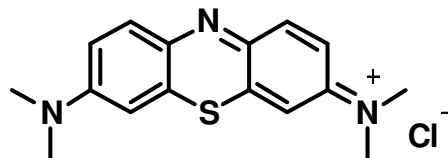
- ¹ Baik, N. S.; Sakai, G.; Miura N.; Yamazoe, N. *Sens. Actuators B*, **2000**, 63, 74.
- ² Parida, K. M.; Dash, S. S.; Das, D. P. *J. Colloid Interface Sci.* **2006**, 298, 787.
- ³ Tebby, Z.; Babot, O.; Toupance, T.; Park, D. H.; Campet, G.; Delville, M. H. *Chem. Mater.* **2008**, 20, 7260.
- ⁴ Wachs, I. E.; Roberts, C. A. *Chem. Soc. Rev.* **2010**, 39, 5002.
- ⁵ Choi, H. C.; Jung, Y. M.; Kim, S. B. *Vib. Spectrosc.* **2005**, 37, 33.
- ⁶ (a) Scherrer, P. *Göttinger Nachrichten Gesell.* **1918**, 2, 98. (b) Patterson, A. *Phys. Rev.* **1939**, 56, 978.
- ⁷ Barrett, E. P.; Joyner, L.; Halenda, P. P. *J. Am. Chem. Soc.* **1951**, 73, 373.
- ⁸ Davis, E. A.; Mott, N. F. *Phil. Mag.* **1970**, 22, 903.
- ⁹ Sanchez, E.; Lopez, T. *Mater. Lett.* **1995**, 25, 271.
- ¹⁰ Niemantsverdriet, J. W. *Spectroscopy in Catalysis*, Wiley-VCH: Weinheim, **2000**.
- ¹¹ Moulder, J. F. *Handbook of x-ray photoelectron spectroscopy: a reference book of standard spectra for identification and interpretation of XPS data*, Perkin-Elmer Corporation: Eden Prairie, **1992**.

Appendix

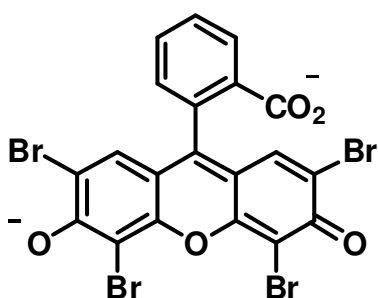
Chemical structure of some organics



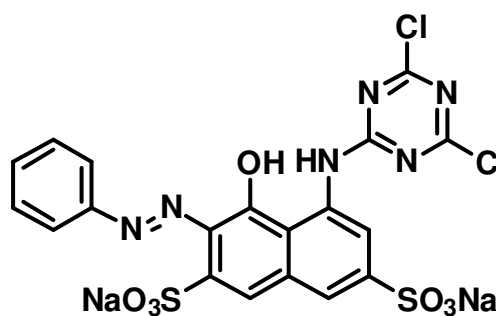
Methyl orange



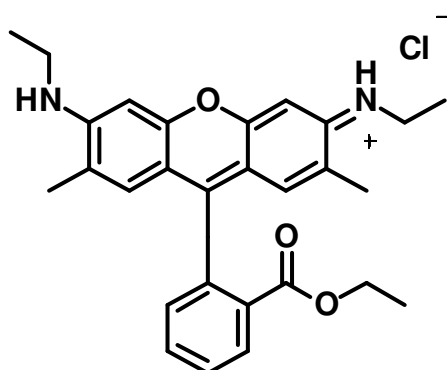
Methylene blue



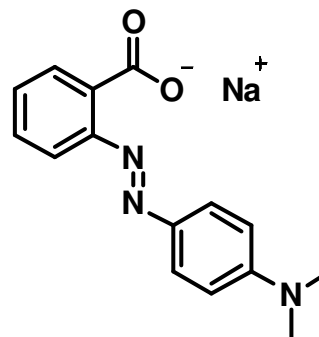
Eosin Y



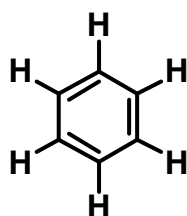
Active red X-3B



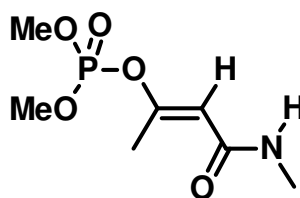
Rhodamine 6G



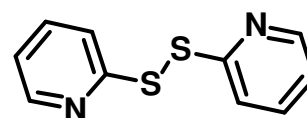
Sodium methyl red



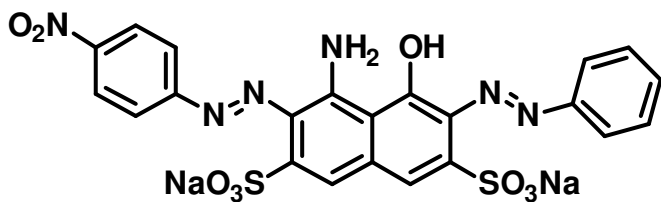
Benzene



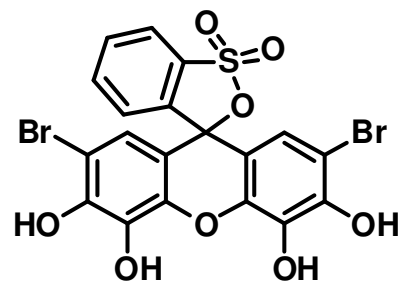
Monocrotophos



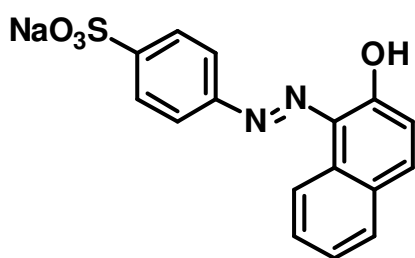
Bis(2-dipyridyl) disulfide



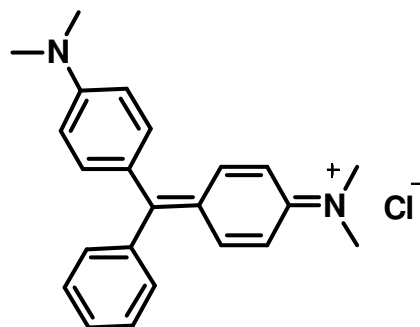
Naphthol blue black



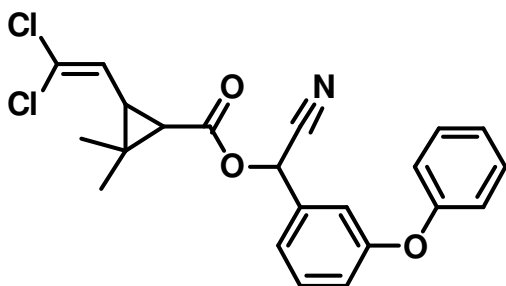
Bromopyrogallol red



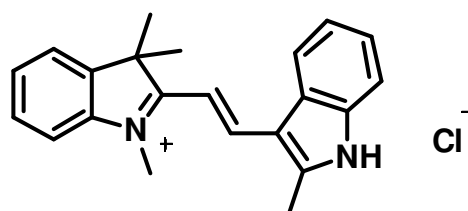
Acid orange 7



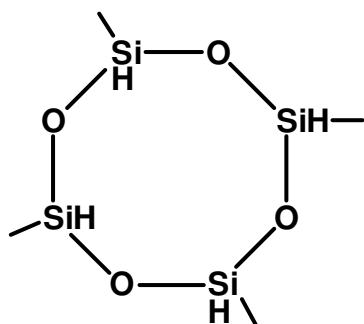
Malachite green



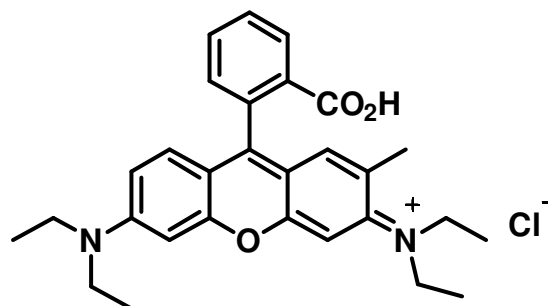
Beta-cypermethrin



Astrazone orange G



1, 3, 5, 7-tetramethylcyclotetrasiloxane



Rhodamine B

Determination of crystallite size by Raman shift

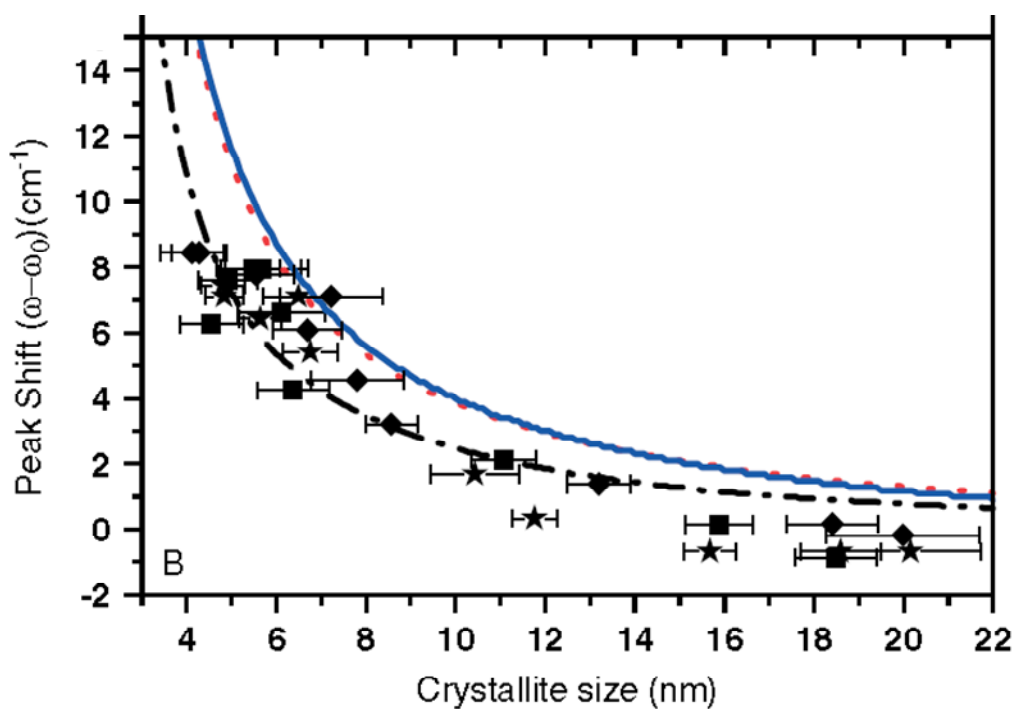


Figure A-1: Peak shift of Raman line shape of anatase TiO_2 as a function of particle size. Dashed and dotted curves show the peak position vs crystallite size. Balaji *et al.* *J. Raman Spectrosc.* **2006**, 37, 141

Published article

Nanostructured SnO₂–ZnO Heterojunction Photocatalysts Showing Enhanced Photocatalytic Activity for the Degradation of Organic Dyes

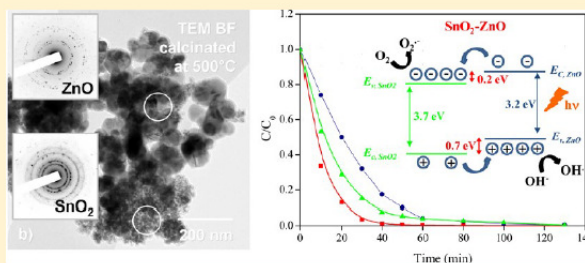
Md. Tamez Uddin,[†] Yohann Nicolas,[†] Céline Olivier,[†] Thierry Toupance,^{*,†} Laurent Servant,[†] Mathis M. Müller,[‡] Hans-Joachim Kleebe,[‡] Jürgen Ziegler,[‡] and Wolfram Jaegermann[‡]

[†]University of Bordeaux, Institut des Sciences Moléculaires, UMR 5255 CNRS, 351 Cours de la Libération, F-33405 Talence Cedex, France

[‡]Institute of Material Science, Technische Universität Darmstadt, Petersenstrasse 23, D-64287 Darmstadt, Germany

Supporting Information

ABSTRACT: Nanoporous SnO₂–ZnO heterojunction nanocatalyst was prepared by a straightforward two-step procedure involving, first, the synthesis of nanosized SnO₂ particles by homogeneous precipitation combined with a hydrothermal treatment and, second, the reaction of the as-prepared SnO₂ particles with zinc acetate followed by calcination at 500 °C. The resulting nanocatalysts were characterized by X-ray diffraction (XRD), FTIR, Raman, X-ray photoelectron spectroscopy (XPS), nitrogen adsorption–desorption analyses, transmission electron microscopy (TEM), and UV–vis diffuse reflectance spectroscopy. The SnO₂–ZnO photocatalyst was made of a mesoporous network of aggregated wurtzite ZnO and cassiterite SnO₂ nanocrystallites, the size of which was estimated to be 27 and 4.5 nm, respectively, after calcination. According to UV–visible diffuse reflectance spectroscopy, the evident energy band gap value of the SnO₂–ZnO photocatalyst was estimated to be 3.23 eV to be compared with those of pure SnO₂, that is, 3.7 eV, and ZnO, that is, 3.2 eV, analogues. The energy band diagram of the SnO₂–ZnO heterostructure was directly determined by combining XPS and the energy band gap values. The valence band and conduction band offsets were calculated to be 0.70 ± 0.05 eV and 0.20 ± 0.05 eV, respectively, which revealed a type-II band alignment. Moreover, the heterostructure SnO₂–ZnO photocatalyst showed much higher photocatalytic activities for the degradation of methylene blue than those of individual SnO₂ and ZnO nanomaterials. This behavior was rationalized in terms of better charge separation and the suppression of charge recombination in the SnO₂–ZnO photocatalyst because of the energy difference between the conduction band edges of SnO₂ and ZnO as evidenced by the band alignment determination. Finally, this mesoporous SnO₂–ZnO heterojunction nanocatalyst was stable and could be easily recycled several times opening new avenues for potential industrial applications.



1. INTRODUCTION

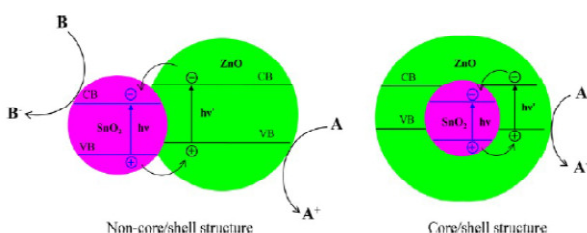
Over the past two decades, the preparation of nanostructured nanoporous metal oxide semiconductors has been the subject of intense research efforts because of their unique chemical, electronic, and optical properties and their numerous potential or demonstrated applications. Thus, nanostructured semiconductor metal oxide photocatalysts, as titanium dioxide (TiO₂) or zinc oxide (ZnO) nanoparticles, have been proposed as an alternative to the conventional methods (i.e., adsorption, biological degradation, chlorination, or ozonation processes) for the complete removal of toxic chemicals from the industrial hazards.¹ In this case, the creation of electron–hole pairs upon UV-irradiation promotes the formation of powerful oxidizing agents on the surface of metal oxide nanocrystals that favors the decomposition of organic compounds and pollutants.² Nonetheless, this approach still suffers from some limitations because of the fast recombination of the photogenerated electron–hole pairs hampering industrial application of photocatalytic techniques in the degradation of

contaminants in water and air.³ As a consequence, minimizing the recombination of photogenerated electron–hole pairs before their participation in redox processes constitutes a key issue for enhancing the photocatalytic efficiency of such materials. To draw a new prospect in this field, heterostructure photocatalysts combining two metal oxide semiconductors of different electron affinity and ionization potentials were developed using contact or core–shell type morphologies (Scheme 1). When such a heterostructure is irradiated with UV-light, valence band (VB) electrons are excited to the conduction band (CB) with simultaneous generation of the same amount of holes in the VB. Photogenerated electrons are then injected from the CB of the semiconductor with an energetically higher CB edge to the CB of the semiconductor with lower CB edge. Simultaneously, holes are injected in the opposite direction for appropriate VB offsets, thus

Received: April 17, 2012

Published: June 26, 2012

Scheme 1. Schematic Representation of the Charge Separation Processes for the Heterostructure Photocatalysts in Contact Type (left) and Core-Shell Type (right) Geometries



increasing the rate of charge separation and reducing the electron–hole pair recombination. In both contact type and core/shell type semiconductors, the charge separation mechanism is the same. However, both holes and electrons are accessible for selective oxidation and reduction processes on different particle surfaces in contact type semiconductor heterostructures, while only one charge carrier is accessible in the core–shell type analogue leading to selective charge transfer at the semiconductor electrolyte interface.⁴ In this context, various semiconductor-based heterostructure photocatalysts have been designed and investigated such as $\text{TiO}_2\text{--ZnO}$,⁵ $\text{TiO}_2\text{--WO}_3$,⁶ and ZnO--WO_3 .⁷ Among the binary metal oxides, tetragonal tin dioxide, SnO_2 , is a well-known large band gap multifunctional material that found widespread applications in the fields of Li-batteries,⁸ field emission,⁹ gas sensing,¹⁰ and photovoltaic conversion.¹¹ Because of its more positive CB edge, SnO_2 is a better electron acceptor than TiO_2 and ZnO that makes it a good candidate for the above-mentioned heterostructures. As a consequence, associating SnO_2 with ZnO has been the subject of several reports for achieving an efficient charge separation and improving the photocatalytic properties of both oxides. In this context, various strategies have been investigated to produce ZnO--SnO_2 heterostructures including co-precipitation method followed by calcination,¹² hydrothermal or solvothermal routes,¹³ and sol–gel process combined with electrospinning techniques.¹⁴ ZnO--SnO_2 heterostructures with a molar ratio $\text{Zn}:\text{Sn}$ of 2:1 prepared by the co-precipitation method showed higher photocatalytic decomposition rates of methyl orange (MO) than pure ZnO and SnO_2 analogues.^{12a,f} A similar trend has been also described by Zhang et al. for one-dimensional ZnO--SnO_2 nanofibers synthesized by an electrospinning technique.¹⁴ However, even though it has been reported that the enhanced photocatalytic properties found with ZnO--SnO_2 heterostructures were related to improved charge separation, no determination of the band alignment in such system has been reported so far to confirm this feature. Thus, the photocatalytic activity of ZnO--SnO_2 systems still remains largely unexplored. On the other hand, one-pot synthesis combined with annealing at high temperature can lead to crystalline impurities as Zn_2SnO_4 ^{12a–e} which requires the development of alternative preparation procedures.

As a consequence, we herein report on the characterization and the photocatalytic properties of $\text{SnO}_2\text{--ZnO}$ materials prepared by a simple two-step procedure. Nanosized SnO_2 particles were first prepared by homogeneous precipitation coupled with hydrothermal treatment and, then, reacted with zinc acetate in acidic medium followed by calcination in air to grow ZnO particles. The photocatalytic activity and recycling ability of the resulting $\text{SnO}_2\text{--ZnO}$ heterostructure were investigated by the degradation of methylene blue (MB) dye under UV irradiation

and compared to those of SnO_2 and ZnO nanopowders. To gain a deeper insight in the relationship between the electronic properties and the photocatalytic activity, the band alignment of the $\text{SnO}_2\text{--ZnO}$ photocatalyst was carefully determined by UV–visible diffuse reflectance and X-ray Photoelectron spectroscopies. The enhanced photocatalytic properties of the $\text{SnO}_2\text{--ZnO}$ photocatalysts were rationalized in terms of a better charge separation related to the effective semiconductor heterojunction.

2. EXPERIMENTAL SECTION

2.1. Preparation of Nanosized Metal Oxide Photocatalysts.

Anhydrous tin tetrachloride (Acros Organic), zinc acetate dihydrate (Alfa Aesar), sodium bicarbonate (Alfa Aesar), and urea (Sigma Aldrich) of analytical grade were used without further purification. Nanocrystalline SnO_2 colloids were first prepared by homogeneous precipitation using a procedure adapted from literature.¹⁵ In a typical experiment, 2.08 g (0.04 M) of anhydrous SnCl_4 and 14.4 g (1.2 M) of urea, used as the precipitant, were mixed in 200 mL of deionized water. The solution was then heated at 90 °C for 4 h. The resulting precipitates were filtered and washed with distilled water. The solids obtained were then dispersed in 100 mL aqueous solution of acetic acid (pH 2) and subjected to hydrothermal treatment in an autoclave at 240 °C for 16 h. The resulting suspension was then condensed to a final SnO_2 concentration of 10–15 wt % by a rotary evaporator. The latter suspension was then divided into two parts. The first one was dried at 90 °C overnight and then calcined in air at 500 °C for 90 min. To prepare the $\text{SnO}_2\text{--ZnO}$ heterostructure with a 1:1 molar ratio, 0.437 g of $\text{Zn}(\text{CH}_3\text{COO})_2\cdot 2\text{H}_2\text{O}$ was added to 5 g of the 12 wt % SnO_2 aqueous suspension. After stirring for 12 h, the resulting mixture was dried at 90 °C overnight and then annealed in air at 500 °C for 2 h to yield the hereafter named $\text{SnO}_2\text{--ZnO}$ photocatalyst. Finally, ZnO was prepared by precipitation method:¹⁶ to a solution of 5.5 g of $\text{Zn}(\text{CH}_3\text{COO})_2\cdot 2\text{H}_2\text{O}$ in distilled water (100 mL), and under continuous stirring, was added an aqueous solution of sodium bicarbonate until reaching a neutral pH. After filtration of the precipitate, the latter was dried at 110 °C overnight and subsequently calcined at 500 °C in air for 2 h to give the hereafter named ZnO photocatalyst. The different powders prepared were crushed with pestle and mortar before further characterization and photocatalytic experiments.

2.2. Characterization. Fourier Transform Infrared (FTIR) studies (KBr pellets) were performed with a Perkin-Elmer spectrum 100 FTIR spectrophotometer. Raman spectra were recorded in the solid state on a Labram 1B spectrometer using a red laser beam (632 nm). X ray diffraction (XRD) studies were carried out with a Bruker AXS diffractometer (D2 PHASER A26 X1-A2B0D3A) using a Cu anode ($K\alpha$ radiation). A continuous scan mode was used to collect 2θ data from 10 to 80° with a 0.1° sampling pitch and a 2° min^{-1} scan rate. The average crystallite size of the materials prepared was estimated by fwhm (full width at half-maximum) according to Scherrer's formula (applied to the $\{110\}$ reflection), $D = (0.9 \lambda) / (\beta_{1/2} \cos \theta_B)$, where D is the average grain size, λ is the wavelength of Cu $K\alpha$ ($= 1.5405 \text{ \AA}$), $\beta_{1/2}$ is the fwhm, and θ_B is the diffraction angle. Transmission electron microscopy was performed using a Jeol/JEM 2100F (Jeol, Tokyo, Japan) operating at an acceleration voltage of 200 kV (wavelength $\lambda = 2.51 \text{ pm}$) equipped with a Schottky-type FEG and an EDS system (Oxford, Wiesbaden, Germany). For transmission electron microscopy (TEM) sample preparation, the photocatalysts were dispersed in an ultrasonic bath (high purity methanol 99.8%, Sigma–Aldrich Co.) and a small droplet of the suspension was placed on holey carbon (Cu) grid. Upon drying, the samples were lightly coated with carbon to avoid charging under the electron beam. Nitrogen sorption isotherms (77 K) were recorded with an Micromeritics ASAP2010 equipment. Before each analysis, samples were degassed at 120 °C in vacuum for a time interval long enough to reach a constant pressure ($<10 \mu\text{m Hg}$). The specific surface areas (S_{BET}) were calculated using the Brunauer–Emmett–Teller (BET) equation between 0.1 and 0.3 relative pressure (P/P_0). Mesopore size distributions were deduced from the Barrett, Joyner, Halenda (BJH) method applied to the adsorption branch of the nitrogen adsorption isotherm.¹⁷ The calculation was performed by the Micromeritics software package which uses the recurrent method and applies the Harkins and Jura equation for the

multilayer thickness. UV–vis diffuse reflectance spectra were measured at room temperature in the 200–800 nm wavelength range using an UV–vis–NIR spectrometer (Lambda 900). Pure powdered BaSO₄ was used as a reference sample. X-ray Photoelectron spectra were recorded using a PHOIBOS 225 (Specs GmbH) spectrometer. Monochromatized X-ray (K_{α} : 1486.61 eV) from an Al anode was used for excitation. The charge effect was evaluated using the main component of the C 1s peak, associated with adventitious hydrocarbons with a binding energy of 284.8 eV as reference for calibration. The base pressure in the sample during the measurements was less than 3×10^{-8} mbar. The energy band diagram of the SnO₂–ZnO heterostructure was determined by X-ray photoelectron spectroscopy (XPS) using well-known procedures from the literature.¹⁸ The technique consists of first measuring the Sn 3d and Zn 2p core levels as well as the VB maximum (VBM) E_V of the bulk SnO₂ and bulk ZnO, respectively. These values were measured by XPS acquisitions on each kind of film deposited by the drop-casting method onto Al substrate. The position of the Sn 3d and Zn 2p core levels of the SnO₂–ZnO heterostructure was then determined. These last values were obtained from XPS acquisitions on the film of SnO₂–ZnO heterostructure deposited on Al substrate. The VB offset (VBO) ΔE_V of the heterostructure SnO₂/ZnO was then calculated according to eq 1¹⁹

$$\Delta E_V = (E_{Zn\ 2p} - E_{V-ZnO/bulk}^{ZnO}) - (E_{Sn\ 3d} - E_{V-SnO_2/bulk}^{SnO_2}) - \Delta E_{CL} \quad (1)$$

where $\Delta E_{CL} = (E_{Zn\ 2p} - E_{Sn\ 3d})_{heterostructure}$ is the energy difference between Zn 2p and Sn 3d core levels (CLs), which were measured in the SnO₂–ZnO sample. $E_{Zn\ 2p}$ and $E_{Sn\ 3d}$ are the binding energies in the bulk of ZnO and SnO₂, respectively; E_{V-ZnO} and E_{V-SnO_2} are the VB maxima in the bulk of ZnO and SnO₂, respectively.

2.3. Photocatalytic Experiments. Photocatalytic activities of the as-synthesized samples were evaluated by the degradation of MB (Alfa Aesar) dye. The MB was reagent grade and was used as supplied. All the experiments were conducted at room temperature in air. In each experiment, 0.1 g of metal oxide catalyst was dispersed in 100 mL of MB solution (10 mg/L) to obtain the concentration of the catalyst at 1.0 g/L. The experiments were carried out in a Pyrex beaker illuminated with a 125 W high pressure mercury lamp (Philips, HPL-N 125 W/S42 E27) emitting UV light (365 and 313 nm). The UV lamp was positioned above the beaker containing the solution. Prior to irradiation, the suspension was stirred in the dark for 30 min to reach adsorption/desorption equilibrium. The solution was continuously stirred during the experiments. At given irradiation time intervals, 4 mL of the suspension were collected, and then centrifuged (4000 rpm, 10 min) to separate the photocatalyst particles. The MB concentration was evaluated by UV–visible Spectrophotometer (Shimadzu, UV-1650 pc) monitoring the absorption maximum at $\lambda_{max} = 664$ nm. A calibration plot based on Beer–Lambert's law was established by relating the absorbance to the concentration. In each case, blank experiments were also conducted with the catalysts in the absence of light and without the catalysts when the solution containing the dissolved dye was illuminated. Moreover, reference experiments were performed under the same conditions with commercial TiO₂ (Degussa, P-25) used as a photocatalytic standard. In some cases, repetitive photodegradation of MB during four consecutive cycles was performed with 1.0 g/L of catalyst at 10 mg/L dye concentration. After each cycle, the catalyst was washed with distilled water and a fresh solution of MB was added before each photocatalytic run.

3. RESULTS AND DISCUSSION

3.1. Particle Characterization. Precipitation of SnO₂ was observed when a clear solution of SnCl₄ and urea was reacted at 90 °C in aqueous medium. The pH of the solution increased gradually because of the progressive decomposition of urea into NH₃ and CO₂, leading to the nucleation and growth of uniformly nanosized particles.²⁰ After annealing in air at high temperature, FTIR studies revealed the complete elimination of the undesirable organics and the formation of metal oxide species (Figure 1A). Thus, above 2000 cm⁻¹, a very broad absorption around 3430 cm⁻¹

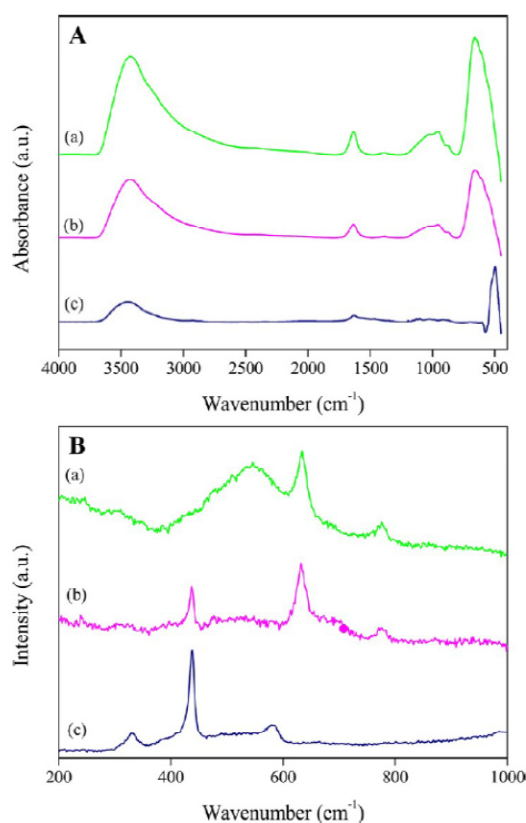


Figure 1. FTIR (A) and Raman (B) spectra of the as-synthesized photocatalysts after annealing in air at 500 °C; (a) SnO₂, (b) SnO₂–ZnO, and (c) ZnO.

ascribed to OH stretching vibration modes was observed for each sample.²¹ Key features observed below 2000 cm⁻¹ include a band at 1634 cm⁻¹ due to the bending vibrations of adsorbed molecular water, and wide bands at 659 cm⁻¹ assigned to Sn–O stretching modes of Sn–O–Sn (Figures 1Aa–b)²² and at 555 cm⁻¹ due to Zn–O stretching modes (Figures 1Aa and 1Ac).²³ Furthermore, the Raman spectrum of the as-prepared SnO₂–ZnO photocatalyst showed three main features at 438, 632, and 776 cm⁻¹ which could be assigned to the vibration modes E_2 for wurtzite ZnO²⁴ as well as A_{1g} and B_{2g} for cassiterite SnO₂.²⁵ Bands at 332 (second-order vibration originating from the zone boundary phonons)²⁶ and 585 ($E_1(LO)$ mode) cm⁻¹ were observed for the pure ZnO sample but were found to be very weak for the heterostructure. It is also worthwhile to mention that the broad resonance observed in the SnO₂ spectrum at 552 cm⁻¹, a feature that could be related to surface modes,²⁷ has collapsed after reaction with zinc acetate and further calcination. As a consequence, the signature of both wurtzite ZnO and cassiterite SnO₂ appeared in the Raman spectrum of the SnO₂–ZnO photocatalyst. This was confirmed by the XRD patterns of the materials calcined at 500 °C (Figure 2). All the diffraction lines in Figure 2a and 2c were those expected for the standard rutile-like, that is, cassiterite, crystalline structure of SnO₂ (space group: $P4_2/mmm$, JCPDS file no. 41-1445) and the standard hexagonal wurtzite ZnO (space group: $P6_3/mc$, JCPDS file no. 36-1451), respectively. The diffraction peaks of pure SnO₂ (Figure 2a) were considerably broadened revealing a small mean crystallite size which was estimated to be 5 ± 0.5 nm. On the other hand, the

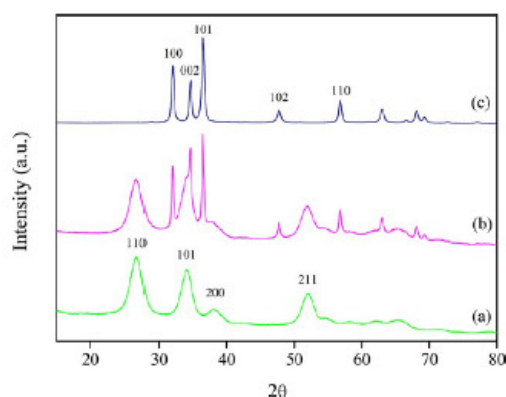


Figure 2. XRD patterns of the as-synthesized photocatalysts after annealing in air at 500 °C; (a) SnO₂, (b) SnO₂-ZnO, and (c) ZnO.

diffraction peaks of ZnO (Figure 2c) were rather sharp indicating a better crystallized sample, with an average crystallite size of about 18 ± 1 nm. ZnO seemed to calcine more easily and, thus,

tends to have larger grain size than SnO₂. Furthermore, Figure 2b shows two sets of diffraction peaks for the SnO₂/ZnO sample ascribed to hexagonal wurtzite ZnO and cassiterite SnO₂. No additional peaks were observed in this sample that confirmed that the sample only contained nanocrystalline ZnO and SnO₂ particles. The full-width half-maximum (fwhm) for SnO₂ in SnO₂-ZnO photocatalyst is slightly larger than that found for pure SnO₂ showing that the size of the SnO₂ crystallite, that is, 4.5 ± 0.5 nm, in the SnO₂-ZnO photocatalyst was smaller than that in pure SnO₂. On the other hand, the crystallite size of ZnO, that is, 27 ± 1 nm, in SnO₂-ZnO was larger than that of pure ZnO. As previously reported for similar heterostructures,^{12a} the presence of SnO₂ causes an increase in the crystallite size of ZnO whereas that of ZnO restrains the growth of SnO₂ nanocrystals.

Figure 3 shows TEM images of SnO₂-ZnO heterostructures dried at 90 °C (Figure 3a) and calcinated at 500 °C (Figure 3b). Moreover, HRTEM micrographs of the calcinated materials are shown to verify the crystallinity of both SnO₂ and ZnO after the heat treatment (Figures 3c,d). The shape of the pure SnO₂ nanoparticles was spherical and of uniform size (not shown here). It is worth mentioning that the diameter of the pure SnO₂ was about 5 nm which was in good agreement with the crystallite

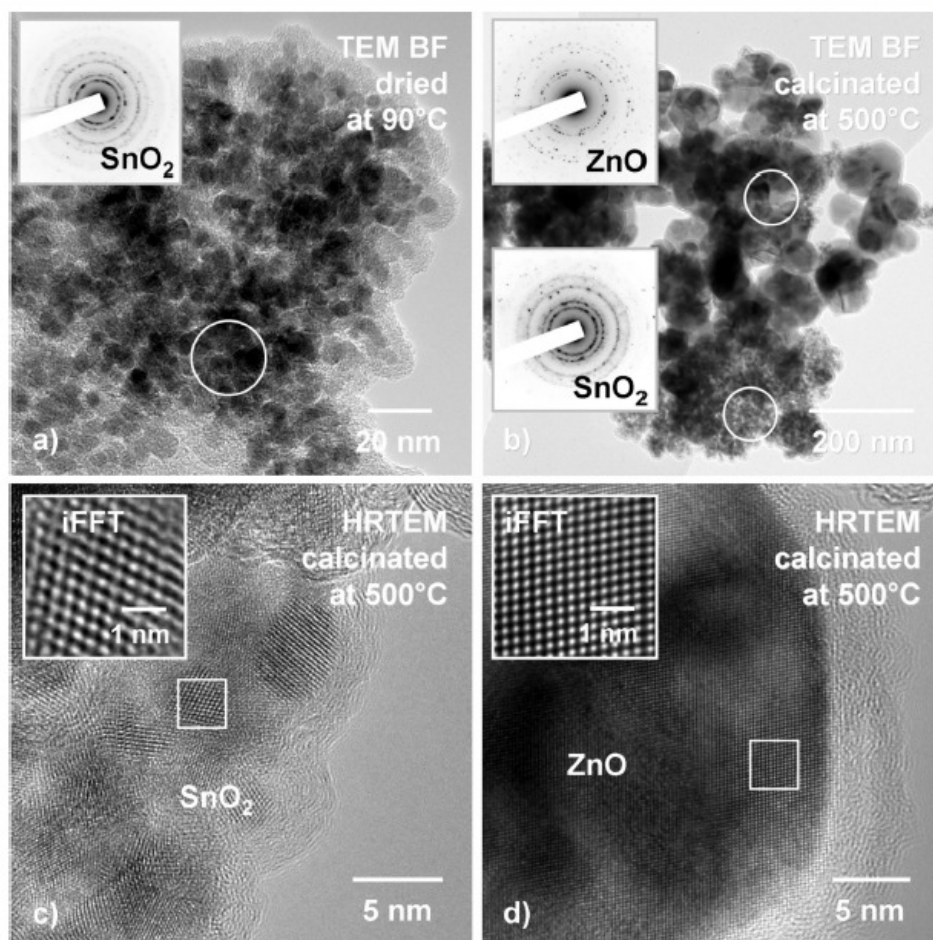


Figure 3. TEM micrographs of the (a) dried SnO₂-ZnO heterostructure and (b) calcinated SnO₂-ZnO photocatalyst. The inset SAED patterns reveal the occurrence of (a) crystalline SnO₂ and (b) crystalline SnO₂ and ZnO. HRTEM images (c,d) verify the crystallinity of both SnO₂ and ZnO after calcination.

size deduced from the XRD patterns. The dried SnO₂–ZnO heterostructure was composed of amorphous ZnO and nanocrystalline SnO₂, while upon hydrothermal treatment both phases were crystalline, as confirmed by the Selected Area Electron Diffraction (SAED) pattern shown in Figure 3b. According to the TEM bright field images, the SnO₂–ZnO photocatalyst was composed of aggregated ZnO particles of approximately 100 nm in diameter and nanosized SnO₂ particles, as also shown in the HRTEM images in Figures 3c and d. These results were consistent with those inferred from the above XRD analysis. Furthermore, a large number of small pores were observed between the nanoparticles suggesting that the SnO₂–ZnO photocatalyst is mesoporous. This feature was then assessed by N₂ sorption analyses. The N₂ adsorption–desorption isotherm of the SnO₂–ZnO heterostructure exhibited a type IV-like behavior including a type H2 hysteresis loop (Figure 4) which is typical of mesoporous

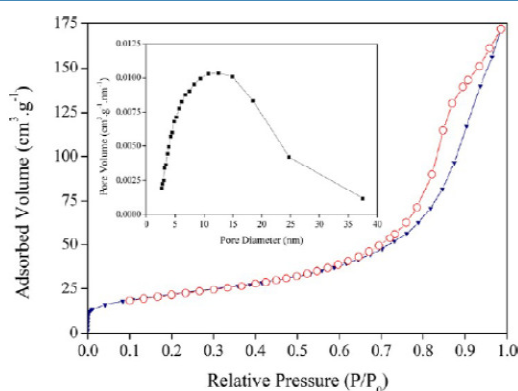


Figure 4. Nitrogen gas adsorption–desorption isotherms and pore-size distribution (inset) of the SnO₂–ZnO photocatalyst.

materials according to the IUPAC classification.²⁸ The H2-hysteresis loop indicated the presence of pores of nonuniform sizes and shapes, characteristic of solids consisting of particles crossed by nearly cylindrical channels or made by aggregates (consolidated) or agglomerates (unconsolidated) of spheroidal particles being fully consistent with the TEM data.²⁹ The BET surface area and pore volume for this system were estimated to be $77 \pm 2 \text{ m}^2 \text{ g}^{-1}$ and $0.26 \pm 0.01 \text{ cm}^3 \text{ g}^{-1}$, respectively; these values lay between those of pure SnO₂ and ZnO analogues (Table 1). Furthermore,

Table 1. Nitrogen Sorption Porosimetry Studies^a of the as-Synthesized SnO₂, ZnO and SnO₂–ZnO Nanomaterials

photocatalyst	S_{BET} ($\text{m}^2 \text{ g}^{-1}$)	pore volume ($\text{cm}^3 \text{ g}^{-1}$)	mean pore size (nm)
SnO ₂	90 ± 2.5	0.22 ± 0.005	10 ± 0.5
ZnO	45 ± 1.5	0.29 ± 0.01	26.5 ± 1
SnO ₂ –ZnO	77 ± 2.0	0.26 ± 0.01	14 ± 0.5

^aSurface areas were determined by the BET technique, mean pore diameters by BJH theory (applied to the adsorption branch), and pore volumes by single-point analysis.

the pore size distribution for the SnO₂–ZnO photocatalyst was rather large with an average pore diameter of $14 \pm 0.5 \text{ nm}$ (Figure 4, inset). As a consequence, all these data were consistent with the formation of mesoporous SnO₂–ZnO nanocatalyst.

The optical properties of the various samples prepared were then investigated by UV–Visible diffuse reflectance. The absorp-

tion edge for the SnO₂–ZnO photocatalyst was estimated to be about 390 nm, which was shifted toward the visible region compared to that of the pure SnO₂ sample (Figure 5A). The

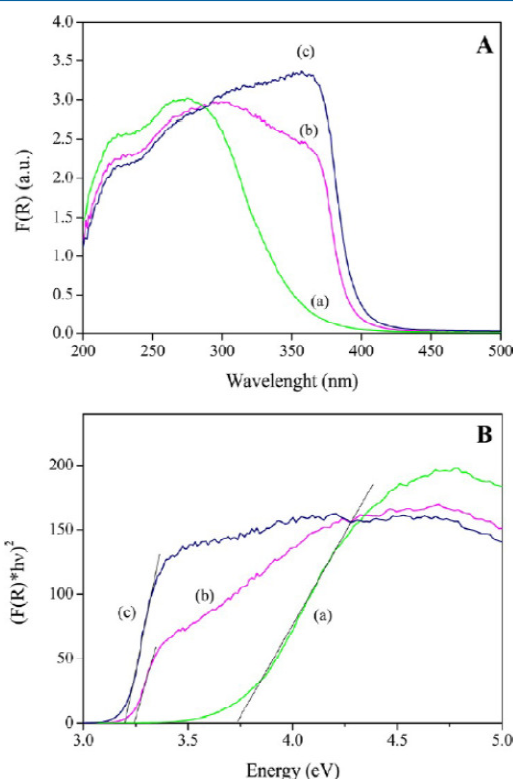


Figure 5. UV–vis diffuse reflectance spectra (A) and plots of $(F(R)h\nu)^2$ versus photon energy ($h\nu$) (B) of the as-synthesized materials after annealing in air at 500 °C; (a) SnO₂, (b) SnO₂–ZnO, and (c) ZnO.

absorption edges of ZnO and SnO₂ were determined to be 394 and 355 nm, respectively. Compared to the SnO₂ sample, the SnO₂–ZnO photocatalyst showed an obvious absorption edge increment of about 35 nm. The absorption edge at higher wavelengths revealed that the heterostructure photocatalysts could more efficiently utilize light for the photocatalytic purpose.³⁰ Nonetheless, it was close to that of ZnO because of the 1:1 composition of the heterostructure, since, to some extent, the absorption edge of the heterostructure should be the combined contribution of each component in the SnO₂–ZnO composite.³¹ Furthermore, it has been shown for a crystalline direct semiconductor that the optical absorption near the band edge follows the equation $\alpha(h\nu) = A(h\nu - E_g)^{1/2}$ where α , ν , E_g , and A are the absorption coefficient, light frequency, band gap energy, and a constant, respectively.³² It is generally admitted that the absorption coefficient (α) can be replaced by the remission function, $F(R)$. The latter can be written in terms of diffused reflectance (R) according to the Kubelka–Munk theory: $\alpha/s = F(R) = (1 - R)^2 / (2R)$ where s is the scattering coefficient.³³ The band gap energies (E_g values) of the as-synthesized samples can then be estimated from a plot of $(F(R)h\nu)^2 = f(h\nu)$, the intercepts of the tangents yielding the band gap energies of the as-synthesized samples (Figure 5B). The estimated band gap energies of the resulting samples were therefore about 3.7, 3.23, and 3.2 eV for SnO₂, SnO₂–ZnO, and ZnO, respectively. The values for ZnO

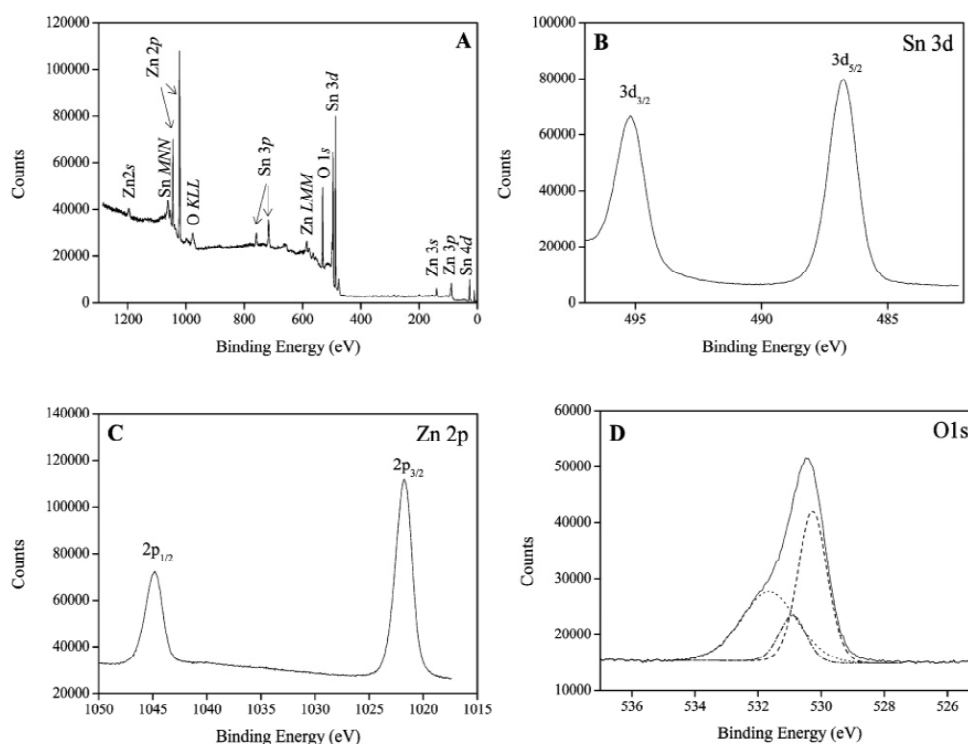


Figure 6. XPS patterns of the SnO_2 -ZnO photocatalyst (A) XPS survey spectrum; (B) Sn 3d region; (C) Zn 2p region; (D) O 1s region (full) with the corresponding fits for OH (dot), O-Zn (dot-dash) and Sn-O-Sn (dash).

and SnO_2 were in good agreement with those reported by others.³⁴

3.2. Surface and Interface Analysis. To gain a better insight into the surface composition and the band alignment in the SnO_2 -ZnO photocatalyst, XPS studies were performed on the SnO_2 , ZnO, and SnO_2 -ZnO samples annealed at 500 °C in air. As shown in the survey spectrum of Figure 6A, the SnO_2 -ZnO heterostructure only shows emissions of Sn, O, and Zn elements with only a very weak C line, the different peaks observed being assigned to Sn 3d, Sn 3p, Sn 4d, Zn 2p, Zn 3s, and Zn 3p core levels and to Sn MNN, Zn LMM, and O KLL Auger features. The high resolution XPS spectra for Sn 3d (Figure 6B) reveals the spin orbital splitting of the Sn $3d_{5/2}$ and Sn $3d_{3/2}$ core level states of tin centered at 486.8 and 495.2 eV, respectively, which were symmetric and were assigned to the lattice tin oxide. The separation between the Sn $3d_{5/2}$ and Sn $3d_{3/2}$ level (8.41 eV) corresponds to the standard spectrum of Sn³⁵ and of commercial SnO_2 reported in the literature.³⁶ The measured emission lines also correspond to a binding energy of Sn⁴⁺ ion in SnO_2 .³⁵ Figure 6C shows the pronounced splitting of the Zn 2p emission into two symmetric peaks. The peak centered at 1021.8 eV was attributed to the Zn $2p_{3/2}$ and the other one at 1044.9 eV to Zn $2p_{1/2}$, indicating a normal oxidation state of Zn²⁺ in the SnO_2 -ZnO photocatalyst. Figure 6D shows the XPS high resolution spectrum of oxygen. The shape of the spectrum is asymmetric which indicates that there are several chemical states according to the measured binding energy. Thus, the region of O 1s could be deconvoluted into three peaks centered at 530.3, 530.8, and 531.5 eV. The lower binding energy peak at 530.3 eV was attributed to oxygen in SnO_2 ,^{37,38} while the peak centered at 530.8 eV is due to the Zn-O binding.³⁹ The peak at 531.5 eV could be

ascribed to adsorbed hydroxyl species.^{35,38,40} The results confirmed that the SnO_2 -ZnO photocatalyst was actually composed of SnO_2 and ZnO entities. To determine the band alignment of the SnO_2 -ZnO photocatalyst, the core level positions and the VBM positions of bulk SnO_2 and bulk ZnO were also determined.⁴¹ With these values as reference of the energy distance ($E_{\text{V}} - E_{\text{CL}}$) for each sample and the energy difference ($E_{\text{CL}}^{\text{ZnO}} - E_{\text{CL}}^{\text{SnO}_2}$) the VB line-up can be determined according to eq 1. The VBM positions in the VB spectra were determined by linear extrapolation of the leading edges of the VB spectra of the bulk SnO_2 and ZnO samples to the base lines (Table 2). The energy difference of the Sn $3d_{5/2}$ CL peak to VBM, ($E_{\text{Sn}3d} - E_{\text{V-SnO}_2/\text{bulk}}^{\text{SnO}_2}$), was

Table 2. XPS Binding Energies of the Core Levels and VBM of SnO_2 , ZnO, and SnO_2 -ZnO Photocatalysts

photocatalyst	state	binding energy (eV)
SnO_2	Sn $3d_{5/2}$	486.70 ± 0.05
	VBM	3.30 ± 0.05
ZnO	Zn $2p_{3/2}$	1021.70 ± 0.05
	VBM	2.60 ± 0.05
SnO_2 -ZnO	Sn $3d_{5/2}$	486.80 ± 0.05
	Zn $2p_{3/2}$	1021.80 ± 0.05

determined to be 483.4 ± 0.05 eV while that of Zn $2p_{3/2}$ to ZnO VBM, ($E_{\text{Zn}2p}^{\text{ZnO}} - E_{\text{V-ZnO/bulk}}^{\text{ZnO}}$) was 1019.10 ± 0.05 eV. The energy difference of Sn $3d_{5/2}$ and Zn $2p_{3/2}$ CLs, ΔE_{CL} , in the SnO_2 -ZnO heterostructure was evaluated to be 535.0 ± 0.05 eV. According to eq 1, the resulting VB offset (VBO), ΔE_{V} , was calculated to be 0.7 eV. Finally the CB offset (CBO) was estimated by the formula $\Delta E_{\text{C}} = \Delta E_{\text{V}} + F_{\text{g}}^{\text{ZnO}} - F_{\text{g}}^{\text{SnO}_2}$, where $F_{\text{g}}^{\text{ZnO}}$ and $F_{\text{g}}^{\text{SnO}_2}$ are the optical band gap of

ZnO and SnO₂, respectively. Using the band gap of SnO₂ (3.7 eV) and ZnO (3.2 eV) determined by UV–visible diffuse reflectance spectroscopy (Figure 5B), the ΔE_C was calculated to be 0.2 ± 0.05 eV that led to the proposed energy band diagram for the SnO₂–ZnO sample shown in Figure 7. This experimentally determined energy diagram is fully consistent with the formation

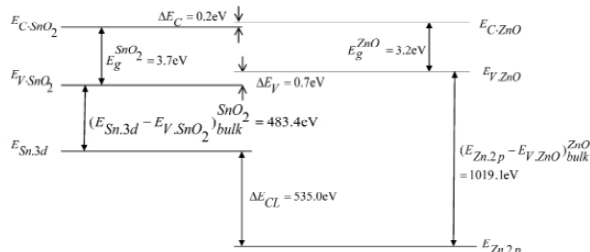


Figure 7. Band alignment diagram of the SnO₂–ZnO photocatalyst.

of mesoporous SnO₂–ZnO type II heterojunction nanomaterials as already schematically drawn in Scheme 1.

3.3. Photocatalytic Activity. To evidence the photocatalytic activities of the as-synthesized SnO₂–ZnO nanomaterials, the photocatalytic decomposition of MB was performed as a test reaction according to the literature.⁴² As depicted in Figure 8A, the maximum absorption peaks of MB at 664 nm diminished gradually and disappeared completely under UV

light irradiation for 80 min in the presence of the SnO₂–ZnO nanocatalyst. Meanwhile, the color of the solution changed gradually, suggesting that the chromophoric structure of MB was decomposed. Furthermore, blank experiments in the absence of irradiation with the photocatalyst or in the presence of irradiation without the photocatalyst, as well as similar experiments with pure SnO₂ and ZnO samples were carried out to rationalize the photocatalytic activity of the as-synthesized SnO₂–ZnO photocatalyst. The degradation efficiency of the as-synthesized samples was defined as C/C_0 , where C_0 is the initial concentration of MB, after equilibrium adsorption, and C its concentration during the reaction. Both blank experiments results showed that MB could not be decomposed without the photocatalyst and/or UV irradiation (Figure 8B). In contrast, the degradation efficiency of the SnO₂–ZnO photocatalyst after 20 min was of about 88%, whereas values of about 72% and 50% were found after 20 min for the SnO₂ and ZnO samples, respectively (Figure 8B). Furthermore, the MB decomposition efficiency found for the SnO₂–ZnO photocatalyst was comparable to that determined under the same experimental conditions for the reference P-25 catalyst, that is, 85% after 20 min. As a result, the heterojunction nanomaterial concept allowed increasing the photocatalytic activities of SnO₂ and ZnO up to that of commercial titania that validates the approach developed in this study. For a better understanding of the photocatalytic efficiency of the as-synthesized samples, the kinetic analysis of MB degradation is discussed in the following. It is generally assumed that reaction kinetics can be described in

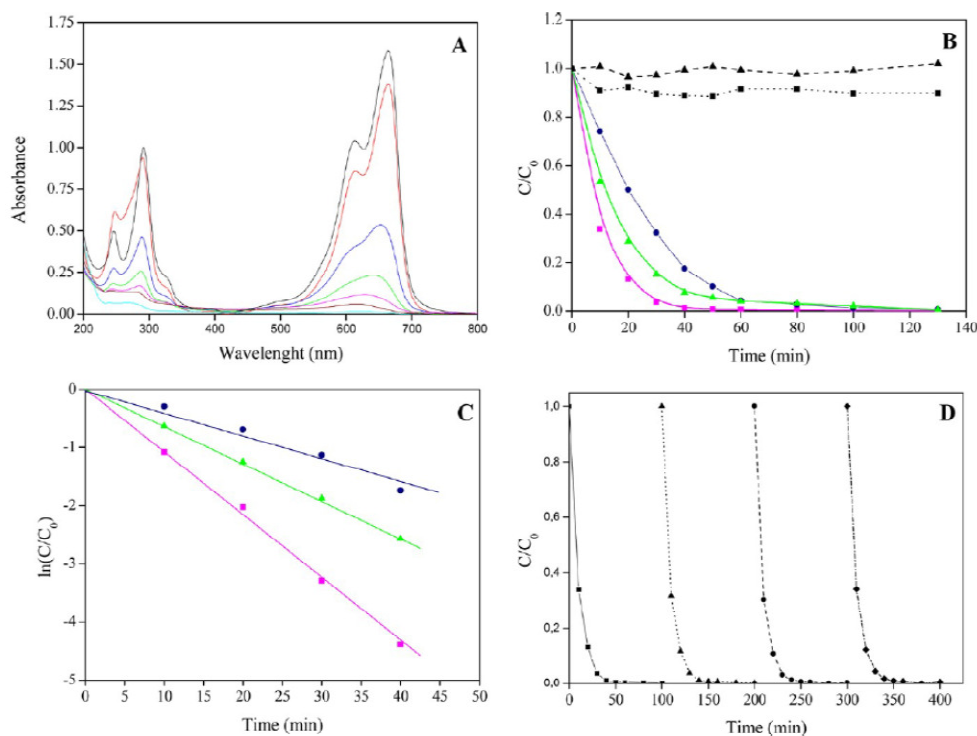


Figure 8. (A) Absorbance changes of MB solution after different irradiation times in the presence of the SnO₂–ZnO sample: initial (black), equilibrium (red), 10 min (blue), 20 min (green), 30 min (magenta), 40 min (brown), and 130 min (cyan). (B) Kinetic of the degradation of MB in the presence of UV only (square, dot), SnO₂–ZnO in the dark (triangle, dash), SnO₂–ZnO under UV (square, plain), SnO₂ under UV (triangle, plain), and ZnO under UV (circle, plain). (C) $\ln(C/C_0)$ as a function of the irradiation time for calcined SnO₂ (triangle), SnO₂–ZnO (square), and ZnO (circle) photocatalysts. (D) Cyclic runs in the photodegradation of MB using the SnO₂–ZnO photocatalyst under UV-light: 1st cycle (square), 2nd cycle (triangle), 3rd cycle (circle), and 4th cycle (diamond).

terms of Langmuir–Hinshelwood model, which can be expressed following eq 2:⁴³

$$-\frac{dC}{dt} = k_r \frac{K_a C}{1 + K_a C} \quad (2)$$

where $(-dC/dt)$ is the degradation rate of MB, C is the concentration of MB, t is the reaction time, k_r is a reaction rate constant, and K_a is the adsorption coefficient of the reactant. As the initial concentration of MB is very low ($C_0 = 10$ mg/L in the as-described experiments), $K_a C$ is negligible, and eq 2 can be described as first-order kinetics. Setting eq 2 at the initial conditions of the photocatalytic procedure, when $t = 0$, $C = C_0$, it can be described as

$$\ln \frac{C}{C_0} = -k_{app} t \quad (3)$$

where k_{app} is the apparent rate constant, used as the basic kinetic parameter for different photocatalysts, since it enables one to determine a photocatalytic activity independent of the previous adsorption period in the dark, and the concentration of the remaining dye in solution. This model was then applied to the present data (Figure 8C), and the apparent first-order rate constants, before and after normalization by the BET surface area, is reported in Table 3. First of all, the degradation of MB followed a first order kinetic rate for all samples. Furthermore, the

Table 3. Apparent (k_{app}) and Normalized (k_{norm}) Rate Constants for the Degradation of MB with the As-Synthesized Materials^a

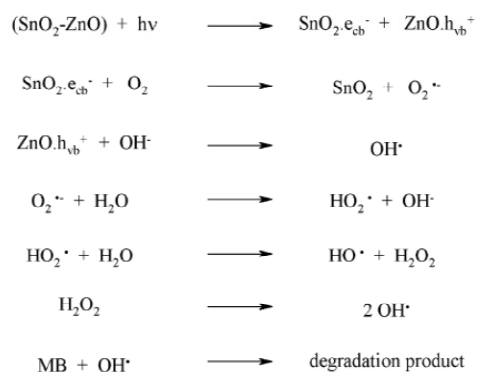
photocatalysts	k_{app} min ⁻¹	k_{norm} g/(m ² min)
SnO ₂ -ZnO	0.0931	12.1 × 10 ⁻⁴
SnO ₂	0.0635	7.1 × 10 ⁻⁴
ZnO	0.0401	8.9 × 10 ⁻⁴

^a k_{norm} calculated from k_{app} and the BET surface area given in Table 1.

mesoporous SnO₂-ZnO heterojunction nanomaterial was clearly a much more effective photocatalyst than the SnO₂ and ZnO analogues with an apparent MB degradation rate constant reaching 0.0931 min⁻¹. In addition, this nanocatalyst can be recycled and reused several times without significant loss of efficiency, which is a key requirement for a possible industrial application. Thus, the photocatalytic efficiency of the SnO₂-ZnO heterojunction photocatalyst for the 4 cycling reuse were 99.3, 99.2, 99.3, and 99.0% after 50 min of reaction time, respectively (Figure 8D). Finally, it is also worth mentioning that the photocatalytic activity collapsed in acidic solution and was improved in basic medium, the SnO₂-ZnO photocatalyst being always the most efficient.⁴¹ This behavior can be rationalized on the basis of the point of zero charge (pH_{pzc}) of SnO₂ and ZnO that is about 4 and 9, respectively. Indeed, since MB is a cationic dye, the dye chemisorption at the oxide surface will be favored by negatively charged metal oxide nanoparticles, that is, in basic medium.

In summary, the improved photocatalytic activity found for the SnO₂-ZnO heterostructure can be rationalized on the basis of the above-determined band alignment as follows (Scheme 1 and 2). Upon UV illumination, electrons in the VB could be excited to the CB of both oxides, with the concomitant formation of the same amount of holes in the VB. According to the type II band alignment and the heterojunction formed, the electrons were collected by the SnO₂ nanosized particles and the holes by the

Scheme 2. Proposed Mechanism for the Degradation of MB under UV Irradiation in the Presence of the SnO₂-ZnO Photocatalyst



ZnO particles as they are transferred to a more stable electronic state, that is, downward for electron transfer from ZnO to SnO₂, upward corresponding to a more stable bonding situation for holes from SnO₂ to ZnO (Comparison between Scheme 1 left, and Figure 7). The resulting charge carrier separation (electrons preferentially on the SnO₂ particle, holes preferentially at the ZnO particle) leads to increased carrier lifetime because of reduced charge recombination. As a consequence, the formation of hydroxyl OH[•] radicals by reaction of holes with surface hydroxyl groups or physisorbed water molecules at the zinc oxide surface is enhanced. On the other side, also the reaction of electrons with dissolved oxygen molecules to give superoxide radical anions, O₂^{•-}, yielding hydroperoxyl radicals HO₂[•] on protonation and finally OH[•] radicals will be more efficient. OH[•] radicals are a strong oxidizing agent well-known to decompose organic substrates as MB dye.⁴⁴ As a result, the enhanced charge separation related to the SnO₂-ZnO heterojunction favors the interfacial charge transfer to physisorbed species forming OH[•] radicals and reduce possible back reactions, and therefore accounts for the higher activity of the SnO₂-ZnO nanomaterials.

4. CONCLUSION

Mesoporous SnO₂-ZnO heterojunction photocatalysts have been successfully prepared using a two-step solution route involving the synthesis of nanosized SnO₂ particles by the homogeneous precipitation combined with a hydrothermal treatment that were further reacted with zinc acetate followed by calcination. The UV-vis diffuse reflectance studies showed that the band gap energy of the heterostructure SnO₂-ZnO photocatalyst was red-shifted compared to that of pure SnO₂ and ZnO. A careful examination of the band alignment by XPS revealed a type-II band alignment with VBO of $\Delta E_V = 0.7 \pm 0.05$ eV and CBO of $\Delta E_C = 0.2 \pm 0.05$ eV for the SnO₂-ZnO heterojunction photocatalyst. This heterojunction photocatalyst showed higher photocatalytic activity than the pure SnO₂ and ZnO nanocatalysts for the degradation of MB dye under UV light irradiation in neutral and basic media because of improved separation of photogenerated electrons and holes. Furthermore, the heterostructure photocatalysts could be easily recycled without significant change in the catalytic activity which evidenced the stability of the catalysts and the reproducibility of the approach. This concept of semiconducting heterojunction nanocatalysts with high photocatalytic activity should find industrial application in the future to remove undesirable organics from the environment.

■ ASSOCIATED CONTENT

■ Supporting Information

Additional information and figures concerning XPS and photocatalytic studies (reference experiment with P25). This material is available free of charge via the Internet at <http://pubs.acs.org>.

■ AUTHOR INFORMATION

Corresponding Author

*E-mail: t.toupance@ism.u-bordeaux1.fr.

Notes

The authors declare no competing financial interest.

■ ACKNOWLEDGMENTS

Dr. Jörg Zimmermann (TUD) and Mrs. Odile Babet (ISM) are thanked for the UV-vis diffused reflectance spectrometry and N₂ sorption measurements, respectively. This work was carried out within the framework of BMML (European Multifunctional Material Institute) and was supported by the Erasmus Mundus Joint Doctoral program International Doctoral School in Functional Materials for Energy, Information Technology and Health (T.U. fellowship), and the Aquitaine Region (Contract no.11002746).

■ REFERENCES

- (1) (a) Hoffmann, M. R.; Martin, S. T.; Choi, W.; Bahnemann, D. W. *Chem. Rev.* 1995, 95, 69. (b) Tennakone, C. T.; Tilakarante, C. T. K.; Kottegoda, I. R. M. *J. Photochem. Photobiol. A: Chem.* 1995, 87, 177. (c) Habibi, M. H.; Vosoughian, H. *J. Photochem. Photobiol. A: Chem.* 2005, 174, 45. (d) Liu, C. C.; Hsieh, Y. H.; Lai, P. F.; Li, C. H.; Kao, C. L. *Dyes Pigm.* 2006, 68, 191.
- (2) (a) Linsebigler, A. L.; Lu, G.; Yates, J. T. *Chem. Rev.* 1995, 95, 735. (b) Mahmoodi, N. M.; Arami, M.; Limaee, N. Y.; Tabrizi, N. S. *J. Colloid Interface Sci.* 2006, 295, 159. (c) Rauf, M. A.; Ashraf, S. S. *Chem. Eng. J.* 2009, 151, 10. (d) Behnadjady, M. A.; Modirshahla, N.; Daneshvar, N.; Rabbani, M. *J. Hazard. Mater.* 2007, 140, 257.
- (3) Zhang, M.; Sheng, G.; Fu, J.; An, T.; Wang, X.; Hu, X. *Mater. Lett.* 2005, 59, 3641.
- (4) Bedja, I.; Kamat, P. V. *J. Phys. Chem.* 1995, 99, 9182.
- (5) (a) Jiang, Y.; Sun, Y.; Liu, H.; Zhu, F.; Yin, H. *Dyes Pigm.* 2008, 78, 77. (b) Liao, D. L.; Badour, C. A.; Liao, B. Q. *Photochem. Photobiol. A: Chem.* 2008, 194, 11. (c) Tian, J.; Chen, L.; Yin, Y.; Wang, X.; Dai, J.; Zhu, Z.; Liu, X.; Wu, P. *Surf. Coat. Technol.* 2009, 204, 205. (d) Darzi, S. J.; Mahjoub, A. R. *J. Alloys Compd.* 2009, 486, 805. (e) Zhang, M.; An, T.; Liu, X.; Hu, X.; Sheng, G.; Fu, J. *Mater. Lett.* 2010, 64, 1883. (f) Liu, R.; Ye, H.; Xiong, X.; Liu, H. *Mater. Chem. Phys.* 2010, 121, 432.
- (6) (a) Shifu, C.; Lei, C.; Shen, G.; Gengyu, C. *Powder Technol.* 2005, 160, 198. (b) Leghari, S. A. K.; Sajjad, S.; Chen, J.; Zhang, J. *Chem. Eng. J.* 2011, 166, 906. (c) Lv, K.; Li, J.; Qing, X.; Li, W.; Chen, Q. *J. Hazard. Mater.* 2011, 189, 329. (d) Ismail, M.; Bousselmi, L.; Zahraa, O. *Photochem. Photobiol. A: Chem.* 2011, 222, 314.
- (7) (a) Li, D.; Haneda, H. *J. Photochem. Photobiol. A: Chem.* 2003, 160, 203. (b) Yu, C.; Yang, K.; Shu, Q.; Yu, J. C.; Cao, F.; Li, X. *Chin. J. Catal.* 2011, 32, 555.
- (8) (a) Wang, Y.; Lee, J. Y.; Zeng, H. C. *Chem. Mater.* 2005, 17, 3899. (b) Lou, X. W.; Wang, Y.; Yuan, C.; Lee, J. Y.; Archer, L. A. *Adv. Mater.* 2006, 17, 2325. (c) Ha, H. W.; Kim, K.; de Borniol, M.; Toupance, T. *J. Solid State Chem.* 2006, 179, 689.
- (9) He, H., Jr.; Wu, T. H.; Hsin, C. L.; Li, K. M.; Chen, L. J.; Chueh, Y. L.; Chou, L. J.; Wang, Z. L. *Small* 2006, 2, 116.
- (10) (a) Gurlo, A. *ChemPhysChem* 2006, 7, 241. (b) Gurlo, A.; Riedel, R. *Angew. Chem., Int. Ed.* 2007, 46, 3826. (c) Nayral, C.; Viola, E.; Fau, P.; Senocq, F.; Jumas, J.-C.; Maisonnat, A.; Chaudret, B. *Chem.—Eur. J.* 2000, 6, 4082. (d) Han, C. H.; Han, S.-D.; Singh, I.; Toupance, T. *Sens. Actuators, B* 2005, 109, 264. (e) Pavelko, R. G.; Daly, H.; Hardacre, C.; Vasiliev, A. A.; Llobet, E. *Phys. Chem. Chem. Phys.* 2010, 12, 2639.
- (f) Marichy, C.; Donato, N.; Willinger, M.-G.; Latino, M.; Karpinsky, D.; Yu, S. H.; Neri, G.; Pinna, N. *Adv. Mater.* 2011, 21, 658.
- (11) (a) Vilaça, G.; Jousseume, B.; Mahieux, C.; Belin, C.; Cachet, H.; Bernard, M.-C.; Vivier, V.; Toupance, T. *Adv. Mater.* 2006, 18, 1073. (b) Gubbala, S.; Chakrapani, V.; Kumar, V.; Sunkara, M. K. *Adv. Funct. Mater.* 2008, 18, 2411. (c) Liu, J.; Luo, T.; Mouli, S.; Meng, F.; Sun, B.; Li, M.; Liu, J. *Chem. Commun.* 2010, 46, 472. (d) Tebby, Z.; Uddin, T.; Olivier, C.; Nicolas, Y.; Toupance, T.; Hirsch, L. *ACS Appl. Mater. Interfaces* 2011, 3, 1485.
- (12) (a) Cun, W.; Jincai, Z.; Xinming, W.; Bixian, M.; Guoying, S.; Ping'an, P.; Jiamo, F. *Appl. Catal., B* 2002, 39, 269. (b) Cun, W.; Wang, X.; Xu, B.; Zhao, J.; Mai, B.; Ping'an, P.; Sheng, G.; Jiamo, F. *J. Photochem. Photobiol. A: Chem.* 2004, 168, 47. (c) Zhang, M.; An, T.; Hu, X.; Wang, C.; Sheng, G.; Fu, J. *Appl. Catal., A* 2004, 260, 215. (d) Zhang, M.; Sheng, G.; Fu, J.; An, T.; Wang, X.; Hu, X. *Mater. Lett.* 2005, 59, 3641. (e) Wang, H.; Baek, S.; Lee, J.; Lim, S. *Chem. Eng. J.* 2009, 146, 355. (f) Yang, Z.; Lv, L.; Dai, Y.; Xu, Z.; Qian, D. *Appl. Surf. Sci.* 2010, 256, 2898.
- (13) (a) Wen, Z.; Wang, G.; Lu, W.; Wang, Q.; Zhang, Q.; Li, J. *Cryst. Growth Des.* 2007, 7, 172. (b) Wang, W.-W.; Zhu, Y.-J.; Yang, L.-X. *Adv. Funct. Mater.* 2007, 17, 59. (c) Zheng, L.; Zheng, Y.; Chen, C.; Zhan, Y.; Lin, X.; Zheng, Q.; Wei, K.; Zhu, J. *Inorg. Chem.* 2009, 48, 1819.
- (14) Zhang, Z.; Shao, C.; Li, X.; Zhang, L.; Xue, H.; Wang, C.; Liu, Y. *J. Phys. Chem. C* 2010, 114, 7920.
- (15) Baik, N. S.; Sakai, G.; Miura, N.; Yamazoe, N. *Sens. Actuators B* 2000, 63, 74.
- (16) Parida, K. M.; Dash, S. S.; Das, D. P. *J. Colloid Interface Sci.* 2006, 298, 787.
- (17) Barrett, E. P.; Joyner, L.; Halenda, P. P. *J. Am. Chem. Soc.* 1951, 73, 373.
- (18) (a) Lang, O.; Klein, A.; Pettenkofer, C.; Jaegermann, W.; Chevy, A. *J. Appl. Phys.* 1996, 80, 3817. (b) Schlaf, R.; Lang, O.; Pettenkofer, C.; Jaegermann, W. *J. Appl. Phys.* 1999, 85, 2732. (c) Mönch, W. In *Semiconductor surfaces and interfaces*; Springer-Verlag: Heidelberg, Germany, 1993.
- (19) Bernède, J. C.; Barreau, N.; Marsillac, S.; Assmann, L. *Appl. Surf. Sci.* 2002, 195, 222.
- (20) Song, K. C.; Kang, Y. *Mater. Lett.* 2000, 42, 283.
- (21) Sibü, C. P.; Kumar, S. R.; Mukundan, P.; Warrior, K. G. K. *Chem. Mater.* 2002, 14, 2876.
- (22) Chen, D.; Gao, L. *J. Colloid Interface Sci.* 2004, 279, 137.
- (23) Ismail, H. M. *J. Anal. Appl. Pyrolysis* 1991, 21, 315.
- (24) (a) Damen, T. C.; Porto, S. P. S.; Tell, B. *Phys. Lett.* 1966, 144, 570. (b) Khan, A.; Kordesch, M. E. *Mater. Lett.* 2008, 62, 230.
- (25) (a) Scott, J. F. *J. Chem. Phys.* 1970, 53, 852. (b) Kumar, V.; Govind, A.; Nagarajan, R. *Inorg. Chem.* 2011, 50, 5637.
- (26) Xu, C. X.; Sun, X. W.; Zhang, X. H.; Ke, L.; Chua, S. J. *Nanotechnology* 2004, 15, 856.
- (27) Lorient, S. *J. Phys. Chem. B* 2002, 106, 13273.
- (28) Sing, K. S. W.; Everett, D. H.; Haul, R. A. W.; Moscou, L.; Pierotti, R. A.; Rouquerol, J.; Siemieniewska, T. *Pure Appl. Chem.* 1985, 57, 603.
- (29) (a) Leofanti, G.; Padovan, M.; Tozzola, G.; Venturelli, B. *Catal. Today* 1998, 41, 207. (b) Toupance, T.; El Hamzaoui, H.; Jousseume, B.; Riague, H.; Saadeddin, I.; Campet, G.; Broetz, J. *Chem. Mater.* 2006, 18, 6364.
- (30) Shifu, C.; Lei, C.; Shen, G.; Gengyu, C. *Powder Technol.* 2005, 160, 198.
- (31) Liu, R.; Ye, H.; Xiong, X.; Liu, H. *Mater. Chem. Phys.* 2010, 121, 432.
- (32) Davis, E. A.; Mott, N. F. *Phil. Mag.* 1970, 22, 903.
- (33) Jahan, F.; Islam, M. H.; Smith, B. E. *Sol. Energy Mater. Sol. Cells* 1995, 37, 383.
- (34) (a) Hagfeldt, A.; Gratzel, M. *Chem. Rev.* 1995, 95, 49. (b) Lin, C. F.; Wu, C. H.; Onn, Z. N. *J. Hazard. Mater.* 2008, 154, 1033. (c) Memming, R. *Electrochim. Acta* 1980, 25, 77. (d) Vogel, R.; Hoyer, P.; Weller, H. *J. Phys. Chem.* 1994, 98, 3183.
- (35) Moulder, J. F.; Sticke, W. F.; Sobol, K. P. E.; Bomben, D. In *Handbook of X-ray photoelectron spectroscopy*; Chastain, J., King, R. C., Jr.,

Eds.; Physical Electronics Division, Perkin-Elmer Corp: Eden Prairie, MN, 1995; p 127.

(36) Babar, A. R.; Shinde, S. S.; Moholkar, A. V.; Rajpure, K. Y. *J. Alloys Compd.* **2010**, *505*, 743.

(37) Chang, S. T.; Leu, I. C.; Hon, M. H. *J. Cryst. Growth* **2004**, *273*, 195.

(38) Li, G.; Leung, M. K. H. *J. Sol-Gel Sci. Technol.* **2010**, *53*, 499.

(39) Ballerini, G.; Ogle, K.; Labrousse, M. G. B. *Appl. Surf. Sci.* **2007**, *253*, 6860.

(40) Mu, J.; Shao, C.; Guo, Z.; Zhang, Z.; Zhang, M.; Zhang, P.; Chen, B.; Liu, Y. *ACS Appl. Mater. Interfaces* **2011**, *3*, 590.

(41) See Supporting Information.

(42) (a) Guo, Y.; Wang, H.; He, C.; Qiu, L.; Cao, X. *Langmuir* **2009**,

25, 4678. (b) Logar, M.; Jancar, B.; Sturm, S.; Suvorov, D. *Langmuir*

2010, *26*, 12215. (c) Hirose, Y.; Mori, T.; Morishita, Y.; Itadani, A.;

Kudoh, T.; Ohkubo, T.; Matsuda, T.; Kittaka, S.; Kuroda, Y. *Inorg. Chem.*

2011, *50*, 9948. (d) Kang, J.; Kuang, Q.; Xie, Z.-X.; Zheng, L. *S. J. Phys.*

Chem. C **2011**, *115*, 7874.

(43) Burch, R.; Breen, J. P.; Meunier, F. C. *Appl. Catal., B* **2002**, *39*,

283.

(44) (a) Tayade, R. J.; Sivakumar, T. S.; Bajaj, H. C. *Ind. Eng. Chem. Res.*

2009, *48*, 10262. (b) Zhang, L.; Yin, L.; Wang, C.; Lun, N.; Qi, Y. *ACS*

Appl. Mater. Interfaces **2010**, *2*, 1769.

Résumé

Les processus photocatalytiques à la surface d'oxydes métalliques semi-conducteurs font l'objet d'intenses recherches au niveau mondial car ils constituent des alternatives efficaces, respectueuses de l'environnement et peu coûteuses aux méthodes conventionnelles dans les domaines de la purification de l'eau et de l'air, et de la production « verte » d'hydrogène. Cependant, certaines limitations pour atteindre des efficacités photocatalytiques élevées ont été mises en évidence avec les matériaux semi-conducteurs classiques du fait de la recombinaison rapide des porteurs de charge générés par illumination. Le développement de photocatalyseurs à base d'hétérostructures obtenues par dépôt de métaux à la surface de matériaux semi-conducteurs ou par association de deux semi-conducteurs possédant des bandes d'énergie bien positionnées devrait permettre de limiter ces phénomènes de recombinaison via un transfert de charge vectoriel. Dans ce contexte, trois types d'hétérostructures telles que des nanomatériaux à base d'hétérojonction semi-conducteur n/semi-conducteur n (SnO_2/ZnO), métal/semi-conducteur n ($\text{RuO}_2/\text{TiO}_2$ and RuO_2/ZnO) et semi-conducteur p/semi-conducteur n (NiO/TiO_2) ont été synthétisées avec succès par différentes voies liquides. Leur composition, leur texture, leur structure et leur morphologie ont été caractérisées par spectroscopies FTIR et Raman, par diffraction des rayons X, microscopie électronique en transmission (MET) et porosimétrie de sorption d'azote. Par ailleurs, une combinaison judicieuse des données issues de mesures effectuées par spectroscopie UV-visible en réflexion diffuse (DRS) et par spectroscopies de photoélectrons X (XPS) et UV (UPS) a permis de déterminer le diagramme d'énergie des bandes pour chaque système étudié. Les catalyseurs ainsi obtenus ont conduit à des efficacités photocatalytiques plus élevées qu'avec le dioxyde de titane P25 pour la dégradation de colorants organiques (bleu de méthylène, l'orangé de méthyle) et la production d'hydrogène. En particulier, les nanocomposites $\text{RuO}_2/\text{TiO}_2$ et NiO/TiO_2 contenant une quantité optimale de RuO_2 (5 % en masse) et de NiO (1% en masse), respectivement, ont conduit aux efficacités photocatalytiques les plus importantes pour la production d'hydrogène. Ces excellentes performances photocatalytiques ont été interprétées en termes d'alignement adéquat des bandes d'énergies des matériaux associé à des propriétés texturales et structurales favorables. Ce concept de photocatalyseurs à base d'hétérojonctions semi-conductrices d'activité élevée devrait à l'avenir trouver des débouchés industriels dans les domaines de l'élimination de l'environnement de composés organiques indésirables et de la production « verte » d'hydrogène.

Mots clés: Oxydes métalliques semi-conducteurs, nanocatalyseurs à hétérojonctions, XPS, UPS, alignement des bandes, activité photocatalytique, production d'hydrogène, dégradation de colorants organiques.

Abstract

Photocatalytic processes over semiconducting oxide surfaces have attracted worldwide attention as potentially efficient, environmentally friendly and low cost methods for water/air purification as well as for renewable hydrogen production. However, some limitations to achieve high photocatalytic efficiencies have been found due to the fast recombination of the charge carriers. Development of heterostructure photocatalysts by depositing metals on the surface of semiconductors or by coupling two semiconductors with suitable band edge position can reduce recombination phenomena by vectorial transfer of charge carriers. To draw new prospects in this domain, three different kinds of heterostructures such as n-type/n-type semiconductor (SnO_2/ZnO), metal/n-type semiconductor ($\text{RuO}_2/\text{TiO}_2$ and RuO_2/ZnO) and p-type/n-type semiconductor (NiO/TiO_2) heterojunction nanomaterials were successfully prepared by solution process. Their composition, texture, structure and morphology were thoroughly characterized by FTIR, X-ray diffraction (XRD), Raman spectroscopy, transmission electron microscopy (TEM) and N_2 sorption measurements. On the other hand, a suitable combination of UV-visible diffuse reflectance spectroscopy (DRS), X-ray photoelectron spectroscopy (XPS) and ultraviolet photoemission spectroscopy (UPS) data provided the energy band diagram for each system. The as-prepared heterojunction photocatalysts showed higher photocatalytic efficiency than P25 TiO_2 for the degradation of organic dyes (i.e. methylene blue and methyl orange) and the production of hydrogen. Particularly, heterostructure $\text{RuO}_2/\text{TiO}_2$ and NiO/TiO_2 nanocomposites with optimum loading of RuO_2 (5 wt %) and NiO (1 wt %), respectively, yielded the highest photocatalytic activities for the production of hydrogen. These enhanced performances were rationalized in terms of suitable band alignment as evidenced by XPS/UPS measurements along with their good textural and structural properties. This concept of semiconducting heterojunction nanocatalysts with high photocatalytic activity should find industrial application in the future to remove undesirable organics from the environment and to produce renewable hydrogen.

Key words: Semiconducting metal oxides, heterojunction nanocatalysts, XPS, UPS, energy band alignment, photocatalytic activity, hydrogen production, organic dye degradation.